

Abstract

AYRES, JENNIFER. Synthesis and Characterization of Nanoparticle Assemblies for Electronic Applications. (Under the direction of Dr. Christopher B. Gorman.)

While significant effort has been made to synthesize molecular wires for electronic applications, the ability to insert these molecules between two metallic contacts with directional control has yet to be demonstrated. Control over molecular orientation is critical to the development of molecular devices such as diodes, capacitors and transistors. In this study, directional control is achieved using orthogonal self-assembly to synthesize electronic junctions between nanoparticles of different compositions. Phenyl ethynylene oligomers were synthesized with different end groups. One molecule was functionalized with a thiol which exhibits preferential binding to gold and an isocyanide which exhibits preferential binding to platinum. The other was functionalized with a thiol for binding to gold and a carboxylic acid which exhibits preferential binding to metal oxides.

One of the major challenges of this work was the synthesis of nanoparticle building blocks that were suitable for the formation of these heterodimeric structures. Metal and metal oxide particles were synthesized with capping ligands that provided stability yet did not sterically hinder heterodimer formation. Once appropriate nanoparticles had been identified, preliminary studies indicated heterodimer formation. However, characterizing these structures presented additional challenges.

Several characterization techniques, including transmission electron microscopy (TEM), size-exclusion chromatography (SEC), several types of electrophoresis and small-angle x-ray scattering (SAXS), were evaluated for their ability to characterize these structures with statistical accuracy. While all of these techniques did indicate the presence of dimers or larger aggregates in solution, accurate statistical information was not obtained using any single method.

Synthesis and Characterization of Nanoparticle Assemblies for Electronic Applications

by
Jennifer Ayres

A dissertation submitted to the Graduate Faculty of
North Carolina State University
in partial fulfillment of the requirements
for the Degree of
Doctor of Philosophy

Chemistry

Raleigh, North Carolina

2009

APPROVED BY:

Dr. Edmond Bowden, Chemistry

Dr. Gregory Parsons, Chemical and
Biomolecular Engineering

Dr. Stefan Franzen, Chemistry

Dr. Christopher B. Gorman, Chemistry
Chair of the Advisory Committee

Dedication

This work is dedicated to my parents, Helen and Charles Ayres without whom this would not have been possible. I am eternally grateful for their unconditional love and support.

Biography

Jennifer Ayres grew up in Chapel Hill, N.C. and got a B.S. in Applied Science from UNC-Chapel Hill with a concentration in polymeric materials. She spent two years working in product development for fiber optic assemblies before returning to school as a graduate student in Materials Science and Engineering at N.C. State. She received an M.S. in MSE in 2004 for her work with sol-gel systems that prevent the nucleation and adhesion of ice on military aircraft before pursuing her PhD in Chemistry.

Acknowledgements

The following people are acknowledged for their contribution to this work:

Dr. Christopher B. Gorman, advisor

Dr. Gregory Parsons, collaborator and member of the advisory committee

Dr. Edmond Bowden, Dr. Daniel Feldheim, Dr. Stefan Franzen, members of the advisory committee

Dr. Kusum L. Chandra, organic synthesis

Dr. Changwoong Chu, Jeong-Seok Na, lithography and electronic characterization

Wallace Ambrose, TEM assistance

Dr. David Cliffl and Brian Hixson, CFFE

Dr. Matthew Marcus, SAXS

Table of Contents

List of Tables.....	xiv
List of Figures.....	xviii

1. Introduction 1

1.1. Molecular Electronics	1
1.1.1. Molecular Structure	2
1.1.2. Molecular Contacts	7
1.2. Project Impetus	23
1.2.1. General Concepts	23
1.2.2. Orthogonal Self-Assembly	26
1.2.3. Objectives	33
1.3. References	37

2. Synthesis, Stability and Properties of Metal Nanoparticles 43

2.1. Introduction and Background	45
2.1.1. Colloid Stability.....	45
2.1.1.1. Electrostatic Stabilization	45
2.1.1.2. Steric Stabilization	51
2.1.2. Particle Formation	53
2.1.2.1. Mechanisms for Particle Formation.....	53
2.1.2.2. Size Control	60
2.1.2.3. Shape Control	64
2.1.2.4. Ligand Exchange and Phase Transfer	70

2.1.3. Organization of Particles	76
2.1.4. Properties of Nanoparticles	80
2.1.4.1. Optical Properties.....	80
2.1.4.1.1 Effects of Nanoparticle Geometry	82
2.1.4.1.2 Effects of the Dielectric Constant and Surface Chemistry.....	86
2.1.4.2. Optical Properties of Platinum, Palladium and Nickel	87
2.1.4.3. Electrical Properties	89
2.1.5. Literature Summary.....	90
2.2. Results and Discussion	92
2.2.1. Synthetic Requirements for Heterodimer Formation.....	92
2.2.2. Gold Particles	94
2.2.2.1. Citrate-capped Gold Particles	94
2.2.3. Platinum and Palladium Particles.....	99
2.2.3.1. Evaluation of literature methods for platinum and palladium nanoparticle synthesis.....	99
2.2.3.2. Synthesis of Tiopronin-Capped Platinum Nanoparticles	106
2.2.3.3. Attempted Synthesis of Glutathione-Capped Platinum Nanoparticles.....	108
2.2.3.4. Synthesis of 4-Mercaptobenzoic Acid capped Platinum Particles.....	109
2.2.3.5. Reverse Micelle Synthesis of Platinum Particles	115
2.2.4. Nickel Particles.....	118
2.2.4.1. Evaluation of literature methods for nickel nanoparticle synthesis....	118
2.2.4.2. Synthesis of Nickel Nanoparticles with CTAB and PTAB.....	122
2.2.5. Summary and Conclusions	126
2.2.6. Experimental	128
2.2.6.1. Synthesis of Tiopronin-capped Platinum Particles	128
2.2.6.2. Synthesis of Glutathione-capped Platinum Particles.....	129
2.2.6.3. Synthesis of Platinum Particles with 4-mercaptobenzoic acid.....	129

2.2.6.4. Reverse Micelle Synthesis of Platinum Particles	130
2.2.6.5. Synthesis of Nickel Particles	131
2.2.6.6. Particle Characterization	132
2.3. References	133

3. Synthesis and Stability of Metal Oxide Nanoparticles ... 150

3.1. Introduction and Background	152
3.1.1. Synthesis of Metal Oxide Particles through Sol-Gel Methods. 152	
3.1.1.1. Sol-gel concepts	152
3.1.1.1.1. The Sol-gel Process.....	153
3.1.1.1.2. Steric and Inductive Effects.....	157
3.1.1.1.3. Additional Kinetic Effects.....	164
3.1.1.1.4. Titanium and Other Transition Metal Oxides.....	166
3.1.1.1.5. Summary	173
3.1.1.2. Overview of Literature Methods for TiO ₂ Particle Synthesis.....	173
3.1.1.2.1. Stability of Metal Oxide Particles.....	174
3.1.1.2.2. Synthesis of TiO ₂ Particles – General Considerations	176
3.1.1.2.3. Effects of the Molecular Precursor	179
3.1.1.2.4. The Synthesis of TiO ₂ Particles from Titanium Chloride	179
3.1.1.2.5. The Synthesis of TiO ₂ Particles from Titanium Alkoxides	183
3.1.1.2.6. Titanium Sol-gel Reactions within Reverse Micelles	188
3.1.1.2.7. Non-Hydrolytic Methods.....	194
3.1.1.2.8. Hydrothermal and Solvothermal Methods	202
3.1.1.2.9. Optical Properties of TiO ₂ Nanoparticles.....	210
3.1.1.2.10. Summary	210
3.1.1.3. Overview of Literature Methods for the Synthesis of Iron Oxide Particles	213
3.1.1.3.1. Sonochemical Methods.....	215

3.1.1.3.2. Coprecipitation of Fe ²⁺ and Fe ³⁺ Ions.....	219
3.1.1.3.2.1. General Considerations.....	219
3.1.1.3.2.2. Particles Coated with Polymers and Surfactant Molecules ..	222
3.1.1.3.2.3. Iron Oxide Particles Synthesized With Micelles and Liposomes	225
3.1.1.3.3. Thermal Decomposition of Iron Complexes	228
3.1.1.3.4. Summary	233
3.2. Results and Discussion	235
3.2.1. Synthesis of TiO₂ Nanoparticles.....	235
3.2.1.1. Synthesis of Stearic-Acid Capped TiO ₂ Particles	235
3.2.1.2. Ligand-Exchange Involving Stearic Acid-Capped TiO ₂ Particles	237
3.2.1.3. Synthesis of TiO ₂ Particles from TiCl ₄	241
3.2.1.4. Synthesis of TiO ₂ Particles from Titanium (IV) Isopropoxide.....	243
3.2.1.5. Synthesis of TiO ₂ Particles from Titanium (IV) Ethoxide	250
3.2.1.6. Synthesis of TiO ₂ Particles Using Solvothermal Methods	252
3.2.1.7. Summary and Conclusions	258
3.2.2. Synthesis of Iron Oxide Nanoparticles	260
3.2.2.1. Synthesis of Iron Oxide Particles by Coprecipitation.....	260
3.2.2.2. Solvothermal Synthesis of Iron Oxide	262
3.2.2.3. Summary.....	266
3.3. Experimental	267
3.3.1. Particle Synthesis	267
3.3.1.1. Synthesis of Hexanethiol-capped Platinum Particles	268
3.3.1.2. Synthesis of Stearic Acid-capped TiO ₂ Particles.....	269
3.3.1.3. Synthesis of TiO ₂ Particles from TiCl ₄	269
3.3.1.4. Synthesis of TiO ₂ Particles from TIP in the presence of HCl and EtOH	270
3.3.1.5. Synthesis of TiO ₂ Particles from TEO in the presence of KCl and EtOH.....	270

3.3.1.6. Synthesis of TiO ₂ Particles Using a Solvothermal Method	271
3.3.1.7. Synthesis of Fe ₃ O ₄ Particles by Coprecipitation	272
3.3.1.8. Solvothermal Synthesis of Fe ₃ O ₄	272
3.3.2. Particle Characterization	274
3.3.2.1. Transmission Electron Microscopy (TEM).....	274
3.3.2.2. Transmission Infrared Spectroscopy	274
3.3.2.3. UV-VIS Spectroscopy.....	274
3.4. References	275
4. Synthesis of Nanoparticle Assemblies.....	286
4.1. Overview of Literature Methods for Forming Particle Assemblies	286
4.1.1. Formation of Nanoparticle Assemblies on Surfaces	286
4.1.2. Synthesis of Solution-Based Nanoparticle Networks	293
4.1.3. Synthesis of Isolated Nanoparticle Aggregates	296
4.1.4. Solution-Based Synthesis of Molecularly-Linked Nanoparticle Dimers and Trimers	301
4.1.5. Synthesis of Nanoparticle Assemblies Using Solid Phase Place-Exchange.....	309
4.1.6. Optical Properties of Nanoparticle Assemblies	315
4.1.7. Summary.....	323
4.2. Results and Discussion	327
4.2.1. Synthesis of Gold Homodimers and Homotrimers	328
4.2.2. Synthesis of Nanoparticle Gold-Platinum Heterodimers	337
4.2.3. Synthesis of Nanoparticle Gold-Nickel Heterodimers	346
4.2.4. Synthesis of Nanoparticle Gold-Metal Oxide Heterodimers....	348
4.2.5. Summary and Conclusions	357

4.3. Experimental	360
4.3.1. Sample Preparation	360
4.3.2. Particle Characterization	362
4.4. References	362
5. Size-Exclusion Chromatography of Particles and Particle Assemblies	368
5.1. Introduction and Background	369
5.1.1. Size-Exclusion Chromatography – General Theory	369
5.1.2. Liquid Chromatography of Nanoparticles in Organic Solution ..	374
5.1.3. Aqueous Chromatography of Nanoparticles	378
5.1.4. Recycling Size-Exclusion Chromatography	388
5.1.5. SEC of Nanoparticle Assemblies	390
5.1.6. Summary	392
5.2. Results and Discussion	393
5.2.1. Organic SEC	393
5.2.2. Aqueous SEC	394
5.2.2.1. Normal Phase Chromatography	394
5.2.2.2. Reverse-Phase Chromatography	410
5.2.3. Summary	426
5.3. Experimental	429
5.4. References	431
6. Electrophoresis of Particles and Particle Assemblies ...	434
6.1. Background and Introduction	434

6.1.1. Electrophoresis – General Theory	434
6.1.2. Capillary Electrophoresis	392
6.1.3. Micellar Electrokinetic Chromatography.....	436
6.1.4. Particle Electrophoresis	441
6.1.5. Gel Electrophoresis of Particles	460
6.2. Results and Discussion	462
6.2.1. Gel Electrophoresis of Particle and Assemblies	462
6.2.2. Capillary Electrophoresis of Particles and Assemblies – General Considerations.....	466
6.2.3. Capillary Electrophoresis of Gold-Citrate Particles	470
6.2.4. Capillary Electrophoresis of Nanoparticle Assemblies.....	478
6.2.5. Capillary Electrophoresis of Platinum Particles.....	485
6.2.6. Continuous Free-Flow Electrophoresis of Particles and Assemblies – General Considerations.....	487
6.2.7. Continuous Free-Flow Electrophoresis of Particles and Assemblies – Results and Discussion	489
6.2.8. Conclusions.....	444
6.3. Experimental	498
6.3.1. Sample Preparation.	498
6.3.2. Gel Electrophoresis.....	500
6.3.3. Capillary Electrophoresis	500
6.3.4. Continuous Free-Flow Electrophoresis	502
6.4. References	503
 7. Small Angle X-Ray Scattering	 508
7.1. Background and Introduction	508

7.2. Results and Discussion	513
7.3. Experimental	515
7.4. References	516
8. Ligand-Exchange Kinetics	518
8.1. Infrared Spectroscopy	519
8.2. Fluorescence Quenching	522
8.3. Summary and Conclusions	528
8.4. Experimental	528
8.4.1. Synthesis of 1-Isocyano-4-phenylethynyl-benzene	529
8.4.2. Synthesis of Hexanethiol-capped Platinum Particles	531
8.4.3. Synthesis of Polyacrylate-capped Platinum Particles	532
8.4.4. Analytical Techniques	532
8.4.4.1. Transmission Infrared Spectroscopy	532
8.4.4.2. Attenuated Total Reflectance Spectroscopy	533
8.4.4.3. Optical Absorbance Spectroscopy	533
8.4.4.4. Fluorescence Spectroscopy	533
8.5. References	533
9. Conclusions and Project Outlook	536

Appendices	541
Appendix 1. Collaborative Publications Involving the Integration of Nanoparticles and Nanoparticle Assemblies into Lithographic Architectures	542
A-1.1. References.....	553
Appendix 2. Geometric Calculations Involving Nanoparticle Dimers and Trimers	554
A-2.1 Hydrodynamic Radii of Nanoparticle Dimers	554
A-2.2 Hydrodynamic Radii of Nanoparticle Trimers	565
A-2.3 Geometry of Nanoparticle Trimers.....	571
A-2.4 References	574

List of Tables

1. Introduction

2. Synthesis, Stability and Properties of Metal Nanoparticles

Table 2-1.	Concentrations of citrate-capped gold particles as received by Ted Pella, Inc. The values below were reported by the supplier.....	96
Table 2-2.	Observations recorded for platinum particles with 4-mercaptopbenzoic acid	111
Table 2-3.	Nickel-CTAB particle Synthesis 1: Variables = NiCl_2 and N_2H_4 conc. and stirring.....	123
Table 2-4.	Nickel-CTAB particle Synthesis 2: Variable = CTAB concentration	125

3. Synthesis and Stability of Metal Oxide Nanoparticles

Table 3-1.	Effects of Relative Hydrolysis and Condensation Rates on Material Structure	159
Table 3-2.	Gelation Times (hours) for Silicon Alkoxides in Different Solvents	164
Table 3-3.	Partial positive charges associated with the metal atoms in several ethoxides	167
Table 3-4.	Hydrolysis Rate Constants for Silicon and Titanium Alkoxides	169
Table 3-5.	Effects of Reaction Parameters on the Size and Dispersity of TiO_2 Particles	187
Table 3-6.	Reaction Conditions for the Hydrolysis of TIP in the Presence of Hydrochloric Acid and Ethanol.....	248
Table 3-7.	Observations for the Hydrolysis of TIP in the Presence of Hydrochloric Acid and Ethanol.....	249

4. Synthesis of Nanoparticle Assemblies

Table 4-1.	Statistics obtained for heterodimer assemblies consisting of citrate-capped gold particles (20 nm) and mercaptobenzoic acid-capped platinum particles	340
Table 4-2.	Statistics Obtained for Heterodimer Assemblies Consisting of Citrate-capped Gold Particles (15 nm) and Tartaric-acid-Capped Fe ₃ O ₄ Particles	356
Table 4-3.	Concentrations of gold particles.....	361

5. Size-Exclusion Chromatography of Particles and Particle Assemblies

Table 5-1.	Retention Volumes Observed for Platinum Particles with Different Capping Ligands	396
Table 5-2.	Retention Volumes Observed for Platinum Particles with Different Capping Ligands	416
Table 5-3.	Data Obtained from SEC Chromatograms of Nanoparticle Assemblies	423

6. Electrophoresis of Particles and Particle Assemblies

Table 6-1.	Approximate k_a values for 5.3 nm and 19 nm gold particles in 10 mM CAPS buffer with varying concentrations of SDS.	454
Table 6-2.	Ionic strengths, Debye lengths and k_a values for buffers used in CE experiments	471
Table 6-3.	Data obtained from plots of migration time vs. particle diameter for buffers at different pH values.....	475
Table 6-4.	Retention times of platinum particles obtained using capillary electrophoresis	486
Table 6-5.	Statistics for particle solutions containing dimers determined by TEM before CFFE separation.....	495

Table 6-6.	Statistics for fractions collected after CFFE of gold dimers.....	495
Table 6-7.	Concentrations of gold particles used in separations.....	498
Table 6-8.	Concentrations of gold particles in solutions containing dimers and trimers	499
Table 6-9.	Buffer conditions for CFFE separations	502

7. Small Angle X-Ray Scattering

8. Ligand-Exchange Kinetics

Table 8-1.	Stern-Volmer Quenching Constants	525
Table 8-2.	Concentrations of gold particles.....	529

9. Conclusions and Project Outlook

Appendix 1. Collaborative Publications Involving the Integration of Nanoparticles and Nanoparticle Assemblies into Lithographic Architectures

Appendix 2. Geometric Calculations Involving Nanoparticle Dimers and Trimers

Table A-2-1.	Hydrodynamic radii calculated for homodimers of various sizes using both the rod-approximation and the dumbbell model.	558
Table A-2-2.	Hydrodynamic radii calculated for heterodimers of various sizes using the dumbbell model.....	559
Table A-2-3.	Hydrodynamic radii calculated for homotrimers composed of nanoparticles of various sizes using both the rod-approximation and the cylindrical model based on the axial ratio.	565
Table A-2-4.	Maximum particle sizes feasible for nanoparticle trimers with different linker lengths.....	568

Table A-2-5. Values calculated for the gap between particles both with and without consideration for the citrate capping layer 573

List of Figures

1. Introduction

- Figure 1-1. (A) Semilogarithmic plots of current vs. voltage for Au/SAM/Pd nanowires junctions formed from dodecanethiol, an oligomeric phenyleneethylene (OPE) and an oligomeric phenylenevinylene (OPV). (B) General structure of an OPE (C) General structure of an OPV 2
- Figure 1-2. (A) Schematic of an acceptor-bridge-donor molecular junction. (B) Example of an acceptor-bridge-donor molecule. (C) Another example of an acceptor-bridge-donor molecule. (D) Electronic energy levels associated with an acceptor-bridge-donor junction..... 4
- Figure 1-3. Schematic of OPE functionalized with a nitro group and an amine..... 5
- Figure 1-4. Schematics of molecular junctions formed through vapor deposition (A) Titanium and gold evaporated onto a monolayer of 4-thioacetyl biphenyl. (B) Reaction of magnesium with a methoxy-terminated self-assembled monolayer. (C) Schematic of a pattern formed through the selective deposition of magnesium onto carboxylic acids. 8
- Figure 1-5. Schematic showing a crossed-wire tunnel junction consisting of two, 10 μm gold wires, one of which is modified with a molecular monolayer 11
- Figure 1-6. Schematic of a Hg-SAM/SAM-M' junction created using a mercury drop. The magnified view shows the presence of some solvent molecules (ethanol) at the interface..... 12
- Figure 1-7. (A) A metal-molecule-metal junction formed by contacting a self-assembled monolayer with a gold-coated AFM tip (B) Schematic of a single-molecule molecular junction consisting of an OPE inserted into an alkanethiol mololayer and then contacted with an STM tip 13
- Figure 1-8. Schematic of a dithiol OPE, which was inserted into an alkanethiol film and then bound to a nanoparticle..... 15
- Figure 1-9. (A) Schematic of 1,8'-octanedithiol covalently bound to a gold substrate and a gold-plated CP-AFM tip (B) Schematic of a thiol-

terminated OPE bridged between a gold surface and a gold STM tip	16
Figure 1-10. (A) Method used to form a mechanical break junction by coating xylyl dithiol onto a gold wire, stretching it until fracture and then bringing it back together until conductance was achieved. (B) Junction formed using the process shown in (A) (C) Differential conductance curve measured for this junction.....	17
Figure 1-11. (A) Linear oligomeric phenylene ethylene (OPE) used to synthesize nanoparticle dimers (B) Trigonal planar OPE used to synthesize nanoparticle trimers (C) Tetrahedral OPE used to synthesize nanoparticle tetramers (D) Tetragonal planar OPE used to synthesize nanoparticle tetramers (E) Dimer composed to 30 nm silver particles (F) Trimer composed of 10 nm gold particles (G) Planar tetramer composed of 10 nm gold particles (H) Tetrahedral trimer composed of 10 nm gold particles	19
Figure 1-12. (A) Schematic showing an OPE-linked gold nanoparticle dimer trapped within a lithographic trench (B) Current-voltage measurements through a trapped dimer indicating long-term stability under vacuum	21
Figure 1-13. (A) The structures of three molecules used to form nanoparticle dimers: 1,4-benzenedimethanethiol (BDMT), 4,4'-biphenyldithiol (BPD) and bis-(4-mercaptophenyl)-ether (BPE) (B) Schematic of a nanoparticle dimer (C) The differential conductance curves for nanoparticle dimers with three different molecular linkers	22
Figure 1-14. Long-term vision for a molecular-scale transistor self-assembled into a silicon-based architecture.	23
Figure 1-15. Possible method for functionalizing the TiO ₂ gate electrode with redox-active molecules.	24
Figure 1-16. Schematic of a lithographic trench after reactive ion etching of the SiO ₂ layer and assembly of a nanoparticle trimer. Here the S, D, and G indicate the source, drain and gate for the proposed transistor.....	25
Figure 1-17. Orthogonal self-assembly of isocyanide on platinum and disulfide on gold	27

Figure 1-18. Kinetic effects on bridging a bifunctional molecule between two electrodes using orthogonal self-assembly (A) One functional group binds at a faster rate, facilitating the formation of a molecular bridge (B) Both functional groups bind at similar rates, and electrochemical stripping is required for the formation of a molecular bridge	29
Figure 1-19. Molecules used to evaluate orthogonal self-assembly (A) Monofunctional OPE used as a control (B) Bifunctional linker molecule	30
Figure 1-20. The binding of the bifunctional OPE observed using grazing angle infrared spectroscopy on planar substrates (left) and transmission IR (right). (A) Spectrum of bifunctional OPE shown in Figure 1-19 (B) Spectrum of isocyanide-terminated control molecule shown in Figure 1-19 (A) after incubation with a platinum substrate (C) Spectrum of the bifunctional OPE after incubation with a gold substrate (D) Spectrum of the bifunctional OPE after incubation with a platinum substrate (E) Spectrum of the bifunctional OPE (F) Spectrum of the bifunctional OPE after incubation with hexanethiol-capped gold particles (G) Spectrum of OPE after incubation with hexanethiol-capped platinum particles.....	32
Figure 1-21. Schematics of the proposed molecularly-linked nanoparticle heterodimers (A) Gold-metal heterodimer linked by an OPE terminated with a thiol and an isocyanide. The metal could be either platinum, palladium or nickel. (B) Gold-metal oxide heterodimer linked by an OPE terminated with a thiol and a carboxylic acid. Possible metal oxides include titania and iron oxide.....	33

2. Synthesis, Stability and Properties of Metal Nanoparticles

Figure 2-1 Schematic showing mechanisms for particle stability (A) Electrostatic stabilization (B) Steric stabilization	45
Figure 2-2. The relative magnitudes of various double-layer potentials of interest.....	48
Figure 2-3. Potential energy curves for the interaction of two colloidal particles (A) Total interaction energy as a function of particle separation distance calculated from the sum of the van der Waals attractive energy and the energy due to electrostatic repulsion. (B) Changes	

	in total interaction energy observed for different values of ionic strength.....	49
Figure 2-4.	Nanoparticles of different shapes achieved through kinetic control of reaction conditions (A) Gold nanocubes (B) Rod-shaped gold particles (C) Gold multipods (D) Silver nanowires. (E) Triangular silver nanoparticles.	65
Figure 2-5.	Branched structures created through nucleation on seed crystals. (A) Two-dimensional representation of crystal structure of a tetrapod (B) Schematic of the formation of heterostructured rods through the controlled addition of CdSe extensions to CdS nanorods (C) CdTe tetrapods. (D) Branched tetrapods formed from the nucleation of CdTe on the branches of CdS tetrapods	67
Figure 2-6.	Different shapes of copper nanocrystals formed in reverse micelles	68
Figure 2-7.	Sacrificial polystyrene template used to form triangular gold nanoparticles (A) deposition of polystyrene spheres on a substrate (B) thermal evaporation of gold onto substrate (C) removal of polystyrene spheres to leave triangular gold nanoparticles	69
Figure 2-8.	Schematic of encapsulating hydrophobic nanoparticle with amphiphilic polymer and then subsequent cross-linking of the polymer chains.....	74
Figure 2-9	(A) Superlattice of thiolated gold particles. (B) Ordered chains of BaCrO ₄ nanorods. (C) Bimodal superlattice of gold and silver nanoparticles.	76
Figure 2-10.	Noncovalent linking of nanoparticles (A) Network of gold particles capped with 1,10 phenanthroline and lithium ions. (B) Network of cyclodextrin-capped gold nanoparticles induced by fullerene molecules.....	78
Figure 2-11.	Schematic of Plasmon oscillation for a sphere, showing the displacement of the conduction electron charge cloud relative to the nuclei	80
Figure 2-12.	(A) Optical spectra calculated for gold ellipsoids of varying aspect ratios (R) using the dipole approximation and a dielectric constant of 2.05. (B) Optical spectra of gold nanorods obtained for gold nanorods of different aspect ratios.....	82

Figure 2-13. (A) Gold colloid nanoshells with decreasing shell thickness	84
Figure 2-14. Absorption spectra calculated for a gold ellipsoid (aspect ratio = 3.3) with as the dielectric constant of the surrounding medium changes from 1.3 to 2.3	86
Figure 2-15. Absorption spectra for 10nm spherical particles of platinum, palladium and nickel calculated using Mie theory	88
Figure 2-16. Schematic of nanoparticle heterodimer (not to scale). Two nanoparticles bound with an organic linker molecule terminated with different functional groups. Nanoparticles can be either electrostatically or sterically stabilized.	92
Figure 2-17. OPE used to synthesize heterodimers.....	93
Figure 2-18. (A) Citrate ion (B) Tannic Acid	95
Figure 2-19 (A). UV-VIS absorption spectra of gold nanoparticles as received from Ted Pella, Inc. (B) Relationship between particle diameter and the wavelength of the absorbance maximum for gold particles, both theoretical calculations and experimental data. (C) Particle concentrations and extinction coefficients at 520 nm were plotted as a function of particle diameter for gold nanoparticles as received from Ted Pella, Inc.....	97
Figure 2-20. Capping ligands used in the synthesis of platinum particles (A) glutathione (B) tiopronin (C) 4-mercaptobenzoic acid.....	104
Figure 2-21 Pt-tiopronin particles (A) TEM image (B) absorption spectrum	107
Figure 2-22. Pt particles with 4-mercaptobenzoic acid (A) TEM image and (B) absorption spectrum	110
Figure 2-23. Platinum particles with 4-mercaptobenzoic acid (A) thiol/gold ratio of 0.5:1; particle size 2.1 ± 0.5 nm (B) thiol/gold ratio of 1:1; particle size 3.0 ± 0.5 nm	114
Figure 2-24. Sodium 2-mercaptoethanesulfonate	115
Figure 2-25. Platinum particles synthesized using reverse micelles and capped with 2-mercaptoethanesulfonate in formamide (A) TEM of particles synthesized with 10% solution of surfactant in pentane; particle size 4.7 ± 0.9 nm (B) TEM of particles synthesized with 7% solution of	

	surfactant in pentane (C) Absorption spectrum of particles synthesized with 10% surfactant solution	117
Figure 2-26.	Schematic of surfactant bilayer surrounding a nanoparticle.....	120
Figure 2-27	(A) Cetyltrimethylammonium bromide (CTAB) (B) Phenyltrimethylammonium bromide (PTAB)	122
Figure 2-28.	Aqueous solution containing Nickel-CTAB particles	124
Figure 2-29.	(A) TEM of nickel particles (A) synthesized with 0.05 M CTAB (B) synthesized with 0.05 M PTAB	126

3. Synthesis and Stability of Metal Oxide Nanoparticles

Figure 3-1.	OPE used to synthesize heterodimers.....	150
Figure 3-2.	Shrinkage of gel with condensation	157
Figure 3-3.	TEOS precursor substitution reactions and the resulting hydrolysis rates.....	158
Figure 3-4.	Gel structures for acid and base catalyzed reactions	161
Figure 3-5.	Computer simulations of structures formed by monomer-cluster and cluster-cluster aggregation under reaction and diffusion-limited conditions.....	165
Figure 3-6.	Schematic structures of (A) $[\text{Ti}(\text{OR})_4]_4$ (R = Me, Et) (B) $\text{Ti}_2(\text{OR})_8$ (C) $\text{Ti}_2(\text{OR})_8(\text{LH})_2$ (LH = ROH or RNH_2).....	168
Figure 3-7.	Schematic of nucleation and growth process assumed for alkoxide hydrolysis.....	177
Figure 3-8.	Images of TiO_2 particles synthesized via the hydrolysis of TiCl_4 in aqueous solution (A) SEM image of a film of TiO_2 particles (B) TEM image of TiO_2 particles (C) TEM image of micron-sized TiO_2 particles formed in the presence of Na_2SO_4	181
Figure 3-9.	TiO_2 Nanostructures formed from the hydrolysis of TiCl_4 in the presence of HCl (A) Mixture of rutile (elongated) and brookite (spherical) structures (B) Brookite particles after separation through selective peptization.	184

Figure 3-10. TEM images of TiO ₂ particles synthesized from the hydrolysis of titanium isopropoxide under acidic conditions. The reaction conditions associated with images A-D are listed in Table 3-5.	186
Figure 3-11. Surfactants and polymers used to create reverse micelles for TiO ₂ synthesis (A) Polyoxyethylene nonylphenyl ether; tradename Igepal® CO-520 for n~5 (B) Triton® X-100, n = 9-10 (C) Ammonium carboxylate perfluoroether (D) bis(2-ethylhexyl) sulfosuccinate sodium salt (AOT) (E) Copolymer consisting of a dimethyl amino ethyl methacrylate block and a perfluorooctyl methacrylate block.	190
Figure 3-12. TEM images of titanium oxide nanostructures formed in reverse micelles in the presence of (A) hydrochloric acid (B) nitric acid (C) sulfuric acid (D) phosphoric acid. The acid concentrations in all cases were equivalent to 2.5 M HCl. The insert in (A) is an electron diffraction pattern indicating the rutile crystal phase	193
Figure 3-13. TiO ₂ particles synthesized using non-hydrolytic methods (A) Particles synthesized from the reaction of TiCl ₄ with benzyl alcohol, approximately 15 nm in diameter (B) Particles synthesized from the reaction of TiCl ₄ with TIP in the presence of TOPO	199
Figure 3-14. Image and cross-sectional schematic of a stainless steel autoclave, specifically a General Purpose Acid Digestion Bomb manufactured by the Parr Instrument Company	202
Figure 3-15. TiO ₂ nanoparticles synthesized using solvothermal methods (A) Anatase particles synthesized from the reaction of TiCl ₄ in ethanol at 150 °C. (B) Rutile particles synthesized from the reaction of TiCl ₄ in glycerol and acetic acid at 150 °C (C) Anatase particles synthesized from the reaction of titanium isopropoxide with acetone at 130 °C	205
Figure 3-16. TEM images of TiO ₂ synthesized using a solvothermal method (A) Nanoparticles synthesized through the hydrolysis of Ti(OBu) ₄ in the presence NH ₄ HCO ₃ and linoleic acid (B) Nanorods synthesized from the non-hydrolytic reactions between Ti(OBu) ₄ and linoleic acid.	207
Figure 3-17. Titania nanocrystals synthesized through the hydrolysis and condensation of titanium isopropoxide (TIP) in the presence of trimethylammonium hydroxide (Me ₄ NOH). (A) Triangular prismatic nanocrystals synthesized with a 4.4:1 ratio of TIP to Me ₄ NOH (B)	

Rectangular particles formed after autoclaving the particles shown in (A) at 200 °C.	209
Figure 3-18. Absorption spectrum of anatase TiO ₂ particles	210
Figure 3-19. Iron oxide particles synthesized using sonochemical reactions (A) Fe ₃ O ₄ particles (9 nm) synthesized from iron pentacarbonyl in the presence of sodium dodecyl sulfate (B) FeO particles (3 – 8 nm) synthesized from iron pentacarbonyl in the presence of poly(vinylpyrrolidone). (C) Fe ₃ O ₄ particles (10 nm) synthesized sonochemically from iron (II) acetate in water.....	216
Figure 3-20. (A) Oleic acid (B) Stearic acid.....	217
Figure 3-21. Iron oxide particles synthesized via the coprecipitation of Fe ²⁺ and Fe ³⁺ ions in the presence of NH ₄ OH (A) and N(CH ₃) ₄ OH (B)	221
Figure 3-22. (A) Schematic of interdigitated bilayer formed from undecanoic acid and the ester formed from undecanoic acid and poly(ethyleneglycol) (B) Fe ₃ O ₄ particles stabilized with this interdigitated bilayer after gamma irradiation.	222
Figure 3-23. Iron oxide particles synthesized via the coprecipitation of Fe ²⁺ and Fe ³⁺ ions. (A) Fe ₃ O ₄ particles coated with poly(vinylalcohol). (B) Fe ₃ O ₄ particles coated with a bilayer consisting of lauric acid and decanoic acid. (C) Fe ₃ O ₄ particles coated with sulfonated poly(acrylic acid) (D) Fe ₃ O ₄ particles coated with a graft copolymer, poly(glycerol monoacrylate)-g-(PEG methyl ether acrylate) (F) Fe ₃ O ₄ particles synthesized in the presence of tetramethylammonium hydroxide	223
Figure 3-24 Schematic of a liposome.....	225
Figure 3-25. TEM images of Fe ₃ O ₄ particles (A) Particles synthesized in reverse micelles of sodium dodecylbenzenesulfonate. (B) α-FeOOH particles synthesized in phosphatidylcholine vesicles.....	226
Figure 3-26 TEM images of Fe ₃ O ₄ particles synthesized by the coprecipitation of Fe ²⁺ and Fe ³⁺ ions both with (A) and without (B) the presence of polyoxyethylene nonyl phenyl ether micelles.	227
Figure 3-27. TEM images of iron oxide particles (A) γ-Fe ₂ O ₃ particles synthesized from the thermal decomposition of Fe(Cup) ₃ in trioctylamine. (B) Fe ₃ O ₄ particles synthesized from the thermal	

	decomposition of Fe(acac) ₃ in the presence of phenyl ether, 1,2-hexadecanediol, oleic acid and oleylamine.....	228
Figure 3-28.	γ -Fe ₂ O ₃ nanoparticles (7 nm) synthesized via the decomposition of an iron-oleate complex.....	229
Figure 3-29.	(A) Schematic of the reaction between iron acetylacetonate and 2-pyrrolidone (B) Fe ₃ O ₄ particles coated with 2-pyrrolidone, 5 nm in diameter.....	231
Figure 3-30.	Fe ₃ O ₄ nanoparticles synthesized through the solvothermal reaction of Fe(acac) ₃ in benzyl alcohol (A) Particles as synthesized, 12 nm in diameter (B) Particles dispersed in hexane after coating with undecanoic acid, 8 nm in diameter (C) Particles dispersed in water after coating with dopamine, 12 nm in diameter	232
Figure 3-31.	(A) TEM Image of TiO ₂ particles capped with stearic acid (B) Absorption spectrum of TiO ₂ synthesized in the presence of stearic acid and hexanoic acid	236
Figure 3-32.	Molecules and bonds associated with the Pt/TiO ₂ Orthogonal Self-Assembly Study (A) Control Molecule (B) Linker Molecule (C) Bidentate carboxylic acid – titanium bond (D) Bridging carboxylic acid – titanium bond.....	232
Figure 3-33.	Transmission IR data of carboxylic acid and isocyanide terminated molecules in the presence of TiO ₂ and Pt nanoparticles. (A) Free stearic acid (B) Stearic acid upon binding to TiO ₂ (C) Control molecule terminated with carboxylic acid (D) Control molecule after incubation with TiO ₂ particles (E) Bifunctional linker molecule terminated with carboxylic acid and isocyanide functionalities (F) Bifunctional linker after incubation with TiO ₂ particles (G) Bifunctional linker after incubation with Pt particles.	239
Figure 3-34	TiO ₂ nanostructures formed from the hydrolysis of TiCl ₄ in an aqueous hydrochloric acid solution. (A) Spherical particles 7.2 ± 0.8 nm in diameter (B) A mixture of TiO ₂ nanorods and spherical aggregates (C) Lower magnification image indicating the extent of aggregation.....	242
Figure 3-35.	TEM images of TiO ₂ particles synthesized from the hydrolysis of TIP in the presence of hydrochloric acid and ethanol	244

Figure 3-36. TiO ₂ particles synthesized from the hydrolysis of TEO in the presence of potassium chloride	250
Figure 3-37. TiO ₂ particles synthesized using a solvothermal method	252
Figure 3-38. Ligands used for attempted-ligand exchange (A) glycerol (B) succinic acid (C) tartaric acid.	253
Figure 3-39. TiO ₂ nanostructures observed after attempted ligand-exchange with (A) glycerol (B) succinic acid (C) tartaric acid	254
Figure 3-40. Proposed mechanism for the formation of anisotropic nanostructures from smaller nanocrystals through selective desorption of ligands from the (001) crystal face	255
Figure 3-41. TiO ₂ nanostructures observed after attempted ligand-exchange with (A) glycerol (B) succinic acid (C) tartaric acid.	256
Figure 3-42. Fe ₃ O ₄ particles synthesized by the coprecipitation of FeCl ₂ and FeCl ₃ in tetramethyl ammonium hydroxide (N(CH ₃) ₄ OH) (A) Particles synthesized in the presence of 58 mmol (N(CH ₃) ₄ OH) (B) Particles synthesized in the presence of 29 mmol mmol (N(CH ₃) ₄ OH)	261
Figure 3-43. Iron oxide particles synthesized solvothermally from iron acetylacetonate in benzyl alcohol (A) particles coated with tridecanoic acid and dispersed in hexane (B) Particles coated with glycerol (C) Particles coated with succinic acid (D) Particles coated with tartaric acid. The insets in (C) and (D) show larger aggregates also present in these solutions.....	264

4. Synthesis of Nanoparticle Assemblies

Figure 4-1. Schematics of nanoparticle assemblies on solid substrates. (A) Gold nanoparticles covalently bound to a self-assembled monolayer; the terminal functional group, A, binds to nanoparticles and adheres them to the surface (B) Gold nanoparticles adsorbed to the substrate through non-covalent interactions; nanoparticles coated with streptavidin interact with a biotinylated surface.....	287
---	-----

Figure 4-2.	Microcontact printing of palladium colloids (A) Method used to form surface patterns (B, C) SEM images of patterns formed after electroless copper deposition	288
Figure 4-3.	Schematics of nanoparticle assemblies formed on substrates (A) Bilayer created using two different sizes of CdSe quantum dots bound by 1,4-benzenedimethanethiol. (B) Bilayer of gold particles capped with 12-aminododecane bound by 1,8-octanedithiol on a patterned substrate	290
Figure 4-4.	(A) Reaction scheme showing asymmetric functionalization of CdTe tetrapods. Step 1: spin-coat polymer to partially cover tetrapods. Step 2: addition of hexanedithiol. Step 3: attach gold nanoparticles (red dots). Step 4: dissolve polymer layer (B) TEM image of formation from CdTe tetrapod functionalized with 5 nm gold nanoparticles (C) Schematic showing nanrod formation by breaking tetrapods using a TEM grid (D) TEM image of CdTe nanorods asymmetrically functionalized with 5 nm gold nanoparticles	292
Figure 4-5.	Schematic representation of DNA-directed assembly of gold nanoparticles	294
Figure 4-6.	The formation of a cadmium sulfide particle network through the reaction of α,α' -dibromo-p-xylene with pyridine functionalities on adjacent particles.	295
Figure 4-7.	Dimers formed through controlled aggregation (A) SEM image of silica particles (330 nm) and dimers. Dimers are marked with a black line. (B) TEM image of gold particles (15 nm) and dimers coated with a polymer shell.....	297
Figure 4-8.	(A) Method for coating the top of silica beads with a gold film. (B) SEM images of SiO ₂ beads (600 nm) after coating with Ti/W alloy (5 nm) and gold (25 nm) and annealing at 700 °C (C) TEM image of Au/SiO ₂ dimers after removal from substrate.....	299
Figure 4-9.	(A) Formation of heterodimeric structures through the thermal decomposition of iron pentacarbonyl in the presence of gold particles. (B) TEM image of heterodimer formed in non-polar solvent. (C) TEM image of 'flower-like' structures formed in polar solvent	300

Figure 4-10.	(A) Schematic showing the formation of Fe ₃ O ₄ -Ag heterodimers at a micellar interface and the subsequent selective functionalization (B) TEM image showing Fe ₃ O ₄ -Ag heterodimer (C) TEM image showing FePt-Ag heterodimer	301
Figure 4-11	(A) Schematic for the formation of a gold nanoparticle dimer from gold nanoparticles functionalized with complementary DNA strands (B) Schematic for the formation of a dimer from DNA-functionalized gold nanoparticles bound by a longer, complimentary strand (C) TEM image of a dimer formed using the method shown in (B). (D) Schematic of a trimer formation from complimentary thiolated-DNA strands bound to nanoparticles (E) TEM images of trimer formed using the method shown in (D)	302
Figure 4-12.	Nanoparticle assembly consisting of a gold core (31 nm) surrounded by smaller gold satellites (8 nm)	303
Figure 4-13.	(A) Linear oligomeric phenylene ethylene (OPE) used to synthesize nanoparticle dimers (B) Trigonal planar OPE used to synthesize nanoparticle dimers (C) Tetrahedral OPE used to synthesize nanoparticle tetramers (D) Tetragonal planar OPE used to synthesize nanoparticle tetramers (E) Dimer composed to 30 nm silver particles (F) Trimer composed of 10 nm gold particles (G) Planar tetramer composed of 10 nm gold particles (H) Tetrahedral trimer composed of 10 nm gold particles.	305
Figure 4-14.	Diruthenium-bis(OPE) compounds used to synthesize nanoparticle dimers and linear chains	306
Figure 4-15.	(A) Structure of bis(acyl hydrazide) (B) TEM image of CdSe homodimers linked by bis(acyl hydrazine) after repeated size-selective precipitation to isolate dimers.....	307
Figure 4-16.	Gold nanoparticle dimers synthesized using a solid phase approach (A) Reaction scheme showing dimer formation (B) TEM images of gold nanoparticle dimers synthesized from particles 2.8 nm in diameter.....	310
Figure 4-17.	Synthesis of dimers from mono-functionalized gold nanoparticles. The particles were functionalized using both polystyrene Wang and poly(ethylene glycol)acrylamide (PEGA) copolymer-based resins.....	311
Figure 4-18.	Gold nanoparticle dimers synthesized using asymmetrical functionalization (A) Reaction scheme showing dimer formation (B)	

11-mercapto-1-undecanol (MUOH) (C) 16-mercaptohexadecanoic acid (MHA) (D) Mercaptoethylamine (MEA) (E) Amide linkage formed from the reaction of MHA with MEA (F) TEM image of gold nanoparticle dimers synthesized from particles 41 nm in diameter (G) TEM image of a dimer consisting of a 41 nm and a 30 nm particle	313
Figure 4-19. Optical absorption of gold nanoparticle assemblies (A) Calculated extinction spectra of spherical aggregates each containing 2,600 Au nanospheres for increasing gold volume fraction. (B) Calculated extinction spectra for spherical aggregates of gold nanospheres in water for increasing aggregate size at a fixed Au volume fraction.	316
Figure 4-20. Core-satellite structures with reconfigurable tether in both the hairpin (A) and extended (B) states	317
Figure 4-21 A) Schematics of gold particles with carboxylic acid functionalities, PAMAM dendrimers, the self-assembly of gold particles with dendrimers and the decreased coupling that occurs with increasing dendrimer generation (B) Optical absorption spectra for gold nanoparticles self-assembled in the presence of dendrimers	318
Figure 4-22. (A) Optical absorption spectra of 8 nm gold nanoparticles both before (lower spectrum) and after (upper spectrum) the addition of the OPE linker in (B). The inset shows the time evolution of the absorbance at 535 nm	319
Figure 4-23. Optical spectra for silver nanoparticle dimers (A) Spectra calculated for 60 nm silver particles as a function of inter-particle distance. (B) Optical absorption spectra for 30 nm silver nanoparticles linked by OPE molecules	320
Figure 4-24. (A) Method for assembling nanoparticle multi-layers on a surface (B) Photograph of Au, Au/Ag and Ag nanoparticle multilayer samples	321
Figure 4-25. Oligomeric phenylene ethylene (OPE) molecules used to synthesize homodimers of gold nanoparticles (A) 3-ring linker (B) 5-ring linker (C) 7-ring linker	328
Figure 4-26. TEM images of gold nanoparticle homodimers (A) Solution containing 15 nm citrate-capped gold homodimers (B) Homodimer of 20 nm citrate-capped gold particles. Dimers were linked with linked with a 3-ring OPE	329

Figure 4-27. (A) Graph shows the percentages of particles that appeared to be in dimers on a TEM grid for citrate-capped gold particles of various sizes both without and with the addition of an OPE linker. (B) The percentage of particles that appeared to be in dimers in the presence of three different linker molecules.	330
Figure 4-28. Three-armed oligomeric phenylene ethylene (OPE) molecules used to synthesize gold nanoparticle trimers (A) Linker with 7 rings (B) Linker with 10 rings.....	331
Figure 4-29. TEM images of gold nanoparticle trimers (A) Solution containing 5 nm citrate-capped gold trimers linked with a 10-ring three-armed OPE. (B) Trimer of 15 nm particles linked with a 7-ring OPE. (C) Trimer of 15 nm particles linked with a 7-ring OPE.....	332
Figure 4-30. (A) Graph shows the percentage of particles that appeared to be in trimers on a TEM grid for citrate-capped gold particles of various sizes both without and with the addition of a three-armed OPE linker. These values reflect averages measured for 2-3 experiments (B) The percentage of 15 nm particles that appeared to be in dimers and trimers in the presence of two different linker molecules.....	333
Figure 4-31. Optical absorption spectra for citrate-capped gold nanoparticle solutions containing dimers and trimers. (A) Solutions of 5 nm particles (B) Solutions of 15 nm particles.....	336
Figure 4-32. Bifunctional linkers used to link gold particles to platinum and nickel	338
Figure 4-33. TEM images of citrate-capped gold particles (20 nm) and mercaptobenzoic-acid-capped platinum particles (7 nm) in the presence of the bifunctional linker shown in Figure 4-32 (A)	339
Figure 4-34. TEM image of citrate-capped gold particles (10 nm) and platinum particles capped with 2-mercaptoethanesulfonate in the presence of the linker shown in Figure 4-32 (B)	342
Figure 4-35. TEM image of citrate-capped gold particles (5 nm) in the presence of tiopronin-capped platinum particles and the bifunctional linker shown in Figure 4-32 (A).....	342
Figure 4-36. Optical absorption spectra of gold and platinum particles upon the addition of a bifunctional linker (A) 20 nm gold particles with	

	mercaptobenzoic acid (MBA) – capped platinum particles (B)	
	10 nm gold particles with tiopronin-capped platinum particles	344
Figure 4-37.	TEM image of aggregated citrate-capped gold particles (10 nm) in the presence of PTAB-capped nickel particles	347
Figure 4-38.	Bifunctional linker used to link gold particles to TiO ₂ and Fe ₃ O ₄	349
Figure 4-39.	TEM image of citrate-capped gold particles (15 nm) with succinic acid-capped TiO ₂ particles (9 nm) in the presence of the bifunctional linker shown in Figure 4-38	350
Figure 4-40.	TEM images of hetero-assemblies formed between citrate-capped gold particles (15 nm) and tartaric acid-capped Fe ₃ O ₄ particles (7 nm)	351

5. Size-Exclusion Chromatography of Particles and Particle Assemblies

Figure 5-1.	Schematic of column used for size-exclusion chromatography	369
Figure 5-2.	Sample van Deemter plot calculated from Equation 5-5 indicating the effects of flow rate on the plate height of a chromatographic separation	374
Figure 5-3.	Chromatograms of monodispersed hexanethiol-capped gold nanoparticles before and after ligand-exchange with a ferrocenyl-octanethiol ligand	375
Figure 5-4.	(A) TEM image of dodecanethiol-capped gold particles. The majority of particles appeared to be 3-4 nm, but lower contrast particles of approximately 1.4-1.6 nm were also observed in this region. (B) Size-exclusion chromatograms of dodecanethiol-capped gold particles	377
Figure 5-5.	Chromatograms of CdS particles (5.7 nm) obtained using Nucleosil 500 C ₄ and Nucleosil 1000 C ₄ columns in series at various sodium chloride concentrations	379
Figure 5-6.	Size-exclusion chromatograms of citrate-capped gold particles (5.3 nm and 38.3 nm) with varying concentrations of sodium dodecyl sulfate in the mobile phase. (A) 0 mM (B) 0.1 mM (C) 1 mM (D) 5 mM (E) 80 mM	380

Figure 5-7.	Schematics of possible interactions between sodium dodecyl sulfate (SDS) and both gold particles and size-exclusion chromatography columns (A) Interactions between SDS and silica column material coated with an alkyl chain (B) No interactions between SDS and gold particles; SDS micelles act independently of gold particles (C) Hydrophobic tails of SDS associate with gold particles (D) Inter-digitated bi-layer structure	381
Figure 5-8.	(A) Effects of the sodium dodecyl sulfate (SDS) concentration on retention the times of gold nanorods (a) and gold nanoparticles (b) in size-exclusion experiments. (B) Effects of the concentration of Brij-35 added to a mobile phase consisting of 40 mM SDS	382
Figure 5-9.	Schematic of SDS hemimicelles formed at a moderately-charged gold electrode	383
Figure 5-10.	Structure of Brij-35®, polyoxyethylene (23) lauryl ether.....	386
Figure 5-11.	Three-dimensional size-exclusion chromatogram for a solution containing gold nanoparticles (5.3 nm and 19.3 nm) and nanorods. Mobile phase = 40 mM SDS with 10 mM Brij-35®.....	387
Figure 5-12.	Closed-loop recycling chromatography of broadly distributed 1-decanethiol-gold nanoparticles (A) The configuration of the closed-loop recycling system. (B) Closed-loop recycling chromatogram of 1-decanethiol-gold nanoparticles taken on a 1000 Å column with a flow rate of 0.5 mL/min.....	388
Figure 5-13.	Alternate-recycling chromatography of broadly distributed 1-decanethiol-gold nanoparticles (A) configuration of the alternate-recycling system. (B) Alternate-recycling chromatograms for a broadly distributed 1-decanethiol-gold nanoparticle sample at a flow rate of 1.0 mL/min.....	389
Figure 5-14.	(A) Size-exclusion chromatogram showing the retention times of citrate-capped gold nanoparticles: (a) 10 nm particles (b) 30 nm particles (c) solution containing both 10 nm and 30 nm particles (B) Chromatograms for assemblies if 10 nm particles: (a) isolated particles (b) solution containing nanoparticle trimers (c) solution containing nanoparticle dimers	391
Figure 5-15.	(A) SEC Chromatograms of various sizes of citrate-capped gold particles (B) Plot showing linear relationship between retention volume and log(particle diameter).....	395

Figure 5-16. SEC Chromatograms (A) citrate-capped gold particles (5 nm) upon addition of OPE linker molecule; chromatograms were taken as a function of time after linker addition and offset along the y-axis for clarity. (B) citrate-capped gold particles (10 nm), mercaptobenzoic acid-capped platinum particles, and a solution of both particles after incubation with a bifunctional linker molecule	397
Figure 5-17. SEC chromatograms of citrate-capped gold particles with varying mobile phase compositions.....	399
Figure 5-18. SEC Chromatograms (A) citrate-capped gold particles (B) citrate-capped gold particles after ligand-exchange with BSPP.....	400
Figure 5-19. Bis(p-sulfonatophenyl) phenylphosphine (BSPP)	401
Figure 5-20. (A) SEC chromatograms of BSPP-capped gold particles. (B) Normalized peak areas as a function of particle size for different separation conditions.....	402
Figure 5-21. SEC chromatograms of BSPP-capped gold particles at various SDS concentrations.....	404
Figure 5-22. (A) Retention of BSPP-capped gold particles as a function of SDS concentration in the mobile phase (B) Resolution between 5 and 20 nm particles as a function of SDS concentration	405
Figure 5-23. The plate height and the resolution between 5 nm and 20 nm particle as a function of flow rate	407
Figure 5-24. SEC chromatograms of BSPP-capped gold particles at (A) 0 mM SDS, (B) 10 mM SDS and (C) 40 mM SDS	408
Figure 5-25. SEC chromatograms of gold nanoparticles (5 nm) and particle assemblies (A) After ligand-exchange with BSPP (B) In the absence of BSPP.....	409
Figure 5-26. SEC Chromatograms of citrate-capped gold particles	411
Figure 5-27. SEC Chromatograms of citrate-capped gold particles at various SDS concentrations	412
Figure 5-28. SEC chromatograms of citrate-capped gold particles and tannic acid	413

Figure 5-29. Normalized peak areas for citrate-capped gold particles characterized with several different SEC columns.....	414
Figure 5-30. (A) Plot showing linear relationships between retention volume and log(particle diameter) for citrate-capped gold particles in both Macrosphere (300 Å) and Nucleosil (500 Å) columns in series and a silica-C18 column (500 Å) (B) Resolution between 5 and 20 nm particles as a function of SDS concentration.	415
Figure 5-31. (A) SEC chromatograms of citrate-capped gold particles (10 nm) as a function of time after the addition of an OPE linker molecule. (B) Magnified view of chromatograms shown in (A)	417
Figure 5-32. SEC Chromatograms of a solution of citrate-capped gold particles (10 nm) in a solution containing additional sodium citrate and organic solvent taken as a function of time	418
Figure 5-33. Optical absorption spectra for a solution of citrate-capped gold particles (10 nm) as a function of time after the addition of a molecular linker. The inset shows the absorption at 460 nm and 520 nm as a function of sqrt(time)	419
Figure 5-34. OPE molecule used in control experiment.....	420
Figure 5-35. (A) SEC chromatograms of a solution of citrate-capped gold particles (10 nm) as a function of time after addition of the molecule shown in Figure 5-34 (B) Optical absorption spectra corresponding to the sample in (A). The inset shows the absorption at 460 nm and 520 nm as a function of sqrt(time)	420
Figure 5-36. (A) SEC chromatograms of citrate-capped gold particles (10 nm) as a function of time after the addition of a three-armed OPE linker molecule. (B) Magnified view of chromatograms shown in (A)	421
Figure 5-37. Peak heights observed in SEC chromatograms plotted as a function of sqrt(time). These data correspond to chromatograms shown in Figure 5-31 and Figure 5-36. (A) Observed heights for peaks associated with individual particles (B) Observed heights for peaks associated with dimers and trimers	422
Figure 5-38. SEC chromatograms of mixed particle solutions (A) citrate-capped gold particles (5 nm) with succinic acid-capped titania particles (B) citrate-capped gold particles (5 nm) with glycerol-capped iron oxide particles..	424

Figure 5-39. SEC chromatograms of particle solutions containing citrate-capped gold particles (5 nm) and tartaric acid-capped Fe ₃ O ₄ particles.....	425
---	-----

6. Electrophoresis of Particles and Particle Assemblies

Figure 6-1	Electrophoretic velocity of charged molecules in an electric field is dependent upon charge-to-size ratio	435
Figure 6-2.	(A) Electrical double layer along capillary wall creates electroosmotic flow (B) The total velocity of ions is determined by the sum of the electrophoretic and electroosmotic components	438
Figure 6-3.	Forces acting on a charged particle in an electric field $k_1 =$ electrophoretic force exerted on particle by electric field; $k_2 =$ Stokes friction; $k_3 =$ retarding force; $k_4 =$ force due to relaxation effect.....	445
Figure 6-4.	The limits of Smoluchowski and Huckel in terms of particle radius and double-layer thickness compared to the domain in which the majority of colloids exist.	446
Figure 6-5.	Variation of mobility with zeta potential for a spherical colloidal particle in KCl at ka values > 3	449
Figure 6-6.	Electrophoretic mobility of nanoparticles with ζ -potential of 102.6 mV	451
Figure 6-7.	Effects of SDS concentration on the electrophoretic mobility of gold nanoparticles. CAPS, 10 mM, pH 10.0, applied voltage 20 kV (A) 5.3 nm (B) 19.0 nm	452
Figure 6-8.	(A) Electrophoretic mobilities of α,γ -Al ₂ O ₃ and Fe ₂ O ₃ as a function of pH (B) Electrophoretic mobilities of γ -Al ₂ O ₃ and TiO ₂ as a function of pH (C) Electropherograms of γ -Al ₂ O ₃ and TiO ₂ at pH 9.0 (D) Electropherograms of a mixture of (a) α,γ -Al ₂ O ₃ , (b) γ -Al ₂ O ₃ and (c) TiO ₂ as a function of pH.....	457
Figure 6-9.	Gel electrophoresis of gold particles in 2% agarose gel (A) A mixture of 5 nm, 10 nm, 15 nm, 20 nm, 30 nm and 60 nm particles (B) A plot of migration distance vs. particle diameter showing that mobility decreases with particle size	463

Figure 6-10. Gel electrophoresis of particle assemblies in 2% agarose gel (A) Solution containing dimers of 5 nm particles compared to solution of isolated 5 nm particles (B) Solutions containing dimers and trimers composed of 10 nm and 15 nm particles compared to solutions of isolated particles.	465
Figure 6-11. Molecules involved in CE experiments (A) Gold-citrate particles underwent ligand-exchange with BSPP for added stability (B) CAPS buffer (C) SDS was added to mobile phase (D) Mesityl oxide was added to the sample and elutes at t_0 (E) Octanophenone was added to the sample and elutes at t_{mc}	468
Figure 6-12. Electropherograms of 5 nm, 10 nm, 15 nm and 20 nm gold-citrate particles (A) CAPS Buffer, pH 9.8 (B) Phosphate Buffer, pH 8.0 Applied voltage = 18 kV, $\lambda_{det} = 254$ nm; EOF marker = mesityl oxide (t_0); Micellar marker = octanophenone (t_{mc})	470
Figure 6-13 The dependence of pH on gold particle migration times, mobilities and interaction parameters (A) Migration times of mesityl oxide (t_0) and octanophenone (t_{mc}) as a function of pH (B) Migration time relative to EOF vs. nanoparticle diameter at several pH values (C) Electroosmotic and electrophoretic mobilities as a function of pH. (D) Interaction parameters of gold particles vs. nanoparticle diameter as several pH values.....	472
Figure 6-14. Migration time vs. nanoparticle diameter for gold particles in 10 mM CAPS Buffer, 70 mM SDS, pH ~ 8-9	474
Figure 6-15. Electroosmotic and electrophoretic mobilities as a function of applied voltage.....	476
Figure 6-16. Capillary electropherogram of solution containing 5nm nanoparticles and dimers linker contained three phenyl rings	478
Figure 6-17 (A) Capillary electropherograms of solutions containing 10 nm particles, dimers and trimers (B) electropherograms altered to reflect time relative to EOF (toluene)	480
Figure 6-18 (A). Capillary electropherogram of solution containing 5nm particles and dimers (B) electropherograms of solutions containing 10nm particles and dimers.....	482

Figure 6-19	(A). Capillary electropherograms of solutions containing 5 nm particles and dimers (B) electropherograms of solution containing 10 nm particles, dimers and trimers	484
Figure 6-20.	Schematic of Continuous Free-Flow Electrophoresis Apparatus	487
Figure 6-21.	Photograph taken of 5nm particles in the CFFE chamber	489
Figure 6-22.	Concentrated fractions collected after the CFFE separation of particle solution containing dimers of 5 nm particles.....	490
Figure 6-23.	UV-VIS spectra of fraction collected after CFFE separation of 5 nm gold particles (A) Intensity increases for fractions 9-12 (B) Intensity decreases for fraction 12-21 (C) Plot of the peak maximum versus fraction number.....	491
Figure 6-24.	UV-VIS spectra of concentrated fractions collected after the CFFE separation of particle solution containing 5nm dimers	492
Figure 6-25.	Sample TEM images of fractions collected after CFFE separation of particle solution containing dimers of 5 nm gold particles.....	494

7. Small Angle X-Ray Scattering

Figure 7-1.	(A) Schematic of x-rays interacting with crystalline lattice (B) Higher magnification view of (A) showing the trigonometric basis for Bragg's Law.....	508
Figure 7-2.	(A) Schematic of small x-ray scattering associated with a colloidal solution (B) Images of SAXS set-up at Lawrence Berkeley National Lab. The flight path was adjustable from 1.3 m to 4.3 m.....	511
Figure 7-3.	Calculated scattering intensity profiles for nanoparticle solutions containing nanoparticle homodimers (10 nm).....	512
Figure 7-4.	(A) Scattering profiles for citrate-capped gold particles (10 nm) in the presence of sodium citrate and organic solvent taken over a period of six hours (B) The scattering profiles in (A) plotted on a logarithmic scale.	513
Figure 7-5.	(A) Scattering profiles for citrate-capped gold particles (10 nm) as a function of time after the addition of a stoichiometric amount of	

an OPE linker molecule (B) The scattering profiles in (A) plotted on a logarithmic scale	514
--	-----

8. Ligand-Exchange Kinetics

Figure 8-1. Psuedo-first-order rate plots for the exchange of phenylethanethiolate by p-nitrophenol onto Au ₁₄₀ (SC ₂ Ph) ₅₃ . The natural log of the free ligand concentration was plotted versus time.....	518
Figure 8-2. Isocyanide-functionalized OPE molecule used in IR kinetic experiments	519
Figure 8-3. (A) IR spectra of the isocyanide-functionalized OPE shown in Figure 8-2 during incubation with hexanethiol-capped platinum particles monitored over a period of 75 minutes. (B) The disappearance of the free isocyanide at 2120 cm ⁻¹ with time.	520
Figure 8-4. IR spectra of isocyanide-functionalized OPE obtained both after deposition onto a KBr plate and in aqueous solution	521
Figure 8-5. Fluorescence quenching observed upon binding of a fluorescent carboxylic acid-terminated thiophene to stearic-acid coated TiO ₂	522
Figure 8-6. Bifunctional linker molecules used in fluorescence quenching experiments	523
Figure 8-7. Optical absorbance and fluorescence spectra for Linker B. Fluoresence spectrum was obtained after excitation at 380 nm.	524
Figure 8-8. Fluorescence spectra of Linker A in aqueous solution recorded over a period of 1200 minutes.	525
Figure 8-9. (A) Fluorescence spectra taken for Linker B as citrate-capped gold particles (5 nm) were added to the solution (B)Stern-Volmer plot of quenching observed as citrate-capped gold particles (5 nm) were added to solutions of Linker A and Linker B.....	526

9. Conclusions and Project Outlook

Appendix 1. Collaborative Publications Involving the Integration of Nanoparticles and Nanoparticle Assemblies into Lithographic Architectures

Appendix 2. Geometric Calculations Involving Nanoparticle Dimers and Trimers

Figure A-2-1. Nanoparticle homodimer approximated as a rod 554

Figure A-2-2. Calculated linker lengths..... 556

Figure A-2-3. Nanoparticle trimer approximated as a cylinder 565

Figure A-2-4 Translational diffusion coefficient and hydrodynamic radius as a function of cylindrical radius for a cylinder with a constant length of 5nm..... 568

Figure A-2-5. (A) Schematic of three-armed linker molecule with different linker lengths (B) trimer geometry (C) high magnification schematic of trimer geometry showing how maximum particle size was calculated..... 571

Figure A-2-6 (A) Trimer geometry showing gap between particles (B) High-magnification schematic showing how the gap between the particles was calculated 573

1. Introduction

1.1. Molecular Electronics

The current trend in electronics is to manufacture faster devices with higher circuit densities and processing speeds. As processing speeds are limited by the time it takes for an electron to travel between devices,⁸ higher circuit densities (i.e. smaller feature sizes) are required for improved device performance. However, industry cannot sustain this trend with current silicon-based architectures as there is a limit to the feature size achievable via a lithographic, top-down approach to device fabrication. As of 2001, the feature size on microchips was less than 0.1 μm . Once this size approaches 0.01 μm , silicon no longer retains its fundamental band structure and quantum limitations will most likely hinder device performance.^{4,17} The bottom-up approach of molecular-based device fabrication offers the possibility of continuing the trend towards miniaturization while avoiding the limitations imposed by current lithographic techniques. Using devices on the molecular length scale, it could be possible to incorporate 10^{14} devices per cm^2 , which is a million-fold increase over the density of the current Pentium chip, which contains 10^7 - 10^8 devices per cm^2 .⁴ In addition to performance improvements, molecular electronics offer potential cost and processing advantages over current semiconductor fabrication facilities. Large quantities of devices could be synthesized within a single reaction flask. However, in the bottom-up approach, an as yet unmet challenge is

finding efficient ways to link the molecular devices to the macroscale, outside world. Bridging the length scales between molecules (ca. 1 nm) and lithographic patterns (ca. 100 nm) will be necessary in a bottom-up approach for electronics fabrication.

1.1.1. Molecular Structure

One of the first challenges associated with developing nano-scale devices is identifying candidates for molecular 'wires' that are suitable for conduction.

Oligomeric

phenylene

ethynylene (OPE)

and phenylene

vinylene (OPV)

structures have been

identified as

promising structures

based on their linear,

rigid structures and

extended

conjugation. Figure

1-1 shows that these

molecules are

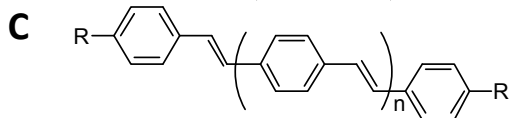
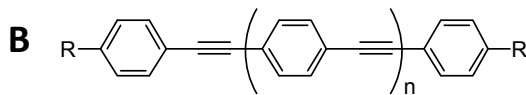
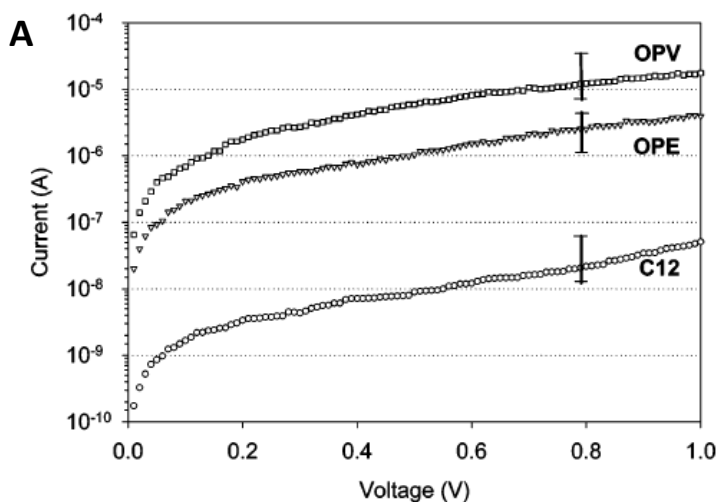


Figure 1-1. (A) Semilogarithmic plots of current vs. voltage for Au/SAM/Pd nanowires junctions formed from dodecanethiol, an oligomeric phenyleneethynylene (OPE) and an oligomeric phenylenevinylene (OPV). Error bars were based on 10 or more electronic junctions. Figure taken from Cai et al.¹⁹ (B) General structure of an OPE (C) General structure of an OPV

several orders of magnitude more conductive than a similarly-terminated alkane chain.^{14,19,24} Research focus has been directed towards OPEs, and significant efforts have been expended to develop facile methods for synthesizing long-chain OPEs for electronic applications.^{4,8,17,26,27} In addition, many variations of the basic OPE structure have been prepared. The molecular approach to electronics offers the advantage that each structure can be synthetically tailored to achieve the properties desired for a particular application. For example, electron-donating substituents can be added to increase the conductivity along the molecular backbone.¹⁷ In contrast, insulating methylene groups can be incorporated to disrupt conductivity.^{4,17}

One of the first examples of a molecule that was tailored to exhibit device characteristics was demonstrated in 1974 by Aviram et al.,¹³ who incorporated electron-donating, electron-withdrawing and insulating groups within a single molecule so that current could only flow in one direction. An example of this type of acceptor-bridge-donor molecule is shown in Figure 1-2 (B). The quinone groups decreased the electron density of the ring to which they were attached, increasing its electron affinity and allowing it to function as an electron acceptor. In contrast, the methoxy groups increased the electron density so that the ring to which they are attached had a lowered ionization potential and functioned as an electron donor. The donor and acceptor sites were insulated from each other with a methylene

bridge so that the π -levels of these two groups did not interact on the time-scale of electronic motion. It was necessary that the LUMO of the acceptor molecule lie at or above the Fermi level of the electrode so that electron flow did not occur in the absence of an applied field. An applied field raised the Fermi level of the cathode and facilitated electron transfer to the acceptor as shown in Figure 1-2 (C). Electron transfer across the bridge occurred via either tunneling or thermally-activated hopping to the donor, which then transferred current to the anode. Current did not flow in the reverse direction, because this pathway was energetically uphill.^{13,28}

Another example shows how the addition of functional groups to an OPE backbone

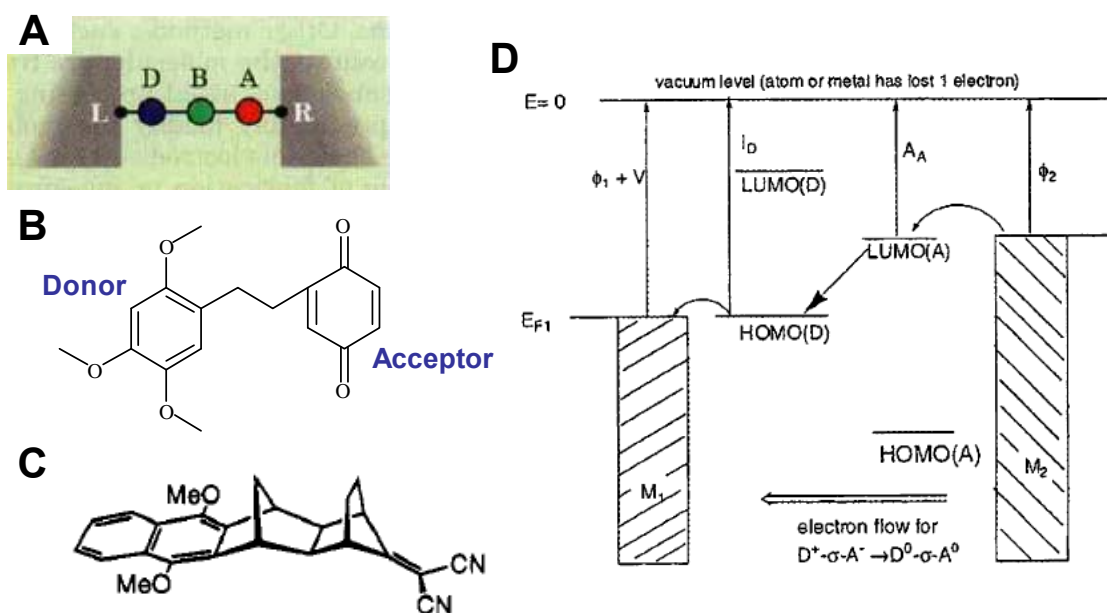


Figure 1-2. (A) Schematic of an acceptor-bridge-donor molecular junction. Figure taken from Heath et al.¹ (B) Example of an acceptor-bridge-donor molecule. Figure adapted from Aviram et al.¹³ (C) Another example of an acceptor-bridge-donor molecule. Figure taken from Paddon-Row et al.²¹ (D) Electronic energy levels associated with an acceptor-bridge-donor junction. Figure taken from Metzger.²⁸

can alter the molecular electronic behavior.¹⁷ The molecule in Figure 1-3 shows a modified OPE with two adjacent rings functionalized with an amine group and a nitro group. As free rotation could occur about the single bond between these rings, this structure was not planar in the ground state due to steric interactions associated with the substituent groups. As a result, there was minimal π -overlap and consequently low molecular conductivity. In the presence of an external electric field, the pendant functional groups were proposed to ionize resulting in a zwitterionic resonance form.

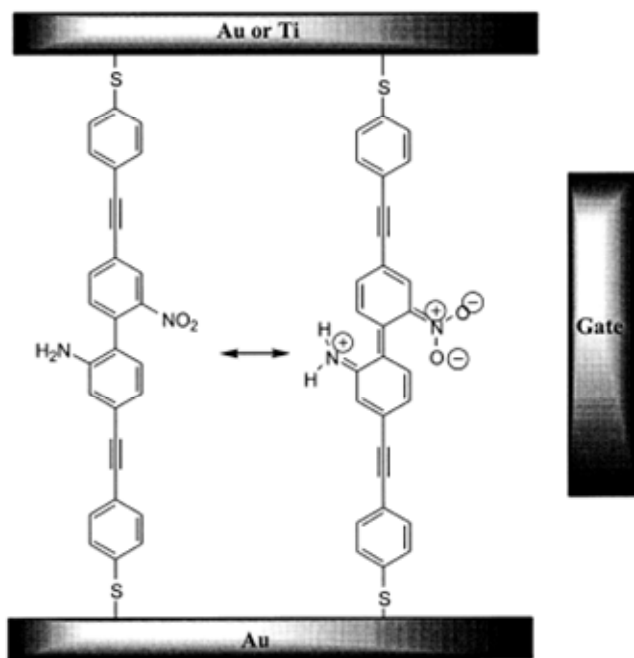


Figure 1-3. Schematic of OPE functionalized with a nitro group and an amine. The zwitterionic resonance form induced by an external field increases molecular planarity and consequently conductivity. Image taken from Tour et al.⁴

Due to the presence of double bonds, this resonance form had increased planarity, π -overlap and conductivity. It was predicted that the conductivity changes exhibited by this molecule in the presence of an external field could allow it to function as a molecular-scale electronic switch.¹⁷

While significant efforts have been expended to tailor the

electronic properties of a molecule, only a few of which were mentioned above, these properties cannot be utilized unless they are connected to a larger-scale electrode. Thus, another important consideration in the synthesis of molecular wires is the choice of terminal functional groups. These molecular 'alligator clips' bind to external electrodes, creating junctions that are crucial to the performance of any device. The tunneling barrier associated with these junctions is reduced greatly when the Fermi level of the metal electrode aligns with the molecular LUMO. The Fermi level of gold correlates most closely to the energy levels of selenium, and then to sulfur and tellurium.²⁹ Because of both the strength of the gold-sulfur bond and the electronic overlap, this junction is commonly used for molecular electronic applications. Isocyanides, on the other hand, are often bound to platinum or palladium. The electron delocalization associated with an isocyanide bound to these metals allows the electron density to shift between the molecule and the metal, lowering the contact resistance associated with this junction.³⁰

While some reports claim there is a high contact resistance associated with the gold-isocyanide bond,²⁹ and higher conductivities have been observed for gold-thiol contacts than for similar contacts with isocyanides,³¹ Chu et al.³² observed conductances approximately an order of magnitude greater for molecules terminated with an isocyanide functionality compared to the same molecules terminated with thiols. These discrepancies suggest that in addition to the nature of the functional

group, other factors such as the molecular conformation and contact geometry likely affect conductivity.³² These variables are likely affected by the method used to form the contact, a subject which is addressed in the next section.

1.1.2. Molecular Contacts

Despite all of the potential efforts expended to synthesize and characterize molecular wires, there are still significant challenges associated with attaching these molecular structures to larger-scale electrodes. This attachment is necessary in order to both measure the electrical properties and fabricate devices. Binding molecules between two macroscopic electrodes is not practical due to the drastic size differences between these contacts. Any defects or surface roughness associated with the larger-scale electrodes would likely disrupt the molecular monolayer, leading to metal-metal contact and electrical shorting.¹⁶ It is also unclear how to bring two macroscopic metal surfaces together without damaging the bridging molecular monolayer. It is therefore necessary to develop methods for bridging molecular length scales (i.e. 1 nm) with the lithographic (i.e. 0.01 to 0.1 μm). The methods described in the literature to address this problem include metal evaporation^{9,20,25,33-46} and electroless deposition,^{39,47-49} crossed-wire junctions,¹⁴ mercury-drop electrodes,^{16,33} scanning probe microscopy,^{3,15,22,24,31,50-62} and mechanical break junctions.³ While many of these techniques have been useful for observing molecular electronic properties, none of them are really suitable for device

fabrication because none offer an obvious way to integrate more than one molecular device into a circuit. Nevertheless, these are the currently available methods for measuring the electronic properties of one or a very small number of molecules, so all we have learned thus far comes from these methods.

One method used to create molecular electronic junctions involves forming a molecular monolayer on a solid substrate, and then creating the top contact through metal vapor deposition.^{9,20,25,33-46} The interactions of metal atoms with organic molecules are complex, and not completely understood.^{20,38} Atoms can interact with the terminal functionality of a monolayer to form an adlayer, they can penetrate the organic layer to the substrate or they can react with and degrade the molecular

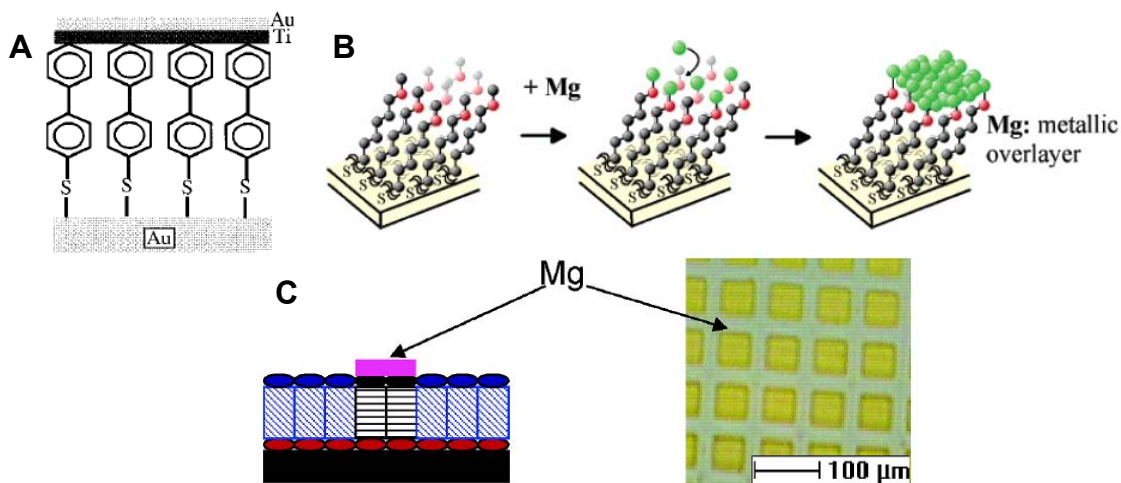


Figure 1-4. Schematics of molecular junctions formed through vapor deposition (A) Titanium and gold evaporated onto a monolayer of 4-thioacetylbiaryl. Schematic taken from Zhou et al.⁹ (B) Reaction of magnesium (green) with a methoxy-terminated self-assembled monolayer. Schematic taken from Walker et al.²⁰ (C) Schematic of a pattern formed through the selective deposition of magnesium onto carboxylic acids. Schematic taken from Zhou et al.²⁵

structures. This behavior depends upon the nature of the metal, the monolayer and the reaction conditions. The schematic in Figure 1-4 (A) shows a monolayer of 4-thioacetylbiphenyl on gold onto which a layer of titanium was deposited followed by a layer of gold.^{9,34} While the exact nature of this junction was not characterized, it was assumed that contact was made through physical interactions between the molecules and the titanium. In contrast, chemical bonds are reported to dominate the contact formed between vapor-generated magnesium atoms and a methoxy-terminated monolayer (Figure 1-4 (B)).²⁰ In this case, the adsorbed atoms inserted into the O-C bonds, and the resulting Mg-O-R groups acted as nucleation sites for the growth of a magnesium adlayer.

As mentioned above, the ability of a metal to form a top contact on a monolayer depends on the interactions between the metal atoms and the monolayer. While copper and silver interacted with a methoxy-terminated monolayer on gold to form a top contact, some atoms also penetrated the monolayer. Under the same conditions, all vaporized gold atoms penetrated the monolayer and deposited onto the substrate, and no top contact was observed.³⁷ In addition to incomplete formation of a top contact, penetration of the monolayer can create undesirable shorting paths to the bottom electrode.⁴³ Even if an adlayer is formed, these junctions would likely be unstable due to the tendency of atoms to penetrate the monolayer.⁴³ While under many circumstances the penetration of metal atoms is

undesirable, this behavior has also been exploited to form patterns as shown in (Figure 1-4 (C)).²⁵ In this case, magnesium was deposited onto a patterned monolayer. While the metal complexed with carboxylic-acid terminated molecules to form a top contact, it penetrated through regions of the monolayer consisting of alkane terminated molecules. A top contact was therefore only observed on areas of the substrate patterned with a carboxylic acid.²⁵ There have also been several reports indicating that high reactivity metals such as titanium react with and degrade molecular monolayers, forming inorganic materials such as metal oxides and carbides.^{40,43-46}

Electroless deposition has been proposed as an alternative method for depositing metals, which could limit the tendency for atoms to penetrate and degrade the monolayer.^{39,47-49} This process involves the chemical reduction of metal ions without an externally applied potential. While this process often requires a catalyst,⁴⁷ the electroless deposition of copper ions onto carboxylic acids has been demonstrated in the absence of a catalyst.^{39,47-49} Cu^{2+} ions formed complexes with acid-terminated monolayers before reduction by formaldehyde to form $\text{Cu}(0)$. These copper complexes acted as nucleation sites for the deposition of additional Cu^{2+} ions. As Cu^{2+} ions typically exhibit higher affinities for copper than the organic structures, they have added preferentially to the reduced copper to form discrete copper islands rather than a uniform adlayer.³⁹ Some reports also claim that copper does penetrate

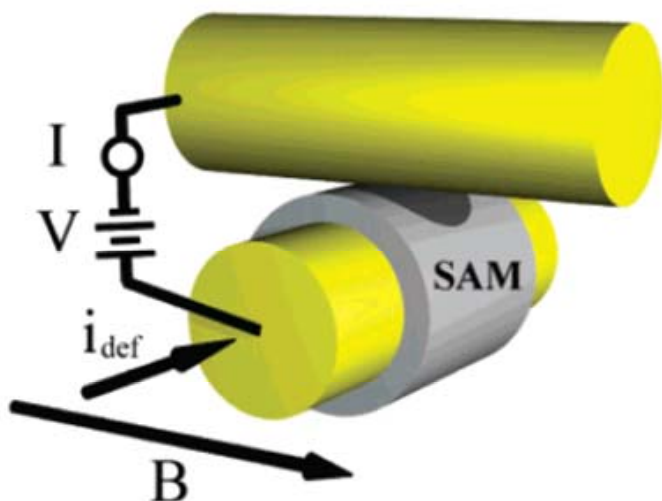


Figure 1-5. Schematic showing a crossed-wire tunnel junction consisting of two, 10 μm gold wires, one of which is modified with a molecular monolayer. Image taken from Blum et al.¹⁴

through the monolayer, even under the milder conditions associated with electroless deposition.³⁹ Copper atoms were observed to penetrate even after removal from plating conditions suggesting the nature of these contacts may change with time,

which would make them unsuitable electronic junctions.³⁹

Molecular contacts have also been created using crossed-wire tunnel junctions as shown in Figure 1-5. This junction consisted of two 10 μm diameter gold wires, one of which was modified with a monolayer of dithiol.¹⁴ The spacing between the wires was controlled by an electromagnetic force (Hall effect) until contact was achieved. While the electrical properties of several dithiol molecules were successfully measured using this set-up, the electrodes were significantly larger than the molecular length scale. Calculations indicated that approximately 10^3 dithiol molecules were present in this junction.¹⁴

Another larger-scale molecular junction has been formed using a mercury droplet as shown in Figure 1-6.^{16,33} In the example shown, a mercury droplet coated with a thiol monolayer was brought into close contact with a thiol-coated metal substrate. The two monolayers interacted only through van der Waals interactions. The advantages of using mercury include the fact that small droplets are easily formed (1–100 μm), and that mercury is a liquid at room temperature. When a mercury droplet is brought in close proximity to a solid substrate, its liquid nature allows it to conform to the topography of the surface. However, the high surface tension associated with mercury does not allow it to completely conform and some defects in the junction were anticipated. Figure 1-6 shows a cartoon illustrating the presence of solvent molecules in a region where molecular contact was not achieved.

Electrical measurement
 s were performed
 using these junctions with
 observed behavior
 similar to

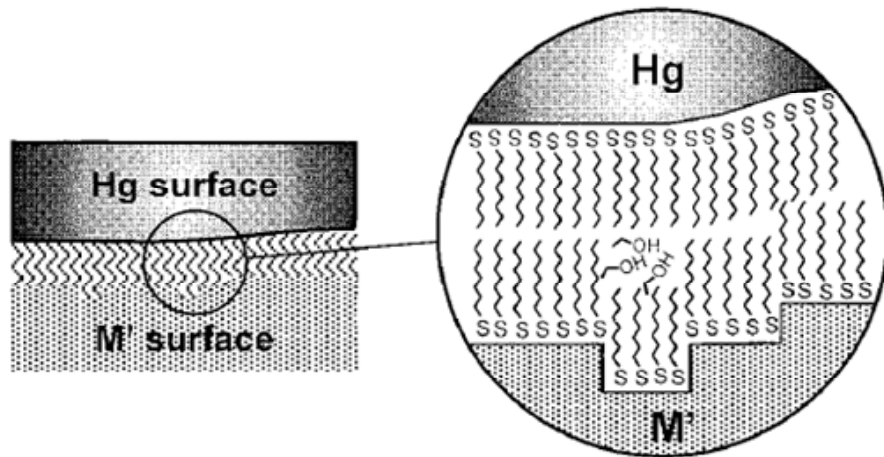


Figure 1-6. Schematic of a Hg-SAM/SAM-M' junction created using a mercury drop. The magnified view shows the presence of some solvent molecules (ethanol) at the interface. Schematic taken from Haag et al.¹⁶

demonstrated by the donor-bridge-acceptor structures discussed in Section 1.1.1 (page 2). These data confirmed limited electronic interaction between the adjacent monolayers.³³ Contact areas as small as 0.01 nm^2 were achieved by controlling the size of the mercury droplets and the pressure applied to them.^{16,33} However, these dimensions again do not compare to the molecular length scale. In addition, this approach only facilitates junctions where molecules interact with the electrodes through physical interactions rather than covalent linkages. Attraction between the two metals under an applied field could also deform the monolayers.¹⁶ While this approach may be suitable for measuring molecular electronic properties, it is not suitable for device fabrication.

One of the most common methods for creating and evaluating molecular electronic

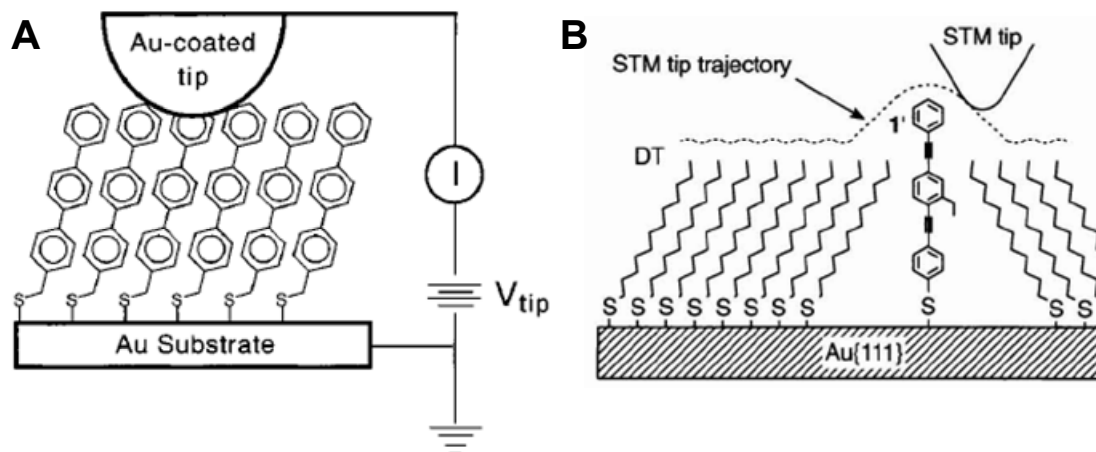


Figure 1-7. (A) A metal-molecule-metal junction formed by contacting a self-assembled monolayer with a gold-coated AFM tip (not to scale). Schematic taken from Wold et al.¹⁵ (B) Schematic of a single-molecule molecular junction consisting of an OPE inserted into an alkanethiol monolayer and then contacted with an STM tip. Schematic taken from Bumm et al.²²

junctions and evaluating involves the use of scanning probe microscopies (SPM), either conductive-probe atomic force microscopy (CP-AFM) or scanning tunneling microscopy (STM).^{3,15,22,24,31,50-62} Surface-bound molecules are probed the tip of either an AFM or STM, and junctions are formed through either physical contact between the molecule and the probe or through covalent bonds. Figure 1-7 (A) shows a monolayer of oligophenylene thiolates on gold, which was probed with a gold-coated AFM tip.¹⁵ In this case, the tip was approximately 15 nm^2 so that each junction contained approximately 75 molecules.⁵¹ While this contact was significantly smaller than those discussed previously, it was still not capable of measuring a single molecule.

It is also noted that the molecules interacted with the tip through non-bonded interactions. The currents measured through these types of junctions are sensitive to the applied stress, and can disagree with calculated values by several orders of magnitude.^{51,52} These discrepancies are attributed to the nature of these contacts, which exhibit properties significantly different than junctions formed through covalent bonds. These ill-defined contacts can dominate the measured electrical properties.⁵³ In the previous section, it was noted that Kim et al.³¹ and Chu et al.³² observed different trends when comparing the conductivity of gold-thiol and gold-isocyanide molecular junctions. The fact that these experiments involved different geometries of non-covalent interactions could account for these differences.

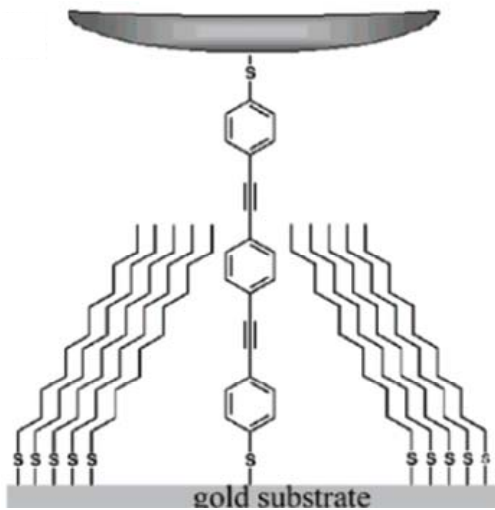


Figure 1-8. Schematic of a dithiol OPE, which was inserted into an alkanethiol film and then bound to a nanoparticle. Schematic taken from Blum et al.¹⁴

Single-molecule contacts have been made using a technique similar to that shown in Figure 1-7 (B). In this case, an OPE molecule was inserted into an alkanethiol monolayer. In this type of experiment, the alkanethiol serves to isolate the conductive molecules from each other.^{52,54} These molecules were then probed with the tip of either an AFM or STM probe.^{3,22,54} Similar experiments have been performed in

which dithiol molecules were inserted into a molecular monolayer.^{14,52,53} These molecules could then be bound to nanoparticles as shown in Figure 1-8. The SPM tip was then brought into contact with the particles. These covalently-bound molecular junctions exhibited significantly different properties than those observed for junctions formed from non-bonded interactions, and typically showed better agreement with theoretical calculations.⁵² However, there was still a contact resistance between the gold particle and the SPM tip.⁵⁰

The contact resistance between the particle and the SPM tip was later circumvented by covalently linking bifunctional molecules directly to the SPM tip, as shown in

Figure 1-9.^{10,23,50,56-63} The most common method used to fabricate these junctions involved moving the SPM tip into and out of contact with a solid substrate in the presence of a solution containing the bifunctional molecules.^{23,50,57-60} During this process, one end of the molecule binds to the substrate and another binds to the moving tip to create an electronic junction. The conductance of molecules measured through these junctions was in good agreement with theory and was dependent upon the molecular structure and the applied force.^{57,60} However, these junctions were highly sensitive to the contact geometry, which is difficult to

consistently reproduce. In order to accurately measure the electronic properties of the bifunctional molecules, many measurements and statistical analyses were performed.^{59,61,63}

The irreproducibility

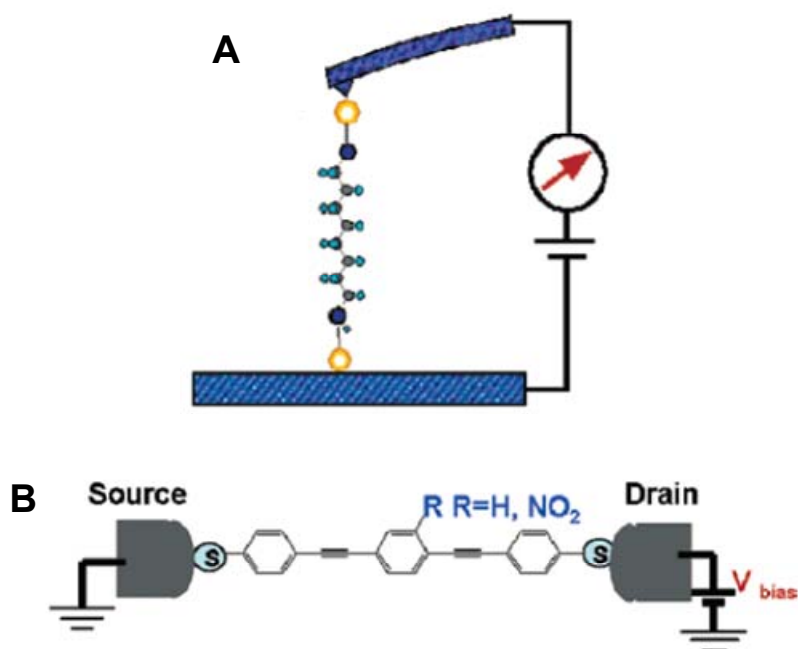


Figure 1-9. (A) Schematic of 1,8'-octanedithiol covalently bound to a gold substrate and a gold-plated CP-AFM tip. Figure taken from Huang et al.¹⁰ (B) Schematic of a thiol-terminated OPE bridged between a gold surface and a gold STM tip. Figure taken from Xiao et al.²³

of these contacts makes them undesirable for device fabrication. In addition, these contacts are typically short-lived.⁶³ Breakdown of these junctions has been observed at gold-gold bonds near the molecule-electrode contacts.^{60,63}

Another method that has been used to bridge a single molecule between two larger electrodes is a mechanical break junction.³ As shown in Figure 1-10 (A), a monolayer of xylyl dithiol was coated on the exterior of a gold wire, which was then

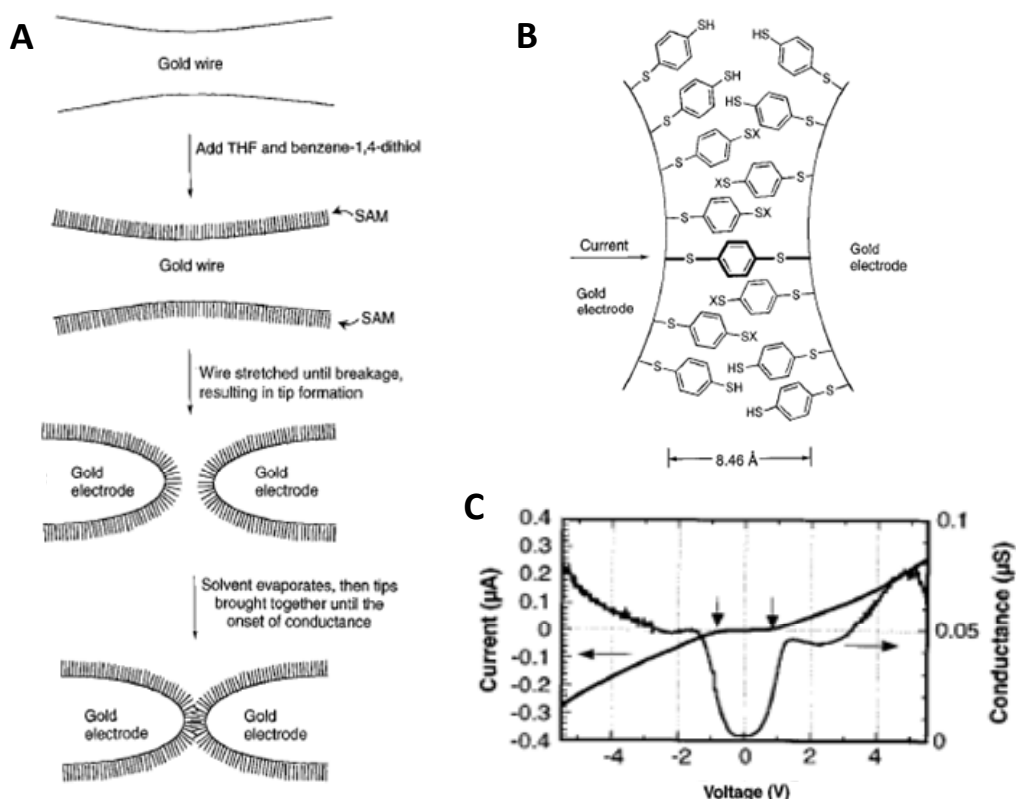


Figure 1-10. (A) Method used to form a mechanical break junction by coating xylyl dithiol onto a gold wire, stretching it until fracture and then bringing it back together until conductance was achieved. (B) Junction formed using the process shown in (A) (C) Differential conductance curve measured for this junction. Images taken from Reed et al.³

stretched until fracture. The two electrodes were then gradually brought back together until conductance was achieved indicating the presence of the molecular junction shown in Figure 1-10 (B). The non-linear shape of the differential conductance curves measured for this junction (Figure 1-10 (C)) suggests that the conductivity was directly related to the electronic structure of the molecule, and was in good agreement with theory. The Fermi level of the substrate increases with applied voltage until it aligns with the HOMO of the molecule, creating a low-resistance pathway for electron flow.²⁴ This maximum conductivity is indicated by the peak in the differential conductance curve. As the bias continues to increase, the Fermi level no longer aligns with the molecular HOMO yielding a decrease in the differential conductance. This phenomenon is referred to as negative differential resistance.

While the methods described above have proved useful for measuring the properties of molecular 'wires', they are somewhat impractical for use in commercial electronic devices. The use of metal evaporation, crossed-wire tunnel junctions and mercury drop electrodes all involve significantly large molecular monolayers rather than individual molecules. The methods used to form these junctions are sensitive to defects in the monolayers and could potentially damage or deform the molecular layers. In addition, non-bonded contacts are often difficult to reproduce and do not necessarily reflect the properties of the molecular wire.

While single-molecule, covalently-linked molecular junctions have been formed using SPM and mechanical break junctions, they require complicated fabrication methods and have high probabilities of failure due to electrical shorting.¹⁶ In addition, both the SPM and gold wire electrodes were significantly larger than the molecular 'wires'. The main motivation for developing molecular-scale electronics are the possibilities they offer for higher circuit densities. However, this million-fold increase in circuit density cannot be achieved if each molecular device requires a

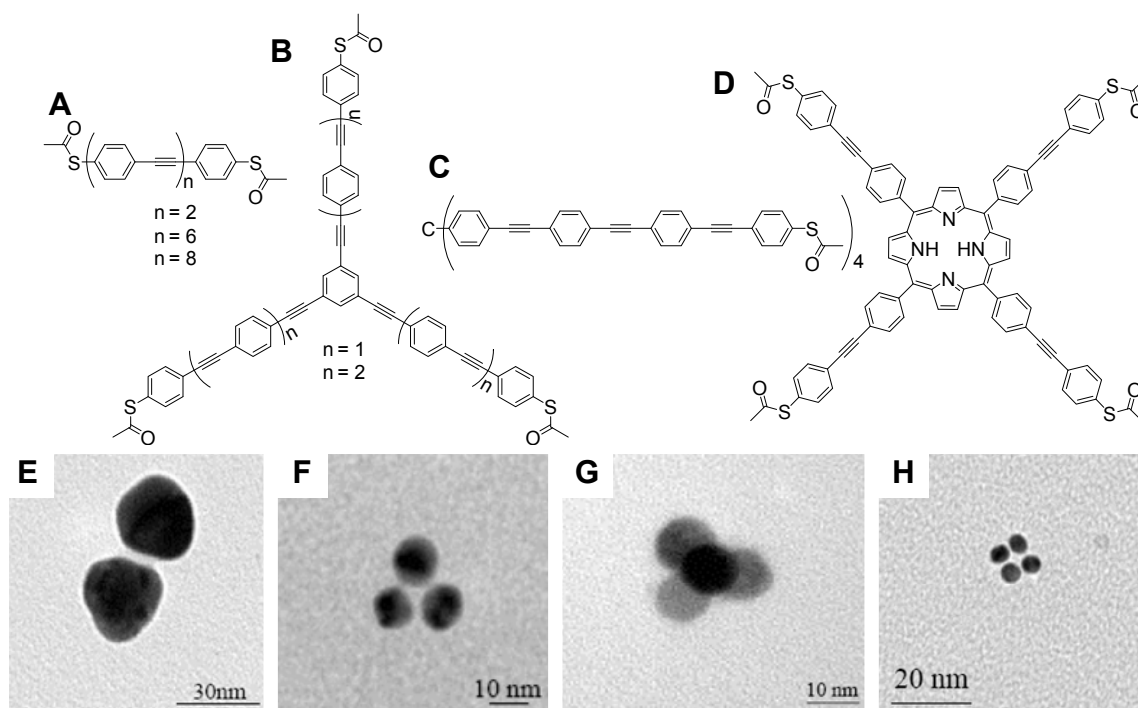


Figure 1-11. (A) Linear oligomeric phenylene ethylene (OPE) used to synthesize nanoparticle dimers (B) Trigonal planar OPE used to synthesize nanoparticle trimers (C) Tetrahedral OPE used to synthesize nanoparticle tetramers (D) Tetragonal planar OPE used to synthesize nanoparticle tetramers (E) Dimer composed to 30 nm silver particles (F) Trimer composed of 10 nm gold particles (G) Tetrahedral trimer composed of 10 nm gold particles (H) Planar tetramer composed of 10 nm gold particles. Images were taken from the Doctoral Thesis of James Novak.⁷

large-scale contact. These methods, therefore, do not represent true miniaturization.

An attractive alternative for creating molecular junctions involves self-assembling molecular wires between nanoparticles and then using these assemblies to contact lithographically defined electrodes. Not only would this method facilitate the formation of covalently-linked single-molecule devices, but it would minimize the size of the electrode contact allowing for higher circuit densities. Because thermodynamics govern the formation of self-assembled structures, it was predicted that the reproducibility of these contacts would be greater. In addition, many molecular junctions could be fabricated in parallel within a single reaction flask, an advantage over the more tedious methods described previously. In 2000, Novak et al.⁷ successfully demonstrated the formation of nanoparticle arrays using self-assembly. As will be discussed in more detail in Chapter 4, OPEs with thioacetate terminal groups were bound to both gold and silver nanoparticles after in-situ deprotection of the acetyl group. Because these molecules are conformationally rigid, they were able to bridge nanoparticles in a variety of geometries and keep them at a fixed distance.⁶⁴ Both gold and silver nanoparticles were bound to form the dimer, trimer and tetramer geometries shown in Figure 1-11. The authors were later able to show that a single molecule bridged these particles.⁷

In 2007, Na et al.⁵ inserted OPE-linked dimers into a lithographically defined trench and evaluated the electronic properties of these junctions. A schematic of this junction is shown in Figure 1-12 (A). The electronic properties of these junctions reflected the molecular structure of the OPE and exhibited stability over long time periods (Figure 1-12 (B)). Similar experiments were performed by Dadosh et al.¹¹ who bridged several different molecules between two lithographically defined electrodes on a silicon substrate as shown in Figure 1-13. Again, the electrical properties reflected the molecular structures. Biphenyl dithiol (BPD) exhibited greater conductance than 4,4'-benzenedimethylthiol (BDMT) and bis-(4-mercaptophenyl)-ether (BPE). The methylene groups in BDMT reduced the overlap of the delocalized molecular orbitals with the gold particles and limited conduction. Similarly, the oxygen atom in the BPE structure disrupted the conjugation

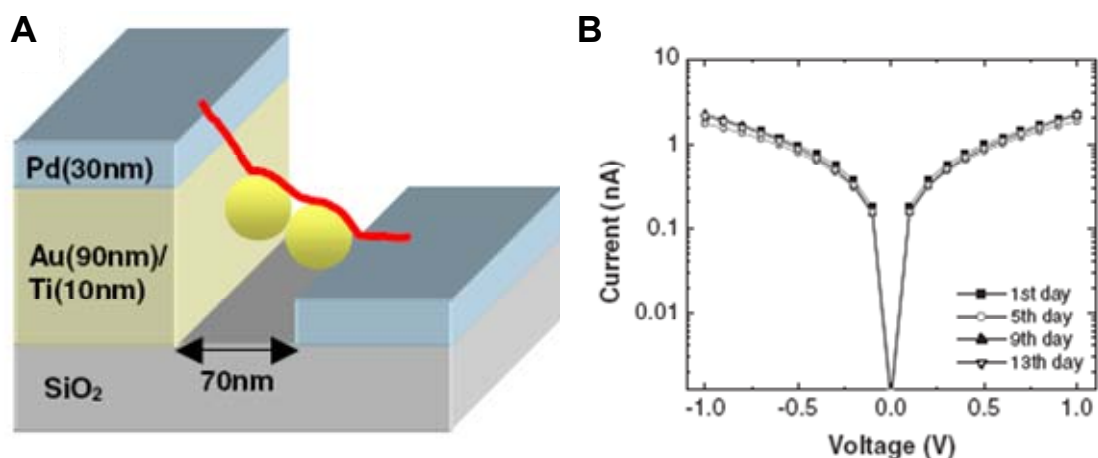


Figure 1-12. (A) Schematic showing an OPE-linked gold nanoparticle dimer trapped within a lithographic trench (B) Current-voltage measurements through a trapped dimer indicating long-term stability under vacuum. Images taken from Na et al.⁵

substantially limiting
electron transport.¹¹

Both of these

examples demonstrate

that molecularly-

bridged nanoparticle

dimers effectively

bridge the molecular

and lithographic length

scales and show

promise in the

development of

molecular-scale electronics.

All of the examples above demonstrating electronic junctions formed from

molecularly-linked nanoparticles used dithiol molecules to bridge nanoparticles of

identical composition. This approach provides no control over molecular orientation

in the junction. If a molecule is acting just as a wire, perhaps the orientation is less

important. However, for any other device (i.e. diodes and transistor) molecular

orientation is critical to function. This work was focused on developing

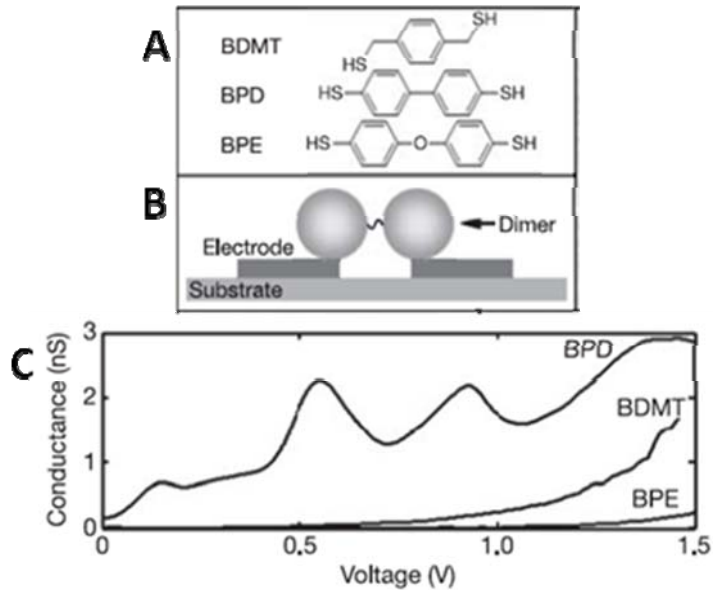


Figure 1-13. (A) The structures of three molecules used to form nanoparticle dimers: 1,4-benzenedimethanethiol (BDMT), 4,4'-biphenyldithiol (BPD) and bis-(4-mercaptophenyl)-ether (BPE) (B) Schematic of a nanoparticle dimer (C) The differential conductance curves for nanoparticle dimers with three different molecular linkers. Images taken from Dadosh et al.¹¹

methodologies for controlling the orientation of molecular-wires within nanoparticle-based electronic junctions for eventual device fabrication.

1.2. Project Impetus

1.2.1. General Concepts

The long-term goal of this project is to synthesize and characterize a molecular-scale transistor, the basic structure of which is shown in Figure 1-14. The proposed methodology involves synthesizing a three-armed OPE similar to the one shown in Figure 1-11 (B), but with different functional groups to facilitate selective binding to nanoparticles of varying compositions. The three nanoparticles bound to the OPE would serve as the source, the drain and the gate electrodes. As with conventional lithographic transistors, the gate will serve as a switch to control current flow

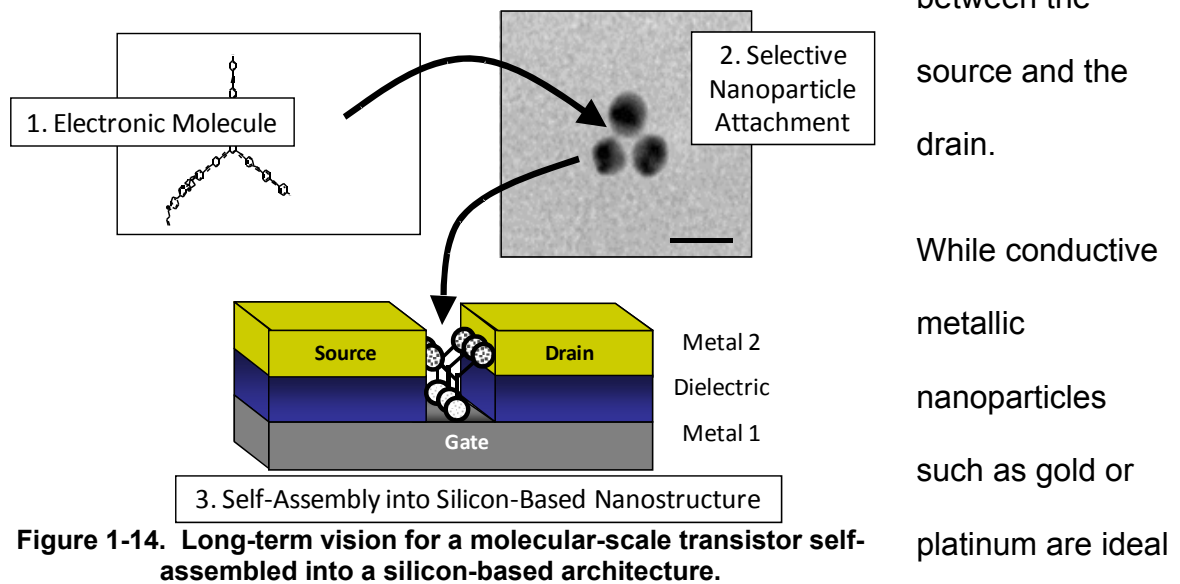


Figure 1-14. Long-term vision for a molecular-scale transistor self-assembled into a silicon-based architecture.

candidates for the source and drain electrodes, a non-conducting particle such as TiO_2 is desirable for the gate electrode in order to avoid current leakage. Incorporating an insulating functionality in the third arm of the OPE molecule could also help to prevent current leakage. The three-terminal device would then be inserted into a silicon-based architecture. One method proposed for achieving the gate functionality involves

functionalizing the gate electrode with electroactive groups such as the viologen groups shown in Figure 1-15. A voltage applied across the gate electrode would reduce the redox-active functional groups, and the resulting negative charge would prevent electron transfer from the source to the drain.

This long-term vision incorporates many novel concepts, which must each be individually addressed before any attempt can be made to demonstrate device functionality. Synthetic techniques must be devised that result in selective functionalization of three-armed molecules in ways that allow purification by common laboratory techniques and that produce high yields. Methodologies need to be established to fabricate sub-100 nm trenches in which to assemble the resulting structures. In addition, the ability to selectively bind OPEs to nanoparticles of

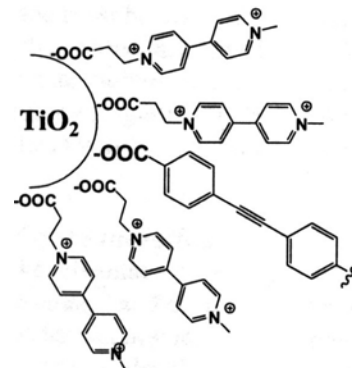


Figure 1-15. Possible method for functionalizing the TiO_2 gate electrode with redox-active molecules.

different compositions much be demonstrated and then methods for both synthesizing and characterizing the resulting nanoparticle arrays must be developed.

A former postdoctoral research assistant in the Gorman group, Kusum L. Chandra, developed synthetic methodologies for synthesizing OPEs with different functional groups. While these efforts were critical to this project, they are not the focus of this dissertation and are reported elsewhere.⁶⁵ The Parsons group at NCSU has

successfully fabricated a trench with a width of approximately 50 nm using a shadowed evaporation technique.⁶⁶ As mentioned above, these lithographic trenches have successfully been used to trap molecularly-bridged nanoparticle dimers and measure their electronic properties.^{5,67,68} A slightly modified trench was fabricated to contact nanoparticle trimers.² The thickness of the SiO₂ layer was decreased using a reactive ion etching technique so that the gate nanoparticle could contact the heavily-doped silicon back gate as shown in Figure 1-16. A thin layer of SiO₂ was

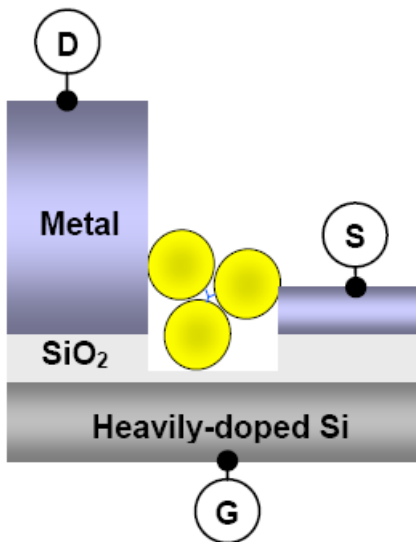


Figure 1-16. Schematic of a lithographic trench after reactive ion etching of the SiO₂ layer and assembly of a nanoparticle trimer. Here the S, D, and G indicate the source, drain and gate for the proposed transistor. Schematic taken from Na et al.² (unpublished manuscript).

maintained to avoid any current leakage between the nanoparticle and the silicon layer. This work is reported in an as yet unpublished manuscript.²

In addition to the synthesis of the molecular wires and the fabrication of the lithographic trenches, the success of this project depends on the ability to insert the OPEs between nanoparticles with directional control. This was attempted using orthogonal self-assembly.

1.2.2. Orthogonal Self-Assembly

Orthogonal self-assembly (OSA) describes a way to selectively bind different functional groups to different regions on a chemically heterogeneous substrate and was first demonstrated by Hickman et al.⁶ who achieved the selective attachment of an isocyanide on platinum and a disulfide on gold as shown in Figure 1-17. Very little information is available on what factors control the relative affinity of a given substrate for one functional group over another. However, this study demonstrated that strict control over reaction conditions was required to achieve OSA. The oxidation state of the platinum substrate appeared to be important. When platinum was oxidized by treatment with O₂ plasma, it showed a 200:1 preference for the isocyanide over the disulfide, which is greater than the 20:1 ratio detected on a reduced platinum substrate. The oxidation state of gold did not appear to play a role in the binding selectivity; the ratio of isocyanide to gold on both oxidized and reduced gold surfaces was 8:1. OSA was only achieved using oxidized platinum

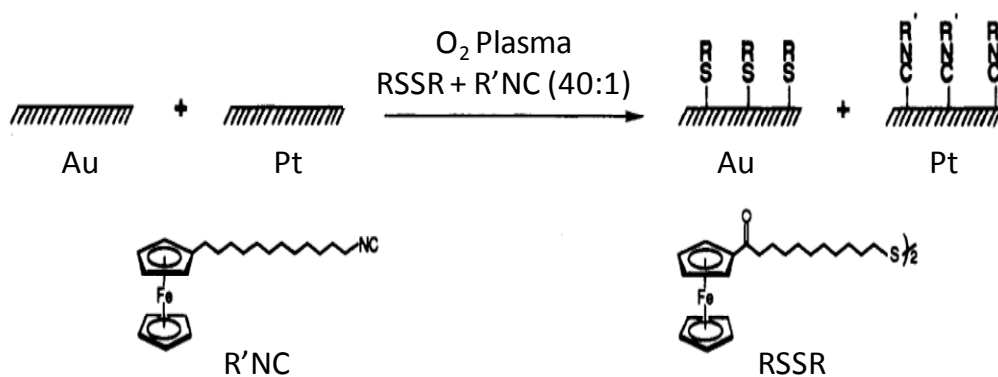


Figure 1-17. Orthogonal self-assembly of isocyanide on platinum and disulfide on gold. Image taken from Hickman et al.⁶

and a 1:40 ratio of the two molecules in solution. As both substrates exhibited an affinity for isocyanide, the excess of disulfide was necessary to ensure that significant concentrations of this molecule were adsorbed. Under these conditions, a 10:1 ratio of isocyanide to thiol was detected on platinum and a 1:10 ratio detected on gold.

A few years later Gardner et al.¹² demonstrated the orthogonal self-assembly of thiols to gold and both carboxylic and phosphonic acids to $\text{In}_2\text{O}_3/\text{SnO}_2$ (ITO). A higher degree of selectivity was achieved in this study with fewer restrictions on reaction conditions. No surface treatment was performed and equimolar solutions of thiol and carboxylic acid resulted in a 100:1 ratio on gold and a 1:45 ratio on ITO. Similarly, equimolar solutions of thiol and phosphonic acid resulted in a 30:1 ratio on gold and a 1:100 ratio on ITO.

While these two studies demonstrated orthogonal self-assembly, they did not offer significant information on what factors control the selectivity of binding. Achieving OSA with a bifunctional molecule creates additional challenges as the stoichiometry of the two functional groups is dictated to be 1:1. In the initial study performed by Hickman et al.⁶ the selectivities of the two functional groups for the two substrates was not 1:1. In addition, the kinetics of binding could be a factor in forming a molecular bridge. While Gardner et al.¹² never attempted to create a molecular junction using OSA, they acknowledged that this phenomenon could be used to achieve orientation of a molecule within an electronic junction and that understanding the relative binding kinetics of the two terminal groups could be crucial to developing appropriate methodologies.

Figure 1-18 illustrates the role binding kinetics could play in bridging a molecule between two lithographic electrodes. If one functional group binds at a significantly greater rate than the other, the second functional group can bind to an essentially bare electrode to form a covalently-linked molecular bridge (Figure 1-18 (A)). If the binding kinetics of the two functional groups are essentially the same, both functional groups will bind and one electrode must be stripped in order for successful formation of a molecular bridge (Figure 1-18 (B)). While the mechanism for bridging molecules between nanoparticles in solution differs from that associated with that associated with bridging lithographic features, understanding the relative binding kinetics could

still play an important role in optimizing conditions to maximize the efficiency of binding two particles together.

The binding of a single molecule between two different nanoparticles also requires an understanding of additional variables such as how the surface structure and geometry of the particle and the composition of the capping ligand affect binding affinity. Walker et al.¹⁸ demonstrated that the selectivity of thiols and isocyanides for gold and platinum nanoparticles was different than that observed for planar

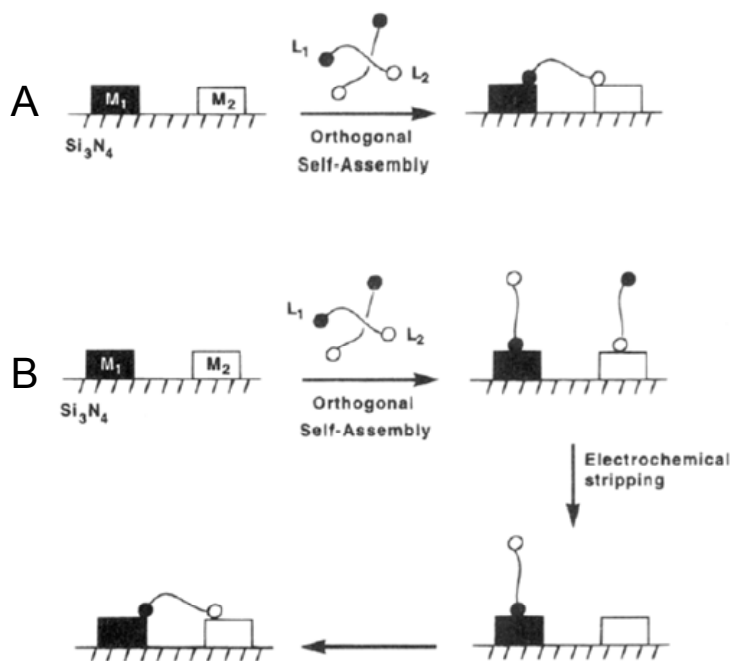


Figure 1-18. Kinetic effects on bridging a bifunctional molecule between two electrodes using orthogonal self-assembly (A) One functional group binds at a faster rate, facilitating the formation of a molecular bridge (B) Both functional groups bind at similar rates, and electrochemical stripping is required for the formation of a molecular bridge. Schematic was taken from Gardner et al.¹²

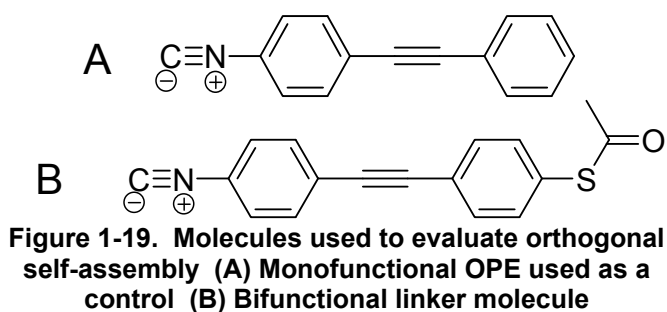
substrates. The molecules used in these studies are shown in Figure 1-19 and the selectivity data are shown in Figure 1-20.

Initial experiments were performed on planar surfaces on which molecular binding to form a self-assembled monolayer

(SAM) could be verified through ellipsometry. Grazing angle infrared reflectance spectroscopy was then used to determine which functional group was bound. A 50-70 cm^{-1} shift in the isocyanide peak upon binding was expected based on previous studies.^{30,69-73} This behavior was verified by forming a monolayer of the control molecule (Figure 1-19 (A)) on a platinum substrate. The free isocyanide peak at 2120 cm^{-1} (Figure 1-20 (A)) broadened and shifted to 2158 cm^{-1} (Figure 1-20 (B)) indicating that binding did occur. The peak broadening is attributed to the inhomogeneity of binding sites.³⁰

The intensity of the shifted isocyanide peak was minimal in the spectra of the bifunctional OPE after in situ deprotection of the thiol and incubation with gold and platinum substrates (Figure 1-20 (C, D)).¹⁸ This result indicated that most of the isocyanide remained unbound. Ellipsometric measurements indicated the presence of a monolayer, suggesting these molecules were bound via the thiol groups. An enhanced acetylene stretch was also observed in these spectra at 2216 cm^{-1} . The exact mechanism for the

surface enhancement of this particular infrared signal is not well known, but this phenomenon has been documented for acetylene-



containing molecules on several metals⁷⁴⁻⁷⁸ and is used here as another indication of binding. These data indicate that isocyanide binding to platinum does occur, but not under the competing influence of the thiol group. These results differ from those obtained by Hickman et al.⁶, but this difference was possibly due to the higher binding affinity of the thiolate compared to the disulfide employed previously by them.

Similar experiments were performed using hexanethiol-capped gold⁷⁹ and platinum⁸⁰ nanoparticles (Figure 1-20, right).¹⁸ Transmission infrared spectroscopy was used to evaluate the binding of the bifunctional oligomer after in situ deprotection of the thioacetate group and evaporation of the solution on a KBr plate. The carbonyl peak shifted from 1710 cm^{-1} to 1671 cm^{-1} confirming the removal of the acetyl group to form free acetic acid. After incubation with the gold nanoparticles, there was no shift in the isocyanide stretch indicating a lack of binding between the isonitrile and the gold. The enhanced acetylene stretch, also observed upon binding the linker molecule to a gold surface, does suggest that some degree of binding through the thiol groups did occur, via either ligand exchange or insertion into a defect site. Upon incubation of the linker molecule with platinum particles, a complete shift in the isocyanide stretch was observed indicating that binding of the linker molecule through this functionality did occur and that orthogonal self-assembly was achieved.

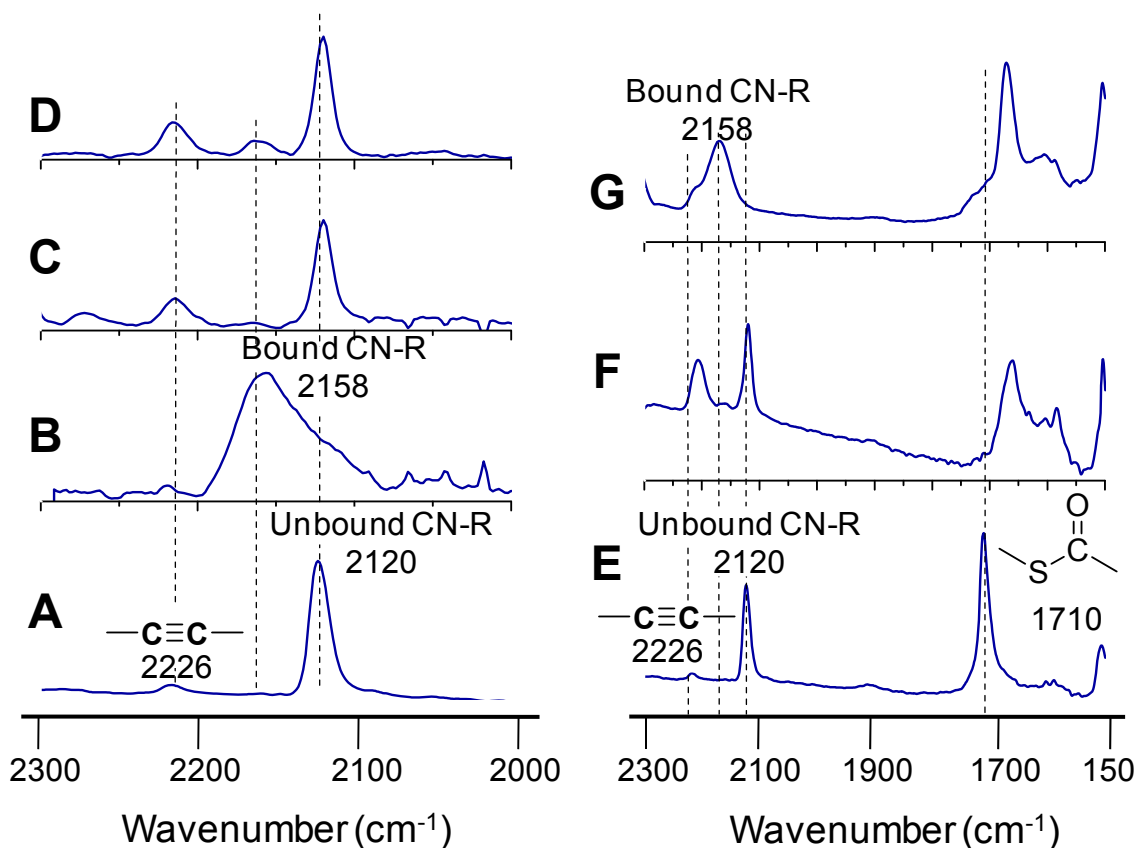


Figure 1-20. The binding of the bifunctional OPE observed using grazing angle infrared spectroscopy on planar substrates (left) and transmission IR (right). (A) Spectrum of bifunctional OPE shown in Figure 1-19 (B) Spectrum of isocyanide-terminated control molecule shown in Figure 1-19 (A) after incubation with a platinum substrate (C) Spectrum of the bifunctional OPE after incubation with a gold substrate (D) Spectrum of the bifunctional OPE after incubation with a platinum substrate (E) Spectrum of the bifunctional OPE (F) Spectrum of the bifunctional OPE after incubation with hexanethiol-capped gold particles (G) Spectrum of OPE after incubation with hexanethiol-capped platinum particles. Figure adapted from Walker et al.¹⁸

The relative binding affinity of the two functional groups was significantly different upon exposure to hexanethiol-capped nanoparticles compared to nominally bare substrates.¹⁸ The factors that govern orthogonal self-assembly are not understood nor is it known how the selectivity would vary with different sizes of nanoparticles,

different capping ligands or different solvents. However, the results suggest the possibility of using OSA to bridge molecules between two nanoparticles of different composition.

1.2.3. Objectives

The main objective of this work was to synthesize and characterize nanoparticle heterodimers consisting of a bifunctional molecules bridged between nanoparticles of different compositions. While the long-term goal of this work was to synthesize a nanoparticle transistor similar to that shown in Figure 1-14, this concept is dependent upon the ability to control the orientation of a molecular wire within a nanoparticle-based electronic junction. The data obtained by Walker et al.¹⁸ suggested this orientation could be achieved by means of OSA. However, this

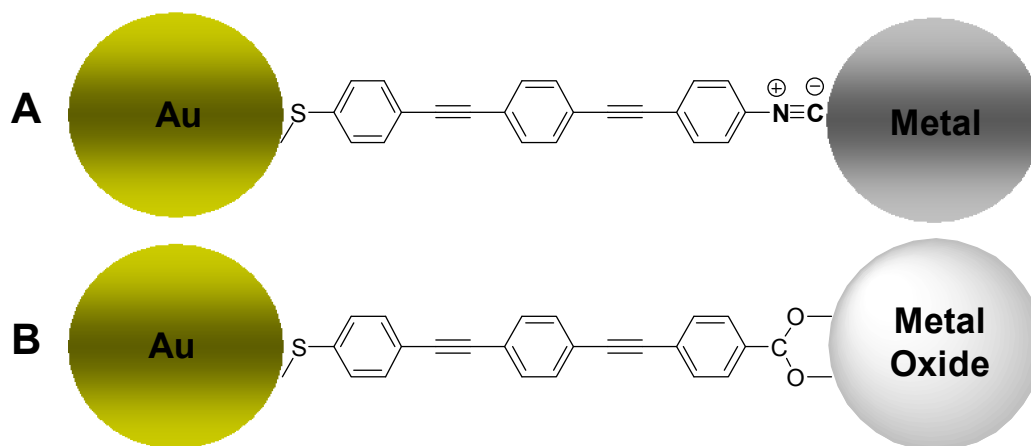


Figure 1-21. Schematics of the proposed molecularly-linked nanoparticle heterodimers (A) Gold-metal heterodimer linked by an OPE terminated with a thiol and an isocyanide. The metal could be either platinum, palladium or nickel. (B) Gold-metal oxide heterodimer linked by an OPE terminated with a thiol and a carboxylic acid. Possible metal oxides include titania and iron oxide. These images are not drawn to scale.

concept has yet to be applied to the formation of discreet nanoparticle assemblies. Initial efforts were focused on dimers in order to identify the variables that affect binding. There are fewer geometric constraints associated with the formation of dimers relative to trimers and fewer binding events to control for the formation of each structure. In addition, there were fewer synthetic obstacles associated with the formation of linear bifunctional OPEs relative to three-armed multi-functional structures.

As Walker et al.¹⁸ demonstrated the possibility of the selective binding of thiols and isocyanides to gold and platinum nanoparticles, attempts were made to synthesize heterodimers from these building blocks as shown in Figure 1-21 (A). In addition to platinum,^{6,18,69-71,81} isocyanides have been reported to bind to the other group ten transition metals, palladium^{30,73,82} and nickel.^{29,83,84} These materials were also investigated as components for heterodimers. The selective binding of carboxylic acids to metal oxides reported by Gardner et al.¹² was also applied to synthesize gold-metal oxide heterodimers as shown in Figure 1-21 (B). Based on the results of Gardner's work, it was speculated that higher degrees of selectivity could be attained for this system compared to the one in Figure 1-21 (A). Both metal-metal junctions and metal-metal oxide junctions will be required for the eventual fabrication of the device shown in Figure 1-14.

While the general heterodimers structures are represented in Figure 1-21, these schematics are not drawn to scale. In addition, they do not show the presence of any stabilizing ligands on the nanoparticle surfaces, which could sterically hinder heterodimer formation. One of the biggest challenges associated with this project was the synthesis of suitable nanoparticles. As will be discussed in detail in subsequent chapters, it was difficult to engineer particles that were stable yet did not have sterically-bulky capping ligands.

Once suitable nanoparticles were synthesized, the ability to bridge these particles with a bifunctional linker using OSA was explored. As discussed previously, there are many factors which affect the selectivity of binding, many of which are not fully understood. In addition, the chemistry and the stability of the nanoparticles were likely significant as homogeneous mixing of the two particle solutions is necessary for efficient dimer formation.

In order to fully evaluate how the size and composition of the nanoparticles, the structure and concentration of the bifunctional linker and other reaction conditions affect both OSA and the formation of heterodimers, it was necessary to develop methods of characterizing these solutions. Transmission Electron Microscopy (TEM) can suggest the presence of heterodimers. However, as discussed in more detail in Chapters 2 and 4, there is some ambiguity associated with TEM data and these images reflect such a small amount of each sample that accurate statistical

information cannot be obtained. Solution-based techniques including size-exclusion chromatography, electrophoresis and small-angle x-ray scattering were investigated as methods to accurately determine the concentrations of heterodimers in solution.

The characterization methods evaluated in this work were mainly developed to show the presence of nanoparticle assemblies in solution. The chemistry associated with the binding of the different functional groups to nanoparticles of different compositions was not fully explored. Experiments similar to those performed by Walker et al.¹⁸ were performed to demonstrate the selectivity of binding for isocyanides and carboxylic acids on platinum and titanium nanoparticles in organic solution. As indicated in Figure 1-20, it was significantly more difficult to confirm the binding of a thiol.

As discussed in reference to Figure 1-18, the relative binding kinetics of the two different functional groups could be significant to both understanding heterodimer formation and optimizing the reaction conditions. However, these measurements required analytical techniques capable of detecting binding, which, as mentioned above, are not fully developed. However, preliminary kinetic experiments were performed using infrared spectroscopy and fluorescence quenching.

As described above, one of the major challenges associated with this project was the synthesis of stable nanoparticles that were suitable for heterodimer formation. Nanoparticle synthesis of both metal and metal oxide particles is described in

Chapters 2 and 3, respectively. Chapter 4 describes efforts to synthesize heterodimers, the general structures of which are shown in Figure 1-21. Methods developed to characterize these nanoparticle assemblies and separate them from both isolated particles and larger aggregates in solution are then described. Size-exclusion chromatography, electrophoresis and small-angle x-ray scattering are discussed in Chapters 5, 6 and 7, respectively. Kinetic considerations are briefly discussed in Chapter 8.

1.3. References

- (1) Heath, J. R.; Ratner, M. A., *Physics Today* **2003**, *56*, 43-49.
- (2) Na, J. S.; Ayres, J.; Chandra, K. L.; Gorman, C. B.; Parsons, G. N., *Unpublished Work* **2008**
- (3) Reed, M. A.; Zhou, C.; Muller, C. J.; Burgin, T. P.; Tour, J. M., *Science* **1997**, *278*, 252-254.
- (4) Tour, J. M., *Acc. Chem. Res.* **2000**, *33*, 791-804.
- (5) Na, J. S.; Ayres, J.; Chandra, K. L.; Chu, C.; Gorman, C. B.; Parsons, G. N., *Nanotechnology* **2007**, *18*, 035203.
- (6) Hickman, J. J.; Laibinis, P. E.; Auerbach, D. I.; Zou, C. F.; Gardner, T. J.; Whitesides, G. M.; Wrighton, M. S., *Langmuir* **1992**, *8*, 357-359.
- (7) Novak, J., Doctoral Thesis, **2001** Chemistry, North Carolina State University
- (8) Pearson, D. L.; Tour, J. M., *J. Org. Chem.* **1997**, *62*, 1376-1387.
- (9) Zhou, C.; Deshpande, M. R.; Reed, M. A.; Jones, L.; Tour, J. M., *Appl. Phys. Lett.* **1997**, *71*, 611-613.

- (10) Huang, Z. F.; Xu, B. Q.; Chen, Y. C.; Di Ventra, M.; Tao, N. J., *Nano Lett.* **2006**, *6*, 1240-1244.
- (11) Dadosh, T.; Gordin, Y.; Krahne, R.; Khivrich, I.; Mahalu, D.; Frydman, V.; Sperling, J.; Yacoby, A.; Bar-Joseph, I., *Nature* **2005**, *436*, 677-680.
- (12) Gardner, T. J.; Frisbie, C. D.; Wrighton, M. S., *J. Am. Chem. Soc.* **1995**, *117*, 6927-6933.
- (13) Aviram, A.; Ratner, M. A., *Chem. Phys. Lett.* **1974**, *29*, 277-283.
- (14) Blum, A. S.; Kushmerick, J. G.; Pollack, S. K.; Yang, J. C.; Moore, M.; Naciri, J.; Shashidhar, R.; Ratna, B. R., *J. Phys. Chem. B* **2004**, *108*, 18124-18128.
- (15) Wold, D. J.; Haag, R.; Rampi, M. A.; Frisbie, C. D., *J. Phys. Chem. B* **2002**, *106*, 2813-2816.
- (16) Haag, R.; Rampi, M. A.; Holmlin, R. E.; Whitesides, G. M., *J. Am. Chem. Soc.* **1999**, *121*, 7895-7906.
- (17) Tour, J. M.; Rawlett, A. M.; Kozaki, M.; Yao, Y. X.; Jagessar, R. C.; Dirk, S. M.; Price, D. W.; Reed, M. A.; Zhou, C. W.; Chen, J.; Wang, W. Y.; Campbell, I., *Chem.-Eur. J.* **2001**, *7*, 5118-5134.
- (18) Walker, B. R.; Wassel, R. A.; Stefanescu, D. M.; Gorman, C. B., *J. Am. Chem. Soc.* **2004**, *126*, 16330-16331.
- (19) Cai, L. T.; Skulason, H.; Kushmerick, J. G.; Pollack, S. K.; Naciri, J.; Shashidhar, R.; Allara, D. L.; Mallouk, T. E.; Mayer, T. S., *J. Phys. Chem. B* **2004**, *108*, 2827-2832.
- (20) Walker, A. V.; Tighe, T. B.; Cabarcos, O.; Haynie, B. C.; Allara, D. L.; Winograd, N., *J. Phys. Chem. C* **2007**, *111*, 765-772.
- (21) Paddonrow, M. N., *Acc. Chem. Res.* **1994**, *27*, 18-25.
- (22) Bumm, L. A.; Arnold, J. J.; Cygan, M. T.; Dunbar, T. D.; Burgin, T. P.; Jones, L.; Allara, D. L.; Tour, J. M.; Weiss, P. S., *Science* **1996**, *271*, 1705-1707.
- (23) Xiao, X. Y.; Nagahara, L. A.; Rawlett, A. M.; Tao, N. J., *J. Am. Chem. Soc.* **2005**, *127*, 9235-9240.
- (24) McCreery, R. L., *Chem. Mater.* **2004**, *16*, 4477-4496.

- (25) Zhou, C. Z.; Nagy, G.; Walker, A. V., *J. Am. Chem. Soc.* **2005**, *127*, 12160-12161.
- (26) Jones, L.; Schumm, J. S.; Tour, J. M., *J. Org. Chem.* **1997**, *62*, 1388-1410.
- (27) Price, D. W.; Dirk, S. M.; Maya, F.; Tour, J. M., *Tetrahedron* **2003**, *59*, 2497-2518.
- (28) Metzger, R. M., *Chem. Rev.* **2003**, *103*, 3803-3834.
- (29) Seminario, J. M.; Zacarias, A. G.; Tour, J. M., *J. Am. Chem. Soc.* **1999**, *121*, 411-416.
- (30) Swanson, S. A.; McClain, R.; Lovejoy, K. S.; Alamdari, N. B.; Hamilton, J. S.; Scott, J. C., *Langmuir* **2005**, *21*, 5034-5039.
- (31) Kim, B.; Beebe, J. M.; Jun, Y.; Zhu, X. Y.; Frisbie, C. D., *J. Am. Chem. Soc.* **2006**, *128*, 4970-4971.
- (32) Chu, C.; Ayres, J. A.; Stefanescu, D. M.; Walker, B. R.; Gorman, C. B.; Parsons, G. N., *J. Phys. Chem. C* **2007**, *111*, 8080-8085.
- (33) Holmlin, R. E.; Haag, R.; Chabinyk, M. L.; Ismagilov, R. F.; Cohen, A. E.; Terfort, A.; Rampi, M. A.; Whitesides, G. M., *J. Am. Chem. Soc.* **2001**, *123*, 5075-5085.
- (34) Zhou, C.; Deshpande, M. R.; Reed, M. A.; Jonesll, L.; Tour, J. M., *Appl. Phys. Lett.* **1997**, *71*, 2857-2857.
- (35) McCreery, R. L.; Viswanathan, U.; Kalakodimi, R. P.; Nowak, A. M., *Faraday Discuss.* **2006**, *131*, 33-43.
- (36) Metzger, R. M.; Xu, T.; Peterson, I. R., *J. Phys. Chem. B* **2001**, *105*, 7280-7290.
- (37) Walker, A. V.; Tighe, T. B.; Cabarcos, O. M.; Reinard, M. D.; Haynie, B. C.; Uppili, S.; Winograd, N.; Allara, D. L., *J. Am. Chem. Soc.* **2004**, *126*, 3954-3963.
- (38) Nagy, G.; Walker, A. V., *J. Phys. Chem. B* **2006**, *110*, 12543-12554.
- (39) Lu, P.; Walker, A. V., *Langmuir* **2007**, *23*, 12577-12582.

- (40) Nagy, G.; Walker, A. V., *J. Phys. Chem. C* **2007**, *111*, 8543-8556.
- (41) Lu, P.; Demirkan, K.; Opila, R. L.; Walker, A. V., *J. Phys. Chem. C* **2008**, *112*, 2091-2098.
- (42) Carpenter, P. D.; Lodha, S.; Janes, D. B.; Walker, A. V., *Chem. Phys. Lett.* **2009**, *472*, 220-223.
- (43) Walker, A. V.; Tighe, T. B.; Stapleton, J.; Haynie, B. C.; Uppili, S.; Allara, D. L.; Winograd, N., *Appl. Phys. Lett.* **2004**, *84*, 4008-4010.
- (44) Tighe, T. B.; Daniel, T. A.; Zhu, Z. H.; Uppili, S.; Winograd, N.; Allara, D. L., *J. Phys. Chem. B* **2005**, *109*, 21006-21014.
- (45) Konstadinidis, K.; Zhang, P.; Opila, R. L.; Allara, D. L., *Surf. Sci.* **1995**, *338*, 300-312.
- (46) Walker, A. V.; Tighe, T. B.; Haynie, B. C.; Uppili, S.; Winograd, N.; Allara, D. L., *J. Phys. Chem. B* **2005**, *109*, 11263-11272.
- (47) Zangmeister, C. D.; van Zee, R. D., *Langmuir* **2003**, *19*, 8065-8068.
- (48) Garino, J. C.; Zangmeister, C. D.; Batteas, J. D., *Langmuir* **2007**, *23*, 7874-7879.
- (49) Zhu, P. X.; Masuda, Y.; Koumoto, K., *J. Mater. Chem.* **2004**, *14*, 976-981.
- (50) Xu, B. Q.; Tao, N. J. J., *Science* **2003**, *301*, 1221-1223.
- (51) Wold, D. J.; Frisbie, C. D., *J. Am. Chem. Soc.* **2001**, *123*, 5549-5556.
- (52) Cui, X. D.; Primak, A.; Zarate, X.; Tomfohr, J.; Sankey, O. F.; Moore, A. L.; Moore, T. A.; Gust, D.; Harris, G.; Lindsay, S. M., *Science* **2001**, *294*, 571-574.
- (53) Cui, X. D.; Primak, A.; Zarate, X.; Tomfohr, J.; Sankey, O. F.; Moore, A. L.; Moore, T. A.; Gust, D.; Nagahara, L. A.; Lindsay, S. M., *J. Phys. Chem. B* **2002**, *106*, 8609-8614.
- (54) Cygan, M. T.; Dunbar, T. D.; Arnold, J. J.; Bumm, L. A.; Shedlock, N. F.; Burgin, T. P.; Jones, L.; Allara, D. L.; Tour, J. M.; Weiss, P. S., *J. Am. Chem. Soc.* **1998**, *120*, 2721-2732.

- (55) Andres, R. P.; Bein, T.; Dorogi, M.; Feng, S.; Henderson, J. I.; Kubiak, C. P.; Mahoney, W.; Osifchin, R. G.; Reifenberger, R., *Science* **1996**, *272*, 1323-1325.
- (56) Tian, W. D.; Datta, S.; Hong, S. H.; Reifenberger, R.; Henderson, J. I.; Kubiak, C. P., *J. Chem. Phys.* **1998**, *109*, 2874-2882.
- (57) Xu, B. Q.; Xiao, X. Y.; Tao, N. J., *J. Am. Chem. Soc.* **2003**, *125*, 16164-16165.
- (58) Xiao, X. Y.; Xu, B. Q.; Tao, N. J., *J. Am. Chem. Soc.* **2004**, *126*, 5370-5371.
- (59) Tao, N. J., *J. Mater. Chem.* **2005**, *15*, 3260-3263.
- (60) Xu, B. Q. Q.; Li, X. L. L.; Xiao, X. Y. Y.; Sakaguchi, H.; Tao, N. J. J., *Nano Lett.* **2005**, *5*, 1491-1495.
- (61) Li, X. L.; He, J.; Hihath, J.; Xu, B. Q.; Lindsay, S. M.; Tao, N. J., *J. Am. Chem. Soc.* **2006**, *128*, 2135-2141.
- (62) Chen, F.; Li, X. L.; Hihath, J.; Huang, Z. F.; Tao, N. J., *J. Am. Chem. Soc.* **2006**, *128*, 15874-15881.
- (63) Huang, Z. F.; Chen, F.; Bennett, P. A.; Tao, N. J., *J. Am. Chem. Soc.* **2007**, *129*, 13225-13231.
- (64) Brousseau, L. C.; Novak, J. P.; Marinakos, S. M.; Feldheim, D. L., *Adv. Mater.* **1999**, *11*, 447-+.
- (65) Chandra, K. L.; Zhang, S.; Gorman, C. B., *Tetrahedron* **2007**, *63*, 7120-7132.
- (66) Chu, C., Doctoral Thesis, **2005** Chemical and Biomolecular Engineering, North Carolina State University
- (67) Na, J. S.; Ayres, J.; Chandra, K. L.; Gorman, C. B.; Parsons, G. N., *Nanotechnology* **2007**, *18*, 424001.
- (68) Na, J. S.; Ayres, J. A.; Chandra, K. L.; Gorman, C. B.; Parsons, G. N., *J. Phys. Chem. C* **2008**, *112*, 20510-20517.

- (69) Bong, D.; Tam, I.; Breslow, R., *J. Am. Chem. Soc.* **2004**, *126*, 11796-11797.
- (70) Horswell, S. L.; Kiely, C. J.; O'Neil, I. A.; Schiffrin, D. J., *J. Am. Chem. Soc.* **1999**, *121*, 5573-5574.
- (71) Avery, N. R.; Matheson, T. W., *Surf. Sci.* **1984**, *143*, 110-124.
- (72) Shih, K. C.; Angelici, R. J., *Langmuir* **1995**, *11*, 2539-2546.
- (73) Murphy, K. L.; Tysoe, W. T.; Bennett, D. W., *Langmuir* **2004**, *20*, 1732-1738.
- (74) Olsen, C. W.; Masel, R. I., *J. Vacuum Sci. Technol. a-Vacuum Surf. and Films* **1988**, *6*, 845-847.
- (75) Johnson, E.; Aroca, R., *J. Phys. Chem.* **1995**, *99*, 9325-9330.
- (76) Zhang, J.; Zhao, J.; He, H. X.; Zhang, H. L.; Li, H. L.; Liu, Z. F., *Langmuir* **1998**, *14*, 5521-5525.
- (77) Zhang, Z. J.; Imae, T., *J. Colloid Interface Sci.* **2001**, *233*, 99-106.
- (78) Ross, D.; Aroca, R., *J. Chem. Phys.* **2002**, *117*, 8095-8103.
- (79) Brust, M.; Walker, M.; Bethell, D.; Schiffrin, D. J.; Whyman, R., *J. Chem. Soc.-Chem. Commun.* **1994**, 801-802.
- (80) Eklund, S. E.; Cliffler, D. E., *Langmuir* **2004**, *20*, 6012-6018.
- (81) Geissler, M.; Chen, J. Y.; Xia, Y. N., *Langmuir* **2004**, *20*, 6993-6997.
- (82) Stapleton, J. J.; Daniel, T. A.; Uppili, S.; Cabarcos, O. M.; Naciri, J.; Shashidhar, R.; Allara, D. L., *Langmuir* **2005**, *21*, 11061-11070.
- (83) Lee, Y. G.; Morales, G. M.; Yu, L. P., *Angew. Chem.-Int. Ed.* **2005**, *44*, 4228-4231.
- (84) Friend, C. M.; Stein, J.; Muetterties, E. L., *J. Am. Chem. Soc.* **1981**, *103*, 767-772.

2. Synthesis, Stability and Properties of Metal Nanoparticles

One of the first steps associated with creating nanoparticle assemblies is the synthesis of the nanoparticle building blocks. While there are reports of colloidal gold and silver that date back to the middle ages,^{19,20} the development of nanoscience and nanotechnology in the last fifteen years has led to an explosion in the number of nanoparticle syntheses reported in the literature. On the nanometer length scale, the electrical and optical properties of particles often differ from those of the corresponding bulk metals, and these properties have been exploited for many different applications. Due to the large surface area/volume ratio associated with nanoparticles, they have been used for catalytic purposes.^{19,22,24-39} Their optical properties have been tailored for a variety of sensing applications including surface enhanced Raman spectroscopy (SERS),^{13,14,41-50} surface plasmon resonance spectroscopy (SPR).⁵²⁻⁵⁴ and the optical sensing of ions,^{5,19,55-59} proteins and DNA.⁶⁰⁻⁶³ Nanoparticles have also been used for drug delivery,^{21,65-71} medical diagnostics⁷²⁻⁷⁵ and as the building blocks for optical and electronic devices.⁷⁶⁻⁷⁸ With the wide variety of properties and applications associated with nanoparticles, there has been extensive work performed to tailor the size, dispersity, shape and surface chemistry of these structures.

Before describing the nanoparticle synthetic work done on this project, this chapter includes a review of the factors affecting particle stability, synthetic considerations and a brief description of the electrical and optical properties of nanoparticles. These concepts are relevant to both the syntheses of nanoparticles described in this chapter and their characterization, which is discussed in more detail in later chapters. While nanoparticles have been synthesized using a variety of different techniques including metal evaporation and laser ablation, most syntheses in the literature are solution-based, and they are the focus of this work.⁷²

In the early stages of nanoparticle development, the term metal colloid was used to describe these structures. Today, this term is still used, but is generally associated with structures on the order of 100 nm or greater. The term nanocluster is also prevalent in the literature, and generally refers to structures on the order of a few nanometers. A quantum dot is defined as a semi-conductor particle. In this chapter, the term nanoparticle is intended to encompass all of these terms. The term colloid is used to describe concepts that apply to all colloidal materials, not just metallic nanoparticles.

2.1.Introduction and Background

2.1.1.Colloid Stability

There are several mechanisms associated with stabilizing colloids against aggregation. Broadly, these mechanisms can be classified in terms of either electrostatic or steric stabilization.

2.1.1.1. Electrostatic Stabilization

Electrostatic stabilization is generally the result of surface-adsorbed anions. The cations in solution are attracted to the negatively-charged particle surface creating

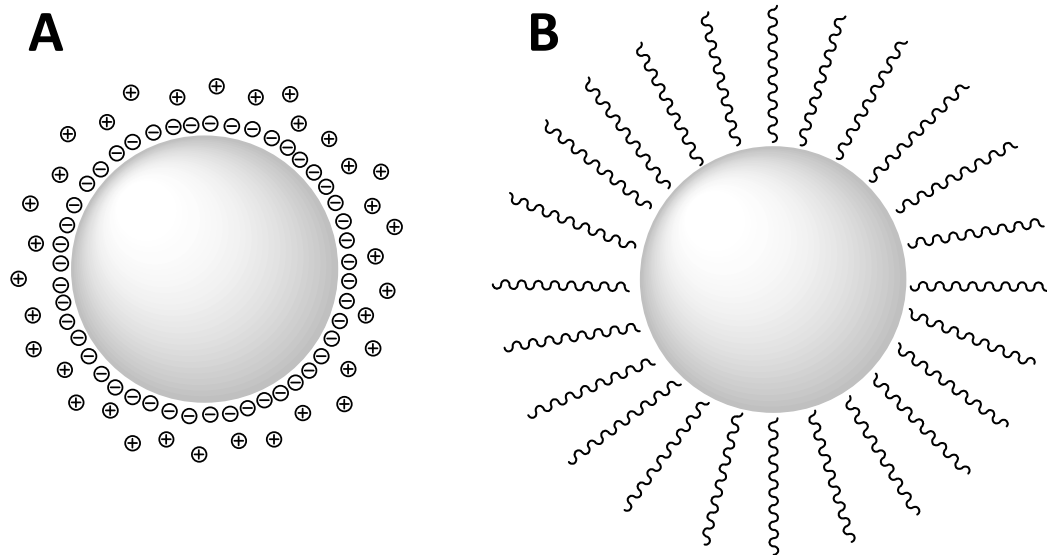


Figure 2-1 Schematic showing mechanisms for particle stability (A) Electrostatic stabilization (B) Steric stabilization

an electrical double-layer as shown in Figure 2-1(A). When the electrostatic repulsion between adjacent double-layers outweighs the attractive Van der Waals forces, particles are stable in solution. As discussed in more detail below, the thickness of the electrical double-layer, often referred to as the Debye length, is critical to particle stability and decreases with the solution electrolyte concentration (Equation 2-1).

$$\lambda_D = \frac{1}{\kappa} = \left(\frac{\epsilon_0 \epsilon_r RT}{2F^2 C_0} \right)^{1/2} \approx C_0^{-1/2} \quad 2-1$$

λ_D = Debye length for a monovalent electrolyte solution

κ = Debye-Huckel parameter

ϵ_0 = permittivity of free space = $8.854 \times 10^{-12} \text{ C}^2/\text{Jm}$

ϵ_r = dielectric constant = 80.10 in H_2O at 20°C

R = gas constant = 8.3144 J/Kmol

T = temperature (Kelvin)

F = Faraday constant = $N_A q = 96,485 \text{ C/mol}$

C_0 = molar concentration of electrolyte (mol/m^3)

The theory that describes the relative forces between particles is called DLVO theory after the two groups of scientists that independently came up with it, Derjaguin and Landau (Soviet Union) and Verwey and Overbeek (Netherlands). They claimed that the total force between two particles is the sum of the attractive and the repulsive forces, which can be calculated according to Equations 2-2 and 2-3, respectively.

$$V_A = \frac{-A}{12\pi D^2} \quad 2-2$$

V_A = attractive force between two charged spheres per unit area^{3,83-86}

A = Hamaker constant

D = distance between spheres

$$V_R = \frac{64kTn_\infty Z^2}{\kappa} e^{-\kappa D} \quad 2-3$$

V_R = repulsive force between two charged spheres⁸⁵

k = Boltzmann constant

Z = particle charge

n_∞ = bulk ion concentration

The attractive forces between the particles are the result of Van der Waals interactions. These are induced-dipole interactions present at the atomic level.^{3,83-87} These Van der Waals interactions are summed over the total volume of each particle, and thus the magnitude of these forces increases with particle size.³ The constant, A , is known as the Hamaker constant and is dependent upon the material properties of each particle, particularly the atomic density and the magnitude of the Van der Waals interactions (Equation 2-4). This equation assumes that the particles are in a vacuum. Solvent molecules generally decrease the magnitude of the Van der Waals attraction.

$$A = \left(\frac{\rho N_A \pi}{M} \right)^2 \beta \quad 2-4$$

A = Hamaker constant (units of energy)³

ρ = number of atoms per unit volume

M = atomic mass

β = Van der Waals interaction parameter

For electrostatic stabilization, the repulsive forces increase with particle charge and decrease with the thickness of the electrical double layer. While Equation 2-3 defines the repulsive forces in terms of particle charge, the relative magnitude of these forces is often discussed in terms of ζ -potential, the potential at the surface of

shear (Figure 2-2). This potential is generally more negative at high pH values, increasing the degree of electrostatic repulsion and consequently the stability of particles.⁸⁸ Particle stability is therefore dependent upon both solution pH and ionic strength.

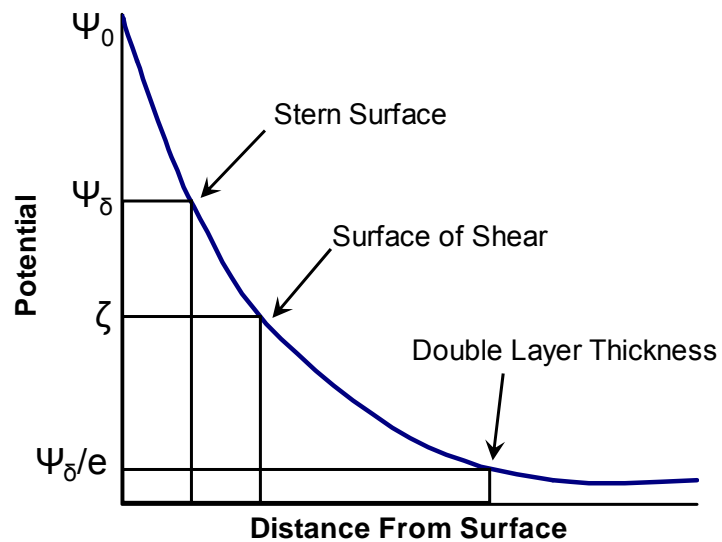


Figure 2-2. The relative magnitudes of various double-layer potentials of interest
 Figure adapted from Hiemenz and Rajagopalan³

As stated above, the total interaction energy between two particles is the sum of the Van der Waals attractive energy and the energy due to electrostatic repulsion as shown in Figure 2-3(A). Similar trends have been reported in the literature.³ These curves were calculated according to Equations 2-2 and 2-3 assuming a temperature of 20°C and using various ionic strengths. However, an arbitrary value was used for the particle charge, and the value used for the Hamaker constant was only approximate.⁴⁰ These energy curves are therefore only intended for qualitative purposes.

The dependence of particle spacing on colloidal stability can be seen in Figure 2-3(A). When the distance between particles is large, their interaction energy is effectively zero. At smaller inter-particle spacings, electrostatic repulsion creates a potential energy barrier to aggregation, corresponding to the shaded area of the plot. If a collection of particles acquires enough energy to overcome this barrier, aggregation will occur. This energy can come from a number of sources, most notably heat or mechanical stirring.³ It is also noted that when electrostatically-stabilized particles are removed from solution, the distance between them goes to

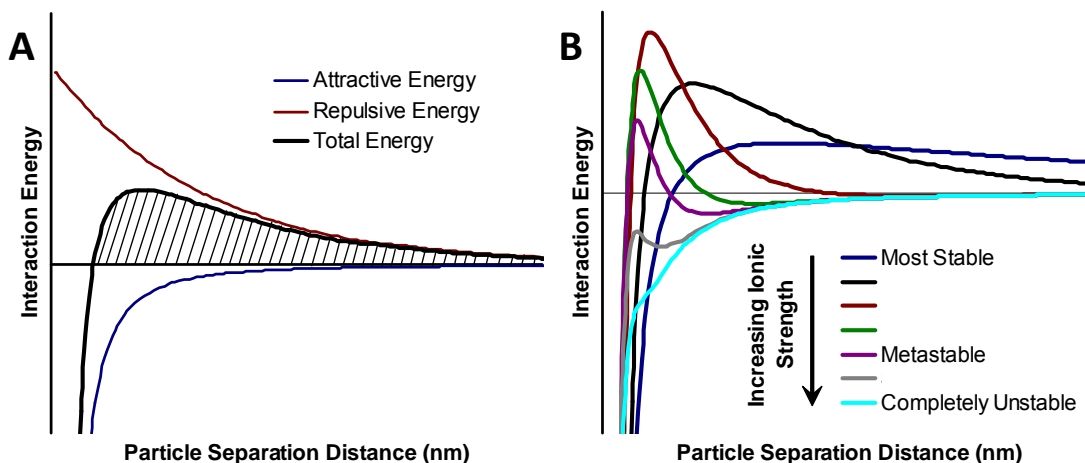


Figure 2-3. Potential energy curves for the interaction of two colloidal particles (A) Total interaction energy as a function of particle separation distance calculated from the sum of the van der Waals attractive energy and the energy due to electrostatic repulsion. The shaded area represents the potential energy barrier to aggregation. (B) Changes in total interaction energy observed for different values of ionic strength; the black curve in this plot corresponds to the black curve in (A). Similar trends have been reported in the literature.³

These calculations were performed according to Equations 2-2 and 2-3 assuming a temperature of 20 °C and using various ionic strengths. However, an arbitrary value was used for the particle charge and the value used for the Hamaker constant was only approximate.⁴⁰ These energy curves are therefore only intended for qualitative purposes.

zero and irreversible aggregation occurs. At this point, particles cannot be re-dissolved into solution.

One of the most significant factors that affects the inter-particle spacing and colloidal stability is the thickness of the electrical double layer, which decreases with the ionic strength of the particle solution (Equation 2-1). For instance, it has been shown that the addition of NaClO_4^- to gold particles results in aggregation due to the compression of the electrical double-layer.⁸⁹ However, the adsorption of ClO_4^- ions to the surface also leads to slight increases in the stabilizing surface potential. Both of these factors contribute to the expression for repulsive energy in Equation 2-3. The repulsive energy decreases exponentially with the Debye-Huckel parameter and thus with the ion concentration (Equation 2-1). However, the barrier height increases slightly before it decreases due to the increased charge on the particle surface, which is accounted for by the pre-exponential term. This behavior is shown in Figure 2-3(B), which qualitatively depicts how the potential energy curves change with ionic strength. It can be seen that the distances over which the repulsive forces act decrease with ionic strength. It is also noted that as both the magnitude of the repulsive energy and the barrier height decrease, secondary minima are observed (purple curve) indicative of metastable particle solutions. With further decreases in the repulsive energy, the attractive forces dominate at all separation distances and

particles become unstable (aqua curve). The concentration of ions at which particles become unstable is known as the critical flocculation concentration (cfc).

This is a simplified view of particle interactions contributing to electrostatic stabilization and assumes no overlap of the electrical double layers around different particles. In addition, when aggregation occurs on a slower time scale, the process can be complicated by the movement of surface-adsorbed ions between particles.⁹⁰ After two particles have coagulated, the potential is not uniform around the aggregate, and this affects the mechanism for future flocculation.

2.1.1.2. Steric Stabilization

While the mechanism associated with electrostatic stabilization is associated with surface charges, steric stabilization is attributed to molecules or polymers bound to the surface as shown in Figure 2-1(B). These capping ligands mask the strong Van der Waals attraction between particles in addition to generating steric repulsion. Both of these effects increase particle stability. Unlike electrostatic stabilization, stability in this case is generally not as sensitive to pH and ionic strength. The capping ligand can even be chosen so that particles are soluble in non-aqueous solvents. In contrast to electrostatically-stabilized particles which irreversibly aggregate when removed from solution, sterically-stabilized particles can often be precipitated from solution and then re-suspended.

There are several factors that determine the degree of stability provided by a steric capping layer, including the packing density of molecules on the surface, the strength of the interaction between the molecule and the particle, and the size and the solubility of the adsorbed molecules. In the case of polymers, the degree of steric repulsion is also affected by their free energy of mixing with both the solvent and adjacent polymers.⁸⁴ Because of the demonstrated strength of the gold-sulfur interaction, thiols are most commonly used to stabilize gold particles.^{88,91} However, partial desorption of the thiol capping ligand has often been observed with negative effects on colloid stability.⁸⁸ Attempts to minimize these effects have included using ligands with multiple thiol-functionalities⁹¹ and longer chain lengths,² both of which improved overall stability. There are disadvantages associated with steric stabilization for particle applications where surface activity is desirable, i.e. for catalysis. Steric hindrance significantly limits the access of other molecules to the particle surface, and there is an obvious tradeoff between particle stability and reactivity.

Some particles are stabilized by both steric and electrostatic forces, a mechanism often referred to as electrosteric stabilization. The molecular layer bound to the particle contains ionizable groups, which form an electrostatic barrier. For example, carboxylic-acid terminated thiols allow gold particles to be dispersed in water, and, within a certain pH range, the carboxylate is deprotonated creating an electrostatic

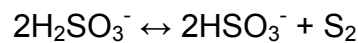
barrier in addition to the steric protection offered by the molecular capping layer.⁸⁸ These negatively charged groups can also be used to react with or adsorb to other organic or biological species, adding functionality and reactivity to the particles.⁸⁸ Polyelectrolytes, proteins and surfactants are also used as electrosteric stabilizing agents.

2.1.2. Particle Formation

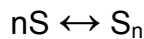
2.1.2.1. Mechanisms for Particle Formation

Most solution-based particle formation occurs through nucleation and growth. Typically, a heterogeneous colloid solution is formed from a homogeneous reactant solution. Something in solution, such as the reduction of a metal salt, triggers the formation of nuclei, which then grow into particles until the reactant is exhausted. The key to obtaining a monodispersed colloid solution is the separation of the two processes, nucleation and growth. If nuclei continue to form during particle growth, the solution will contain particles in various stages of growth and the final particles will be significantly polydispersed. Monodispersity requires that nucleation be completed once growth has begun. In order to synthetically control these factors, a more detailed, mechanistic understanding of particle formation is desired. A few mechanisms have been proposed, although their general applicability has yet to be demonstrated.

In 1950 LaMer proposed a mechanism for the formation of sulfur particles, which suggested that effective separation of nucleation and growth could be achieved through proper control of solution concentration.^{8,92} With this control, a short burst of nucleation followed by slow, diffusion-controlled growth could yield monodispersed particles.^{8,92} His observations were based on the formation of molecularly-dissolved sulfur from thiosulfate according to the reaction scheme:



As the reaction progresses, the concentration of sulfur increases to supersaturation at which point nuclei begin to form through a series of bimolecular additions:

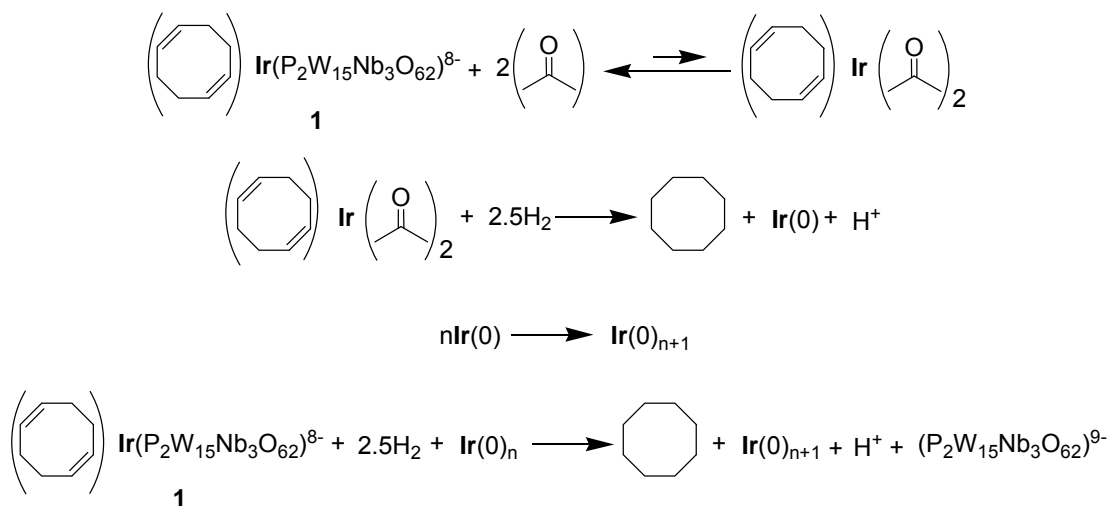


LaMer argued that supersaturation is a requirement for nucleation as the probability for bimolecular interactions is not high enough at lower concentrations to overcome the thermodynamic energy barrier to nucleation.^{8,92} Once the concentration of sulfur in solution drops below this critical value, nucleation ceases. Thus, with proper control over the initial reagent concentrations, a short burst of nucleation could consume enough sulfur to sufficiently lower the solution concentration and prevent further nucleation. If the initial solution is concentrated enough such that nucleation does not relieve the supersaturation, nuclei will continue to form during particle growth resulting in significant polydispersity.

Particle growth occurs as molecularly-dissolved sulfur diffuses to the existing nuclei. This process is thermodynamically-favorable and occurs spontaneously with diffusion as the limiting factor to the rate of growth. The size of the monodispersed colloid is then dependent upon both the number of nuclei which initially form and the amount of sulfur in solution. The rate of particle growth is dependent upon the diffusion coefficient which increases with solution temperature and decreases with solution viscosity. It has been reported that during a slow growth process, the atoms that attach to the surface of the nucleus are in equilibrium with the atoms in solution.⁹³ If they attach in a manner that is not the most thermodynamically stable, they can detach and return to solution. In addition, surface diffusion and possibly even interparticle exchanges of atoms occur to achieve the most thermodynamically stable structure.⁹⁴

In 1997 Watzky et al.⁸ argued that LaMer's mechanism, while possibly relevant for sulfur particle growth, is not applicable to all colloidal systems. They proposed an alternate mechanism based on their studies of iridium nanoclusters. While LaMer claimed monodispersed particle formation could be achieved through a short burst of nucleation followed by slower, diffusion-controlled growth, Watzky provided evidence for a slow nucleation step followed by fast autocatalytic surface growth.⁸

The iridium nanoclusters studied by Watzky et al.⁸ were formed from a five-coordinate precursor involving cyclooctadiene and a polyoxoanion as shown in



Scheme 2-1. Mechanism proposed for the autocatalytic nucleation and growth of iridium clusters. Scheme adapted from Watsky et al.⁸

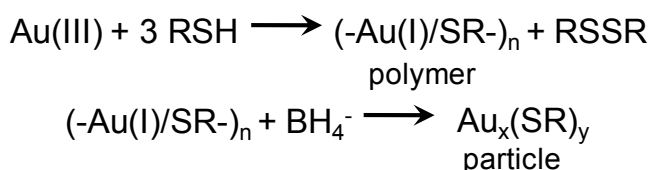
Scheme 2-1. The reduction of this complex occurs by a two-step process involving first the complexation with acetone and then the subsequent reduction by hydrogen. As iridium is reduced, nuclei begin to form.

According to the mechanism proposed by Watsky et al.,⁸ two competing effects determine the critical nucleus size. There is an enthalpic gain associated with the formation of iridium bonds within the nucleus, but an enthalpic cost due to the surface energy created upon nucleation. It is the balance between these energy contributions that determines the nucleus size, and supersaturation is not required. Once these nuclei are formed, they act as the catalyst for the reduction of additional iridium atoms, facilitating the growth process. The autocatalyzed growth process occurs at a much faster rate than nucleation but is not diffusion-limited. Because the

iridium reduced in the autocatalytic reaction contributes to growth rather than nucleation, one can achieve the sufficient separation of these two processes required for monodispersed particles.⁸

Turkevich et al. proposed yet a different mechanism for the nucleation and growth of gold particles, which involves the organization of ions into a polymeric form before nucleation.⁹⁵⁻⁹⁷ In both acidic and neutral solutions, the copolymer consists of gold ions while in basic solutions, the polymerization likely involves gold hydroxide.

When binding to gold, the reducing agent must be a polydentate, coordinating species so it can bind to multiple gold ions. In the case of gold-citrate particles, it was shown that it was actually not the citrate that was incorporated into the polymer, but rather acetone dicarboxylic acid (ADCA), one of the products of citrate reduction. There is an induction period before nucleation begins which is attributed to the time required to produce ADCA. Once a sufficient concentration of gold ions is achieved, the polymer is reduced and a nucleus forms. Similar to Watsky's theory, nucleation



Scheme 2-2. Proposed mechanism for the formation of thiol-terminated gold particles^{1,2}

is believed to occur when the favorable, cohesive lattice energy is greater than the unfavorable surface energy created upon particle formation.⁹⁷

Nuclei were observed to be approximately 3 to 5 nm upon formation which supports this type of mechanism.^{95,96} The number of gold atoms associated with nuclei of this size is on the order of a million, and it seems unlikely that this number of ions would associate by collision as described by LaMer.

Once a sufficient number of nuclei are formed, the growth process takes over. The growth process is a one-step autocatalytic process catalyzed by the nucleus while the nucleus formation is a multi-step process dependent on the polymerization of the gold ions and the capping ligands.⁹⁷ Standard citrate sols are often composed of several crystallites,⁹⁷ which supports the theory of fast growth in contrast to the single crystals expected for slower growth processes. A similar mechanism involving the formation of a precursor polymer has been reported for the formation of thiol-terminated gold particles.^{1,2,91,98-100} As shown in Scheme 2-2, a 3:1 ratio of thiol/gold is necessary for a stoichiometric polymer.^{1,2} Lower ratios yield particles with increased polydispersity.

LaMer, Watzky and Turkevich each provided significant evidence to support their proposed mechanisms, indicating that there is not a general mechanism that applies to all colloidal systems. In the subsequent discussion of various nanoparticle syntheses, other mechanisms and variables will be discussed. However, the underlying theme throughout all synthetic procedures is control over both the kinetics and thermodynamics of nucleation and growth. For example, fast nucleation

and slow growth results in a large number of nuclei and smaller particle sizes. Likewise, slow nucleation and fast growth yield a smaller number of larger particles.

The rate of nucleation can be affected the concentration and the strength of the reducing agent used.^{72,101,102} For thiolated gold particles, it has been reported that increasing the amount of reducing agent increases particle size.² For some particles, however, this increase leads to significant polydispersity and larger degrees of aggregation.¹⁰² Likewise, replacing a strong reducing agent such as tetrabutylammonium borohydride (TBAB) with a weaker one such as hydrazine increased the average particle size of gold particles.¹⁰¹ Using a combination of hydrazine and TBAB yielded more control over the particle size. It was assumed that TBAB was consumed during the nucleation process and then hydrazine participated in particle growth.¹⁰¹ A similar procedure was adapted for gold-citrate particles.¹⁰³ Tannic acid is a stronger reducing agent than sodium citrate and increasing the concentration of tannic acid in solution led to distinctly smaller particles. In addition, the rate at which reducing agent is added to the solution affects particle dispersity with faster addition yielding more monodispersed particles.^{101,102}

Another factor that affects the kinetics of nucleation and growth and consequently particle size for sterically-stabilized particles is the concentration of the stabilizing ligand in solution. These molecules can hinder particle growth yielding smaller

particles.^{2,19,72,101,102,104} The stronger the interaction between the molecule and the particle, the greater this effect. Decreasing the concentration of stabilizing ligand can result in increased particle size; however, there is a point at which this decrease leads to larger polydispersity and aggregation.² There have also been cases where the presence of stabilizing ligands hinders nucleation, resulting in a small number of nuclei and larger particles.¹⁰¹

In addition to the selection of the type and concentration of the capping ligands, there are several other techniques that can be used to control the size, shape, dispersity and surface chemistry of particles. The size and dispersity can be controlled using seed-mediated growth and digestive ripening techniques. The shape can be controlled by the nature of the stabilizing ligand or by the use of micelles or templates. In addition, ligand-exchange processes can be used to tailor the surface chemistry of particles.

2.1.2.2. Size Control

In general, both thermodynamic and kinetic factors affect particle size, geometry and dispersity. One method for controlling the size and dispersity of nanoparticles is through seed-mediated growth.^{19,72} Seed-mediated growth is a method of synthesizing larger particles without the increased polydispersity and aggregation associated with decreasing the amount of capping ligand or increasing the amount of reducing agent in solution. Smaller nanoparticle 'seeds' are synthesized and then

injected into a solution containing additional metal salt and reductant. Reduction of the metallic salt facilitates growth onto the smaller seeds yielding larger particles. This process can be repeated to grow multiple generations of increasingly larger particles. It is possible that the nanoparticle seeds can catalyze additional nucleation with negative effects on polydispersity, but this is generally not a significant effect.⁷² In general, particles synthesized in this manner are more monodispersed than larger particles formed through a one-step synthesis.¹⁰⁵ The slower growth process allows for particle structures to be formed according to thermodynamic considerations rather than kinetic ones and the final particle structures are generally more thermodynamically stable.

Similarly, digestive ripening allows for particles to form more monodispersed, more thermodynamically stable particles. The process generally involves heating a colloidal suspension in the presence of the stabilizing ligand, and yields smaller, more monodispersed particles.^{6,19,101,106,107} There are some reports in the literature that argue that the enthalpy gained through the ligand-gold binding balances the enthalpy lost by creating smaller particles with higher surface energy.¹⁰⁷ Therefore, smaller particles are observed when employing ligands that exhibit stronger binding to the particle. For example, gold particles were smaller after digestive ripening in the presence of thiols than they were in the presence of amines, which exhibit weaker bonds with gold.¹⁰⁷

Additional methods developed to control the nucleation and growth processes, and consequently the size and dispersity of the resulting particles, include the hot-injection method and the thermal decomposition of metal-surfactant complexes. The hot injection method involves injecting the metallic precursors into a solution to achieve supersaturation and fast nucleation.¹⁰⁸⁻¹¹⁰ For example, CdSe particles were synthesized by injecting the organometallic precursors, CdMe₂ and Se in trioctylphosphine, into a solution of trioctylphosphine oxide (TOPO) at 300 °C.¹⁰⁹ This rapid increase in reactant concentration incited the immediate formation of CdSe nuclei. According to LaMer's theory, nucleation relieved the supersaturation and nucleation ceased when the solution was no longer supersaturated.¹⁰⁸ In addition, in this example, the solution temperature decreased to 170°C after the injection of the room temperature precursor solution. As the nucleation process in this instance was temperature-dependent, this decrease also contributed to the cessation of nucleation.^{108,109}

In the hot-injection method, after the injection of metallic precursors and the subsequent nucleation, growth occurs through slow, controlled heating of the solution.¹⁰⁸ The size of the particles increases with the solution temperature; although increasing the temperature by too much can lead to uncontrolled growth. Proper control over the growth kinetics can yield thermodynamically stable particles. In addition to temperature effects on the growth kinetics, the TOPO molecules

interact with the particle surface affecting the growth kinetics. The composition of the hot solution can be altered with shorter chain alkylphosphine oxides yielding faster growth rates.¹⁰⁹

Another method applied to control the size and dispersity of palladium particles involved the thermal decomposition of palladium-surfactant complexes¹¹¹. This method was initially developed by Hyeon et al. for the synthesis of metal oxide particles.¹¹²⁻¹¹⁸ Rather than forming particles from a metal salt, a metal-surfactant complex was synthesized and then slowly heated to temperatures in the range of 300 °C. Initial data associated with the formation of metal oxide particles, obtained using both thermogravimetric analysis and differential scanning calorimetry, suggested that one ligand in the complex disassociated at a lower temperature than the others.¹¹⁴ Nucleation occurred with the dissociation of the first ligand and growth occurred at higher temperatures with the dissociation of the remaining ligands.¹¹⁴ The efficient separation in time of nucleation and growth led to the formation of monodispersed particles. A more recent study indicates that the separation of nucleation and growth occurs in a way similar to that proposed by LaMer.¹¹² The decomposition of the metal-surfactant complex creates the active species in solution. Once the concentration of this intermediate species reaches super-saturation, nucleation occurs followed by growth once the super-saturation is

relieved. The monodispersity of the particle solution can be attributed to digestive ripening, which occurs at these higher temperatures.

Yet another method for controlling the size and dispersity of particles is through the use of microwave heating. In general, microwave heating has been able to produce nanostructures with smaller sizes, narrower size distributions, and higher degrees of crystallization than those obtained through convention oil-bath heating.¹¹⁹ In oil-bath heating, the solvent is heated by conduction and convection, so that there is a large temperature distribution within the solvent. The rapid and uniform heating typically achieved in microwave procedures accelerates the reduction of metal precursors and the nucleation of the metal clusters, resulting in small, monodispersed nanostructures.¹¹⁹

2.1.2.3. Shape Control

The shape of nanostructures is also determined by both thermodynamic and kinetic considerations. The most stable nanostructure geometries are spherical particles as they have the least surface area and thus the least total surface energy. Likewise, the surface of a particle generally consists of low-index crystallographic planes, which have the lowest surface energy.⁷² However, as particles of different shapes exhibit unique optical, electronic and catalytic properties, there have been significant efforts to gain kinetic control of particle reaction conditions in order to synthesize particles of various shapes.^{10,12,22,23,110,120-122}

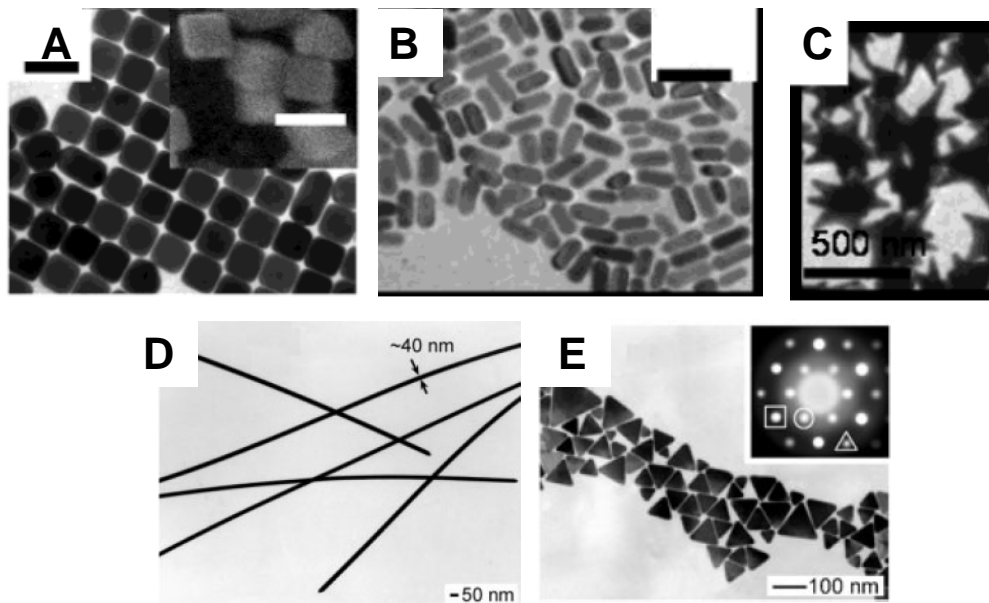


Figure 2-4. Nanoparticles of different shapes achieved through kinetic control of reaction conditions (A) Gold nanocubes, scale bar = 100 nm (B) Rod-shaped gold particles scale bar = 100 nm (C) Gold multipods. Images of gold particles were taken from Sau et al.¹⁰ (D) Silver nanowires. Image taken from Xia et al.¹²⁻¹⁴ (E) Triangular silver nanoparticles. Image taken from Wiley et al.²³

One of the most common methods for achieving shape control during particle syntheses is by incorporating ligands that promote anisotropic growth. Some ligands bind preferentially to certain crystallographic planes hindering growth in these directions and, under kinetic control, yielding particles of different shapes.^{4,110,120,121,123-126} For example cetyltrimethylammonium bromide (CTAB) appears to bind more strongly to the [100] faces of gold particles than the [111] faces.¹⁰ Injecting gold seeds into a solution containing a moderate amount of CTAB and a sufficient concentration of reducing agent promoted growth on the [111] faces yielding cubic structures.¹⁰ The concentration of reducing agent should be high

enough to facilitate the fast deposition of gold atoms so that kinetic factors overcome any thermodynamic barriers to the formation of these shapes. Likewise, poly(vinylpyrrolidone) (PVP) binds more strongly to the [100] faces of silver particles promoting growth in the [111] direction. By changing the ratio of AgNO_3 to PVP in solution, one can achieve cubes²³ and wires.^{12,23} Figure 2-4 shows gold and silver particles synthesized using various concentrations of seed particles, reducing agent and stabilizing ligands.

The preferential adsorption of ions to different crystalline faces can also yield particles of different shapes.⁴ In the presence of NaCl, copper particles have been shown to form rods with an aspect ratio determined by the chloride concentration.⁴ Changing the nature and concentration of the anion from Br^- to F^- and NO_3^- yielded a variety of shapes in many different sizes.

The kinetically controlled growth of particles can be further applied to the formation of more intricate particle geometries through oriented attachment.^{7,80,110,127} This process, which has been applied to several different semiconductor nanoparticles, involves injecting particle seeds of one crystal structure into a solution which facilitates growth of a different crystal structure. As shown in Figure 2-5 (A), this can be done so that the crystallographic faces align creating branched structures. CdSe nanocrystals injected into hot trioctylphosphine oxide (TOPO) with hexylphosphonic acid (HPA) yielded a wide variety of structures including rods, arrows, teardrops and

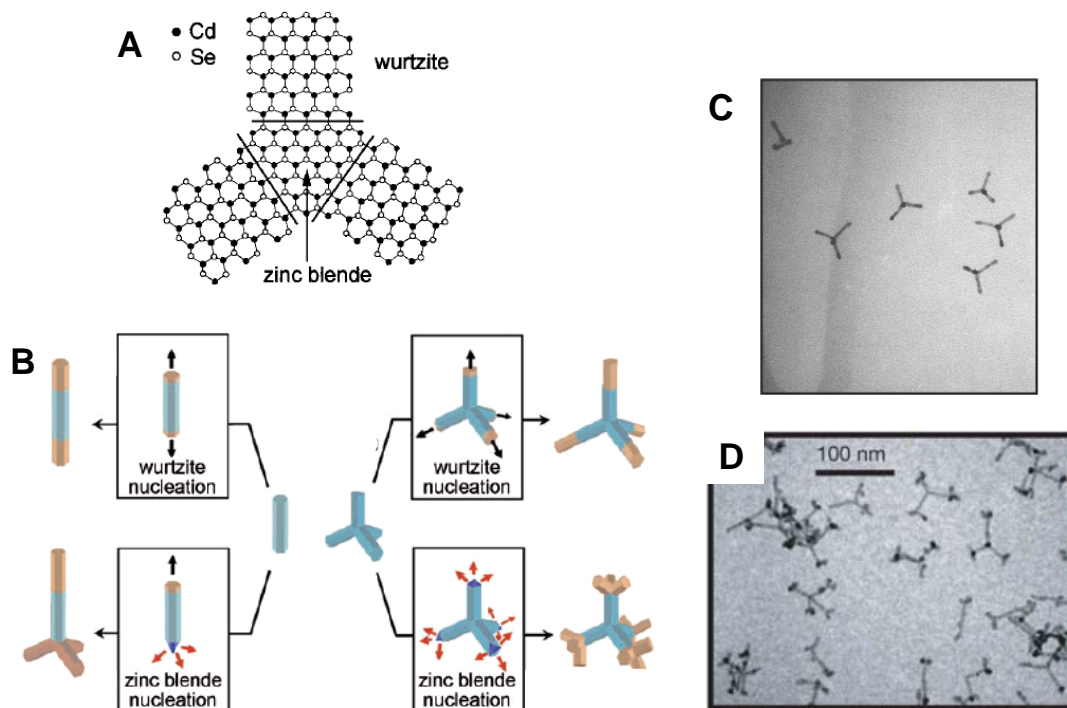


Figure 2-5. Branched structures created through nucleation on seed crystals. (A) Two-dimensional representation of crystal structure of a tetrapod. Figure taken from Manna et al.⁷ (B) Schematic of the formation of heterostructured rods through the controlled addition of CdSe extensions to CdS nanorods. Figure adapted from Jun et al.^{14,22} (C) CdTe tetrapods. Image taken from Manna et al.⁸⁰ (D) Branched tetrapods formed from the nucleation of CdTe on the branches of CdS tetrapods. Image taken from Milliron et al.^{54,82}

tetrapods. The final particle morphology was controlled by the ratio of surfactants, i.e. TOPO:HPA, the injection volume and the monomer concentration.⁷ The presence of HPA appeared to promote growth on the [001] faces relative to all other faces. It is unclear whether this effect was due to interactions of the HPA with the particle surface or whether the acidic conditions resulted in partial protonation of crystal facets controlling growth.⁷ Repeated injections can lead to intricate

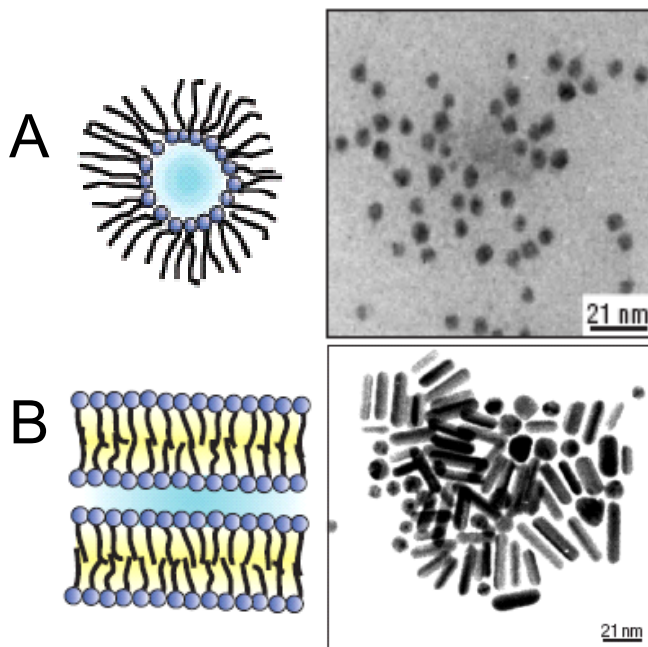


Figure 2-6. Different shapes of copper nanocrystals formed in reverse micelles.
 Figure adapted from Pileni et al.⁴

branching patterns and structures resembling inorganic dendrimers.¹¹⁰ Some examples of these structures are shown in Figure 2-5.

Another method for controlling particle shape and size is through the use of templates, often in the form of reverse micelles.^{4,6,128-133} Surfactant molecules with small polar heads and branched

hydrocarbon chains form reverse micelles as shown in Figure 2-6, the size of which increases linearly with the amount of water present in the system.^{4,128} As the water concentration increases further, the shape of the micelle changes, yielding particles of different shapes. Copper structures formed in micelles of $\text{Cu}(\text{AOT})_2$ are shown in Figure 2-6. In addition to control over particle size and shape, the use of reverse micelles facilitates the formation of particles from metals that are easily oxidized (e.g. iron and nickel). and the use of strong reducing agents, which are easily hydrolyzed (e.g. LiBH_4).⁶

In addition to reverse micelles, other types of templates have been used for synthesizing particles.

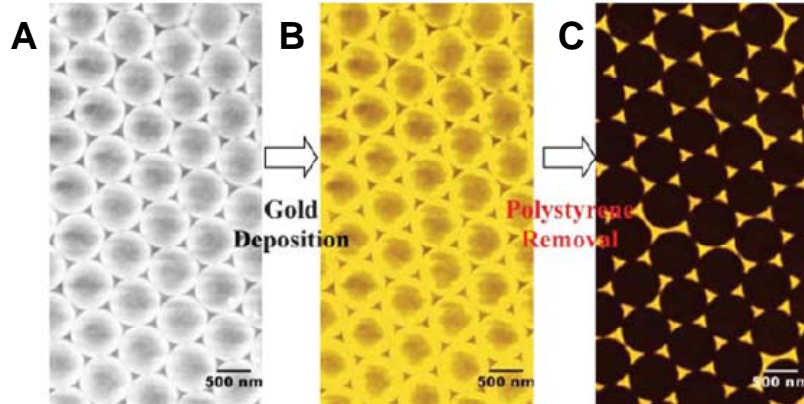


Figure 2-7. Sacrificial polystyrene template used to form triangular gold nanoparticles (A) deposition of polystyrene spheres on a substrate (B) thermal evaporation of gold onto substrate (C) removal of polystyrene spheres to leave triangular gold nanoparticles. Figure taken from Eutis et al.⁹

Dendrimers have been used as templates for the synthesis of copper, platinum and palladium particles.¹³⁴⁻¹³⁶ The amine groups in the interior of poly(amido-amine) dendrimers adsorbed metal ions from solution. These ions were subsequently reduced to form particles. The number of atoms in each particle corresponds to the number of amine functionalities in the dendrimer, and thus the size of the particles can be altered by tailoring the size and structure of the dendrimer template. Palladium particles have also been synthesized using a liquid crystal template.¹³⁷ The palladium salt was incorporated into the cylindrical channels within the lyotropic crystal before reduction with hydrogen gas. Figure 2-7 shows a method for synthesizing triangular gold particles using a sacrificial template of polystyrene particles.

2.1.2.4. Ligand Exchange and Phase Transfer

Previous sections have discussed how the nature of the stabilizing ligands present during particle synthesis can affect the size, dispersity and shape of the resulting structures. However, the surface functionality is important for many nanoparticle applications, especially when the reactivity of particles is important. For this reason, it is sometimes desirable to exchange the capping ligands after particle synthesis. This exchange can be done within the same phase or to effect phase transfer.

A general mechanism for ligand-exchange has not been identified, and likely varies with particle composition and the ligands involved. Exchange typically involves two steps. Fast exchange usually occurs at places on the particle surface easily accessible to an incoming molecule, such as edge and vertex sites.¹³⁸⁻¹⁴¹ On crystalline faces where the molecules are tightly packed, exchange is slower. For ligand-exchange reactions where one thiol is replaced by another, the proposed mechanism is associative, i.e. S_N2 , with rate-determining step being the protonation of the bound thiol by the incoming thiol.^{91,142} In this case, the rate decreases with the bulkiness of the incoming ligand. It has been observed that long ligands replace short ligands, but not vice versa.¹⁴³ In addition to steric issues, the Van der Waals forces between long alkyl chains create a larger barrier to displacement.^{141,143} In contrast, the proposed mechanism for replacing weakly-bound ligands such as sulfides and amines is dissociative, i.e. S_N1 , with the rate-determining step being the

desorption of the bound ligand.¹⁴² Another mechanistic study involving the replacement of phosphines with thiols on gold indicated that the reaction was not purely associative or dissociative, but involved several steps specific to the particular reaction.¹⁴²

There are several factors that affect the rate and the extent of ligand-exchange for a reaction in solution. For exchange reactions that occur in organic media, the critical factors are the amount of ligand added to solution, and the relative steric bulk and chain lengths of the two ligands involved.⁹¹ For the exchange of triphenylphosphine (TPP) -coated gold particles with thiol, it was observed that a significant excess of thiol was required in order to achieve complete exchange; however, too large an excess led to particle decomposition.¹⁴² The rate and the extent of exchange also decreased with the steric bulk of the incoming ligand. In addition, the strength of the particle-ligand interaction plays a role. There are several reports in which particles were synthesized in the presence of weakly adsorbing ligands, which were then replaced with more strongly-binding thiols.^{101,144,145} It has also been reported that the rate and extent of ligand-exchange increases with the positive charge of the metallic core of gold particles.¹⁴⁰

For ligand-exchange reaction in aqueous solutions, the ionic strength and pH of the solution likely play a role as well.^{142,146} For gold particles capped with phosphine ligands, ligand-exchange with thiols required a pH between 5 and 8.¹⁴² Lower pH

values resulted in particle decomposition while higher pH values resulted in disulfide formation. In addition, the pH must be high enough that any acidic ligands used in ligand-exchange are ionized. A negative charge is required to ensure stability through electrostatic stabilization of the particles against aggregation.

Additional complications arise when ligands are introduced to electrostatically-stabilized particles. For example, citrate readily desorbs from gold particles. When gold citrate particles are in the presence of thiols, the electrostatic repulsion is quickly diminished due to the fast desorption of the citrate, which sometimes leads to irreversible adsorption of one particle onto another.¹³⁸ Slower desorption of the bound capping layer is necessary to prevent against aggregation during exchange. This has been accomplished through a two-step functionalization process wherein the adsorbed citrate and chloride ions were displaced by thioctic acid (TA) before the thiols were introduced.¹³⁸ The desorption of TA from the gold particle surface is significantly slower than that of citrate so that that electrostatic stabilization is not lost until sufficient steric stabilization has been achieved.

Ligand-exchange can be used to alter the size of nanoparticles in addition to their surface chemistry.¹⁴⁷ This size modulation is generally not observed when the exchange involves molecules of similar functionality. For example, while there were negligible size differences observed for gold particles after the ligand-exchange of one thiol for another,¹⁴⁸ TPP-capped gold particles exhibited an increase in core

size after ligand exchange with thiolates.^{142,148} Similarly, when TPP-capped particles underwent an exchange with 1-pentadecylamine, the core diameter increased by a factor of almost four.¹⁴⁴ There have been other reports where ligand-exchange yielded particles with deformed shapes and broadened size distributions.¹⁴⁹ The mechanisms associated with these changes in size are not clearly understood; however there has been some speculation that differences in stability and basicity of the ligands involved is relevant to the mechanism.¹⁴⁸

There have been significant efforts expended in transferring particles from organic to aqueous phases. There are many applications, especially biological applications, where water-soluble particles are desirable. However, aqueous particle syntheses are often subject to detrimental ionic interactions and can only be carried out at extremely low concentrations.¹⁵⁰ Particles synthesized in organic solvents do not suffer either of these limitations and are generally more monodispersed.¹⁵⁰ For this reason, particles are often synthesized in organic solvents and then transferred to the aqueous phase. This transfer has been achieved by exchanging the hydrophobic ligands with hydrophilic ones.^{101,150-153}

Particles synthesized in organic solvent have also been brought into aqueous solution by encapsulating particles and their capping layers with surfactants or amphiphilic polymers. For example, CTAB was used to bring gold particles capped with dodecyl amine in chloroform into the aqueous phase.¹⁵⁴ The hydrophobic tail of

the surfactant molecule was attracted to the hydrophobic capping layer and was thought to form an inter-digitated bilayer while the ammonium groups were believed to impart water-solubility. Hydrophobic quantum dots and iron oxide particles have similarly been brought into the aqueous phase using surfactants and lipids.¹⁵⁵⁻¹⁵⁷ In addition to promoting solubility in the aqueous phase, the surfactants provide additional stability through both steric and electrostatic interactions. Amphiphilic

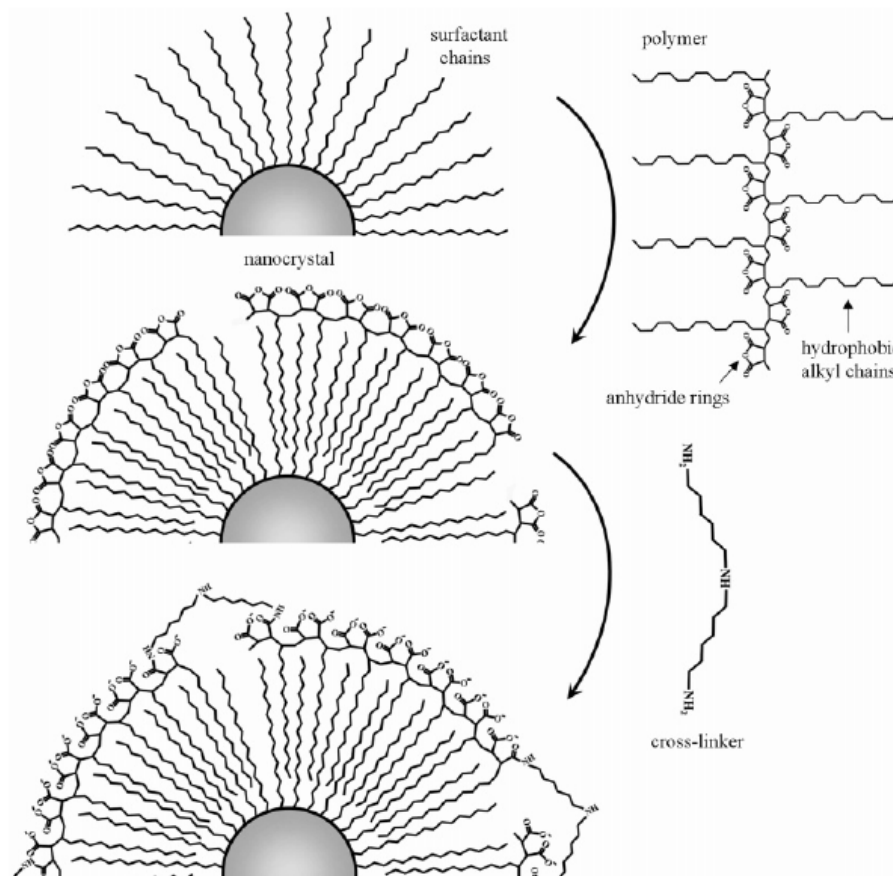


Figure 2-8. Schematic of encapsulating hydrophobic nanoparticle with amphiphilic polymer and then subsequent cross-linking of the polymer chains. Figure taken from Pellearino et al.¹¹

polymers have also been used to encapsulate hydrophobic particles and transfer them into the aqueous phase. For example, poly(maleic anhydride alt-1-tetradecene), which has hydrophobic side chains has been shown to promote the phase transfer of several particles.¹¹ As shown in Figure 2-8, the side chains are proposed to form an inter-digitated bilayer while the hydrophilic groups provide water-solubility. An amine was added to crosslink the polymer chains and impart additional stability. Yet another method used to bring particles into the aqueous phase involved 'threading' the hydrophobic capping layer through cyclodextrin molecules.¹⁵⁸ Cyclodextrin is a cyclic oligosaccharide with a semi-hydrophobic interior and a hydrophilic exterior. These molecules threaded themselves onto oleic acid imparting water-solubility to iron oxide particles.¹⁵⁸ While encapsulating particles has shown to be effective for phase transfer, the thick stabilizing layer provides a steric barrier to additional ligand-exchange or surface functionalization. Yet another method used to control the surface functionality is to chemically react the capping ligand with another molecule. For example, amide and ester linkages can be formed from carboxylic acids reacted with amines and alcohols, respectively.^{91,146,152,159} Gold particles functionalized with norbornenyl groups have been used to initiate ring-opening metathesis polymerization of norbornenyl ferrocene derivatives so that a block copolymer encapsulated the original particle.¹⁶⁰ One of the major challenges associated with this type of modification is that these

reactions must be carried out under conditions that do not negatively affect particle stability.

2.1.3. Organization of Particles

As the goal of this project is to synthesize and characterize covalently-bound nanoparticle assemblies, it is important to understand other particle interactions so that they may be excluded when characterizing the bound structures. One of the most commonly observed types of structures involves the self-assembly of particles into two-dimensional and three-dimensional superlattices.^{3,19,22,72,81,161-172} These structures are often formed simply by the slow evaporation of solvent,^{22,81,162,170,172} and the degree of order increases with particle monodispersity.^{19,81,93} The inter-particle spacing is determined by the attractive and repulsive forces between particles discussed in more detail in Section 2.1.1. When the attractive forces between particles are weak, there is no significant driving force for lattice formation,

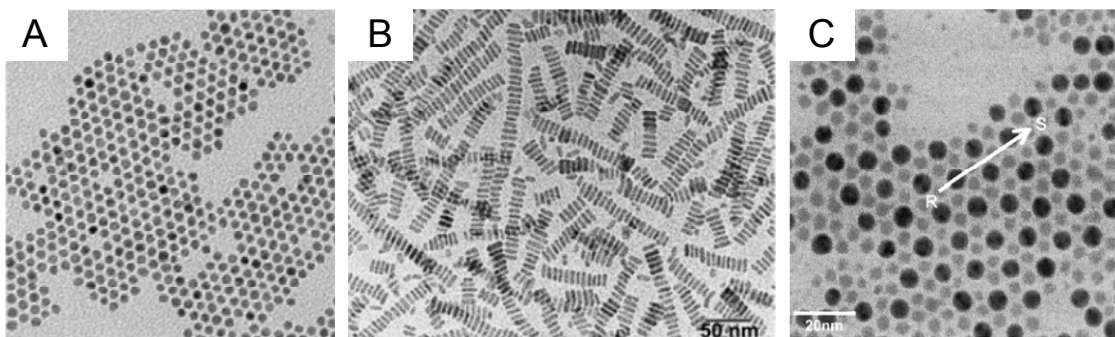


Figure 2-9 (A) Superlattice of thiolated gold particles. Image taken from Martin et al.⁶ (B) Ordered chains of BaCrO₄ nanorods. Image taken from Burda et al.²² (C) Bimodal superlattice of gold (dark) and silver nanoparticles. Image taken from Brust et al.^{50,81}

and weak repulsive forces lead to aggregation. Figure 2-9(A) shows a superlattice formed from thiolated gold particles. Superlattices have also been observed for CdSe, AgS, TiO₂, Ag, Co, Ni, Fe, Fe₂O₃, CoO, BaCrO₄ and FePt particles.^{22,166} Ordered structures are not limited to spherical particles. Figure 2-9(B) shows ordered chains of BaCrO₄ nanorods.²²

While the collective inter-particle forces generally determine the spacing between particles in a lattice or other ordered structure, there are many factors that affect these particle interactions and contribute to the final structure. There are several reports indicating that the ratio of core size to the length of the capping ligand is critical in determining the lattice packing.^{22,163-167} There have also been reports that the thickness of the electrical double-layer plays a role with large values yielding body-centered cubic (bcc) structures and smaller values yielding face-centered cubic (fcc) structures.³ The rate of evaporation, the wetting properties of the substrate, particle geometry¹²² and the orientation of crystal facets on the nanoparticle surface are also important.^{163,165} Stoeva et al.¹⁶³ observed that the crystallinity of the individual nanoparticles plays a role with single crystals forming fcc structures and polycrystalline particles favoring hexagonal close-packed (hcp) structures.¹⁶³ Interactions between capping ligands on adjacent particles also contribute to the formation of these structures. The distances measured between particles using both TEM¹⁰² and x-ray diffraction¹⁶¹ in superlattices containing alkane-thiol capped

particles indicate that the alkane chains on adjacent particles interdigitate, increasing the stability of these organized structures.^{81,102,161,163,167,171,173}

Superlattices can also be formed from particles of multiple sizes and compositions.

Bimodal superlattices have been formed from gold particles of two different sizes.⁸¹

The relative sizes and particle concentrations were adjusted in order to obtain the desired structure.²² This concept has also been applied to the formation of bimodal superlattices of gold and silver particles as shown in Figure 2-9 (C).⁸¹ In this image

the larger, darker particles are gold and the smaller particles are silver. Similar

structures have been formed from PbSe quantum dots and γ -Fe₃O₄ particles.^{22,174}

As with lattices formed from particles of only one composition, the solvent

evaporation rate, the substrate and the particle capping ligands play a role in the

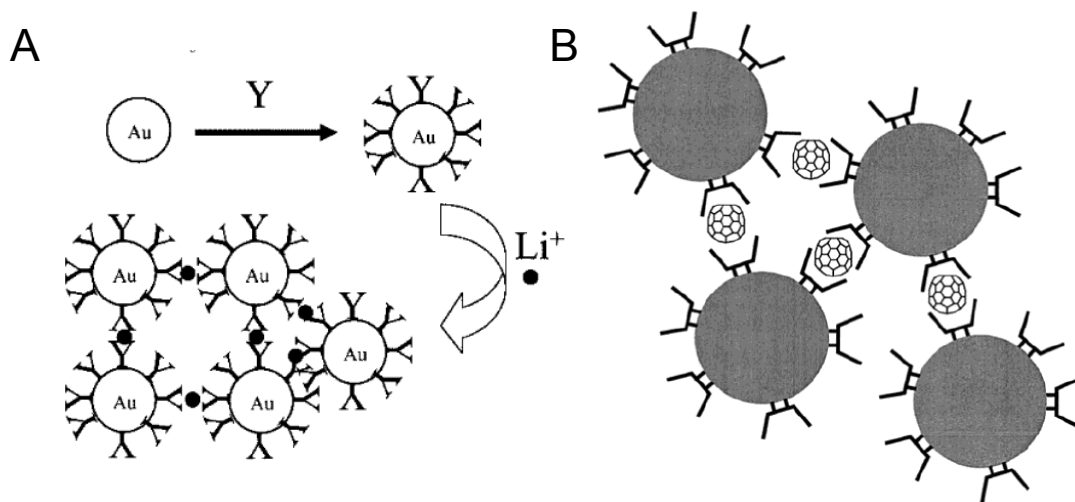


Figure 2-10. Noncovalent linking of nanoparticles (A) Network of gold particles capped with 1,10 phenanthroline and lithium ions. Schematic taken from Obare et al.⁵ (B) Network of cyclodextrin-capped gold nanoparticles induced by fullerene molecules. Schematic taken from Liu et al.^{14,51}

final structure.

Particle aggregates and assemblies can also be formed through non-covalent interactions such as hydrogen-bonding¹⁷⁵ and electrostatics. Johnson et al.¹⁷⁶ looked at the effects of the terminal functionality of the capping ligand on the properties of gold particles and observed significant aggregation due to hydrogen bonding between terminal functionalities on adjacent particles for particles terminated with amines and carboxylic acids. Su et al.¹⁷⁷ observed aggregation, which was attributed to hydrogen bonding between carboxylic acid-terminated thiols at low pH values and suggested electrostatic interactions between carboxylate groups on adjacent particles and adsorption of a mutual counter-ion may occur at higher pH values. Similar types of electrostatic interactions were reported for gold particles capped with 1,10 phenanthroline in the presence of lithium ions.⁵ A schematic of this type of network is shown in Figure 2-10 (A). The 1,10 phenanthroline selectively binds to lithium ions in a 1:2 ratio and facilitates the formation of larger nanoparticle networks. Fullerene has also been used as a non-covalent linker in the presence of cyclodextrin-capped gold particles as shown in Figure 2-10 (B).⁵¹ Fullerene molecules were attracted the hydrophobic interior of the cyclodextrin, and each fullerene formed a complex with two cyclodextrins on adjacent particles.

2.1.4. Properties of Nanoparticles

As mentioned earlier in this chapter, the properties of materials at the nanoscale often differ from those of the corresponding bulk materials. As many of the particles synthesized in this work were characterized by their optical properties, a brief discussion of their origin is included below. The electrical properties are also mentioned as they are relevant to the application of particles to electronic devices.

2.1.4.1. Optical Properties

When light interacts with a material, part of the incident radiation is scattered and part of it is absorbed. This phenomenon can be explained by Maxwell's equations, which describe how both the electric and magnetic vectors of light interact with matter. In 1908, Gustav Mie solved Maxwell's equations for the interaction of light with spherical metal particles smaller than the wavelength of light, a solution that

later became known as Mie Theory.¹⁷⁸ Mie's calculations showed that the oscillating electric field associated with electromagnetic radiation causes

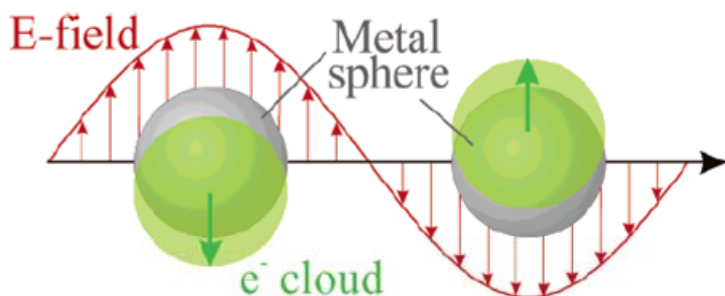


Figure 2-11. Schematic of Plasmon oscillation for a sphere, showing the displacement of the conduction electron charge cloud relative to the nuclei. Figure taken from Kelly et al.¹⁶

coherent oscillation of the electrons in the conduction band of the particle as shown in Figure 2-11^{9,16,179}. The incident field displaces the cloud of conductive electrons relative to the particle core and atomic nuclei. The attractive force between the atomic nuclei and electrons restores the position of the electron cloud before it is displaced in the other direction.¹⁶ This collective oscillation of electrons is known as the surface plasmon resonance (SPR) and greatly enhances both the absorption and scattering of light at the SPR frequency.¹⁷⁹ Smaller particles (i.e. < ~40-60 nm diameter) primarily absorb while both scattering and absorption occur with larger particles.¹⁷⁹ The enhancement of absorption and scattering associated with SPR can lead to emission more intense than many common molecular fluorophores. For instance, some reports claim that a single 40 nm gold particle scatters light with an intensity comparable to that emitted by 10^4 fluorescein molecules.^{179,180}

The frequency of SPR is determined by the electron density and the size and shape of the charge distribution.¹⁶ These variables are affected by both the particle and solution properties such as the nanoparticle geometry and the dielectric constant of the surrounding medium.^{9,16} The SPR frequency for a few metals, including gold, silver and copper, occurs within the ultraviolet and visible regions of the electromagnetic spectrum resulting in well-resolved absorption bands. However, as discussed in Section 2.1.4.2 in reference to platinum, palladium and nickel particles,

many metal colloids exhibit a continuous absorption in this range with apparent absorption maxima close to 200 nm.¹⁷

2.1.4.1.1 Effects of Nanoparticle Geometry

The electric field density on the particle surface, and consequently the SPR, changes with particle size and shape. For spherical noble metal particles, such as gold and silver, the absorption wavelength does not change significantly with size. Data presented later in Section 2.2.2.1 show that the absorption maximum for gold particles shifted from 520 nm to 540 nm as the particle size increased from 5 nm to 60 nm in diameter.

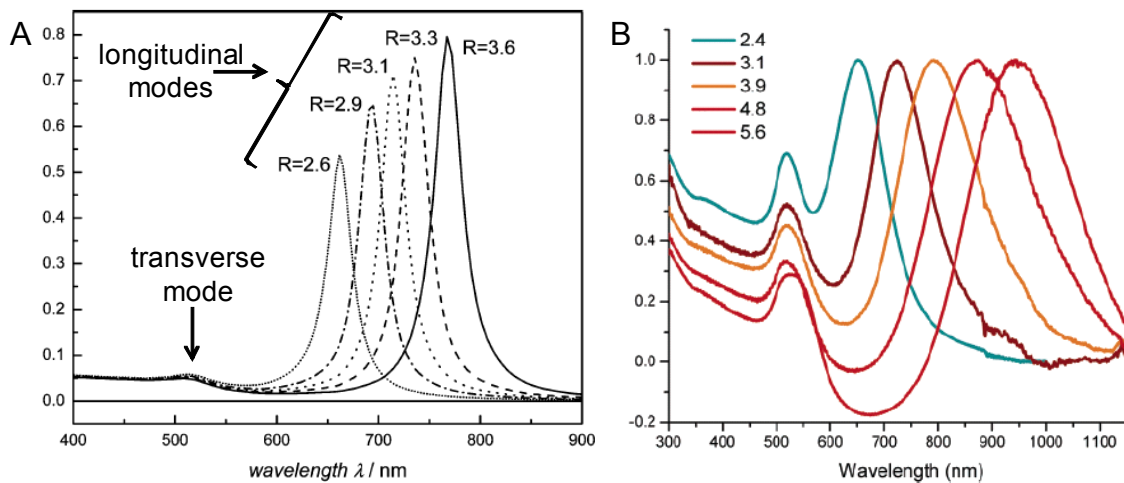


Figure 2-12. (A) Optical spectra calculated for gold ellipsoids of varying aspect ratios (R) using the dipole approximation and a dielectric constant of 2.05. Figure taken from Link et al.¹⁵ (B) Optical spectra of gold nanorods obtained for gold nanorods of different aspect ratios. Figure taken from Huang et al.⁶⁴

While the absorption wavelength did not change significantly with size for spherical particles of noble metals, more substantial changes have been observed for particles of varying shapes. According to Mie theory, anisotropic particles should exhibit more than one SPR band.^{16,21,181} However, analytical solutions that compute the optical absorption spectrum are not available for non-spherical particle shapes, and numerical methods are often used to predict their optical behavior. These include the discrete dipole approximation (DDA), the T-matrix method and the modified long-wavelength approximation (MLWA).^{16,180-189} Figure 2-12 (A) shows spectra calculated using the dipole approximation for ellipsoids, which clearly had two distinct SPR modes, a transverse mode corresponding to electronic oscillation along the short axis and a longitudinal mode corresponding to oscillation along the long axis.^{9,15,179,190} The peak due to the transverse oscillation occurred in the same region as that observed for spherical gold particles, while the peak due to the longitudinal oscillation occurred at significantly longer wavelengths depending on the aspect ratio of the rod or ellipsoid. Calculations showed that both the wavelength and the intensity of this peak increase with aspect ratio, which agreed with the experimental data shown in Figure 2-12(B). These data demonstrate the possibility of tuning the optical properties of a nanostructure by controlling the geometry.

The more distinct axes a particle has, the more SPR resonances it exhibits, and significant variation in optical properties have been observed when comparing spectra of particles with different, unique shapes. The absorption spectra of silver nanospheres were monitored as they were converted into triangular nanoprisms and while the peak at 400 nm disappeared, peaks grew in at 335, 470 and 670 nm.¹⁸¹ An additional peak grew in at 770 nm when the triangular corners were truncated. Complex optical behavior has also been observed in the calculated spectra of

truncated tetrahedral particles.^{183,187}

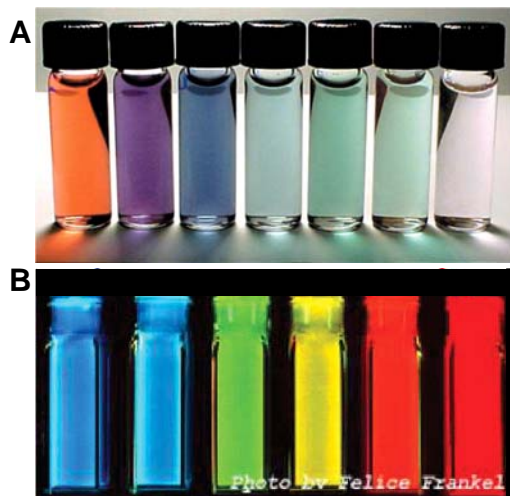


Figure 2-13. (A) Gold colloid nanoshells with decreasing shell thickness. Nanoshells consist of silica cores surrounded by a thin gold shell. The vial on the far left (red) contains gold colloids (no shell) The second vial (purple) contains gold nanoshells with a 60nm core and a 20 nm shell. The shell thickness decreases from left to right and is 5 nm for the vial on the far right. Figure taken from West et al.^{9,21}

(B) Fluorescence emission of (CdSe)ZnS quantum dots for particle sizes between 2.3 nm (blue) and 5.5 nm (red). Figure taken from Dabbousi et al.⁷⁹

The optical properties of particles can be further tailored through the synthesis of core-shell particles.^{21,191} By controlling both the overall particle size and the core/shell ratio, both the degree of absorption and scattering can be optimized to obtain optical resonances over most of the visible region and into the mid-infrared.²¹

Figure 2-13(A) shows gold nanoshells consisting of a silica

core and a thin gold shell. The SPR wavelength of the samples shown here spanned from approximately 750 nm to 1050 nm as the thickness of the gold shell decreased from 20 nm to 5 nm on a 60 nm silica core. Few molecular chromophores absorb in this region where biological tissue is relatively transparent, making these particles applicable for biomedical applications such as drug delivery and cell ablation.²¹ Other core/shell particles that have been reported include CdSe/CdS and Au/Ag.²¹

The optical properties of semiconductor particles are more sensitive to particle size than those consisting of noble metals. The bright colors associated with semiconductor particles are not generally associated with SPR frequencies, but with absorption due to electronic transitions from the valence band to the conduction band. Such transitions increase in energy with decreasing particle size. This energy gap is due to the quantum effect, a phenomenon discussed in Section 2.1.4.3. The size dependence on the optical properties of (CdSe)ZnS particles ranging in size from 2.3 to 5.5 nm is shown in Figure 2-13(A). The larger band gap associated with the smaller particles made them appear blue compared to the red color observed for the larger particles.^{9,21} These data are yet another example of how the size and geometry of a nanoparticle can be used to tailor the optical properties.

As discussed in more detail in Chapter 4, the optical properties of nanoparticles can change when they come in close contact with one another in either a dimer, trimer or

larger scale array due to interactions between the SPR-induced fields associated with each individual particle.

2.1.4.1.2 Effects of the Dielectric Constant and Surface Chemistry

The dielectric constant of the surrounding medium affects the ability of the particle surface to accommodate the oscillating electron density,⁹ and higher values yield higher SPR wavelengths.^{179,188} This phenomenon is shown in Figure 2-14 for gold ellipsoids with an aspect ratio of 3.3. It has also been noted that the sensitivity of particles to the dielectric environment increases with aspect ratio.¹⁸⁸

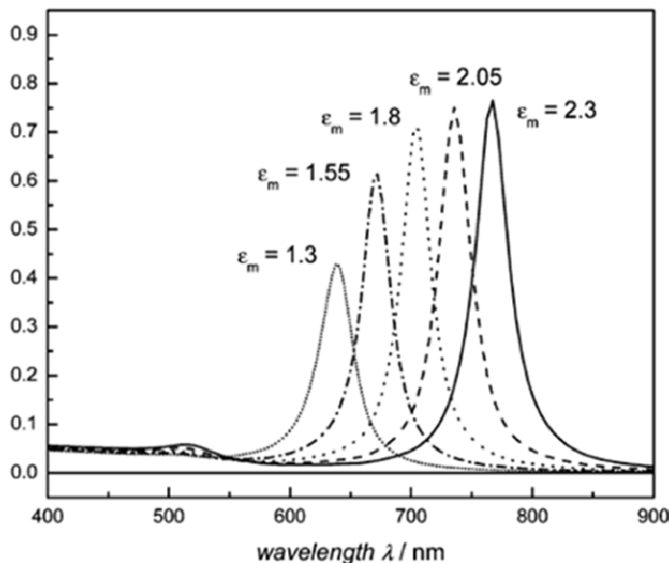


Figure 2-14. Absorption spectra calculated for a gold ellipsoid (aspect ratio = 3.3) with as the dielectric constant of the surrounding medium changes from 1.3 to 2.3. Figure taken from Link et al.¹⁵

The dielectric constant of the surrounding medium is affected by both the solvent and the capping ligands on the particle surface. It has been documented that the SPR of surfactant-stabilized gold particles varies between 520 and 550 nm depending on solvent.¹⁹² The shift in the

absorption maximum of silver particles upon adsorption of SH^- and I^- ions has been attributed to changes in the effective dielectric constant around the particles.¹⁹³ Likewise, spectral shifts of up to 27 nm were observed upon the binding of streptavidin to silver nanotriangles,⁵² and a shift of approximately 40 nm was observed upon binding alkanethiols to silver nanoparticles.¹⁹⁴ Some of these spectral changes were attributed to simple changes in the electron density on the surface with chemically bound molecules.⁹ Other changes have been attributed to charge transfer interactions between the particle and the chemisorbed molecules. For example, when thiols bound to silver particles, a blue shift of 8.5 nm was attributed to the Ag-S charge transfer interaction.⁵² Charge transfer interactions have been more significant between nanoparticles and chromophores, for instance a pyrene amine bound to gold.¹⁹⁵ These spectral changes have made nanostructures of interest for molecular sensing applications.

2.1.4.2. Optical Properties of Platinum, Palladium and Nickel

As mentioned above, only a few colloidal metals show sharp and prominent absorption bands in the ultraviolet and visible ranges. The absorption spectra of platinum, palladium and nickel are typically broad and featureless in this region, which explains the brown color typically associated with platinum particles. However, the properties of these metals are mentioned here as they are relevant to discussion later in this chapter. The optical spectra of these metals calculated by

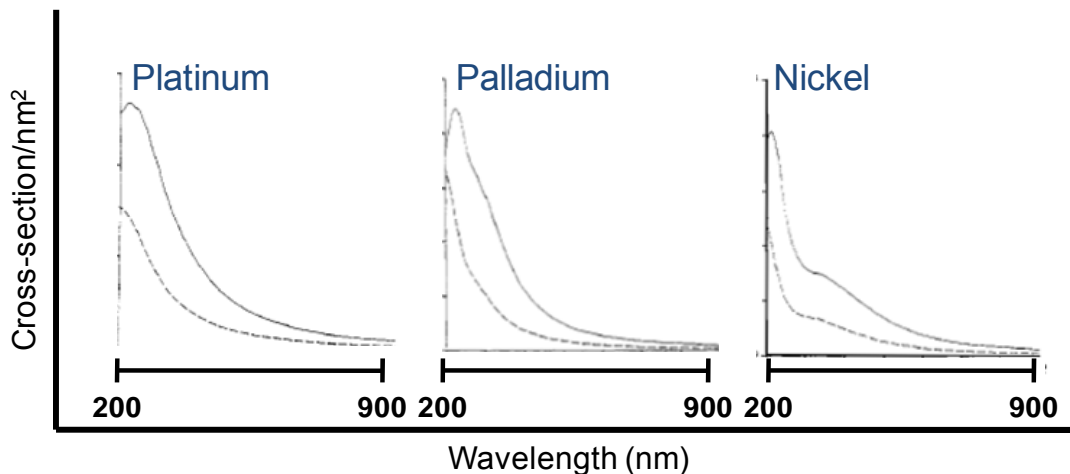


Figure 2-15. Absorption spectra for 10nm spherical particles of platinum, palladium and nickel calculated using Mie theory. Dashed lines indicate spectra in vacuo and solid lines indicate spectra in a dielectric medium with the refractive index equal to that of water (1.33). Figure adapted from Creighton et al.¹⁷

Creighton et al.¹⁷ are shown in Figure 2-15. It can be seen that platinum colloids exhibit a tailing absorbance which decreases with increasing wavelength.^{17,196} It was predicted that these spectra were independent of particle size.^{17,196} However, it has been observed that the linear slope obtained from the plot of $\log(\text{absorbance})$ vs. $\log(\text{wavelength})$ is dependent on particle size.^{197,198} The slope is defined by the parameter, S , which is defined in Equation 2-5, and decreases with particle size. S decreases rapidly upon aggregation.^{197,198}

$$S = \frac{d(\log \text{ absorbance})}{d(\log \text{ wavelength})} \quad 2-5$$

2.1.4.3. Electrical Properties

The electronic structure and properties of materials are very complex subjects, which are beyond the scope of this work.¹⁹⁹ However, a brief description is included here as the electronic structure is relevant to the application of particles to electronic devices. The electronic structures of metals at the nanoscale differ both from those of the individual atoms and the corresponding bulk materials. The delocalized electrons in bulk metals collectively form overlapping valence and conduction bands of continuous energy levels. However, as the size of the material decreases to sizes on the same order as the Bohr radius²² of the bulk material or the deBroglie wavelength,¹⁹ a gap forms between the conduction and valence bands and energy levels become quantized or discreet.^{19,22,200} These changes in electronic energy levels as a function of particle size are known as quantum size effects.

When the energy between discreet levels exceeds the thermal energy at a given temperature, significant, size-dependent changes in the electrical and optical properties have been observed.^{19,200} This critical size is significantly greater for semiconductor materials, which exhibit band gaps in the bulk, and has been documented to be as large as 10,000 atoms.²⁰⁰ Significantly smaller sizes are required in order to observe quantum size effects in metals. Because of the presence of quantum size effects, semiconductor particles are often called quantum dots. The bright colors observed for semiconductor particles in Figure 2-13 (B) can

be described by the size-dependent spacing of the electronic energy levels. As the particle size decreases, electronic transitions shift to higher energy.²⁰⁰

As the electronic structure changes with particle size and the onset of quantum size effects, so do the electronic properties. The electron transport behavior associated with metal particles is significantly different than that of the corresponding bulk metals. A significant amount of energy is required to add a single extra electron to a nanoparticle, and the presence of this additional charge prevents the addition of a subsequent electron, a phenomenon called the Coulomb blockade.^{19,200,201}

Therefore, current passes through particles one electron at a time and current-voltage curves resemble a staircase, with each 'stair' corresponding to a single charging event. Because this phenomenon is attributed to the Coulomb blockade, it is frequently referred to as the Coulomb staircase.

2.1.5. Literature Summary

The literature review above was intended to outline the challenges associated with synthesizing and working with nanoparticles and to set the stage for the work reported in the next section.

The factors that contribute to particle stability were discussed in Section 2.1.1. As discussed below, maintaining particle stability proved to be a challenge not only with particle synthesis, but also with particle assembly and characterization. These

concepts will be referred to in several subsequent chapters. For applications where accessibility to the particle surface is important, the tradeoff between particle stability and reactivity needs to be considered.

The mechanisms for particle formation in solution and the variables that affect particle size, shape, dispersity and surface chemistry were described in Section 2.1.2. Nanoparticle synthesis is far from an exact science. Particles are generally extremely sensitive to small changes in reaction conditions, which typically do not convey from one particle synthesis to the next. As a result, strict control over reaction conditions is required and synthetic methods need to be optimized for each new particle. An understanding of the general trends determining particle size and dispersity is critical to developing and optimizing particle syntheses. Several literature examples were presented to demonstrate how nanoparticle structure can be optimized through proper control of both thermodynamic and kinetic variables.

Of significant relevance to this work are the complications associated with synthesizing particles in aqueous solution. Aqueous particles are subject to ionic interactions, which can be difficult to control and detrimental to particle stability. Particles synthesized in organic solvent avoid these problems, and are typically more monodispersed. However, organic ligands are typically sterically bulky, which, as discussed in the next section, would most likely inhibit assembly formation. The studies reported on ligand-exchange and phase transfer (Section 2.1.2.4) indicate

that limited exchange occurs when the initial ligands are sterically bulky. Particles synthesized in organic solvents have been brought into aqueous solution through encapsulation with a surfactant or an amphiphilic polymer rather than through ligand exchange. However, these encapsulating layers further limit particle reactivity.

2.2. Results and Discussion

2.2.1. Synthetic Requirements for Heterodimer Formation

As discussed in Chapter 1, the overall goal of this work was to synthesize and characterize heterodimers consisting of oligomeric phenylethylenes (OPEs) inserted

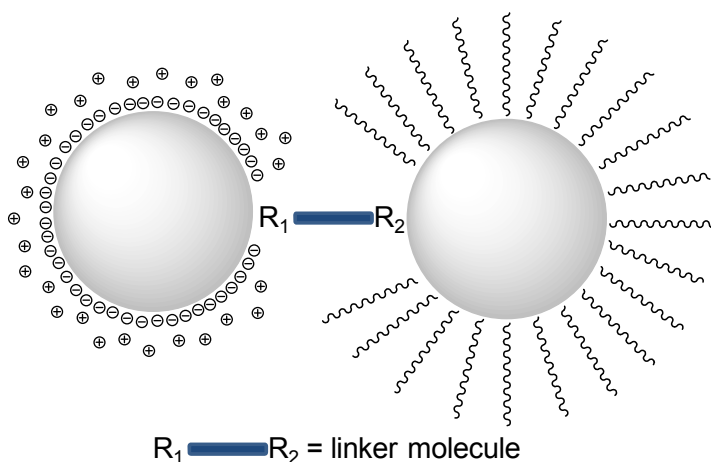


Figure 2-16. Schematic of nanoparticle heterodimer (not to scale). Two nanoparticles bound with an organic linker molecule terminated with different functional groups. Nanoparticles can be either electrostatically or sterically stabilized.

between two nanoparticles of different compositions using orthogonal self-assembly (Figure 2-16). The basic structure of the OPE molecules used in this study is shown in Figure 2-17. The thiol functionality was intended to bind to gold particles while the isocyanide functionality was intended to

bind to one of the group ten transition metals: platinum,²⁰²⁻²⁰⁷ palladium²⁰⁸⁻²¹⁰ or nickel.²¹¹⁻²¹³ The metal particles synthesized in this work therefore included gold, platinum and nickel.

There were several factors that needed to be considered before choosing the capping ligands and synthetic procedures described here. There have been several reports indicating that alkane thiols on adjacent nanoparticles interdigitate, allowing for interparticle distances smaller than the sum of the two molecular capping ligands (Section 2.1.3).^{81,102,161,163,167,171} However, it was assumed that the capping ligands should be shorter than half of the linker length. Assuming that interdigitation is not necessarily going to take place in the general case, steric hindrance would likely prohibit the formation of dimers consisting of two particles with long capping ligands. In addition, ligand-exchange is more efficient when the initial capping ligand is less sterically-bulky (Section 2.1.2.4).⁹¹ For these reasons, short capping ligands were desirable. In order to accommodate the linker lengths used in this study, which vary between 2 and 3.3 nm, all

attempts at particle synthesis involved capping ligands less than 1 nm. There was an obvious tradeoff between particle

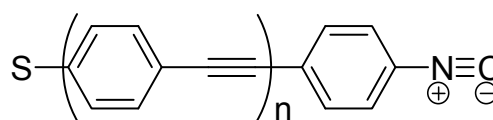


Figure 2-17. OPE used to synthesize heterodimers. $n=3,4,5$.

stability and reactivity making it difficult to synthesize stable nanoparticles with these short capping ligands.

The focus of this work was also on aqueous particles. As summarized in Section 2.1.5, the syntheses of particles in organic solvents typically involve sterically bulky capping ligands, which were undesirable for heterodimer formation. In addition, no reports were found in the literature describing the successful exchange of a sterically bulky ligand for a shorter one. This concern contributed to the choice of water as a solvent despite problems associated with ionic interactions. In addition, aqueous, electrostatically-stabilized, citrate-capped gold particles were commercially available in numerous sizes, and several of the characterization methods evaluated required aqueous solvent.

The synthesis and properties of the commercially available gold-citrate particles are briefly discussed below. The remainder of this chapter focuses on synthesizing aqueous platinum and nickel particles with short capping ligands.

2.2.2. Gold Particles

2.2.2.1. Citrate-capped Gold Particles

Although all of the gold particles used in this study were purchased, a brief overview of the literature routes for their synthesis is given here. One of the first methods developed for synthesizing nanoparticles was the citrate reduction of

tetrachloroaurate,
which was first
reported by
Turkevich et al.⁹⁵ in
the 1950's. In this
case, the citrate
acts not only as a

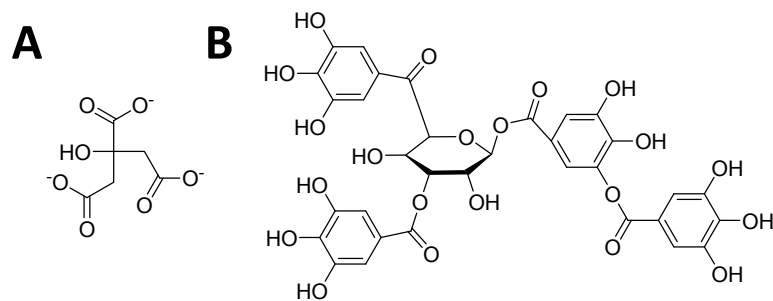


Figure 2-18. (A) Citrate ion (B) Tannic Acid

reductant, but adsorbs to the particle surface and acts as a stabilizing agent. Particles synthesized using this method are generally monodispersed and among the most-commonly used.⁷²

Citrate-capped gold particles prepared using the Turkevich method yielded particles with a minimum diameter of 12 nm.^{19,90,103} Decreasing the concentration of sodium citrate yielded significantly larger particles. Many years later Slot et al.¹⁰³ developed a method for preparing monodisperse gold particles of various sizes ranging from 3 to 150 nm through the use of two reducing agents, sodium citrate and tannic acid (Figure 2-18). Tannic acid is a stronger reducing agent than sodium citrate; it reduced the gold salt at a faster rate, yielding a greater number of nuclei and smaller particles. Stricter size control was achieved using varying ratios of the two reducing agents. It was determined that pH values between 7.5 and 8.0 were ideal for the synthesis of these particles and potassium carbonate was therefore added to

compensate for the decrease in pH attributed to the tannic acid. Lower pH values resulted in larger particle sizes and higher pH values yielded samples with a larger polydispersity.^{103,214}

The exact nature of the interaction between the gold particles between the citrate and the tannic acid is not known. However, it is noted here that the tannic acid molecule is considerably larger than the citrate anion, and could pose a steric barrier to dimer formation when present at higher concentrations.

The citrate-capped gold particles used in this work were purchased from Ted Pella, Inc., and were available in sizes ranging from 2 to 250 nm. While the supplier does not provide information on the exact method used to synthesize these particles, it was assumed that they were synthesized according to the protocol established by Slot et al.¹⁰³ The supplier described the solutions of gold particles as being aqueous with trace amounts of citrate, tannic acid and potassium carbonate. The pH of these

Table 2-1. Concentrations of citrate-capped gold particles as received by Ted Pella, Inc. The values below were reported by the supplier.

Particle Diameter (nm)	Particle Concentration (particles/mL*10 ¹⁰)	Particle Concentration (nM)
5	5000	83.0
10	570	9.46
15	140	2.32
20	70	1.16
30	20	0.33
40	9.0	0.15
50	4.5	0.07
60	2.6	0.04

values. As faster reduction leads to a greater number of nuclei and smaller particles (Section 2.1.2), the concentrations of gold particles in solution increased with decreasing particle sizes. The concentrations of particles in solution reported by the supplier are listed in Table 2-1.

The optical properties of these particle solutions were evaluated using UV-VIS

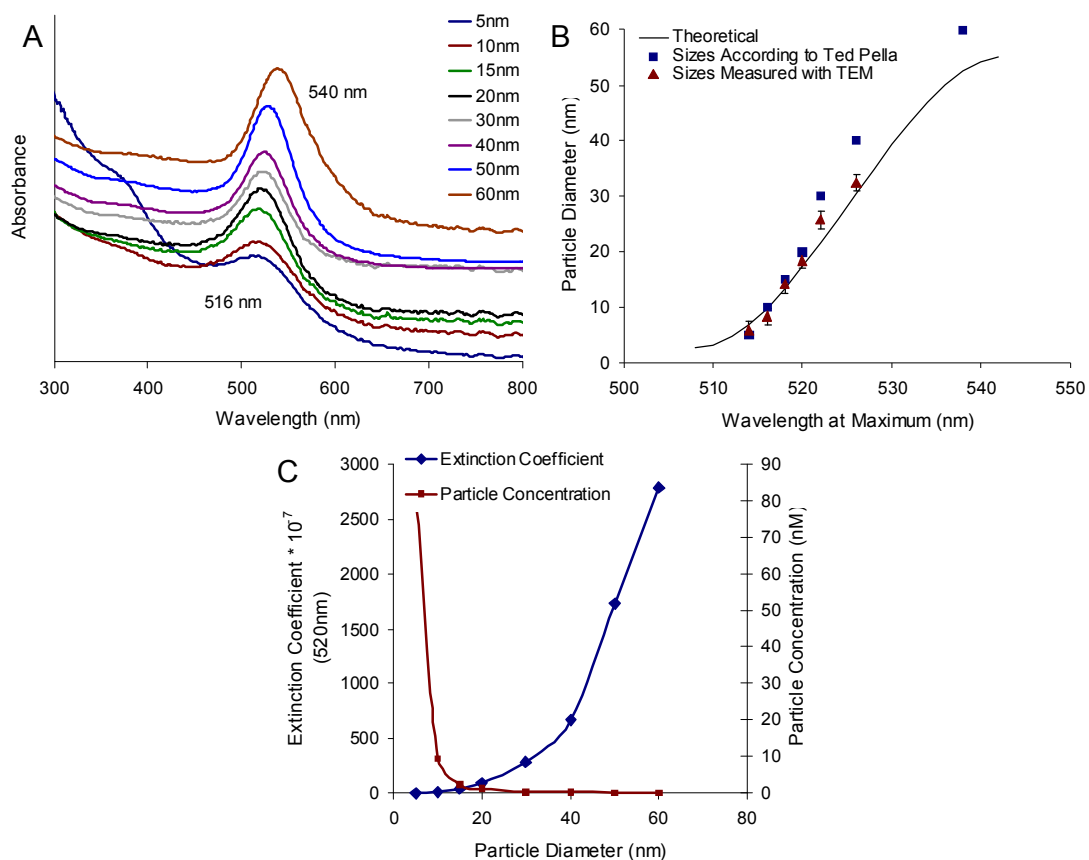


Figure 2-19 (A). UV-VIS absorption spectra of gold nanoparticles as received from Ted Pella, Inc. Spectra were offset along the y-axis for clarity. **(B)** Relationship between particle diameter and the wavelength of the absorbance maximum for gold particles, both theoretical calculations and experimental data. Theoretical calculations were based on the work of Khlebstov et. al.¹⁸ **(C)** Particle concentrations and extinction coefficients at 520 nm were plotted as a function of particle diameter for gold nanoparticles as received from Ted Pella, Inc.

spectroscopy as shown in Figure 2-19 (A). As expected, the wavelengths at the absorption maxima increased only slightly with particles size (Section 2.1.4.1). These results were then compared to the theory of Khlebtsov et al.¹⁸ who derived the relationship between particle diameter and the absorption maximum for gold particles from the best-fit polynomial relating spectrophotometric and electron-microscopic data (Equation 2-6). Figure 2-19 (B) compares this expression to values obtained from the spectra in (A) and shows reasonably good agreement. Initial data (blue) were based on particle diameters provided by Ted Pella, Inc. and shows some deviation from the trend, esp. at larger particle sizes. However, electron-microscopic data (red) provided more accurate sizes and showed better agreement. The microscope data also indicated that the size of the gold particles supplied by Ted Pella, Inc., for at least some of their product, deviated from what they claimed. This deviation appeared to be greater for larger particles sizes.

$$d_m (nm) = \sum_{n=0}^3 A_n (\lambda_{\max} - 500)^n \quad 2-6$$

$A_0 = 12.558; A_1 = -2.593; A_2 = 0.1921; A_3 = -0.00253$

While the wavelength of the absorption maximum did not change significantly with particle size, Figure 2-19 (C) shows that the extinction coefficients at 520 nm (blue) increased substantially with particle size. These values were calculated using the absorbance at 520 nm and the particle concentration reported by the manufacturer. This result is in agreement with literature reports that the extinction coefficient

increases with particles size up to approximately a diameter of 80 nm, at which point it decreases again.²¹⁵ This behavior was less obvious in (A) as the particle concentrations in solutions obtained from Ted Pella, Inc. (red) also decreased substantially with particle size.

2.2.3. Platinum and Palladium Particles

2.2.3.1. Evaluation of literature methods for platinum and palladium nanoparticle synthesis

The first task at hand was to select an appropriate method for the preparation of platinum and palladium nanoparticles. For the synthesis of heterodimers, stable, monodispersed particles with short capping ligands were desired. A survey of the literature indicated that most synthetic methods involved stabilization by either citrate, a polymer or a thiolate ligand. These three classes of particles are reviewed below after some general statements about platinum and palladium.

Platinum and palladium nanoparticles are discussed together as they are both Group 10 transition metals, they exhibit similar properties, and many of the preparation methods discussed here can be applied to both metals.²¹⁶ The stability of platinum and palladium particles is significantly lower than that observed for gold, and thus these particles aggregate more readily.²¹⁷ It has also been noted that platinum particles typically exhibit highly faceted and irregular surfaces, making spherical particles more difficult to produce.^{6,72}

While citrate has been used to reduce both platinum^{196,218-221} and palladium,²¹⁷ these methods do not offer the stability or the size control observed for gold. There have been several reports indicating that citrate does not reduce hydrogen hexachloroplatinate (H_2PtCl_6) at temperatures less than 90 °C.^{217,219,220} Citrate has successfully reduced H_2PtCl_6 at higher temperatures to produce particles approximately 3 nm in diameter.^{218,220,222,223} However, higher temperatures have also been reported to favor aggregation.²¹⁹ The increases in particle size observed with reactant concentration, temperature and time after reduction have been attributed to aggregation rather than growth.^{217,223} All attempts by a previous group member, Brandon Walker, to synthesize platinum particles using these methods were unsuccessful. While the efficacy of citrate as a reducing agent has not been demonstrated with platinum and palladium, its ability to stabilize these particles has been observed. There have been reports of the reduction of platinum salts by hydrogen and methanol in the presence of citrate, which acted solely as a stabilizing agent.^{216,219}

More commonly, platinum and palladium salts have been reduced by hydrogen or an alcohol in the presence of a stabilizing polymer. There have been many reports of the reduction of H_2PtCl_6 , H_2PdCl_6 and K_2PdCl_6 in the presence of polymers such as polyacrylate,^{72,196,219,224,225} poly(vinylpyrrolidone) (PVP),^{197,198,203,219,224-228} Carbowax,^{219,224} and poly(methyl methacrylate) (PMMA).²²⁴ The size and stability of

these particles were affected by the nature and the concentrations of both the reducing agent and the stabilizing polymer. Stronger reducing agents and higher reductant concentrations yielded smaller particles.^{219,227} Similarly, higher molecular weight polymers and higher polymer concentrations yielded smaller particles.^{197,227} Particle stability was dependent upon both the solvency of the polymer chains and the strength of their interaction with the metal particle. For example, in aqueous media, particle stability increased with polymer hydrophilicity.¹⁹⁷ While Carbowax is a block copolymer containing two poly(ethylene glycol) (PEG) chains linked by a short hydrophobic epoxide chain, simple PEG chains were deemed poor protective agents.²²⁴ This was attributed to the weak adsorption of PEG to Pt. In the case of Carbowax, it was the epoxide chain that adsorbed to the particle surface.

Despite the prevalent use of polymers as stabilizing agents for platinum and palladium, they were not suitable for this work as their steric bulk would likely prohibit ligand-exchange and heterodimer formation. For these reasons, the focus of this work was on the synthesis of particles with small molecule capping ligands, more specifically thiolate ligands. The synthesis of thiolate-capped particles was initially developed for gold. As the methods used for platinum are based on these, a review of thiolate-capped gold particles is included below. These general concepts were then applied to the synthesis of platinum particles.

While Giersig et al.¹⁷³ were actually the first to publish the synthesis of alkanethiolate-capped particles through ligand exchange, the direct synthesis developed by Brust et al. was not published until 1994, a year later.^{19,98} This method was a two-phase process wherein the anionic gold salt, AuCl_4^- was transferred into the organic phase (toluene), by means of the phase-transfer agent, tetraoctylammonium bromide. The gold salt was then reduced with sodium borohydride in the presence of alkanethiols yielding particles ranging in size from 1.5 to 5.2 nm, depending on the reaction conditions.^{19,91,98,102} This was one of the first accounts of sterically-stabilized particles that were air-stable, thermally-stable and that could be precipitated and re-dissolved in solution.

After the initial report published by Brust et al.⁹⁸, many other reports of thiol-stabilized gold particles appeared in the literature along with descriptions of how reaction conditions affected particle size.^{19,91,102,143,161,176,229,230} While the differences between particles of 1.5 and 5.2 nm may initially seem insignificant, the core sizes in these particles range from approximately 110 to 4800 atoms, and the number of molecules in each capping layer range from 53 to 520 ligands/core.¹⁹ It has been determined that the greatest factor contributing to the average particle size was the molar ratio between the thiol and the gold atoms, with larger ratios yielding smaller particles.^{19,91,102,230} This trend has been explained by the mechanism in Scheme 2-2 (pg. 57) where the particle size is determined by the stoichiometry in the precursor

polymer. While lower ratios yielded larger particles, they also yielded increased polydispersity and aggregation.² Similar results were observed for increased borohydride/gold ratios.^{19,100} Other factors that have affected the final particle size and dispersity are the steric bulkiness of the capping ligand, the solution temperature and the rate of reactant addition. Smaller particles have been observed with sterically bulky capping ligands and particle dispersity has improved with cooler reaction temperatures and faster rates of reductant addition.^{19,91}

The two-phase synthesis of thiol-stabilized organic gold particles was later extended to a single-phase synthesis of water-soluble, thiol-stabilized particles. The capping ligands used in aqueous particle syntheses include *p*-mercaptophenol,¹⁹ glutathione,^{100,231} tipronin,^{146,232} and 4-hydroxythiophenol.²³³ In 2005, Ackerson et al.² reported a survey where 36 water-soluble organothiols were used in nanoparticle syntheses, and only 13 resulted in stable gold nanoparticles. This survey provided several interesting observations. While small, neutral and negatively charged thiolates were capable of stabilizing gold particles, small, positively charged ligands were not. Mercaptopropionic acid was the smallest, negatively charged thiolate yielding stable particles. These particles exhibited stability over time periods ranging from days to weeks. 3-Mercapto-1,2-propanediol was the smallest, uncharged thiolate yielding particles; however, these particles

were only stable over a period of days. As discussed in Section 2.1.1.2, larger ligands yielded particles with greater stability in all cases.²

Approximately ten years after the initial report of thiolate-protected gold particles, Eklund et al.³⁸ reported methods for synthesizing monolayer-protected platinum clusters in both aqueous and organic solvents. They concluded that the mechanism for the formation of platinum particles was different than that observed for gold. This conclusion was based on the observations that the two-phase process initially used to synthesize organic-soluble gold particles was unsuccessful and yielded only

precipitates.³⁸

Organic-soluble

particles were

instead

synthesized using

a single-phase

system with

lithium

triethylborohydride

as the reducing

agent. It was also

observed that

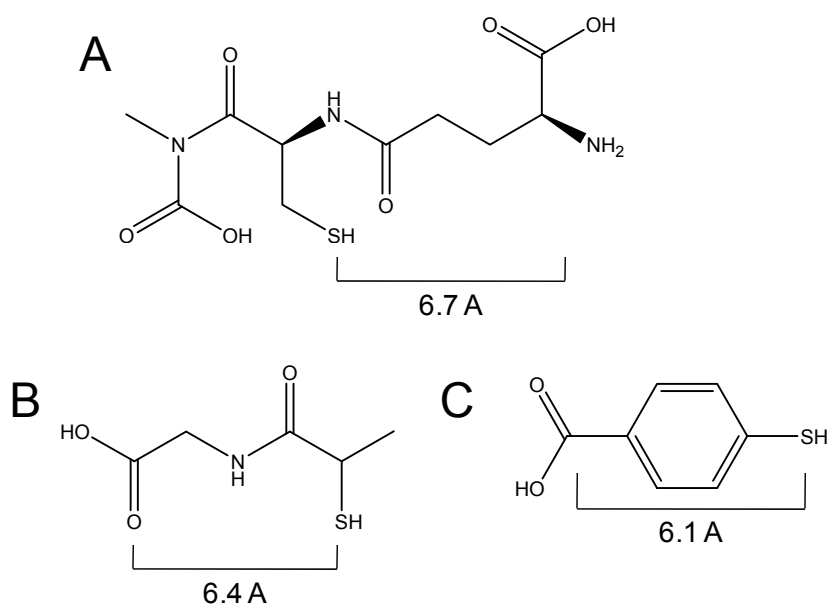


Figure 2-20. Capping ligands used in the synthesis of platinum particles (A) glutathione (B) tiopronin (C) 4-mercaptobenzoic acid Lengths were measured using Chem3D software after MM2 Energy Minimization

while thiols play a role in the reduction of gold salts, they did not appear to do so in the case of platinum. While there are inconsistencies in the literature, the syntheses of gold MPCs typically involve a thiol/gold ratio of 3:1, where two thirds of the thiols are used to reduce Au(III) to Au(I) as described in Section 2.1.2.1 and shown in Scheme 2-2 (pg. 57).^{*} However, no reduction was observed for platinum in the presence of thiols, and the best results were achieved using a 1:1 thiol/Pt ratio.³⁸ This behavior indicated that the precursor polymer believed to form between thiolates and gold ions (Scheme 2-2 - pg. 57) does not form in the case of platinum. For thiol/Pt ratios greater than 1:1, the particle yield suffered and lower ratios resulted in aggregation. It was also noted that the size distribution was wider for platinum particles compared to gold particles synthesized using similar methods. This was attributed to the higher prevalence of particle aggregation.³⁸

The three water-soluble ligands used by Eklund et al.³⁸ to synthesize platinum particles were tiopronin, glutathione, and (11-mercapto-undecyl)-trimethylammonium. While the trimethylammonium compound was longer than desirable for our application, the effective lengths of tiopronin and glutathione are significantly shorter (Figure 2-20), and of more interest for this work. Despite the presumed differences in the particle formation mechanisms, the methods used to

^{*} Some data suggest that thiolated gold particles do form at lower thiol/gold ratios. Templeton et al. varied this ratio between 1:12 and 3:1 for gold-tiopronin particles and demonstrated that lower ratios yielded larger particles. The corresponding particle sizes were 3.9 and 1.8 nm.

synthesize these platinum particles were similar to those previously developed for gold with the main differences being the thiol/gold ratios. Attempts were made to synthesize platinum particles with both tiopronin and glutathione capping ligands according to the methods reported by Eklund et al.³⁸

2.2.3.2. Synthesis of Tiopronin-Capped Platinum Nanoparticles

Platinum particles capped with tiopronin were synthesized according to the method described by Eklund et al.³⁸ This method was based on one reported by Templeton et al.^{146,232} for the synthesis of tiopronin-capped gold particles, with the main difference being the thiol/platinum ratio.^{38,146,232} A 1:1 ratio of tiopronin/H₂PtCl₆ was stirred in a solution of 6:1 methanol/acetic acid before platinum reduction with sodium borohydride. For gold particles, it was reported that irreversible aggregation occurred in the absence of acid suggesting that particles with deprotonated tiopronin capping ligands were not stable in methanol.²³² Once particles were formed, they were purified by dialysis in water. The size distribution for the platinum-tiopronin particles synthesized in this work was 1.75 ± 0.24 nm as determined by TEM (Figure 2-21 (A)). This was in reasonable agreement with the values reported by Eklund et al. (1.9 ± 1.3 nm).³⁸ Decreasing the thiol/gold ratio to 0.7:1 was expected to increase particle size. However, negligible differences were observed. The measured size distribution was 1.41 ± 0.32 nm, which is actually smaller than that observed in the previous experiment. The 1:1 ratio was maintained for all further

syntheses. The absorption spectrum in Figure 2-21(B) appeared to be in agreement with both that reported by Eklund et al.³⁸ for platinum-tiopronin particles and the general spectrum for platinum particles calculated by Creighton et al.¹⁷ (Figure 2-15, pg. 88).

It is relevant to mention a few properties of the tiopronin capping layer reported in the literature, which may be significant when performing ligand-exchange and attempting heterodimer formation. As mentioned above, the carboxylic-acid functionality is ionizable, and thus in aqueous solutions with pH values above its pKa (3.51) both electrostatic and steric forces contribute to particle stability.²³² In addition to the terminal carboxylic acid functionality, tiopronin also contains an amide

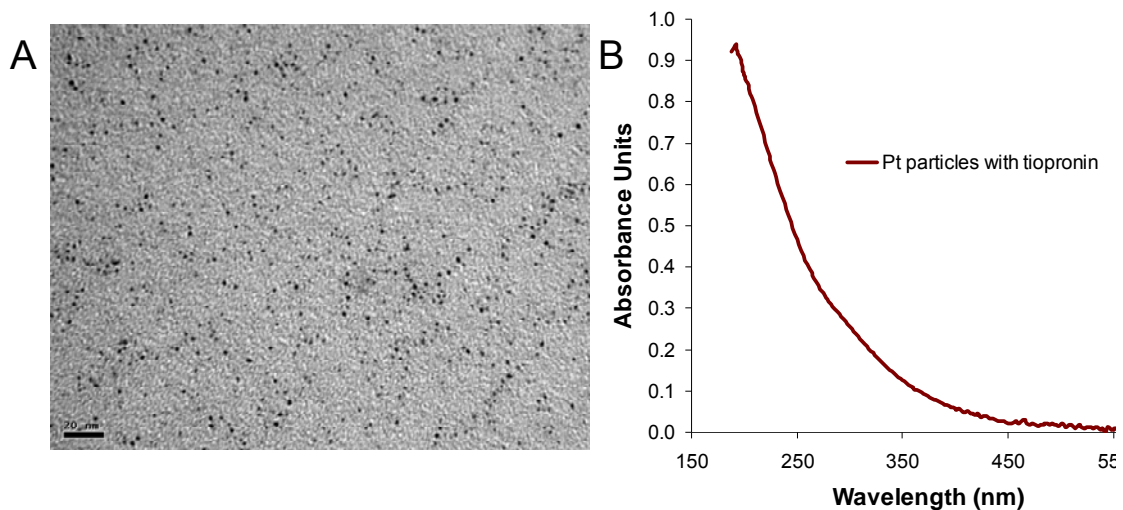


Figure 2-21 Pt-tiopronin particles (A) TEM image (B) absorption spectrum. These data correspond to particles 1.75 ± 0.24 nm in diameter

functionality (Figure 2-20, pg. 104). Templeton et al.²³² suggested that both inter- and intramolecular hydrogen bonding occur between both the carboxylic acid and amide functionalities.²³² In the solid-phase, inter-particle amide hydrogen bonding has been observed using infrared (IR) spectroscopy.¹⁴⁶ This hydrogen bonding was believed to occur through the interdigitation of capping ligands similar to that observed for alkanethiolate clusters (Section 2.1.3).^{81,102,161,163,167,171,173} Based on IR data, Templeton et al.²³² reported that hydrogen bonding between amides was more prevalent than that between carboxylic acid groups; however, it is unclear how the relative strengths of these forces would differ in aqueous media.¹⁴⁶ The hydrogen bonding stabilization of gold particles was one of the factors used to rationalize the low-extent of ligand-exchange described in the literature observed for gold-tiopronin particles. Specifically, Templeton et al.¹⁴⁶ attempted ligand-exchange with tiopronin-capped gold particles and five different ligands, and consistently observed that only about half of the expected ligand-exchange occurred.

2.2.3.3. Attempted Synthesis of Glutathione-Capped Platinum Nanoparticles

All attempts to synthesize glutathione-capped platinum particles according to the methods described by Eklund et al.³⁸ were unsuccessful. Significant aggregation was observed using TEM. Possible reasons for this may be found in the discrepancies between Eklund's method and a similar procedure reported by Schaff et al.^{100,231} for the synthesis of gold-glutathione particles. Schaff et al.¹⁰⁰ performed

the particle synthesis in a 2:1 methanol/water solution claiming that this composition was necessary to prevent uncontrolled growth. However, Eklund et al. used a completely aqueous solution with no explanation for the discrepancy with the earlier statement. It was also noted that Eklund et al. used a 19:1 ratio of the reducing agent to the gold salt while the ratio used by Schaff et al. was 10:1.

Future experiments to improve this synthetic method could involve systematic variations in reaction conditions. It is possible that incorporating methanol into the reaction solution or increasing the thiol/platinum ratio could have yielded better results. Eklund et al. reported a 0.7:1 thiol/platinum ratio compared to the 1:1 reported for other platinum syntheses. It is also possible that aggregation occurred only after precipitation from solution and washing with ethanol, and different purification methods could have yielded better results. However, at this point, efforts were shifted to the synthesis of other platinum particles.

2.2.3.4. Synthesis of 4-Mercaptobenzoic Acid capped Platinum Particles

Platinum particles were synthesized using 4-mercaptobenzoic acid based on a similar procedure reported for synthesis of gold particles. While the syntheses reported in the literature for platinum particles stabilized with thiols were limited, they were all adapted from methods developed for gold. The literature was therefore surveyed for gold particles stabilized with short, hydrophilic thiols so that these procedures could be applied to platinum.

As mentioned in Section 2.2.3.1, Ackerson et al.² performed a survey of 36 water-soluble organothiols for stabilizing gold nanoparticles. Of these 36 ligands, only 13 resulted in stable particles, and the stabilities ranged from minutes to months.² The four ligands, with the greatest stability (months) were 4-mercaptobenzoic acid, tiopronin, 1-thio- β -D-glucose and glutathione. Glucose is a sterically bulky ligand and both glutathione and tiopronin have been previously evaluated so efforts were focused on 4-mercaptobenzoic acid (Figure 2-20(C)).

The procedure Ackerson et al.² referenced for the synthesis of 4-mercaptobenzoic acid-capped gold particles was one previously reported by Johnson et al.¹⁷⁶ Again, there were some discrepancies between the two reports. While Ackerson et al.² claim to have used a 3:1 thiol/gold ratio for all of the ligands they surveyed, the ratio reported by Johnson et al. was 1.8:1. While there was no explanation given for this

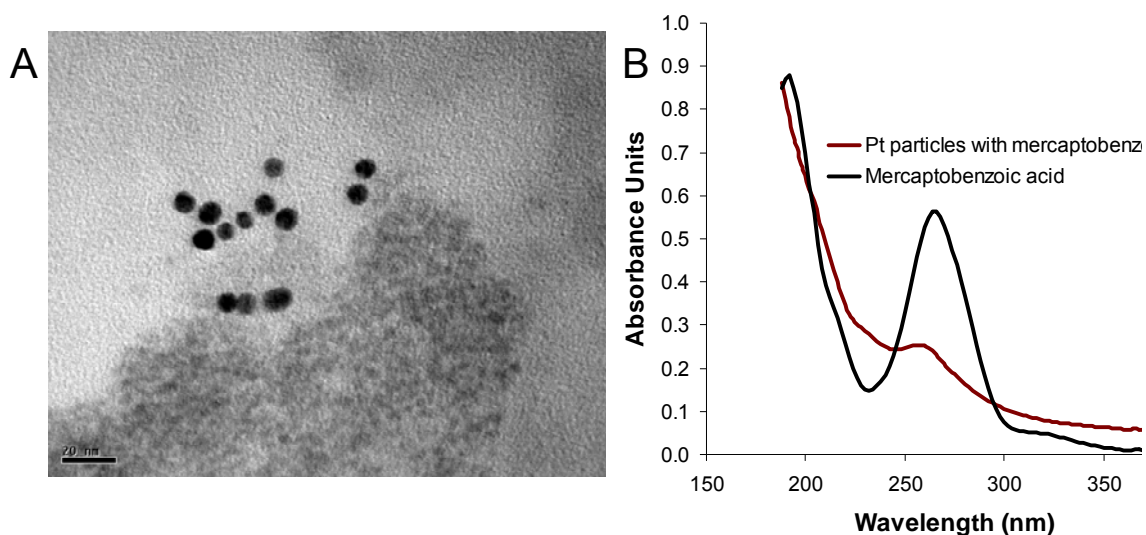


Figure 2-22. Pt particles with 4-mercaptobenzoic acid (A) TEM image and (B) absorption spectrum. These data correspond to particles of 7.2 +/- 0.6 nm

discrepancy, it appears that the lower thiol/gold ratio yielded larger particles.

Johnson et al.¹⁷⁶ reported a size of 2.9 ± 0.5 nm for their particles (1.8:1 ratio) while

Ackerson et al.² reported a size of 1.8 ± 0.4 nm

Initial attempts to synthesize 4-mercaptobenzoic acid capped platinum particles involved substituting H_2PtCl_6 for $HAuCl_4$ in the procedure reported by Johnson et al.¹⁷⁶ H_2PtCl_6 and 4-mercaptobenzoic acid were dissolved in a 5:1 ratio of methanol/acetic acid before reduction with sodium borohydride. Johnson et al. claimed that the acetic acid was necessary to prevent deprotonation of the capping ligand. This procedure initially yielded platinum particles averaging 7.2 ± 0.6 nm in diameter. These particles were significantly larger than those reported for gold particles; however, larger particles were desirable for the TEM characterization of heterodimers. Both TEM and UV-VIS data for these particles are shown in Figure 2-23. The tailing absorbance in the absorption spectrum was consistent with that predicted for platinum particles (Figure 2-15, pg. 88).¹⁷ The small peak at 262 nm

Table 2-2. Observations recorded for platinum particles with 4-mercaptobenzoic acid

Thiol/Au Ratio	Observed Particle Size Distribution
1.8:1	7.2 ± 0.6 nm
1.8:1	6.1 ± 1.3 nm
1.5:1	Two distinct particles sizes: 5.4 ± 0.6 nm 17.4 ± 1.5 nm possibly some aggregation of smaller particles into larger particles
1.5:1	aggregation
1.8:1	aggregation
1.8:1	1.8 ± 0.4 nm with some aggregates observed

most likely corresponds to bound 4-mercaptobenzoic acid. This peak is slightly blue-shifted compared to the absorbance of 4-mercaptobenzoic acid. However, this discrepancy was attributed to charge-transfer interactions, which are commonly observed between chromophores and metallic particles (Section 2.1.4.1).^{52,195}

Decreasing the thiol/platinum ratio from 1.8:1 to 1.5:1 was predicted to yield larger particles; however, this appeared only to contribute to aggregation. Results obtained at both thiol/platinum ratios were inconsistent as shown in Table 2-2. The results are reported in chronological order.

The inconsistencies observed for the formation of platinum particles with 4-mercaptobenzoic acid were later explained by NMR spectra indicating that this molecule has formed disulfide, as is common with aromatic thiols. The inconsistent results were attributed to varying ratios of thiol and disulfide in solution.

In October of 2007, several years after the initial synthesis was published, another report of 4-mercaptobenzoic acid gold particles appeared in the literature.²³⁴ This method differed significantly from that published by Johnson et al.¹⁷⁶ This modified procedure for the synthesis of gold particles with 4-mercaptobenzoic acid was evaluated in attempt to understand the differences between the two reported syntheses and determine whether the more recently published method could be applied to platinum. This procedure was deduced from slightly varying accounts gathered from both private correspondence with Christopher J. Ackerson and his

recently published paper.²³⁴ A 3.4:1 ratio of thiol/Au was mixed in an aqueous solution containing 47-50% methanol. The pH was adjusted to ~ 13 using a 300 mM solution of NaOH. After stirring overnight, this stock solution was diluted to between 27% and 47% methanol before being reduced by a 3:1 excess of sodium borohydride.²³⁴ While the pH in the previous report was acidic in order to prevent the deprotonation of the capping ligand,^{176,235} this procedure was performed in extremely basic conditions. The reasons for this were unclear. However, the solubility of the deprotonated capping ligand was most likely not an issue as water was incorporated into the reaction solution whereas previous accounts involved only methanol.

The structural information reported for the gold particles also provided some insight into the formation mechanism. X-ray crystal structures of the gold particles indicated alternating gold and sulfur atoms on the surfaces, consistent with gold-thiol polymers predicted as intermediates by Brust et al. (Section 2.1.2.2; Scheme 2-2, pg. 57).⁹⁵⁻⁹⁷ It was therefore presumed that the higher pH and incubation time before reduction was conducive to the formation of the precursor gold-thiol polymer, which, as mentioned above, most likely does not form in the case of platinum.

As it has been speculated that the mechanism for forming platinum particles differs from that observed for gold (Section 2.2.3),³⁸ it was unclear how these conditions would affect the formation of platinum particles. A series of experiments indicated that particle formation was indeed more consistent at higher pH values with optimum results observed when the pH was approximately 12-13. This could have simply been due to higher concentrations of disulfide in solution, which is favored over the thiol at higher pH values. Ill-defined colloids and aggregates were observed using a 3:1 ratio of NaBH₄/Pt and better results were achieved using the higher ratios associated with the initial synthesis. Figure 2-23 shows particles synthesized at two different thiol/platinum ratios. As expected, the lower ratio yielded slightly larger particles.

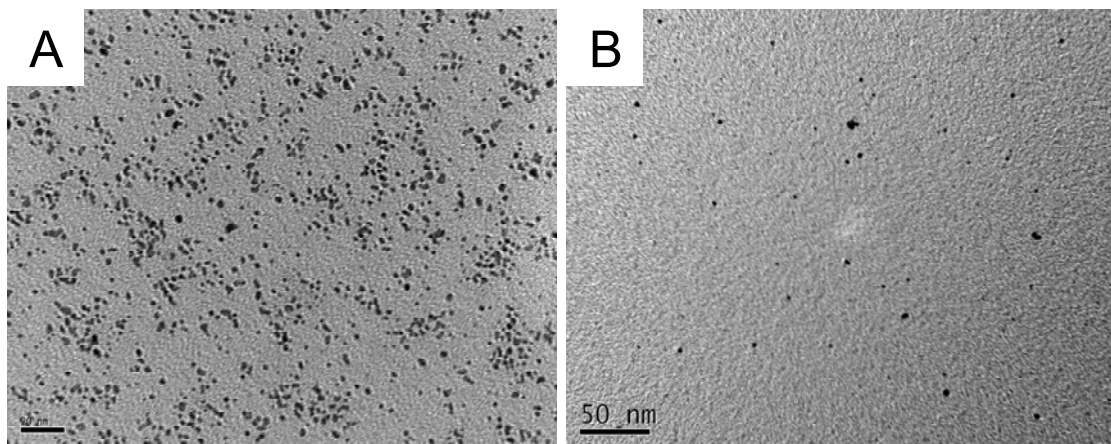


Figure 2-23. Platinum particles with 4-mercaptopbenzoic acid (A) thiol/gold ratio of 0.5:1; particle size 2.1 ± 0.5 nm (B) thiol/gold ratio of 1:1; particle size 3.0 ± 0.5 nm

While a method was developed that consistently yielded platinum particles with mercaptobenzoic acid capping ligands, the exact mechanism for this particle formation is still unclear and particle stability remains an issue. All attempts at purifying these particle solutions resulted in irreversible aggregation.

2.2.3.5. Reverse Micelle Synthesis of Platinum Particles

Another method used to synthesize platinum particles is through the use of reverse micelles, a concept described in (Section 2.1.2.3)^{4,6,128-133}. The procedure used here was based on one described by Martin et al.⁶ for the synthesis of both platinum and palladium particles. While applicable to palladium, efforts were focused on the synthesis of platinum particles. A 10% solution of surfactant in oil was used to create the reverse micelles. The surfactant was Brij® 30, C₁₂H₂₅(OCH₂CH₂)₄OH, in pentane. While Martin et al.⁶ used oils ranging from pentane to hexadecane and claimed that the type of oil had an effect

on the size and dispersity of the resulting particles, this trend was not explained and pentane was most readily available in the lab. H₂PtCl₆ was then added to the surfactant solution, which was stirred overnight to ensure the metal salt was distributed between the

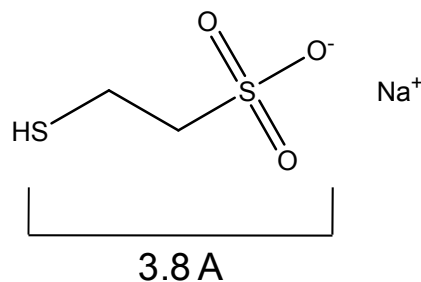


Figure 2-24. Sodium 2-mercaptoethanesulfonate. Distance measured using Chem3D Software after MM2 energy minimization

micelles before reduction with lithium borohydride (LiBH_4) in THF. The use of reverse micelles permitted the use of this stronger reducing agent, which hydrolyzes in water, and dissolving the reducing agent in THF increased the rate of reduction. THF is completely soluble in the oil phase and facilitated fast mixing within the solution.⁶

After reduction was complete, the capping ligand was introduced to the particle solution. The literature reported that either a hydrophobic or hydrophilic capping ligand could be used.⁶ However, the hydrophilic ligands were introduced in organic solvents. In this work, 2-mercaptoethanesulfonate was introduced as a solution in formamide. This ligand was chosen as it was reported to yield discreet particles with high stability and it satisfied the length requirements of this project (Figure 2-24).

Platinum particles synthesized in a 10% Brij® 30 solution with 2-mercaptoethanesulfonate are shown in Figure 2-25(A), and exhibited a particle size of 4.7 ± 0.9 nm. It was speculated that lower surfactant concentrations might yield larger particles; however, as shown in Figure 2-25(B), small aggregates were observed when 7% Brij® was used. After particle synthesis was complete, attempts were made to reduce particle size dispersity by thermal annealing at 70 °C for 96 hours. However, only minimal size differences and some aggregation were observed. For the particles synthesized with 7% Brij® 30, complete aggregation

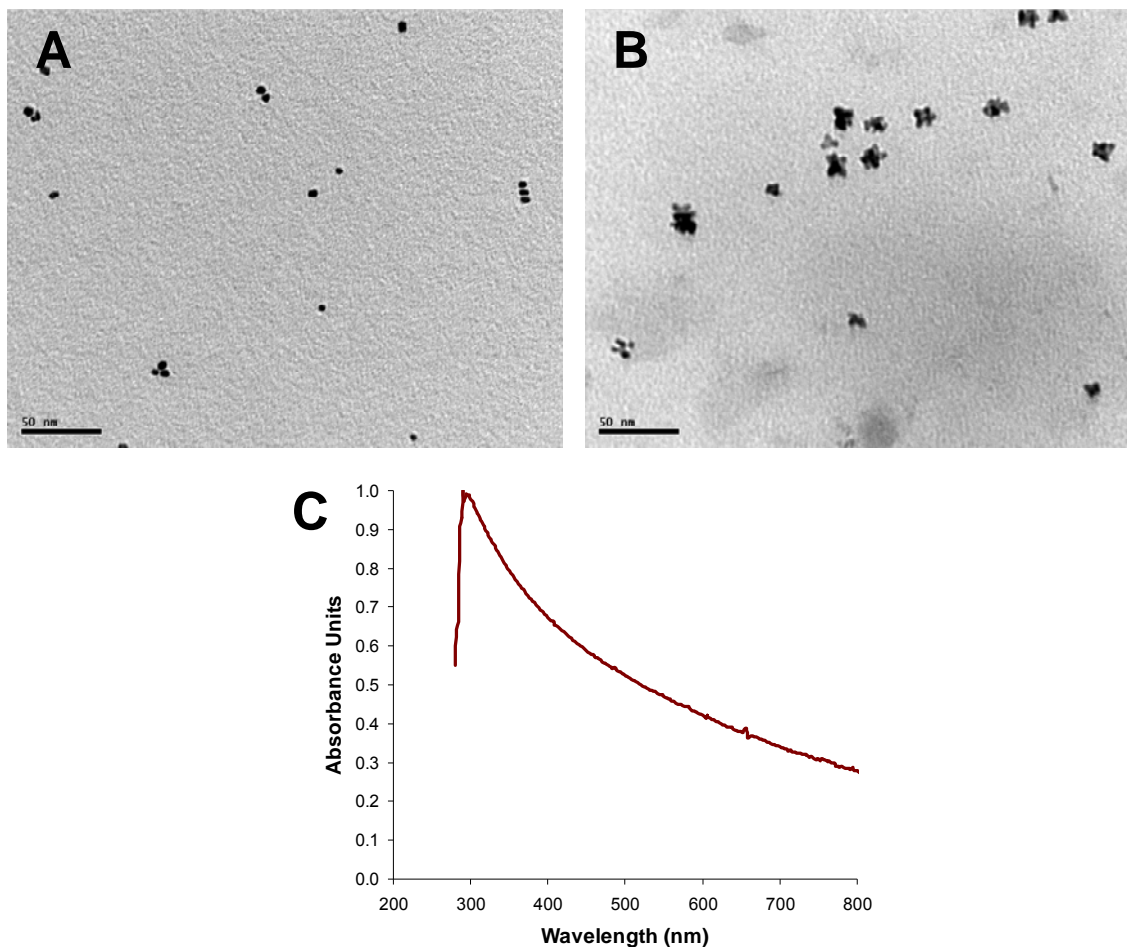


Figure 2-25. Platinum particles synthesized using reverse micelles and capped with 2-mercaptoethanesulfonate in formamide (A) TEM of particles synthesized with 10% solution of surfactant in pentane; particle size 4.7 ± 0.9 nm (B) TEM of particles synthesized with 7% solution of surfactant in pentane (C) Absorption spectrum of particles synthesized with 10% surfactant solution

occurred upon annealing and the tailing optical absorbance shown in Figure 2-25(C) completely disappeared.

The major disadvantage of particles synthesized using this method was solubility.

While they exhibited high degrees of stability in some hydrophilic solvents, including

formamide, these particles aggregated upon suspension in aqueous solution.

Future experiments could involve the subsequent ligand-exchange with a molecule that is more stable in water.

2.2.4. Nickel Particles

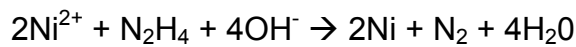
2.2.4.1. Evaluation of literature methods for nickel nanoparticle synthesis

Nickel particles were also investigated for heterodimer formation as strong binding has been reported between isocyanides and nickel surfaces.²¹¹⁻²¹³ Again, the first task at hand was to select an appropriate method for the preparation of water-soluble nickel nanoparticles. Lee et al.²¹¹ observed that both the surface coverage and stability of isocyanide monolayers were significantly greater on reduced nickel surfaces than on oxidized nickel. However, synthesizing pure nickel particles is difficult as nickel is easily oxidized in the presence of air.²³⁶⁻²³⁸ The most commonly reported methods for synthesizing nickel particles involve organic solvents to avoid the formation of nickel oxide or hydroxide. More specifically, nickel particles have often been formed through the decomposition of metallic precursors such as $\text{Ni}(\text{COD})_2$ ²³⁹⁻²⁴³ and $\text{Ni}(\text{acac})_2$ ²⁴⁴⁻²⁴⁷ in the presence of a basic reducing agent and often a stabilizing polymer (Section 2.1.2.2).* Stabilizing polymers such as poly(vinylpyrrolidone) (PVP) are commonly used as PVP has little interaction with the

* COD = cycloocta-1,5-diene; acac = acetylacetonate

surface and does not alter the electronic and magnetic structure of the particles.^{240,242}

Due to the tendency of nickel to oxidize, there are far fewer reports of nickel particles synthesized in aqueous solution. However, in 2002, Chen et al.²³⁶ reported the successful synthesis of nickel particles through the reduction of NiCl₂ with hydrazine. This reaction, which has also been performed in ethylene glycol²³⁸ and reverse micelles²⁴⁸ produces nitrogen as shown below.



It was believed that the continuous flow of nitrogen generated during the reduction prevented the nickel from oxidizing.^{236-238,248} X-ray diffraction experiments indicated that the resulting particles contained only metallic nickel. No oxides or hydroxides such as NiO, Ni₂O₃ or Ni(OH)₂ were observed.^{236,237,248}

Several reports of particle formation through the reduction of nickel chloride with hydrazine have been described in the literature. The initial procedure reported involved the reduction of nickel chloride with hydrazine in an aqueous solution of mixed cationic surfactants, sodium hydroxide (NaOH) and acetone at elevated temperatures.²³⁶ However, two years later a similar procedure was reported in which both the organic solvent and the elevated temperature were unnecessary.²³⁷ The reduction was carried out at room temperature in the presence of the cationic surfactant, cetyltrimethylammonium bromide (CTAB). It was speculated that the

formation of CTAB micelles was not critical to particle formation; CTAB acted simply as a stabilizing ligand. It was speculated that the formation of CTAB micelles were not critical to particle formation

The room temperature synthesis was also evaluated in attempt to determine how reaction conditions affected both particle size and dispersity. It was reported that the particle diameter increased with nickel chloride concentration,²³⁶ except at high hydrazine concentrations where particle size was independent of the nickel chloride concentration.²⁴⁸ The particle diameter also appeared to decrease with hydrazine concentration.^{236-238,248} While particles

did not form in the absence of NaOH, its role in particle formation was unclear. The solution pH increased from 10.2 to 10.6 upon the addition of NaOH, however when the pH was increased to the same extent with hydrazine, particles did not form.²³⁶⁻²³⁸ It was therefore suggested that NaOH somehow catalyzed the particle formation. In ethylene glycol, the required amount of NaOH appeared to

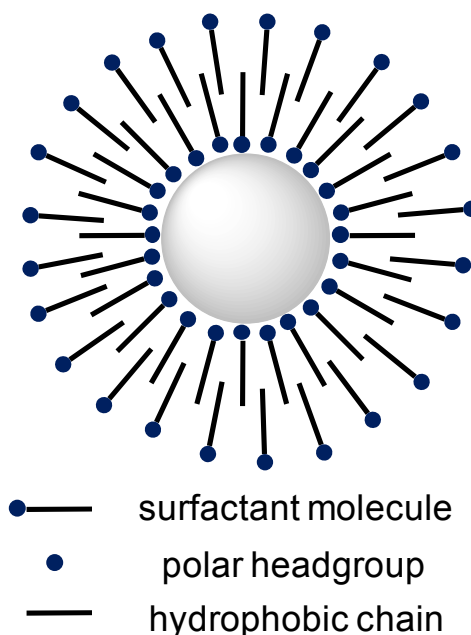


Figure 2-26. Schematic of surfactant bilayer surrounding a nanoparticle. The extent of interdigitation of the alkyl chains is not known.

increase with nickel chloride concentration.²³⁸ In aqueous solution, Ba(OH)₂, KOH and tetramethylammonium hydroxide also appeared to catalyze particle formation.²³⁷

The exact nature of the interaction between CTAB and the nickel particles is also a little unclear. Thermogravimetric analysis of the nickel particles indicated that CTAB stabilized the particles through a bilayer structure as shown in Figure 2-26.²³⁷ The positively-charged, hydrophilic headgroups of the inner layer were adsorbed to the particle surface while the headgroups of the outer layer were in the aqueous solution. The two layers were connected through hydrophobic interactions. Similar behavior was reported for the interactions of CTAB and tetraoctylammonium bromide (TOAB) with gold nanorods in aqueous solution.²⁴⁹ For this case, the adsorption of the surfactant to the gold surface was attributed to hydrogen bonding between water molecules present at the particle surface and the bromide counterions. Similarly, a study involving quaternary ammonium compounds on flat surfaces suggested that the interaction of the positively-charged headgroups could be through direct interaction with negatively-charged sodium oxalate.²⁵⁰ However, it was determined more likely that this adsorption occurred indirectly through interactions involving other ions in solution.

In addition to unclear interactions between the CTAB and the particle surface, the extent of interaction between the two layers is also uncertain. For bilayers of hexadecyltrimethylammonium bromide on a silica surface, neutron reflectivity data

indicated that the layer thickness was substantially less than twice the extended chain length, suggesting the interdigitation of alkyl chains.²⁵¹ However, another theoretical study claimed that minimal interdigitation should occur as the electrostatic repulsion between the two headgroups is greater than any energy gain associated with the hydrophobic interactions.²⁵²

2.2.4.2. Synthesis of Nickel Nanoparticles with CTAB and PTAB

Nickel particles were synthesized through the reduction of NiCl_2 in aqueous solution with CTAB at room temperature according to the procedure outlined by Wu et al.²³⁷

While CTAB is longer than what is desirable for heterodimer formation (Figure 2-27), this method was then adapted to the much shorter compound,

phenyltrimethylammonium bromide (PTAB). It was hypothesized that PTAB could stabilize nickel particles

assuming that the

presence of micelles was

not critical to particle

formation and

interdigitation of ligands in

bilayer structures was not

crucial for particle stability.

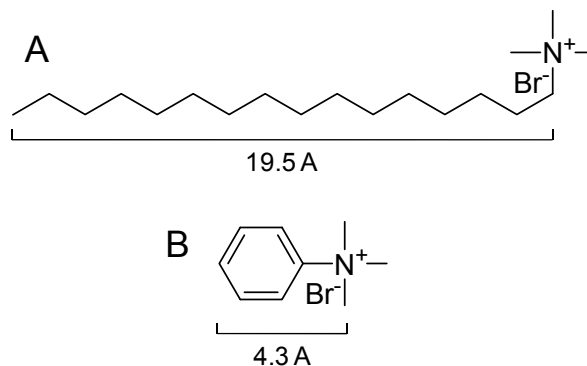


Figure 2-27. (A) Cetyltrimethylammonium bromide (CTAB) (B) Phenyltrimethylammonium bromide (PTAB)

As detailed in Section 2.2.6.5 (pg. 131), the procedure reported in the literature was rather ambiguous and thus several experiments were necessary in order to determine the optimum reaction conditions.

Table 2-3 shows the results obtained as both the nickel chloride and hydrazine

Table 2-3. Nickel-CTAB particle Synthesis 1: Variables = NiCl₂ and N₂H₄ conc. and stirring

Reactant	Conc. (M)	[NiCl ₂]/[CTAB]	[NiCl ₂]/[N ₂ H ₄]	Stirred?	Observations
NiCl ₂	0.025	2.5	0.1	Yes	TEM indicated the presence of many large aggregates in addition to particles. Average of 35 particle measurements = 138 +/- 108 nm (78%)
CTAB	0.010				
Hydrazine (N ₂ H ₄)	0.250				
NaOH	0.020				
NiCl ₂	0.025	2.5	0.1	No	TEM indicated the presence of several large aggregates in addition to particles. Average of 35 particle measurements = 2.8 +/- 0.7 nm (25%)
CTAB	0.010				
Hydrazine (N ₂ H ₄)	0.250				
NaOH	0.020				
NiCl ₂	0.025	2.5	0.09	Yes	TEM indicated the presence of several aggregates in addition to particles. Average of 56 particle measurements = 113 +/- 58 nm (51%)
CTAB	0.010				
Hydrazine (N ₂ H ₄)	0.280				
NaOH	0.020				
NiCl ₂	0.025	2.5	0.09	No	TEM indicated the presence of several aggregates in addition to particles. Average of 44 particle measurements = 35.8 +/- 9.3 nm (25%)
CTAB	0.010				
Hydrazine (N ₂ H ₄)	0.280				
NaOH	0.020				
NiCl ₂	0.020	2.0	0.08	Yes	TEM indicated may large aggregates in addition to small particles. Average of 45 particle measurements = 9.3 +/- 6.4 nm (69%)
CTAB	0.010				
Hydrazine (N ₂ H ₄)	0.250				
NaOH	0.020				
NiCl ₂	0.020	2.0	0.08	No	TEM did not indicate aggregates – just particles. Average of 44 particle measurements = 48.3 +/- 25.7 nm (53%)
CTAB	0.010				
Hydrazine (N ₂ H ₄)	0.250				
NaOH	0.020				



Figure 2-28. Aqueous solution containing Nickel-CTAB particles

shown in Figure 2-28. The particle sizes reported are slightly misleading as they do not reflect the extent of aggregation in solution. The major findings in this experiment were that stirring the particle solution yielded higher degrees of aggregation. More uniform particles were observed when stirring was ceased after approximately one minute. Increasing the hydrazine concentration was expected to decrease particle size.

While the data shown here appears to be contradictory, significantly less aggregation was observed in the presence of higher hydrazine concentrations. As expected, lower nickel concentrations yielded resulted in smaller particles and less aggregation. However, none of these reactions yielded monodisperse particles free of aggregation.

These variables were altered in a few more experiments. However, the variable that appeared to play the largest role was the concentration of CTAB as shown in Table 2-4. In the presence of higher CTAB concentrations, TEM did not indicate the presence of aggregates. In addition, the particle sizes decreased slightly. A TEM image of the resulting particles is shown in Figure 2-29(A) from which particles were determined to be 2.5 ± 0.7 nm.

Table 2-4. Nickel-CTAB particle Synthesis 2: Variable = CTAB concentration

Reactant	Conc. (M)	[NiCl ₂]/ [CTAB]	[NiCl ₂]/ [N ₂ H ₄]	Stirred?	Observations
NiCl ₂	0.025	2.5	0.09	No	TEM indicated some aggregation. Average of 50 particle measurements = 2.8 ± 0.8 nm
CTAB	0.010				
Hydrazine (N ₂ H ₄)	0.280				
NaOH	0.020				
NiCl ₂	0.025	0.5	0.09	No	TEM did not indicate the presence of aggregates. Average of 50 particle measurements = 2.5 ± 0.7 nm.
CTAB	0.050				
Hydrazine (N ₂ H ₄)	0.280				
NaOH	0.020				

Once the reaction conditions were optimized for the synthesis of nickel particles with CTAB, these conditions were applied to the synthesis of PTAB-capped nickel particles. The resulting particles were determined to be 3.6 ± 0.9 nm (Figure 2-29(B)), which is slightly larger than the corresponding CTAB particles. The fact that particles were synthesized in the presence of PTAB supported the belief that micelles were not necessary for particle formation. The capping ligands most likely adsorbed to the surface after particle formation. It was unclear, however, if the PTAB formed a bilayer structure similar to that observed for CTAB.

The major difficulty associated with the synthesis of nickel particles with both capping ligands is that all attempts at purification resulted in particle aggregation. Experiments to rectify this could include ligand-exchange with another capping ligand that would exhibit a stronger interaction with the nickel particles and thus more stability against aggregation.

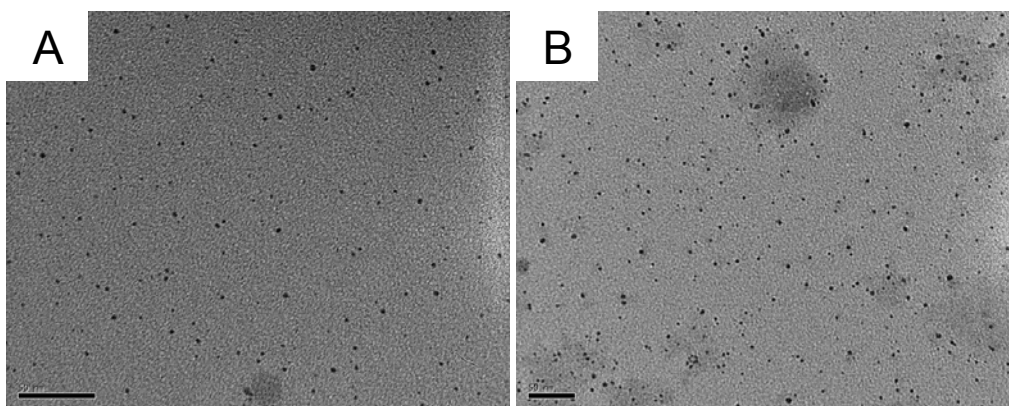


Figure 2-29. (A) TEM of nickel particles (A) synthesized with 0.05 M CTAB (B) synthesized with 0.05 M PTAB

2.2.5. Summary and Conclusions

The properties of commercially-available gold-citrate particles were evaluated.

While the interaction of both citrate and tannic acid with the gold particles is unclear, it was speculated that higher concentrations of tannic acid present in solutions containing smaller particles could contribute to steric bulk on the particle surface.

Methods for synthesizing both platinum and nickel particles with short, hydrophilic capping ligands were evaluated for eventual incorporation into nanoparticle heterodimers.

Platinum particles with tiopronin capping ligands were successfully synthesized and purified according to a literature procedure. The resulting particles were 1.75 ± 0.24 nm. However, attempts to synthesize platinum particles with glutathione

capping ligands according to a literature procedure were unsuccessful, and TEM data indicated aggregation. A few discrepancies with the published procedure were noted, and it is possible that systematic variations in the reaction conditions may have yielded more stable particles. However, these were not explored.

Platinum particles were synthesized with 4-mercaptobenzoic acid capping ligands, based on similar methods published for gold. Initial attempts at synthesizing these particles under acidic conditions were irreproducible. This was attributed to varying concentrations of the aromatic disulfide in solution. Consistent results were achieved when these particles were synthesized in basic conditions. The resulting particles were 3.0 ± 0.5 nm. However, all attempts to purify these particles resulted in aggregation.

Platinum particles were synthesized in reverse micelles and then capped with 2-mercaptoethanesulfonate. The resulting particles were $4. \pm 0.9$ nm. While these particles were successfully purified through precipitation with 1-propanol, aggregation was observed when they were suspended in aqueous solution. These hydrophilic particles were stable in formamide.

Reaction conditions were optimized for the synthesis of nickel particles with CTAB, and then these conditions were applied to the synthesis of nickel particles with PTAB. The resulting particles were 2.5 ± 0.7 nm and $3. \pm 0.9$ nm, respectively. The

observation of nickel particles in the presence of PTAB supported prior claims that micelles were not critical to the formation of nickel particles. While the interaction of PTAB with the particle surface is unclear, these data also support the claim that a highly inter-digitated bilayer is not crucial to particle stability. All attempts to purify these particles resulted in aggregation.

Attempts to synthesize heterodimers using these particles are reported in Chapter 4.

2.2.6. Experimental

2.2.6.1. Synthesis of Tiopronin-capped Platinum Particles

Particles were synthesized according to a literature procedure.³⁸ $\text{H}_2\text{PtCl}_6 \cdot 6\text{H}_2\text{O}$ (0.22 mmol, 0.112 g) and tiopronin (0.15 mmol, 0.025 g) were stirred in 35 mL 6:1 methanol/acetic acid for 30 min. NaBH_4 (4.32 mmol, 0.167 g) was added and the solution was stirred for an additional 30 min. The solvent was evaporated at 38 °C and the residue was dissolved in 50 mL filtered, deionized water. The solution was acidified to pH 1 with concentrated HCl prior to purification by dialysis with Spectrapor CE dialysis tubing (MWCO 10,000). The tubing was stirred in 4 L water, which was changed twice a day for three days. The water was evaporated from the purified solution and the particles dried. The resulting particles were 1.75 ± 0.24 nm as measured by TEM and exhibited a tailing optical absorbance.

2.2.6.2. Synthesis of Glutathione-capped Platinum Particles

Particles were synthesized according to a literature procedure.³⁸ $\text{H}_2\text{PtCl}_6 \cdot 6\text{H}_2\text{O}$ (0.19 mmol, 0.100 g) and glutathione (0.13 mmol, 0.041 g) were added to a round-bottomed flask containing 25 mL deionized water. The solution was stirred for 30 min. before 3 mL aqueous NaBH_4 solution (1.9 mmol, 0.072 g) was added and the solution was stirred for an additional 30 min. The water was evaporated and the particles precipitated with the addition of ethanol, filtered on a fine frit and washed with additional ethanol. After purification, TEM showed large aggregates rather than discrete particles.

2.2.6.3. Synthesis of Platinum Particles with 4-mercaptobenzoic acid

Method 1 – Particle synthesis was adapted from a similar procedure for gold.¹⁷⁶ An aliquot of 20 mL of 0.053 M $\text{H}_2\text{PtCl}_6 \cdot 6\text{H}_2\text{O}$ (1.06 mmol, 0.434 g) in methanol was added to 20 mL 0.095 M (1.90 mmol, 0.293 g) of 4-mercaptobenzoic acid in methanol in a round-bottomed flask. While the solution was stirring, 10 mL acetic acid was added followed by 10 mL 0.891 M aqueous NaBH_4 solution (8.91 mmol, 0.337 g). The solution turned dark brown and was stirred for three hours. The solvent was evaporated and the residue dissolved in water and washed with diethyl ether (x3). The resulting solution contained free 4-mercaptobenzoic acid; the particles were precipitated from solution by centrifugation and the remaining solution was decanted off (x3). This procedure yielded inconsistent results as evidenced by

TEM. The ratio of thiol/Pt was altered slightly for different experiments as indicated in the text.

Method 2- Particle synthesis was adapted from a similar procedure for gold.²³⁴ An aliquot of 3 mL of 40 mM $\text{H}_2\text{PtCl}_6 \cdot \text{H}_2\text{O}$ (0.12 mmol, 0.049 g) in methanol was added to 3 mL of 40 mM 4-mercaptobenzoic acid (0.12 mmol, 0.019 g) in methanol. This solution was diluted with 6 mL of H_2O so that the solution concentration was 50% methanol/50% H_2O , and then the pH was adjusted to ~ 13 with 0.1 M NaOH. After stirring overnight, this solution was further diluted so that the final methanol concentration was 27%, and then a 20-fold excess of NaBH_4 was added (2.4 mmol, 0.090 g) as a solution in 2.5 mL water. The resulting particles were 3.0 ± 0.5 nm as measured by TEM and exhibited a tailing optical absorbance. The ratio of thiol/Pt was altered slightly for different experiments as indicated in the text. All attempts at purification including washing with diethyl ether, precipitation of the particles and rinsing using centrifugation filtration resulted in aggregation.

2.2.6.4. Reverse Micelle Synthesis of Platinum Particles

Particles were synthesized according to a literature procedure.⁶ A 10% solution of Brij® 30, $\text{C}_{12}\text{H}_{25}(\text{OCH}_2\text{CH}_2)_4\text{OH}$, was made by mixing 5 mL Brij® 30 and 45 mL pentane in a Schlenck flask under positive N_2 flow. The surfactant concentration was altered slightly as indicated in the text. The flask was covered with aluminum foil to shield the solution from light. Then, 0.20 g (0.50 mmol) H_2PtCl_6 was added to

achieve a concentration of 0.01 M. After stirring overnight, a 4-fold excess of LiBH_4 in THF (2.0 mmol, 43.5 mg) was added, and the solution was stirred for approximately 30 min. before the capping ligand was introduced. A solution of 15 mL of 0.5 M sodium 2-mercaptoethanesulfonate (0.008 mol, 1.23 g) in formamide was added to the solution to yield a final concentration of 0.10 M. After stirring for approximately 30 min., particles were precipitated with 1-propanol. The resulting suspension was centrifuged, the supernant decanted and the precipitate re-suspended in 1-propanol (x3). Afterwards, the particles were dissolved in formamide. The resulting particles were 4.7 ± 0.9 nm as measured by TEM, and exhibited a tailing optical absorbance. Thermal annealing was attempted by placing the final particle solution in an oven at 70 °C for 96 hours. However, this did not noticeably improve particle size dispersity and subsequently some aggregates were observed by TEM.

2.2.6.5. Synthesis of Nickel Particles

Nickel-CTAB Particles – Particle synthesis was based on a previously-reported literature procedure.²³⁷ The procedure in the literature was reported as:

“In general the synthesis of Ni nanoparticle, an aqueous solution of 10 mL was first prepared by dissolving [cetyltrimethylammonium bromide] CTAB (0.01 M) and nickel chloride (0.005-0.05 M) in water. Then hydrazine (0.25-2 M) and NaOH solutions (0.02 M) were added in sequence. At 25 °C, Ni particles were formed after about 20 hours in a capped bottle.”

The concentrations of the reactants were varied as indicated in the text. The best results were achieved when 59.4 mg (0.25 mmol) of $\text{NiCl}_2 \cdot 6\text{H}_2\text{O}$ and 36.4 mg (0.50 mmol) of CTAB were dissolved in 10 mL H_2O , and 88.5 μL (2.8 mmol) hydrazine was then added followed by 50 μL of 4 mM NaOH solution. The solution was stirred for approximately one minute and then incubated in a capped vial at room temperature overnight.

Nickel-PTAB Particles – Particles were synthesized using the same method described above with 182 mg (0.50 mmol) of phenyltrimethylammonium bromide (PTAB) substituted for CTAB.

2.2.6.6. Particle Characterization

TEM Images were taken with a Philips CM12 TEM operated at 100 kV. Images were captured using a Gatan 780 camera and DigitalMicrograph software. Particle sizes were measured using Image J software and setting the scale using the scale bars captured with the images. A minimum of 30-50 particles were measured when calculating average particle sizes.

Absorbance measurements were made using a Hewlett-Packard 8452A Diode Array Spectrometer and a path length of 1.0 cm. All particles were analyzed in water with the exception of the particles synthesized in reverse micelles, which were analyzed in formamide.

2.3.References

- (1) Alvarez, M. M.; Khoury, J. T.; Schaaff, T. G.; Shafiqullin, M.; Vezmar, I.; Whetten, R. L., *Chem. Phys. Lett.* **1997**, *266*, 91-98.
- (2) Ackerson, C. J.; Jadzinsky, P. D.; Kornberg, R. D., *J. Am. Chem. Soc.* **2005**, *127*, 6550-6551.
- (3) Heimenz, P. C.; Rajagopalan, R. *Principles of Colloid and Surface Chemistry*, Marcel Dekker, Inc.: New York, 1997.
- (4) Pileni, M.-P., *Nature Mater.* **2003**, *2*, 145-150.
- (5) Obare, S. O.; Hollowell, R. E.; Murphy, C. J., *Langmuir* **2002**, *18*, 10407-10410.
- (6) Martin, J. E.; Wilcoxon, J. P.; Odinek, J.; Provencio, P., *J. Phys. Chem. B* **2002**, *106*, 971-978.
- (7) Manna, L.; Scher, E. C.; Alivisatos, A. P., *J. Am. Chem. Soc.* **2000**, *122*, 12700-12706.
- (8) Watzky, M. A.; Finke, R. G., *J. Am. Chem. Soc.* **1997**, *119*, 10382-10400.
- (9) Eustis, S.; El-Sayed, M. A., *Chem. Soc. Rev.* **2006**, *35*, 209-217.
- (10) Sau, T. K.; Murphy, C. J., *J. Am. Chem. Soc.* **2004**, *126*, 8648-8649.
- (11) Pellegrino, T.; Manna, L.; Kudera, S.; Liedl, T.; Koktysh, D.; Rogach, A. L.; Keller, S.; Radler, J.; Natile, G.; Parak, W. J., *Nano Lett.* **2004**, *4*, 703-707.
- (12) Xia, Y. N.; Yang, P. D.; Sun, Y. G.; Wu, Y. Y.; Mayers, B.; Gates, B.; Yin, Y. D.; Kim, F.; Yan, Y. Q., *Adv. Mater.* **2003**, *15*, 353-389.
- (13) Lim, I. I. S.; Njoki, P. N.; Park, H. Y.; Wang, X.; Wang, L. Y.; Mott, D.; Zhong, C. J., *Nanotechnology* **2008**, *19*.
- (14) Tripp, R. A.; Dluhy, R. A.; Zhao, Y. P., *Nano Today* **2008**, *3*, 31-37.
- (15) Link, S.; El-Sayed, M. A.; Mohamed, M. B., *J. Phys. Chem. B* **2005**, *109*, 10531-10532.

- (16) Kelly, K. L.; Coronado, E.; Zhao, L. L.; Schatz, G. C., *J. Phys. Chem. B* **2003**, *107*, 668-677.
- (17) Creighton, J. A.; Eadon, D. G., *J. Chem. Soc.-Faraday Trans.* **1991**, *87*, 3881-3891.
- (18) Khlebtsov, N. G.; Bogatyrev, V. A.; Dykman, L. A.; Melnikov, A. G., *J. Colloid Interface Sci.* **1996**, *180*, 436-445.
- (19) Daniel, M. C.; Astruc, D., *Chem. Rev.* **2004**, *104*, 293-346.
- (20) Feldhiem, D. L.; Foss, C. A. In *Metal Nanoparticles: Synthesis, Characterization and Applications*; Feldhiem, D. L., Foss, C. A., Eds.; Marcel Dekker: New York, 2002, pp 1-13.
- (21) West, J. L.; Halas, N. J., *Annual Review of Biomedical Engineering* **2003**, *5*, 285-292.
- (22) Burda, C.; Chen, X. B.; Narayanan, R.; El-Sayed, M. A., *Chem. Rev.* **2005**, *105*, 1025-1102.
- (23) Wiley, B.; Sun, Y. G.; Mayers, B.; Xia, Y. N., *Chem. Eur. J.* **2005**, *11*, 454-463.
- (24) Phan, N. T. S.; Van Der Sluys, M.; Jones, C. W., *Adv. Synth. Catal.* **2006**, *348*, 609-679.
- (25) Haruta, M., *Gold Bulletin* **2004**, *37*, 27-36.
- (26) Schlogl, R.; Abd Hamid, S. B., *Ang. Chem. Int. Edit.* **2004**, *43*, 1628-1637.
- (27) Thomas, J. M.; Johnson, B. F. G.; Raja, R.; Sankar, G.; Midgley, P. A., *Acc. Chem. Res.* **2003**, *36*, 20-30.
- (28) Campbell, C. T.; Parker, S. C.; Starr, D. E., *Science* **2002**, *298*, 811-814.
- (29) Somorjai, G. A.; Borodko, Y. G., *Catal. Lett.* **2001**, *76*, 1-5.
- (30) Waszczuk, P.; Solla-Gullon, J.; Kim, H. S.; Tong, Y. Y.; Montiel, V.; Aldaz, A.; Wieckowski, A., *J. Catal.* **2001**, *203*, 1-6.

- (31) Hermans, S.; Raja, R.; Thomas, J. M.; Johnson, B. F. G.; Sankar, G.; Gleeson, D., *Angew. Chem. Int. Ed.* **2001**, *40*, 1211-+.
- (32) Toshima, N.; Shiraishi, Y.; Teranishi, T.; Miyake, M.; Tominaga, T.; Watanabe, H.; Brijoux, W.; Bonnemann, H.; Schmid, G., *Appl. Organomet. Chem.* **2001**, *15*, 178-196.
- (33) Raja, R.; Sankar, G.; Hermans, S.; Shephard, D. S.; Bromley, S.; Thomas, J. M.; Johnson, B. F. G., *Chem. Commun.* **1999**, 1571-1572.
- (34) Shiraishi, Y.; Toshima, N., *J. Molec. Catal. A: Chem.* **1999**, *141*, 187-192.
- (35) Toshima, N.; Yonezawa, T., *New J. Chem.* **1998**, *22*, 1179-1201.
- (36) Mayer, A. B. R.; Mark, J. E., *Colloid. Polym. Sci.* **1997**, *275*, 333-340.
- (37) Niesz, K.; Koebel, M. M.; Somorjai, G. A., *Inorg. Chim. Acta* **2006**, *359*, 2683-2689.
- (38) Eklund, S. E.; Cliffler, D. E., *Langmuir* **2004**, *20*, 6012-6018.
- (39) Okura, I. In *Encyclopedia of Nanoscience and Nanotechnology*; Nalwa, H. S., Ed.; American Scientific Publishers: Stevenson Ranch, CA, 2004; Vol. 8, pp 41-48.
- (40) Kane, V.; Mulvaney, P., *Langmuir* **1998**, *14*, 3303-3311.
- (41) Moskovits, M., *J. Raman Spectroscopy* **2005**, *36*, 485-496.
- (42) Tian, Z. Q., *J. Raman Spectroscopy* **2005**, *36*, 466-470.
- (43) Vo-Dinh, T.; Yan, F.; Wabuyele, M. B., *J. Raman Spectroscopy* **2005**, *36*, 640-647.
- (44) Qian, X. M.; Nie, S. M., *Chem. Soc. Rev.* **2008**, *37*, 912-920.
- (45) Porter, M. D.; Lipert, R. J.; Siperko, L. M.; Wang, G.; Narayanan, R., *Chem. Soc. Rev.* **2008**, *37*, 1001-1011.
- (46) Alexander, T. A., *Anal. Chem.* **2008**, *80*, 2817-2825.

- (47) Stewart, M. E.; Anderton, C. R.; Thompson, L. B.; Maria, J.; Gray, S. K.; Rogers, J. A.; Nuzzo, R. G., *Chem. Rev.* **2008**, *108*, 494-521.
- (48) Sun, L. L.; Song, Y. H.; Wang, L.; Guo, C. L.; Sun, Y. J.; Liu, Z. L.; Li, Z., *J. Phys. Chem. B* **2008**, *112*, 1415-1422.
- (49) Anderson, D. J.; Moskovits, M., *J. Phys. Chem. B* **2006**, *110*, 13722-13727.
- (50) Doering, W. E.; Nie, S. M., *J. Phys. Chem. B* **2002**, *106*, 311-317.
- (51) Liu, J.; Alvarez, J.; Ong, W.; Kaifer, A. E., *Nano Lett.* **2001**, *1*, 57-60.
- (52) Haes, A. J.; Van Duyne, R. P., *J. Am. Chem. Soc.* **2002**, *124*, 10596-10604.
- (53) Hutter, E.; Pileni, M. P., *J. Phys. Chem. B* **2003**, *107*, 6497-6499.
- (54) Hutter, E.; Cha, S.; Liu, J. F.; Park, J.; Yi, J.; Fendler, J. H.; Roy, D., *J. Phys. Chem. B* **2001**, *105*, 8-12.
- (55) Watanabe, S.; Sonobe, M.; Arai, M.; Tazume, Y.; Matsuo, T.; Nakamura, T.; Yoshida, K., *Chem. Commun.* **2002**, 2866-2867.
- (56) Lin, S. Y.; Liu, S. W.; Lin, C. M.; Chen, C. H., *Anal. Chem.* **2002**, *74*, 330-335.
- (57) Kim, Y. J.; Johnson, R. C.; Hupp, J. T., *Nano Lett.* **2001**, *1*, 165-167.
- (58) Liu, J. W.; Lu, Y., *J. Am. Chem. Soc.* **2004**, *126*, 12298-12305.
- (59) Liu, J. W.; Lu, Y., *J. Am. Chem. Soc.* **2003**, *125*, 6642-6643.
- (60) Liu, J. W.; Lu, Y., *Anal. Chem.* **2004**, *76*, 1627-1632.
- (61) Elghanian, R.; Storhoff, J. J.; Mucic, R. C.; Letsinger, R. L.; Mirkin, C. A., *Science* **1997**, *277*, 1078-1081.
- (62) Storhoff, J. J.; Elghanian, R.; Mucic, R. C.; Mirkin, C. A.; Letsinger, R. L., *J. Am. Chem. Soc.* **1998**, *120*, 1959-1964.
- (63) Chakrabarti, R.; Klibanov, A. M., *J. Am. Chem. Soc.* **2003**, *125*, 12531-12540.

- (64) Huang, X. H.; El-Sayed, I. H.; Qian, W.; El-Sayed, M. A., *J. Am. Chem. Soc.* **2006**, *128*, 2115-2120.
- (65) Yang, W.; Peters, J. I.; Williams, R. O., *Int. J. Pharm.* **2008**, *356*, 239-247.
- (66) Azarmi, S.; Roa, W. H.; Loeberberg, R., *Adv. Drug Delivery Rev.* **2008**, *60*, 863-875.
- (67) Murakami, T.; Tsuchida, K., *Mini-Rev. Med. Chem.* **2008**, *8*, 175-183.
- (68) Vijayaraghavalu, S.; Raghavan, D.; Labhasetwar, V., *Current Opinion in Investigational Drugs* **2007**, *8*, 477-484.
- (69) Xu, Z. P.; Zeng, Q. H.; Lu, G. Q.; Yu, A. B., *Chem. Eng. Sci.* **2006**, *61*, 1027-1040.
- (70) Lockman, P. R.; Mumper, R. J.; Khan, M. A.; Allen, D. D., *Drug Dev. Ind. Pharm.* **2002**, *28*, 1-13.
- (71) Kreuter, J., *Adv. Drug Deliv. Rev.* **2001**, *47*, 65-81.
- (72) Tan, Y.; Li, Y.; Zhu, D. In *Encyclopedia of Nanoscience and Nanotechnology*; Nalwa, H. S., Ed.; American Scientific Publishers: Stevenson Ranch, CA, 2004, pp 9-40.
- (73) Ito, A.; Shinkai, M.; Honda, H.; Kobayashi, T., *J. Biosci. Bioeng.* **2005**, *100*, 1-11.
- (74) Gao, X. H.; Yang, L. L.; Petros, J. A.; Marshal, F. F.; Simons, J. W.; Nie, S. M., *Curr. Opin. Biotechnol.* **2005**, *16*, 63-72.
- (75) Mornet, S.; Vasseur, S.; Grasset, F.; Duguet, E., *J. Mater. Chem.* **2004**, *14*, 2161-2175.
- (76) Andres, R. P.; Bein, T.; Dorogi, M.; Feng, S.; Henderson, J. I.; Kubiak, C. P.; Mahoney, W.; Osifchin, R. G.; Reifenger, R., *Science* **1996**, *272*, 1323-1325.
- (77) Davidovic, D.; Tinkham, M., *Appl. Phys. Lett.* **1998**, *73*, 3959-3961.
- (78) Trindade, T.; O'Brien, P.; Pickett, N. L., *Chem. Mater.* **2001**, *13*, 3843-3858.

- (79) Dabbousi, B. O.; RodriguezViejo, J.; Mikulec, F. V.; Heine, J. R.; Mattoussi, H.; Ober, R.; Jensen, K. F.; Bawendi, M. G., *J. Phys. Chem. B* **1997**, *101*, 9463-9475.
- (80) Manna, L.; Milliron, D. J.; Meisel, A.; Scher, E. C.; Alivisatos, A. P., *Nature Mater.* **2003**, *2*, 382-385.
- (81) Brust, M.; Kiely, C. J., *Colloids and Surfaces A:Physicochem. Eng. Aspects* **2002**, *202*, 175-186.
- (82) Milliron, D. J.; Hughes, S. M.; Cui, Y.; Manna, L.; Li, J. B.; Wang, L. W.; Alivisatos, A. P., *Nature* **2004**, *430*, 190-195.
- (83) Hamaker, H. C., *Physica* **1937**, *4*, 1058-1072.
- (84) Tadros, T. F. In *Colloid Stability: The Role of Surface Forces - Part I*; Tadros, T. F., Ed.; Wiley-VCH: Weinheim, Germany, 2007; Vol. 1, pp 2-22.
- (85) Hunter, R. J. *Foundations of Colloidal Science*; Oxford University Press: New York, 2001.
- (86) Ross, S.; Morrison, I. D. *Colloidal Systems and Interfaces*; John Wiley & Sons: New York, 1988.
- (87) Hunter, R. J. *Introduction to Modern Colloid Science*; Oxford University Press: New York, 1993.
- (88) Roux, S.; Garcia, B.; Bridot, J. L.; Salome, M.; Marquette, C.; Lemelle, L.; Gillet, P.; Blum, L.; Perriat, P.; Tillement, O., *Langmuir* **2005**, *21*, 2526-2536.
- (89) Enustun, B. V.; Turkevich, J., *J. Am. Chem. Soc.* **1963**, *85*, 3317-&.
- (90) Turkevich, J., *Gold Bull.* **1985**, *18*, 125-131.
- (91) Templeton, A. C.; Wuelfing, W. P.; Murray, R. W., *Acc. Chem. Res.* **2000**, *22*, 27-36.
- (92) LaMer, V. K.; Dinegar, R. H., *J. Am. Chem. Soc.* **1950**, *72*, 4847-4854.
- (93) Brown, L. O.; Hutchison, J. E., *J. Phys. Chem. B* **2001**, *105*, 8911-8916.

- (94) Wilcoxon, J. P.; Provencio, P. P., *J. Am. Chem. Soc.* **2004**, *126*, 6402-6408.
- (95) Turkevich, J.; Stevenson, P. C.; Hillier, J., *J. Phys. Chem.* **1953**, *57*, 670-673.
- (96) Turkevich, J.; Stevenson, P. C.; Hillier, J., *Discussions of the Faraday Society* **1951**, 55-&.
- (97) Turkevich, J., *Gold Bull.* **1985**, *18*.
- (98) Brust, M.; Walker, M.; Bethell, D.; Schiffrin, D. J.; Whyman, R., *J. Chem. Soc. - Chem. Commun.* **1994**, 801-802.
- (99) Chen, S. W.; Templeton, A. C.; Murray, R. W., *Langmuir* **2000**, *16*, 3543-3548.
- (100) Schaaff, T. G.; Whetten, R. L., *J. Phys. Chem. B* **2000**, *104*, 2630-2641.
- (101) Jana, N. R.; Peng, X. G., *J. Am. Chem. Soc.* **2003**, *125*, 14280-14281.
- (102) Hostetler, M. J.; Wingate, J. E.; Zhong, C. J.; Harris, J. E.; Vachet, R. W.; Clark, M. R.; Londono, J. D.; Green, S. J.; Stokes, J. J.; Wignall, G. D.; Glish, G. L.; Porter, M. D.; Evans, N. D.; Murray, R. W., *Langmuir* **1998**, *14*, 17-30.
- (103) Slot, J. W.; Geuze, H. J., *Eur. J. Cell Bio* **1985**, *38*, 87-93.
- (104) Ahmadi, T. S.; Wang, Z. L.; Henglein, A.; ElSayed, M. A., *Chem. Mater.* **1996**, *8*, 1161-1163.
- (105) Brown, K. R.; Natan, M. J., *Langmuir* **1998**, *14*, 726-728.
- (106) Stoeva, S.; Klabunde, K. J.; Sorensen, C. M.; Dragieva, I., *J. Am. Chem. Soc.* **2002**, *124*, 2305-2311.
- (107) Prasad, B. L. V.; Stoeva, S. I.; Sorensen, C. M.; Klabunde, K. J., *Chem. Mater.* **2003**, *15*, 935-942.
- (108) Murray, C. B.; Norris, D. J.; Bawendi, M. G., *J. Am. Chem. Soc.* **1993**, *115*, 8706-8715.

- (109) Donega, C. D.; Liljeroth, P.; Vanmaekelbergh, D., *Small* **2005**, *1*, 1152-1162.
- (110) Yin, Y.; Alivisatos, A. P., *Nature* **2005**, *437*, 664-670.
- (111) Kim, S. W.; Park, J.; Jang, Y.; Chung, Y.; Hwang, S.; Hyeon, T.; Kim, Y. W., *Nano Lett.* **2003**, *3*, 1289-1291.
- (112) Kwon, S. G.; Piao, Y.; Park, J.; Angappane, S.; Jo, Y.; Hwang, N. M.; Park, J. G.; Hyeon, T., *J. Am. Chem. Soc.* **2007**, *129*, 12571-12584.
- (113) Hyeon, T.; Lee, S. S.; Park, J.; Chung, Y.; Bin Na, H., *J. Am. Chem. Soc.* **2001**, *123*, 12798-12801.
- (114) Park, J.; An, K. J.; Hwang, Y. S.; Park, J. G.; Noh, H. J.; Kim, J. Y.; Park, J. H.; Hwang, N. M.; Hyeon, T., *Nature Mater.* **2004**, *3*, 891-895.
- (115) Hyeon, T., *Chem. Commun.* **2003**, 927-934.
- (116) Park, J.; Kang, E. A.; Bae, C. J.; Park, J. G.; Noh, H. J.; Kim, J. Y.; Park, J. H.; Park, J. H.; Hyeon, T., *J. Phys. Chem. B* **2004**, *108*, 13594-13598.
- (117) Kang, E.; Park, J.; Hwang, Y.; Kang, M.; Park, J. G.; Hyeon, T., *J. Phys. Chem. B* **2004**, *108*, 13932-13935.
- (118) Park, J.; Lee, E.; Hwang, N. M.; Kang, M. S.; Kim, S. C.; Hwang, Y.; Park, J. G.; Noh, H. J.; Kini, J. Y.; Park, J. H.; Hyeon, T., *Angew. Chem. Int. Ed.* **2005**, *44*, 2872-2877.
- (119) Tsuji, M.; Hashimoto, M.; Nishizawa, Y.; Kubokawa, M.; Tsuji, T., *Chem. Eur. J.* **2005**, *11*, 440-452.
- (120) Kumar, S.; Nann, T., *Small* **2006**, *2*, 316-329.
- (121) Jun, Y. W.; Choi, J. S.; Cheon, J., *Angew. Chem. Int. Ed.* **2006**, *45*, 3414-3439.
- (122) Ren, J. T.; Tilley, R. D., *J. Am. Chem. Soc.* **2007**, *129*, 3287-3291.
- (123) Wang, S. H.; Yang, S. H., *Langmuir* **2000**, *16*, 389-397.
- (124) Agnoli, F.; Zhou, W. L.; O'Connor, C. J., *Adv. Mater.* **2001**, *13*, 1697-1699.

- (125) Wikander, K.; Petit, C.; Holmberg, K.; Pileni, M. P., *Langmuir* **2006**, *22*, 4863-4868.
- (126) Nair, P. S.; Fritz, K. P.; Scholes, G. D., *Small* **2007**, *3*, 481-487.
- (127) Wang, D. L.; Lieber, C. M., *Nature Mater.* **2003**, *2*, 355-356.
- (128) Pileni, M. P., *Langmuir* **1997**, *13*, 3266-3276.
- (129) Pileni, M. P.; Gulik-Krzywicki, T.; Tanori, J.; Filankembo, A.; Dedieu, J. C., *Langmuir* **1998**, *14*, 7359-7363.
- (130) Lisiecki, I.; Pileni, M. P., *Langmuir* **2003**, *19*, 9486-9489.
- (131) Naoe, K.; Petit, C.; Pileni, M. P., *Langmuir* **2008**, *24*, 2792-2798.
- (132) Smetana, A. B.; Wang, J. S.; Boeckl, J.; Brown, G. J.; Wai, C. M., *Langmuir* **2007**, *23*, 10429-10432.
- (133) Lisiecki, I.; Billoudet, F.; Pileni, M. P., *J. Phys. Chem.* **1996**, *100*, 4160-4166.
- (134) Zhao, M. Q.; Crooks, R. M., *Angew. Chem. Int. Ed.* **1999**, *38*, 364-366.
- (135) Zhao, M. Q.; Sun, L.; Crooks, R. M., *J. Am. Chem. Soc.* **1998**, *120*, 4877-4878.
- (136) Balogh, L.; Tomalia, D. A., *J. Am. Chem. Soc.* **1998**, *120*, 7355-7356.
- (137) Ding, J. H.; Gin, D. L., *Chem. Mater.* **2000**, *12*, 22-24.
- (138) Lin, S. Y.; Tsai, Y. T.; Chen, C. C.; Lin, C. M.; Chen, C. H., *J. Phys. Chem. B* **2004**, *108*, 2134-2139.
- (139) Guo, R.; Song, Y.; Wang, G. L.; Murray, R. W., *J. Am. Chem. Soc.* **2005**, *127*, 2752-2757.
- (140) Song, Y.; Murray, R. W., *J. Am. Chem. Soc.* **2002**, *124*, 7096-7102.
- (141) Hostetler, M. J.; Templeton, A. C.; Murray, R. W., *Langmuir* **1999**, *15*, 3782-3789.

- (142) Woehrle, G. H.; Brown, L. O.; Hutchison, J. E., *J. Am. Chem. Soc.* **2005**, *127*, 2172-2183.
- (143) Ingram, R. S.; Hostetler, M. J.; Murray, R. W., *J. Am. Chem. Soc.* **1997**, *119*, 9175-9178.
- (144) Brown, L. O.; Hutchison, J. E., *J. Am. Chem. Soc.* **1999**, *121*, 882-883.
- (145) Rucareanu, S.; Gandubert, V. J.; Lennox, R. B., *Chem. Mater.* **2006**, *18*, 4674-4680.
- (146) Templeton, A. C.; Cliffler, D. E.; Murray, R. W., *J. Am. Chem. Soc.* **1999**, *121*, 7081-7089.
- (147) Brown, L. O.; Hutchison, J. E., *J. Am. Chem. Soc.* **1999**, *121*, 882-883.
- (148) Balasubramanian, R.; Guo, R.; Mills, A. J.; Murray, R. W., *J. Am. Chem. Soc.* **2005**, *127*, 8126-8132.
- (149) Son, S. U.; Jang, Y.; Yoon, K. Y.; Kang, E.; Hyeon, T., *Nano Lett.* **2004**, *4*, 1147-1151.
- (150) Gittins, D. I.; Caruso, F., *Angew. Chem. Int. Ed.* **2001**, *40*, 3001-3004.
- (151) Nikolic, M. S.; Krack, M.; Aleksandrovic, V.; Kornowski, A.; Forster, S.; Weller, H., *Angew. Chem. Int. Ed.* **2006**, *45*, 6577-6580.
- (152) Chan, W. C. W.; Nie, S. M., *Science* **1998**, *281*, 2016-2018.
- (153) Mitchell, G. P.; Mirkin, C. A.; Letsinger, R. L., *J. Am. Chem. Soc.* **1999**, *121*, 8122-8123.
- (154) Swami, A.; Kumar, A.; Sastry, M., *Langmuir* **2003**, *19*, 1168-1172.
- (155) Fan, H. Y.; Leve, E. W.; Scullin, C.; Gabaldon, J.; Tallant, D.; Bunge, S.; Boyle, T.; Wilson, M. C.; Brinker, C. J., *Nano Lett.* **2005**, *5*, 645-648.
- (156) Fan, H. Y.; Chen, Z.; Brinker, C. J.; Clawson, J.; Alam, T., *J. Am. Chem. Soc.* **2005**, *127*, 13746-13747.
- (157) Yavuz, C. T.; Mayo, J. T.; Yu, W. W.; Prakash, A.; Falkner, J. C.; Yean, S.; Cong, L. L.; Shipley, H. J.; Kan, A.; Tomson, M.; Natelson, D.; Colvin, V. L., *Science* **2006**, *314*, 964-967.

- (158) Wang, Y.; Wong, J. F.; Teng, X. W.; Lin, X. Z.; Yang, H., *Nano Lett.* **2003**, *3*, 1555-1559.
- (159) Latham, A. H.; Williams, M. E., *Langmuir* **2006**, *22*, 4319-4326.
- (160) Watson, K. J.; Zhu, J.; Nguyen, S. T.; Mirkin, C. A., *J. Am. Chem. Soc.* **1999**, *121*, 462-463.
- (161) Whetten, R. L.; Khoury, J. T.; Alvarez, M. M.; Murthy, S.; Vezmar, I.; Wang, Z. L.; Stephens, P. W.; Cleveland, C. L.; Luedtke, W. D.; Landman, U., *Adv. Mater.* **1996**, *8*, 428-&.
- (162) Martin, J. E.; Wilcoxon, J. P.; Odinek, J.; Provencio, P., *J. Phys. Chem. B* **2000**, *104*, 9475-9486.
- (163) Stoeva, S. I.; Prasad, B. L. V.; Uma, S.; Stoimenov, P. K.; Zaikovski, V.; Sorensen, C. M.; Klabunde, K. J., *J. Phys. Chem. B* **2003**, *107*, 7441-7448.
- (164) Wang, Z. L., *Adv. Mater.* **1998**, *10*, 13-+.
- (165) Wang, Z. L.; Harfenist, S. A.; Vezmar, I.; Whetten, R. L.; Bentley, J.; Evans, N. D.; Alexander, K. B., *Adv. Mater.* **1998**, *10*, 808-812.
- (166) Korgel, B. A.; Fitzmaurice, D., *Phys. Rev. B: Condens. Matter* **1999**, *59*, 14191-14201.
- (167) Pileni, M.-P. In *Metal Nanoparticles: Synthesis, Characterization and Applications*; Feldhiem, D. L., Foss, C. A., Eds.; Marcel Dekker: New York, 2002, pp 207-331.
- (168) Eychmuller, A. In *Nanoparticles: From Theory to Application*; Schmid, G., Ed.; Wiley-VCH: Weinheim, 2004, pp 239-304.
- (169) Murray, C. B.; Kagan, C. R.; Bawendi, M. G., *Annu. Rev. Mater. Sci.* **2000**, *30*, 545-610.
- (170) Korgel, B. A.; Fitzmaurice, D., *Phys. Rev. Lett.* **1998**, *80*, 3531-3534.
- (171) Teranishi, T.; Hasegawa, S.; Shimizu, T.; Miyake, M., *Adv. Mater.* **2001**, *13*, 1699-1701.
- (172) Lin, X. M.; Jaeger, H. M.; Sorensen, C. M.; Klabunde, K. J., *J. Phys. Chem. B* **2001**, *105*, 3353-3357.

- (173) Giersig, M.; Mulvaney, P., *Langmuir* **1993**, *9*, 3408-3413.
- (174) Redl, F. X.; Cho, K. S.; Murray, C. B.; O'Brien, S., *Nature* **2003**, *423*, 968-971.
- (175) Kinge, S. S.; Crego-Calama, M.; Reinhoudt, D. N., *Langmuir* **2007**, *23*, 8772-8777.
- (176) Johnson, S. R.; Evans, S. D.; Brydson, R., *Langmuir* **1998**, *14*, 6639-6647.
- (177) Su, C. H.; Wu, P. L.; Yeh, C. S., *Bull. Chem. Soc. Jpn.* **2004**, *77*, 189-193.
- (178) Mie, G., *Annalen Der Physik* **1908**, *25*, 377-445.
- (179) Jain, P. K.; Huang, X.; El-Sayed, I. H.; El-Sayad, M. A., *Plasmonics* **2007**, *2*, 107-118.
- (180) Jain, P. K.; Eustis, S.; El-Sayed, M. A., *J. Phys. Chem. B* **2006**, *110*, 18243-18253.
- (181) Jin, R. C.; Cao, Y. W.; Mirkin, C. A.; Kelly, K. L.; Schatz, G. C.; Zheng, J. G., *Science* **2001**, *294*, 1901-1903.
- (182) Srivastava, S.; Frankamp, B. L.; Rotello, V. M., *Chem. Mater.* **2005**, *17*, 487-490.
- (183) Jensen, T.; Kelly, L.; Lazarides, A.; Schatz, G. C., *J. Cluster Sci.* **1999**, *10*, 295-317.
- (184) Lazarides, A. A.; Schatz, G. C., *J. Phys. Chem. B* **2000**, *104*, 460-467.
- (185) Miller, M. M.; Lazarides, A. A., *J. Opt. A-Pure Appl. Opt.* **2006**, *8*, S239-S249.
- (186) Lazarides, A. A.; Kelly, K. L.; Jensen, T. R.; Schatz, G. C., *Theochem-J. Mol. Struct.* **2000**, *529*, 59-63.
- (187) Yang, W. H.; Schatz, G. C.; Vanduyne, R. P., *J. Chem. Phys.* **1995**, *103*, 869-875.

- (188) Miller, M. M.; Lazarides, A. A., *J. Phys. Chem. B* **2005**, *109*, 21556-21565.
- (189) Su, K. H.; Wei, Q. H.; Zhang, X.; Mock, J. J.; Smith, D. R.; Schultz, S., *Nano Lett.* **2003**, *3*, 1087-1090.
- (190) Link, S.; Mohamed, M. B.; El-Sayed, M. A., *J. Phys. Chem. B* **1999**, *103*, 3073-3077.
- (191) Oldenburg, S. J.; Averitt, R. D.; Westcott, S. L.; Halas, N. J., *Chem. Phys. Lett.* **1998**, *288*, 243-247.
- (192) Ghosh, S. K.; Nath, S.; Kundu, S.; Esumi, K.; Pal, T., *J. Phys. Chem. B* **2004**, *108*, 13963-13971.
- (193) Linnert, T.; Mulvaney, P.; Henglein, A., *J. Phys. Chem.* **1993**, *97*, 679-682.
- (194) Malinsky, M. D.; Kelly, K. L.; Schatz, G. C.; Van Duyne, R. P., *J. Am. Chem. Soc.* **2001**, *123*, 1471-1482.
- (195) Thomas, K. G.; Kamat, P. V., *J. Am. Chem. Soc.* **2000**, *122*, 2655-2656.
- (196) Henglein, A.; Ershov, B. G.; Malow, M., *J. Phys. Chem.* **1995**, *99*, 14129-14136.
- (197) Chen, C. W.; Tano, D.; Akashi, M., *J. Colloid Interface Sci.* **2000**, *225*, 349-358.
- (198) Duff, D. G.; Edwards, P. P.; Johnson, B. F. G., *J. Phys. Chem.* **1995**, *99*, 15934-15944.
- (199) Hummel, R. E. *Electronic Properties of Materials*; Third ed.; Springer-Verlag, Inc.: New York, 2001.
- (200) Alivisatos, A. P., *J. Phys. Chem.* **1996**, *100*, 13226-13239.
- (201) Kastner, M. A., *Rev. Mod. Phys.* **1992**, *64*, 849-858.
- (202) Geissler, M.; Chen, J. Y.; Xia, Y. N., *Langmuir* **2004**, *20*, 6993-6997.

- (203) Horswell, S. L.; Kiely, C. J.; O'Neil, I. A.; Schiffrin, D. J., *J. Am. Chem. Soc.* **1999**, *121*, 5573-5574.
- (204) Avery, N. R.; Matheson, T. W., *Surf. Sci.* **1984**, *143*, 110-124.
- (205) Hickman, J. J.; Laibinis, P. E.; Auerbach, D. I.; Zou, C. F.; Gardner, T. J.; Whitesides, G. M.; Wrighton, M. S., *Langmuir* **1992**, *8*, 357-359.
- (206) Bong, D.; Tam, I.; Breslow, R., *J. Am. Chem. Soc.* **2004**, *126*, 11796-11797.
- (207) Walker, B. R.; Wassel, R. A.; Stefanescu, D. M.; Gorman, C. B., *J. Am. Chem. Soc.* **2004**, *126*, 16330-16331.
- (208) Stapleton, J. J.; Daniel, T. A.; Uppili, S.; Cabarcos, O. M.; Naciri, J.; Shashidhar, R.; Allara, D. L., *Langmuir* **2005**, *21*, 11061-11070.
- (209) Swanson, S. A.; McClain, R.; Lovejoy, K. S.; Alamdari, N. B.; Hamilton, J. S.; Scott, J. C., *Langmuir* **2005**, *21*, 5034-5039.
- (210) Murphy, K. L.; Tysoe, W. T.; Bennett, D. W., *Langmuir* **2004**, *20*, 1732-1738.
- (211) Lee, Y. G.; Morales, G. M.; Yu, L. P., *Angew. Chem. Int. Ed.* **2005**, *44*, 4228-4231.
- (212) Seminario, J. M.; De la Cruz, C. E.; Derosa, P. A., *J. Am. Chem. Soc.* **2001**, *123*, 5616-5617.
- (213) Friend, C. M.; Muetterties, E. L.; Gland, J. L., *J. Phys. Chem.* **1981**, *85*, 3256-3262.
- (214) Chiang, Y.; Turkevich, J., *J. Colloid Sci.* **1963**, *18*, 772-&.
- (215) Turkevich, J.; Garton, G.; Stevenson, P. C., *J. Colloid Sci.* **1954**, *9*, S26-S35.
- (216) Henglein, A.; Giersig, M., *J. Phys. Chem. B* **2000**, *104*, 6767-6772.
- (217) Turkevich; Kim, G., *Science* **1970**, *169*, 873-&.
- (218) Leheny, A. R.; Rossetti, R.; Brus, L. E., *J. Phys. Chem.* **1985**, *89*, 211-213.

- (219) Lin, C. S.; Khan, M. R.; Lin, S. D., *J. Colloid Interface Sci.* **2006**, 299, 678-685.
- (220) Lin, C. S.; Khan, M. R.; Lin, S. D., *J. Colloid Interface Sci.* **2005**, 287, 366-369.
- (221) Furlong, D. N.; Sasse, W. H. F., *Aust. J. Chem.* **1983**, 36, 2163-2167.
- (222) Henglein, A., *J. Phys. Chem. B* **2000**, 104, 6683-6685.
- (223) Furlong, D. N.; Launikonis, A.; Sasse, W. H. F.; Sanders, J. V., *J. Chem. Soc. - Faraday Trans.* **1984**, 80, 571-&.
- (224) Brugger, P. A.; Cuendet, P.; Gratzel, M., *J. Am. Chem. Soc.* **1981**, 103, 2923-2927.
- (225) Wang, Z. L.; Petroski, J. M.; Green, T. C.; El-Sayed, M. A., *J. Phys. Chem. B* **1998**, 102, 6145-6151.
- (226) Narayanan, R.; El-Sayed, M. A., *J. Am. Chem. Soc.* **2003**, 125, 8340-8347.
- (227) Teranishi, T.; Hosoe, M.; Tanaka, T.; Miyake, M., *J. Phys. Chem. B* **1999**, 103, 3818-3827.
- (228) Li, Y.; El-Sayed, M. A., *J. Phys. Chem. B* **2001**, 105, 8938-8943.
- (229) Hostetler, M. J.; Green, S. J.; Stokes, J. J.; Murray, R. W., *J. Am. Chem. Soc.* **1996**, 118, 4212-4213.
- (230) Chen, S. W.; Murray, R. W., *Langmuir* **1999**, 15, 682-689.
- (231) Schaaff, T. G.; Knight, G.; Shafiqullin, M. N.; Borkman, R. F.; Whetten, R. L., *J. Phys. Chem. B* **1998**, 102, 10643-10646.
- (232) Templeton, A. C.; Chen, S. W.; Gross, S. M.; Murray, R. W., *Langmuir* **1999**, 15, 66-76.
- (233) Chen, S. W., *Langmuir* **1999**, 15, 7551-7557.
- (234) Jadzinsky, P. D.; Calero, G.; Ackerson, C. J.; Bushnell, D. A.; Kornberg, R. D., *Science* **2007**, 318, 430-433.

- (235) Brust, M.; Fink, J.; Bethell, D.; Schiffrin, D. J.; Kiely, C., *J. Chem. Soc. - Chem. Commun.* **1995**, 1655-1656.
- (236) Chen, D. H.; Hsieh, C. H., *J. Mater. Chem.* **2002**, *12*, 2412-2415.
- (237) Wu, S. H.; Chen, D. H., *Chem. Lett.* **2004**, *33*, 406-407.
- (238) Wu, S. H.; Chen, D. H., *J. Colloid Interface Sci.* **2003**, *259*, 282-286.
- (239) Cordente, N.; Respaud, M.; Senocq, F.; Casanove, M. J.; Amiens, C.; Chaudret, B., *Nano Lett.* **2001**, *1*, 565-568.
- (240) Ould-Ely, T.; Amiens, C.; Chaudret, B.; Snoeck, E.; Verelst, M.; Respaud, M.; Broto, J. M., *Chem. Mater.* **1999**, *11*, 526-+.
- (241) Kolytyn, Y.; Fernandez, A.; Rojas, T. C.; Campora, J.; Palma, P.; Prozorov, R.; Gedanken, A., *Chem. Mater.* **1999**, *11*, 1331-1335.
- (242) deCaro, D.; Bradley, J. S., *Langmuir* **1997**, *13*, 3067-3069.
- (243) Cheng, G. J.; Puentes, V. F.; Guo, T., *J. Colloid Interface Sci.* **2006**, *293*, 430-436.
- (244) Hou, Y. L.; Gao, S., *J. Mater. Chem.* **2003**, *13*, 1510-1512.
- (245) Hou, Y.; Kondoh, H.; Ohta, T.; Gao, S., *Appl. Surf. Sci.* **2005**, *241*, 218-222.
- (246) Green, M.; O'Brien, P., *Chem. Commun.* **2001**, 1912-1913.
- (247) Park, J.; Kang, E.; Son, S. U.; Park, H. M.; Lee, M. K.; Kim, J.; Kim, K. W.; Noh, H. J.; Park, J. H.; Bae, C. J.; Park, J. G.; Hyeon, T., *Adv. Mater.* **2005**, *17*, 429-+.
- (248) Chen, D. H.; Wu, S. H., *Chem. Mater.* **2000**, *12*, 1354-1360.
- (249) Nikoobakht, B.; El-Sayed, M. A., *Langmuir* **2001**, *17*, 6368-6374.
- (250) Hind, A. R.; Bhargava, S. K.; Grocott, S. C., *Langmuir* **1997**, *13*, 3483-3487.
- (251) Rennie, A. R.; Lee, E. M.; Simister, E. A.; Thomas, R. K., *Langmuir* **1990**, *6*, 1031-1034.

(252) Yeskie, M. A.; Harwell, J. H., *J. Phys. Chem.* **1988**, 92, 2346-2352.

|

3. Synthesis and Stability of Metal Oxide Nanoparticles

As discussed in Chapter 1, the overall goal of this work was to synthesize and characterize heterodimers consisting of oligomeric phenylethylenes (OPEs) inserted between nanoparticles of different compositions using orthogonal self-assembly. Chapter 2 discussed the synthesis of the metal nanoparticle building blocks used in these studies. Gold particles were desirable for binding a thiolate functionality, and platinum and nickel particles were synthesized for binding an isocyanide functionality. This chapter describes the synthesis of metal oxide particles, particularly titanium dioxide and iron oxide. Carboxylic acids have been reported to bind selectively to metal oxide particles. Metal oxide particles were therefore synthesized with the intent of forming heterodimers with gold particles using linker molecules, the basic structure of which is shown in Figure 3-1.

As described in Section 2.2.1 for metal particles, there were several factors that needed to be considered before choosing the capping ligands and synthetic procedures described here for metal oxide particles. Aqueous metal oxide particles were desirable as the gold-citrate particles used for heterodimer formation were in aqueous solution. Also, aqueous capping

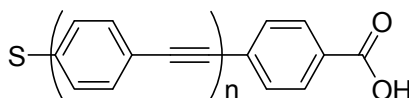


Figure 3-1. OPE used to synthesize heterodimers. $n = 1, 2$

ligands are typically less sterically-bulky than those utilized in organic solvents and several of the characterization methods evaluated required aqueous solvent. In addition, capping ligands with lengths less than 1 nm were desirable in order to minimize steric hindrance, which would prohibit dimer formation. Therefore, the focus of this work was on the synthesis of metal oxide particles with short hydrophilic ligands. As with metal particles, there is an obvious tradeoff between particle stability and reactivity making the synthesis of stable particles with short capping ligands quite challenging.

While many of the concepts associated with metal particles can also be applied to metal oxide particles, the synthetic methods can differ significantly. As with metal particles, these syntheses are extremely sensitive to small changes in reaction conditions, which typically do not convey from one particle synthesis to the next. An understanding of the chemistry involved with particle synthesis is therefore critical to developing and optimizing each procedure. The most commonly reported method for synthesizing titanium dioxide (TiO_2) involves sol-gel chemistry. More recently, non-hydrolytic and hydrothermal methods have been reported for the synthesis of these particles. The general concepts associated with both of these chemistries are described before more detailed particle syntheses are discussed. Likewise, the chemistries associated with the synthesis of iron oxide particles are discussed,

including the co-precipitation of Fe^{2+} and Fe^{3+} ions and the thermal decomposition of an iron complex resulting in the formation of iron oxide particles.

3.1. Introduction and Background

3.1.1. Synthesis of Metal Oxide Particles through Sol-Gel Methods

3.1.1.1. Sol-gel concepts*

While the sol-gel method for producing glasses and ceramics has not replaced other more traditional methods, the complex chemistry has been applied to prepare a wide variety of materials for many different applications. The ability to form extremely pure metal oxides using these techniques has led to their use in optical components including lenses and optical fibers.³⁵⁻³⁷ The liquid nature of the precursor solutions creates the ability to mold ceramics to unique shapes including thin films, fibers, particles, coatings and powders.^{6,24,37-40} Sol-gel solutions are applied to polymer and glass surfaces using spin or dip coating techniques to create coatings resistant to heat, abrasion and chemicals.^{2,6} There is also interest in using sol-gel materials for electronic applications. They form extremely pure, transparent, conductive films for coating semi-conductor wafers² and have been explored as alternatives to sputtering.³⁶

* Some of these concepts have also been reported in my Masters Thesis, J. Ayres, NCSU, 2004, Materials Science and Engineering

The chemical nature of the sol-gel process also creates the possibility of incorporating organic functional groups into metal oxide structure.^{3,46-49} Organic molecules can either be trapped within the inorganic network or covalently bound to it.⁵⁰ Organic modifiers have been incorporated into sol-gel materials to impart hydrophobicity, anti-static properties and UV-resistance to the final network.⁵⁰⁻⁵² Materials can be synthesized with properties of both an inorganic oxide, and an organic material.^{6,48,50} The ratio of organic to inorganic material in the final structure can also be tailored to create materials ranging from a brittle solid to an elastic or thermoplastic.^{6,50}

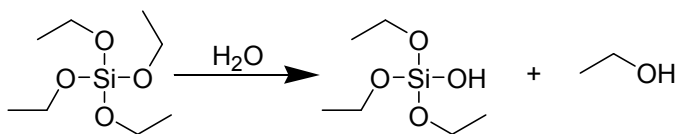
While sol-gel chemistry can be used to create a wide variety of materials with significantly differing properties, it is extremely complex. Both an understanding of the chemistry and strict control over reaction conditions are required in order to achieve the desired product. The discussion below includes a brief overview of the chemistry and what factors can affect the final structure of the metal oxide.

3.1.1.1.1. The Sol-gel Process

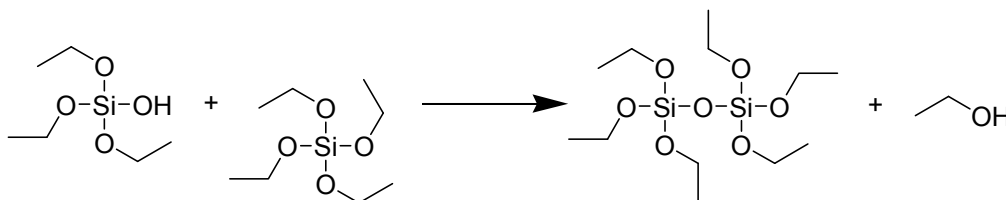
As mentioned above, the sol-gel process originates with a solution of molecular precursors which then undergo a series of hydrolysis and condensation reactions to produce a metal oxide. The molecular precursors used in this process can include inorganics such as metal chlorides, nitrates and sulfides.^{39,53} However, the use of metal or silicon alkoxide precursors is more versatile and more frequently reported in

the literature.^{53,54} The most common sol-gel reaction involves the hydrolysis and condensation of tetraethoxysilane (TEOS) to form silica (SiO₂), and this reaction is shown below as a model for the overall sol-gel reaction. These concepts will later be applied to titania (TiO₂).

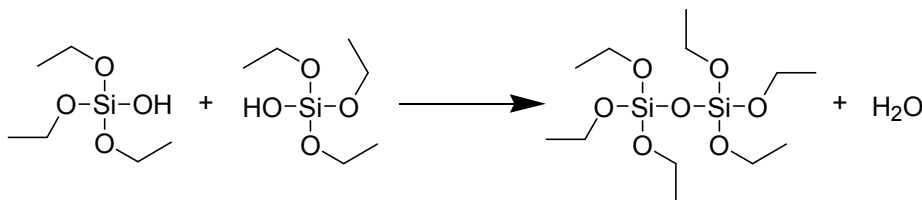
The initial solution for a sol-gel reaction consists of molecular precursor molecules, which undergo hydrolysis upon exposure to water. The hydrolysis of TEOS is shown in Scheme 3-1. Ethanol is produced as the side-product of this reaction. The electronegative alkoxy ligands withdraw electron density from the central silicon atom making it prone to nucleophilic attack.⁷



Scheme 3-1. Hydrolysis of tetraethoxysilane



Scheme 3-2. Alcohol condensation of hydrolyzed TEOS



Scheme 3-3. Dehydration of hydrolyzed TEOS

After hydrolysis, TEOS undergoes one of two possible condensation reactions. A hydroxide group can react with an adjacent ethoxy group to produce ethanol and a siloxane oligomer as shown in Scheme 3-2. The hydroxide group can also react with another hydroxide group as shown in Scheme 3-3. This reaction produces water in addition to the siloxane oligomer. The alcohol condensation occurs much more often than the dehydration, because the ethoxy group is a better leaving group than the hydroxide anion. In addition, there is a larger concentration of ethoxy groups in the early stages of the reaction. Both hydrolysis and condensation continue several stages of the sol-gel process, described below, until a pure SiO_2 network is formed.^{4,7,39,40,55} This process is often called inorganic polymerization.

The chemistry involved with the sol-gel process can be very complex. Hydrolysis and condensation cannot be separated and generally occur simultaneously.^{5,47,56-58} As a result, a wide range of intermediates can be present at any given time, which makes these solutions very difficult to characterize. In addition, foreign species are always present either as counter ions, solvents, or chemical additives.³⁹ Reactions can also occur between organic side-reactions, which further complicate things.

While the chemical reactions occur at the molecular scale, the larger-scale sol-gel also goes through several different stages as it transforms from a solution to a solid. The first stage associated with the sol-gel process is, of course, the formation of gel, which consists of growing metal-oxide chains surrounding solvent molecules. This

stage is accompanied by a sharp increase in viscosity. Gelation is succeeded by the formation of additional metal-oxide crosslinks, which pull chains together and result in shrinkage of the gel as shown in Figure 3-2. This contraction brings additional –OH groups together, resulting in further condensation. Ostwald ripening also occurs in this stage; small oligomeric metal-oxide structures migrate towards each other to form larger, polymeric structures with less surface energy.^{37,53,57,59} The result is phase separation of the solid network from the solvent, and precipitation of solid crystals is often observed. This process is thermodynamically driven to reduce energy associated with the solid-liquid interface. However, since this process is not kinetically favored, Ostwald ripening is limited in systems with high reaction rates. In this case, condensation occurs with minimal migration yielding a final product with significant cracking and a high concentration of oligomers.

The next stage of the sol-gel process is aging, which involves the loss of water, solvent and any alcohols produced during hydrolysis and condensation.^{1,2,57} These liquids are first removed through syneresis; a consequence of the gel shrinkage shown in Figure 3-2, which expels liquids from the pores. Liquid on the surface of the gel evaporates, creating a concentration gradient that leads to diffusion. Liquid evaporation can also cause pressure gradients and capillary stresses within the network, which are relieved by cracking and the release of additional liquid.¹

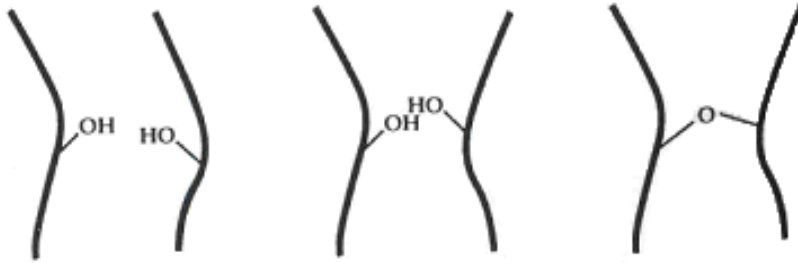


Figure 3-2. Shrinkage of gel with condensation. Figure taken from Scherer et al.¹

Once aging is complete, the resulting network can be subjected to thermal treatment; above approximately

1000°C, densification occurs.¹⁰ This process involves additional condensation reactions and structural relaxation which cause shrinkage and produce a dense ceramic.^{1,2}

3.1.1.1.2. Steric and Inductive Effects

In order to achieve a desired SiO₂ structure, strict control over all stages of the sol-gel process is required. Any small change in reaction conditions including the structure of the precursor molecule, temperature, pH and solvent can affect the hydrolysis and condensation kinetics, and consequently the final structures of the resulting inorganic network. Slow kinetics are often desirable, because slower kinetics make it easier to control the morphology of the gel. Specific examples of how the structure of the precursor molecule and the pH and affect the reaction kinetics and the structure of the final oxide are described below.

Sol-gel reactions are influenced by both steric and inductive effects. As both hydrolysis,

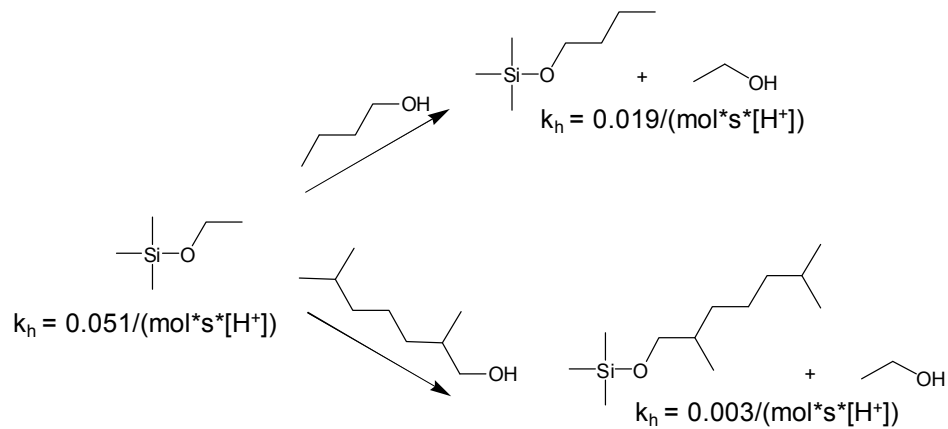


Figure 3-3. TEOS precursor substitution reactions and the resulting hydrolysis rates. Data was taken from Scherer et al.¹

and condensation occur through an $\text{S}_{\text{N}}2$ substitution mechanism,^{5,53,56,60} reaction rates are limited by steric effects and therefore decrease with the length of the alkyl substituent on the alkoxide precursor.^{1,2,7,47,54,56,61} In addition, the positive charge on the silicon atom decreases with the size of the alkoxy substituent. This phenomenon reduces the driving force for hydrolysis and also contributes to slower kinetics.⁵⁴ As slower kinetics allow for more control over the reaction and typically yield larger networks with limited cracking, alcohol exchange, also known as precursor substitution, reactions are often utilized to increase the length of the alkoxy substituents and limit reaction kinetics. Figure 3-3 shows two alcohol exchange reactions involving TEOS and indicates their effects on hydrolysis rates. Nucleophilic substitution of butanol decreases the hydrolysis rate by a factor of approximately 2.7 while substitution of 2, 6 – dimethyl-heptanol decreases the

hydrolysis rate by a factor of 17.¹ It has also been observed that larger alkoxy substituents yield smaller inorganic polymers.⁶

Another factor that affects both the rate and extent of condensation reactions is the flexibility of the inorganic chains.⁴⁰ The condensation reaction shown in Figure 3-2 assumes some flexibility in the backbone chains. This reaction would not occur in an extremely rigid system. Chain flexibility decreases with the extent of condensation in any given gel. Likewise, the viscosity of the pore liquid affects condensation as its movement through the network is required for condensation and concurrent shrinkage. Increasing the temperature of reaction often increases the reaction rates; however, proportional increases in the liquid viscosity and chain flexibility are most often not observed. When liquid is not expelled at a rate comparable to the rate of condensation, pressure builds up in the network and

Table 3-1. Effects of Relative Hydrolysis and Condensation Rates on Material Structure

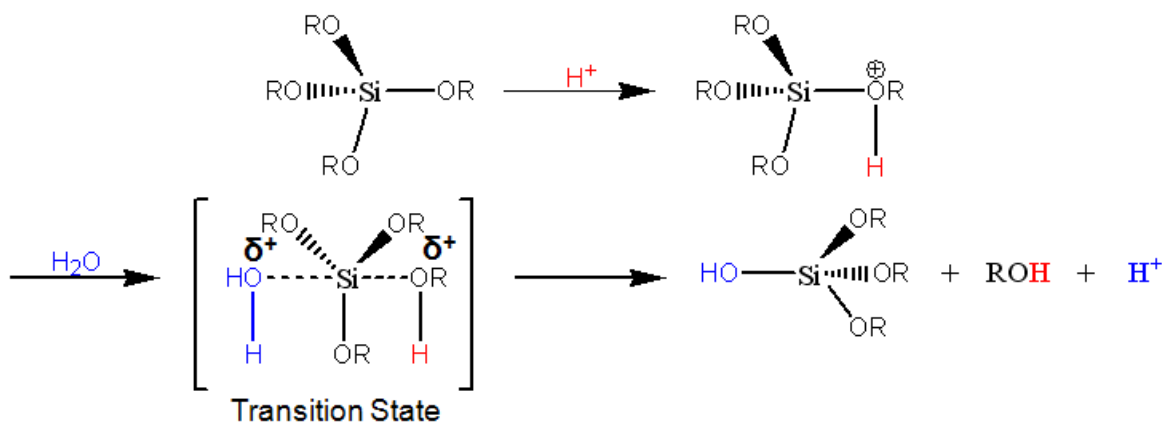
Hydrolysis Rate	Condensation Rate	Result
Slow	Slow	Colloids/sols
Fast	Slow	Polymeric Gels
Fast	Fast	Colloidal Gel or Gelatinous Precipitate
Slow	Fast	Controlled Precipitation

This table was adapted from Livage et al.⁶ and Sanchez et al.⁷

causes additional cracking.⁴⁰

The relative rates of hydrolysis and condensation also play a large role in the final structure of the metal oxide produced in the sol-gel process. Table 3-1 lists the different structures that can be obtained for varying reaction rates, and illustrates why control over reaction kinetics is critical in the sol-gel process.

One of the most common methods for controlling the relative rates of hydrolysis and condensation is through acid or base catalysis.^{1,5,6,55,62,63} The mechanisms for hydrolysis and condensation are different for each case resulting in significantly different reaction rates and oxide structures. Hydrolysis involves the nucleophilic attack of water through an S_N2 mechanism.^{5,53,56,60} In the case of acid catalysis, the pentacoordinate transition state is positively charged as shown in Scheme 3-4. This partial positive charge is stabilized by the electron-donating alkoxy substituents.



Scheme 3-4. Acid catalyzed hydrolysis of an alkoxy silane

With each successive reaction, the number of stabilizing alkoxy substituents decreases. As a result, the stability of the transition states and consequently the reaction rates decrease throughout the course of the sol-gel process.^{1,2,5,7,47,54,57,58,60,62,64,65} Hydrolysis initially happens extremely rapidly, but as the reaction rates decrease, the system has sufficient time for reorganization and Ostwald ripening resulting in a highly crosslinked network as shown in Figure 3-4.^{1,2} Acid catalysis generally results in crystalline powders formed from fully hydrolyzed precursors.⁴⁰ It has also been observed that in acidic solution, condensation reactions are favored between silanol groups on monomers or the end of a growing polymer chain.^{60,62} As a result, these gels are typically composed of entangled linear chains with limited

branching.^{5,47,54,57,}

^{58,60,62,64,65} This

phenomenon is

also shown in

Figure 3-4.

In contrast, the

reaction rates

increase

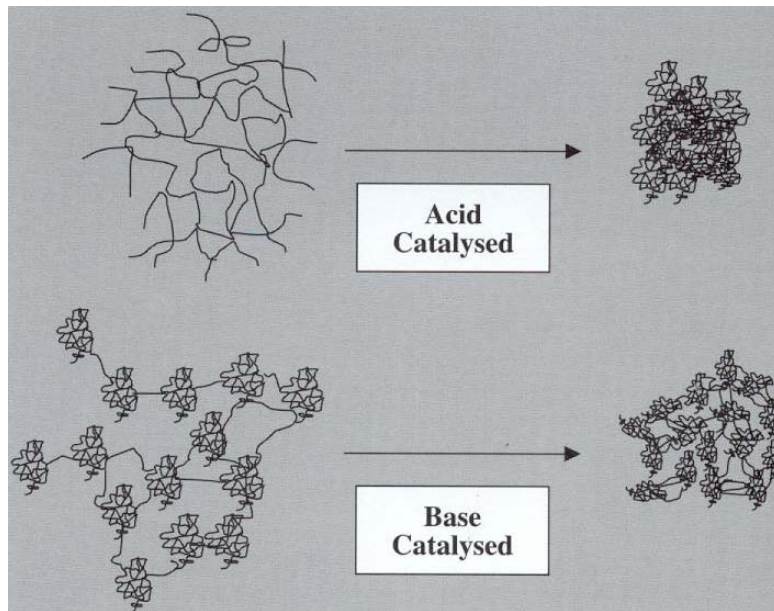
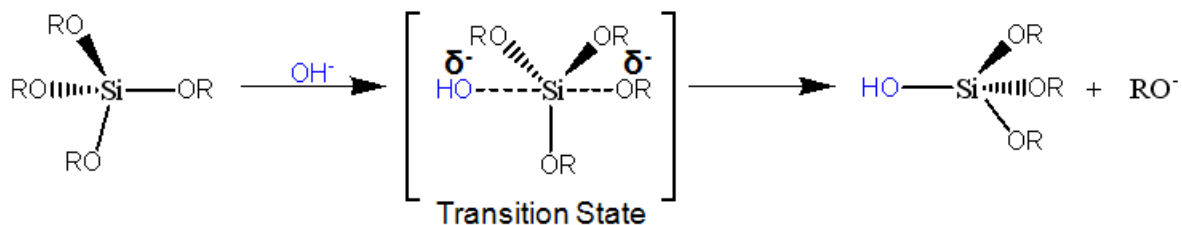


Figure 3-4. Gel structures for acid and base catalyzed reactions. Figure taken from Sommerdijk et al.²

throughout the sol-gel process in the presence of base, leading to amorphous powders containing unhydrolyzed alkoxide ligands.⁴⁰ The deprotonated hydroxide anion attacks the initial alkoxide to form the negatively charged transition state shown in Scheme 3-5.^{1,2,5} In this case, the electron-donating alkoxy substituents destabilize the negatively-charged transition state. Thus, as the number of destabilizing substituents decreases with successive reactions, the reaction rates increase. For example, the presence of formamide has been reported to decrease the hydrolysis rate while slightly increasing the rate of condensation.⁶⁰ The slow kinetics in the early stages of the condensation process facilitate Ostwald ripening and the formation of highly-crosslinked particles. However, as the reaction rates increase, the kinetics do not favor structural reorganization, and the final structure is extremely porous as shown in Figure 3-4.² This final structure is also attributed in part to the formation of highly branched oligomers, which has been observed in basic solutions in contrast to the linear chains observed in acid.^{5,47,58,60,62,64,65}

As discussed above, the addition of acid generally increases the hydrolysis rates for



Scheme 3-5. Base catalyzed hydrolysis of an alkoxy silane

silicon alkoxides. Some reports claim that the presence of acid increases the hydrolysis rate by a factor or two.⁶⁰ Another report claims that the gelation time for TEOS decreases by an order of magnitude in the presence of HCl.⁷ However, the nature of the acid also plays a role. For example, the pH of HCl is greater than that of acetic acid so HCl was expected to have a greater effect on hydrolysis kinetics. However, it has been shown that acetic acid decreases hydrolysis rates to a greater extent despite the higher pH.^{6,7} This was attributed to interactions between the acetate ligand and the alkoxide precursor, a phenomenon discussed in more details with respect to titanium alkoxide chemistry.

The significant structural differences observed for products of acidic and basic sol-gel solutions are yet another indication that strict control of reaction conditions is required to achieve a desired product. While the complexity of these systems can seem like a disadvantage when trying to obtain a specific product, it also allows for the synthesis of kinetics and consequently the structure of the gel or metal oxide can be changed by the nature of the molecular precursor, solution pH, and the solvent or any other solution additives which interact with the precursor.^{7,66} Table 3-2 shows how solvent affects the gelation time for two silicon alkoxides. Reaction rates are also affected by precursor concentration, water concentration and reaction temperature.^{4,6,40,55} The next section describes how slow kinetics can facilitate the formation of thermodynamically-stable particles.

Table 3-2. Gelation Times (hours) for Silicon Alkoxides in Different Solvents

Alkoxide	Solvent	
	MeOH	EtOH
Si(OCH ₃) ₄	44	152
Si(OCH ₂ CH ₃) ₄	108	242

Data taken from Sanchez et al.⁷

3.1.1.1.3. Additional Kinetic Effects

While condensation reactions typically involve the formation of a siloxane polymer, the reverse reactions can also occur.⁵ These reactions facilitate a means for less-stable bonds to break and reform in a more stable configuration. These 'depolymerization' reactions occur much more readily under basic conditions with rates reported to increase by over three orders of magnitude as the pH was increased from 3 to 8.⁵ Thus, more stable colloids are often observed under basic conditions. These reverse reactions also decrease the effective reaction kinetics allowing for Ostwald ripening, which minimizes surface energy.

The slow kinetics facilitated by these 'depolymerization' reactions have been reported to lead to the formation of stable, spherical silica particles through nucleation and growth, a mechanism described in Chapter 2 in reference to metal particles.⁵ Nuclei form from a supersaturated precursor (monomer) solution, and then growth occurs through the slow addition of monomer to the growing nuclei. Depolymerization helps to maintain a sufficient monomer concentration so that

growth occurs through the addition of a monomer to a growing particle rather than through aggregation of smaller clusters.⁵

Figure 3-5 shows computer-simulated data indicating that thermodynamically stable particles only form through reaction-limited growth involving the addition of monomer to a growing particle.⁵ When reaction rates are faster and depolymerization does not occur, kinetics are typically diffusion-limited. This behavior results in the formation of non-stable branches. Likewise, cluster-cluster aggregation yields irregularly-shaped precipitates. It has been observed that aggregation is more

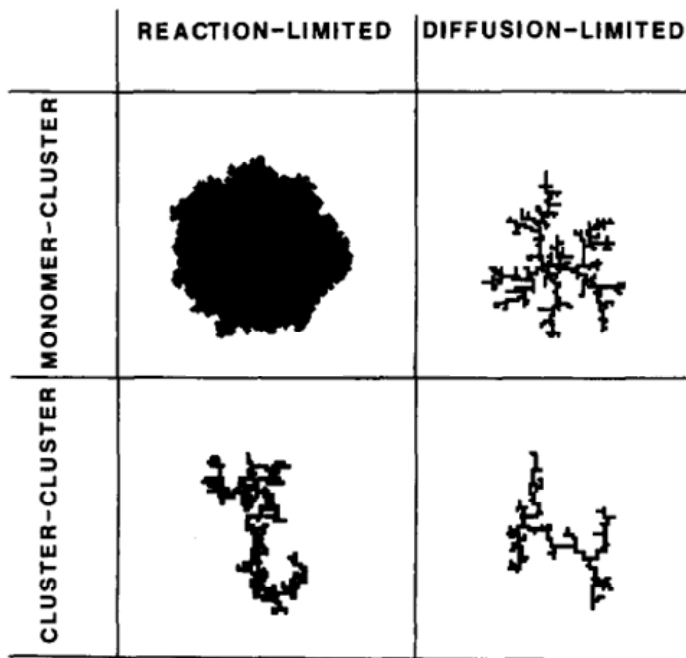


Figure 3-5. Computer simulations of structures formed by monomer-cluster and cluster-cluster aggregation under reaction and diffusion-limited conditions. Figure taken from Brinker et al.⁵

prevalent than growth at high precursor concentrations.⁶

For the case of silica, basic conditions are generally required to achieve reaction-limited monomer-cluster growth. As mentioned in Section 3.1.1.1.2 (page 157), hydrolysis rates are retarded in the presence of

base. Likewise, it is mentioned above that depolymerization and thus decreased effective condensation kinetics occur under basic conditions.⁵ Thus, silica particles can be formed in basic solution with slow hydrolysis and slow condensation.^{5,7} This trend is also shown in Table 3-1. Basic pH also facilitates a negative charge on the particle surface leading to particle stability through electrostatic stabilization.^{5,47}

Werner Stober was one of the first to report the synthesis of stable, micron-sized silica particles, and his method is often referred to as the Stober method. Stober used ammonia as the basic catalyst, noting that particle size increased with ammonia concentration and aggregation occurred in the absence of ammonia.^{55,67} Unfortunately, this method is specific to the synthesis of silica particles and does not apply to the synthesis of particles of titania or other transition metal oxides.

3.1.1.1.4. Titanium and Other Transition Metal Oxides

While silica is the most prevalent type of sol-gel network, there is increasing interest in systems synthesized from titanium and other transition metal alkoxides, and they are of primary interest in this work. While the principles of these hydrolysis and condensation reactions are similar for the non-silicon systems, the kinetic and thermodynamic aspects are significantly different and much less understood. The reaction kinetics are significantly faster for transition metal alkoxides due to their highly electrophilic nature and their tendency to increase in coordination number. Table 3-3 lists the partial positive charges associated with the metal atoms in several

ethoxides and shows that the partial positive charge on titanium is approximately twice of that associated with silicon in the same environment. The higher charge on the titanium atom increases the driving force for nucleophilic attack and consequently the hydrolysis kinetics.^{3,6,40} While silicon alkoxides do not readily react with water, a vigorous, strongly exothermic reaction is observed for when a titanium alkoxide is exposed to water.^{3,6,7,56}

Table 3-3. Partial positive charges associated with the metal atoms in several ethoxides

Alkoxide	Zr(OEt) ₄	Ti(OEt) ₄	Nb(OEt) ₅	Ta(OEt) ₅	VO(OEt) ₃	W(OEt) ₆	Si(OEt) ₄
δ (M)	+ 0.65	+ 0.63	+ 0.53	+ 0.49	+0.46	+0.43	+0.32

Table was adapted from Livage et al.⁶

The fast hydrolysis kinetics associated with titanium and other transition metal alkoxides can also be attributed, in part, the tendency for their coordination number to increase.^{3,6,7,40} While many monomeric titanium alkoxides have a coordination number of four, this number can increase upon exposure to other nucleophiles, and is often as high as six. Metal alkoxides are Lewis acids and can interact with compounds having a lone pair of electrons (Lewis bases) to increase their coordination number.^{3,6} This phenomenon also makes titanium alkoxides significantly more reactive than their silicon counterparts.

In the absence of other reactive species, some transition metal alkoxides oligomerize to achieve a higher coordination number, a process which further

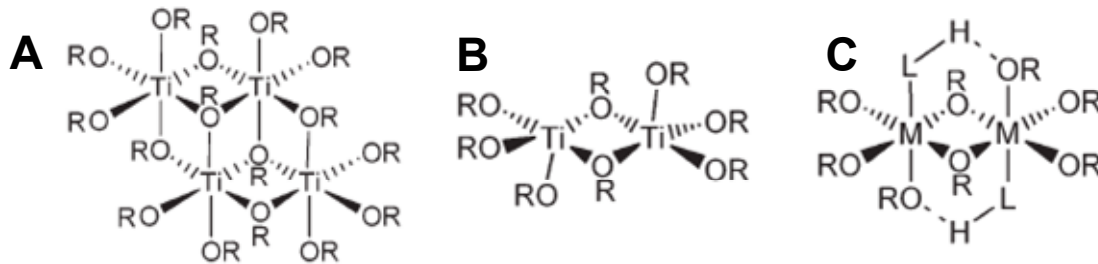


Figure 3-6. Schematic structures of (A) $[\text{Ti}(\text{OR})_4]_4$ ($\text{R} = \text{Me}, \text{Et}$) (B) $\text{Ti}_2(\text{OR})_8$ (C) $\text{Ti}_2(\text{OR})_8(\text{LH})_2$ ($\text{LH} = \text{ROH}$ or RNH_2). Image taken from Schubert³

complicates the sol-gel process.^{3,6,40} In this case, some of the alkoxy ligands bind to two metal atoms. Some examples of titanium alkoxide oligomers are shown in Figure 3-6. As with the extent of hydrolysis and condensation, the extent of oligomerization depends on several factors including the steric bulk of the alkoxy ligands and their ability to bridge between two titanium atoms.^{3,7,66} For example, titanium isopropoxide is a tetracoordinated monomer, while titanium ethoxide forms a trimer and forms a pentacoordinated oligomer.^{7,66}

The reactivity of these oligomeric structures is significantly different than that of the monomers. The bidentate ligands are less easily removed through hydrolysis, and are mainly removed through condensation reactions.³⁹ This process slows down reaction kinetics and can limit simultaneous hydrolysis and condensation. One report claims that oligomeric $[\text{Ti}(\text{OEt})_4]_4$ forms monodispersed spherical particles in contrast to monomeric $\text{Ti}(\text{OPr}^i)_4$, which rapidly precipitates.⁴⁰ However, it has also

Table 3-4. Hydrolysis Rate Constants for Silicon and Titanium Alkoxides

Alkoxide	k_h at pH 7
Si(OEt) ₄	$5 \times 10^{-9} \text{ M}^{-1}\text{s}^{-1}$
Ti(OR) ₄	$1 \times 10^{-3} \text{ M}^{-1}\text{s}^{-1}$

Values for this table were taken from Livage et al.⁶

been reported that oligomerization promotes anisotropic growth and promotes the formation of polymeric gels rather than dense colloids.^{39,55}

Due to both their highly electrophilic nature and their tendency to increase in coordination number, the sol-gel process is significantly more complicated for transition metal alkoxides than for their silicon counterparts. The rapid reaction kinetics and simultaneous hydrolysis and condensation lead to the fast precipitation of metal oxides, making the reactions significantly more difficult to monitor and control.^{3,6,40,53} While there is very little kinetic data available, rate constants for the hydrolysis of titanium alkoxides have been approximated and are listed in Table 3-4 along with values for silicon ethoxide. These data indicate that the reaction rates for titanium alkoxides are greater by approximately five to six orders of magnitude.⁶ The rapid kinetics generally establish diffusion-limited conditions with limited depolymerization, which result in irregular precipitates as indicated in Figure 3-5.^{3,40}

Because of the rapid kinetics and precipitation often observed with titanium alkoxides, chemical additives are often incorporated in the sol-gel process to slow down and gain better control over the hydrolysis and condensation reactions. These

additives can include sterically bulky alcohols to replace the alkoxy substituents on the precursor, acid or base catalysts, solvents, or any species that can complex with the original alkoxide to reduce its reactivity. As mentioned in Section 3.1.1.1.2 (page 157), the hydrolysis rate decreases with the steric bulk of the alkoxy substituent. The titanium-oxygen bond strength (i.e. electronegativity of ligand) also plays a role. Replacing the alkoxy groups with less hydrolysable groups, such as β -diketones,^{7,46,68} carboxylates and β -dicarbonylates,⁴⁸ has been shown to slow down the sol-gel process.

While it has been documented that the addition of acetic acid decreases the gelation times for silicon alkoxides,^{6,7} the reverse effect has actually been observed for transition metal alkoxides.⁶ This effect is not attributed to solution pH, but to the ability of the acetate ligand to bind to more than one titanium atom. While the acetate ligand does not bind strongly to a silicon alkoxide, it replaces an alkoxy ligand when exposed to a titanium alkoxide, forming a new precursor molecule.^{6,7,38,39,46,48} As the acetate ligand is a less effective leaving group than alkoxy ligands, hydrolysis rates decrease. Compared to the instantaneous precipitation observed for pure titanium alkoxides, gelation times as long as several days have been observed in the presence of acetic acid.^{6,7}

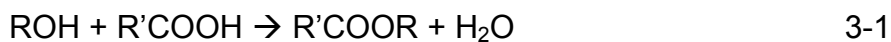
In addition to slower kinetics, introducing acetic acid to a titanium alkoxide affects several changes to the sol-gel chemistry and the structure of the final product. For

example, while the alkoxy ligands are removed through hydrolysis and condensation, the acetate ligands remain bound to the network and are incorporated into the final TiO₂ structure, typically bridging two titanium atoms.^{6,7,39,46,48} If the initial alkoxy ligands is sterically bulky (e.g. isopropoxide), replacing it with a smaller acetate ligands can also lead to coordination expansion and oligomerization, which also affect the sol-gel process.^{39,66} The amount of acetic acid added also plays a role with greater amounts leading to less hydrolysis and condensation.⁷ While titanium isopropoxide typically precipitates upon exposure to water, substitution of one acetate ligand slows down the reaction kinetics and facilitates the formation of smaller, more monodispersed particles.⁴⁰ Substitution of two acetate ligands further limits functionality and results in a more anisotropic, fibrillar structure.⁴⁰ Similar effects have been observed when acetylacetone was added to titanium alkoxides.^{6,40,66,68} While these ligands slow down the reaction kinetics, there are also other consequences to the chemistry and the oxide structure.

In addition to bidentate ligands, other species can alter the molecular precursor and affect reactivity. For example, anions in solution can coordinate to the metal cations.³⁹ Anions also affect aggregation processes due to the formation of an electrical double-layer, which affects the final oxide structure.³⁹ The solvent used can also influences the structure of the molecular precursor and the structure of the final oxide.⁶ Of course, the amount of water present in solution also has a significant

effect on the hydrolysis kinetics and the structure of the final oxide. For the hydrolysis of titanium tetra-n-butoxide, fast precipitation was observed for water:butoxide ratios of three or greater, while a variety of mixed polymers were observed for ratios of less than 2.5.⁴

While the amount of water in solution is critical to sol-gel reactions, it is often difficult to control the amount of water in a given system. In addition to difficulties associated with atmospheric moisture, side reactions can produce water during the sol-gel process. Scheme 3-3 shows the production of a water molecule through the dehydration of hydrolyzed species. However, it is difficult to predict what to what extent condensation will occur through dehydration versus alcohol condensation. In addition, organic side reactions can also produce water. For instance, once an alcohol is removed for the alkoxide, it can react with a free carboxylic acid (e.g. acetic acid) to form an ester and produce a water molecule as shown below.^{3,7,48,63} It has been reported for every two moles of acetic acid or methacrylic acid added to titanium ethoxide, 1.33 moles coordinated with the titanium, while the remainder underwent esterification.⁴⁸ This esterification reaction was likely catalyzed by the titanium.³ Both the water molecule and the ester could then interact with the alkoxides and alter their reactivity.



3.1.1.1.5. Summary

The summary above was intended to provide an outline of the challenges associated with controlling the structure of a metal oxide using the sol-gel process. Sol-gel chemistry is extremely complex, and small changes in reaction conditions can have significant effects on the final product. As a result, reaction conditions need to be strictly controlled and optimized for each reaction. The same conditions cannot typically be applied from one sol-gel synthesis to the next.

In addition to the complexities associated with sol-gel chemistry, the challenges discussed in Chapter 2 in reference to the synthesis of metal particles also apply to metal oxide particles. While particle stability is critical, there is a tradeoff between particle stability and reactivity. In addition, control over both the thermodynamics and kinetics of nucleation and growth is critical in obtaining particles of a desired size, shape and dispersity. The next section provides an overview of sol-gel particle syntheses in the literature.

3.1.1.2. Overview of Literature Methods for TiO₂ Particle Synthesis

Titania nanomaterials have been widely investigated as their unique properties make them useful for many applications. The applications for TiO₂ include

ceramics,^{9,19,20,63,69,70} thin films,^{24,38} coatings,^{9,26,38,71,72} membranes,^{9,19,26,38,63,72}

pigments,^{9,18-20,26,69,70,72-75} catalysts and catalytic supports,^{9,18-20,24,26,33,34,38,63,70-79}

sensors,^{18,20,38,63,69-71,77-79} solar cells,^{9,20,26,33,63,71,73,76,78} optics,^{9,18,34,74} environmental

purification,^{19,24,80} dielectric materials,^{19,34,69} batteries,^{24,33,70} photovoltaics,^{18,69,71,74,77},
electronic and electrochromic devices,^{24,26,38,75} and energy and data storage.⁷⁰

Despite all of the research in this area, there is still no general method for synthesizing discreet, stable, monodispersed TiO₂ particles.^{63,73,81} Many of the methods used to synthesize TiO₂ powders lack control over size and shape, and the resulting structures are polydispersed and agglomerated.⁴ This section provides an overview of the methods that have been used with the intent of portraying the complexity of these systems and the how reaction conditions affect the size, shape and dispersity of the resulting particles. Before describing synthetic methods associated with TiO₂ particles, the general mechanism affecting the stability of metal oxide particles is described.

3.1.1.2.1. Stability of Metal Oxide Particles

Metal oxide particles synthesized in aqueous solution are generally electrostatically stabilized as discussed in Section 2.1.1.1. Depending on the solution pH, water molecules adsorbed to the particle surface ionize to either H₃O⁺ or OH⁻, and electrostatic repulsion between particles prevents aggregation.^{5,6,30,55,82} The electrostatic stability of metal nanoparticles is described in Section 2.1.1.1 in terms of DLVO theory, which describes the interaction between particles as the sum of the attractive and repulsive forces between them.⁸³⁻⁸⁷ While DLVO theory is sufficient to predict the behavior of most nanoparticles, it fails when it comes to extremely

hydrophobic or hydrophilic particles.⁸⁸ One reason for this is that DLVO theory assumes a uniform structure for the aqueous medium. However, especially for hydrophilic and hydrophobic materials, the structure of the medium close to the particle surface may differ from that of the bulk.⁸⁸ To account for this, an additional structural term, also called a secondary hydration force, has been added to the conventional DLVO expression as shown in Equation 3-2.⁸⁸⁻⁹¹ The secondary hydration force is associated with hydrated ions adsorbed to the particle surface, and is termed a 'secondary' force as it is only significant above a critical electrolyte concentration.⁸⁸ This term is also negligible for particles when the corresponding substrate exhibits advancing contact angles between 15 and 64.^{88,91}

$$\begin{aligned}
 V_{TOTAL} &= V_A + V_R + V_S \\
 V_A &= \text{attractive force} \\
 V_R &= \text{repulsive force} \\
 V_S &= \text{structural or secondary hydration force}
 \end{aligned}
 \tag{3-2}$$

As mentioned above, the effects of the secondary hydration force are only significant in the presence of electrolytes. The discussion related to metal particles in Section 2.1.1.1 indicates that their stability decreases with ionic strength due to compression of the electrical double layer. However, for hydrophilic or hydrophobic particles for which the secondary hydration force is significant, the hydrated counter-ions on the surface can contribute to additional electrostatic repulsion. For TiO₂ (rutile), particle stability was significantly greater at high concentrations of NaCl than predicted by conventional DLVO theory.⁸⁸ As the secondary hydration forces increases with

electrolyte concentration, there are cases where particle stability increases with ionic strength.^{88,90,92,93}

In addition to electrostatic forces, some aspects of steric stabilization may also be present in the case of sol-gel derived metal oxides. The alcohol molecules produced throughout the sol-gel process can chemisorb onto the particle surface, also helping to prevent particle aggregation.⁹⁰ While the addition of molecules to act as capping ligands has not been frequently pursued, this concept is discussed later in this chapter.

3.1.1.2.2. Synthesis of TiO₂ Particles – General Considerations

While the synthesis of silica particles is most commonly done under basic conditions as discussed in Section 3.1.1.1.3 (page 164), the most common method for synthesizing titanium particles is through the hydrolysis and condensation of titanium chlorides or alkoxides under acidic conditions.^{4,41,66,68,71,75} This process may initially seem counter-intuitive as acidic conditions promote fast hydrolysis as described in Section 3.1.1.1.2 (page 157). However, condensation is significantly slowed under acidic conditions, thus limiting precipitation.^{9,94} The product of the acid-catalyzed hydrolysis of these titanium precursors is the protonated species, $[\text{Ti}(\text{OH})(\text{OH}_2)_5]^{3+}$.^{19,95} These cations are stable under strong acidic conditions, and do not undergo condensation due to electrostatic repulsion.^{19,95} Condensation only

occurs upon deprotonation of this species, which typically requires an increase in pH.^{19,95}

This mechanism facilitates some separation between hydrolysis and condensation, which is critical to the formation of uniform particles. One possible reaction mechanism is shown in Figure 3-7.⁴ This mechanism is based on the LaMer model for the separation of nucleation growth, described in Section 2.1.2.1 in reference to metal particles.^{96,97} Once a critical concentration of the hydrolyzed species is achieved, nucleation begins. Nucleation ceases once the concentration of hydrolyzed species drops below the critical value.⁴ This model represents an ideal

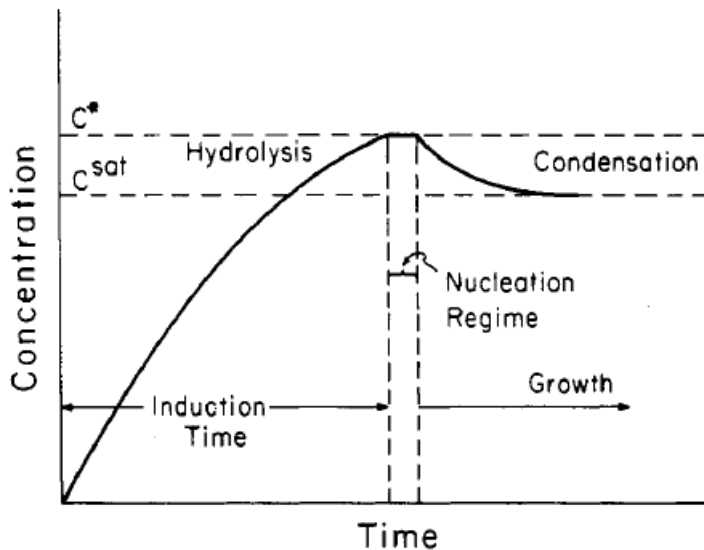


Figure 3-7. Schematic of nucleation and growth process assumed for alkoxide hydrolysis. Schematic taken from Barringer et al.⁴

reaction system; however, complete separation of hydrolysis and condensation has not been achieved.⁴

As the different crystalline forms of titania have different properties and reactivities, there have been significant efforts to tailor not only the size and shape, but also the crystallinity of TiO₂

nanomaterials.^{19,30,95} In most cases, sol-gel materials synthesized at low temperatures are amorphous and thermal annealing or calcination is required in order to induce crystallization.^{18-20,63,69} These processes can also remove any remaining organic materials.⁷⁶ There are three crystallographic forms of TiO₂: rutile (tetragonal), anatase (tetragonal), and brookite (orthorhombic).^{19,30,34,70,72,95} Anatase and brookite are metastable phases typically produced under kinetically-controlled reaction conditions.^{20,30,69,72} However, brookite is observed much less frequently than anatase.⁷² Rutile is the most thermodynamically stable crystalline form, and is generally only formed at higher temperatures.^{34,70,72} While anatase crystals form at temperatures less than 400 °C, rutile typically requires temperatures between 600 °C and 1200 °C, depending on the particle sizes and impurities present.^{69,72}

While these high-temperature processes can induce crystallization, they often lead to particle aggregation, grain growth and loss of surface area.^{20,34,63,69} There may be a few exceptions to this general trend. It has been reported that surface energy plays a significant role in the stability of small particles, and anatase is more stable than rutile for particles smaller than 14 nm.⁷⁰ While the crystal form of the TiO₂ particles synthesized in this work for the demonstration of heterodimers was of little concern, crystallinity will likely need to be tailored for eventual electronic applications.

3.1.1.2.3. Effects of the Molecular Precursor

As discussed above, the nature of the molecular precursor affects the hydrolysis and condensation kinetics of the sol-gel process and thus the structure of the resulting oxide. Titanium ethoxide and titanium isopropoxide rapidly precipitate upon exposure to water.⁶ While stable sols can be obtained through the hydrolysis and condensation of titanium tetra-n-butoxide and titanium amyloxyde ($\text{Ti}(\text{OC}_5\text{H}_{11})_4$), these reactions typically yield linear polymers rather than colloids.⁶ Therefore, the majority of literature reports relating to TiO_2 particle formation from a titanium alkoxide involve either titanium ethoxide (TEO) or titanium isopropoxide (TIP).

Comparing the two viable precursor candidates for TiO_2 particle formation, the reaction kinetics are faster for TIP than for TEO.⁶ This behavior is attributed to the fact that TEO forms oligomeric structures prior to hydrolysis while TIP is monomeric. The faster kinetics associated with the hydrolysis of monomeric TIP make these reactions more difficult to control.

The next few sections summarize literature reports on the synthesis of TiO_2 particles from titanium tetrachloride and titanium tetraalkoxides, specifically TEO and TIP.

3.1.1.2.4. The Synthesis of TiO_2 Particles from Titanium Chloride

The hydrolysis of titanium tetrachloride (TiCl_4) has been performed in both aqueous^{11,41,82,94,98-102} and organic media^{30,99} to yield colloidal TiO_2 . While the

discussion of sol-gel chemistry up to this point has focused on metal alkoxides, titanium tetrachloride can also undergo hydrolysis and condensation to yield TiO₂. In this case, the oxygen in the final network is supplied by either water or an alcohol.³⁴ In the presence of alcohols, metal chlorides react to yield metal chloride alkoxides.⁶ The reaction between TiCl₄ and ethanol is shown below and indicates only partial substitution of the ethoxide ligands.⁶



In this case, it is the substituted product that acts as the precursor in the sol-gel reaction. As with other sol-gel reactions, the reaction rate depends upon the nature of the alcohol, and is much faster for longer alkyl chains. For reactions involving niobium pentachloride, gelation occurs within a few seconds with isopropanol, a few hours with ethanol and several days with methanol.^{7,103}

The most common method of preparing TiO₂ from TiCl₄ involves adding the metal chloride solution to cooled water at acidic pH.^{11,41,94,98,99,102} In most of these reports, particle size was determined from light scattering or x-ray diffraction data, and no TEM images were shown. Thus, it was difficult to evaluate the dispersity and the extent of aggregation for these particles. Figure 3-8 (A) shows an image of TiO₂ particles reported to be approximately 8 nm; however, these data do not clearly indicate whether this method can produce discreet, monodispersed particles. Likewise, the 16 nm particles prepared by Li et al.³⁰ appear to be somewhat

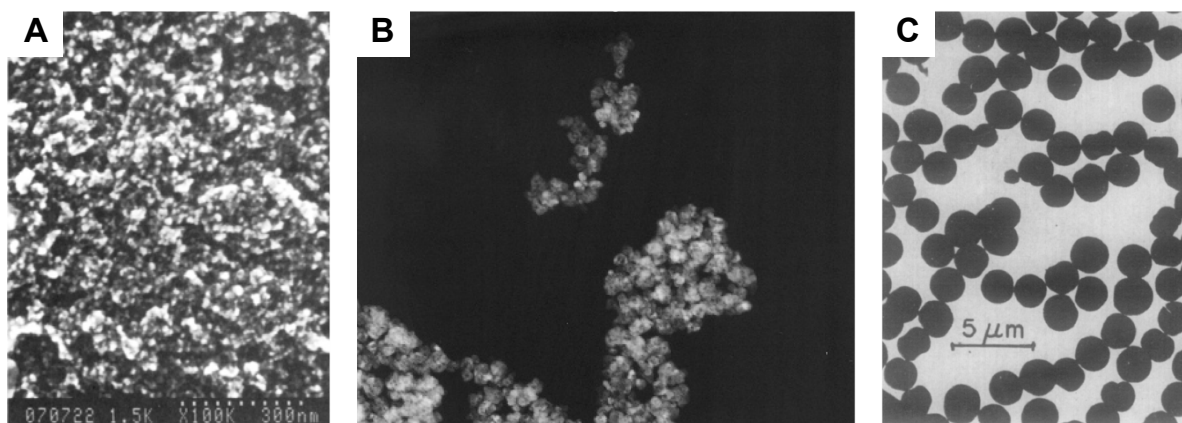


Figure 3-8. Images of TiO₂ particles synthesized via the hydrolysis of TiCl₄ in aqueous solution (A) SEM image of a film of TiO₂ particles (8 nm) taken from Oregan et al.¹¹ (B) TEM image of TiO₂ particles (16 nm) taken from Li et al.³⁰ (C) TEM image of micron-sized TiO₂ particles formed in the presence of Na₂SO₄ taken from Matijevic et al.⁴¹

aggregated as shown in Figure 3-8 (B). There are also some questions about the stability of the TiO₂ particles. One report claims that TiO₂ suspensions are stable for time periods ranging from a few hours to a few days, depending upon the solvent used and the reaction temperature.⁹⁹

There have been attempts to control the sol-gel process, and separate the processes of nucleation and growth. As mentioned in Section 3.1.1.2.2 (page 176), condensation of the hydrolyzed species, $[\text{Ti}(\text{OH})(\text{OH}_2)_5]^{3+}$, does not occur unless the solution pH is high enough to facilitate deprotonation.^{19,95} One method dialyzed an aqueous solution of TiCl₄, initially at a pH of approximately 0-1, against water until the pH was 3.5.¹¹ At this point, it was determined that particle growth was complete. In another method TiCl₄ was hydrolyzed in the presence of Na₂SO₄.^{41,82,94} The

sulfate ions bind strongly with the hydrolyzed titanium ions and therefore limit condensation. The titanium sulfate complexes slowly decompose upon heating, which facilitates particle growth.⁴¹ While this process produces discreet monodispersed particles, it occurs slowly. Growth is favored over nucleation leading to a small number of large particles. Figure 3-8 (C) shows an image of micron-sized particles synthesized using this method. The particle radii increased with the concentration of sulfate ions in solution.⁴¹ The synthesis of nanometer-sized particles using this method was not reported, and would not likely be obtainable due to the low number of nucleation events associated with this method.

Several reaction variables have also been reported to affect the crystallinity of the final TiO₂ particles. For example, one report claims that particles prepared in the presence of low Na₂SO₄ concentrations were rutile, while both anatase and rutile crystalline phases were observed in the presence of high sulfate concentrations.⁴¹ Another report claims that the presence of sulfate ions has led to the formation of anatase, while chloride ions produced anatase, and perchlorate ions resulted in rutile particles.⁹⁴ These discrepancies were attributed to differences in the binding affinities between these additives and the hydrolyzed titanium ions.⁹⁴ The particle shapes also varied with the nature of solution ions.⁹⁴ The solvent has also been reported to affect crystallinity with anatase particles forming in aqueous solution and rutile particles in organic solvent.⁹⁹ Crystallinity also varied with the nature of the

halide; while anatase crystals were formed from the hydrolysis of TiCl_4 , rutile was obtained from the hydrolysis of TiI_4 under the same conditions.³⁴

Pottier et al.⁹⁴ reported the synthesis of TiO_2 nanostructures in which TiCl_4 was added to an aqueous hydrochloric acid solution. Both rutile (elongated particles) and brookite (spherical aggregates) were formed, the mixture of which is shown in Figure 3-9 (A). The two phases were then separated through the selective peptization* of brookite in the presence of nitric acid. Brookite particles were resuspended in aqueous solution due to their smaller size while rutile remained as a precipitate. Brookite particles imaged after separation and aging are shown in Figure 3-9 (B). The authors claim that chloride ions are critical to the formation and stabilization of the brookite phase. This finding contradicts other reports claiming that anatase forms in the presence of chloride ions, and suggests several factors affect the final crystal structure.⁹⁴ Many small changes in solution conditions can greatly affect the size, shape and crystallinity of TiO_2 particles.

3.1.1.2.5. The Synthesis of TiO_2 Particles from Titanium Alkoxides

There are many reports in the literature involving the synthesis of TiO_2 particles from the hydrolysis and condensation of both titanium isopropoxide (TIP)^{9,11,63,68,104-106} and titanium ethoxide (TEO).^{4,75,92,106,107} The most common method for

* The term, peptize, is a verb meaning to disperse a material into a medium as a colloid

synthesizing aqueous particles involves adding the precursor molecule to an acidic solution in the presence of an alcohol.^{4,9,11,105,106} While the role of the alcohol is unclear, it is assumed that it slows the reaction kinetics by shifting the equilibrium to the left. The main factors reported to affect the size and the dispersity of TiO₂ particles synthesized with these methods are the ratio of water/alkoxide, the acid concentration, the reaction temperature and the rate at which the precursor is added to the solution.

The effects of the water/alkoxide ratio on particle size and dispersity are two-fold, affecting both the reaction kinetics and the particle-particle interactions. High ratios favor nucleation over particle growth leading to small particles with a wide size distribution.^{9,107} The higher concentrations of water molecules adsorbed to the particle surfaces at high ratios also increase the extent of hydrogen bonding

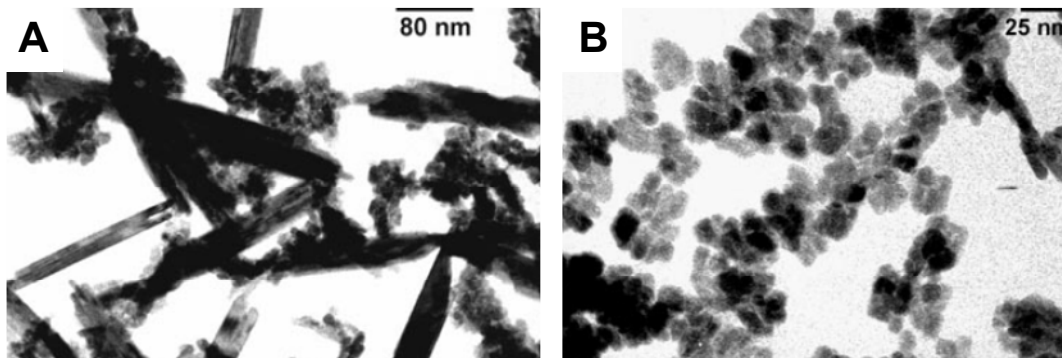


Figure 3-9. TiO₂ Nanostructures formed from the hydrolysis of TiCl₄ in the presence of HCl
(A) Mixture of rutile (elongated) and brookite (spherical) structures (B) Brookite particles after separation through selective peptization.

between particles, and thus the degree of aggregation. While smaller particles are initially formed at high water/alkoxide ratios, larger particles can also be observed due to particle aggregation.^{9,107}

Increasing both the acid concentration and the reaction temperature can lead to smaller particles with a smaller size distribution. As mentioned previously, high acid concentrations are necessary in order to slow condensation reactions and separate nucleation and growth processes.^{9,19,94,95} Thus, smaller particles with narrower size distributions have been observed in the presence of higher HCl concentrations.⁹ In addition, HCl has been reported to act as a catalyst and prevent particle aggregation through electrostatic repulsion.⁹ Higher temperatures increase reaction kinetics so that a larger number of nuclei are formed in a shorter about of time, which also yields smaller particles.^{9,107}

The rate at which the alkoxide precursor is added to the acidic medium also affects particle size and dispersity. The continuously high precursor concentration present in solution at high rates of addition will lead to repetitive nucleation, and thus small particles with a wide size distribution. Lower rates of addition yield shorter nucleation periods and larger, monodispersed particles.⁹ The rate of precursor addition has been controlled using multiple batch⁷⁵ and continuous¹⁰⁷ reaction methods. Continuous reactors yield smaller particles than batch processes due to

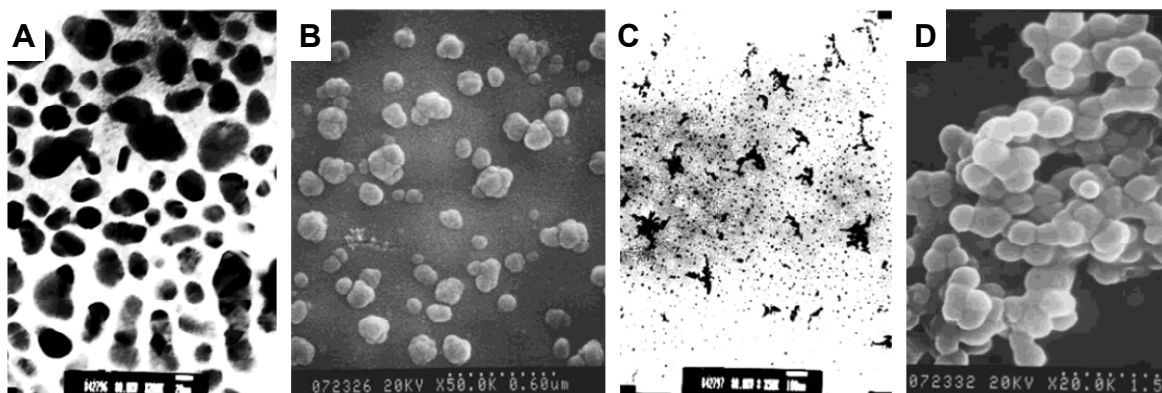


Figure 3-10. TEM images of TiO₂ particles synthesized from the hydrolysis of titanium isopropoxide under acidic conditions. The reaction conditions associated with images A-D are listed in Table 3-5. Images taken from Hsu et al.⁹

short, repetitive nucleation periods while avoiding the polydispersity observed in batch processes.¹⁰⁷

Hsu et al.⁹ synthesized TiO₂ particles by hydrolyzing TIP in the presence of HCl and ethanol systematically varying the water/alkoxide ratio, the acid concentration, the reaction temperature and the rate at which the precursor was added. The results of these experiments are listed in Table 3-5, and images for the first four sets of reaction conditions are shown in Figure 3-10. As expected, the particle size decreased with increasing acid concentrations and decreasing water/alkoxide ratios and feed rates. The authors claim, after further analysis, that small TiO₂ particles (less than 50 nm) with narrow size distributions (less than 5 nm) could be obtained at 0.73 M HCl, a water/alkoxide ratio of 16.6, temperatures above 42.5 °C and feed rates below 14.0 cm³/min.⁹ It is noted, however, that even when the authors report

low size distributions (e.g. Figure 3-10 (C)), some degree of aggregation was also observed.

Another factor that needs to be considered when synthesizing TiO₂ particles is the effect of shear on particle aggregation. While stirring is necessary to ensure mixing of reactants, there is a critical shear rate above which particles aggregate.⁹³ Look et al.⁹³ demonstrated the formation of discrete, spherical, micron-sized TiO₂ particles from the hydrolysis and condensation of TEO. Attempts to synthesize particle under the same conditions but with turbulent mixing resulted in significant aggregation. Similar results were observed for the synthesis of nickel particles reported in Section 2.2.4.2. The critical shear rate required to induce aggregation increased with the

Table 3-5. Effects of Reaction Parameters on the Size and Dispersity of TiO₂ Particles

Image	Water/Alkoxide Ratio	Feed Rate (cm ³ /min)	HCl conc. (M)	Reaction Temperature (°C)	Particle Diameter (nm)	Standard Deviation (nm)
A	1.7	5.8	0.15	25	48.7	13.64
B	33.3	5.8	0.15	60	1571	257
C	1.7	22.2	0.15	60	37	1.2
D	33.3	22.2	0.15	25	1747	336.0
NA	1.7	5.8	0.77	60	14.5	1.9
NA	33.3	5.8	0.77	25	16.5	4.3
NA	1.7	22.2	0.77	25	11	2.8
NA	33.3	22.2	0.77	60	67.5	13.5

The first four sets of reaction conditions correspond to images A-D in Figure 3-10
Data obtained from Hsu et al.⁹

concentration of HCl or NaCl, which is consistent the discussion of metal oxide particle stability in Section 3.1.1.2.1 (page 174). There are some cases where increasing the solution ionic strength can increase particle stability.^{88,90,92,93}

The hydrolysis of titanium alkoxides has also been performed in organic solvents. TiO₂ nanorods have been synthesized by the hydrolysis of TIP in oleic acid.⁶³ The carboxylic acid-terminated molecule reacted with TIP, with the modified precursor exhibiting slower hydrolysis kinetics. After these two compounds were allowed to react, an aqueous solution containing tertiary amines or quaternary ammonium hydroxides was added. These compounds were believed to facilitate crystallization by promoting depolymerization reactions as described in Section 3.1.1.1.3 (page 164).⁶³ Rods are formed as the carboxylic acid functionality of the oleic acid binds preferentially to the {001} crystal faces.¹⁰⁸ Once the formation of nanorods is complete, the oleic acid acts served as a protective capping layer.⁶³ Similarly, TiO₂ nanoparticles have been synthesized by the hydrolysis of TIP starting with a solution of anhydrous chloroform, isopropanol and stearic acid and adding a very controlled amount of water to limit the rate of hydrolysis.¹⁰⁴ In both cases, the particles remained soluble in organic solvents due to the nonpolar capping ligands.^{63,104}

3.1.1.2.6. Titanium Sol-gel Reactions within Reverse Micelles

Attempts have been made to control the size and shape of TiO₂ nanostructures using reverse micelles, similar to the methods described in Section 2.1.2.3 for metal

nanoparticles. Sol-gel reactions similar to those described above, involving the hydrolysis and condensation of titanium halides⁷⁹ and alkoxides,^{19,71,80,81,90,109-111} have been carried out within micellar templates. Micelles facilitate chemical homogeneity at the nanoscale, and have been predicted to yield monodispersed particles.⁸⁰ However, micelles are dynamic structures, and micellar exchange occurs so that reactants are not completely isolated from one another. In one example, TiCl_4 was included in one microemulsion while ammonium was included in another.⁷⁹ No reactions occurred until the solutions were mixed and exchange occurred through micellar collisions. Thus, each micelle does not act as an isolated reaction vessel.

While the discussion in Section 2.1.2.3 in reference to metal particles indicates that the size and shape of the particles is determined by the micellar structure, the literature pertaining to TiO_2 particles emphasizes the importance of micellar exchange. The differences here are likely due to the fact that the water within the micelles is also a reactant in the sol-gel process. In addition, the sol-gel reaction kinetics for titanium can exceed those associated with micellar-exchange. While the size and shape of the micelles do affect the overall particle structure, the relative amounts of the titanium precursor and water within the micelle likely had a greater influence over the final particle size.^{90,110}

For reactions that occur on timescales shorter than those associated with micellar exchange, the composition of the micellar interiors likely vary both from micelle to micelle and throughout the course of the reaction. Fast reactions can lead to particle polydispersity as reactions occur before all of the reactants are completely mixed.⁹⁰ As water is consumed during the sol-gel process, the environment within the micelles also changes as the reaction progresses. For example, when TIP is hydrolyzed within an reverse micelle, part or all of the water is quickly consumed. For every mole of water consumed in this reaction, two moles of isopropanol are produced. In this case, the change in the composition of the micellar interior would

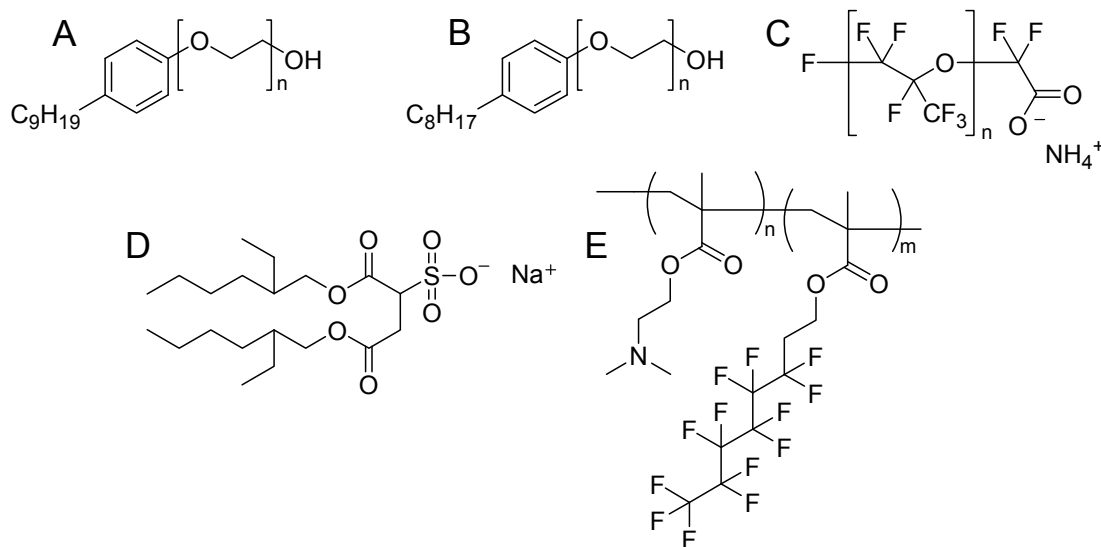


Figure 3-11. Surfactants and polymers used to create reverse micelles for TiO₂ synthesis (A) Polyoxyethylene nonylphenyl ether; tradename Igepal® CO-520 for n~5 (B) Triton® X-100, n = 9-10 (C) Ammonium carboxylate perfluoroether (D) bis(2-ethylhexyl) sulfosuccinate sodium salt (AOT) (E) Copolymer consisting of a dimethyl amino ethyl methacrylate block and a perfluorooctyl methacrylate block.

shift the reaction equilibrium to the left.⁹⁰

The structure of the surfactant used in micellar techniques affects the amount of water available for hydrolysis, and thus the reaction kinetics and particle structure. For example, each Triton X-100 surfactant molecule (Figure 3-11 (B)) contains approximately ten oxyethylene groups. Water within the reverse micelles associates with these polar groups and is therefore not available for hydrolysis.¹¹¹ The reaction kinetics within Triton X-100 micelles were significantly lower than those observed for sodium bis(2-ethylhexyl) sulfosuccinate (AOT - Figure 3-11 (D)), an ionic surfactant with fewer polar groups. The different reaction kinetics observed with the two different surfactants yielded particles of different shapes. In addition, the TiO₂ formed within AOT-micelles contained some organic material, most likely because the fast kinetics did not allow for surfactant rearrangement.¹¹¹

Even when the titanium sol-gel reactions are carried out within micelles, aggregation cannot be avoided. As with bulk sol-gel processes, the extent of aggregation increases with reactant concentrations.^{19,90,110} Moran et al.⁹⁰ claim that uncontrolled aggregation is unavoidable, except at very low precursor concentrations. The authors also suggest a mechanism in which nucleation occurs within a micelle, and growth and aggregation occurs through micellar exchange. A similar mechanism was proposed by Towey et al.¹¹² for the synthesis of CdS nanoparticles.⁹⁰ Under these conditions, the micellar structure would not necessarily prevent aggregation.

Colloid stability also depends upon the size of the micelle and the nature of the surfactant. Colloid stability decreases with increasing micelle size.⁹⁰ While no rationale was given for the following observations, TiO₂ particles synthesized in micelles composed of a block copolymer (Figure 3-11 (E)) were stable for twenty-four hours while particles synthesized in micelles composed of ammonium carboxylate perfluoropolyether (Figure 3-11 (C)) quickly aggregated.¹¹⁰ Particles synthesized in both types of micelles were significantly larger than the size of the micelles, determined by dynamic light-scattering indicating surfactant reorganization.¹¹⁰

As with the bulk sol-gel process, TiO₂ prepared in reverse micelles is typically amorphous and requires calcination for crystallization.^{19,71,79,81,90,109} Again, calcinations can lead to unwanted particle growth and aggregation.^{20,34,63,69,71} However, there have been some reports of crystalline products being formed upon particle ageing or annealing TiO₂ particles in the presence of micelles.^{71,81,90} These processes occurred at temperatures significantly lower than those required for calcination and did not significantly alter the particle size and shape.

Zhang et al.¹⁹ reported the formation of crystalline TiO₂ formed from the hydrolysis of titanium tetra-n-butoxide within reverse micelles of Igelpal® CO-520 (Figure 3-11 (A)) containing acidic solution.⁷¹ As discussed in Section 3.1.1.2.2 (page 176) condensation reactions involving titanium precursors are retarded in the presence of

acid. The relatively slow kinetics observed under these conditions facilitated the arrangement of TiO_2 into crystalline structures.¹⁹ Both the concentration and the nature of the acid significantly affected the particle crystallinity. While pure rutile was formed at hydrochloric acid concentrations of 2.5 M, amorphous materials were produced when the acidity was much lower or much higher.⁷¹

Figure 3-12 shows how the structure of the particles changed as the nature of the acid was changed from hydrochloric to nitric, sulfuric and phosphonic at

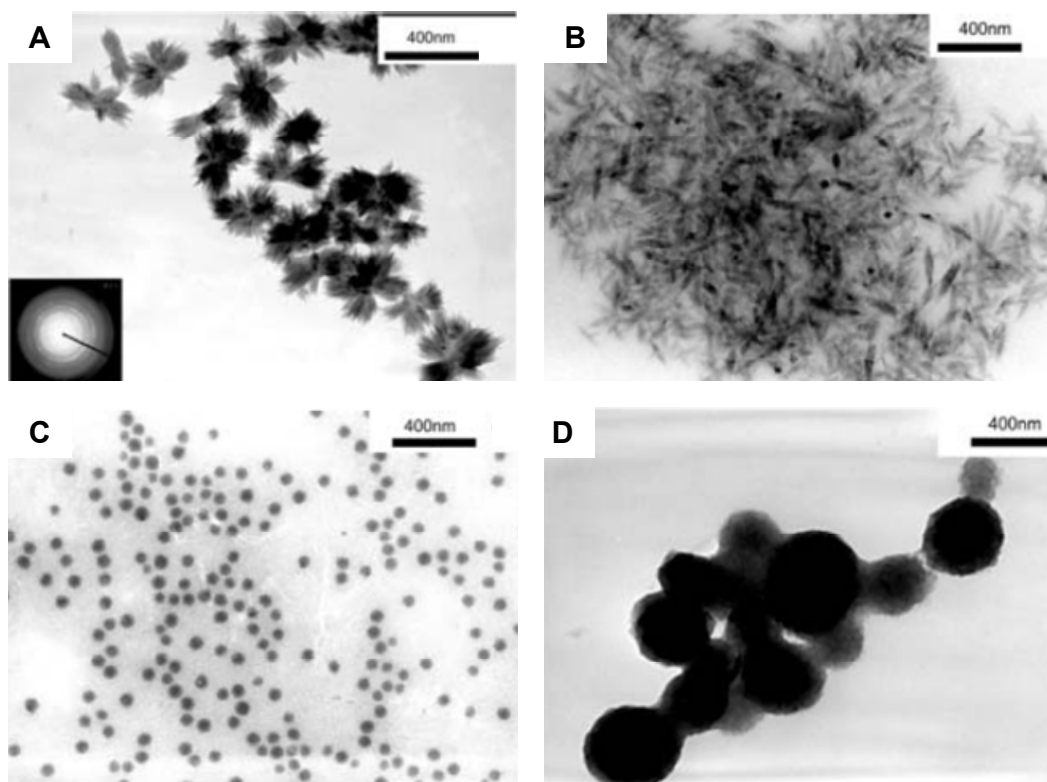


Figure 3-12. TEM images of titanium oxide nanostructures formed in reverse micelles in the presence of (A) hydrochloric acid (B) nitric acid (C) sulfuric acid (D) phosphoric acid. The acid concentrations in all cases were equivalent to 2.5 M HCl. The insert in (A) is an electron diffraction pattern indicating the rutile crystal phase. Images taken from Zhang et al.¹⁹

concentrations equivalent to 2.5 M HCl. The use of both hydrochloric and nitric acid yielded rutile particles, however they were not spherical, but 'shuttle-like'.¹⁹

Amorphous, spherical particles were obtained in the presence of both sulfuric acid and phosphoric acids. However, the particles synthesized with phosphoric acid were significantly larger (240 nm) and aggregated compared to those synthesized with sulfuric acid (40 nm). These differences were attributed to the different affinities between the titanium ions and the acidic ions. For example, SO_4^{2-} ions have a much stronger affinity for titanium than Cl^- and NO_3^- ions, and therefore inhibit the structural rearrangement required for crystal formation.¹⁹

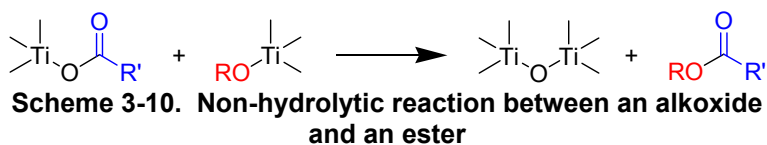
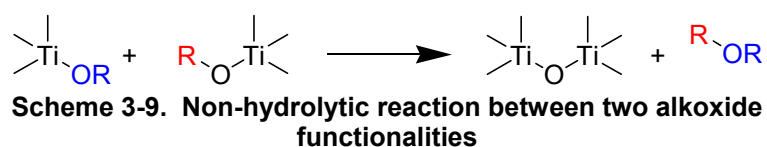
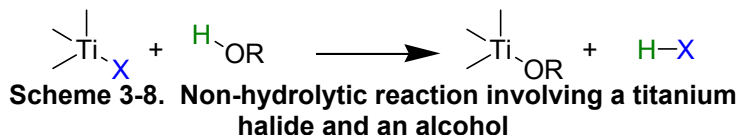
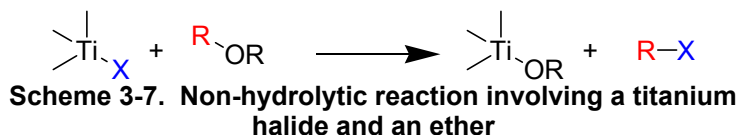
3.1.1.2.7. Non-Hydrolytic Methods

The previous sections describe many of the difficulties associated with synthesizing TiO_2 nanoscale materials using the sol-gel method. Because of the high reactivity of titanium precursors, it is often difficult to control kinetics. While many attempts have been made to control reaction kinetics, these often involve additives which cannot subsequently be removed, and aggregation is typically observed even under optimized reaction conditions. Particles formed using sol-gel methods are typically amorphous without further heat treatment. In addition, because such small changes in reaction conditions can significantly alter the structure of the final product, reproducibility is often difficult to obtain using sol-gel methods.^{92,113}

Non-hydrolytic methods have been developed to avoid some of the problems associated with the sol-gel method.^{18,26,53,78,113,114} For the case of titanium, these reactions typically involve the reaction of a titanium halide with an oxygen donor, such as a titanium alkoxide, an ether or an alcohol.^{8,18,33,49,53,71,72,113} A reaction involving a titanium alkoxide is shown in Scheme 3-6. In this case, a Ti-O-Ti bridge is formed, and an alkyl halide is eliminated. When an alcohol or ether is used as an



Scheme 3-6. Non-hydrolytic reaction involving a titanium halide and a titanium alkoxide



oxygen donor, an alkoxide

is formed in-situ, as

shown in Scheme 3-7 and

Scheme 3-8.^{18,33,71}

These species can then

react further to produce

TiO₂ networks. Two

adjacent alkoxy groups

can react to form a Ti-O-Ti

bridge through the

elimination of an ether as

shown in Scheme 3-9.³

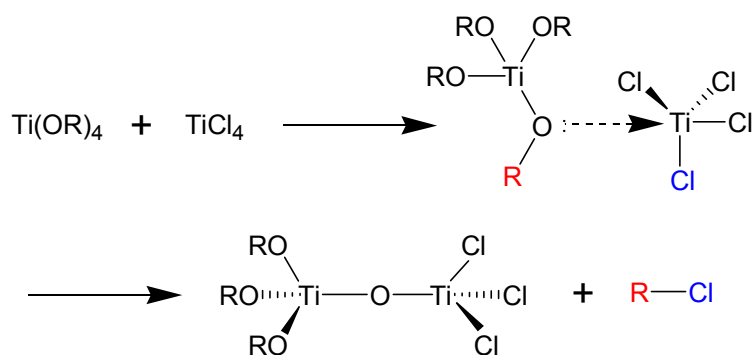
Similarly, carboxylic acids

react readily with titanium

alkoxides, and the product of these reactions can also form a Ti-O-Ti bridge through elimination of an ester and can be removed upon heating to create a pure oxide.^{8,18,33,115}

Advantages of the non-hydrolytic approach include slower reaction kinetics than observed for conventional sol-gel reactions, which allow for more control over the process, and the possibility of controlling the surface chemistry of the particles. While metal oxides are extremely reactive with water, complete condensation in non-hydrolytic reactions typically does not occur without heat and an excess of the oxygen donor.^{8,72} In addition, these reactions occur in one stage, rather than the two associated with the conventional sol-gel process (i.e. hydrolysis and condensation), which also facilitates better control over the process.¹¹⁵ In the presence of water, particle surfaces are coated with hydroxyl groups, which affect the catalytic and electron transfer properties.^{20,33,78} Synthesizing particles in organic solvents creates the possibility of

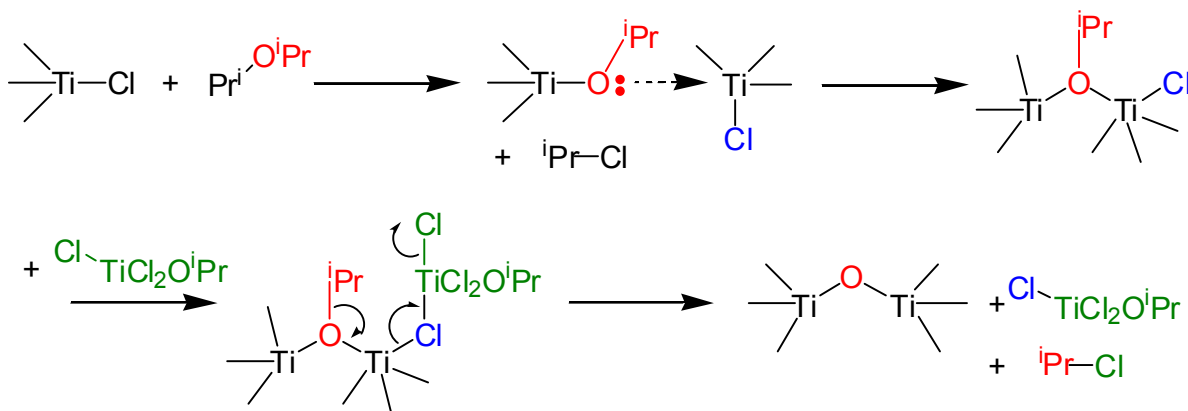
using organic capping ligands.^{33,78} In some cases, the solvent or the organic species



Scheme 3-11. Non-hydrolytic reaction of titanium alkoxide with TiCl₄

formed during the course of the reaction can act as capping ligands.¹¹³

The mechanism associated with non-hydrolytic reactions differs from that described for conventional sol-gel processes.^{33,113-115} For the reaction between a titanium alkoxide and TiCl_4 (Scheme 3-11) the oxygen atom of one of the alkoxy ligands coordinates with the titanium atom in the chloride, creating a pentacoordinated reaction intermediate.¹¹⁵ A similar process occurs when an alcohol or an ether is used as an oxygen donor.^{49,114} The reaction then proceeds via the nucleophilic attack of the chloride ion (blue) on the carbocation (red) to form an alkyl halide.^{33,113-115} This reaction is catalyzed by Lewis acids, the most common being iron (III) chloride.^{8,49} The slower reaction rates observed for these reactions are attributed to the moderate reactivity of the C-O bond, which breaks in this process.¹¹³ While hydrolytic sol-gel reactions are hindered by sterically-bulky alkoxy ligands, these



Scheme 3-12. Reaction mechanism for the $\text{TiCl}_3(\text{O}^i\text{Pr})$ -catalyzed condensation between titanium chloride and di-isopropyl ether. Schematic adapted from Arnal et al.⁸

reactions are favored in the presence of sterically bulky R groups, which are able to stabilize a positive charge.^{33,72,115}

More detailed mechanisms have been proposed for specific systems; for example, the reaction between titanium chloride and di-isopropyl ether. While the general mechanism for the condensation between M-Cl and M-OR bonds discussed above is catalyzed by Friedel-Crafts catalysts such as FeCl₃ or AlCl₃,^{8,49} Arnal et al.⁸ claim that the reaction between TiCl₄ and di-isopropyl ether is catalyzed by the reaction intermediate, Ti(OⁱPr)Cl₃, as shown in Scheme 3-12. The molecular precursors in this reaction are likely a mixture of titanium chloro-isopropoxides in equilibrium. The reaction kinetics are dependent upon the concentration of Ti(OⁱPr)Cl₃ in solution and thus the initial ratio of titanium to ether.⁸

As with the conventional sol-gel process, there are several factors that affect the reaction kinetics, the particle size and distribution for non-hydrolytic reactions. As mentioned above, the nature of the R group affects the reaction kinetics.^{33,72,115} For example, the reactions between TiCl₄ and titanium alkoxides significantly increased as the R group was changed from methyl to ethyl, then isopropyl and tert-butyl.³³ Similarly, reactions rates between TiCl₄ and ethers increased as the ether was changed from dimethyl ether to diethyl ether and di-isopropyl ether.⁷² While one report claims that the varying reaction rates had minimal affect on particle size,³³ another claimed that the particles formed from titanium tetrabutoxide were smaller

than those formed from titanium isopropoxide.²⁶ While the nature of the halide did not affect reaction kinetics, it was observed that more nucleophilic halides yielded smaller particles. For one reaction, particle sizes ranged from 9.2 nm for TiF_4 to 3.8 nm for TiI_4 .³³

The nature of the precursors has also been reported to affect the crystal structure of the resulting particles. For example, anatase was formed from the reaction between TiCl_4 and diethyl ether,^{72,114} while the rutile was formed from a similar reaction with ethanol⁷² and tert-butanol yielded brookite.¹¹⁴ For another reaction, rutile was formed from TiI_4 while anatase was formed from TiCl_4 .³³ While the rationale for these differences is not clearly understood, these data suggest that both the particle size and crystal structure of TiO_2 particles can be controlled by proper choice of

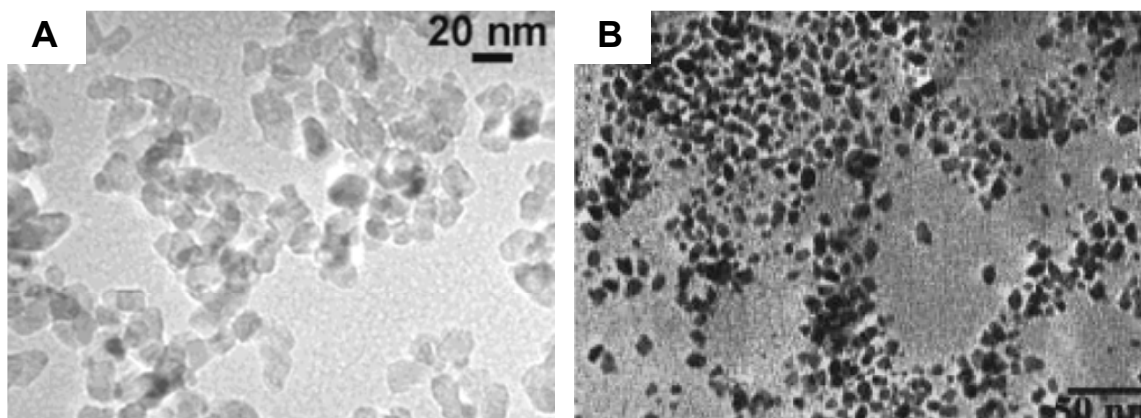


Figure 3-13. TiO_2 particles synthesized using non-hydrolytic methods (A) Particles synthesized from the reaction of TiCl_4 with benzyl alcohol, approximately 15 nm in diameter. Image taken from Niederberger et al.¹⁸ (B) Particles synthesized from the reaction of TiCl_4 with TIP in the presence of TOPO. Image taken from Trentler et al.³³

molecular precursors.

A method commonly reported in the literature for the formation of TiO₂ particles is the reaction of TiCl₄ with benzyl alcohol.^{18,25,71,74,77,113} The size of the resulting particles was tailored by altering the temperature and the ratio of TiCl₄ to benzyl alcohol; particle size decreased with the concentration of TiCl₄.^{18,71} This synthesis has also been done in the presence of stabilizing ligands, which add stability to the resulting particles.^{25,74} TiO₂ particles have also been synthesized through the reaction of benzyl alcohol with titanium alkoxides.¹¹³ For example, anatase particles are formed through the reaction of TIP with benzyl alcohol. This method eliminates halide impurities, which can be problematic for some applications.¹¹³ A TEM image of particles synthesized using this method is shown in Figure 3-13 (A).

Similar to the methods discussed for metal particles (Sections 2.1.2.2 and 2.1.2.3), metal oxide particles can also be synthesized through non-hydrolytic reactions in the presence of surfactants.^{25,33,70,78,108,113} For example, TiO₂ particles have been synthesized from the reaction between TIP and TiCl₄ in the presence of trioctylphosphine oxide (TOPO) and lauric acid.^{108,113} Similar to the hot injection method discussed in Section 2.1.2.2, TIP was added to a solution containing TOPO, lauric acid and TiCl₄ at 300 C.^{33,108} The presence of surfactant slowed down the reaction kinetics and limited the particle growth.^{33,70} A TEM image of particles synthesized using this method is shown in Figure 3-13 (B). While these particles

were highly crystalline, they exhibited some degree of polydispersity and appeared to be loosely aggregated.³³ As lauric acid has a higher affinity for {001} crystalline faces, the ratio of TOPO to lauric acid can also be used to achieve shape control.^{25,108} While there are advantages to surfactant-controlled methods including slower reaction kinetics and added stability, there are consequences regarding surface reactivity. In addition, the presence of surfactants can decrease the purity of the final oxide.¹¹³ The methods developed for surfactant-controlled syntheses are generally specific to one system and the mechanisms cannot be generally applied.¹¹³

While there are numerous reports of non-hydrolytic reactions in the literature, surprisingly few of them contain TEM images. This paucity of data makes it difficult to evaluate the particle morphology. Despite the greater control these methods provide over reaction kinetics, the few TEM images shown in Figure 3-13 do not show completely discrete particles. However, the degree of aggregation observed here is less than that observed for some of the nanometer-sized TiO₂ particles in Figure 3-8, Figure 3-9, Figure 3-10 and Figure 3-12, which were synthesized using hydrolytic techniques. In addition, these particles are typically only dispersible in organic solvents.

3.1.1.2.8. Hydrothermal and Solvothermal Methods

Hydrothermal and solvothermal methods have also been used to synthesize metal oxide particles.^{24,34,71,76,116,117} The only distinction between the two methods is that hydrothermal syntheses are carried out in an aqueous environment while solvothermal reactions are performed in organic media. In both methods, reactions are carried out in sealed reaction vessels called autoclaves.^{24,116,117} A schematic of an autoclave is shown in Figure 3-14. The inert liner protects the stainless steel vessel from any corrosive reagents used in these processes.¹¹⁶ The sealed vessel facilitates heating at temperatures above the boiling point of the solvent as the vapor cannot escape. The pressure within the autoclave drastically increases with

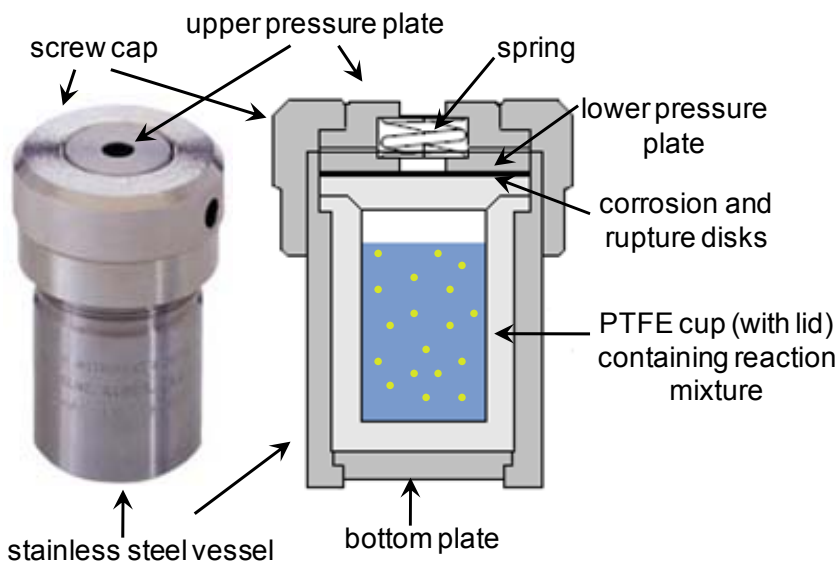


Figure 3-14. Image and cross-sectional schematic of a stainless steel autoclave, specifically a General Purpose Acid Digestion Bomb manufactured by the Parr Instrument Company. The image was taken from and the schematic adapted from the Parr Product Catalog.

temperature, but is also dependent upon the volume of solution in the autoclave and the presence and amount of any dissolved salts.^{71,116} For hydrothermal reactions, pressures of several hundred atmospheres can be achieved even below temperatures of 200 °C.¹¹⁶ The high pressures and associated with hydrothermal and solvothermal methods can facilitate crystal formation at temperatures much lower than those used for calcination, and thus avoids the aggregation which typically occurs during calcination.^{69,81,116}

The high temperatures and pressures associated with hydrothermal and solvothermal methods can also affect reagent solubility and reactivity.^{24,76,116,117} For example, the solubility of rutile TiO₂ increased by two orders of magnitude as the temperature was increased from 100 °C to 300 °C under hydrothermal conditions.¹¹⁶ As the solvent viscosity decreases with increasing temperature, the mobility of dissolved molecules and ions is also higher under solvothermal conditions than at ambient temperature and pressure.^{116,117} In addition, some oxidation states of transition metal compounds can be obtained under hydrothermal conditions that are difficult to obtain in ambient conditions.¹¹⁷ For example, chromium (IV) oxide can be produced from the hydrothermal reactions involving Cr₂O₃ and CrO₃ at 350 °C and 440 bar as shown below. This oxidation state is stabilized by the buildup of oxygen pressure within the autoclave.¹¹⁷



TiO₂ particles have been synthesized in an autoclave using both hydrolytic^{20,24,34,69,71} and non-hydrolytic^{20,24,43,71} processes. The reaction of TiCl₄ with various alcohols yielded TiO₂ particles, the size and crystallinity of which were dependent up on the nature of the alcohol and the concentration of HCl in solution.^{20,34} The reaction of TiCl₄ with alcohols produced HCl as indicated in Scheme 3-8. Due to the high pressure within the autoclave, HCl remained dissolved in solution and catalyzed the etherification reactions depicted in Scheme 3-9.^{20,34} While these reactions are non-hydrolytic, it was proposed that water could be produced as a byproduct of etherification and could contribute to the formation of TiO₂ nanostructures.²⁰ When acetic acid was included in the reaction mixture, it was predicted that hydrolysis was the dominant process once water was produced through esterification reactions (Scheme 3-10).³⁴ TiO₂ particles have also been formed from reactions between TIP with both ketones and aldehydes under solvothermal conditions.⁴³ The size of these particles varied with the nature of the ketone or aldehyde used. Smaller particles were observed with aromatic ligands, suggesting they exhibited stronger interactions with the titania surfaces.⁴³

Better control over the size, shape and crystallinity of TiO₂ particles can be achieved using solvothermal methods compared to hydrothermal methods, which are

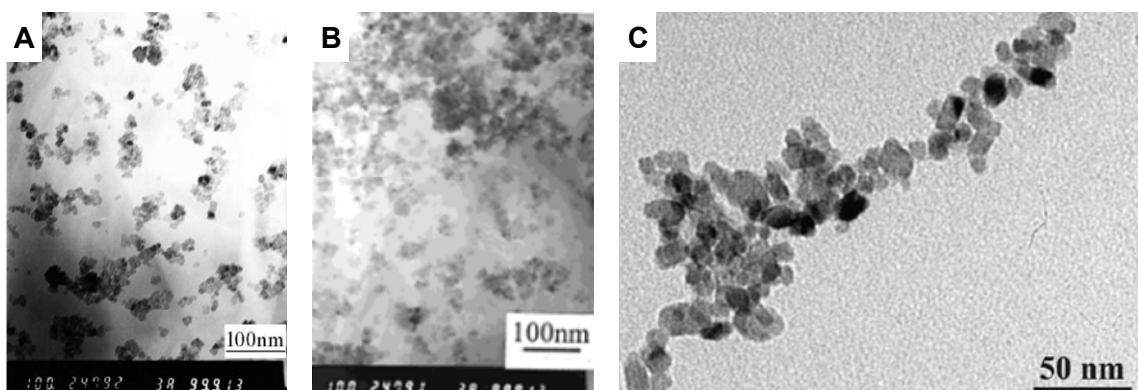


Figure 3-15. TiO₂ nanoparticles synthesized using solvothermal methods (A) Anatase particles synthesized from the reaction of TiCl₄ in ethanol at 150 °C. Image taken from Wang et al.²⁰ (B) Rutile particles synthesized from the reaction of TiCl₄ in glycerol and acetic acid at 150 °C Image taken from Wang et al.³⁴ (C) Anatase particles synthesized from the reaction of titanium isopropoxide with acetone at 130 °C Image taken from Garnweitner et al.⁴³

associated with large size distributions and aggregation.^{63,71,81} However, the particles shown in Figure 3-15, which were synthesized using solvothermal methods, still indicate some degree of aggregation. More discreet particles have been synthesized in the presence of long-chain capping ligands, which prevent aggregation.

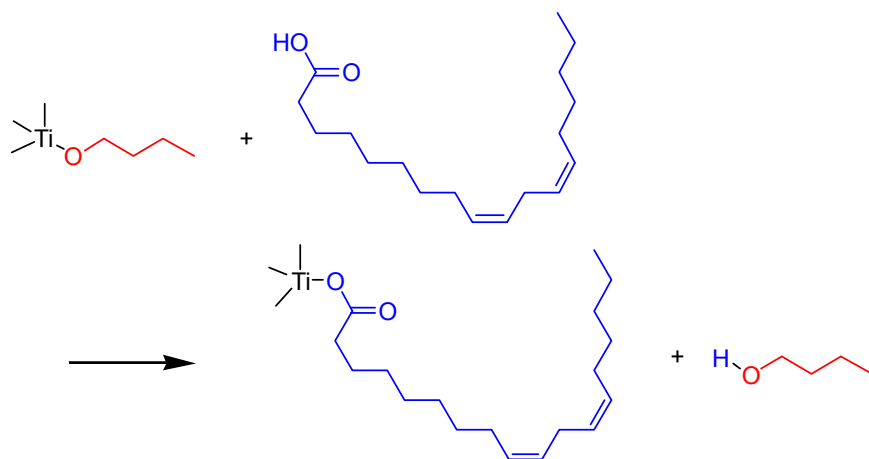
Li et al.²⁴ used the solvothermal method to control the hydrolysis of titanium tetrabutoxide (Ti(OBu)₄) in the presence of ammonium bicarbonate (NH₄HCO₃) and linoleic acid (LA). Both nanoparticle and nanorods structures were achieved by varying the reactant concentrations and the temperature. While water was not added to the reaction, NH₄HCO₃ rapidly decomposed to produce water at temperatures greater than 150 °C according to the equation below:



3-6

The gases released during this reaction could not escape the pressure-sealed vessel, and thus the water produced in this reaction was available to hydrolyze the $\text{Ti}(\text{O}i\text{Bu})_4$. The large amount of water produced at once facilitated fast nucleation and growth of TiO_2 particles, which are shown in Figure 3-16 (A).²⁴ The spacing of the particles on the grid was attributed to the long-chain, linoleic acid capping ligands.

While TiO_2 nanostructures were formed through hydrolysis and condensation in the presence of NH_4HCO_3 , non-hydrolytic reactions involving LA also took place. While LA acted as a solvent and a capping ligand and promoted crystallization, it also reacted with $\text{Ti}(\text{O}i\text{Bu})_4$ as shown in Scheme 3-13. The resulting compound can then



Scheme 3-13. Reaction between titanium tetrabutoxide and linoleic acid

react with another butoxide group to form a Ti-O-Ti bridge through the elimination of an ester as shown in Scheme 3-10.²⁴ In the absence of NH_4HCO_3 , these

reactions led to the formation of TiO_2 nanorods (Figure 3-16 (B)), the length of which increased with LA concentration. This shape control was attributed to the preferential binding of LA to the $\{001\}$ crystalline faces.^{25,108} As LA acts as a stabilizing agent, an amorphous precipitate was obtained when it was excluded from the reaction.²⁴ TiO_2 nanoparticles were formed with an excess of LA, and moderate concentrations of NH_4HCO_3 .²⁴ Extremely high concentrations of NH_4HCO_3 resulted in aggregation. Images of both nanoparticles and nanorods formed using this method are shown in Figure 3-16.

The effects of reaction temperature, duration and the nature of the carboxylic acid on the formation of these TiO_2 nanostructures was also investigated.²⁴ While the crystallinity of TiO_2 increased with reaction temperature, the size of the nanoparticles

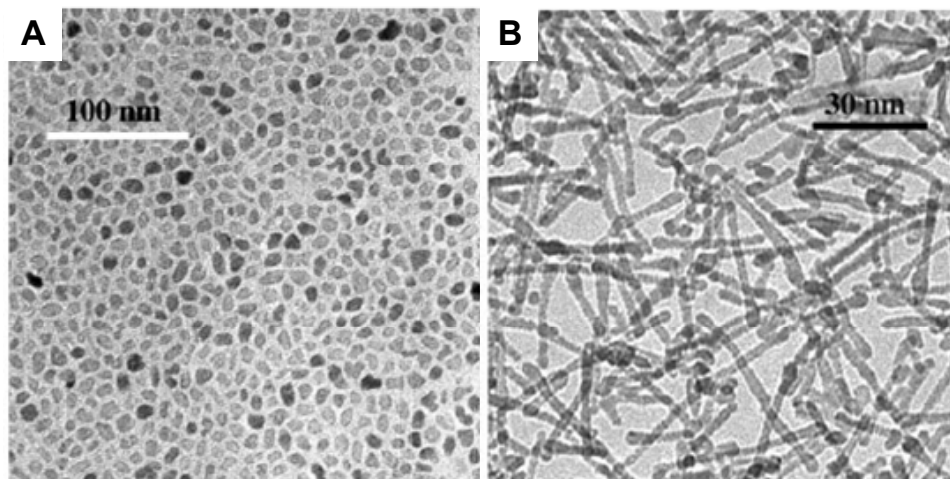


Figure 3-16. TEM images of TiO_2 synthesized using a solvothermal method (A) Nanoparticles synthesized through the hydrolysis of $\text{Ti}(\text{OBu})_4$ in the presence NH_4HCO_3 and linoleic acid (B) Nanorods synthesized from the non-hydrolytic reactions between $\text{Ti}(\text{OBu})_4$ and linoleic acid. Images taken from Li et al.²⁴

and nanorods were not significantly affected. Crystallinity also improved with increased reaction time. Attempts to synthesize TiO₂ particles using a series of carboxylic acids indicated that long-chain carboxylic acids were critical to the formation of these structures. Both nanoparticles and nanorods were formed using linoleic acid (C₁₇H₃₁COOH) and decanoic acid (C₉H₁₉COOH); however, nanostructures were not obtained in the presence of valeric acid (C₄H₉COOH) or acetic acid (C₁H₃COOH).²⁴ While these long-chain acids on the particle surface limit reactivity, it was observed that LA could be removed from the particles by washing them with cyclohexane or ethanol.²⁴ This result suggests the possibility of post-synthesis ligand-exchange with a smaller capping ligand.

While Chemseddine et al.²⁶ did not synthesize particles using hydrothermal methods, the authors altered the size and shape of TiO₂ nanoparticles through post-synthetic treatment in an autoclave. Figure 3-17 shows images of TiO₂ particles both before and after autoclaving at 200 °C. The authors initially achieved shape control over TiO₂ nanostructures by varying the ratio of TIP to Me₄NOH. Because Me₄N⁺ ions preferentially interacted with the [101] crystalline surface, low concentrations favored growth in the [101] direction while high concentrations favored growth in the [001] direction.²⁶ The Me₄N⁺ ions also complex with the growing titania networks, retarding the reaction kinetics and adding stability. The high temperatures and pressures that occurred upon post-synthetic autoclaving

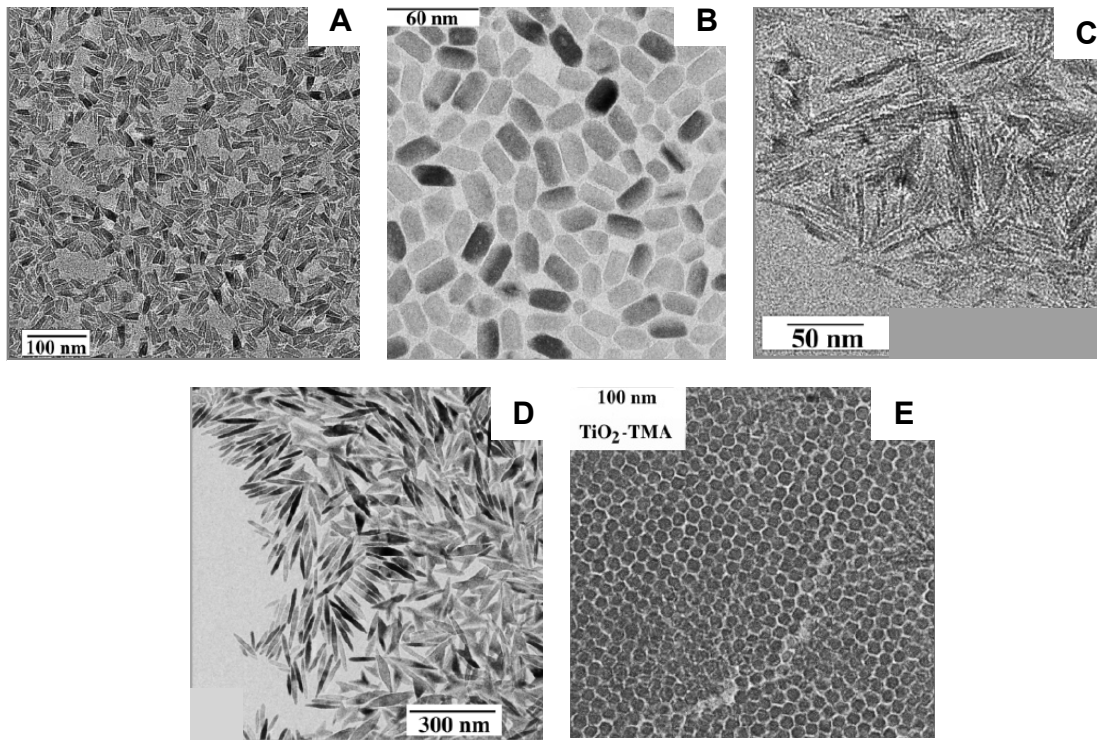


Figure 3-17. Titania nanocrystals synthesized through the hydrolysis and condensation of titanium isopropoxide (TIP) in the presence of trimethylammonium hydroxide (Me_4NOH). (A) Triangular prismatic nanocrystals synthesized with a 4.4:1 ratio of TIP to Me_4NOH (B) Rectangular particles formed after autoclaving the particles shown in (A) at 200 °C. (C) Elongated nanocrystals synthesized with a 1.4:4 ratio of TIP to Me_4OH (D) Nanocrystals obtained after autoclaving the particles shown in (C) at 200 °C. (E) 13.5 nm nanoparticles synthesized using a 0.84:1 ratio of TIP to Me_4NOH . Images taken from Chemseddine et al.²⁶

decomposed the Me_4N^+ ions, which led to further changes in the size and shape of the particles through chemical etching and further growth.²⁶ The size of the particles was also affected by the autoclave temperature, with higher temperatures yielding smaller particles.²⁶

3.1.1.2.9. Optical Properties of TiO₂ Nanoparticles

As many of the particles synthesized in this chapter were characterized by their optical properties, a brief discussion of their origin is included below. Similar to the behavior discussed in Section 2.1.4.1.1, the optical absorption observed for TiO₂ particles is attributed to electronic transitions from the valence band to the conduction band. While no absorption is observed in the visible region, the absorption rises sharply for wavelengths closer to the UV, approximately 380-390 nm, as shown in Figure 3-18.^{18,78,92,101,105} This corresponds to the band gap of approximately 3.2 eV associated with both amorphous and anatase TiO₂.^{71,92,101,105} Blue shifts have been observed for the onset of absorption for extremely small

particles (i.e. less than 4 nm) due to the increase in the band energy.⁷¹

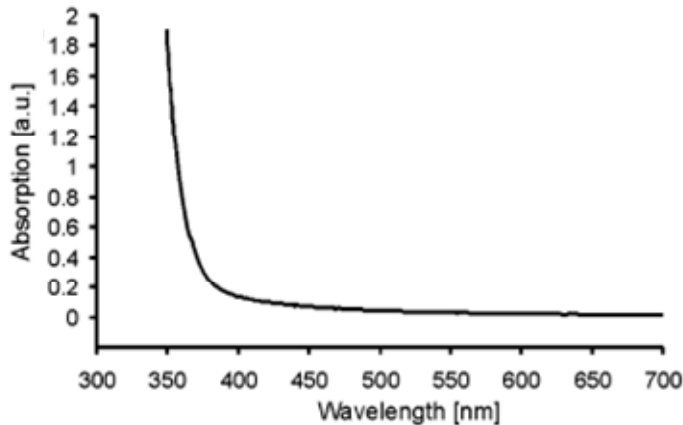


Figure 3-18. Absorption spectrum of anatase TiO₂ particles. Data was taken from Niederberger et al.¹⁸

3.1.1.2.10. Summary

Section 3.1.1.1 discussed some of the challenges associated with controlling the structure of metal

oxides using the sol-gel process. This section was intended to build on those concepts and describe the difficulties associated with synthesizing discreet, stable TiO₂ nanoparticles. While many different methods have been developed, very few produce isolated particles, which are stable over any length of time. In addition, because such small changes in reaction conditions can significantly alter the structure of the final product, reproducibility is often difficult to obtain using sol-gel methods.

The most common methods for synthesizing TiO₂ nanoparticles involve the hydrolysis of TiCl₄, TIP or TEO in acidic media. While these particles are primarily stabilized through electrostatic repulsion between surface-adsorbed ions, some elements of steric stabilization may also be present as alcohol molecules produced during the sol-gel process may also adsorb to the particle surface. There have been attempts to slow down the reaction kinetics in order to limit polydispersity and aggregation. The most successful attempt involved the addition of Na₂SO₄ to solutions of TiCl₄. However, under these conditions, growth is favored over nucleation resulting in monodispersed micron-sized particles. This method is not applicable to the synthesis of structures in the nanometer-size regime.

For reactions involving titanium alkoxides, the effects of the water/alkoxide ratio, acid concentration, reaction temperature and precursor feed rate have been evaluated. While optimal conditions have been reported for several methods, these procedures

still contain some ambiguity, and TEM images do not indicate the presence of isolated particles. Stability also remains a question. More controlled hydrolysis has been achieved in organic solvents. However, these methods typically involve long-chain capping ligands and are not suitable for aqueous applications. Reverse micelles have also been investigated for the synthesis of TiO₂ particles; however, these methods also typically lead to aggregation.

Non-hydrolytic methods have been developed to avoid many of the problems associated with sol-gel methods. The reaction kinetics are much slower, and aggregation does not occur due to hydrogen-bonding between surface hydroxyl groups. In addition, these methods introduce the possibility of capping the particles with organic ligands for additional stability. Despite the greater control these methods provide over reaction conditions, completely discrete particles are not observed. In addition, these particles are typically only dispersible in organic solvents. Solvothermal methods have also been successfully used to synthesize TiO₂ particles. Again, however, the most successful attempts involve long-chain organic capping ligands.

As the goal of this work was to synthesize aqueous TiO₂ particles without bulky capping ligands, initial attempts were focused on the hydrolysis of titanium precursors in acidic media. TiO₂ particles were synthesized using TiCl₄, TIP and TEO. A solvothermal method was also investigated. While this method involved

particle synthesis in organic media with long-chain capping ligands, post-synthesis ligand-exchange and phase-transfer were attempted in order to bring the particles into the aqueous phase.

3.1.1.3. Overview of Literature Methods for the Synthesis of Iron Oxide Particles

In addition to titanium dioxide, the synthesis of iron oxide particle was investigated for the purpose of forming heterodimers with the molecule shown in Figure 3-1.

There are several different crystal structures for iron oxide including Fe_3O_4 (magnetite), $\gamma\text{-Fe}_2\text{O}_3$ (maghemite) and $\alpha\text{-Fe}_2\text{O}_3$ (hematite), all of which exhibit magnetic properties. The magnetic properties of these materials are enhanced in the nanometer-size regime,^{13-16,28,32,118-123} and superparamagnetism has been observed for particles smaller than 10 – 20 nm.^{15,32,121,123} As magnetite is less sensitive to oxidation than other magnetic transition metal nanoparticles such as cobalt, iron and nickel,¹²⁴ the synthesis of iron oxide nanoparticles have been investigated for a wide variety of applications. Iron oxide particles exhibit low toxicity^{23,125} and are therefore of interest for many biomedical applications including magnetic resonance imaging,^{10,14,16,23,28,31,42,45,119,120,122,126-131} targeted drug delivery,^{10,14,16,23,31,42,45,119,120,122,124,127-130,132-137} hyperthermia and other magnetic field-assisted cancer therapies,^{10,14,23,28,31,45,120,125,127,128,130,137} biosensors,^{42,120,122} the separation of cells and biomolecules,^{10,42,45,119,120,122,132,133,135,136,138} immunoassays,⁴² and the detoxification of biological fluids.^{120,133} Solutions of iron oxide nanoparticles

can also be used as ferrofluids,^{14,16,28,31,32,42,120,122,124,127,130,133,139} for information storage media,^{13,14,16,32,42,45,120,122,130,132,138,140} magnetic recording media,^{130,141} magnetic inks,^{120,122} computer hard drives,^{132,136} magnetic sealing,^{28,32,132,136} dynamic loudspeakers,^{132,136} magnetic refrigeration,^{16,32,122,130,132} and catalysis^{16,130,141}

Similar to the situation described for TiO₂ particles, there is no general method for synthesizing discreet, stable, monodispersed iron oxide particles, despite the significant research efforts in this area. Due to the attractive forces between magnetic particles, it is extremely difficult to prevent particle aggregation. In addition to the Van der Waals forces between particles (Section 2.1.1.1), particles are attracted to each other by magnetic dipolar forces.^{17,21,120,124,132,133} As a result, iron oxide particles exhibit extremely high surface energies, often greater than 100 dyne/cm.^{124,132,133} Because of their tendency to aggregate, iron oxide particles are often encompassed within polymer or silica shells.^{121,142-145} While iron oxide has been incorporated into many composite materials, this section is focused on methods that have been used to synthesize pure iron oxide nanoparticles.

While sol-gel methods have been developed for many metal oxide particles and were the focus of the section on TiO₂, these methods are significantly less developed for the synthesis of iron oxides and other ferrite materials.¹⁴⁶ There have been a few reports of the synthesis of iron oxide from the precursor, Fe(NO₃)₃,^{130,147-149} however, these materials were typically aggregated and amorphous.^{120,149} Sol-

gel syntheses for iron alloys such as CoFe_2O_4 and NiFe_2O_4 are more common, but even these are typically aggregated.¹⁴⁹ Commercial iron oxide nanoparticle solutions are generally produced by milling iron oxide in the presence of surfactant in either a ball or vibratory mill.^{17,32} However, these processes take several weeks and lead to broad particle size distributions; particle sizes typically range between 2 and 50 nm.^{17,32} The methods discussed in this chapter include sonochemical methods, the coprecipitation of Fe^{2+} and Fe^{3+} ions, and the thermal decomposition of an iron complex.

3.1.1.3.1. Sonochemical Methods

Sonochemical reactions occur, as the name suggests, by exposing a solution to sonic waves either by sonication or exposure to ultrasound radiation. Under these conditions, bubbles or cavities form within the solution, a process called acoustic cavitation.^{32,44} The collapse of these bubbles generates localized hot spots with transient temperatures up to 5000 K.^{21,32,120} Volatile organometallic compounds within these bubbles can decompose to yield individual metal atoms, which then aggregate to yield metallic nanostructures.

This technique has been used to synthesize iron oxide nanoparticles from ferrous salts in the presence of surfactant.^{21,32,120} The particles sonochemically synthesized using volatile solutes were amorphous,²¹ and the morphology depended upon the nature of the surfactant. For instance, the sonolysis of iron pentacarbonyl ($\text{Fe}(\text{CO})_5$)

in an aqueous solution of sodium dodecyl sulfate yielded water-soluble Fe_3O_4 particles approximately 9 nm in diameter (Figure 3-19 (A)).^{21,120} However, a similar reaction in which $\text{Fe}(\text{CO})_5$ was sonicated in a solution of poly(vinylpyrrolidone) in octanol yielded iron nanoparticles ranging from 3 – 8 nm.³² These particles crystallized into FeO upon irradiation with a high-intensity electron beam (Figure 3-19 (B)). More uniform iron particles (8 nm) were obtained when $\text{Fe}(\text{CO})_5$ was sonicated in a solution of oleic acid in hexadecane. Upon crystallization, these

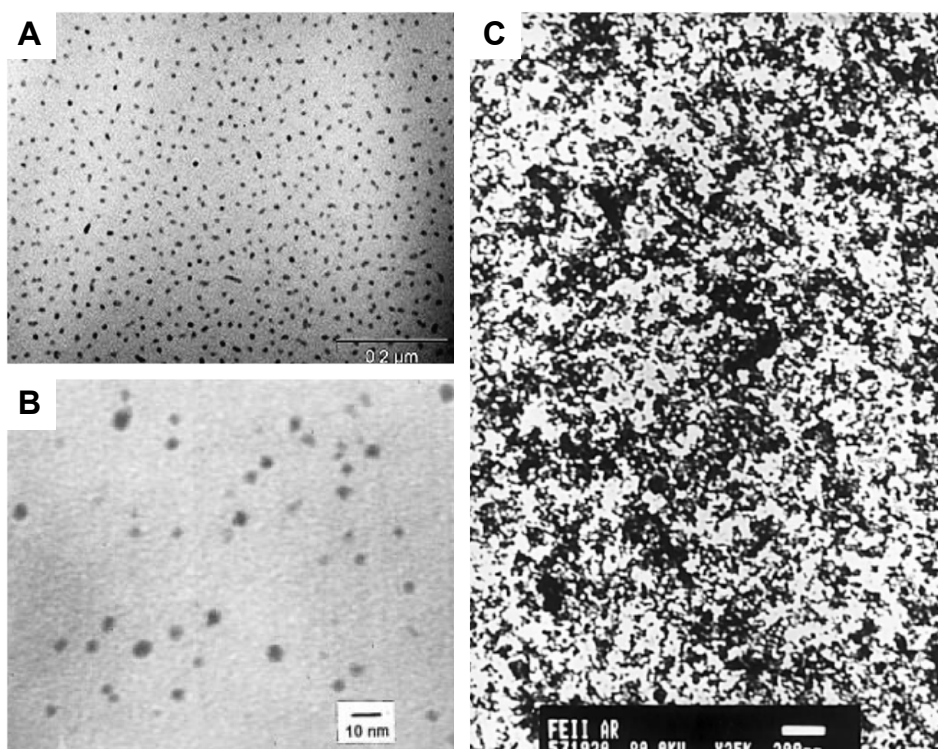


Figure 3-19. Iron oxide particles synthesized using sonochemical reactions (A) Fe_3O_4 particles (9 nm) synthesized from iron pentacarbonyl in the presence of sodium dodecyl sulfate. Image taken from Mukh-Qasem et al.²¹ (B) FeO particles (3 – 8 nm) synthesized from iron pentacarbonyl in the presence of poly(vinylpyrrolidone). Image taken from Suslick et al.³² (C) Fe_3O_4 particles (10 nm) synthesized sonochemically from iron (II) acetate in water. Image taken from Vijayakumar et al.⁴⁴

particles were a mixture of Fe and FeO.³² It was noted that while particles were successfully synthesized in the presence of oleic acid, stearic acid was not effective. As shown in Figure 3-20, these two molecules contain the same number of carbons; however, oleic acid contains a double bond. This indicates that even small differences in the surfactant conformation can greatly affect the synthesis of iron oxide using sonochemical methods.

Fe₃O₄ nanoparticles have also been synthesized from the sonochemical reaction of iron (II) acetate in water.⁴⁴ As this is a non-volatile precursor, the reaction mechanism was different and crystalline particles were obtained. This reaction occurred in the interfacial region between the acoustically-generated cavities and the bulk solution.⁴⁴ In this case, iron oxide particles were formed from a series of reactions initiated by the formation of radical species from water upon absorption of ultrasonic radiation as shown in Equation 3-7. Some of the Fe(II) generated from the iron(II) acetate

was oxidized to Fe(III) by H₂O₂ (Equation 3-11), which was generated upon the recombination of

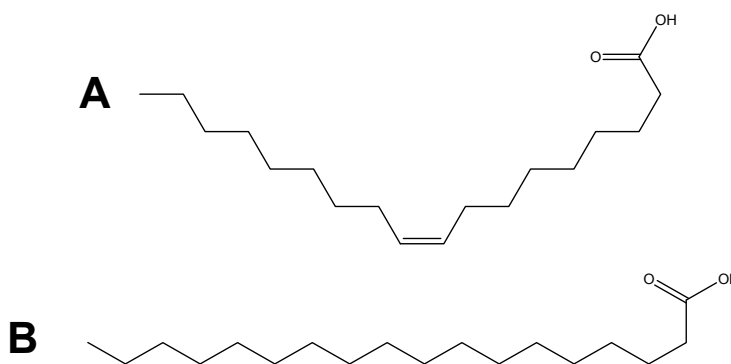
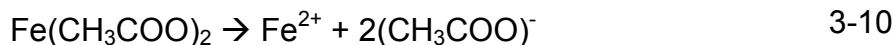
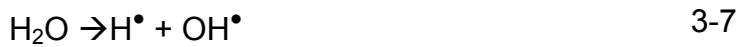


Figure 3-20. (A) Oleic acid (B) Stearic acid

hydroxide radicals (Equation 3-8).⁴⁴ Both Fe²⁺ and Fe³⁺ ions were necessary for the formation of Fe₃O₄. The yield of iron oxide particles was greater under an argon atmosphere as the hydrogen produced in Equation 3-8 can scavenge hydroxide radicals as shown in Equation 3-12, limiting the formation of H₂O₂. In the absence of H₂O₂, pure iron nanoparticles were formed. The 10 nm iron oxide particles synthesized using this method are shown in Figure 3-19 (C), and appear to be somewhat aggregated.



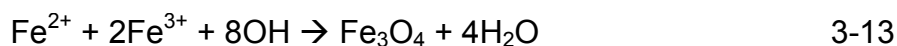
The majority sonochemical methods developed for synthesizing iron oxide particles involve long-chain surfactants, which limit the reactivity of the particle surface. The nature of these surfactants have significant effects on the effectiveness of these techniques and the morphology of the final particles; however, these effects are not clearly understood. While iron oxide particles have been synthesized in the absence of surfactant, these particles appeared to be somewhat aggregated and often led to the formation of both iron and iron oxide nanoparticles. If a mixture of particles was

obtained, a post-synthetic separation technique would be required in order to isolate the iron oxide.

3.1.1.3.2. Coprecipitation of Fe²⁺ and Fe³⁺ Ions

3.1.1.3.2.1. General Considerations

The most common method for the synthesis of iron oxides, specifically Fe₃O₄, involves the coprecipitation of ferrous and ferric ions in the presence of a base such as NH₄OH or NaOH according to the reaction below.^{13,14,17,23,28,29,31,42,45,119-121,123-127,132,133,135,136,138,139,141,150,151}



The size and shape of particles synthesized in this way are affected by the ratio of Fe²⁺/Fe³⁺, the reaction temperature, pH and ionic strength, and the nature of the iron salts.^{120,121} While iron chlorides are most commonly used, sulfates, nitrates and perchlorates have also been used. High pH values favor the formation of Fe₃O₄ according to the reaction above.¹⁵ While one author claims that particle size and size distribution decrease with both solution pH and ionic strength¹²⁰, another report claims that these variables have opposite effects.¹³³ The crystal size decreased from 6 nm to 3 nm as the pH was increased from 11.5 to 14.0 at a constant NaOH concentration of 1.5 M, but increased from 1.3 to 3.0 nm as the NaOH concentration increased from 0.9 to 1.5 M at a constant pH value of 14.¹³³

The pH and ionic strength of the particle solution also affect the nature of the particle surfaces and, thus, particle stability.¹³⁸ In aqueous solution, Fe atoms coordinate with water, which ionizes to either OH⁻ or H₃O⁺, depending upon the solution pH.^{120,151} Particle stability is affected by the concentration of ions on the surface as well as counter-ions in solution, and aggregate at pH values between 5 and 9.^{121,151} While high pH values are necessary for the formation of Fe₃O₄ particles, they can be stabilized in acidic solution post-synthesis. After synthesis, iron oxide colloids have been peptized with both tetramethylammonium hydroxide and perchloric acid.^{121,151} One of the disadvantages of this method is that the pH has to be controlled not only during the reaction, but afterwards as well.

The atmosphere under which particles are synthesized also affects the size and crystal structure of iron oxide. Magnetite (Fe₃O₄) particles are not very stable under ambient conditions and are easily oxidized to maghemite (γ-Fe₂O₃).^{28,42,120,121,150} It has also been reported that in aqueous solution, magnetite can be oxidized to an iron hydroxide as shown below.¹³³



Bubbling nitrogen through the reaction solution has not only limited the oxidation of Fe₃O₄, but to yielded smaller particle sizes.^{120,133} Oxidation of Fe₃O₄ has also been achieved by annealing at high temperatures; the transformation to γ-Fe₂O₃ occurred at approximately 200 °C while the transformation to α-Fe₂O₃ occurred at 400 °C.^{22,28}

The size and shape of the iron oxide structures can also change during the oxidation process. Spherical Fe_3O_4 nanoparticles of 8.5 ± 1.3 nm were oxidized by adjusting the solution pH to 3.5, and the resulting 'needlelike' $\gamma\text{-Fe}_2\text{O}_3$ particles had widths of approximately 4 – 6 nm and lengths of 20 – 50 nm.¹⁵⁰

Despite the prevalence of the coprecipitation method for synthesizing iron oxide particles, this method yields very little control over the resulting particle size and distribution.¹²⁰ Particles synthesized using these methods are typically polydispersed^{15,120,121} and frequently aggregated (Figure 3-21)^{31,141} While the majority of coprecipitation reactions were carried out in the presence of a base such as NaOH or NH_4OH , particles synthesized in the presence of tetramethylammonium hydroxide ($\text{N}(\text{CH}_3)_4\text{OH}$) yielded more well-dispersed particles.^{31,127} In this case, the

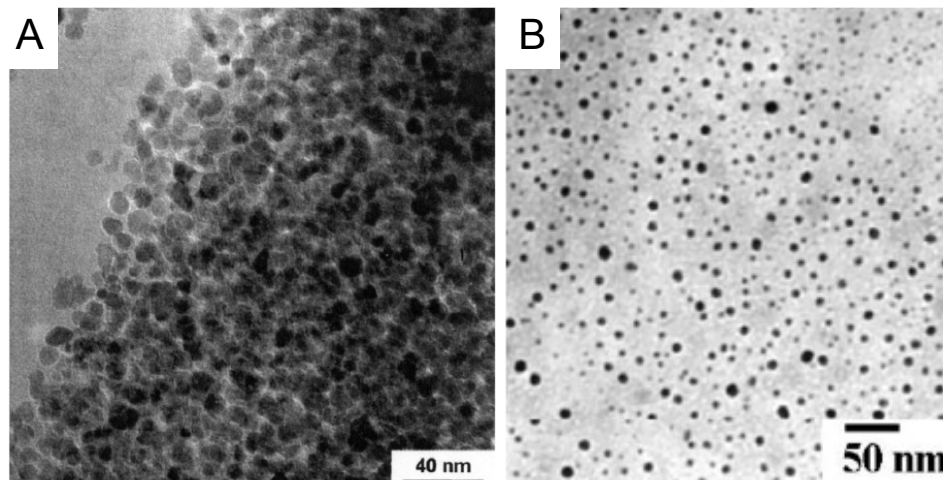


Figure 3-21. Iron oxide particles synthesized via the coprecipitation of Fe^{2+} and Fe^{3+} ions in the presence of NH_4OH (A) and $\text{N}(\text{CH}_3)_4\text{OH}$ (B). Images taken from Hsu et al.¹³ and Cheng et al.³¹, respectively

tetramethylammonium cations in solution interacted with the hydroxide anions on the particle surface and contributed to particle stability. Figure 3-21 shows Fe_3O_4 particles synthesized in the presence of both NaOH and $\text{N}(\text{CH}_3)_4\text{OH}$ and indicates how the nature of the counterions affected the electrostatic stabilization and aggregation behavior of the particles.¹³² In addition to the discrete particles shown in this image, aggregates were also observed.³¹

3.1.1.3.2.2. Particles Coated with Polymers and Surfactant Molecules

Polymers and surfactants have been used not only to stabilize iron oxide particles

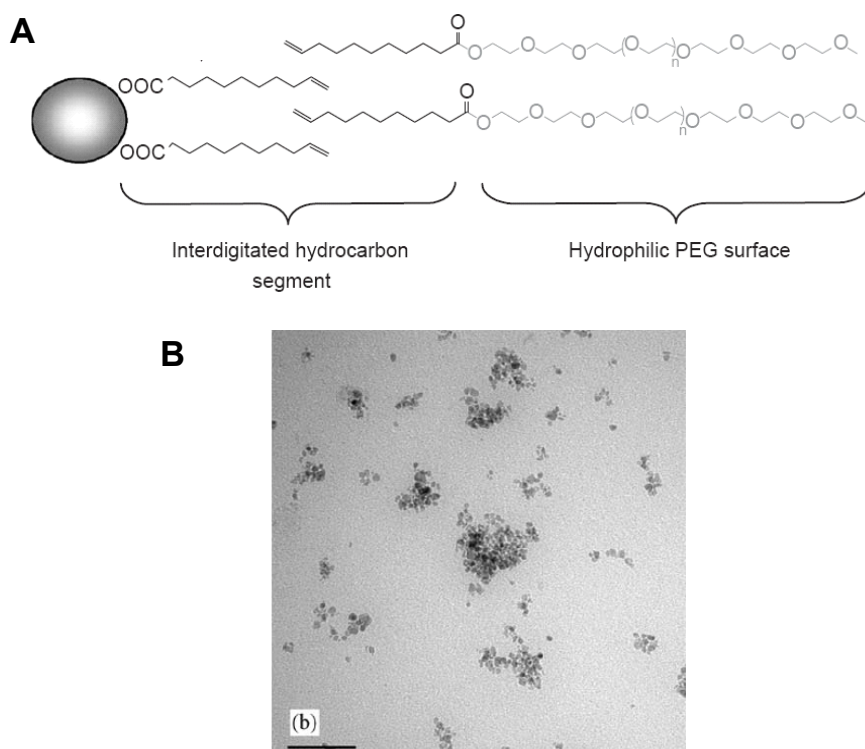


Figure 3-22. (A) Schematic of interdigitated bilayer formed from undecanoic acid and the ester formed from undecanoic acid and poly(ethyleneglycol) (B) Fe_3O_4 particles stabilized with this inter-digitated bilayer after gamma irradiation. Schematic and image were both taken from Acar et al.²³

against aggregation, but also to add functionality to the particle surfaces.

Biocompatible polymers have been used to coat iron particle for biomedical applications such as targeted drug delivery and magnetic resonance imaging.^{120,121}

Functional groups have

also been included to promote interactions with other molecules.¹³⁶

While there are some

examples in the

literature of capping

ligands added during

particle formation, most

particles are coated

post-synthesis.

The molecules used to

coat the surface of iron

oxide particles typically

contain carboxylic

acids, phosphates or

sulfates as these

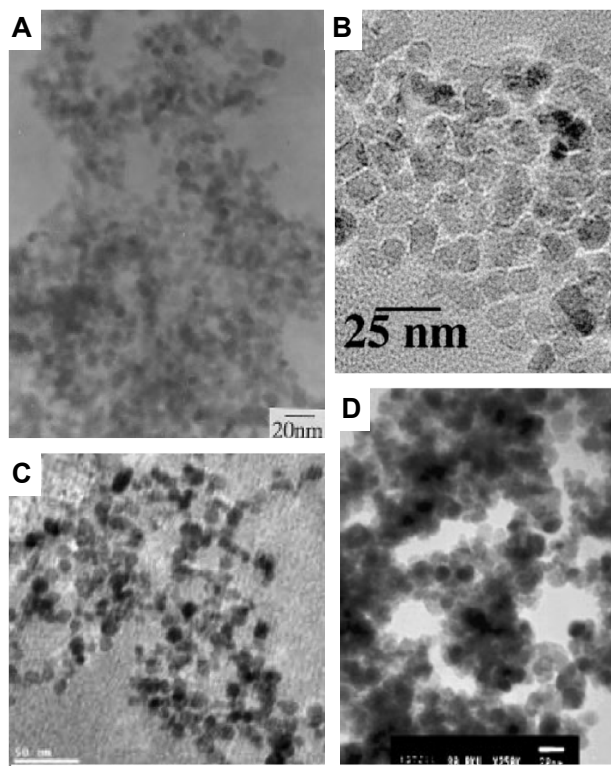


Figure 3-23. Iron oxide particles synthesized via the coprecipitation of Fe^{2+} and Fe^{3+} ions. (A) Fe_3O_4 particles coated with poly(vinylalcohol). Image taken from Lee et al.¹⁷ (B) Fe_3O_4 particles coated with a bilayer consisting of lauric acid and decanoic acid. Image taken from Fu et al.²⁹ (C) Fe_3O_4 particles coated with sulfonated poly(acrylic acid). Image taken from Mak et al.⁴² (D) Fe_3O_4 particles coated with a graft copolymer, poly(glycerol monoacrylate)-g-(PEG methyl ether acrylate). Image taken from Wan et al.⁴⁵ (E) Fe_3O_4 particles synthesized in the presence of tetramethylammonium hydroxide. Image taken from Cheng et al.³¹

functional groups bind to the surface of magnetite.^{120,121} Some of the most common coatings used are dextran,^{120,121} starch,^{120,121} poly(ethylene glycol),^{120,128} poly(vinylalcohol),^{17,120,121,123} and poly(acrylic acid).^{42,122} Iron oxide particles have also been coated with block¹²⁴ and graft⁴⁵ copolymers.

Iron oxide particles have also been stabilized with surfactant bi-layers, the general structure of which is shown in Figure 2-26. Typically, after the synthesis, the particles were coated with a fatty acid. The acid group adsorbed to the iron oxide while the long alkyl chain extended away from the particle surface, making these structures hydrophobic. When aggregation was present, the molecular layer adsorbed to the surface of the aggregate rather than each individual particle.²⁹ Then, a second fatty acid,^{29,132,136} surfactant¹²⁹ or polymer²³ was introduced to form an inter-digitated bilayer and rendering the particles water-dispersible. Figure 3-22 (A) shows a schematic of an inter-digitated bilayer formed between undecanoic acid and the ester formed between undecanoic acid and poly(ethylene glycol). These types of bilayer structures break down at concentrations below the critical micellar concentration of the outer surfactant.^{23,136} In attempt to prevent this behavior and increase particle stability, the terminal olefin groups were polymerized by exposure to gamma radiation.²³ A similar procedure was performed for a bilayer in which both layers consisted of undecanoic acid.¹³⁶ Fe₃O₄ particles stabilized with the polymerized bilayer are shown in Figure 3-22 (B).

While there are many reports in the literature of iron oxide particles stabilized with surfactants, polymers and bilayers, these thin coatings are often not sufficient to prevent particle oxidation.¹²¹ Figure 3-23 shows TEM images of particles coated with various polymers and bilayers in aqueous solution. These particles exhibited aggregated morphologies not unlike those observed for uncoated particles (Figure 3-21). In addition, these types of coatings are typically not stable in air or acidic solutions.¹²¹

3.1.1.3.2.3. Iron Oxide Particles Synthesized With Micelles and Liposomes

Coprecipitation reactions have also been performed within reverse micelles, similar to the methods described in Sections 2.1.2.3 for metal particles and 3.1.1.2.6 for TiO₂. In addition to

preventing aggregation, it has been suggested that these methods can be used to tailor the size and shape of the resulting particles by varying the nature and concentrations of the surfactants.^{14,15,120}

Both ionic and non-ionic surfactants have been used;

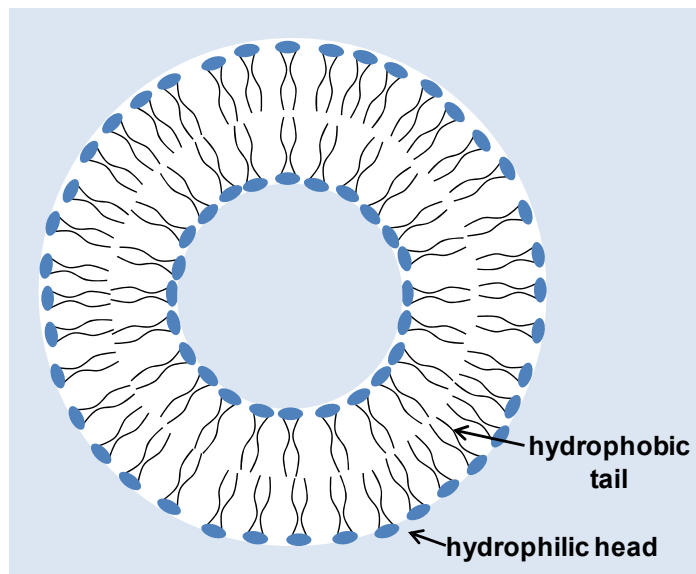


Figure 3-24. Schematic of a liposome

however, it has been reported that ionic functional groups within the micelle interfere with the crystallization of magnetite.¹²⁰

Magnetite has been synthesized in reverse micelles consisting of bis(2-ethylhexyl) sulfosuccinate sodium salt (Figure 3-11 (D)) in n-heptane.^{13,119,130,141} FeCl_2 and FeCl_3 were dissolved in one microemulsion and ammonium hydroxide was dissolved in another. Particles were formed upon mixing the two micellar solutions. While no TEM image was shown, one report claimed that the resulting particles were well-separated compared to those synthesized using the regular coprecipitation method.¹⁴¹ Another report claims that the use of micelles typically leads to aggregated particles.¹⁴ Iron oxide particles synthesized in the presence of sodium dodecylbenzenesulfonate are shown in Figure 3-25 (A).

Iron oxide particles have also been synthesized within liposomes, bilayer structures

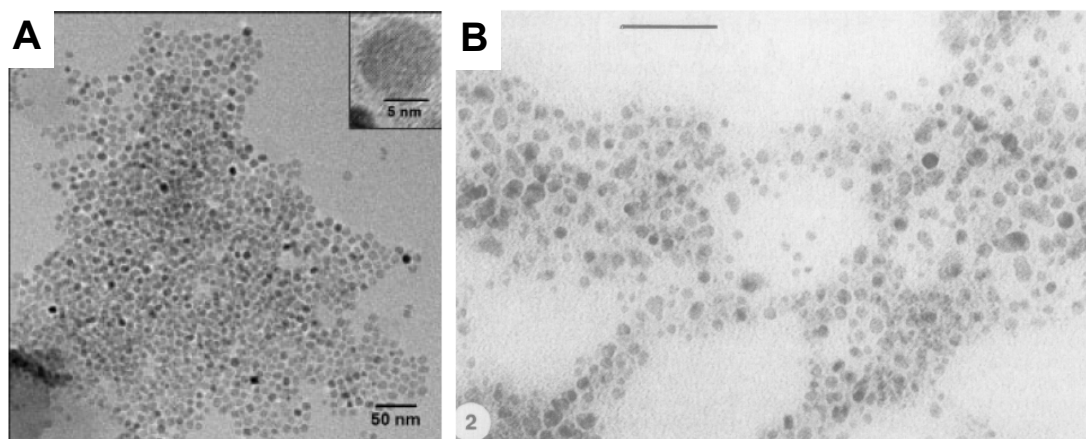


Figure 3-25. TEM images of Fe_3O_4 particles (A) Particles synthesized in reverse micelles of sodium dodecylbenzenesulfonate. Image taken from Lee et al.¹⁴ (B) $\alpha\text{-FeOOH}$ particles synthesized in phosphatidylcholine vesicles. Image taken from Mann et al.²⁷

consisting to phospholipids.^{27,120} The main difference between liposomes and reverse micelles is that liposomes are soluble in aqueous media. Iron oxide particles are formed as hydroxide ions diffuse from the bulk solution into the intravesicular space, a process which is retarded by the vesicle membrane.^{27,120} The slow diffusion of hydroxide ions limits the reaction kinetics, which could provide

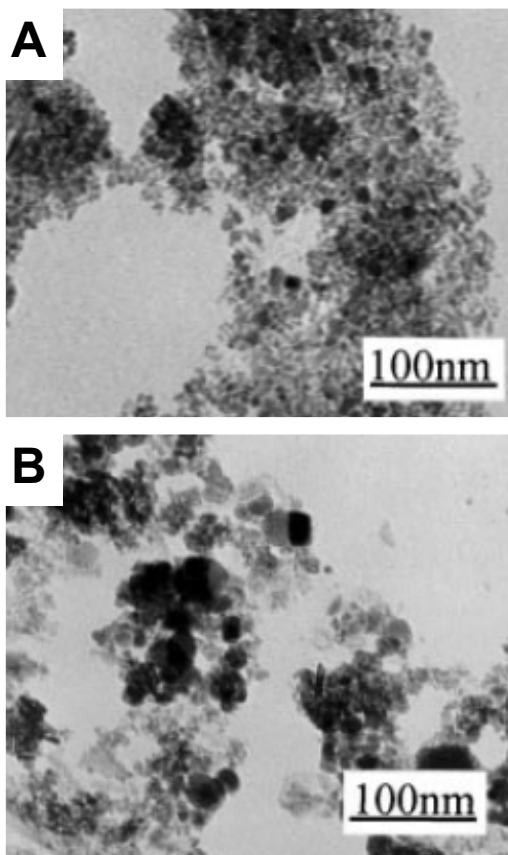


Figure 3-26 TEM images of Fe_3O_4 particles synthesized by the coprecipitation of Fe^{2+} and Fe^{3+} ions both with (A) and without (B) the presence of polyoxyethylene nonyl phenyl ether micelles. Images taken from Zhou et al.¹⁵

additional control over the size and shape of the final particles.²⁷ Goethite ($\alpha\text{-FeOOH}$), magnetite and ferrihydrite ($5\text{Fe}_2\text{O}_3 \cdot 9\text{H}_2\text{O}$) nanoparticles were synthesized upon the addition of NaOH to solutions of phosphatidylcholine vesicles containing Fe(III), Fe(II) and Fe(II)/Fe(III), respectively.²⁷ The goethite particles synthesized using this method are shown in Figure 3-25 (B). An increase in particle size was observed upon aging, which was attributed to the fusion of the liposomes and subsequent aggregation.²⁷

Iron oxide particles have also been

synthesized in solutions containing traditional micelles (i.e. oil in water). Mixed surfactants of polyoxyethylene (5) nonyl phenyl ether (NP-5) and polyoxyethylene (9) nonyl phenyl ether (NP-9) were used to disperse small volumes of hexane in an aqueous solution containing iron(II) sulfate and iron(III) nitrate.¹⁵ While the iron oxide particles were not formed within these micelles, particle nucleation was correlated to the complexation between iron cations and surfactant molecules.¹⁵ While irregular, polydispersed Fe_3O_4 particles were observed in the absence of NP-5 and NP-9 mixed micelles, uniform particles less than 10 nm in diameter were observed in the presence of these micelles (Figure 3-26). The size and morphology of these particles was dependent upon the surfactant concentration.¹⁵

3.1.1.3.3. Thermal Decomposition of Iron Complexes

Another method commonly used to synthesize iron oxide particles involves the

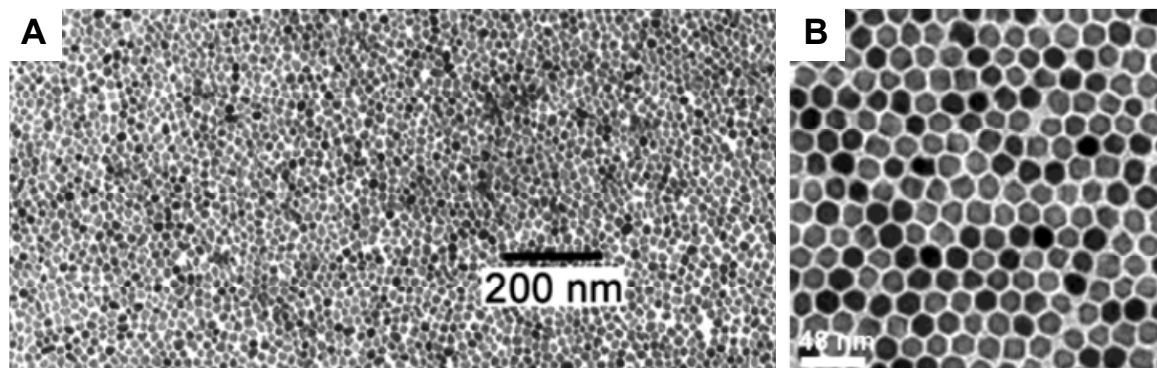


Figure 3-27. TEM images of iron oxide particles (A) $\gamma\text{-Fe}_2\text{O}_3$ particles synthesized from the thermal decomposition of $\text{Fe}(\text{Cup})_3$ in trioctylamine. Image taken from Rockenberger et al.¹² (B) Fe_3O_4 particles synthesized from the thermal decomposition of $\text{Fe}(\text{acac})_3$ in the presence of phenyl ether, 1,2-hexadecanediol, oleic acid and oleylamine. Image taken from Sun et al.²⁸

thermal decomposition of an iron precursor.^{12,16,28,113,121,140,152} While solvothermal reactions have been used, these methods typically involve the rapid injection of the iron complex into a hot surfactant solution followed by aging at high temperature, similar to the hot-injection method described in Section 2.1.2.2.¹⁶ A large number of nuclei are formed upon injection leading to the growth of small, monodispersed particles.¹⁶ The size of these particles can then be increased through a seeded-growth mechanism.^{16,28} For example, reactions with iron Cupferron* complexes ($\text{Fe}(\text{Cup})_3$) complexes in octylamine at temperatures between 250 and 300 °C yield

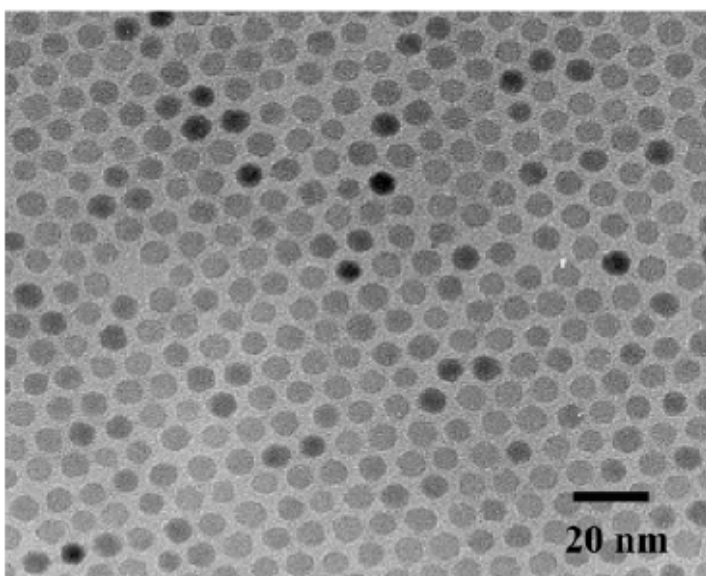


Figure 3-28. $\gamma\text{-Fe}_2\text{O}_3$ nanoparticles (7 nm) synthesized via the decomposition of an iron-oleate complex. Image taken from Hyeon et al.¹⁶

$\gamma\text{-Fe}_2\text{O}_3$ particles (Figure 3-27

(A)).¹² The reaction iron acetylacetonate ($\text{Fe}(\text{acac})_3$) in phenyl ether in the presence of 1,2-hexadecanediol, oleic acid and oleylamine at 265 °C yielded 4 nm magnetite particles.²⁸ These particles were grown to sizes up to

* Cupferron = N-nitrosophenylhydroxylamine

20 nm through the subsequent addition of reagents (Figure 3-27 (B)).

Hyeon et al.^{16,140,152} synthesized monodispersed iron nanoparticles via the decomposition of an iron-oleate, similar to the method discussed in Section 2.1.2.2. The iron-oleate complex ($\text{Fe}(\text{oleate})_3$) was formed in-situ from the reaction between iron pentacarbonyl ($\text{Fe}(\text{CO})_5$) and oleic acid, and size control on the order of 1 nm was achieved by varying the ratio of these two compounds. These particles were then oxidized with trimethylamine N-oxide. The dominant phase in the smaller particles (4 nm) was $\gamma\text{-Fe}_2\text{O}_3$ while the fraction of Fe_3O_4 increased with particle size. Particles larger than 11 nm again required a seeded growth process.¹⁶ The mechanism for the formation of these monodispersed particles (Figure 3-28) was initially believed to be due the temperature-dependence of the decomposition process. One oleate ligand dissociated from the precursor at approximately 200-240 °C leading to particle nucleation. The remaining two oleate ligands dissociated at 300 °C leading to particle growth.¹⁴⁰ Thus, this method provided effective separation of nucleation and growth. A more recent study indicated that this temperature-dependence was not necessarily present, and that nucleation occurred upon solution supersaturation as proposed by LaMer (Section 2.1.2.1).¹⁵³ Monodispersity was attributed to digestive ripening, which occurs at high temperatures (Section 2.1.2.2).

While the majority of particle syntheses involving thermal decomposition were performed in organic solvent in the presence of fatty acids, water dispersible particles have also been synthesized. Li et al.¹⁰ reported the synthesis of Fe_3O_4 particles through the decomposition of $\text{Fe}(\text{acac})_3$, $\text{Fe}(\text{Cup})_3$ and FeCl_3 in 2-pyrrolidone. 2-pyrrolidone was used as it has a high-boiling point and it coordinated with metal ions.^{10,120} The carbonyl group coordinated with the particle surface adding a stabilizing capping layer as shown in Figure 3-29 (A). In addition, carbon monoxide was produced from the decomposition of 2-pyrrolidone at high temperature, which reduced Fe^{3+} to Fe^{2+} . The particles shown in Figure 3-29 (B) were approximately 5 nm in diameter and appear to be discrete and monodispersed. Larger particles were synthesized using seed-mediated growth.¹⁰

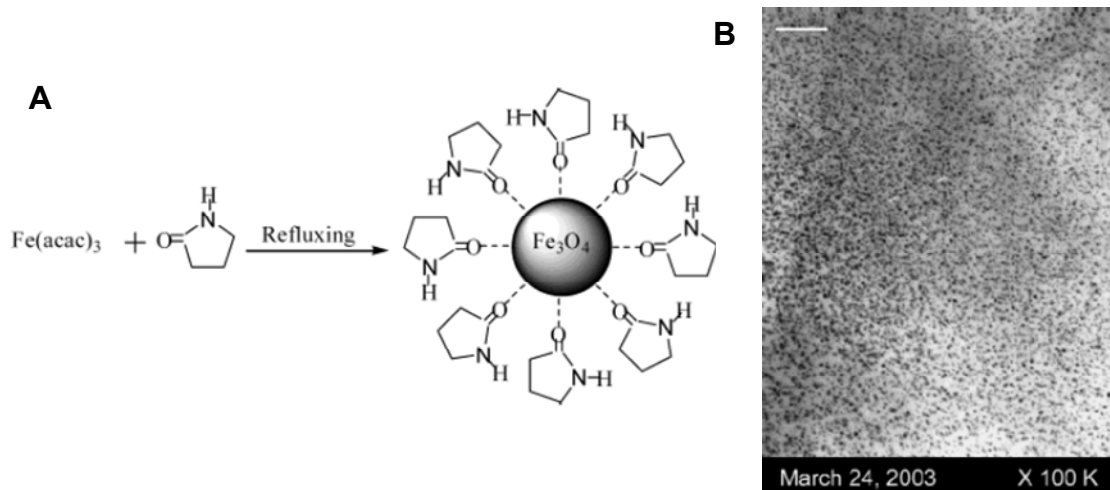


Figure 3-29. (A) Schematic of the reaction between iron acetylacetonate and 2-pyrrolidone (B) Fe_3O_4 particles coated with 2-pyrrolidone, 5 nm in diameter. Schematic and image taken from Li et al.¹⁰

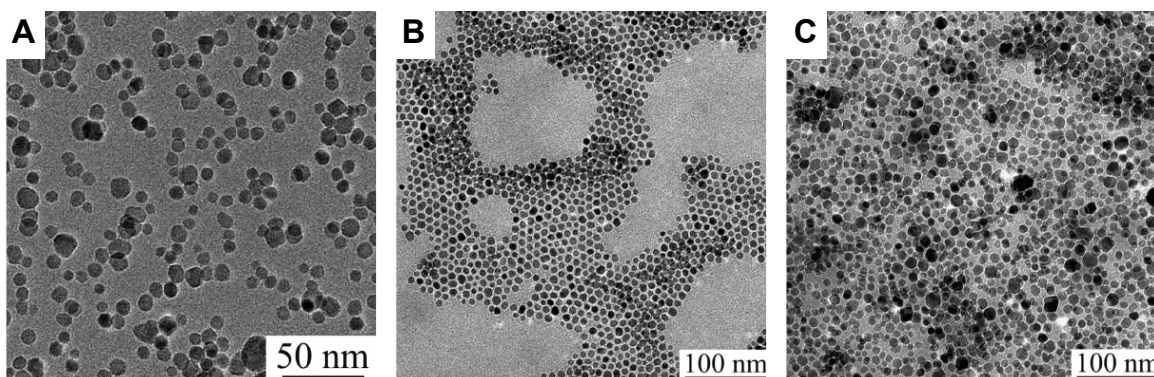


Figure 3-30. Fe_3O_4 nanoparticles synthesized through the solvothermal reaction of $\text{Fe}(\text{acac})_3$ in benzyl alcohol (A) Particles as synthesized, 12 nm in diameter (B) Particles dispersed in hexane after coating with undecanoic acid, 8 nm in diameter (C) Particles dispersed in water after coating with dopamine, 12 nm in diameter. Images taken from Pinna et al.²²

Fe_3O_4 particles have been synthesized solvothermally from the reaction of $\text{Fe}(\text{acac})_3$ in benzyl alcohol in the absence of surfactants²². Both the particle size and size distribution increased with temperature above 175 °C. While particles synthesized at 175 °C were pure magnetite, some oxidation to hematite was observed at 200 °C. After extensive washing, these particles could be redispersed in both nonpolar and polar solvents by coating them with either undecanoic acid or dopamine. As shown in Figure 3-30, both the size and the size distribution of the particles decreased when they were coated with undecanoic acid in hexane. While the size and dispersity of the particles remained approximately the same (12 nm) after coating with dopamine, they exhibited reasonable stability when dispersed in aqueous solution.

3.1.1.3.4. Summary

This section was intended to convey the difficulties associated with synthesizing iron oxide particles. The large surface energies associated with magnetic particles increase the tendency for particle aggregation and make the formation of discrete, stable particles significantly more difficult. The methods described included sonochemical methods, the coprecipitation of Fe^{2+} and Fe^{3+} ions, and the thermal decomposition of iron precursors.

The majority of sonochemical methods involve long-chain surfactants in organic solvents. The nature of the surfactant appeared to have significant effects on the particle morphology, but these effects are not clearly understood. In addition, the sterically-bulky ligands on the particle surfaces limit their reactivity. While iron oxide particles have been synthesized in the absence of surfactant, this method yielded a mixture of iron and iron oxide particles which appeared to be somewhat aggregated. For these reasons, sonochemical reactions were not investigated in this work.

The most common method for synthesizing iron oxide particles involves the coprecipitation of Fe^{2+} and Fe^{3+} ions in the presence of a base. Despite the prevalence of these methods, they yield very little control over the particle size and distribution. Particles synthesized using these methods are typically polydispersed and frequently aggregated. While the stability of these particles has been improved by coating them with polymers and bilayers, the TEM images still indicated

aggregated morphologies. In addition, these coatings limit surface reactivity. Some success has been achieved by coprecipitation within reverse micelles or liposomes. However, the use of tetramethylammonium hydroxide appeared to yield the most well-dispersed particles.

Extremely stable, discreet, monodispersed particles have been synthesized by the thermal decomposition of iron complexes such as $\text{Fe}(\text{Cup})_3$, $\text{Fe}(\text{acac})_3$ and $\text{Fe}(\text{CO})_5$ in the presence of a surfactant or fatty acid. Again, the sterically-bulky capping ligands on these particles limit their reactivity. The decomposition of an iron complex in 2-pyrrolidone is a more promising route as it yielded monodispersed, water-soluble particles with a relatively short capping ligand. Particles synthesized using these methods were typically small and seed-mediated growth was necessary to achieve particles sizes larger than 5 nm. The decomposition of $\text{Fe}(\text{acac})_3$ in benzyl alcohol appeared to be a somewhat versatile synthetic method as the resulting particles could be re-dispersed in either organic or aqueous solution by introducing a capping ligand.

As the goal of this work was to synthesize discreet, aqueous iron oxide particles without bulky capping ligands, initial attempts were focused on the coprecipitation of Fe^{2+} and Fe^{3+} ions in the presence of ammonium hydroxide. The solvothermal reaction of $\text{Fe}(\text{acac})_3$ in benzyl alcohol was also investigated with subsequent ligand-exchange to disperse these particles in aqueous solution.

3.2. Results and Discussion

3.2.1. Synthesis of TiO₂ Nanoparticles

3.2.1.1. Synthesis of Stearic-Acid Capped TiO₂ Particles

While the final goal of this work was to synthesize water-soluble metal oxide particles without sterically bulky capping ligands, initial efforts involving the synthesis of TiO₂ particles involved sol-gel reactions within organic media. The hydrolysis was significantly more controlled in organic solvents, and these particles were used to demonstrate orthogonal self-assembly while aqueous methods were being developed.

TiO₂ particles capped with stearic acid were synthesized using a method reported in the literature.¹⁰⁴ Very small amounts of TIP and water were added to a solution of distilled chloroform (100 mL), isopropanol (4 mL), and stearic acid. The reaction kinetics were presumably slow due to the low concentrations of both water and the titanium precursor; the reaction was stirred for three days. The slow reaction kinetics yielded monodispersed TiO₂ particles approximately 2 nm in diameter and coated with stearic acid. Figure 3-31 shows both a TEM image and an absorption spectrum for these particles. The absorption spectrum was taken in chloroform, the spectrum of which was also plotted here to indicate the range of valid data. This spectrum agrees with the published cutoff wavelength of 245 nm.¹⁵⁴ While the onset

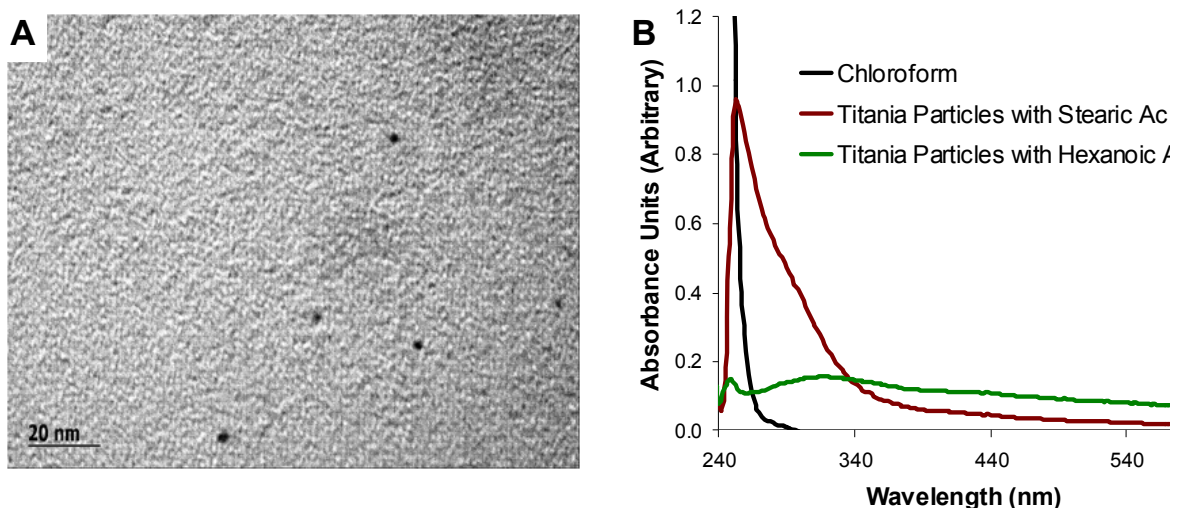


Figure 3-31. (A) TEM Image of TiO₂ particles capped with stearic acid (B) Absorption spectrum of TiO₂ synthesized in the presence of stearic acid and hexanoic acid

of absorption for these TiO₂ particles is slightly blue-shifted compared to the reported values of 380 to 390 nm,^{71,92,101,105} this is expected due to the larger band gap associated with such small particles.⁷¹

Stearic acid has a long hydrocarbon tail (C₁₇COOH), and attempts were made to increase surface reactivity by synthesizing these particles with a shorter capping ligand, hexanoic acid (C₅COOH). The absorption spectrum shown in Figure 3-31 (B) does not show a substantial absorption in the UV range indicating that pure titania was not formed. The small peak at approximately 250 nm is below the observed cutoff for chloroform and does not reflect any solution properties. While the exact reasons why this synthesis did not work are unclear, similar results were observed by Li et al.²⁴ for the hydrolysis of titanium tetrabutoxide in organic media. The

authors concluded that long-chain carboxylic acids were critical to the formation of TiO₂ nanostructures.

3.2.1.2. Ligand-Exchange Involving Stearic Acid-Capped TiO₂ Particles

While the long-chain capping ligands on these particles were not desirable for heterodimer formation, they were used to demonstrate ligand-exchange, the binding of carboxylic acids to a TiO₂ surface and orthogonal self-assembly. Beek et al.¹⁰⁴ reported the functionalization of these stearic acid-capped particles with other carboxylic acid terminated oligomers. It was therefore predicted that similar behavior would occur with the oligomeric phenylene ethylenes (OPEs) used in this work. Transmission Infrared spectroscopy was used to monitor the binding of both isocyanide and carboxylic acid functional groups in a manner similar to that reported by Walker et al.¹⁵⁵ for thiols and isocyanides.

Before the orthogonal self-assembly experiments were performed, the carboxylic

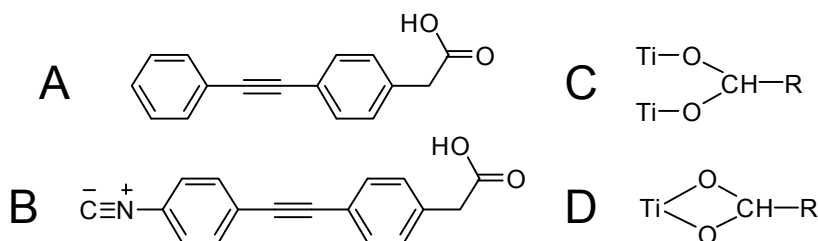


Figure 3-32. Molecules and bonds associated with the Pt/TiO₂ Orthogonal Self-Assembly Study (A) Control Molecule (B) Linker Molecule (C) Bidentate carboxylic acid – titanium bond (D) Bridging carboxylic acid – titanium bond.

acid binding modes were investigated, and ligand-exchange between the carboxylic acid-terminated

molecules in Figure 3-32 (A) and (B) and the TiO₂ particles was demonstrated. Figure 3-33(A) shows the transmission IR spectrum of free stearic acid and spectrum (B) shows stearic acid upon binding to TiO₂. The carbonyl peak at 1700 cm⁻¹ disappeared in lieu of peaks at 1540 and 1590 cm⁻¹. These peaks were attributed to the bidentate and bridging stretches shown in Figure 3-32 (C) and (D).¹⁰⁴ Figure 3-33 (C) shows the IR spectrum of the control molecule (Figure 3-32 (A)), which exhibits a carbonyl stretch at a slightly lower frequency than that observed for stearic acid (1680 cm⁻¹). Figure 3-33 (D) shows the spectrum obtained after the control molecule was incubated with stearic acid-capped TiO₂. The ratio of molecule to particle was approximately 10:1, based on an approximated molecular weight for the particles.* This spectrum shows two carbonyl peaks corresponding to both the control molecule and free stearic acid. These data indicate that stearic acid was displaced from the particle surface, and that ligand exchange occurred to some extent. The presence of free stearic acid in solution was verified using NMR. The disappearance of the bridging and bidentate peaks (1590 and 1540 cm⁻¹) attributed to bound stearic acid supports the conclusion that stearic acid was displaced from the particle surface. It is not clear whether the small peak at 1560 cm⁻¹ was present in the original particle spectrum and simply obscured by the larger peaks or if it could be attributed to the binding of the conjugated oligomer to the TiO₂ surface.

* The molecular weight was approximated based on the particle size determined by TEM, the density of TiO₂ and the reported number of capping ligands associated with each particle.

Once ligand-exchange was demonstrated, the linker molecule shown in Figure 3-32 (B) was incubated with both TiO_2 and platinum particles in order to explore preferential binding. It was expected that the carboxylic acid group would bind to the TiO_2 particles, leaving the isocyanide group free. Conversely, it was expected that the isocyanide group would bind to the Pt particles, leaving the carboxylic acid

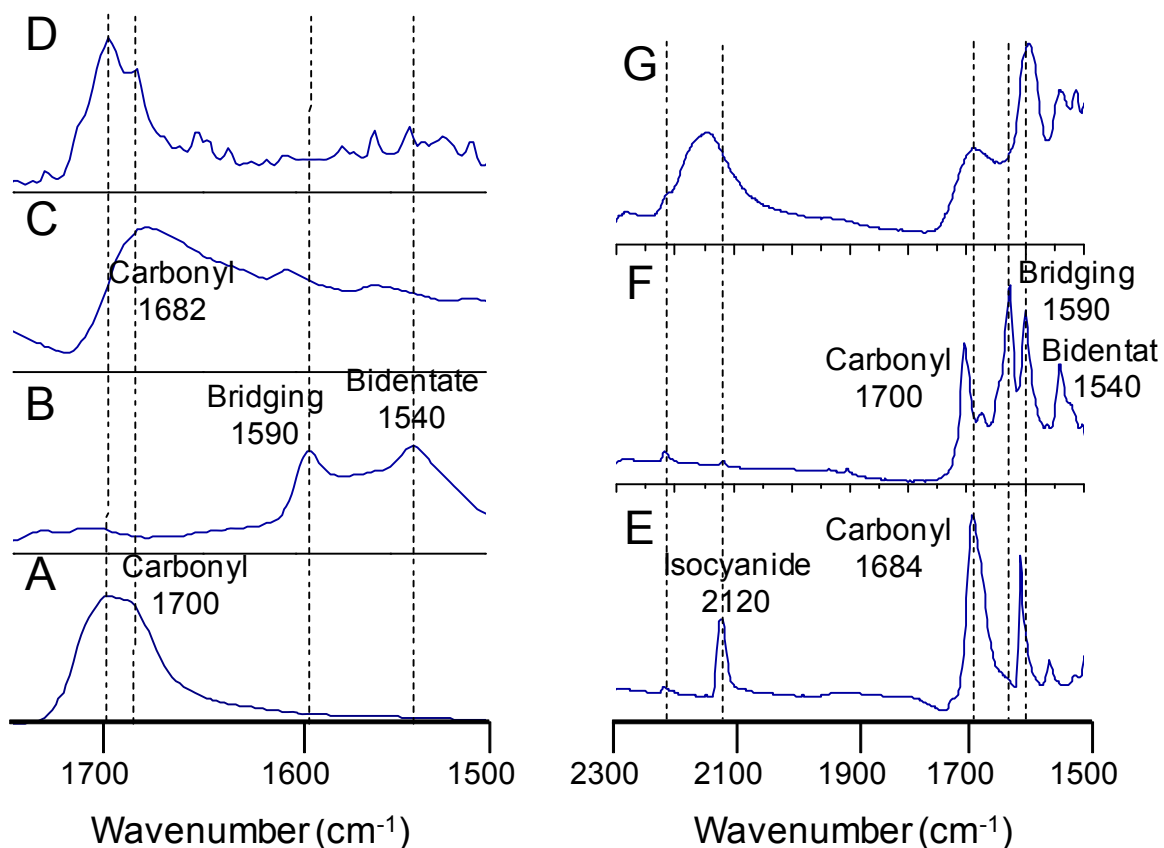


Figure 3-33. Transmission IR data of carboxylic acid and isocyanide terminated molecules in the presence of TiO_2 and Pt nanoparticles. (A) Free stearic acid (B) Stearic acid upon binding to TiO_2 (C) Control molecule terminated with carboxylic acid (D) Control molecule after incubation with TiO_2 particles (E) Bifunctional linker molecule terminated with carboxylic acid and isocyanide functionalities (F) Bifunctional linker after incubation with TiO_2 particles (G) Bifunctional linker after incubation with Pt particles. The structures of the molecules and bonds associated with this study are shown in Figure 3-32.

groups free. The isocyanide functionality was chosen as it exhibits a 50-70 cm^{-1} shift upon binding, which is easily detectable.¹⁵⁵⁻¹⁶¹ Figure 3-33 (F) shows the bifunctional linker molecule (E) in the presence of TiO_2 particles (10:1 ratio). Although the intensity of the 2120 cm^{-1} peak was low, no shift was observed indicating that no binding through the isocyanide functionality occurred. However, the evolution of the carbonyl peak at 1700 cm^{-1} indicates some extent of ligand exchange occurred resulting in some free stearic acid. The bridging and the bidentate peaks at 1540 and 1590 cm^{-1} remain present in addition to a new peak at 1626 cm^{-1} . Figure 3-33 (G) shows the linker molecule in the presence of hexanethiol-capped platinum particles. The isocyanide stretch shifted from 2120 cm^{-1} to 2140 cm^{-1} consistent with binding. The broadened carbonyl stretch at 1684 cm^{-1} could be attributed to the overlapping absorbance of free stearic acid (1700 cm^{-1}), which would also indicate displacement.

Again, the variables that control the selectivity of binding are not well understood, but this study demonstrates orthogonal self-assembly of isocyanides on platinum and carboxylic acids on titania and suggests the possibility of binding these two nanoparticles together with a bifunctional oligomer.

Once the orthogonal self-assembly had been demonstrated, efforts were shifted to synthesizing TiO_2 particles in aqueous solution without long-chain capping ligands so that they could be used for heterodimer formation.

3.2.1.3. Synthesis of TiO₂ Particles from TiCl₄

As discussed in Section 3.1.1.2.4 (page 179), the most common method for preparing TiO₂ from TiCl₄ involves adding the metal chloride solution to cooled water at acidic pH.^{11,41,94,98,99,102} TiO₂ nanostructures were synthesized according to a procedure reported by Pottier et al.⁹⁴ in which TiCl₄ was added to an aqueous solution containing hydrochloric acid. The authors reported two different crystalline phases: rutile (elongated particles) and brookite (spherical aggregates), which were then separated by the selective peptization of brookite in the presence of nitric acid as shown in Figure 3-9. This method was chosen as it was one of the few reports that included a TEM image, and indicated the formation of spherical particles even if they were somewhat aggregated.

Figure 3-34 shows TEM images of structures synthesized using this method. While discrete spherical particles measuring 7.2 ± 0.8 nm were measured on isolated parts of the TEM grid (A), other images indicated the presence of both spherical aggregates and elongated nanorods (B), and lower magnification images suggested the presence of larger aggregates (C). Two attempts were made to synthesize particles using this method, both with the same results. The authors claim that the ratio of Cl⁻ to Ti⁺ ions corresponding to the maximum concentration of spherical brookite particles ranges from seventeen to thirty-five.⁹⁴ The ratio applied here was an intermediate value of twenty-five. Both the final HCl (1.9 M) and titanium

(0.09 M) concentrations were within the ranges reported by the authors, 1 – 5 M and 0.05 - 0.4 M, respectively. However, it is possible better results would have been achieved if these concentrations were varied while maintaining the optimal ratio of Cl^- to Ti^+ .

Another possible source of error is the concentration of nitric acid used in the selective peptization. While the authors used a 3 M HNO_3 solution, the

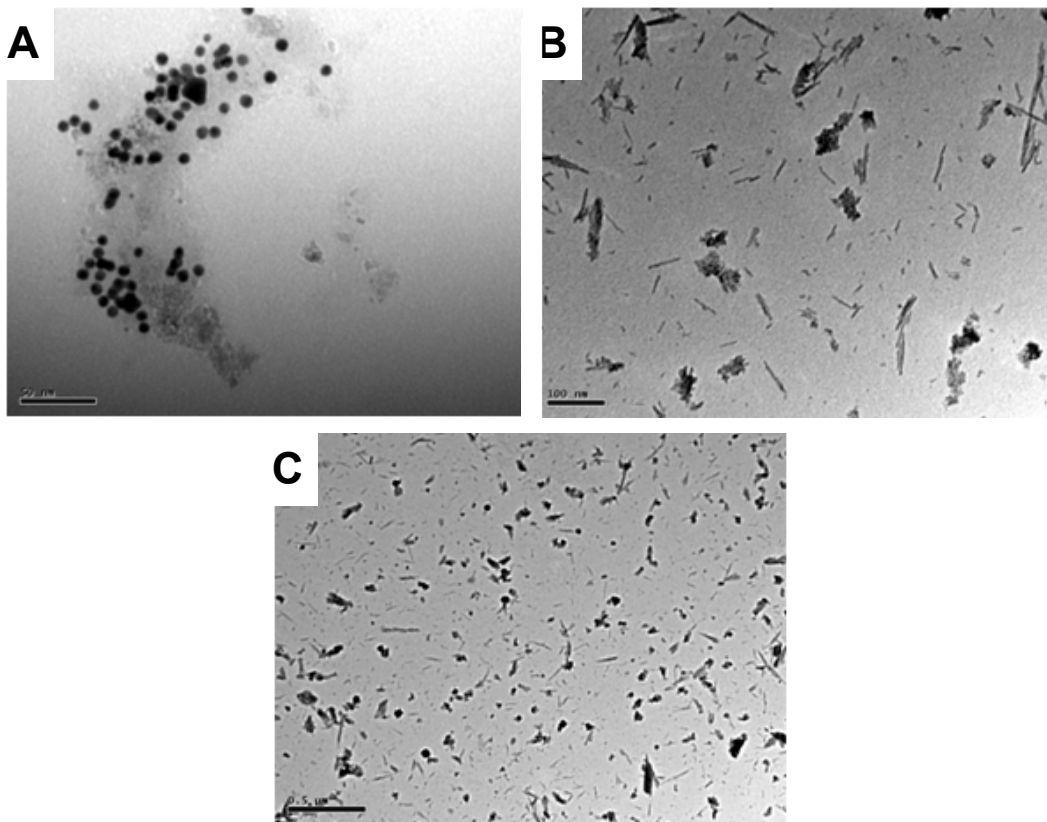


Figure 3-34 TiO_2 nanostructures formed from the hydrolysis of TiCl_4 in an aqueous hydrochloric acid solution. (A) Spherical particles 7.2 ± 0.8 nm in diameter (scale bar = 50 nm) (B) A mixture of TiO_2 nanorods and spherical aggregates (scale bar = 100 nm) (C) Lower magnification image indicating the extent of aggregation (scale bar = 500 nm)

concentration used here was not recorded. A high concentration could have brought larger particles into solution along with the smaller ones, resulting in inefficient separation. This behavior would explain the presence of both spherical aggregates and elongated particles in Figure 3-34 (B). This morphology is similar to that shown in Figure 3-9 (A) for TiO₂ nanostructures before separation. It is also possible that removing particles from solution by rotary evaporation could have caused the observed aggregation.

While there are several variables that could be altered in order to optimize this procedure, the exact effects of these variables are unclear, and the published TEM images still indicate some degree of aggregation (Figure 3-9). Efforts were shifted to a procedure for which the variables affecting both the size and the dispersity of the TiO₂ particles were more clearly understood.

3.2.1.4. Synthesis of TiO₂ Particles from Titanium (IV) Isopropoxide

Hsu et al.⁹ synthesized TiO₂ particles by hydrolyzing TIP in the presence of hydrochloric acid and ethanol, evaluating the effects of the water/alkoxide ratio, the acid concentration, the reaction temperature and the rate at which the precursor was added as discussed in Section 3.1.1.2.5 (page 183). In these reactions, a mixture of TIP and ethanol was added to a flask containing H₂O, HCl and EtOH. The authors claim that the optimal reaction conditions involved an HCl concentration of 0.73 M, a water/alkoxide ratio of 16.6, a temperature greater than 42.5 °C and a feed rate less

than $14.0 \text{ cm}^3/\text{min}$. Under these conditions, particles smaller than $50 \pm 5 \text{ nm}$ in diameter could be obtained. The paper did not indicate the ideal ethanol concentration, but did claim that the alkoxide/alcohol ratio was crucial to obtaining a monodispersed sol. Even in a paper in which the reaction variables were explicitly investigated, there was some ambiguity in the experimental procedure. The first set of experiments was therefore designed with the intent of ascertaining the effects of

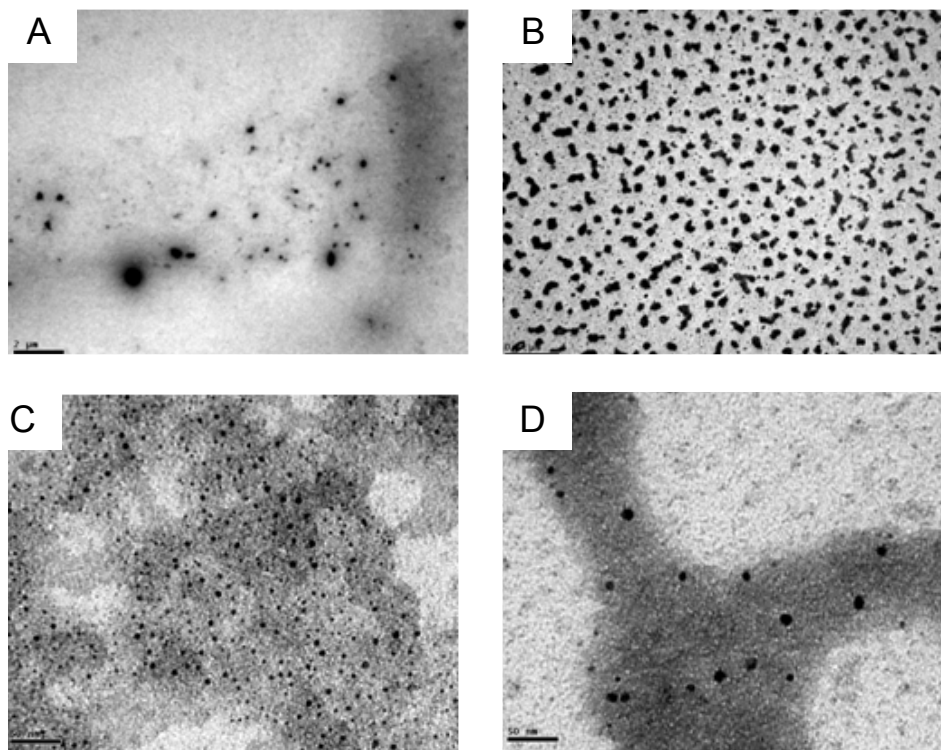


**Figure 3-35. TEM images of TiO_2 particles synthesized from the hydrolysis of TIP in the presence of hydrochloric acid and ethanol (A) Particles synthesized in Experiment 2, sizes ranged from 20 – 740 nm (B) Particles synthesized in Experiment 5, large aggregates observed in addition to particles of $6.2 \pm 0.8 \text{ nm}$ (C) Particles synthesized in Experiment 5 exhibited an average diameter of 3.1 ± 1.3 (D) Particles synthesized in Experiment 7 exhibited an average diameter of $4.5 \pm 2.3 \text{ nm}$
Experiment numbers correspond to conditions listed in Table 3-6**

the ethanol concentration on particle size and dispersity.

The reaction conditions used in this set of experiments are listed in Table 3-6, and the corresponding observations in Table 3-7 at the end of this section. The first three reactions involved adding a TIP/ethanol solution (50/50 % by volume) to a 50 mL solution containing 0.73 M HCl and varying ratios of H₂O/ethanol.

Unfortunately, this set of experiments did not isolate the ethanol concentration as a variable. In order to maintain the desired water/alkoxide ratio, different amounts of precursor solution were added to each flask resulting in different titanium and acid concentrations. While these experiments did not clearly show the effects of the ethanol concentration, they did demonstrate the effects of acid concentration on the aggregation behavior of TiO₂ particles. Upon addition of the precursor solution, the acid concentrations decreased from their initial value of 0.73 M. Immediate precipitation was observed for final HCl concentrations of 0.31 and 0.38 M, while a stable colloidal solution was obtained in a 0.50 M HCl solution. The presence of HCl limits aggregation processes by retarding condensation kinetics and increasing particle stability through electrostatic repulsion.

As the particle solution obtained during this first set of experiments was polydispersed (Figure 3-35 (A)), the remaining attempts involved increasing the acid concentrations so that the concentration after precursor addition was 0.73 M. The only difference between the conditions for Experiments 4 and 5 was the amount of

acid added to the solution. The results were the opposite of what was expected; aggregation was observed at the higher acid concentration (Figure 3-35 (B)) while discrete particles were obtained at the lower acid concentration (Figure 3-35 (C)). In order to verify these results, a similar experiment was again performed. While the amounts of water and TIP were slightly greater than those used for Experiments 4 and 5, the opposite trend was observed for Experiments 6 and 7 with the higher acid concentration yielding discrete, monodispersed particles (Figure 3-35 (D)). While the initial data could have been due to some unappreciated variation in the experimental conditions, it indicates the sensitivity of this reaction to minimal changes in reaction conditions. Several reports indicate that reproducibility in sol-gel methods is often difficult to attain.^{92,113}

In Experiments 8 - 10, a few other variables were investigated. The volume of the aqueous HCl solution was taken into consideration when calculating the water/alkoxide ratio in Experiment 9; this is reported as a lower ratio of pure water/TIP in solution. In Experiment 10, the precursor solution was diluted in a larger volume of ethanol. No obvious effects were observed with these changes in reaction conditions. Within the limited variability in across this set of reactions, the HCl concentration seemingly had the greatest effect on the resulting TiO₂ particles.

While there was some definite ambiguity in the procedure reported by Hsu et al.,⁹ discrete TiO₂ particles of approximately 5 – 6 nm were synthesized using their method. The stability of these particles was questionable, and aggregation was observed within just a few days. Minor changes in reaction conditions also yielded aggregation. More reproducible results may be achievable by controlling the rate of precursor addition. The authors claim an optimal feed rate of less than 14.0 cm³/min. While the precursor solution was added dropwise at a rate significantly less than this, the rate was not reproducibly controlled. It is also noted that no attempts were made to purify the particle solutions. The TEM images shown in Figure 3-35 also indicate some non-particulate matter in the grid, which could be due to unreacted material within the solution.

Table 3-6. Reaction Conditions for the Hydrolysis of TIP in the Presence of Hydrochloric Acid and Ethanol

Expt. #	Reactant Amounts mL (mmol)								
	Before Precursor Addition			After Precursor Addition					
	HCl	H ₂ O	EtOH Initial	EtOH Final	TIP	H ₂ O/TIP volume ratio (molar ratio)	EtOH/TIP volume ratio (molar ratio)	[HCl] in initial solution (M)	[HCl] after addition of TIP (M)
1	3.0 (36)	23.5 (1300)	23.5 (400)	63.5 (1080)	23.0 (78)	1.0 (16.6)	2.8 (14.3)	0.73	0.38
2	3.0 (36)	11.7 (650)	35.3 (600)	46.7 (800)	11.5 (39)	1.0 (16.6)	4.0 (20.0)	0.73	0.50
3	3.0 (36)	35.3 (1960)	11.7 (200)	46.7 (800)	34.5 (117)	1.0 (16.6)	1.3 (6.7)	0.73	0.31
4	3.0 (36)	6.7 (370)	40.3 (690)	46.9 (800)	6.6 (22)	1.0 (16.6)	2.0 (10.9)	0.73	0.57
5	3.9 (47)	6.7 (370)	40.3 (690)	46.9 (800)	6.6 (22)	1.0 (16.6)	2.0 (10.9)	0.93	0.73
6	3.0 (36)	8.5 (470)	38.5 (660)	46.8 (800)	8.3 (28)	1.0 (16.6)	5.6 (23.6)	0.73	0.55
7	4.1 (50)	8.5 (470)	38.5 (660)	46.8 (800)	8.3 (28)	1.0 (16.6)	5.6 (23.6)	0.97	0.73
8	4.0 (48)	7.0 (390)	42.0 (720)	48.8 (840)	6.8 (23)	1.0 (16.6)	7.2 (36.5)	0.91	0.73
9	4.0 (48)	3.0 (170)	42.0 (720)	48.8 (840)	6.8 (23)	0.44 (7.4)	7.2 (36.5)	0.98	0.77
10	4.5 (54)	7.0 (390)	42.0 (720)	55.7 (950)	6.8 (23)	1.0 (16.6)	8.2 (41.3)	1.01	0.73

Table 3-7. Observations for the Hydrolysis of TIP in the Presence of Hydrochloric Acid and Ethanol

Expt. #	Observations	Particle Sizes (nm)	# Particle Measurements	Aggregates Observed
1	White precipitate visible upon TIP addition, which seemed to dissolve upon significant stirring	NA	NA	NA
2	Opaque solution (whitish), no visible precipitate	Sizes ranged from 20 - 740 (most between 100 - 200)	NA	NA
3	White precipitate formed before TIP addition was complete	NA	NA	NA
4	Clear solution, no visible precipitate	3.1 ± 1.3	79	NO
5	White solution, no visible precipitate	6.2 ± 0.8	33	YES
6	Clear solution, no visible precipitate	6.9 ± 1.4	35	YES
7	Clear solution, no visible precipitate	4.5 ± 2.3	36	NO
8	Clear solution, no visible precipitate	2.8 ± 1.0	36	YES
9	Clear solution, no visible precipitate	3.2 ± 0.8	40	YES
10	Clear solution, no visible precipitate	1.9 ± 0.6	53	YES

Experiment numbers correspond to the reaction conditions listed in Table 3-6

3.2.1.5. Synthesis of TiO₂ Particles from Titanium (IV) Ethoxide

Attempts were also made to synthesize TiO₂ particles from TEO according to a procedure published by Eiden-Assman et al.⁹² The authors claim that large colloidal particles were formed through the aggregation of smaller particles in a manner similar to the cluster-cluster aggregation depicted in Figure 3-5 (page 165). The extent of aggregation and thus the final particle size was controlled through both the nature and concentration of ions in solution. On this premise, the authors synthesized particles ranging in size from 50 – 2500 nm. Particles synthesized in the presence of potassium chloride exhibited smaller sizes and narrower size distributions than those synthesized in the presence of other alkali halides (e.g. LiCl and NaCl). The particle size was also reduced at higher KCl concentrations. For example, the particle size decreased from approximately 300 to 50 nm when the KCl

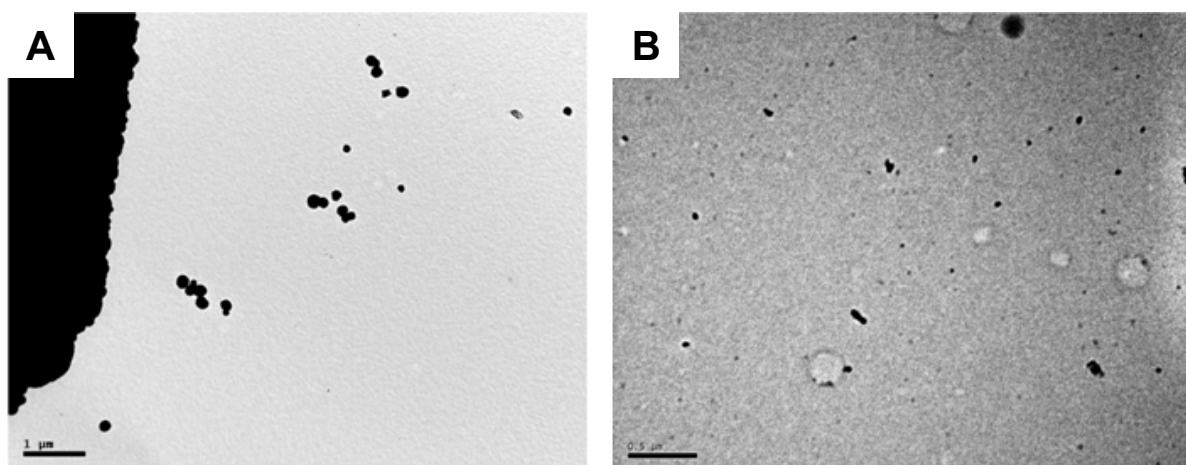


Figure 3-36. TiO₂ particles synthesized from the hydrolysis of TEO in the presence of potassium chloride. A second attempt at the same method yielded different results (A) Particles exhibited diameters of 175 ± 35 nm. The dark area on the left is the copper TEM grid and not TiO₂. (B) Large aggregates observed, in addition to particles of approximately 30 – 40 nm.

concentration was increased from 4×10^{-4} M to 8×10^{-4} M. However, no particles were obtained when the concentration was increased beyond this value.

The first attempt to reproduce this particle synthesis yielded particles of 175 ± 35 nm as shown in Figure 3-36 (A). TEO was added to an absolute ethanol solution (100 mL) containing a small volume of aqueous salt solution (1.7 mL). It is unclear why the particles were so much bigger than those reported in the literature. While it was possible that smaller particle sizes could be achieved by further increasing the salt concentration, this could also prohibit the formation of any particles as reported in the literature.

It was also speculated that distilling the ethanol used in this process could yield greater control over the hydrolysis reactions, and thus particle size. The procedure was repeated using distilled ethanol. Figure 3-36 (B) shows particles of approximately 30 – 40 nm amidst larger aggregates. It is unclear why the particle sizes were smaller while the extent of aggregation was larger. There were problems in the filtering process, which could account for the extent of aggregation. The filter repeatedly clogged, presumably with unreacted TEO. Attempts were made to isolate particles from solution using centrifugation rather than filtration; however, this also resulted in aggregation. Similar results were obtained when the procedure was repeated a third time.

Despite some problems with reproducibility, this method displays potential for synthesizing discrete TiO_2 particles. Additional efforts would need to be expended to optimize the filtration process so that no aggregation occurred.

3.2.1.6. Synthesis of TiO_2 Particles Using Solvothermal Methods

As the goal of this work was to synthesize aqueous TiO_2 particles without bulky capping ligands, non-hydrolytic and solvothermal methods were not initially explored. However, the uniformity and stability of particles synthesized in the presence of long-chain capping ligands appeared to be significantly greater than that achievable using other methods. In a report by Li et al.,²⁴ particles were synthesized solvothermally in the presence of ammonium bicarbonate and linoleic acid (LA).

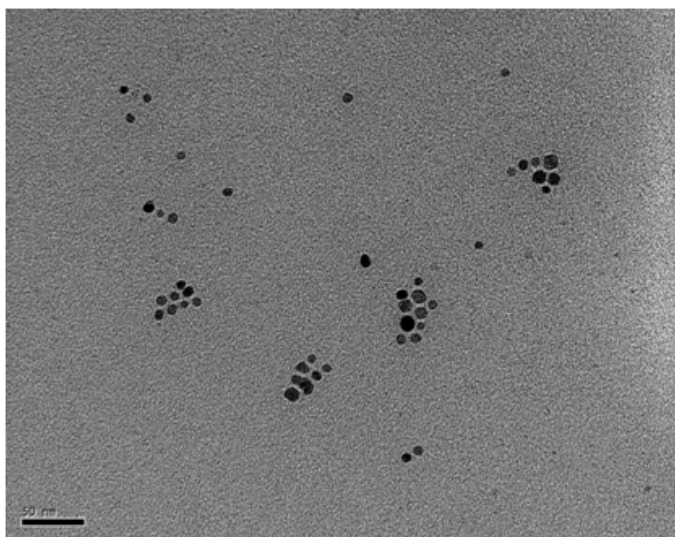


Figure 3-37. TiO_2 particles synthesized using a solvothermal method. Particles were 9.1 ± 1.6 nm, capped with linoleic acid and dispersed in hexane.

They observed that LA could be removed from the particle surfaces by washing them with cyclohexane or ethanol. If a large enough amount of the LA capping ligand was removed, the particles were no longer dispersible in organic solvent. However, they could be re-dispersed when additional LA

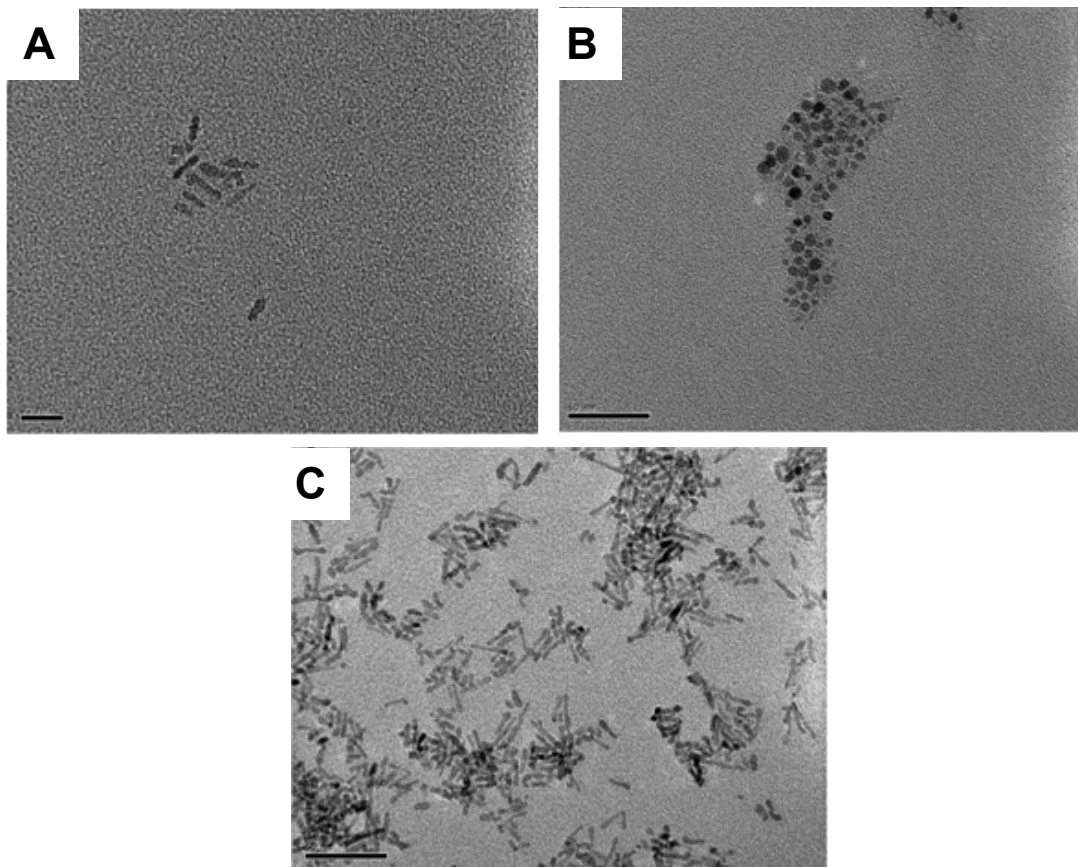


Figure 3-38. TiO₂ nanostructures observed after attempted ligand-exchange with (A) glycerol (B) succinic acid (C) tartaric acid. All ligand-exchange reactions were carried out in a 2:1 solution of ethanol/water

was added to the solution. These results suggested the possibility of post-synthesis ligand-exchange with a smaller capping ligand. These particles were synthesized according to the method developed by Li. et al.,²⁴ and then ligand-exchange was attempted with small, aqueous capping ligands.

Figure 3-37 shows an image of particles synthesized in the presence of a 13:1 ratio of LA to NH₄HCO₃. These particles were dispersed in hexane and exhibited a

uniform particle size of 9.1 ± 1.6 nm. The spacing between particles on the grid is attributed to the long-chain LA capping ligands.

Attempts were made to exchange the LA capping ligands with glycerol, succinic acid and tartaric acid (Figure 3-39). These ligands were chosen based on a report by Jiang et al.,¹⁶² who peptized

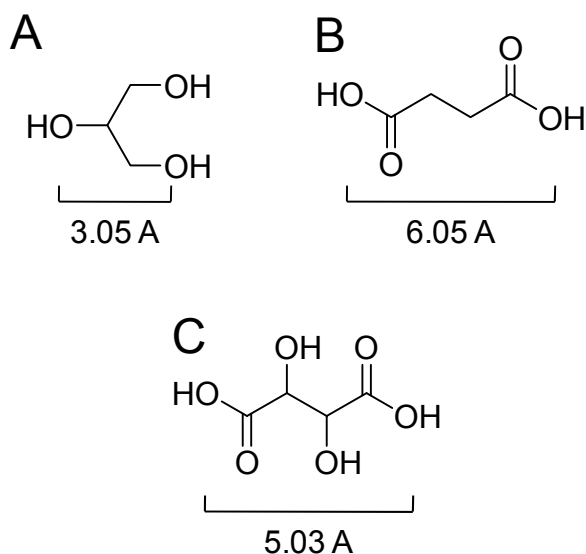


Figure 3-39. Ligands used for attempted-ligand exchange (A) glycerol (B) succinic acid (C) tartaric acid. Lengths were measured using Chem 3D Software after energy minimization.

amorphous titania in the presence of organic modifiers. It is known that carboxylic acid groups bind to TiO_2 , and it was believed that the hydroxyl group on glycerol interacted with the protonated TiO_2 surface.¹⁶² As it was reported that ethanol facilitated the removal of LA from the particle surfaces, the first attempt at ligand exchange was performed in a solution containing a 2:1 ratio of ethanol/water on the premise that ethanol would facilitate ligand-exchange.

After washing with ethanol and drying, the TiO_2 particles were placed in a vial containing the 2:1 ratio of ethanol/water solution and an excess of the capping ligand. The vials were then sonicated for approximately twenty minutes, and the majority of particles appeared to become dispersed within the solutions. The

solutions appeared white with a small amount of yellow precipitate remaining at the bottom of the vial. Figure 3-38 shows TEM images of TiO₂ nanostructures after attempted ligand-exchange with glycerol, succinic acid and tartaric acid. While the particles in the presence of succinic acid maintained their spherical shape, nanorods were observed in the presence of glycerol and tartaric acid.

The formation of nanorods in the presence of additional capping ligands can be explained by the process of oriented attachment, the general concept of which is illustrated in Figure 3-40.²⁵ In this example, selective desorption of benzyl alcohol and Trizma® (2-amino-

2-(hydroxymethyl)-1,3-propanediol) occurred on the (001) crystalline face of TiO₂ particles. These particles then join each other along this planar interface to create anisotropic

structures. While this mechanism could explain the formation

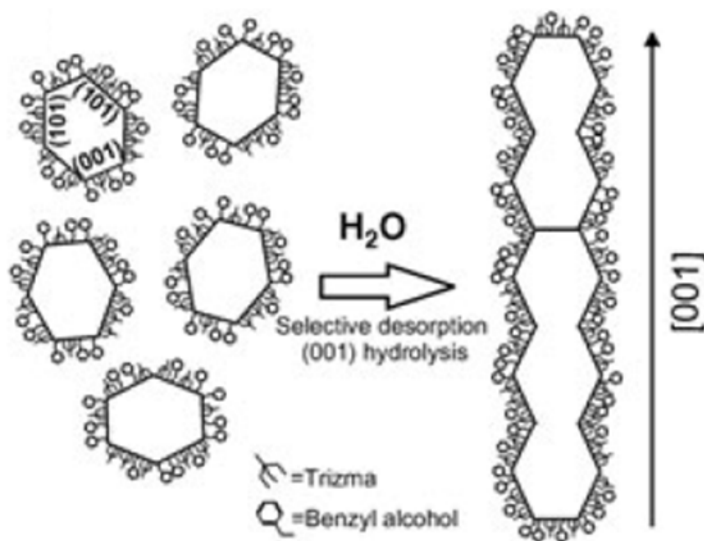


Figure 3-40. Proposed mechanism for the formation of anisotropic nanostructures from smaller nanocrystals through selective desorption of ligands from the (001) crystal face. In this example of oriented attachment, the ligands involved were Trizma® (2-amino-2-(hydroxymethyl)-1,3-propanediol) and benzyl alcohol. Schematic was taken from Polleux et al.²⁵

of rods from particulate structures, the thicknesses of these rods are significantly smaller (3 – 4 nm) than the diameter of the initial particles (~ 9 nm). This suggests some type of chemical etching process also took place.

As it was believed that the desorption of linoleic acid was facilitated by the presence of ethanol, a second attempt a ligand-exchange was made in which a minimal amount of ethanol was included in the vials during ligand-exchange; the solution was

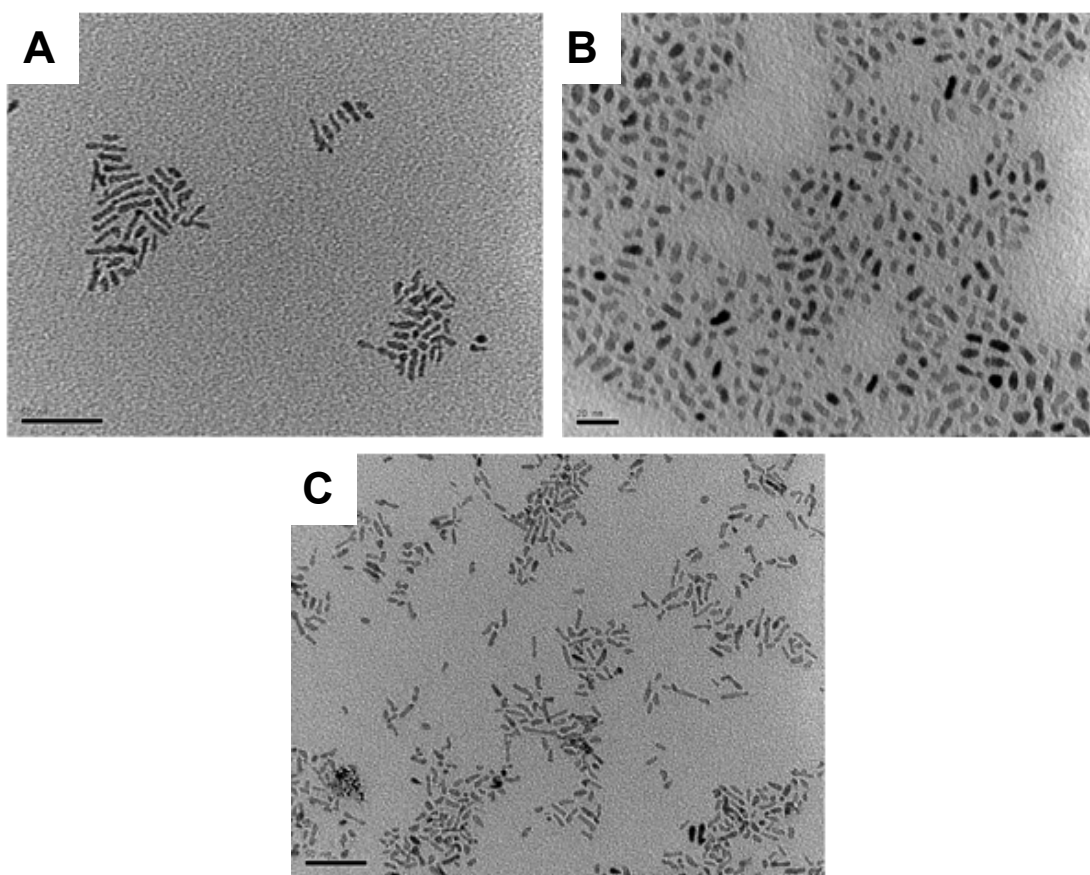


Figure 3-41. TiO₂ nanostructures observed after attempted ligand-exchange with (A) glycerol (B) succinic acid (C) tartaric acid. All ligand-exchange reactions were carried out in an aqueous solution containing 3% ethanol.

97% water. A small amount of ethanol was necessary in order to transfer the TiO₂ powder into the vial. After sonication, particles were again dispersible in water with only a small amount of yellowish precipitate at the bottom of the vials. Figure 3-41 shows the structures obtained after ligand-exchange under these conditions.

Elongated structures were observed for all cases, although the length of the structures observed in the presence of succinic acid appeared somewhat shorter.

No general statements can be made about the differences between the two data sets. It was predicted that in the absence of high ethanol concentrations, LA would desorb to a lesser extent, which would limit the formation of rod-like structures.

While this did not appear to be the case, it is noted that the distances between the rods in Figure 3-41 are greater than those observed in Figure 3-38 (B) and (C). This observation suggests that some LA remains on the surface of the rods, which were formed in the solution containing 97% water. Despite the apparent presence of LA, these structures were dispersible in water. It is plausible that only partial ligand-exchange was necessary in order to affect this change. One report claims that a 27% surface coverage of dopamine on TiO₂ particles was sufficient to provide water solubility.⁷⁴

3.2.1.7. Summary and Conclusions

Several methods for synthesizing TiO₂ particles were evaluated. While discrete, monodispersed particles were obtained; there were issues with reproducibility of the methods used and particle stability towards aggregation.

Isolated, monodispersed TiO₂ particles of approximately 2 nm in diameter were synthesized through the controlled hydrolysis of TIP in organic solvent in the presence of stearic acid. While this method was successfully implemented to synthesize particles, the long-chain organic capping ligands were unsuitable for heterodimer synthesis. However, these particles were used to demonstrate ligand-exchange, the binding of carboxylic acids to a TiO₂ surface and orthogonal self-assembly. The synthesis of TiO₂ in aqueous solution without sterically-bulky capping ligands proved significantly more challenging.

The synthesis of TiO₂ particles via the hydrolysis of TiCl₄ in the presence of nitric acid yielded some discrete particles (Figure 3-34 (A)); however, this result appeared to be the exception rather than the rule. In general, a mixture of nanorods and spherical aggregates was obtained. The variables that could be altered to optimize this procedure were somewhat unclear, and efforts were shifted to a procedure for which the variables affecting both particles size and dispersity were more clearly understood.

Isolated, monodispersed TiO₂ particles were synthesized by hydrolyzing TIP in the presence of hydrochloric acid and ethanol. The extent of aggregation decreased as the acid concentration increased. There were also some issues associated with the reproducibility of this method. While particle stability was not fully evaluated, particle precipitation was observed within a day or two following synthesis. Developing a method for purifying these particle solutions could be advantageous.

Isolated TiO₂ particles were also synthesized by hydrolyzing TEO in the presence of potassium chloride. However, the sizes of these particles were somewhat irreproducible and some larger-scale aggregate were observed. The aggregation was attributed to the post-synthetic filtration process, which would need to be optimized.

TiO₂ particles were successfully synthesized solvothermally in the presence of ammonium bicarbonate and LA. Ligand-exchange and phase-transfer was then attempted using glycerol, succinic acid and tartaric acid. In general, this process led to the formation of nanorods, likely through a combination of chemical etching and oriented attachment processes. The extent to which LA was removed from the particle surface is believed to play a role in this process; however, this variable is difficult to control reproducibly. Even for the cases where LA appeared to be present on the TiO₂ surface, particles were dispersible in water.

In addition to optimizing the methods described above, it may be possible to synthesize isolated TiO₂ particles within reverse micelles. While reverse micelle procedures typically yield aggregated particles, the synthesis of TiO₂ within Igepal® CO-520 micelles could yield monodispersed particles as shown in Figure 3-12 (C). Other efforts to improve the stability of TiO₂ particles could involve the post-synthetic functionalization of particles synthesized in aqueous solution with short-chain, water soluble capping ligands. As this process would not involve ligand-exchange, it is likely that this functionalization could occur without significantly altering the particle morphology.

3.2.2. Synthesis of Iron Oxide Nanoparticles

3.2.2.1. Synthesis of Iron Oxide Particles by Coprecipitation

While the most common method for synthesizing iron oxide particles involves the coprecipitation of Fe²⁺ and Fe³⁺ in the presence of either NaOH or NH₄OH, less aggregation was reported for coprecipitation in the presence of tetramethylammonium hydroxide (N(CH₃)₄OH). The tetramethylammonium cations provided additional electrostatic repulsion and increased particle stability. This was the first method used to synthesize aqueous Fe₃O₄ particles without sterically-bulky capping ligands. N(CH₃)₄OH was added to a solution containing a 2:1 ratio of ferric (Fe(III)) to ferrous (Fe (II) chloride until a pH of 13 as achieved. A black precipitate was quickly formed.

While Cheng et al.³¹ isolated the precipitate using a magnet, there were some difficulties with removing the black solid from the round-bottomed flask using this technique and not all of the particles adhered to a stir bar. This could indicate at least partial oxidation of Fe_3O_4 . It is well-documented that Fe_3O_4 is easily oxidized to $\gamma\text{-Fe}_2\text{O}_3$,^{28,42,120,121,150} and as shown in Equation 3-14 (page 220), Fe_3O_4 can also be oxidized to $\text{Fe}(\text{OH})_3$ in the presence of water and oxygen.¹³³ While the authors did not report synthesizing these particles in a nitrogen atmosphere, this could have yielded better results. The particles were separated by centrifugation and washed repeatedly with de-ionized water. While discrete particles of 3.8 ± 0.7 nm were observed (Figure 3-42 (A)), there also appeared to be some non-particulate material indicating inadequate purification.

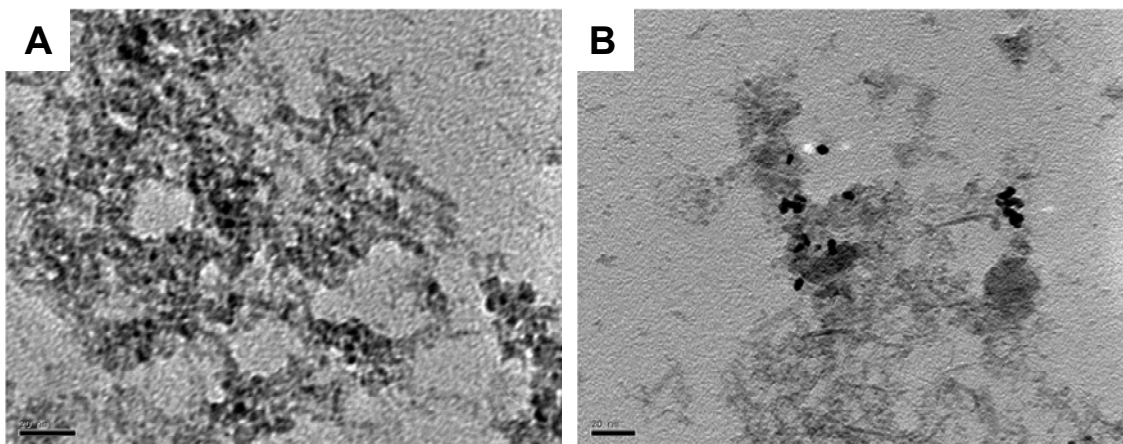


Figure 3-42. Fe_3O_4 particles synthesized by the coprecipitation of FeCl_2 and FeCl_3 in tetramethyl ammonium hydroxide ($\text{N}(\text{CH}_3)_4\text{OH}$) (A) Particles synthesized in the presence of 58 mmol ($\text{N}(\text{CH}_3)_4\text{OH}$) (B) Particles synthesized in the presence of 29 mmol ($\text{N}(\text{CH}_3)_4\text{OH}$)

The authors claim that they added the 21 mL $N(CH_3)_4OH$ until a pH of 13 was reached. It was noted that the solution pH was approximately 13 after half of this volume was added. A TEM image of the resulting particles is shown in Figure 3-42 (A). While these particles were approximately the same size, they did not exhibit any attraction to a magnet compared to the partial attraction observed with the previous sample. This suggested that these particles were not crystalline Fe_3O_4 . Despite the high solution pH, this observation suggests that a higher hydroxide concentration was required for the formation of Fe_3O_4 .

3.2.2.2. Solvothermal Synthesis of Iron Oxide

Iron oxide particles were also synthesized solvothermally through the decomposition of iron (III) acetylacetonate in benzyl alcohol at 175 °C according to a method reported by Pinna et al.²² These particles could be reportedly dispersed in both organic and aqueous media. While larger particles were obtained at 200 °C, they exhibited larger size distributions and were composed of a mixture of magnetite and hematite (Section 3.1.1.3.3, page 228). For these reasons, the lower temperature was chosen for these experiments.

After synthesis the particles were washed with both ethanol and dichloromethane to remove any organics from the particle surfaces, which could facilitate the subsequent addition of a capping ligand. The particles were then sonicated in hexane in attempt to separate particles by size and reduce polydispersity. After

sonication, some of the particles were dispersed in solution and some of them remained as a precipitate. It was assumed that the smaller particles remained dispersed. This was confirmed with TEM measurements after the particles were coated with tridecanoic acid and dispersed in solution. Tridecanoic acid is a long-chain carboxylic acid similar to undecanoic acid, which was reported in the literature. The particles in the precipitate were 9.6 ± 2.1 nm (Figure 3-43 (A)) while the supernatant particles measured 7.7 ± 1.3 nm indicating some degree of size separation. As discussed in 3.1.1.1.3 (page 164), the size of the particles from 12 nm to 8 nm after coating with undecanoic acid. Therefore these sizes likely do not reflect the sizes after the selective peptization and before coating. These organically-coated particles also confirmed the formation of iron oxide particles before attempts were made to disperse them with shorter, water-soluble capping ligands.

While the authors dispersed particles in water using dopamine, shorter capping ligands were used here in attempt to make these particles stable in aqueous solution. Shorter ligands were desirable for heterodimer formation. The same ligands used for attempted ligand-exchange with TiO_2 particles were used here, glycerol, succinic acid and tartaric acid (Figure 3-39). An excess of each capping ligand was added to a vial containing the washed iron oxide powder and sonicated in water for approximately 30 min. The particles appeared to go into solution.

However, it was noted that while all particles stuck to a magnetic stir bar before sonication, the nature of the capping ligand affected their magnetic properties after sonication.

The particles coated with tartaric acid completely adhered to the stir bar while only a

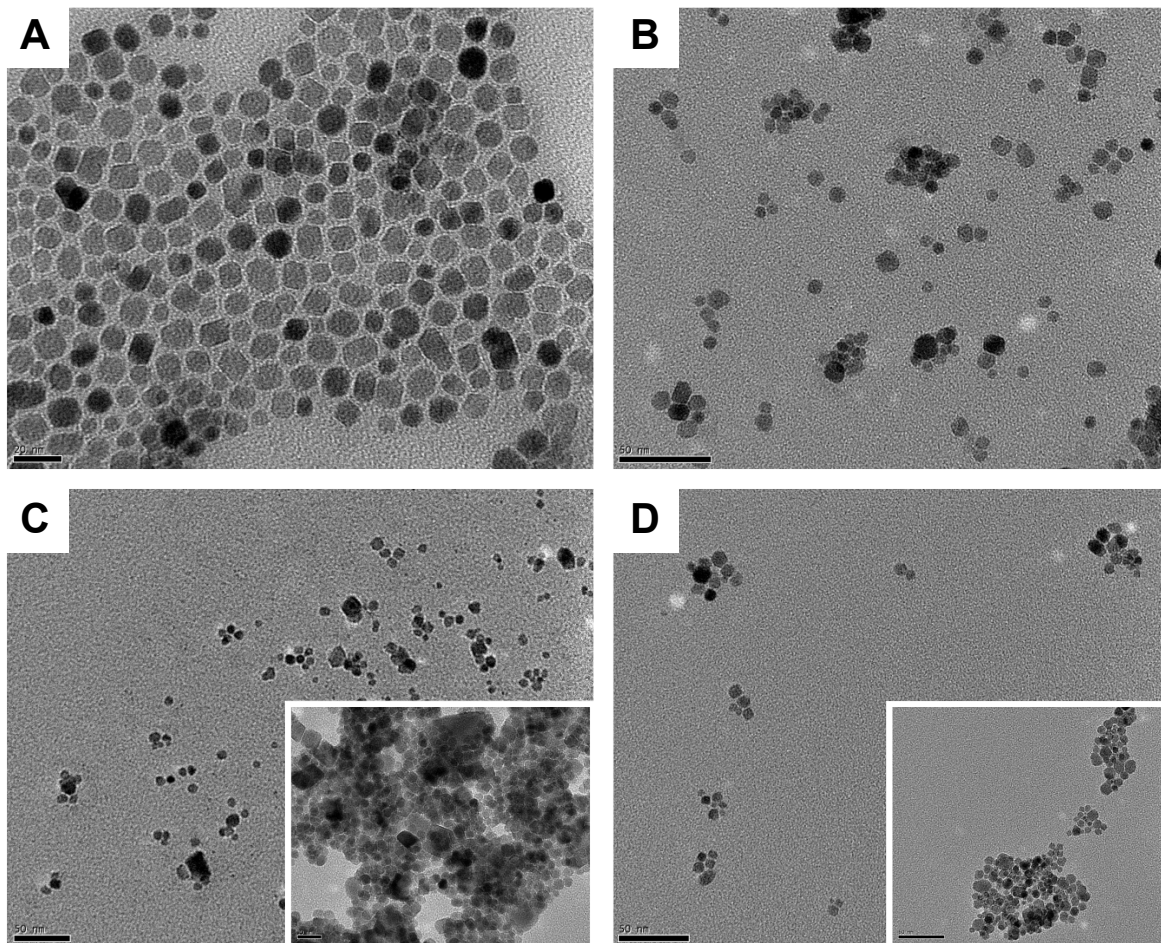


Figure 3-43. Iron oxide particles synthesized solvothermally from iron acetylacetonate in benzyl alcohol (A) particles coated with tridecanoic acid and dispersed in hexane (B) Particles coated with glycerol (C) Particles coated with succinic acid (D) Particles coated with tartaric acid. The insets in (C) and (D) show larger aggregates also present in these solutions.

fraction of the particles coated with succinic acid adhered and those in glycerol remained completely dispersed in solution. The reasons for this were unclear. While the crystal structures were not characterized, it was speculated that interactions between the iron oxide and the capping ligands could have affected the crystal structure and/or magnetic properties of these particles. As indicated in the previous section Fe_3O_4 can be oxidized to either $\gamma\text{-Fe}_2\text{O}_3$ ^{28,42,120,121,150} or $\text{Fe}(\text{OH})_3$ in the presence of water and oxygen.¹³³ As the interactions with iron oxide were expected to be different for the different capping ligands, it is highly possible they could have affected the crystal structure in different ways. As mentioned in Section 3.2.1.6 (page 252) in reference to TiO_2 , the binding mode for glycerol was different than that for the carboxylic acids. It was postulated that the hydroxyl group on the glycerol interacted with the protonated TiO_2 surface.¹⁶²

TEM images of iron oxide particles after sonication with glycerol, succinic acid and tartaric acid are shown in Figure 3-43 (B-D). The measured sizes were 7.30 ± 1.60 nm, 7.36 ± 1.20 nm and 7.75 ± 2.13 nm, respectively indicating negligible size differences between the three particles. Figure 3-43 (B) shows some small aggregates observed for particles coated with glycerol; however, most of the particles appeared to be discrete. While discrete particles were also observed for particles coated with succinic and tartaric acids, the insets in Figure 3-43 (C-D) show larger aggregates, which were also observed. As it seemed that the particles coated

with succinic and tartaric exhibited much stronger magnetic properties, the magnetic dipolar forces (Section 3.1.1.3, page 213) could explain the greater extent of aggregation. Purification of the tartaric acid-coated particles was made possible as they could be removed from solution using a magnet, washed, and then re-dispersed in water.

It is also possible that aggregation could have been limited by not performing the size-selection process in hexane. While Pinna et al.²² indicated in the Experimental Section that the size-selection process was performed after synthesis and before a capping ligand was introduced, the text of the article indicated that this process was performed after coating with undecanoic acid. Precipitating the particles in a non-solvent without a capping ligand could very likely have contributed to particle aggregation.

3.2.2.3. Summary

Iron oxide particles were synthesized both through the coprecipitation of FeCl_2 and FeCl_3 in the presence of ammonium hydroxide and through the thermal decomposition of $\text{Fe}(\text{acac})_3$ in benzyl alcohol. The particles obtained through coprecipitation were 3.8 ± 0.7 nm, and exhibited some attraction to a magnet. Not all of the particles were strongly drawn to the magnet suggesting that partial oxidation may have occurred. Better results may have been obtained by performing this synthesis in a nitrogen atmosphere. Because not all of the particles could be

removed from solution using a magnet, purification was difficult. In addition to particles, non-particulate matter was observed on the TEM grid.

The particles synthesized by thermal decomposition were approximately 7 – 8 nm in diameter. While they exhibited magnetic behavior as synthesized, the magnetic properties appeared to differ dependent upon the nature of the capping ligand used. The particles coated with tartaric acid could be separated from solution using a magnet. After ligand-exchange, some aggregation was observed especially for the particles coated with succinic and tartaric acids. The extent of aggregation may have been less if the size-selection process in hexane had not been performed.

Attempts to synthesize heterodimers using both TiO_2 and iron oxide are reported in Chapter 4.

3.3. Experimental

3.3.1. Particle Synthesis

Unless otherwise noted, all reagents were purchased from Fischer Scientific. All glassware was cleaned with aqua regia (3:1 HCl/ HNO_3) prior to use in order to remove any contaminants, which could act as sites for nucleation or aggregation.

3.3.1.1. Synthesis of Hexanethiol-capped Platinum Particles

Particles were synthesized as reported in the literature.¹⁶³ $\text{H}_2\text{PtCl}_6 \cdot 6\text{H}_2\text{O}$ (0.30 g, 0.58 mmol) and 20 mL anhydrous THF were added to a Schlenk flask inside an N_2 -filled dry box. The flask was sealed with a septum and removed from the box. While stirring under nitrogen, 83 μL hexanethiol was added and the solution stirred for 30 min. Then, 15 mL lithium triethylborohydride (LiTEBH) was added dropwise to the solution, which turned dark brown. After stirring for an additional 30 min, ethanol was added to quench the excess LiTEBH. The majority of solvent was removed via rotary evaporation and the particles precipitated from solution with acetonitrile. The particles were filtered on a fine frit and washed with ethanol and acetonitrile. The resulting particles were approximately 2 nm as evidenced by TEM and exhibited a tailing optical absorbance.

3.3.1.2. Synthesis of Stearic Acid-capped TiO_2 Particles

Particles were synthesized as reported in the literature.¹⁰⁴ Freshly distilled chloroform (100 mL), distilled isopropanol (4 mL) and doubly distilled water (15 μL) were added to a Schlenk flask containing stearic acid (88 mg, 0.31 mmol). The resulting solution was stirred under nitrogen, and 95 μL titanium (IV) isopropoxide (0.32 mmol) was added. The clear solution was stirred for three days before the majority of the solvent was evaporated and the particles were precipitated with acetonitrile. The white particles were filtered on a fine frit and washed with

additional acetonitrile. The resulting particles were approximately 2 nm as evidenced by TEM.

3.3.1.3. Synthesis of TiO₂ Particles from TiCl₄

This procedure was adapted from one reported in the literature⁹⁴ Titanium (IV) chloride (1 mL, 9.1 mmol) was added dropwise to a round-bottomed flask containing deionized water (75 mL) and 12.1 N hydrochloric acid (15.7 mL, 190 mmol) under nitrogen. The final concentrations of HCl and titanium in solution were 1.9 M and 0.09 M, respectively. The ratio of Cl⁻ ions to Ti⁺ ions in solution was thus 25:1. Upon addition of TiCl₄, the solution turned white for a few seconds before turning clear again. Once addition was complete, the solution was aged in an oven at 100 °C for 24 hours. At this point, a white precipitate had formed along with a yellowish supernant. The supernant was decanted and the precipitate was centrifuged and washed with deionized water.

In attempt to separate the rutile and brookite phases through selective peptization, the white solid was stirred in a nitric acid solution for approximately twenty minutes and then centrifuged. The solid precipitate was then dispersed in water, and centrifuged again. At this point it was assumed that the supernant contained spherical brookite particles while the precipitate consisted of rutile. The supernant was subject to rotary evaporation using a vacuum pump yielding a white solid. TEM indicated a mixture of spherical aggregates and elongated rods.

3.3.1.4. Synthesis of TiO₂ Particles from TIP in the presence of HCl and EtOH

This procedure was adapted from one reported in the literature.⁹ Titanium (IV) isopropoxide was measured into Schlenk flasks in a dry box under nitrogen atmosphere. These flasks were then sealed with septa and removed from the dry box. Absolute ethanol was then injected into each of these flasks while under nitrogen flow. Meanwhile, solutions of de-ionized water, absolute ethanol and hydrochloric acid were mixed in round-bottom flasks as outlined in Table 3-6. These flasks were equipped with reflux condensers and heated to 45 °C under nitrogen flow. The TIP/ethanol solutions were then added dropwise. The reactions were stirred for 12 hours. The resulting particles were characterized without further purification.

3.3.1.5. Synthesis of TiO₂ Particles from TEO in the presence of KCl and EtOH

This procedure was adapted from one reported in the literature.⁹² Absolute ethanol (100 mL) and potassium chloride (0.4 mL of 0.2 M solution) were added to a Schlenk flask, which was capped with a septum and stirred under nitrogen. Titanium (IV) ethoxide (1.7 mL) was then added dropwise, and the solution was vigorously stirred for approximately 15 min. Stirring was then discontinued and the reaction was allowed to progress for another 3 hours at which point the particles were collected and washed using a Millipore filter.

3.3.1.6. Synthesis of TiO₂ Particles Using a Solvothermal Method

This procedure was adapted from one reported in the literature.²⁴ Linoleic acid (10 mL, 32.2 mmol), ammonium bicarbonate (0.2 g, 2.5 mmol), distilled triethylamine (2 mL) and distilled cyclohexane (2 mL) were added to a Schlenk flask in a nitrogen-filled dry box. The flask was capped with a septum and removed from the dry box. While the solution was stirred under nitrogen, titanium tetra-n-butoxide (0.4 mL, 1.2 mmol) was added dropwise. During this process, the solution turned from clear to pale yellow in color. After stirring in the flask for an additional five minutes, the solution was transferred to a stainless steel autoclave, specifically a Model #4749 General Purpose Acid Digestion Bomb manufactured by the Parr Instrument Company (Figure 3-14). The sealed autoclave was kept in an oven at 150 °C for 24 hours. After cooling to room temperature, the yellow supernatant was discarded and the white precipitate centrifuged in the presence of ethanol. After washing with ethanol three times, any remaining solvent was removed through rotary evaporation at 30 °C. Particles were then dispersed in hexane. Additional linoleic acid was added as needed to facilitate particle solubility.

Ligand-exchange on the resulting particles was attempted using glycerol, tartaric acid and succinic acid. In each case, a small amount of the dried white powder of nanoparticles (15 mg) was added to a vial along with an excess of the capping ligand. Glycerol (0.1 mL, 1.34 mmol), tartaric acid (0.1 g, 0.67 mmol) and succinic

acid (0.1 g, 0.85 mmol) were added in each case. In retrospect, equivalent molar amounts should have been used for proper comparison rather than an undetermined excess. These reagents were sonicated for approximately 30 min in ethanol/water solutions (20 mL), the composition of which is described in the text.

3.3.1.7. Synthesis of Fe₃O₄ Particles by Coprecipitation

This procedure was adapted from on in the literature.³¹ Iron (III) chloride (1.6 g, 10 mmol) was dissolved in 2 M HCl (10 mL) and iron (II) chloride tetrahydrate (1.0 g, 5 mmol) was dissolved in 2 M HCl (2.5 mL). The two iron chloride solutions were mixed in a round-bottomed flask followed by the slow addition of a tetramethylammonium hydroxide solution (10.44 g N(CH₃)₄OH•5H₂O (58 mmol) in 21 mL H₂O). After addition, the solution pH was 13. Upon stirring for 20 minutes, the solution turned from orange to black and a precipitate was observed. The solution was centrifuged and the supernant decanted. The precipitate was washed with de-ionized water (x 3) to remove any excess, and the particles were re-dispersed in water.

3.3.1.8. Solvothermal Synthesis of Fe₃O₄

This procedure was adapted from on in the literature.²² Benzyl alcohol (10 mL) was placed in the PTFE cup associated with a Model #4749 General Purpose Acid Digestion Bomb manufactured by the Parr Instrument Company (Figure 3-14). The cup was then placed in a bell jar, which was evacuated and brought into a nitrogen-

filled dry box. Iron (III) acetylacetonate (0.5 g, 1.4 mmol) was weighted in the dry box and added to the benzyl alcohol. The red liquid was then sealed within the autoclave, removed from the dry box and placed in an oven at 175 °C for 48 hours. When the reaction was complete, a black precipitate and yellow supernant were observed. The solution was centrifuged and the supernant was decanted. The precipitate was washed several times with ethanol and dichloromethane and re-suspended in hexane. This solution was sonicated for 5 min at which point the supernant was discarded and the precipitate was dried via rotary evaporation at 30 °C.

Ligand-exchange on the resulting particles was attempted using tridecanoic acid, glycerol, tartaric acid and succinic acid. In each case, a small amount of the dried black powder of nanoparticles (15 mg) was added to a vial along with an excess of the capping ligand. Tridecanoic acid (0.1 g, 0.47 mmol), glycerol (0.1 mL, 1.34 mmol), tartaric acid (0.1 g, 0.67 mmol) and succinic acid (0.1 g, 0.85 mmol) were added in each case. In retrospect, equivalent molar amounts should have been used for proper comparison rather than an undetermined excess. These reagents were sonicated for approximately 30 min in either hexane or water (10 mL). The tartaric acid-coated particles were removed from solution using a magnetic stir bar, washed, and then re-dispersed in water.

3.3.2. Particle Characterization

3.3.2.1. Transmission Electron Microscopy (TEM)

Images were taken with a Philips CM12 TEM operated at 100kV. Images were captured using a Gatan 780 camera and DigitalMicrograph software. Particle sizes were measured using Image J software and setting the scale bar using the scale bars captured with the images. A minimum of 30-50 particles were measured when calculating average particle sizes.

3.3.2.2. Transmission Infrared Spectroscopy

Measurements were made using a Perkin-Elmer Spectrum RX1 Spectrometer under an N₂ atmosphere with a resolution of 4 cm⁻¹. Organic solutions were placed on a KBr plate and the solvent was allowed to evaporate.

3.3.2.3. UV-VIS Spectroscopy

Absorbance measurements were made using a Hewlett-Packard 8452A Diode Array Spectrometer and a path length of 1.0 cm. Organic molecules were measured in methylene chloride, hexanethiol-capped nanoparticles were measured in THF and water-soluble particles were measured in water.

3.4. References

- (1) Brinker, J. C.; Scherer, G. W. *Sol-Gel Science: The Physics and Chemistry of Sol-Gel Processing*; Boston Academic Press: Boston, 1990.
- (2) Wright, J. D.; Sommerdijk, N. A. J. M. *Sol-Gel Materials, Chemistry and Applications*; Gordon and Breach Science Publishers, 2001.
- (3) Schubert, U., *J. Mater. Chem.* **2005**, *15*, 3701-3715.
- (4) Barringer, E. A.; Bowen, H. K., *Langmuir* **1985**, *1*, 414-420.
- (5) Brinker, C. J., *J. Non-Cryst. Solids* **1988**, *100*, 31-50.
- (6) Livage, J.; Henry, M.; Sanchez, C., *Prog. Solid State Chem.* **1988**, *18*, 259-341.
- (7) Sanchez, C.; Livage, J.; Henry, M.; Babonneau, F., *J. Non-Cryst. Solids* **1988**, *100*, 65-76.
- (8) Arnal, P.; Corriu, R. J. P.; Leclercq, D.; Mutin, P. H.; Vioux, A., *Chem. Mater.* **1997**, *9*, 694-698.
- (9) Hsu, J. P.; Nacu, A., *Langmuir* **2003**, *19*, 4448-4454.
- (10) Li, Z.; Chen, H.; Bao, H. B.; Gao, M. Y., *Chem. Mater.* **2004**, *16*, 1391-1393.
- (11) Oregan, B.; Moser, J.; Anderson, M.; Gratzel, M., *J. Phys. Chem.* **1990**, *94*, 8720-8726.
- (12) Rockenberger, J.; Scher, E. C.; Alivisatos, A. P., *J. Am. Chem. Soc.* **1999**, *121*, 11595-11596.
- (13) Hsu, K. H.; Wu, J. H.; Huang, Y. Y.; Wang, L. Y.; Lee, H. Y.; Lin, J. G., *J. Appl. Phys.* **2005**, *97*.
- (14) Lee, Y. J.; Lee, J. W.; Bae, C. J.; Park, J. G.; Noh, H. J.; Park, J. H.; Hyeon, T., *Adv. Funct. Mater.* **2005**, *15*, 2036-2036.
- (15) Zhou, Z. H.; Wang, J.; Liu, X.; Chan, H. S. O., *J. Mater. Chem.* **2001**, *11*, 1704-1709.

- (16) Hyeon, T., *Chem. Commun.* **2003**, 927-934.
- (17) Lee, J.; Isobe, T.; Senna, M., *J. Colloid Interface Sci.* **1996**, *177*, 490-494.
- (18) Niederberger, M.; Bartl, M. H.; Stucky, G. D., *Chem. Mater.* **2002**, *14*, 4364-4370.
- (19) Zhang, D. B.; Qi, L. M.; Ma, J. M.; Cheng, H. M., *J. Mater. Chem.* **2002**, *12*, 3677-3680.
- (20) Wang, C.; Deng, Z. X.; Zhang, G. H.; Fan, S. S.; Li, Y. D., *Powder Technol.* **2002**, *125*, 39-44.
- (21) Abu Mukh-Qasem, R.; Gedanken, A., *J. Colloid Interface Sci.* **2005**, *284*, 489-494.
- (22) Pinna, N.; Grancharov, S.; Beato, P.; Bonville, P.; Antonietti, M.; Niederberger, M., *Chem. Mater.* **2005**, *17*, 3044-3049.
- (23) Acar, H. Y. C.; Garaas, R. S.; Syud, F.; Bonitatebus, P.; Kulkarni, A. M., *J. Magn. Magn. Mater.* **2005**, *293*, 1-7.
- (24) Li, X. L.; Peng, Q.; Yi, J. X.; Wang, X.; Li, Y. D., *Chem.-Eur. J.* **2006**, *12*, 2383-2391.
- (25) Polleux, J.; Pinna, N.; Antonietti, M.; Hess, C.; Wild, U.; Schlogl, R.; Niederberger, M., *Chem.-Eur. J.* **2005**, *11*, 3541-3551.
- (26) Chemseddine, A.; Moritz, T., *Eur. J. Inorg. Chem.* **1999**, 235-245.
- (27) Mann, S.; Hannington, J. P., *J. Colloid Interface Sci.* **1988**, *122*, 326-335.
- (28) Sun, S. H.; Zeng, H., *J. Am. Chem. Soc.* **2002**, *124*, 8204-8205.
- (29) Fu, L.; Dravid, V. P.; Johnson, D. L., *Appl. Surf. Sci.* **2001**, *181*, 173-178.
- (30) Li, G. S.; Li, L. P.; Boerio-Goates, J.; Woodfield, B. F., *J. Am. Chem. Soc.* **2005**, *127*, 8659-8666.

- (31) Cheng, F. Y.; Su, C. H.; Yang, Y. S.; Yeh, C. S.; Tsai, C. Y.; Wu, C. L.; Wu, M. T.; Shieh, D. B., *Biomaterials* **2005**, *26*, 729-738.
- (32) Suslick, K. S.; Fang, M. M.; Hyeon, T., *J. Am. Chem. Soc.* **1996**, *118*, 11960-11961.
- (33) Trentler, T. J.; Denler, T. E.; Bertone, J. F.; Agrawal, A.; Colvin, V. L., *J. Am. Chem. Soc.* **1999**, *121*, 1613-1614.
- (34) Wang, C.; Deng, Z. X.; Li, Y. D., *Inorg. Chem.* **2001**, *40*, 5210-5214.
- (35) Ayres, J.; Simendinger, W. H.; Balik, C. M., *J. Coat. Technol. Res.* **2007**, *4*, 463-471.
- (36) Zarzycki, J., *J. Sol-Gel Sci. Technol.* **1997**, *8*, 17-22.
- (37) Narula, C. K. *Ceramic Precursor Technology and Its Applications*; Marcel Dekker, Inc., 1995.
- (38) Boyle, T. J.; Tyner, R. P.; Alam, T. M.; Scott, B. L.; Ziller, J. W.; Potter, B. G., *J. Am. Chem. Soc.* **1999**, *121*, 12104-12112.
- (39) Livage, J.; Sanchez, C.; Henry, M.; Doeuff, S., *Solid State Ion.* **1989**, *32-3*, 633-638.
- (40) Chandler, C. D.; Roger, C.; Hampdensmith, M. J., *Chem. Rev.* **1993**, *93*, 1205-1241.
- (41) Matijevic, E.; Budnik, M.; Meites, L., *J. Colloid Interface Sci.* **1977**, *61*, 302-311.
- (42) Mak, S. Y.; Chen, D. H., *Macromol. Rapid Commun.* **2005**, *26*, 1567-1571.
- (43) Garnweitner, G.; Antonietti, M.; Niederberger, M., *Chem. Commun.* **2005**, 397-399.
- (44) Vijayakumar, R.; Kolytyn, Y.; Felner, I.; Gedanken, A., *Mater. Sci. Eng. A-Struct. Mater. Prop. Microstruct. Process.* **2000**, *286*, 101-105.
- (45) Wan, S. R.; Huang, J. S.; Yan, H. S.; Liu, K. L., *J. Mater. Chem.* **2006**, *16*, 298-303.

- (46) Schubert, U.; Tewinkel, S.; Lamber, R., *Chem. Mater.* **1996**, *8*, 2047-2055.
- (47) Schmidt, H., *J. Non-Cryst. Solids* **1988**, *100*, 51-64.
- (48) Schubert, U.; Arpac, E.; Glaubitt, W.; Helmerich, A.; Chau, C., *Chem. Mater.* **1992**, *4*, 291-295.
- (49) Hay, J. N.; Raval, H. M., *Chem. Mater.* **2001**, *13*, 3396-3403.
- (50) Schmidt, H. In *Sol-Gel Science and Technology*; Aegerter, M. A., Jafelicci, M. J., de Souza, D. F., Zanotto, E. D., Eds.; World Scientific Publishing, 1989.
- (51) Haas, K. H.; Amberg-Schwab, S.; Rose, K., *Thin Solid Films* **1999**, *351*, 198-203.
- (52) Wen, J.; Jordens, K.; Wilkes, G. L. In *Better Ceramics Through Chemistry VII: Organic/Inorganic Hybrid Materials*; Coltrain, B. K., Sanchez, C., Schaefer, D. W., Wilkes, G. L., Eds.; Materials Research Society, 1996.
- (53) Corriu, R. J. P.; Leclercq, D., *Angew. Chem.-Int. Edit. Engl.* **1996**, *35*, 1420-1436.
- (54) Livage, J.; Henry, M.; Sanchez, C., *Progress in Solid State Chemistry* **1988**, *18*, 259-341.
- (55) Brinker, C. J.; Scherer, G. W., *J. Non-Cryst. Solids* **1985**, *70*, 301-322.
- (56) Mehrotra, R. C., *J. Non-Cryst. Solids* **1988**, *100*, 1-15.
- (57) Buckley, A. M.; Greenblatt, M., *J. Chem. Educ.* **1994**, *71*, 599-602.
- (58) Schmidt, H.; Scholze, H.; Kaiser, A., *J. Non-Cryst. Solids* **1984**, *63*, 1-11.
- (59) Sommerdijk, J. D. W. a. N. A. J. M. *Sol-Gel Materials, Chemistry and Applications*; Gordon and Breach Science Publishers, 2001.
- (60) Hench, L. L.; West, J. K., *Chem. Rev.* **1990**, *90*, 33-72.
- (61) Bradley, D. C.; Gaze, R.; Wardlaw, W., *J. Chem. Soc.* **1957**, 469-478.

- (62) Sakka, S.; Kamiya, K., *J. Non-Cryst. Solids* **1982**, *48*, 31-46.
- (63) Cozzoli, P. D.; Kornowski, A.; Weller, H., *J. Am. Chem. Soc.* **2003**, *125*, 14539-14548.
- (64) Pope, E. J. A.; Mackenzie, J. D., *J. Non-Cryst. Solids* **1986**, *87*, 185-198.
- (65) Brinker, C. J.; Keefer, K. D.; Schaefer, D. W.; Assink, R. A.; Kay, B. D.; Ashley, C. S., *J. Non-Cryst. Solids* **1984**, *63*, 45-59.
- (66) Leautic, A.; Babonneau, F.; Livage, J., *Chem. Mater.* **1989**, *1*, 240-247.
- (67) Stober, W.; Fink, A.; Bohn, E., *J. Colloid Interface Sci.* **1968**, *26*, 62-&.
- (68) Leautic, A.; Babonneau, F.; Livage, J., *Chem. Mater.* **1989**, *2*, 248-252.
- (69) Wang, C. C.; Ying, J. Y., *Chem. Mater.* **1999**, *11*, 3113-3120.
- (70) Tang, J.; Redl, F.; Zhu, Y. M.; Siegrist, T.; Brus, L. E.; Steigerwald, M. L., *Nano Lett.* **2005**, *5*, 543-548.
- (71) Chen, X.; Mao, S. S., *Chem. Rev.* **2007**, *107*, 2891-2959.
- (72) Arnal, P.; Corriu, R. J. P.; Leclercq, D.; Mutin, P. H.; Vioux, A., *J. Mater. Chem.* **1996**, *6*, 1925-1932.
- (73) Sugimoto, T.; Zhou, X. P.; Muramatsu, A., *J. Colloid Interface Sci.* **2003**, *259*, 43-52.
- (74) Niederberger, M.; Garnweitner, G.; Krumeich, F.; Nesper, R.; Colfen, H.; Antonietti, M., *Chem. Mater.* **2004**, *16*, 1202-1208.
- (75) Kim, K. D.; Kim, H. T., *Powder Technol.* **2001**, *119*, 164-172.
- (76) Burda, C.; Chen, X. B.; Narayanan, R.; El-Sayed, M. A., *Chem. Rev.* **2005**, *105*, 1025-1102.
- (77) Niederberger, M.; Bard, M. H.; Stucky, G. D., *J. Am. Chem. Soc.* **2002**, *124*, 13642-13643.

- (78) Parala, H.; Devi, A.; Bhakta, R.; Fischer, R. A., *J. Mater. Chem.* **2002**, *12*, 1625-1627.
- (79) Li, G. L.; Wang, G. H., *Nanostruct. Mater.* **1999**, *11*, 663-668.
- (80) Fuerte, A.; Hernandez-Alonso, M. D.; Maira, A. J.; Martinez-Arias, A.; Fernandez-Garcia, M.; Conesa, J. C.; Soria, J., *Chem. Commun.* **2001**, 2718-2719.
- (81) Lin, J.; Lin, Y.; Liu, P.; Meziani, M. J.; Allard, L. F.; Sun, Y. P., *J. Am. Chem. Soc.* **2002**, *124*, 11514-11518.
- (82) Matijevic, E., *Annu. Rev. Mater. Sci.* **1985**, *15*, 483-516.
- (83) Hunter, R. J. *Foundations of Colloidal Science*; Oxford University Press: New York, 2001.
- (84) Hamaker, H. C., *Physica* **1937**, *4*, 1058-1072.
- (85) Tadros, T. F. In *Colloid Stability: The Role of Surface Forces - Part I*; Tadros, T. F., Ed.; Wiley-VCH: Weinheim, Germany, 2007; Vol. 1, pp 2-22.
- (86) Ross, S.; Morrison, I. D. *Colloidal Systems and Interfaces*; John Wiley & Sons: New York, 1988.
- (87) Heimenz, P. C.; Rajagopalan, R. *Principles of Colloid and Surface Chemistry*; Marcel Dekker, Inc.: New York, 1997.
- (88) Yotsumoto, H.; Yoon, R. H., *J. Colloid Interface Sci.* **1993**, *157*, 426-433.
- (89) Yotsumoto, H.; Yoon, R. H., *J. Colloid Interface Sci.* **1993**, *157*, 434-441.
- (90) Moran, P. D.; Bartlett, J. R.; Bowmaker, G. A.; Woolfrey, J. L.; Cooney, R. P., *J. Sol-Gel Sci. Technol.* **1999**, *15*, 251-262.
- (91) Derjaguin, B. V.; Churaev, N. V., *Colloids Surf.* **1989**, *41*, 223-237.
- (92) Eiden-Assmann, S.; Widoniak, J.; Maret, G., *Chem. Mater.* **2004**, *16*, 6-11.
- (93) Look, J. L.; Zukoski, C. F., *J. Colloid Interface Sci.* **1992**, *153*, 461-482.

- (94) Pottier, A.; Chaneac, C.; Tronc, E.; Mazerolles, L.; Jolivet, J. P., *J. Mater. Chem.* **2001**, *11*, 1116-1121.
- (95) Aruna, S. T.; Tirosh, S.; Zaban, A., *J. Mater. Chem.* **2000**, *10*, 2388-2391.
- (96) Watzky, M. A.; Finke, R. G., *J. Am. Chem. Soc.* **1997**, *119*, 10382-10400.
- (97) LaMer, V. K.; Dinegar, R. H., *J. Am. Chem. Soc.* **1950**, *72*, 4847-4854.
- (98) Paunesku, T.; Rajh, T.; Wiederrecht, G.; Maser, J.; Vogt, S.; Stojicevic, N.; Protic, M.; Lai, B.; Oryhon, J.; Thurnauer, M.; Woloschak, G., *Nat. Mater.* **2003**, *2*, 343-346.
- (99) Kormann, C.; Bahnemann, D. W.; Hoffmann, M. R., *J. Phys. Chem.* **1988**, *92*, 5196-5201.
- (100) Moser, J.; Gratzel, M., *J. Am. Chem. Soc.* **1984**, *106*, 6557-6564.
- (101) Moser, J.; Gratzel, M., *J. Am. Chem. Soc.* **1983**, *105*, 6547-6555.
- (102) Makarova, O. V.; Rajh, T.; Thurnauer, M. C.; Martin, A.; Kemme, P. A.; Cropek, D., *Environ. Sci. Technol.* **2000**, *34*, 4797-4803.
- (103) Alquier, C.; Vandenberg, M. T.; Henry, M., *J. Non-Cryst. Solids* **1986**, *79*, 383-395.
- (104) Beek, W. J. E.; Janssen, R. A. J., *Adv. Funct. Mater.* **2002**, *12*, 519-525.
- (105) Duonghong, D.; Borgarello, E.; Gratzel, M., *J. Am. Chem. Soc.* **1981**, *103*, 4685-4690.
- (106) Zhang, H. Z.; Finnegan, M.; Banfield, J. F., *Nano Lett.* **2001**, *1*, 81-85.
- (107) Kim, K. D.; Kim, H. T., *Colloid Surf. A-Physicochem. Eng. Asp.* **2002**, *207*, 263-269.
- (108) Jun, Y. W.; Casula, M. F.; Sim, J. H.; Kim, S. Y.; Cheon, J.; Alivisatos, A. P., *J. Am. Chem. Soc.* **2003**, *125*, 15981-15985.

- (109) Kim, K. D.; Kim, S. H.; Kim, H. T., *Colloid Surf. A-Physicochem. Eng. Asp.* **2005**, *254*, 99-105.
- (110) Lim, K. T.; Hwang, H. S.; Ryoo, W.; Johnston, K. P., *Langmuir* **2004**, *20*, 2466-2471.
- (111) Stathatos, E.; Lianos, P.; DelMonte, F.; Levy, D.; Tsiourvas, D., *Langmuir* **1997**, *13*, 4295-4300.
- (112) Towey, T. F.; Khanlodhi, A.; Robinson, B. H., *J. Chem. Soc.-Faraday Trans.* **1990**, *86*, 3757-3762.
- (113) Niederberger, M., *Acc. Chem. Res.* **2007**, *40*, 793-800.
- (114) Vioux, A., *Chem. Mater.* **1997**, *9*, 2292-2299.
- (115) Corriu, R. J. P.; Leclercq, D.; Lefevre, P.; Mutin, P. H.; Vioux, A., *J. Mater. Chem.* **1992**, *2*, 673-674.
- (116) Walton, R. I., *Chem. Soc. Rev.* **2002**, *31*, 230-238.
- (117) Rabenau, A., *Angew. Chem.-Int. Edit. Engl.* **1985**, *24*, 1026-1040.
- (118) Tartaj, P.; Serna, C. J., *Chem. Mater.* **2002**, *14*, 4396-4402.
- (119) Dresco, P. A.; Zaitsev, V. S.; Gambino, R. J.; Chu, B., *Langmuir* **1999**, *15*, 1945-1951.
- (120) Laurent, S.; Forge, D.; Port, M.; Roch, A.; Robic, C.; Elst, L. V.; Muller, R. N., *Chem. Rev.* **2008**, *108*, 2064-2110.
- (121) Lu, A. H.; Salabas, E. L.; Schuth, F., *Angew. Chem.-Int. Edit.* **2007**, *46*, 1222-1244.
- (122) Si, S.; Kotal, A.; Mandal, T. K.; Giri, S.; Nakamura, H.; Kohara, T., *Chem. Mater.* **2004**, *16*, 3489-3496.
- (123) Albornoz, C.; Jacobo, S. E., *J. Magn. Magn. Mater.* **2006**, *305*, 12-15.
- (124) Harris, L. A.; Goff, J. D.; Carmichael, A. Y.; Riffle, J. S.; Harburn, J. J.; St Pierre, T. G.; Saunders, M., *Chem. Mater.* **2003**, *15*, 1367-1377.

- (125) Chan, D. C. F.; Kirpotin, D. B.; Bunn, P. A., *J. Magn. Magn. Mater.* **1993**, *122*, 374-378.
- (126) Kim, D. K.; Zhang, Y.; Kehr, J.; Klason, T.; Bjelke, B.; Muhammed, M., *J. Magn. Magn. Mater.* **2001**, *225*, 256-261.
- (127) Shieh, D. B.; Cheng, F. Y.; Su, C. H.; Yeh, C. S.; Wu, M. T.; Wu, Y. N.; Tsai, C. Y.; Wu, C. L.; Chen, D. H.; Chou, C. H., *Biomaterials* **2005**, *26*, 7183-7191.
- (128) Zhang, Y.; Kohler, N.; Zhang, M. Q., *Biomaterials* **2002**, *23*, 1553-1561.
- (129) Kim, J.; Lee, J. E.; Lee, J.; Yu, J. H.; Kim, B. C.; An, K.; Hwang, Y.; Shin, C. H.; Park, J. G.; Kim, J.; Hyeon, T., *J. Am. Chem. Soc.* **2006**, *128*, 688-689.
- (130) Machala, L.; Zboril, R.; Gedanken, A., *J. Phys. Chem. B* **2007**, *111*, 4003-4018.
- (131) Jun, Y. W.; Huh, Y. M.; Choi, J. S.; Lee, J. H.; Song, H. T.; Kim, S.; Yoon, S.; Kim, K. S.; Shin, J. S.; Suh, J. S.; Cheon, J., *J. Am. Chem. Soc.* **2005**, *127*, 5732-5733.
- (132) Shen, L. F.; Laibinis, P. E.; Hatton, T. A., *Langmuir* **1999**, *15*, 447-453.
- (133) Kim, D. K.; Zhang, Y.; Voit, W.; Rao, K. V.; Muhammed, M., *J. Magn. Magn. Mater.* **2001**, *225*, 30-36.
- (134) Lubbe, A. S.; Bergemann, C.; Riess, H.; Schriever, F.; Reichardt, P.; Possinger, K.; Matthias, M.; Dorken, B.; Herrmann, F.; Gurtler, R.; Hohenberger, P.; Haas, N.; Sohr, R.; Sander, B.; Lemke, A. J.; Ohlendorf, D.; Huhnt, W.; Huhn, D., *Cancer Res.* **1996**, *56*, 4686-4693.
- (135) Bergemann, C.; Muller-Schulte, D.; Oster, J.; Brassard, L.; Lubbe, A. S., *J. Magn. Magn. Mater.* **1999**, *194*, 45-52.
- (136) Shen, L. F.; Stachowiak, A.; Hatton, T. A.; Laibinis, P. E., *Langmuir* **2000**, *16*, 9907-9911.
- (137) Shang, H.; Chang, W. S.; Kan, S.; Majetich, S. A.; Lee, G. U., *Langmuir* **2006**, *22*, 2516-2522.
- (138) Li, Z.; Sun, Q.; Gao, M. Y., *Angew. Chem.-Int. Edit.* **2005**, *44*, 123-126.

- (139) Hong, C. Y.; Jang, I. J.; Horng, H. E.; Hsu, C. J.; Yao, Y. D.; Yang, H. C., *J. Appl. Phys.* **1997**, *81*, 4275-4277.
- (140) Park, J.; An, K. J.; Hwang, Y. S.; Park, J. G.; Noh, H. J.; Kim, J. Y.; Park, J. H.; Hwang, N. M.; Hyeon, T., *Nat. Mater.* **2004**, *3*, 891-895.
- (141) Lee, H. S.; Lee, W. C.; Furubayashi, T., *J. Appl. Phys.* **1999**, *85*, 5231-5233.
- (142) Yang, C. Q.; Wang, G.; Lu, Z. Y.; Sun, J.; Zhuang, J. Q.; Yang, W. S., *J. Mater. Chem.* **2005**, *15*, 4252-4257.
- (143) Lu, Y.; Yin, Y. D.; Mayers, B. T.; Xia, Y. N., *Nano Lett.* **2002**, *2*, 183-186.
- (144) Ma, D. L.; Guan, J. W.; Normandin, F.; Denomme, S.; Enright, G.; Veres, T.; Simard, B., *Chem. Mat.* **2006**, *18*, 1920-1927.
- (145) Rabelo, D.; Lima, E. C. D.; Reis, A. C.; Nunes, W. C.; Novak, M. A.; Garg, V. K.; Oliveira, A. C.; Morais, P. C., *Nano Lett.* **2001**, *1*, 105-108.
- (146) Willard, M. A.; Kurihara, L. K.; Carpenter, E. E.; Calvin, S.; Harris, V. G., *Int. Mater. Rev.* **2004**, *49*, 125-170.
- (147) Lakeman, C. D. E.; Payne, D. A., *Mater. Chem. Phys.* **1994**, *38*, 305-324.
- (148) Yamaguchi, K.; Fujii, T.; Kuranouchi, S.; Kaneko, A., *J. Appl. Phys.* **1988**, *64*, 5452-5452.
- (149) Takahashi, N.; Kakuda, N.; Ueno, A.; Yamaguchi, K.; Fujii, T., *Jpn. J. Appl. Phys. Part 2 - Lett.* **1989**, *28*, L244-L247.
- (150) Kang, Y. S.; Risbud, S.; Rabolt, J. F.; Stroeve, P., *Chem. Mat.* **1996**, *8*, 2209-&.
- (151) Massart, R., *IEEE Trans. Magn.* **1981**, *17*, 1247-1248.
- (152) Park, J.; Lee, E.; Hwang, N. M.; Kang, M. S.; Kim, S. C.; Hwang, Y.; Park, J. G.; Noh, H. J.; Kini, J. Y.; Park, J. H.; Hyeon, T., *Angew. Chem.-Int. Edit.* **2005**, *44*, 2872-2877.

- (153) Kwon, S. G.; Piao, Y.; Park, J.; Angappane, S.; Jo, Y.; Hwang, N. M.; Park, J. G.; Hyeon, T., *J. Am. Chem. Soc.* **2007**, *129*, 12571-12584.
- (154) Lambert, J. B.; Shurvell, H. E.; Lightner, D. A.; Cooks, R. G. *Organic Structural Spectroscopy*, Prentice Hall: Upper Saddle River, NJ, 1998.
- (155) Walker, B. R.; Wassel, R. A.; Stefanescu, D. M.; Gorman, C. B., *J. Am. Chem. Soc.* **2004**, *126*, 16330-16331.
- (156) Bong, D.; Tam, I.; Breslow, R., *J. Am. Chem. Soc.* **2004**, *126*, 11796-11797.
- (157) Horswell, S. L.; Kiely, C. J.; O'Neil, I. A.; Schiffrin, D. J., *J. Am. Chem. Soc.* **1999**, *121*, 5573-5574.
- (158) Avery, N. R.; Matheson, T. W., *Surface Sci.* **1984**, *143*, 110-124.
- (159) Shih, K. C.; Angelici, R. J., *Langmuir* **1995**, *11*, 2539-2546.
- (160) Murphy, K. L.; Tysoe, W. T.; Bennett, D. W., *Langmuir* **2004**, *20*, 1732-1738.
- (161) Swanson, S. A.; McClain, R.; Lovejoy, K. S.; Alamdari, N. B.; Hamilton, J. S.; Scott, J. C., *Langmuir* **2005**, *21*, 5034-5039.
- (162) Jiang, B. P.; Yin, H. B.; Jiang, T. S.; Jiang, Y. H.; Feng, H.; Chen, K. M.; Zhou, W. P.; Wada, Y. J., *Mater. Chem. Phys.* **2006**, *98*, 231-235.
- (163) Hostetler, M. J.; Wingate, J. E.; Zhong, C. J.; Harris, J. E.; Vachet, R. W.; Clark, M. R.; Londono, J. D.; Green, S. J.; Stokes, J. J.; Wignall, G. D.; Glish, G. L.; Porter, M. D.; Evans, N. D.; Murray, R. W., *Langmuir* **1998**, *14*, 17-30.

4. Synthesis of Nanoparticle Assemblies

As discussed in Chapter 1, the overall goal of this work was to synthesize and characterize heterodimers consisting of oligomeric phenylethylenes (OPEs) inserted between nanoparticles of different compositions using orthogonal self-assembly. Before describing the synthesis of nanoparticle assemblies using the particles discussed in Chapters 2 and 3, an overview of literature methods for forming particle assemblies is presented. A wide variety of methods have been used to form nanoparticle assemblies both on surfaces and in solution.

4.1. Overview of Literature Methods for Forming Particle Assemblies

4.1.1. Formation of Nanoparticle Assemblies on Surfaces

There have been many reports of two-dimensional particle arrays formed on surfaces.^{2,5-11} The most common method for forming particle assemblies on a substrate involves the adsorption of particles to a self-assembled monolayer through either covalent or non-covalent interactions. Figure 4-1(A) shows the general methodology for the covalent attachment of gold particles to a substrate. A self-assembled monolayer is formed on a substrate, which has a terminal functional group with a high affinity for particles in solution. Figure 4-1 (B) shows an example of particle arrays generated by non-covalent interactions. In this case, a monolayer

of biotin on the surface interacts with streptavidin-functionalized particles.⁷ As will be discussed later in this chapter, non-covalent interactions are often reversible.

While both covalent and non-covalent approaches have been reported, monolayers formed through covalent bonds are more frequently reported in the literature. The functional groups typically used for binding to gold include thiols, amines and isocyanides.^{7,8} For example, Andres et al.^{2,8} formed two-dimensional arrays of gold particles on gold surfaces using xylene dithiol, 4,4-biphenyldithiol and oligomeric phenylene ethylene (OPE) di-thiols and di-isocyanides. Chumanov et al.⁹ used self-assembled monolayers of (3-mercaptopropyl)trimethoxysilane on glass and quartz to form monolayers of citrate-capped gold and silver nanoparticles. Similarly gold

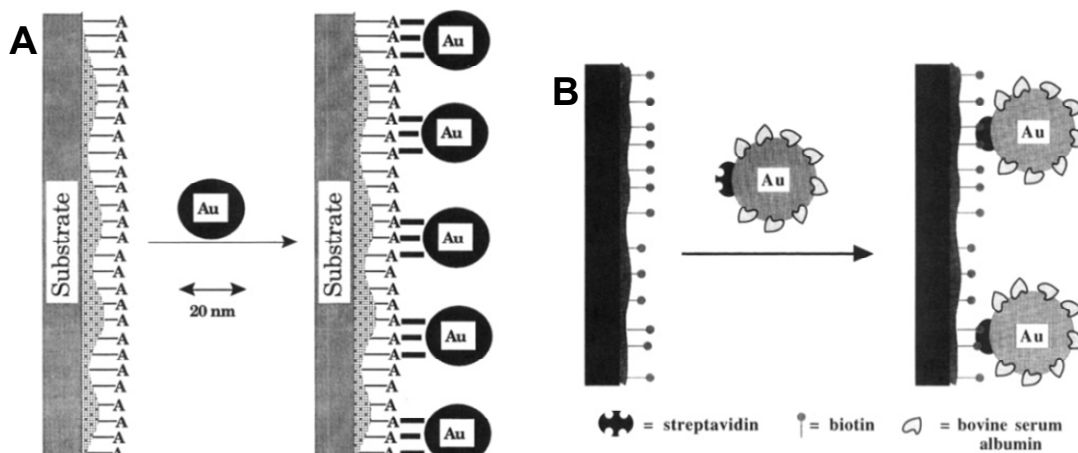


Figure 4-1. Schematics of nanoparticle assemblies on solid substrates. (A) Gold nanoparticles covalently bound to a self-assembled monolayer; the terminal functional group, A, binds to nanoparticles and adheres them to the surface (B) Gold nanoparticles adsorbed to the substrate through non-covalent interactions; nanoparticles coated with streptavidin interact with a biotinylated surface. Schematics taken from Grabar et al.⁷

particles were bound to aluminum with an acid thiolate monolayer.⁶

Arrays of particles covalently bound to a substrate are reported to be extremely stable.^{6,7,9,10} Surface-bound molecules often displace the capping ligands of particles in solution in order to facilitate binding.⁸ However, once bound to the surface, the displacement of the molecular linkers has not been observed.^{7,10} These structures appeared to be extremely resistant to ligand-exchange. In addition to the strong bonds between the particles and the substrate, forces between particles

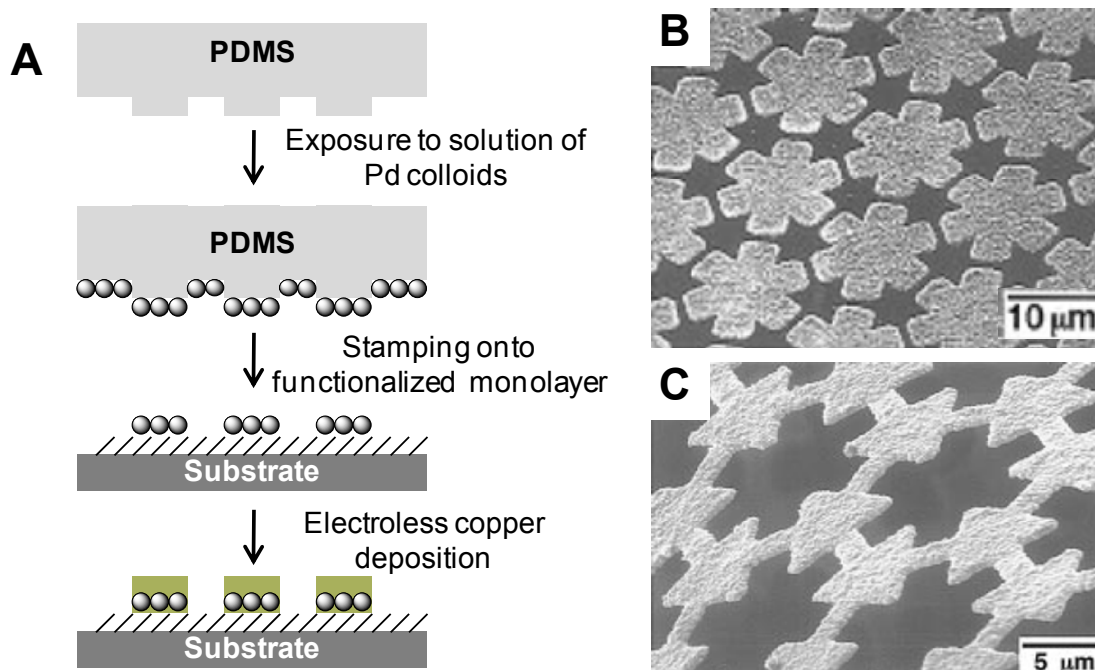


Figure 4-2. Microcontact printing of palladium colloids (A) Method used to form surface patterns (B, C) SEM images of patterns formed after electroless copper deposition. Images taken from Hidber et al.¹³

(Section 2.1.1) also stabilized these arrays and contributed to long-range order.^{7,9}

Both inter-particle repulsion and strong particle-surface bonds have been attributed to the fact that adjacent particles do not coalesce nor do they physically adhere to the substrate.^{7,9,10} Both TEM images and optical absorption spectra indicate that particles were well-separated. In addition, narrower size distributions have been observed for surface-bound particles relative to those in solution.⁶ This phenomenon suggests that either kinetic or thermodynamic factors could favor the binding of one particle size over another.⁶

In addition to uniform particle arrays formed on surfaces, patterns have also been formed using micro-contact printing.¹³ In one example, stamps were formed out of poly(dimethylsiloxane) (PDMS), and then exposed to solution of palladium nanoparticles stabilized with tetraoctadecylammonium bromide (Figure 4-2 (A)). The stamp was then brought into contact with a monolayer-covered substrate to generate a pattern of particles on the surface. In addition to having a strong affinity for the monolayer, the particles used here needed to be sufficiently hydrophobic that they were able to wet the PDMS stamp. This process was ineffective for particles capped with ammonium bromides containing shorter alkyl chains.¹³ As palladium particles can catalyze the electroless deposition of metals, these surface-bound particles were used for the selective deposition of copper. Figure 4-2 shows patterns formed using this technique.

In addition to pattern formation, surface-bound particles can be used as a platform to study inter-particle interactions,⁶ and to measure the electronic properties of molecules between two metallic contacts.² Interactions between particles lead to enhanced Raman scattering and fluorescence,⁹ which makes these assemblies useful as surface-enhanced Raman scattering (SERS) substrates.^{7,9,10} In the context of this work, these studies demonstrate the feasibility of using molecular linkers to create stable nanoparticle assemblies.

These concepts have been extended to bind nanoparticles together on a surface. Andres et al.⁸ formed a monolayer of dodecanethiol-capped gold particles on a

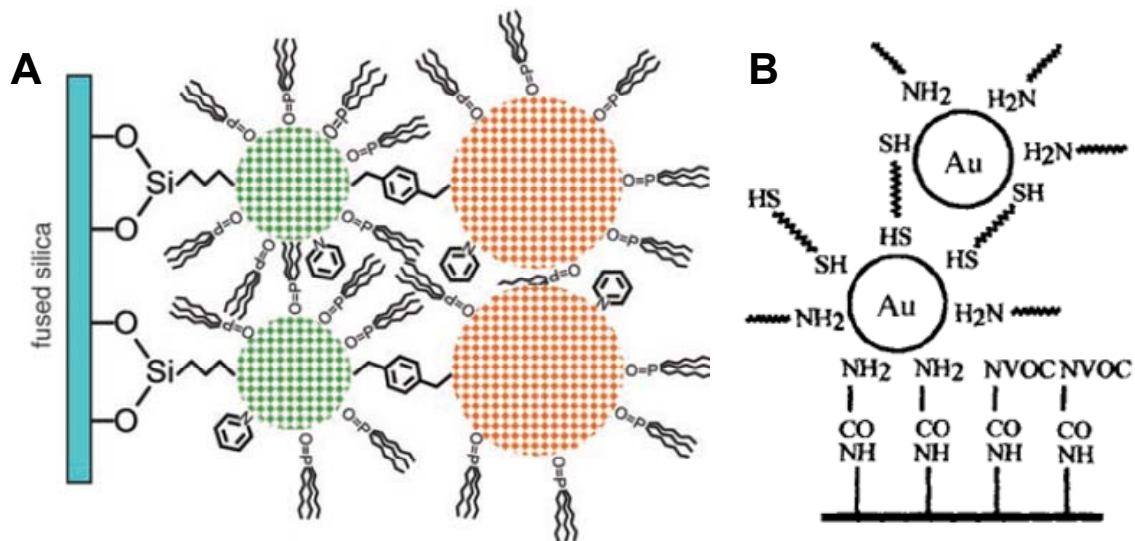


Figure 4-3. Schematics of nanoparticle assemblies formed on substrates (A) Bilayer created using two different sizes of CdSe quantum dots bound by 1,4-benzenedimethanethiol. Schematic taken from Ouyang et al.¹⁵ (B) Bilayer of gold particles capped with 12-aminododecane bound by 1,8-octanedithiol on a patterned substrate. Schematic taken from Vossmeier et al.³⁴

surface, and then exposed the substrate to a solution of aryl dithiol and di-isocyanides. These molecules displaced the dodecanethiol capping ligands and covalently linked adjacent particles. While the distance between particles increased slightly due to the length of the linker molecules, the long-range order of the monolayer was maintained. This process resulted in a two-dimensional network of linked particles. Based on conductivity measurements, approximately thirty-two molecules were found to link adjacent particles.⁸

Ouyang et al.¹⁵ created three-dimensional particle networks by forming layers of particles on a substrate. A monolayer of CdSe quantum dots was bound to a silica substrate by a silane functionalized with a thiol or amine group. This monolayer was exposed to 1,4-benzenedimethanethiol and then another quantum dot solution. Figure 4-3 (A) shows a particle bilayer created using two different sizes of CdSe particles. This process can be repeated to achieve multi-layered structures.¹⁵ A similar procedure was performed by Vossmeier et al.³⁴ They created a surface pattern of gold nanoparticles using a monolayer of 3-aminopropyldimethylethoxysilane treated with nitroveratryloxycarbonylglycine (NVOC-GLY). NVOC is a photo-removable protecting group, which yields an amine upon exposure ultraviolet/visible radiation. Using a mask, selective deprotection was achieved and gold particles capped with 12-aminododecane were bound to the deprotected amine groups as shown in Figure 4-3 (B). These surface-bound

particles were then exposed to 1,8-octanedithiol to create multi-layered structures. It was assumed that the thiol displaced the amine capping ligands to facilitate binding.

More complex structures have been created using similar concepts. Liu et al.⁴

bound gold particles to CdTe tetrapods* as shown in Figure 4-4. A layer of tetrapods

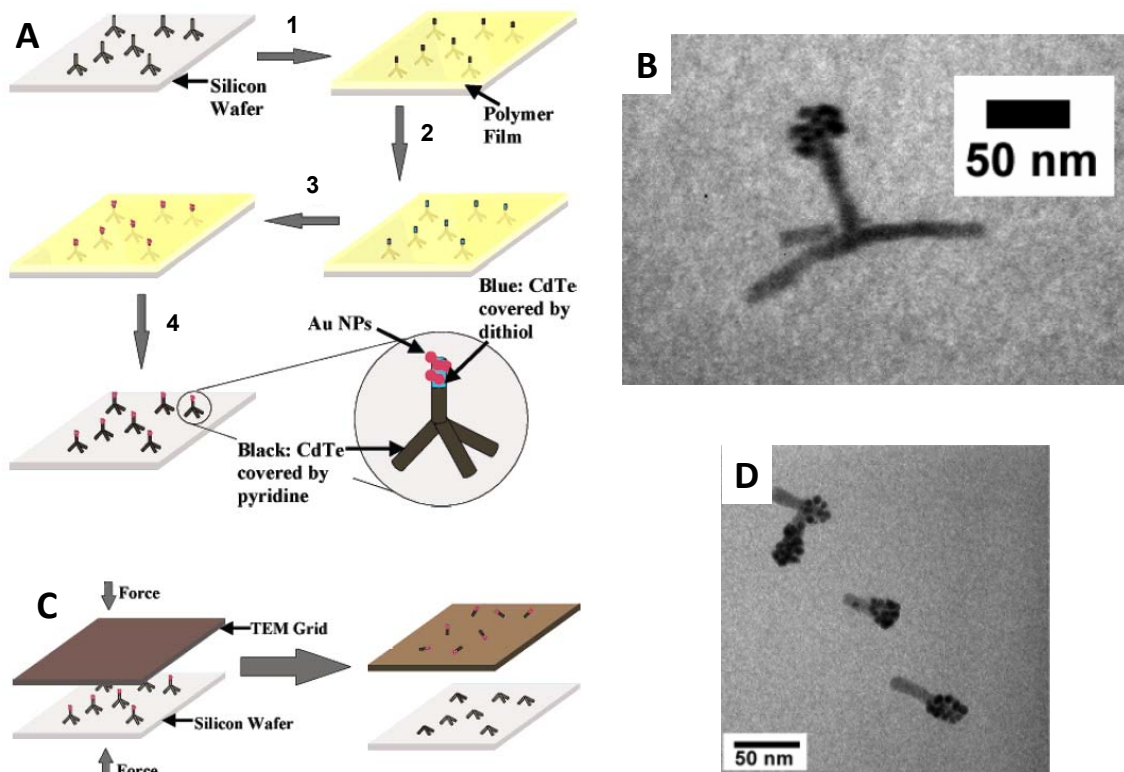


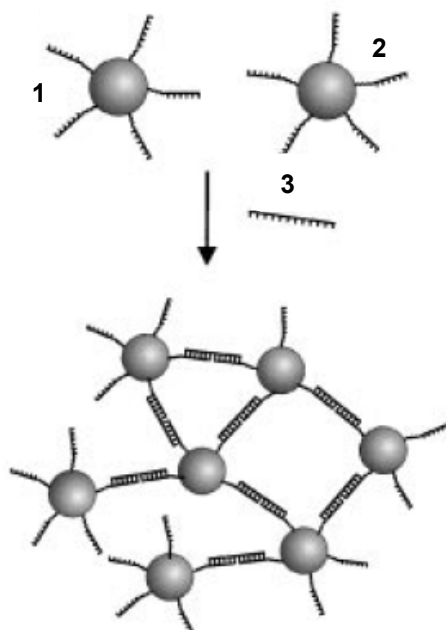
Figure 4-4. (A) Reaction scheme showing asymmetric functionalization of CdTe tetrapods. Step 1: spin-coat polymer to partially cover tetrapods. Step 2: addition of hexanedithiol. Step 3: attach gold nanoparticles (red dots). Step 4: dissolve polymer layer (B) TEM image of formation from CdTe tetrapod functionalized with 5 nm gold nanoparticles (C) Schematic showing nanrod formation by breaking tetrapods using a TEM grid (D) TEM image of CdTe nanorods asymmetrically functionalized with 5 nm gold nanoparticles. Images taken from Liu et al.^{4,5}

* The synthesis of tetrapods was described in Section 2.1.2.3.

was deposited on a substrate in the absence of a molecular monolayer; three arms contacted the surface while one pointed away. While some aggregates were formed, approximately 80% of these structures were isolated on the surface. A polymer film was then deposited to cover the bottom three arms of the tetrapod, leaving only one exposed. The exposed arm was then functionalized with hexanedithiol, which bound gold nanoparticles coated with trioctylphosphine (TOP). This capping ligand was chosen as it is readily displaced by the bound thiol groups. Again, additional exposures to dithiol and gold particles yielded multi-layers. The tetrapods could be re-dispersed into solution upon dissolving the polymer film. As shown in Figure 4-4, the exposed arm could also be broken off using a TEM grid to yield asymmetrically-functionalized nanorods.

4.1.2. Synthesis of Solution-Based Nanoparticle Networks

In addition to nanoparticle assemblies constructed on surfaces, assemblies have also been synthesized in solution both with and without molecular linkers. For example, Brust et al.³⁵ synthesized gold nanoparticles with dithiol capping ligands. Particles capped with 1,5-pentanedithiol, 1,6-hexanedithiol and p-xylenedithiol formed insoluble cross-linked networks.³⁵ The authors also synthesized gold particles stabilized without a thiolate capping ligand, stabilized by only tetraoctylammonium cations. Both p-xylenedithiol and 1,12-dodecanethiol were added to these particles post-synthesis to yield covalently-linked particle networks.



- 1 5' SH(CH₂)₆-A₁₀-CGC ATT CAG GAT 3'
 2 3' SH(CH₂)₃-A₁₀-ATG CTC AAC TCT 5'
 3 5' TAC GAG TTGAGA ATC CTGAAT GCG 3'

Figure 4-5. Schematic representation of DNA-directed assembly of gold nanoparticles Schematic taken from Park et al.²⁵

In both cases, TEM images indicated that the molecular linkers held the particles at a fixed distance, and the particles did not fuse together.³⁵

Similar particle networks have been generated through non-covalent interactions. For example, Park et al.²⁵

functionalized two solutions of gold particles with non-complimentary thiolated DNA strands.²⁵ These two solutions

were then mixed in the presence of a third linker oligonucleotide, which was complementary to both DNA sequences. This third DNA sequence linked the functionalized particles into an extended network as shown in Figure 4-5. The kinetics of this process were slow, most likely due to both the steric and electrostatic repulsion between adjacent oligonucleotide-functionalized particles.³⁶ Similar procedures have been performed by Elghanian et al.³⁶ and Mirkin et al.³⁷ These non-covalent interactions can be reversed upon exposure to heat.^{5,36,37} As the

optical properties of particles change when they are bound into networks, these types of systems have potential as sensors.^{36,37} The formation of particle networks indicates the presence of the linker oligonucleotide.

Nanoparticle networks have also been formed through reactions between the capping ligands on adjacent particles. Brust et al.³⁸ were the first to demonstrate this behavior using gold particles capped with p-mercaptophenol.⁵ Esterification of the terminal hydroxy groups yielded a covalently-linked network. Infrared spectroscopy indicated that the esterification reactions were not complete, a behavior that was attributed to steric hindrance created by the closely-packed monolayer on the particle surface.³⁸ A similar process was performed by Noglik et al.²⁰ to create

networks of cadmium

sulfide quantum dots.

Thiophenol-capped

particles were

synthesized with 8% of

a pyridine capping

functionality, which

reacted with α,α' -

dibromo-p-xylene to

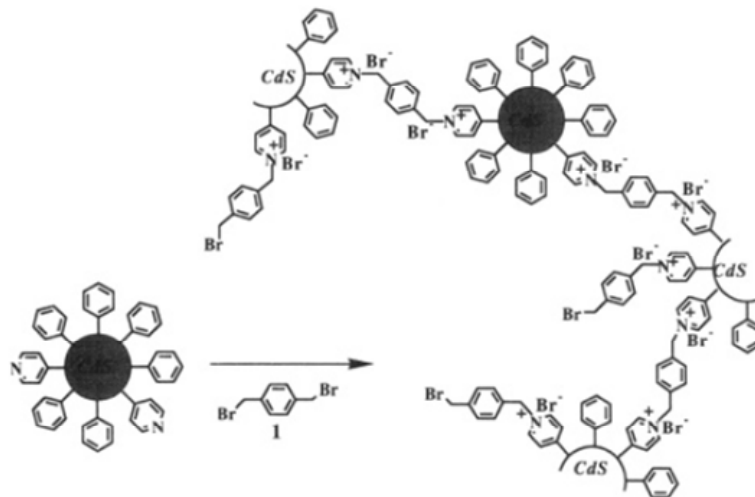


Figure 4-6. The formation of a cadmium sulfide particle network through the reaction of α,α' -dibromo-p-xylene with pyridine functionalities on adjacent particles. Schematic taken from Noglik et al.²⁰

form quantum dot polymeric materials as shown in Figure 4-6.²⁰ Performing organic reactions within a particle solution requires that the reaction conditions are mild enough not to affect particle stability. In addition, the particle solutions should be extremely pure in order to avoid any detrimental side reactions. These requirements limit the applicability of this approach.

4.1.3. Synthesis of Isolated Nanoparticle Aggregates

The methods described up to this point create extensive nanoparticle networks with very little control over the number of particles in each assembly. However, the primary focus of this work was to create nanoparticle dimers and trimers, a process requiring more control over reaction conditions. One method that has been used involves fusing nanoparticles together without a molecular linker through a controlled aggregation process. As discussed in Section 2.1.1.1, the electrostatic repulsive forces between particles are a function of the particle size, the charge density on the particle surface, the dielectric constant and the ionic strength of the solution. With careful control of these variables, one can induce particle collisions and aggregation.^{23,33,39}

McDermott et al.³⁹ gradually increased the ionic strength of both micrometer-sized gold and silver particle solutions to induce aggregation. The aggregation process was then stopped by diluting the solution to decrease the ionic strength. Dilution was performed early enough that some dimers were formed among isolated

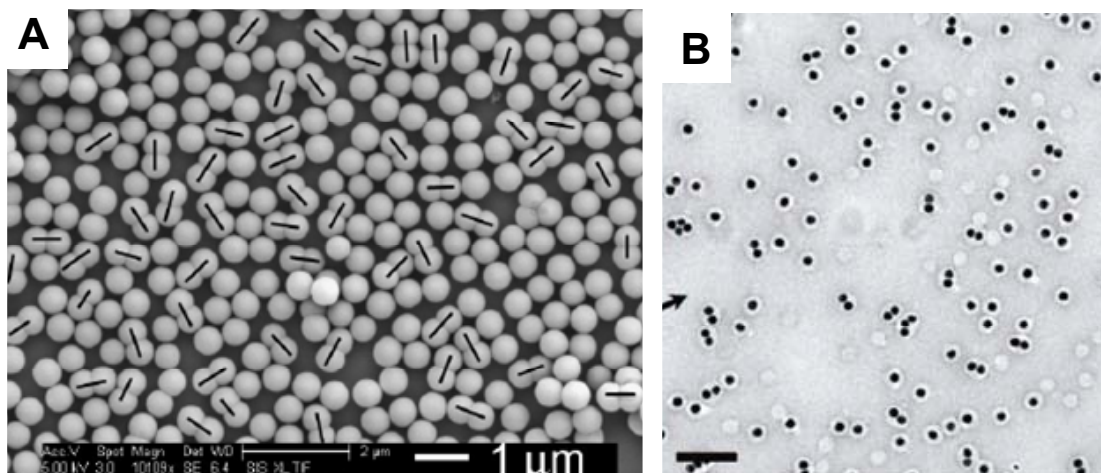


Figure 4-7. Dimers formed through controlled aggregation (A) SEM image of silica particles (330 nm) and dimers. Dimers are marked with a black line. Image taken from Ibisate et al.²³ (B) TEM image of gold particles (15 nm) and dimers coated with a polymer shell. Image taken from Chen et al.³³

particles, but very few higher-order aggregates were observed. The observed yield of dimers was approximately 20%. When this process was performed in a solution containing both gold and silver particles, the dimers were a mix of gold-gold, silver-silver and gold-silver structures. The homodimeric structures exhibited greater mechanical stability than the heterodimers, which separated during sonication.³⁹

A similar process has been performed using silica particles.²³ An ammonia solution was added to protonate the surface silanol groups and induce aggregation. Once the particles aggregated, a fresh solution of the sol-gel precursor, tetraethoxysilane (TEOS) was added. The additional TEOS hydrolyzed and condensed onto the

aggregated colloids, permanently fixing them together.* The yield of dimers appeared to be dependent upon the size of the silica particles with 50% of 280 nm particles forming dimers and 33% of 330 nm particles forming dimers. It was also noted that as the dimer yield increased, so did the yield of higher-order aggregates. Figure 4-7 (A) shows an SEM images of silica dimers synthesized using this method. Figure 4-7 (B) shows a TEM image of gold particles, which were aggregated by the slow addition of NaCl and then coated with a polymer shell. In this case, approximately 24% of the particles formed dimers.³³

Another technique used to form nanoparticle assemblies without a molecular linker involves coating silica particles with a layer of gold. As shown in Figure 4-8 (A), a monolayer of silica particles was formed on a glass surface and then coated by electron-beam evaporation. An adhesion layer of titanium or nickel (0.5-0.8 nm) was deposited followed by a layer of gold (8-15 nm).^{1,3} Due to the orientation of the silica particles on the surface, only the top halves were coated. Upon annealing these composite structures at 700 °C, the mobility of the gold atoms increased and the gold de-wetted the silica bead resulting in the heterodimeric structures shown in Figure 4-8 (B) and (C).³ The relative sizes of the two particles could be tailored by altering the size of the silica particles and the thickness of the gold layers. The heterodimers were removed from the glass surface by sonication.

* Hydrolysis and condensation of TEOS are discussed in Section 3.1.1.1.1.

Heterodimeric

structures of gold and

iron oxide have been

synthesized through

the thermal

decomposition of iron

pentacarbonyl in the

presence of gold

particles.^{18,40,41*}

Upon the nucleation

of Fe_3O_4 on the

surface of the gold particles, the gold particles became electron deficient as

indicated by a red-shift in the optical absorption spectrum. In non-polar solvents,

this phenomenon prevented multiple nucleation events from occurring on the particle

surface, and heterodimeric structures were formed as shown in Figure 4-9 (A) and

(B). The charges present in highly polar solvents compensated for the electron

deficiency on the gold particle surface, and under these conditions multiple

nucleation events occurred on each particle yielding the 'flower-like' structures

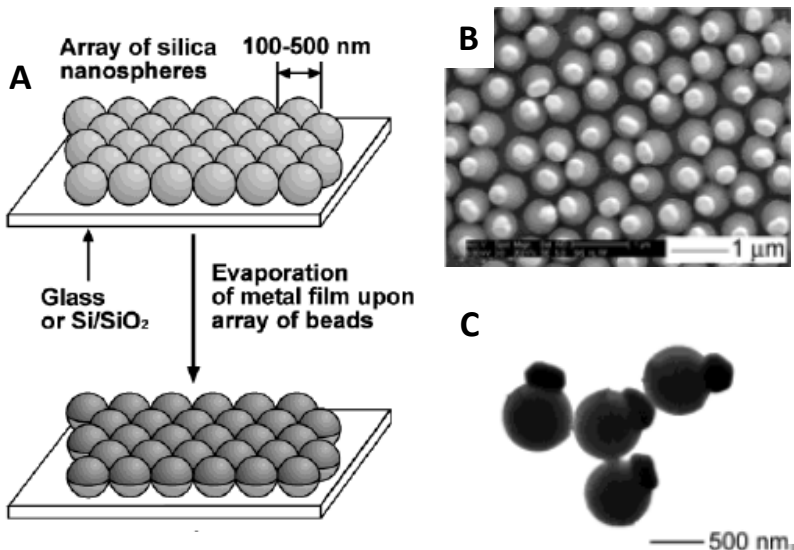


Figure 4-8. (A) Method for coating the top of silica beads with a gold film. Schematic taken from Love et al.^{1,2} (B) SEM images of SiO_2 beads (600 nm) after coating with Ti/W alloy (5 nm) and gold (25 nm) and annealing at 700 °C (C) TEM image of Au/SiO_2 dimers after removal from substrate. Images taken from Lu et al.^{2,3}

* The synthesis of iron oxide particles through the thermal decomposition of iron pentacarbonyl in the presence of oleic acid is described in Section 3.1.1.3.3.

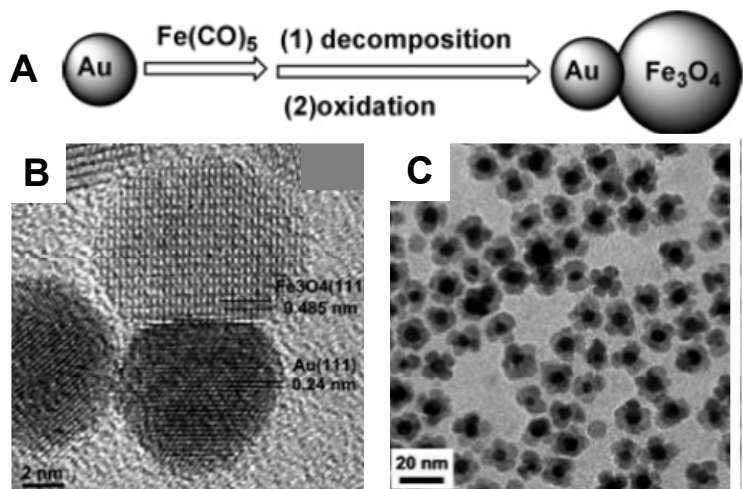


Figure 4-9. (A) Formation of heterodimeric structures through the thermal decomposition of iron pentacarbonyl in the presence of gold particles. (B) TEM image of heterodimer formed in non-polar solvent. (C) TEM image of 'flower-like' structures formed in polar solvent. Images were taken from Yu et al.¹⁸

shown in Figure 4-9 (C).¹⁸

A similar process was reported for heterodimer formation through the nucleation of nickel on CoFe_2O_4 particles.⁴²

Micelles have also been used to control the number of nucleation events in the formation of

heterodimeric structures. A solution of Fe_3O_4 particles in organic solvent was added to an aqueous solution of silver nitrate and then sonicated to form an emulsion as shown in Figure 4-10 (A).²⁸ The iron oxide particles assembled at the liquid-liquid interface. In this case, the Fe(II) acted as a catalyst for the reduction of the silver ions; however, multiple nucleation on the Fe_3O_4 surface was limited as the particles were only partially exposed to the aqueous phase.²⁸ Figure 4-10 (B) shows a TEM image of heterodimers formed using this technique. Similar methods were used to synthesize FePt-Ag (Figure 4-10 (C)) and Au-Ag heterodimers. These structures were soluble in organic solvent. While molecular linkers were not used in this study, post-synthetic particle modification was performed and provided another example of

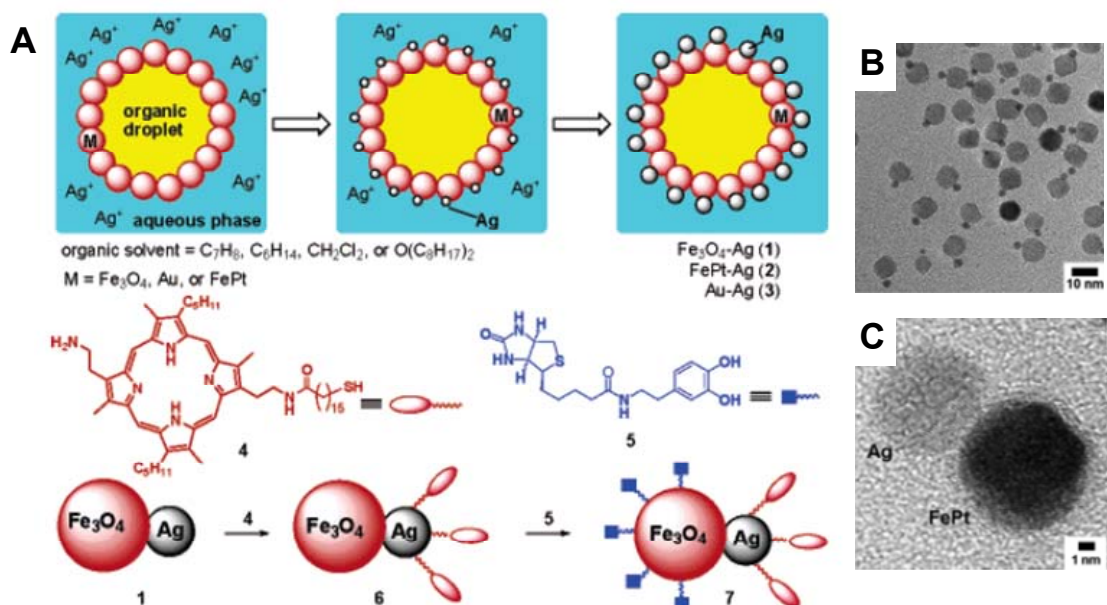


Figure 4-10. (A) Schematic showing the formation of $Fe_3O_4\text{-Ag}$ heterodimers at a micellar interface and the subsequent selective functionalization (B) TEM image showing $Fe_3O_4\text{-Ag}$ heterodimer (C) TEM image showing $FePt\text{-Ag}$ heterodimer. Images taken from Gu et al.²⁸

orthogonal self-assembly. A fluorescent thiol selectively bound to the silver surface while a diol bound to Fe_3O_4 .²⁸

4.1.4. Solution-Based Synthesis of Molecularly-Linked Nanoparticle Dimers and Trimers

While the last several examples have described the formation of homodimers and heterodimers of aggregated particles, the goal of this work was to link particles together with a molecular linker in solution. One of the first examples of this involved non-covalent interactions between DNA oligonucleotides. DNA was ideal as it is similar in size to the nanoparticles.²⁹ Figure 4-11 shows several different ways in which nanoparticles have been linked using DNA. A tail-to-tail configuration was

achieved by binding complimentary oligonucleotides to two different particles (Figure 4-11 (A)).²⁹ A head-to-tail configuration was achieved by mixing DNA-functionalized particles with a longer complimentary chain (Figure 4-11 (B,C)).²⁹ More complex structures were also synthesized by functionalizing thiolated strands with gold nanoparticles and then incubating them with differently-functionalized complimentary strands (Figure 4-11 (D,E)).²⁹ Nanoparticle dimers have also been synthesized by mixing gold particles functionalized with two different oligonucleotides with a third linking oligonucleotide in a process similar to those used for larger networks (Figure

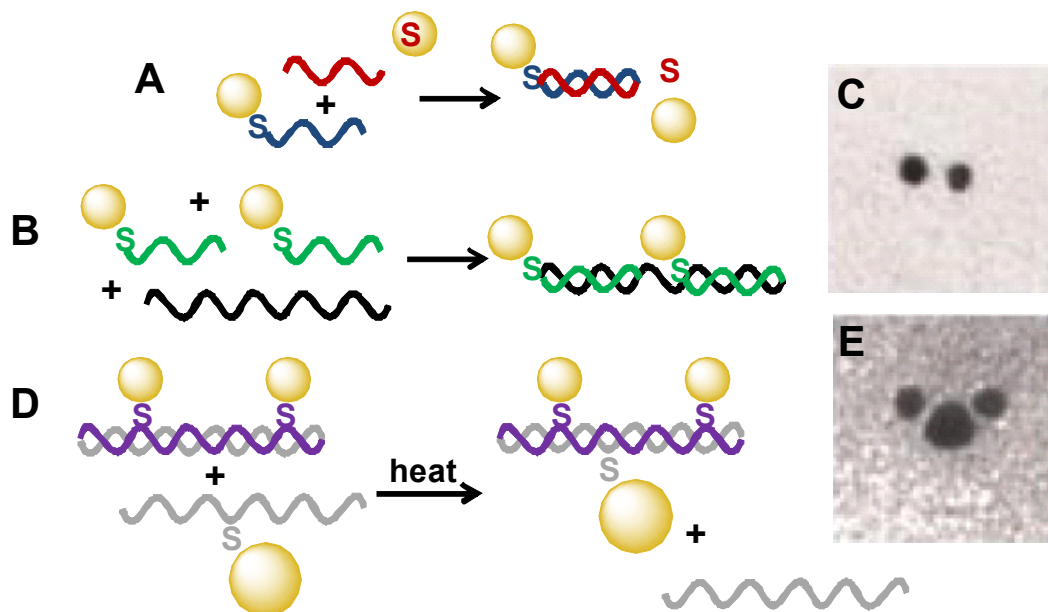


Figure 4-11. (A) Schematic for the formation of a gold nanoparticle dimer from gold nanoparticles functionalized with complementary DNA strands (B) Schematic for the formation of a dimer from DNA-functionalized gold nanoparticles bound by a longer, complimentary strand (C) TEM image of a dimer formed using the method shown in (B). (D) Schematic of a trimer formation from complimentary thiolated-DNA strands bound to nanoparticles (E) TEM images of trimer formed using the method shown in (D). The schematics were adapted from and the images taken from Loweth et al.²⁹

4-5).⁴³ The formation of isolated dimers required that only one DNA strand is bound to each particle; however, the methods used to achieve mono-functionalization were not described.⁴⁴ Similar methods have been applied to synthesize core-satellite structures as shown in Figure 4-12.¹⁶ In this case, 8 nm gold particles were functionalized with one oligonucleotide and 31 nm gold particles were functionalized with another. These particles were mixed in a 120:1 ratio in the presence of a third linking oligonucleotide.

While isolated nanoparticle assemblies were synthesized using DNA linkers, several purification steps were required to remove side products and isolate the desired structures. Loweth et al.²⁹ did not report initial dimer yields. However, they performed two preparative-scale gel electrophoretic separations and obtained a solution of 5 nm gold particles in which

90% of the particles were dimerized.

For the case of the core-satellite structures, there was no evidence of 31 nm particles without any neighboring satellites; however, the number of satellites per core varied.¹⁶

Nanoparticle assemblies have also been synthesized in solution using covalently-

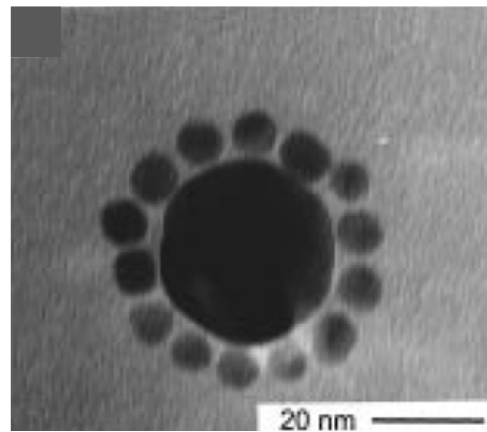


Figure 4-12. Nanoparticle assembly consisting of a gold core (31 nm) surrounded by smaller gold satellites (8 nm). Images taken from Mucic et al.¹⁶

linked organic molecules. As the molecules used are typically significantly smaller than the corresponding particles, controlling the number of functional groups on a nanoparticle surface proved challenging. Dadosh et al.⁴⁵ synthesized homodimers of gold particles linked by 4,4'-biphenyldithiol, bis(4-mercaptophenyl) ether and 1,4-benzenedimethanethiol. The authors varied the concentrations of the linker molecules and determined that a 1:10 ratio of ligand to particle was required in order to limit the formation of trimers and larger aggregates. The dimers were then separated from the individual particles by centrifugation through glycerol or sucrose density gradients. Surface-enhanced Raman scattering measurements were performed to verify the presence of the molecular linkers between the particles. The 'blinking' observed in the Raman signal supported the conclusion that a single molecule bridged the two particles.⁴⁵

Similar nanoparticle assemblies were synthesized by Novak et al.^{12,46-49} who bridged oligomeric phenylene ethylenes (OPEs) between gold and silver nanoparticles. In this case, a stoichiometric amount of linker was added to the particle solution over a period of 1-1.5 hours while stirring.^{12,46} The slow linker addition appeared to limit the formation of larger aggregates. Figure 4-13 shows the molecular linkers used to synthesize nanoparticle dimers, trimers, tetragonal planar tetramers and tetrahedral tetramers. These molecules bound to nanoparticles after in-situ deprotection of the acetyl protecting group. It can be seen that the rigid molecules hold the particles at

a fixed distance. It was noted that similar experiments with 1,6-hexanedithiol did not yield dimers.¹² The reported yields for these structures ranged from 30%¹² to 50%⁴⁷ for dimers, from 25%¹² to 30%⁴⁷ for trimers and were 10% for tetramers.^{12,47} For dimeric structures, blinking was observed in surface-enhanced Raman scattering experiments to indicate the presence of a single molecule between the two particles.¹²

Ying et al.¹⁷ synthesized similar nanoparticle dimers and linear chains using a series

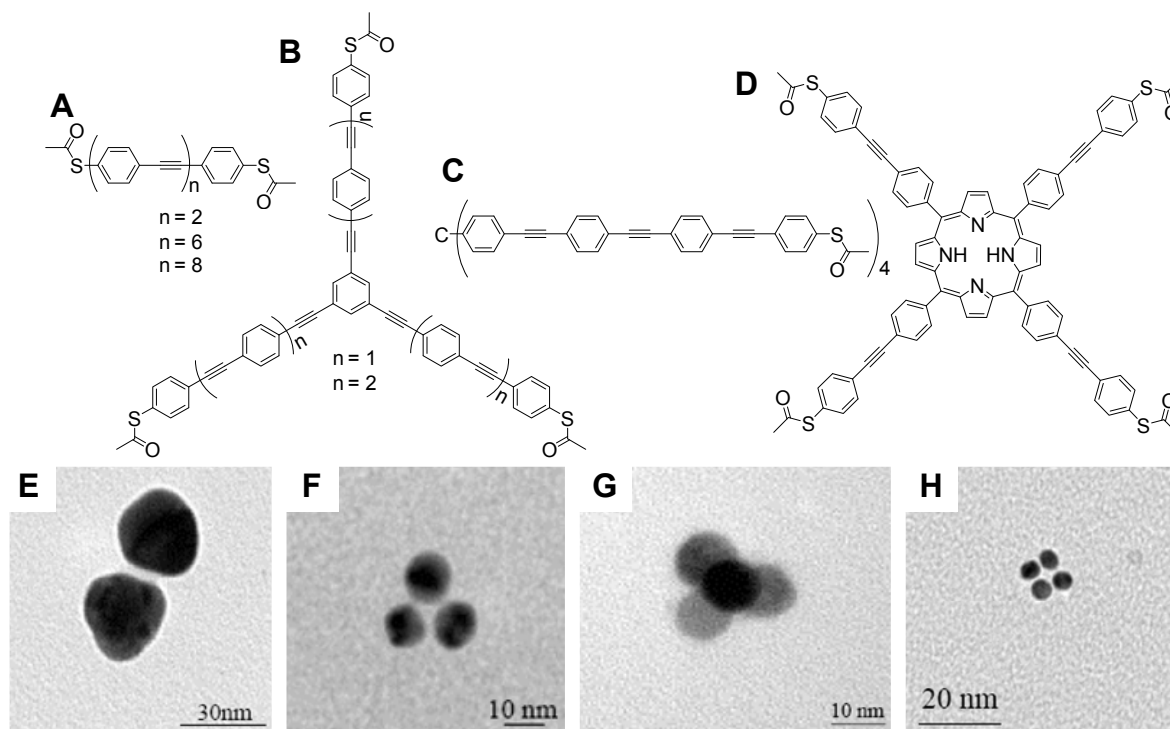


Figure 4-13. (A) Linear oligomeric phenylene ethylene (OPE) used to synthesize nanoparticle dimers (B) Trigonal planar OPE used to synthesize nanoparticle dimers (C) Tetrahedral OPE used to synthesize nanoparticle tetramers (D) Tetragonal planar OPE used to synthesize nanoparticle tetramers (E) Dimer composed to 30 nm silver particles (F) Trimer composed of 10 nm gold particles (G) Tetrahedral trimer composed of 10 nm gold particles (H) Planar tetramer composed of 10 nm gold particles. Images were taken from the Doctoral Thesis of James Novak.¹²

of diruthenium-bis(OPE) compounds as shown in Figure 4-14. The authors used a trimethylsilane thiol protecting group rather than the acetyl group used by Novak et al. Similar to Novak et al.,⁴⁷ the authors observed a 30-35% yield of dimers in solution.¹⁷ Larger aggregates, specifically linear chains, were also observed.

In both studies, the distance measured between particles in the TEM images was smaller than the corresponding linker lengths. Novak et al.¹² attributed this phenomenon to uncertainties regarding the thiol-gold bond angle. Self-assembled monolayers of thiols on gold form a 30 ° angle with respect to the substrate. While this is attributed to interactions between adjacent molecules in the monolayer which are not present in this scenario, there could have been some flexibility in this bond angle affecting the observed inter-particle distance. A change in the bond angle of 5 ° can decrease this distance by more than a nanometer.¹² Ying et al.¹⁷ attributed these discrepancies to the orientation of the dimers on the TEM grid, which may be

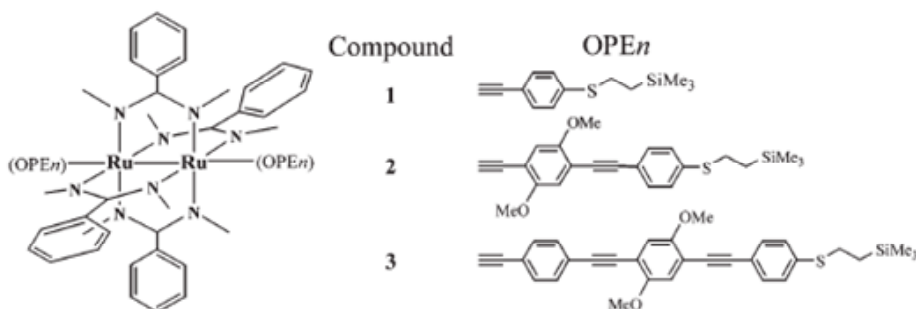


Figure 4-14. Diruthenium-bis(OPE) compounds used to synthesize nanoparticle dimers and linear chains. Image taken from Ying et al.¹⁷

angled away from the plane of view. This behavior could easily be observed as the result of

any surface roughness on the grid. As will be discussed later in this chapter, the inability to correlate the distance between particles leads to some uncertainty as to whether a linker is actually present between two particles observed by TEM.

Another report of homodimer synthesis involved bridging CdSe nanoparticles with bis(acyl hydrazide).²⁶ The authors used a 0.5:1 ratio of bis(acyl hydrazide) to particles and observed the presence of many large aggregates. These aggregates were removed through size-selective precipitation. Several purification steps were required in order to obtain the enriched homodimer sample shown in Figure 4-15 (B).

There has also been a reported attempt to synthesize nanoparticle heterodimers using a bifunctional linker and orthogonal self-assembly.⁵⁰ A bifunctional linker of the form HS-(CH₂)_n-COOH (n = 1-3) was used to bind CdS and TiO₂ particles. The thiol was intended to bind to the CdS particles while the carboxylic acid was intended

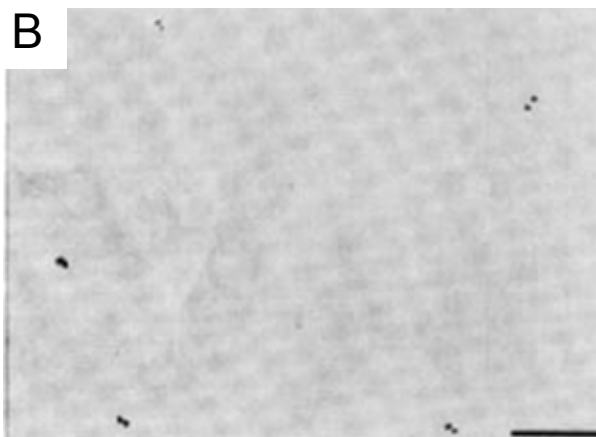
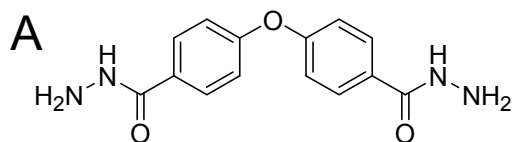


Figure 4-15. (A) Structure of bis(acyl hydrazide) (B) TEM image of CdSe homodimers linked by bis(acyl hydrazine) after repeated size-selective precipitation to isolate dimers. Image taken from Peng et al.²⁶

to bind to the TiO₂. The CdS particles used were capped with mercaptopropionic acid and the TiO₂ particles were electrostatically stabilized (i.e. no capping ligand) after the hydrolysis of TiCl₄.^{*} The concentration of CdS particles (2.1 nm) used was approximately 50 times larger than that of TiO₂ (6.6 nm) on the premise that this decreased the likelihood that more than one TiO₂ particle would bind to each CdS particle. The authors were interested in studying the electron transfer between the conduction band of the CdS to the TiO₂ particles upon binding. They claim that this quenching phenomenon would not be affected if more than one CdS particle was bound to any given TiO₂; thus, no efforts were made to limit this behavior.¹⁷

The only indication that nanoparticle assemblies involving TiO₂ and CdS particles were formed was the observed electron transfer between the two materials. While it should have been possible to differentiate between the two particle sizes in a TEM image, the authors claim that their imaging attempts failed due to the negligible contrast between the two materials.¹⁷ This lack of data creates uncertainty regarding the morphology of these nanoparticle assemblies and the extent of binding. It was noted, however, that the observed binding was reversible. When high concentrations of NaClO₄ were added to solution, the TiO₂ particles preferentially precipitated leaving unbound CdS particles in solution.¹⁷

* The synthesis and stability of TiO₂ particles synthesized from the hydrolysis of TiCl₄ is discussed in Section 3.1.1.2.4.

The solution-phase syntheses of nanoparticle dimers described above exhibited low yields due to difficulties associated with the mono-functionalization of nanoparticles. High concentrations of the molecular linkers led to higher-order aggregates. Attempts to limit aggregation by incorporating low concentrations of the linkers resulted in high concentrations of unreacted monomers. As both the particle and linker concentrations were lowered, the collision efficiency decreased. Post-synthetic separation techniques were required to separate out both individual particles and higher-order aggregates.

4.1.5. Synthesis of Nanoparticle Assemblies Using Solid Phase Place-Exchange

One method utilized to monofunctionalize nanoparticles and increase the yield of dimers in solution involves a solid-phase place-exchange reaction.^{14,22} These methods take advantage of the low-packing density of functional groups on many solid-phase supports. A commonly-used solid-phase support is a polystyrene Wang resin. Each hydroxide functional group on a Wang resin suspended in DMF occupies a volume of approximately 9 nm³. Because of the large distance between functional groups, nanoparticles with diameters of approximately 2 nm or less can be added to the solid support with only one bond forming on each particle.²²

The mono-functionalization of butanethiol-capped gold particles shown in Figure 4-16 (A) involved binding a protected 6-mercaptohexanoic acid to a polystyrene

Wang resin.¹⁴ After deprotection of the acetyl group, gold nanoparticles were bound to the exposed thiols. After removing any unbound particles, the bound particles were cleaved from the surface using a solution of trifluoroacetic acid in methylene dichloride. The resulting particles were functionalized with a single carboxylic-acid terminated ligand. Upon the addition of an excess of 1,7-diamino heptane, adjacent carboxylic acids reacted to form homodimers.¹⁴ The yield of dimers using this method was approximately 60-70%. Less than 5% of the particles were bound in trimers or larger aggregates suggesting that some of the particles were functionalized by more than one ligand. In addition, about 25% of the particles appeared to be isolated.¹⁴ It was not clear whether the isolated particles were not

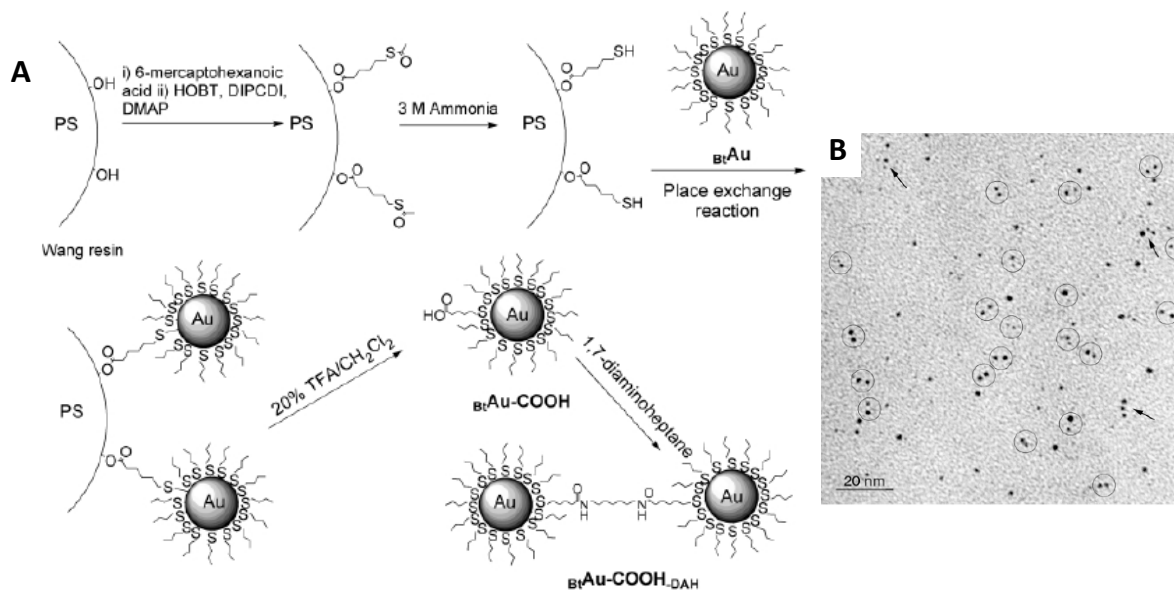


Figure 4-16. Gold nanoparticle dimers synthesized using a solid phase approach (A) Reaction scheme showing dimer formation (B) TEM images of gold nanoparticle dimers synthesized from particles 2.8 nm in diameter. Images taken from Worden et al.¹⁴

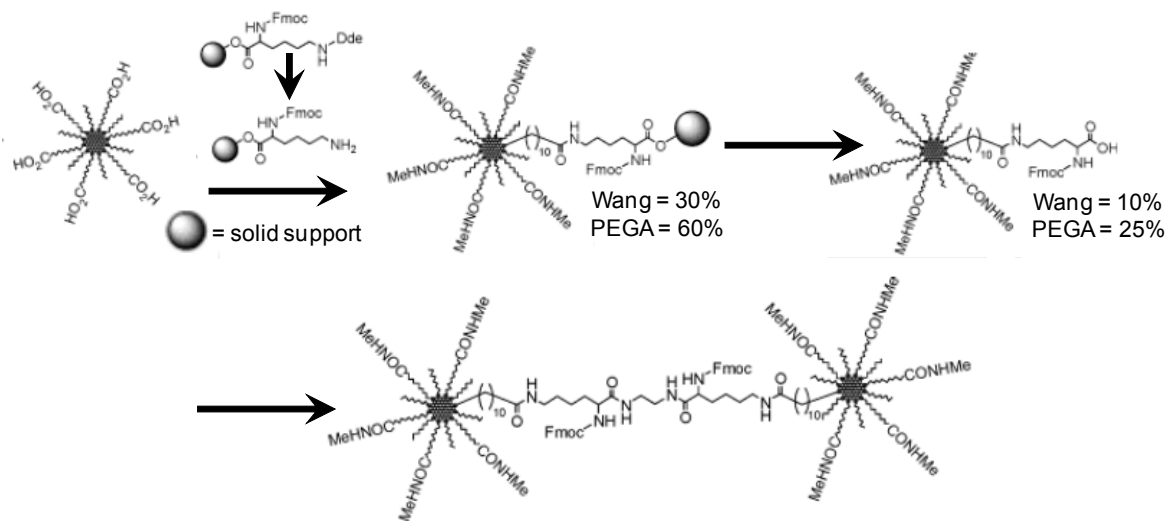


Figure 4-17. Synthesis of dimers from mono-functionalized gold nanoparticles. The particles were functionalized using both polystyrene Wang and poly(ethylene glycol)acrylamide (PEGA) copolymer-based resins. Schematic taken from Sung et al.²²

effectively functionalized using the solid-phase approach or whether they were just not coupled with the diamine.

A similar process was performed to functionalize 2.0 nm gold particles capped with an amphiphilic mixed monolayer of 11-mercaptoundecanoic acid and octanethiolate.²² Both a polystyrene Wang resin and a poly(ethylene glycol)acrylamide (PEGA) copolymer-based resin were used to functionalize these particles with lysine. The nanoparticles were bound to a Fmoc-Lys(Dde)-functionalized resins* after deprotection of the amine as shown in Figure 4-17. Again, the nanoparticles were removed from the solid substrate using trifluoroacetic

* Fmoc = 9-fluorenylmethoxycarbonyl; Dde = 1-(4,4-dimethyl-2,6-dioxocyclohexylidene)ethyl

acid, and the carboxylic functional groups reacted with a diamine to form nanoparticle dimers.²² Based on TEM images, the yield of nanoparticle dimers was approximately 55-60%, comparable to that observed for particle mono-functionalized with 6-mercaptohexanoic acid.¹⁴ However, this yield reflects the number of particles that successfully formed dimers after being cleaved from the solid support. The authors reported relatively low yields associated with both the loading and subsequent cleaving of particles from the resins. The loading of the nanoparticles onto the solid supports occurred with a 30% yield for the Wang resin and a 60% yield for the PEGA-resin. Of those particles successfully bound, only 10% were cleaved from the Wang resin and 25% from the PEGA resin.²² The overall yield for the mono-functionalization reaction using the PEGA-resin (15%) was approximately five times greater than that observed for the Wang-resin, a phenomenon attributed to the increased permeability of the copolymer substrate due to swelling in DMF.²²

While the solid-phase approach facilitates the mono-functionalization of nanoparticles, the overall yields for this process were low. In addition, these methods were not applicable to particles larger than 2 nm. With the density of functional groups on most commercial resins, larger particles would likely be bound by more than one functional group.

An alternative to mono-functionalization is asymmetric functionalization.³⁰ As shown in Figure 4-18 (A), this approach also involves binding particles to a solid substrate.

particle surfaces. Particles asymmetrically-functionalized with MHA were reacted with MEA-capped particles in the presence of the coupling reagents, 1-ethyl-3-(3-dimethylaminopropyl)carbodiimide hydrochloride (EDAC) and pentafluorophenol (PFP), to yield an amide linkage (Figure 4-18 (E)).³⁰ Asymmetrical functionalization of the nanoparticles limited the formation of higher-order aggregates. Based on TEM analysis, the yield of dimers was ranged from 46% to 65%. However, these values only reflect the number of dimers formed from particles successfully cleaved from the solid surface. It is unclear how efficiently the particles bound to and disassociated from the surface. It also appeared that the efficiency of dimerization depended upon particle size.³⁰ The yield of dimers between 16 nm particles was 65% while the corresponding yields for 30 nm particles and 41 nm particles were 57% and 46%, respectively.³⁰

Heterodimers consisting of gold particles of different sizes were also synthesized using the asymmetrical functionalization method (Figure 4-18 (G)). Dimers of 41 nm-30 nm, 41 nm-16 nm, and 30 nm-16 nm were obtained in similar yields, approximately 20% dimers, 50% trimers, 10% tetramers and 10% individual particles.³⁰ The fact that such high yields of trimers and tetramers were observed was attributed to the relative surface areas of the two differently-sized particles. The greater surface area associated with the larger particles is accessible to binding more than one of the smaller particles.³⁰

4.1.6. Optical Properties of Nanoparticle Assemblies

As with isolated nanoparticles, nanoparticle assemblies are often characterized by their optical properties, and a brief discussion of their origin is included below.

Section 2.1.4.1 discussed the enhanced absorption and scattering of nanoparticles due to the surface plasmon resonance (SPR). This property is dependent upon the size, shape and electron density of the material. In addition, the optical properties change when particles are brought in close proximity to one another. This phenomenon is due to the coupling of adjacent SPRs. When the distance between particles is less than the sum of their radii, their plasma dipoles interact.^{29,30,51,52}

This inter-particle electromagnetic coupling results in a strong, localized enhancement of the electric field in the gap between the particles, which has been exploited for spectroscopic techniques such as surface-enhanced Raman scattering.⁵³

The magnitude of the coupling between particles and the resulting optical changes are factors of the distance between the particles, the number of particles grouped together, and their orientation in relation to the incident radiation. When nanoparticles couple, the surface plasmon band displays a red shift, broadens and decreases in intensity.^{29,30} Similar to electron tunneling phenomena, the magnitude of these changes increase exponentially with decreasing inter-particle distances.^{19,21,31,52,54} The spectra for nanoparticles separated by distances greater

than the sum of their radii exhibit some broadening and a decrease in intensity, but with no noticeable red shift.²⁹

The extent of coupling also increases with the number of gold particles bound together.^{19,21,31,54} Both of these effects can be seen from the calculated absorption spectra shown in Figure 4-19. Figure 4-19 (A) shows the spectra for gold nanoparticle assemblies or aggregates consisting of 2600 nanoparticles with increasing volume fractions of gold (i.e. decreasing inter-particle distances). Similar effects can be seen in Figure 4-19 (B) as the size of the assemblies increased (i.e. the number of coupled particles) at a constant volume fraction.³¹ While a solution of dispersed gold particles appears red due to the absorption of green light, aggregated particles appear purple.^{55,56} Several thousand particles need to be grouped together

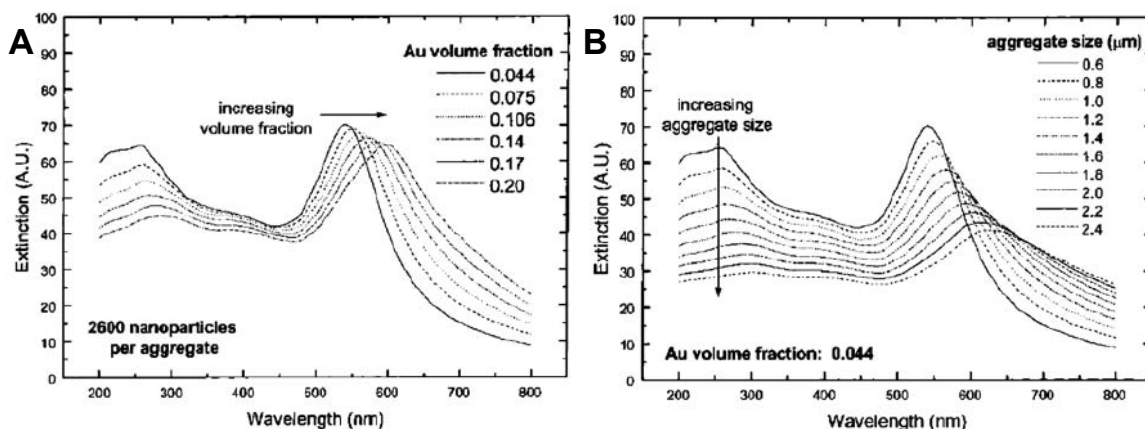


Figure 4-19. Optical absorption of gold nanoparticle assemblies (A) Calculated extinction spectra of spherical aggregates each containing 2,600 Au nanospheres for increasing gold volume fraction. (B) Calculated extinction spectra for spherical aggregates of gold nanospheres in water for increasing aggregate size at a fixed Au volume fraction. Figures taken from Jain et al.³¹

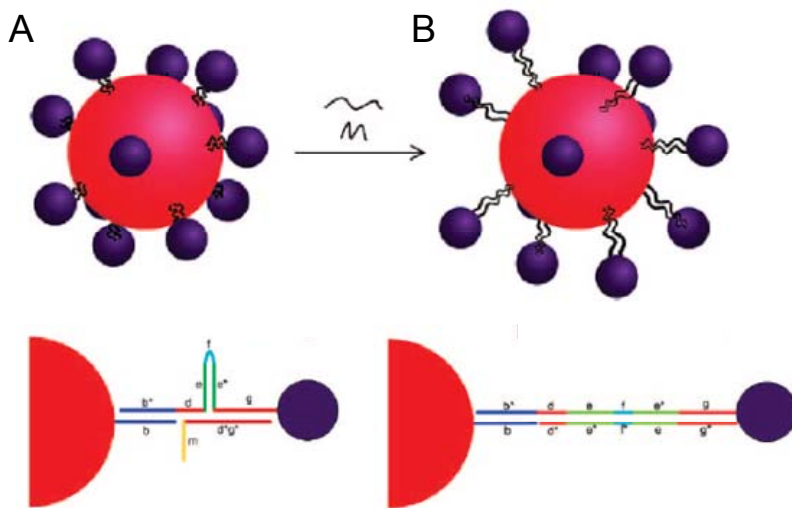


Figure 4-20. Core-satellite structures with reconfigurable tether in both the hairpin (A) and extended (B) states. Image taken from Sebba et al.¹⁹

in order to observe the maximum red-shift in the SPR band for ordered arrays.⁵⁴

The observed shifts in the optical spectrum have been used to determine the inter-particle spacing

between nanoparticles, a technique referred to as a 'plasmon ruler'.^{31,55,57} The spectral shifts can be converted to distance based on either theoretical calculations or an empirical calibration.⁵⁷ These types of measurements can be somewhat difficult, however, as spectral shifts can also occur due to variations in particle size and shape, the refractive index of the solution and the orientation of a nanoparticle dimer relative to the polarization of the incident light.⁵⁷

An example of how optical shifts can be used to obtain structural information is shown in Figure 4-20. A core-satellite structure was formed using a reconfigurable tether. The plasmon resonance for the hairpin configuration was red-shifted relative to the extended confirmation due to increased inter-particle coupling.¹⁹ In another example, gold particles with a carboxylic acid-terminated capping ligand were mixed

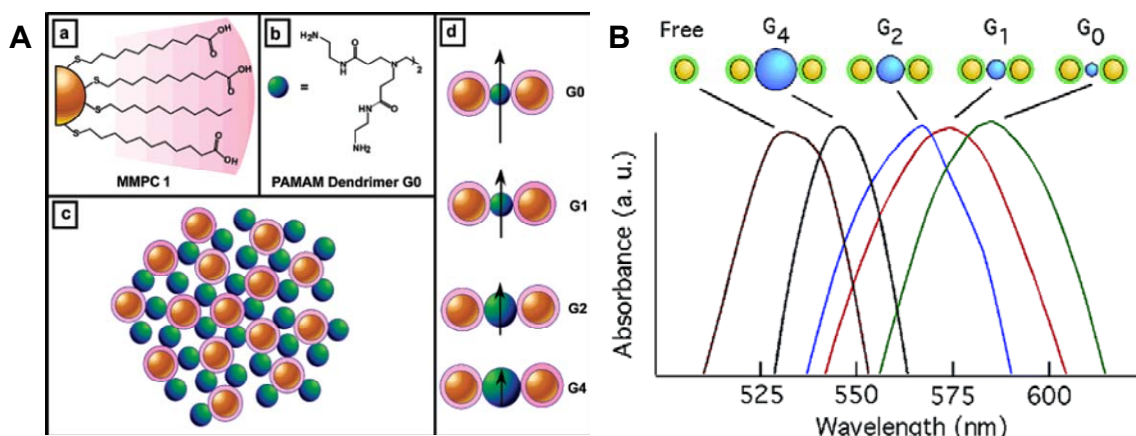


Figure 4-21. (A) Schematics of gold particles with carboxylic acid functionalities, PAMAM dendrimers, the self-assembly of gold particles with dendrimers and the decreased coupling that occurs with increasing dendrimer generation (B) Optical absorption spectra for gold nanoparticles self-assembled in the presence of dendrimers. Images taken from Srivastava et al.²¹

with poly(amidoamine) (PAMAM) dendrimers of several different generations as shown in Figure 4-21 (A).²¹ Due to interactions between the carboxylic acid and amine functionalities, the dendrimers self-assemble among the gold particles. As the space between particles increases with dendrimer generation, the SPR was tuned over an 84 nm range²¹ The absorption maximum shifted to lower wavelength with increasing generation due to decreased electromagnetic coupling.²¹

In addition to the number of particles and the inter-particle spacing, the observed plasmonic shift also varies with orientation of the particle assemblies.

Electromagnetic coupling phenomena are typically only observed when the particles are aligned with the polarization of the incident light.⁵⁵ The optical effects observed in a solution of randomly-oriented dimers are often insignificant.⁵⁵ Novak et al.^{12,27}

observed the changes in the optical properties for a solution of 8 nm gold nanoparticles upon the addition of an OPE linker (Figure 4-22 (B)). Only a slight shift and broadening were observed as dimers were formed. This small shift could be attributed to the dimers being randomly oriented in solution and the fact that this spectrum represented the average properties of the isolated particles, dimers and trimers in solution (Section 4.1.4). Similar results have been observed for 12 nm gold-citrate particles linked by diruthenium-bis(OPE) compounds (Figure 4-14).¹⁷ A slightly larger red-shift (20 nm)

was observed for solutions of dimers synthesized using the solid-phase approach to monofunctionalization (Figure 4-16), which could simply be due to the larger concentration of dimers in solution (60-70%).¹⁴

The magnitude of the spectral shift observed upon nanoparticle coupling also depends upon the composition of the metal nanoparticles. The

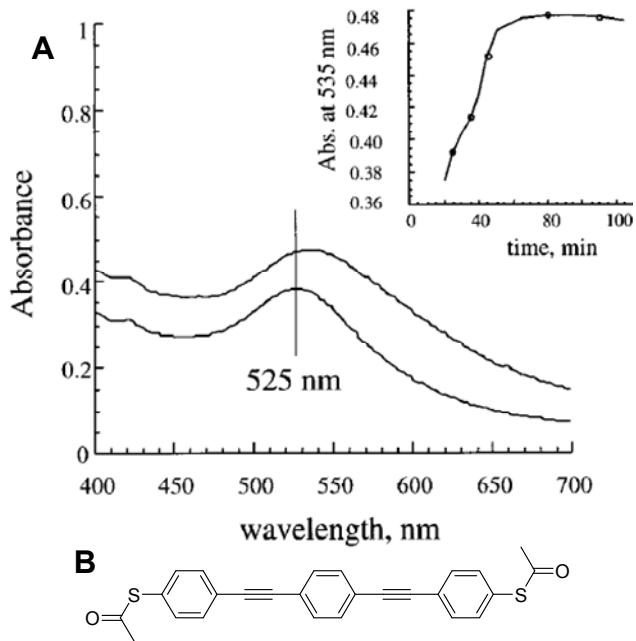


Figure 4-22. (A) Optical absorption spectra of 8 nm gold nanoparticles both before (lower spectrum) and after (upper spectrum) the addition of the OPE linker in (B). The inset shows the time evolution of the absorbance at 535 nm. Figure taken from McConnell et al.²⁷

optical shift observed upon coupling silver particles was significantly greater than that observed for gold.^{24,27} The more obvious shifts have been attributed to narrower plasmon bands, which are a result of the smaller imaginary dielectric constant associated with silver.³¹ Calculated spectra for dimers of silver nanoparticles are shown in Figure 4-23 (A). A small red-shift was observed for silver particles separated by 30 nm.^{24,27} As the distance between particles decreased, the red-shift increased and a high-energy shoulder (~ 370 nm) appeared. Figure 4-23(B) shows data collected for silver particles in the presence of linkers of different lengths. The absorption maximum red-shifted with decreasing linker length and a shoulder appeared in the presence of a 3-ring OPE (sulfur-sulfur distance = 2 nm).²⁷

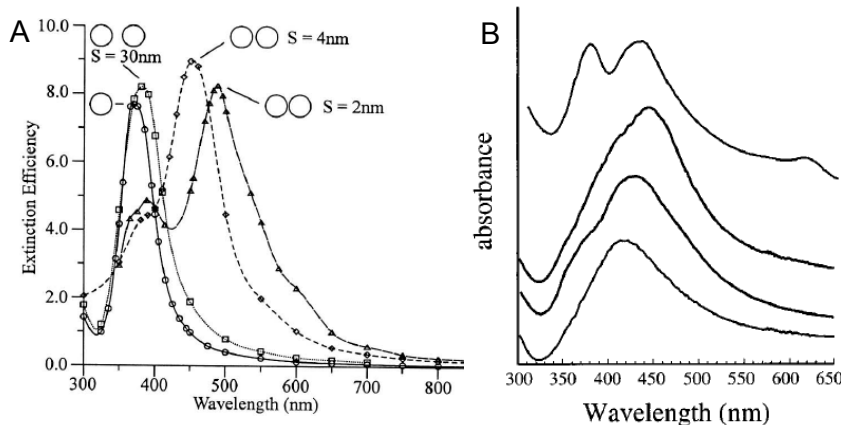


Figure 4-23. Optical spectra for silver nanoparticle dimers
(A) Spectra calculated for 60 nm silver particles as a function of inter-particle distance. Figure taken from Jensen et al.²⁴
(B) Optical absorption spectra for 30 nm silver nanoparticles linked by OPE molecules. From bottom to top the spectra correspond to isolated silver particles, dimers connected by a 9-ring OPE, dimers connected by a 7-ring OPE, and dimers connected by a 3-ring OPE. Spectra were offset along the absorbance axis for clarity. Figure taken from McConnell et al.²⁷

The differences between the experimental and the calculated spectra were attributed to both the orientation of dimers and the presence of monomers and

higher-order aggregates in solution.²⁷

Most of the literature describes the linking of particles composed of the same material. The formation of heterodimers could involve the coupling of two different plasmon bands with some interesting consequences. This has been demonstrated through the assembly of particle multi-layers on a surface with a bifunctional cross-linker according to the method shown in Figure 4-24 (A).³² Strong inter-particle

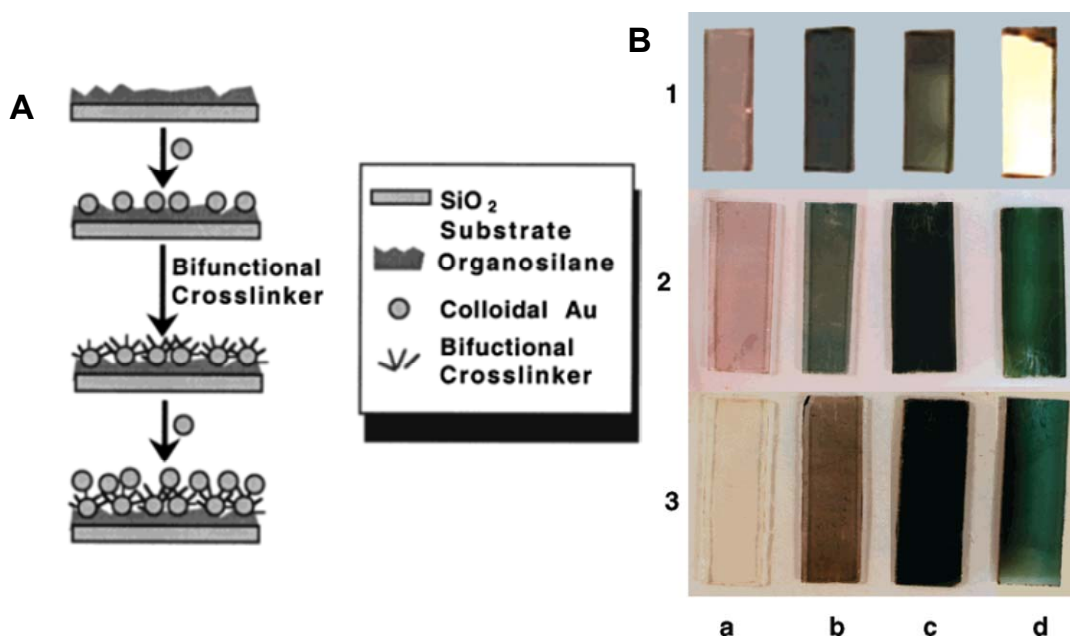


Figure 4-24. (A) Method for assembling nanoparticle multi-layers on a surface (B) Photograph of Au, Au/Ag and Ag nanoparticle multilayer samples. Au multilayers shown in row 1 are from left to right: Au colloid monolayer (a), after five treatments of colloid and four of 2-mercaptoethylamine (b) 12 colloidal Au layers (c) 20 colloidal Au layers. Row 2: Au/Ag mixed-nanoparticle multilayers with exposures to either Au or Ag colloid and HSCH₂CH₂OH. The film compositions are: (a) Au monolayer (b) Au/Ag/Ag (c) Au/Ag/Ag/Ag/Au (d) Au/Ag/Ag/Ag/Au/Ag/Au Row 3: HSCH₂CH₂OH/Ag colloid multilayers after 3 (a), 5 (b), 7 (c) and 9 (d) Ag treatments, respectively. Image taken from Musick et al.³²

coupling was observed, and the optical properties changed with both the thickness and composition of the multi-layers as shown in Figure 4-24 (B). Mixed multi-layers exhibited plasmon bands associated with both gold and silver particles creating the possibility of tailoring the optical properties over most of the visible spectrum. It was also noted that when the bifunctional cross-linker was less than 0.8 nm long, the films exhibited properties similar to those of the bulk material.³²

As discussed in Section 2.1.4.1.1, the optical properties of a nanostructure are strongly dependent upon its shape with nanorods exhibiting both transverse and longitudinal SPR modes. Thus, the coupling between nanorods depends upon their orientation with larger shifts observed for the coupling of longitudinal plasmons upon end-to-end dimerization compared to the coupling of transverse plasmons upon side-by-side dimerization.⁵³ In the case of side-by-side linkages, a blue shift was observed in the longitudinal plasmon band and a red-shift was observed for the transverse plasmon band.^{31,53} The strength of both coupling modes increased with the aspect ratio of the nanorods.⁵³

For the case of gold nanoparticle dimers synthesized through controlled aggregation (Figure 4-7 (B)), the optical properties resembled those of a nanorods. Peaks were observed for both transverse (530 nm) and longitudinal (600 nm) modes. For asymmetrical aggregates such as those shown in Figure 4-9 and Figure 4-10, electronic interactions between the two materials can affect the optical properties.

For example, an 18 nm red-shift was observed for gold-Fe₃O₄ dimers relative to the SPR of pure gold particles.¹⁸ This behavior was attributed to an electron-deficiency in the gold particles, which occurs upon Fe₃O₄ nucleation.

4.1.7. Summary

Several different techniques have been used to synthesize a wide variety of nanoparticle assemblies, all with different properties. Two-dimensional particle arrays have been formed on surfaces using self-assembled monolayers. These structures were extremely stable over long periods, and particles did not aggregate with each other or with the surface. In addition, narrower size-distributions have been observed for surface-bound particles relative to those in solution, suggesting a higher binding affinity for some particle sizes over others. These concepts were extended to the formation of covalently-linked particle networks. Two-dimensional arrays have been synthesized by linking adjacent particles in a surface-bound monolayer, and three-dimensional arrays have been formed through multi-layer deposition.

Nanoparticle networks have also been synthesized in solution. Covalently-linked networks have been formed upon the addition of dithiol to a solution of gold nanoparticles and from particles functionalized with dithiol capping ligands. Similarly, the addition of a complimentary DNA strand to a solution of particles functionalized with oligonucleotides led to the reversible formation of an extended

network. Networks have also been formed through reactions between adjacent capping ligands. However, these types of reactions are limited to those with conditions mild enough not to affect particle stability.

The synthesis of isolated dimers and trimers proved to be significantly more challenging and required more control over reaction conditions. The formation of dimeric nanoparticle aggregates without a linker molecule has been achieved through controlled aggregation processes. In these cases, the dimeric structures were held together either through the addition of additional precursor material or the addition of a polymer shell. The yields of dimers achieved using these methods were typically low, varying between 20-50% depending upon the particle material and size. As the yield of dimers increased, so did the number of higher-order aggregates.

Heterodimeric structures have also been synthesized through the controlled dewetting of silica particles coated with gold, the thermal decomposition of iron pentacarbonyl in the presence of gold particles and the nucleation of silver on Fe_3O_4 particles at a micellar interface. As these aggregates were formed through the deposition or nucleation of one particle onto another one rather than aggregation processes, the yields of dimers were high and higher-order aggregates were not typically observed.

The goal of this work, however, was to synthesize nanoparticle dimers and trimers using a molecular linker. These types of assemblies have been obtained using DNA, which was an ideal template as it is similar in size to many nanoparticles. However, multiple purification steps were required to isolate the dimers from isolated particle and other reaction side products. The formation of nanoparticle assemblies using smaller, organic molecules proved difficult due to the tendency for more than one linker to bind to each particle which resulted in higher-order aggregates. Attempts to limit this behavior included using low concentrations of both particles and linker. However, the frequency of collisions between particles and linker decreases at low concentrations and limits the efficiency of dimer formation. The yield of dimers achieved using these methods ranged from 30-50%, and post-synthetic separation techniques were required in order to isolate the dimeric product. Higher yields of dimers (55-70%) were obtained using a solid-phase place-exchange reaction to mono-functionalize particles. However, these yields reflected the number of particles that formed dimers after being cleaved from the solid resin. One report claims that the efficiencies of particle loading onto the resin and subsequent cleaving are quite low. In addition, these methods are limited to small particles. With the density of functional groups on most commercial resins, larger particles would likely be bound by more than one functional group.

An alternative to mono-functionalization is an asymmetrical functionalization process. This method limits the formation of higher-order aggregates and is applicable to many different particle sizes. The yield of homodimers varied between 46% and 65%, depending upon particle size. Higher order aggregates were more prevalent in solutions containing particles of multiple sizes. This behavior was attributed to the greater surface area of the larger particles accessible to binding more than one of the smaller particles.

While there has been at least one reported attempt at synthesizing heterostructures using orthogonal self-assembly, the only evidence that CdS and TiO₂ particles interacted with one another was observed electron transfer between the two materials. No microscopy was performed, and the morphology of the nanoparticle assemblies and the extent of binding were not characterized. This lack of data creates uncertainty regarding the success of these experiments.

When the distance between nanoparticles is less than the sum of their radii, which is often the case in nanoparticle assemblies, their plasma dipoles interact resulting in a change in their optical properties. These changes are dependent upon the nature of the particle, the number of particles bound together, the inter-particle distances and the orientation of the assembly relative to the polarization of the incident light. While drastic changes in optical properties have been observed, only modest changes have been observed for gold nanoparticle dimers. This behavior is attributed to the

broad plasmon resonance, the low yield of dimers in solution and their random orientation in solution. The interaction of particles with different plasmon resonances through the formation of heterodimers could yield some interesting behaviors. However, with the exception of gold, most of the particles used in this work were not optically active.

4.2. Results and Discussion

The syntheses of homodimers, homotrimers and heterodimers in this work were performed by adapting the methods reported by Novak et al.^{12,46-49} While the yields reported were somewhat low (~30%), these methods proved effective for bridging nanoparticles with conductive, OPE molecules. While solid-phase place exchange produced higher yields, mono-functionalization required extremely small particles sizes (< 2 nm). In addition, the techniques involving both mono- (Figure 4-16 and Figure 4-17) and asymmetrical (Figure 4-18) functionalization methods involved reactions between aliphatic capping ligands on two adjacent particles. As will be discussed later, adapting these methods to conjugated bridges without an insulating functional group would be significantly more challenging.

Before these methods were applied to the synthesis of heterodimers, they were used to synthesize homodimers and trimers consisting of citrate-capped gold particles. The variables affecting the synthesis of these structures, their stability, and characterization were evaluated before being applied to heterodimer formation.

4.2.1. Synthesis of Gold Homodimers and Homotrimers

Homodimers consisting of citrate-capped gold nanoparticles were synthesized using a method adapted from Novak et al.¹² As discussed in Chapters 2 and 3, water-soluble particles were desirable for synthesizing nanoparticle assemblies as they can be synthesized without sterically-bulky capping ligands, which would inhibit dimer formation. In addition, several of the characterization methods discussed in subsequent chapters required aqueous solvents. However, the OPE molecules used in this work (Figure 4-25) were only soluble in organic solutions. Therefore, the linker molecules were introduced to the aqueous particle solution in a 2:3 ratio of THF/ethanol, which was miscible. In addition, aromatic thiols typically react to form disulfides. For this reason, the thiols were protected by an acetyl group, which was removed in-situ under mildly basic conditions. A sodium citrate solution was added to increase the solution pH from approximately 5-6 to 8,* and facilitate deprotection.

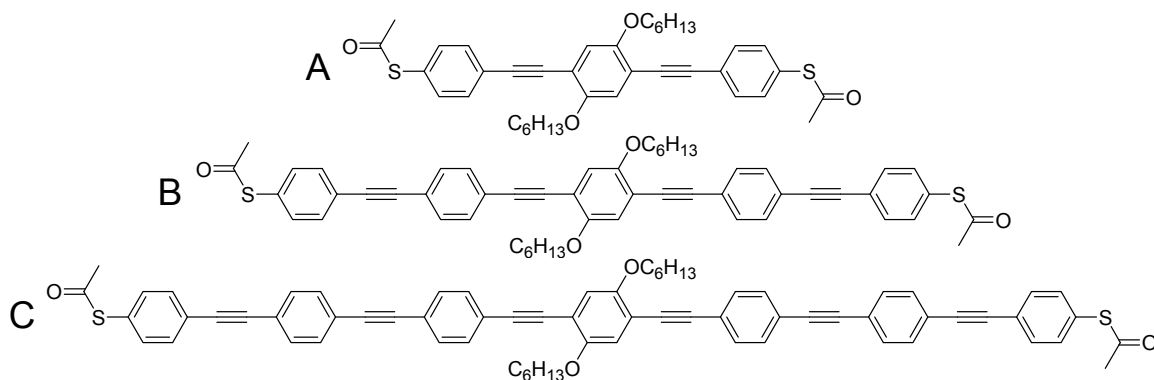


Figure 4-25. Oligomeric phenylene ethylene (OPE) molecules used to synthesize homodimers of gold nanoparticles (A) 3-ring linker (B) 5-ring linker (C) 7-ring linker. The alkoxy groups are present to enhance solubility.

The addition of organic solvent and sodium citrate had consequences regarding particle stability. As discussed in Section 2.1.1.1, the stability of electrostatically-stabilized particles decreases with ionic strength due to the compression of the electrical double-layer. In addition, solvent molecules shield repulsive electrostatic interactions and also affect particle stability. Both of these factors will be addressed both in this chapter and the following chapter.

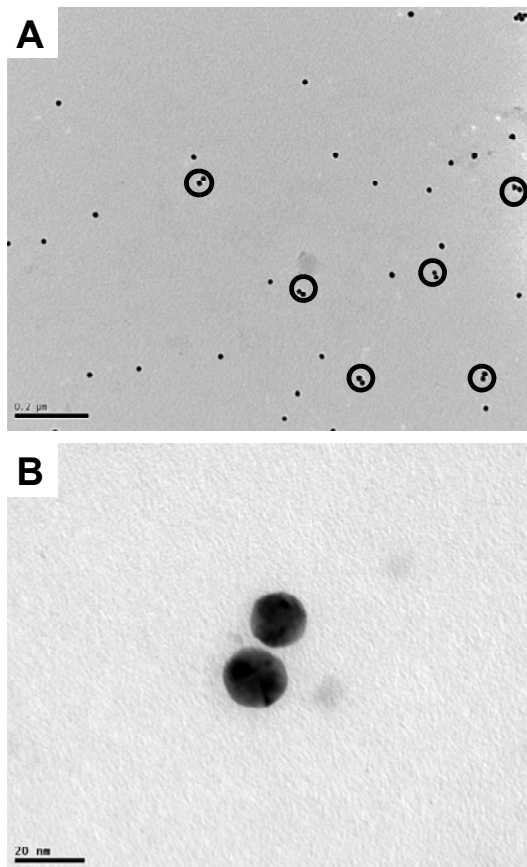


Figure 4-26. TEM images of gold nanoparticle homodimers (A) Solution containing 15 nm citrate-capped gold homodimers (B) Homodimer of 20 nm citrate-capped gold particles. Dimers were linked with linked with a 3-ring OPE (Figure 4-25 (A))

Figure 4-26 shows gold homodimers observed using TEM. The dimer yields observed were approximately 30%, which is consistent with the values reported in the literature.^{12,17,47} However, it is difficult to determine whether or not these

particles were actually linked with a molecular linker. As discussed in Section 2.1.3, particles often self-assemble into lattices. In this scenario, the inter-particle distances are determined by the sum of the attractive and repulsive forces. It is therefore likely that particles could have come together during preparation of the TEM grids even in the absence of linker. As discussed in Section 4.1.4, the distances measured between particle assemblies synthesized using these methods do not correlate with the linker length due to uncertainties in the thiol-gold bond angle and the orientation of dimers on the TEM grid, which may be angled away from the view. This behavior increases the difficulty in determining whether adjacent particles are covalently linked. For these reasons, particle solutions were also

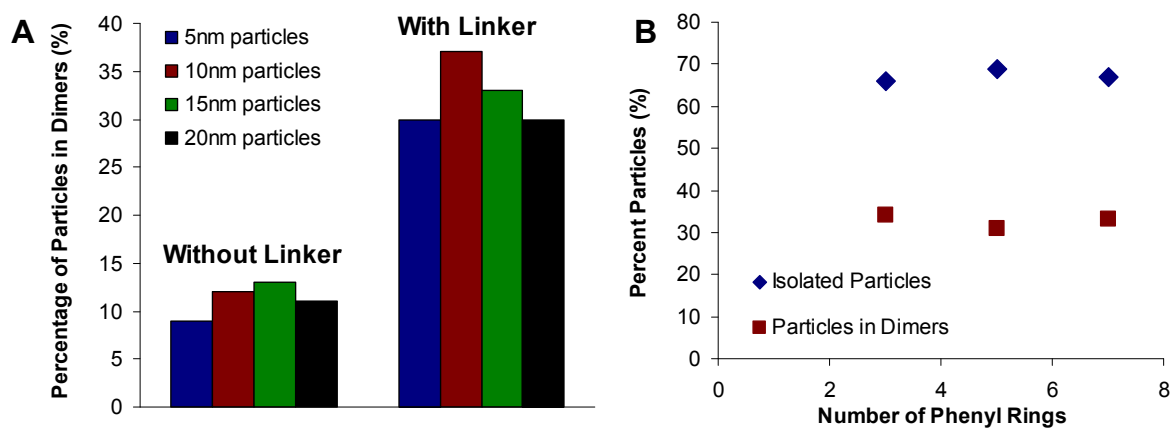


Figure 4-27. (A) Graph shows the percentages of particles that appeared to be in dimers on a TEM grid for citrate-capped gold particles of various sizes both without and with the addition of an OPE linker ((Figure 4-25 (A)). These values reflect an average measured for 2-3 experiments (B) The percentage of particles that appeared to be in dimers in the presence of three different linker molecules (Figure 4-25).

imaged in the absence of linker.

Figure 4-27 (A) shows the number of dimers counted both with and without linker. To eliminate as many variables as possible, the particle solutions without linker also contained sodium citrate and organic solvent. Some dimers were observed even in the absence of linker. These data create some uncertainty about the dimer yields observed in the presence of the molecular linker. The fact that three times as many dimers were observed in the presence of the molecular linker suggests that some covalently-linked dimers were present. In addition, Novak et al.¹² confirmed the presence of the molecular linker for similar structures using Raman spectroscopy,

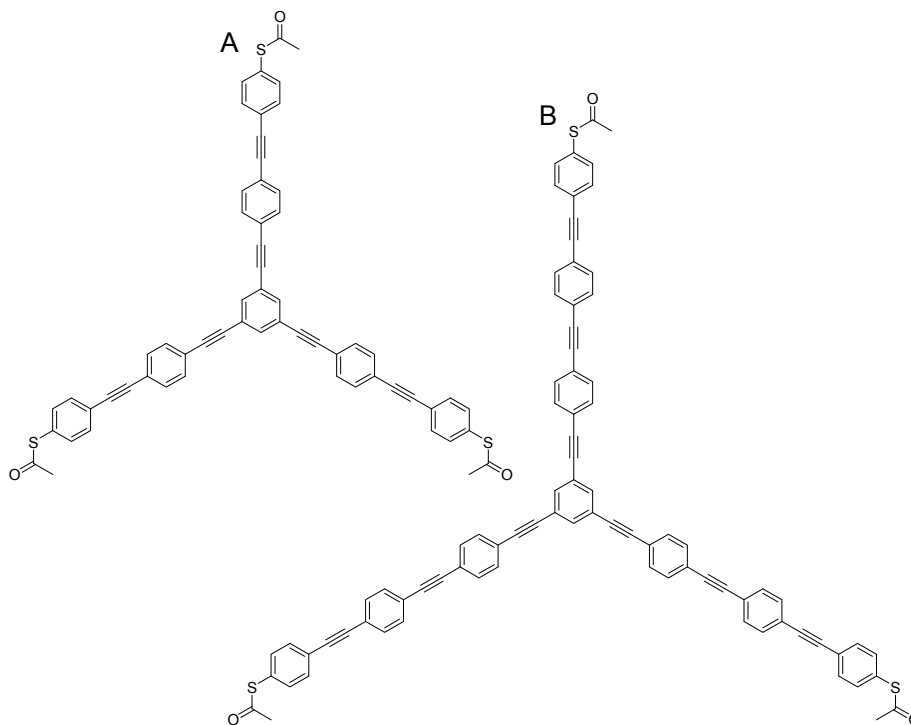


Figure 4-28. Three-armed oligomeric phenylene ethylene (OPE) molecules used to synthesize gold nanoparticle trimers (A) Linker with 7 rings (B) Linker with 10 rings

and Na et al.⁵⁸⁻⁶⁰ reported current measurements through these structures that confirmed the presence of the molecular linker. Regardless, characterizing these structures using electron microscopy remains a challenge.

Similar experiments were performed for nanoparticle trimers, which were formed by linking gold particles using the molecules shown in Figure 4-28. Images of nanoparticles trimers are shown in Figure 4-29. While the distance between particles linked with the 10-ring linker molecule (Figure 4-29 (C)) appeared to be larger than that between particles linked with the 7-ring linker molecule (Figure 4-29

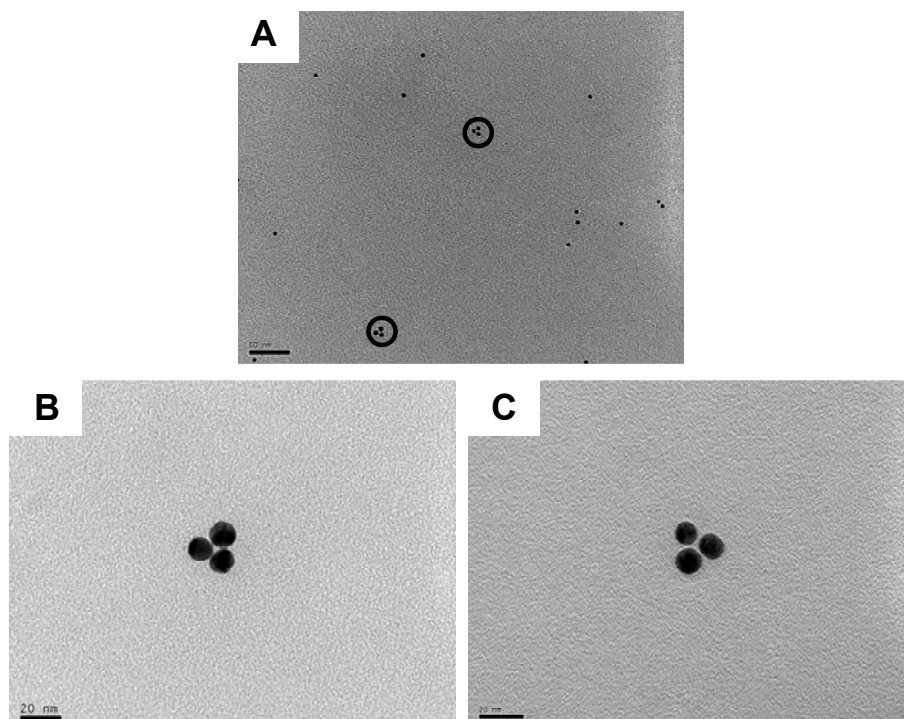


Figure 4-29. TEM images of gold nanoparticle trimers (A) Solution containing 5 nm citrate-capped gold trimers linked with a 10-ring three-armed OPE (Figure 4-28 (B)). (B) Trimer of 15 nm particles linked with a 7-ring OPE (Figure 4-28 (A)). (C) Trimer of 15 nm particles linked with a 7-ring OPE (Figure 4-28 (B)).

(B)), this behavior was not consistent for all samples images and there was again some uncertainty about whether groups of particles on the TEM grid were bound together. However, the number of trimers observed in the presence of linker was significantly higher as shown in Figure 4-30 (A). These data support the formation of covalently-linked nanoparticle assemblies.

In contrast to the data collected for dimers shown in Figure 4-27, the observed trimer yields appeared to be dependent upon nanoparticle size. A significantly greater number of trimers were observed for 15 nm particles compared to the smaller particle sizes.* There have been a few other reports of size-dependent processes in

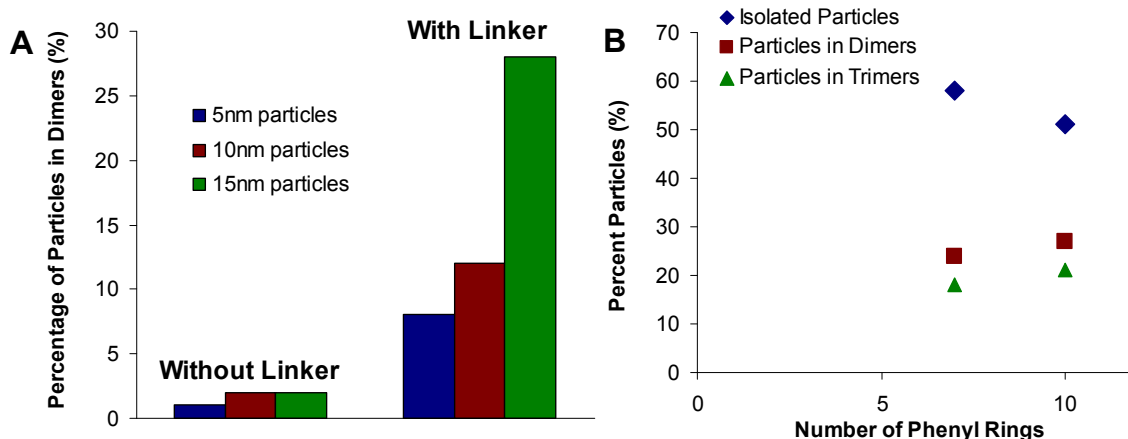


Figure 4-30. (A) Graph shows the percentage of particles that appeared to be in trimers on a TEM grid for citrate-capped gold particles of various sizes both without and with the addition of a three-armed OPE linker (Figure 4-28 (A)). These values reflect averages measured for 2-3 experiments (B) The percentage of 15 nm particles that appeared to be in dimers and trimers in the presence of two different linker molecules (Figure 4-28).

* Trimers were not synthesized with larger particles due to geometrical constraints, which are discussed in Appendix 2 (Table A-2-4).

the literature; however, no rationale has been provided for these observations. For example, Colvin et al.⁶ observed a narrower size distribution for surface-bound cadmium selenide nanoparticles relative to those in solution and suggested that kinetic or thermodynamic factors could favor the binding of one particle size over another. The synthesis of silica dimers through controlled aggregation was also reported to be size-dependent.²³ The yield of dimers was 33% for 330 nm particles and 50% for 280 nm particles. For dimers synthesized through asymmetrical functionalization, the yield for 16 nm particles was 65% while the corresponding yields for 30 nm particles and 41 nm particles were 57% and 46%, respectively.³⁰

There are a few possible reasons why the yields of trimers were greater for 15 nm particles than for smaller particles. The synthesis of citrate-capped gold particles was described in Section 2.2.2.1, which describes how tannic acid was used in the synthesis of particles smaller than 12 nm. Figure 2-18 shows that tannic acid is a significantly larger molecule than citric acid. Thus, it is possible steric considerations limited the formation of trimers for the smaller particles. Steric factors would likely be more significant for nanoparticle trimers as each particle is bound to two other particles and the gap between particles is smaller (Table A-2-5). Another consideration could be the magnitude of the attractive forces between particles. As mentioned in Section 2.1.1.1, the magnitude of the attractive van der Waals forces increases with particle size.⁶¹ However, it is unlikely that these forces would

contribute to the significantly higher yields observed for larger particles, esp. as this behavior contradicts the other reports in the literature. The yields for both the dimerization of silica²³ and gold were greater for smaller particles.³⁰ It is also possible the concentration of particles in solution could affect the yield of nanoparticle trimers. As shown in Table 4-3, the gold particle concentration decreases with increasing particle size. However, it seems unlikely that the yield of trimers would increase with decreasing particle concentration.

The effects of linker length on the yields of dimers and trimers were also investigated. While it was hypothesized that the yields would be higher for longer linker lengths, Figure 4-28 (B) shows negligible differences in dimer yields for the series of OPEs used here. The length differences among these molecules are small and it is possible that greater differences may be observed for longer chain lengths. Figure 4-30 shows a slight increase in the percentage of both dimers and trimers observed in the presence of the longer linker. However, these differences are small and additional experiments with longer linkers would be required in order to confirm this trend.

The optical properties of these nanoparticle assemblies were also investigated. As discussed in Section 4.1.6, Novak et al.^{12,27} observed a 10 nm red-shift in the optical absorption spectra of 8 nm gold particles upon dimerization. Similar trends are shown in Figure 4-31 for assemblies of both 5 nm and 15 nm particles. The peak at

520 nm observed for 5 nm particles red-shifted to 534 nm and broadened upon the formation of dimers and trimers. Some peak broadening was observed when additional sodium citrate and organic solvent was added to the particle solution, even in the absence of linker. This behavior could be due to either a change in the solution dielectric constant or a small number of aggregation events, which occurred due to the decreased stability of particles in the presence of these additives. Similarly, the peak at 522 nm observed for 15 nm particles red-shifted to 540 nm and broadened upon the formation of dimers and trimers. A small shift to 526 nm was observed when sodium citrate and organic solvent were added to the particle solution. Again, the origin of this shift is unclear. The extent of these red-shifts was

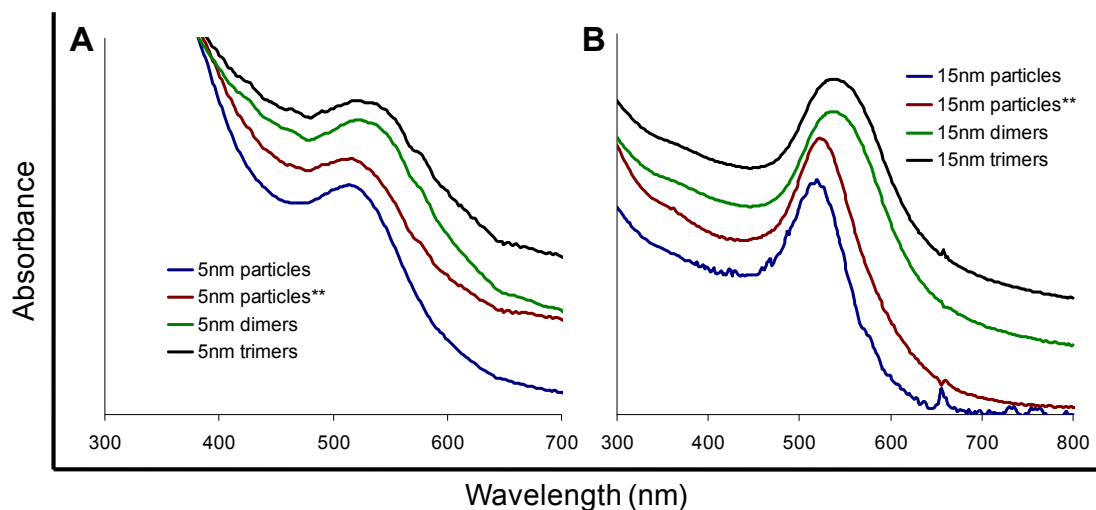


Figure 4-31. Optical absorption spectra for citrate-capped gold nanoparticle solutions containing dimers and trimers. (A) Solutions of 5 nm particles (B) Solutions of 15 nm particles
**** indicates a particle solution containing additional sodium citrate and organic solvent The spectra were off-set along the y-axis for clarity.**

likely dependent upon the yield of dimers and trimers in solution.

These experiments demonstrated the assembly of citrate-capped gold nanoparticles into dimers and trimers using a molecular linker. There were some uncertainties about the yields of these assemblies. Some dimers and trimers were observed on the TEM grid even in the absence of the molecular linker, and the distance between particles could not be correlated with the linker length. However, a significantly greater number of assemblies were observed in the presence of the linker, supporting the conclusion that assemblies were formed. The yield of dimers did not appear to be dependent on either particle size or linker length; however, the yield of trimers increased significantly as the particle size increased from 5 nm to 15 nm particles. The stability of particles in the presence of additional sodium citrate and organic solvent also came into question.

4.2.2. Synthesis of Nanoparticle Gold-Platinum Heterodimers

There are many different variables which could contribute to the effectiveness and the yield of heterodimer formation. In addition to the interactions between the particles and the bifunctional linker, the interactions between the two different particles and their capping ligands could be significant. If interactions between particles of the same type are significant, particle mixing and heterodimer formation will likely be inhibited. In the case of homodimers, there have been several reports indicating that particle size plays a role in the efficiency of dimerization.^{23,30} The

concentration and length of the OPE linker molecules are also significant. In order to properly evaluate these variables, effective characterization methods are required. As will be discussed in subsequent chapters, such methods have not yet been developed. This work was intended to demonstrate heterodimer formation; however, as is elaborated below, not all variables could be explored due to the unavailability of adequate characterization techniques.

The synthesis of nanoparticle heterodimers was carried out using methods similar to those used for gold homodimers. A stoichiometric amount of the OPE linker molecule in organic solvent was added to an aqueous solution containing two different types of particles in a 1:1 ratio and additional sodium citrate to facilitate the in-situ deprotection of the acetyl group. Citrate-capped gold particles were commercially available, and the remainder of the particles were synthesized according to procedures described in Chapters 2 and 3. While the concentrations of citrate-capped gold particles were provided by the manufacturer as indicated in the Experimental

Section (Table

4-3), the

concentrations of

the other

nanoparticles

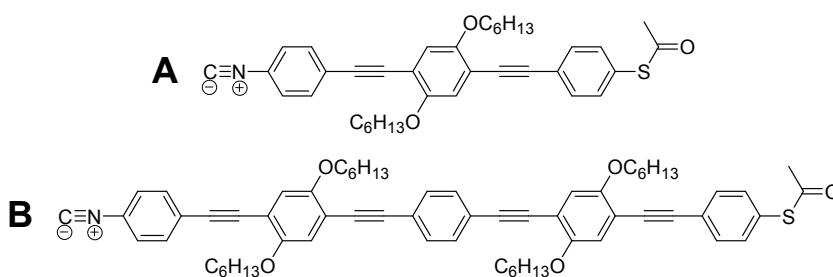


Figure 4-32. Bifunctional linkers used to link gold particles to platinum and nickel

used in this work were more difficult to determine. Calculations assumed 100% yield of the molecular precursor used in the particle synthesis. The approximate volume of an individual particle was calculated from its diameter determined by TEM measurements. This value and the density of the material were then used to determine the final concentration of the particles. As these values were only approximate, the concentrations had to be altered, in some cases, to observe a 1:1 particle ratio using TEM.

The first attempts at heterodimer formation involved linking citrate-capped gold particles (20 nm) with mercaptobenzoic acid-capped platinum particles (Section

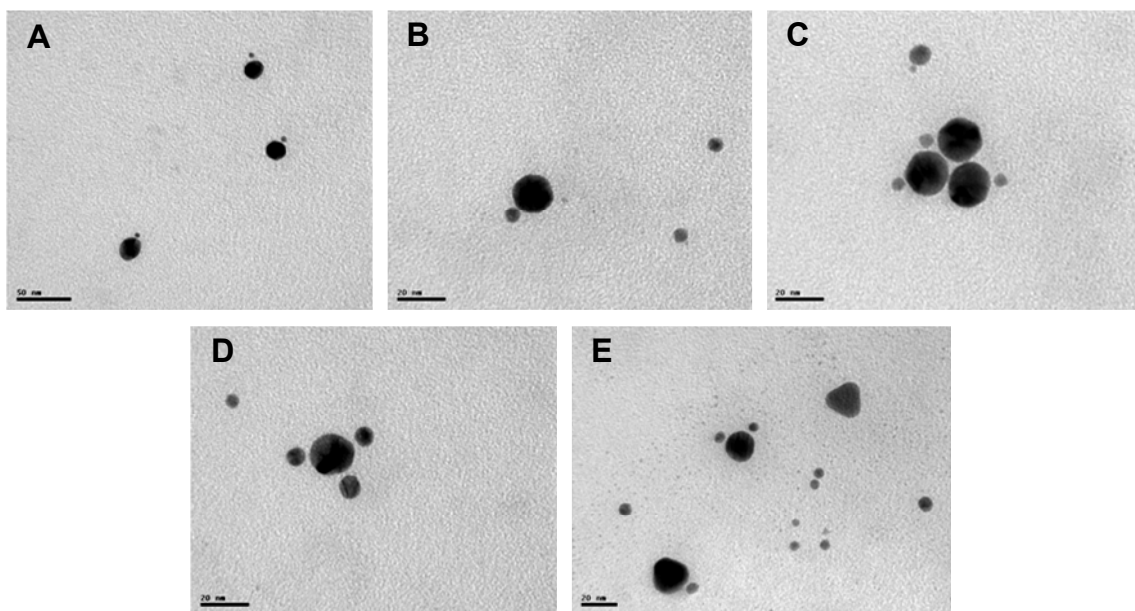


Figure 4-33. TEM images of citrate-capped gold particles (20 nm) and mercaptobenzoic-acid-capped platinum particles (7 nm) in the presence of the bifunctional linker shown in Figure 4-32 (A)

2.2.3.4, Figure 2-22) using the linker molecule shown in Figure 4-32. As discussed in Chapter 1, it was predicted that the thiol functionalities would bind to gold and the isocyanide would bind to platinum in order to create a heterodimer. The TEM images in Figure 4-33 show that heterodimers did form. However, in addition to isolated heterodimers, there were also gold particles that appeared to be bound to more than one platinum (Figure 4-33 (D, E)), gold homodimers, platinum

homodimers, and assemblies containing both gold and platinum (Figure 4-33 (C)).

Table 4-1. Statistics obtained for heterodimer assemblies consisting of citrate-capped gold particles (20 nm) and mercaptobenzoic acid-capped platinum particles

Total # Au Particles Imaged	118
# isolated Au particles	15 (13%)
# Au particles isolated in heterodimers	19 (16%)
# Au bound to more than one Pt	21 (18%)
# Au particles isolated in homodimers	14 (12%)
# Au particles in groups containing both Au-Au and Au-Pt	49 (41%)
# Au Particles bound to at least one Pt.	61 (54%)
Total # Pt Particles Imaged	164
# isolated Pt particles	45 (27%)
# Pt particles isolated in heterodimers	19 (12%)
# Pt particles in assemblies where more than one Pt is bound to a single Au	24 (15%)
# Pt particles isolated in homodimers	14 (9%)
# Pt particles in groups of more than two	29 (18%)
# Pt particles in groups containing both Au-Au and Au-Pt	33 (20%)
# Pt Particles bound to Au	90 (55%)

The numbers of particles within these different structures are reported in Table 4-1.

These numbers were obtained by counting particles observed using TEM, and do not necessarily reflect the statistics of the entire solution. While approximately 54% of gold particles were bound to at least one platinum particle, only 16% appeared to be isolated in heterodimers. More control over reaction conditions would be required in order to limit the formation of higher-order aggregates. As was the case with homodimers, it was difficult to determine whether or not these particles were covalently bound with a molecular linker. A control experiment was necessary in order to determine how many particles appeared to be bound together in the absence of linker. However, as described in Section 2.2.3.4, the synthesis of these mercaptobenzoic acid-capped platinum particles was irreproducible due to varying concentrations of the thiol and disulfide in the reaction. Therefore, additional experiments using these particles could not be performed.

Heterodimer formation was also attempted using mercaptobenzoic acid-capped platinum particles synthesized using a modified method (Figure 2-23). However, these attempts yielded only large aggregates. As discussed in Section 2.2.3.4, attempts at purifying these particle solutions resulted in irreversible aggregation. These solutions of platinum particles likely had high concentrations of chloride, hydroxide and borohydride ions in addition to excess mercaptobenzoic acid and methanol. While the sterically-stabilized platinum particles were stable under these conditions, the combination of high ionic strength and methanol likely facilitated the

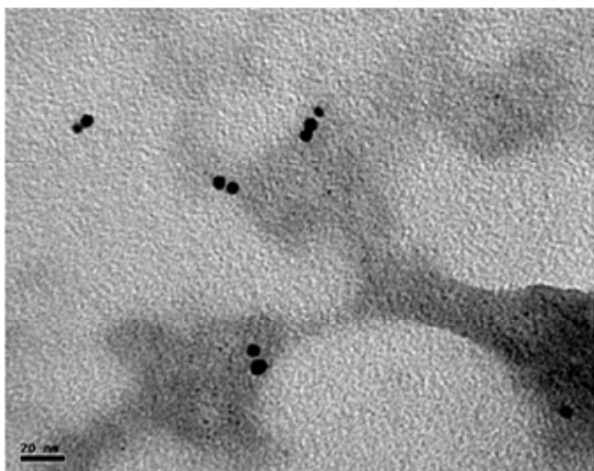


Figure 4-34. TEM image of citrate-capped gold particles (5 nm) in the presence of tiopronin-capped platinum particles and the bifunctional linker shown in Figure 4-32 (A)

aggregation of gold particles. In addition, the organic solvent and sodium citrate solution present during heterodimer formation could have led to aggregation of the platinum particles. The composition of the large aggregates observed in TEM images could not be determined. It was unclear whether the aggregates

consisted primarily of gold or platinum. Isolated particles of both types were also observed.

Attempts to synthesize heterodimers using both tiopronin-capped platinum particles and mercaptoethanesulfonate-capped particles were unsuccessful. Figure 4-34 shows a TEM images taken after

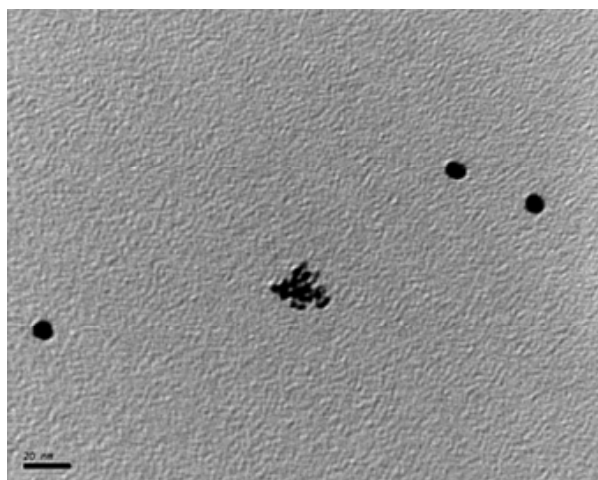


Figure 4-35. TEM image of citrate-capped gold particles (10 nm) and platinum particles capped with 2-mercaptoethanesulfonate in the presence of the linker shown in Figure 4-32 (B)

tiopronin-capped platinum particles were mixed with citrate-capped gold particles (5 nm) in the presence of the bifunctional linker shown in Figure 4-32 (A). No platinum particles were observed suggesting the selective aggregation or precipitation of platinum particles under these reaction conditions. While the presence of the OPE linker cannot be confirmed using TEM, a significant number of homodimers were observed suggesting that the isocyanide functionality bound to gold particles in the absence of platinum.

In the case of 2-mercaptoethanesulfonate-capped platinum particles, platinum aggregates were observed as shown in Figure 4-35. This behavior was not completely unexpected as these particles were only soluble in a few hydrophilic solvents, including formaldehyde.⁶² Irreversible aggregation occurred upon attempts to suspend μM concentrations of these particles in aqueous solution (Section 2.2.3.5). It was speculated that, at the low particle concentrations used in the synthesis of heterodimers (nM), the solubility of these platinum particles would be less of a problem. In addition, it was predicted that the solubility of these particles would improve upon binding to the water-soluble gold particles. While the solubility of these platinum particles did appear to be greater under these conditions, small aggregates were still observed. In contrast to the assemblies shown in Figure 4-34, homodimers were not observed.

It was unclear whether or not any changes in optical properties would be observed upon heterodimer formation. Figure 4-31 shows a small red-shift observed upon the formation of gold homodimers, which was attributed to inter-particle electromagnetic coupling. As platinum particles do not exhibit a strong absorption in the visible region (Section 2.1.4.2), it was difficult to predict what, if any, coupling phenomena would be observed.

Figure 4-36 (A) shows the optical absorption spectra for solutions of citrate-capped gold particles (20 nm) and mercaptobenzoic acid (MBA)-capped platinum particles in the presence of the bifunctional linker. While the general protocol for synthesizing heterodimers involved adding the linker molecule to a solution containing both gold and platinum particles, this particular experiment was designed to determine if there

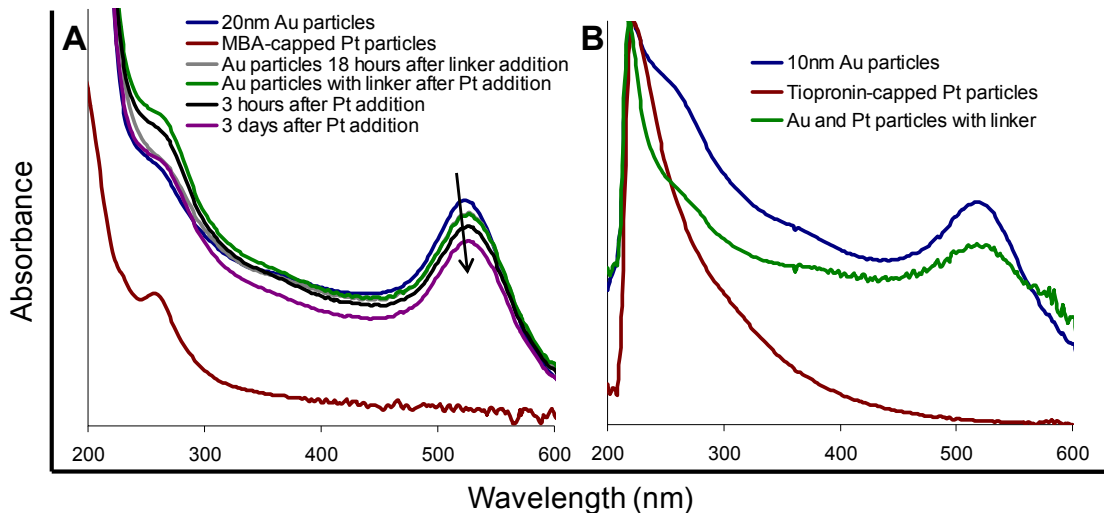


Figure 4-36. Optical absorption spectra of gold and platinum particles upon the addition of a bifunctional linker (A) 20 nm gold particles with mercaptobenzoic acid (MBA) – capped platinum particles (B) 10 nm gold particles with tiopronin-capped platinum particles

was any change in the optical properties of gold particles upon linker addition. While no changes were observed in the optical spectrum for gold particles immediately upon linker addition, a small red-shift and a decrease in absorption intensity were observed after approximately 18 hours. This result may be due to the formation of a small concentration of homodimers. The magnitude of these changes increased upon the addition of platinum particles. It is unclear whether these changes were due to interactions between the gold and platinum particles or due to further aggregation of gold particles. Also, the intensity of the shoulder at approximately 260 nm increased upon the addition of platinum, and then decreased with time. As this shoulder overlaps a small peak at 260 nm in the spectrum of the MBA-capped platinum particles, which is associated with the MBA absorption (Figure 2-22), it is unclear whether this behavior reflects changes in the spectrum for gold or that of platinum. Further investigation coupled with theoretical calculations would be required in order to determine the origin of these optical changes.

Figure 4-36 (B) shows the optical absorption spectra for solutions of citrate-capped gold particles (10 nm) and tiopronin-capped platinum particles in the presence of the bifunctional linker. In this case, the linker molecule was added to a solution containing both gold and platinum particles. Again, a decrease in the intensity and a small red-shift was observed along with some peak broadening. According to TEM

data, heterodimers were not formed for this case. Therefore, the changes in the optical spectra were attributed to the formation of gold assemblies.

4.2.3. Synthesis of Nanoparticle Gold-Nickel Heterodimers

Nickel particles were also investigated for heterodimer formation as strong binding has been reported between isocyanides and nickel surfaces.⁶³⁻⁶⁵ Attempts were made to bind gold particles to nickel particles stabilized with both cetyltrimethylammonium bromide (CTAB) and phenyltrimethylammonium bromide (PTAB).

As described in Section 2.2.4.2, high concentrations of the ionic stabilizing ligands were required to achieve monodispersed nickel particles, and all attempts to purify these particle solutions resulted in aggregation. These particle solutions therefore contained ammonium and bromide ions, chloride ions, sodium and hydroxide ions and hydrazine, all of which could affect the stability of a particle solution. When CTAB-capped nickel particles were added to a solution of citrate-capped gold particles, immediate precipitation was observed. This was attributed to the high ionic strength of the nickel particle solution, which destabilized the gold particles and resulted in aggregation. Immediate precipitation was not observed upon the addition of PTAB-capped nickel particles to solution of citrate-capped gold particles; however the TEM image in Figure 4-37 shows that aggregation of gold particles did occur over a longer time-scale. This image was taken approximately 18 hours after the

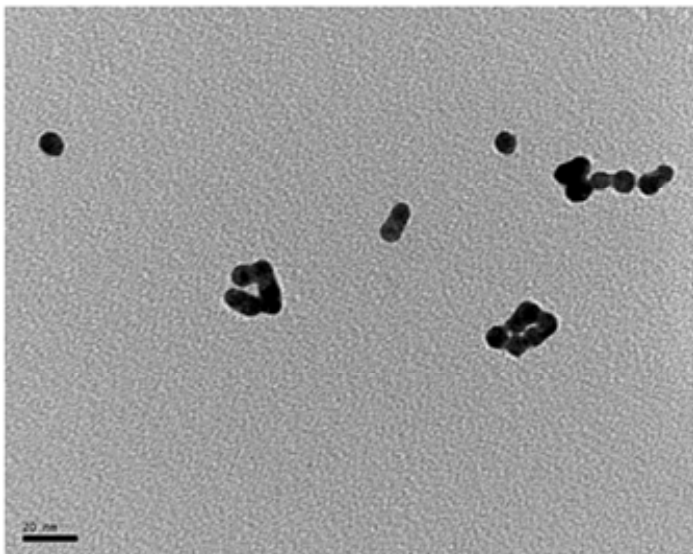


Figure 4-37. TEM image of aggregated citrate-capped gold particles (10 nm) in the presence of PTAB-capped nickel particles

particle solutions were mixed. It was speculated that interactions between the gold particles and the long alkyl chain associated with the CTAB contributed to the faster aggregation kinetics.

Figure 4-37 shows

aggregated gold particles

(10 nm), but nickel particles (3.6 nm) were not observed. As the concentration of nickel particles in this solution was based only on approximate calculations, it was possible that the actual concentration of nickel particles was much lower than the concentration of gold particles. In order to rule out this possibility, a second experiment was performed in which a large excess of nickel particles was added. The TEM images taken of the resulting solution were similar and no nickel particles were observed. These data suggest that nickel particles precipitated. Both the gold and the nickel particles were stable separately, but exhibited aggregation and precipitation upon mixing. It is also likely that the additional sodium citrate and

organic solvent added for heterodimer formation contributed to the precipitation of nickel particles.

Heterodimer formation requires particles that can be easily purified to eliminate problems associated with impurities. In addition, both types of nanoparticles must be stable under the same conditions. As discussed in Chapter 2, there is a tradeoff between particle stability and reactivity. Significant difficulties were encountered in synthesizing stable nanoparticles without sterically-bulky capping ligands. These experiments demonstrated that particle stability can be further decreased in mixed particle solutions.

4.2.4. Synthesis of Nanoparticle Gold-Metal Oxide Heterodimers

As carboxylic acids have been reported to bind selectively to metal oxides, heterodimer synthesis has also been attempted using the bifunctional linker shown in Figure 4-38. As before, the thiolate functionality was intended to bind to gold particles after *in situ* deprotection of the acetate functionality while the carboxylic acid was intended to bind to metal oxide particles, specifically TiO_2 and Fe_3O_4 . These types of assemblies were of interest as a non-conductive particle will be required for the eventual assembly of a three-terminal device. In addition, the selectivity between the thiol and the carboxylic acid functionalities was expected to be greater than that associated with the thiol and isocyanide functionalities.

Attempts were made to synthesize heterodimers by binding citrate-capped gold particles (15 nm) and succinic acid-capped TiO₂

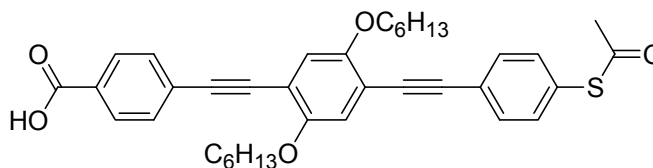


Figure 4-38. Bifunctional linker used to link gold particles to TiO₂ and Fe₃O₄

particles. As described in Section 3.2.1.6, the synthesis of TiO₂ using solvothermal methods yielded stable, dispersed, spherical particles; however, these particles often transformed to nanorods upon ligand-exchange with hydrophilic capping ligands. As TiO₂ particles maintained their spherical shape during initial attempts at ligand-exchange (Figure 3-39 (B)), these particles were chosen for heterodimer formation. Figure 4-39 shows a TEM image of citrate-capped gold particles and succinic acid-capped TiO₂ in the presence of the bifunctional linker shown in Figure 4-38. Negligible binding was observed. Repeated experiments were not performed due to the irreproducibility of the TiO₂ particle synthesis (Section 3.2.1.6).

More promising results were obtained upon binding citrate-capped gold particles to tartaric acid-capped Fe₃O₄ particles. As discussed in Section 3.2.2.2, tartaric acid-coated Fe₃O₄ particles completely adhered to a stir bar, while Fe₃O₄ particles sonicated in the presence of succinic acid and glycerol did not. This behavior suggested that these particles were pure Fe₃O₄ while other oxide or hydroxide species may have been present in the other solutions. In addition, the magnetic

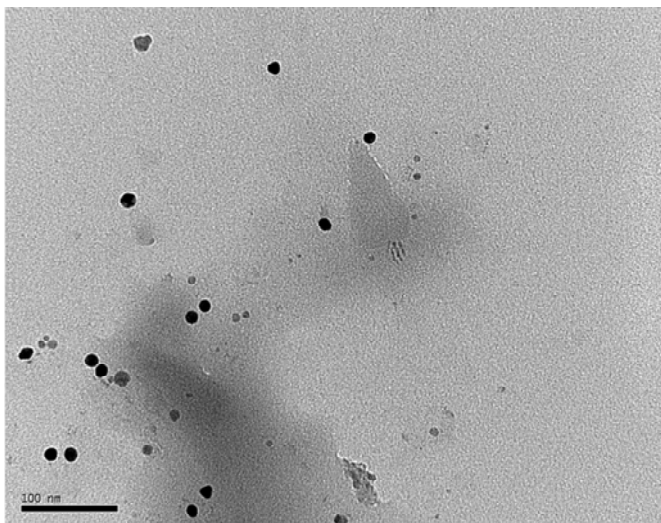


Figure 4-39. TEM image of citrate-capped gold particles (15 nm) with succinic acid-capped TiO₂ particles (9 nm) in the presence of the bifunctional linker shown in Figure 4-38

properties of the tartaric acid-coated particles facilitated their removal from solution allowing them to be washed and re-dispersed in pure water. Effective purification methods had not been developed for the particles capped with succinic acid

or glycerol. For these reasons, the tartaric-acid coated Fe₃O₄ particles were used for the formation of heterodimers.

Figure 4-40 shows TEM images of heterodimers formed between citrate-capped gold particles (15 nm) and tartaric acid-capped Fe₃O₄ particles. As was the case for heterodimers formed between gold particles and mercaptobenzoic acid-capped platinum particles (Figure 4-33), TEM indicated the presence of many different types of structures. In addition to isolated heterodimers, there were also gold particles that appeared to be bound to more than one Fe₃O₄ (Figure 4-40 (C)), gold homodimers, Fe₃O₄ homodimers, and assemblies containing both gold and Fe₃O₄.

The numbers of particles within these different structures are reported in Table 4-2 at the end of this section. These numbers were obtained by counting particles observed using TEM, and do not necessarily reflect the statistics of the entire solution. As described in Section 4.2.2 (page 337), in reference to platinum particles, the concentrations of Fe_3O_4 particles were difficult to determine. A 'molecular' weight for these particles was approximated based on their diameter determined by TEM measurements and the density of Fe_3O_4 . As the tartaric-acid capped Fe_3O_4 particles could be isolated from solution, they were then weighed to make stock solutions of approximately-known concentrations. As these concentrations were only approximate, they required further altering in order to

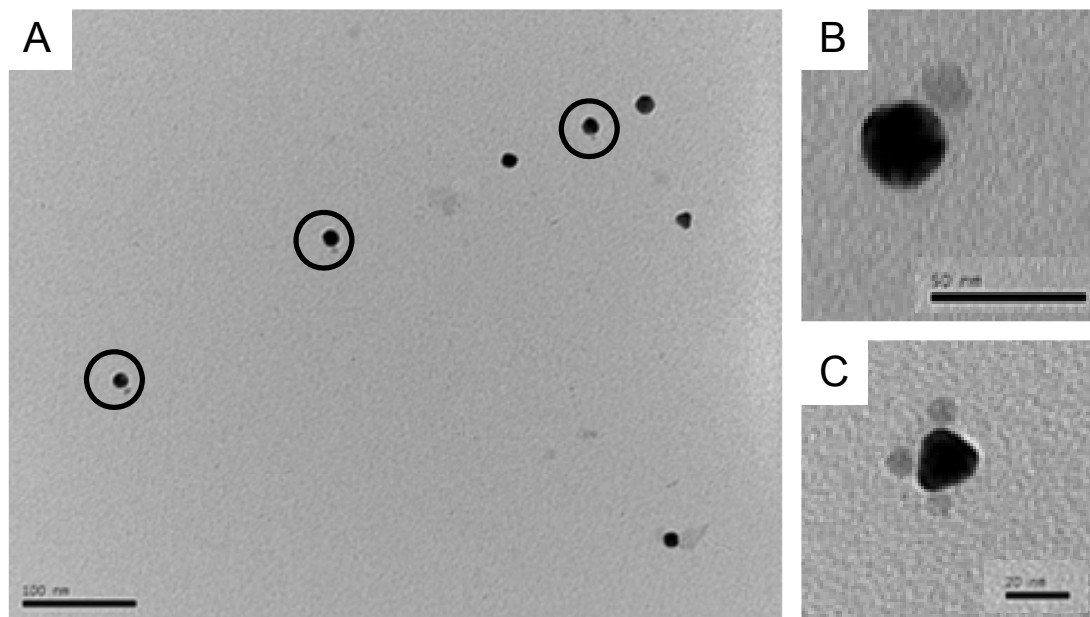


Figure 4-40. TEM images of hetero-assemblies formed between citrate-capped gold particles (15 nm) and tartaric acid-capped Fe_3O_4 particles (7 nm)

observe a 1:1 particle ratio using TEM. Figure 3-43 (D) shows that tartaric acid-capped Fe_3O_4 particles formed large aggregate structures in addition to discrete particles. It is therefore possible that the number of discrete particles observed in heterodimer experiments does not reflect the true particle concentration.

Table 4-2 shows the results for three different heterodimer experiments both with and without the bifunctional linker molecule. In the first experiment, the number of Fe_3O_4 particles observed was approximately 2-3 times greater than the number of observed gold particles. The Fe_3O_4 concentration was then altered to achieve the approximate 1:1 ratios observed in experiments 2 and 3. The statistics recorded for experiment 3 are highlighted as they represent not only comparable numbers of gold and Fe_3O_4 particles, but also similar numbers of particles were counted for samples both with and without the bifunctional linker. As was the case with both homodimers (Section 4.2.1, page 328) and heterodimers formed with mercaptobenzoic acid-capped platinum particles (Section 4.2.2, page 337), it was difficult to determine whether or not these particles were covalently bound with a molecular linker. As discussed in Section 2.1.3, particles often self-assemble into lattices. A control experiment was performed in order to determine how many particles appeared to be bound together in the absence of linker. To eliminate as many variables as possible, the particle solutions without linker also contained sodium citrate and organic solvent.

As with both homodimer and previous heterodimer experiments, some dimers and larger-order aggregates were observed even in the absence of linker. While the percentage of gold particles bound to at least one Fe_3O_4 was slightly higher when the Fe_3O_4 nanoparticle concentration was larger (experiment 1), this value approximately doubled in the presence of linker for all experiments. The number of isolated heterodimers also approximately doubled in the presence of linker. These data suggest that some covalently linked dimers were present in the presence of linker, although there was some uncertainty regarding their exact concentrations.

While the distances measured between particles have not correlated with the linker lengths in previous experiments due to uncertainties in the thiol-gold bond angle and the orientation of the dimers of the TEM grid (Section 4.1.4, page 301), these values were measured here in attempt to determine if there were significant differences between the samples with and without the molecular linker. If the distances between particles were significantly different in the presence of the linker, this information could support the presence of covalently-linked assemblies. While the distance measured between the thiolate and carboxylic acid functionalities for the linker shown in Figure 4-38 was 2.0 nm,* the distance measured between particles in the presence of the linker molecule was 1.13 ± 0.25 nm. This finding was not unexpected as both Novak et al.¹² and Ying et al.¹⁷ also measured inter-particle

* This distance was measured using ChemDraw 3D software after MM2 energy minimization.

distances that were shorter than the linker length. However, the distance measured between particles in the absence of linker was 1.11 ± 0.25 nm. As there were negligible differences between these two values, these data could not be used to support the presence of the molecular linker between the two particles. The large deviations on these values were attributed to differences in particle orientation on the TEM grid and the low-resolution of the images.

While it was predicted that the selectivity between the thiol and carboxylic acid functionalities would be greater than that associated with the thiol and isocyanide functionalities, only 30% of gold particles were bound to at least one Fe_3O_4 particle compared to the 54% of gold particle bound to at least one mercaptobenzoic acid-capped platinum particle. However, similar percentages of heterodimers (16% vs. 18%) were observed for both systems. It is difficult to make a direct comparison between the two systems, because counts were not performed for citrate-capped gold particles and mercaptobenzoic acid-capped platinum particles in the absence of linker. The affinity of the different particles may vary between the two systems. It is noted that the percentages of Fe_3O_4 particles isolated in homodimers (14-18%) and the percentages of Fe_3O_4 particles in group so greater than two (10-39%) are greater than similar percentages observed for mercaptobenzoic acid-capped platinum particles (9% and 18%, respectively). These data suggest that tartaric acid-capped Fe_3O_4 particles may have a higher affinity for one another than

mercaptobenzoic acid-capped platinum particles. This could be due to the magnetic forces between the particles or hydrogen bonding interactions between the capping ligands. Significant inter-particle interactions could limit particle mixing and consequently heterodimer formation.

Table 4-2. Statistics Obtained for Heterodimer Assemblies Consisting of Citrate-capped Gold Particles (15 nm) and Tartaric-acid-Capped Fe₃O₄ Particles

	Experiment 1		Experiment 2		Experiment 3	
	No Linker	Linker	No Linker	Linker	No Linker	Linker
Total # Au Particles Imaged	116	72	152	249	200	230
# isolated Au Particles	70 (60%)	30 (42%)	64 (42%)	102 (41%)	149 (75%)	137 (60%)
# Au particles isolated in heterodimers	9 (8%)	14 (19%)	11 (7%)	28 (11%)	16 (8%)	41 (18%)
# Au particles bound to more than one Fe ₃ O ₄	5 (4%)	2 (3%)	3 (2%)	5 (2%)	5 (2%)	12 (5%)
# Au particles isolated in homodimers	12 (10%)	12 (17%)	38 (25%)	60 (24%)	26 (13%)	16 (7%)
# Au particles in groups containing both Au-Au and Au-Fe ₃ O ₄	20 (17%)	14 (19%)	36 (24%)	54 (22%)	4 (2%)	24 (10%)
# Au Particles bound to at least one Fe ₃ O ₄	23 (19%)	29 (40%)	25 (16%)	75 (30%)	28 (14%)	69 (30%)
Total # Fe ₃ O ₄ Particles Imaged	258	264	133	260	201	216
# Isolated Fe ₃ O ₄ Particles	60 (23%)	126 (48%)	44 (33%)	60 (23%)	66 (33%)	71 (33%)
# Fe ₃ O ₄ particles isolated in heterodimers	9 (3%)	14 (5%)	11 (8%)	28 (11%)	16 (8%)	41 (19%)
# Fe ₃ O ₄ particles in assemblies where more than one Fe ₃ O ₄ is bound to a single Au	0 (0%)	2 (1%)	2 (1%)	4 (2%)	5 (3%)	2 (1%)
# Fe ₃ O ₄ particles isolated in homodimers	46 (18%)	4 (2%)	14 (11%)	48 (18%)	16 (8%)	30 (14%)
# Fe ₃ O ₄ particles in groups of more than two	101 (39%)	87 (33%)	45 (34%)	53 (20%)	79 (39%)	21 (10%)
# Fe ₃ O ₄ particles in groups containing both Au-Au and Au-Fe ₃ O ₄	42 (16%)	31 (11%)	17 (13%)	67 (26%)	19 (9%)	51 (23%)
# Fe ₃ O ₄ Particles bound to Au	35 (14%)	48 (18%)	28 (21%)	99 (38%)	25 (12%)	78 (36%)

Samples with 'No Linker' contained particle mixtures in addition to a sodium citrate solution and organic solvent

4.2.5. Summary and Conclusions

The assembly of citrate-capped gold nanoparticles into dimers and trimers using a molecular linker was demonstrated although there was some uncertainty in the yields of these assemblies. Some dimers and trimers were observed on the TEM grid even in the absence of the molecular linker, and the distance between particles could not be correlated with the linker length. However, a significantly greater number of assemblies were observed in the presence of the linker supporting the conclusion that assemblies were formed. The yield of dimers did not appear to be dependent on either particle size or linker length; however, the yield of trimers increased significantly as the particle size increased from 5 nm to 15 nm particles. The stability of particles in the presence of additional sodium citrate and organic solvent also came into question.

The synthesis of nanoparticle heterodimers was carried out using methods very similar to those used for gold homodimers. However, these procedures presented additional challenges, the most significant of which appeared to be the synthesis of particles that were stable in a solution containing citrate-capped gold particles, sodium citrate and organic solvent. Tiopronin-capped platinum, mercaptoethanesulfonate-capped platinum, CTAB-capped nickel and PTAB-capped nickel particles all aggregated in these solutions. In addition, the high ionic strength of the nickel particle solutions caused the gold particles to aggregate. Chapters 2

and 3 described the difficulties associated with synthesizing stable particles without sterically-bulky capping ligands. These methods would need to be further developed in order to successfully synthesize a wide variety of heterodimeric structures.

Preliminary TEM data suggested the formation of heterodimers consisting of citrate-capped gold particles and mercaptobenzoic acid-capped platinum particles.

Approximately 54% of the gold particles were bound to at least one platinum and 16% of the gold particles were isolated in heterodimers. Other structures included gold particles that were bound to more than one platinum, gold homodimers, platinum homodimers and assemblies containing both gold and platinum. As with the homodimer experiments, it was difficult to confirm the presence of the molecular linker. Further experiments could not be performed due to the irreproducibility of this particle synthesis. Attempts to synthesize heterodimers using mercaptobenzoic acid-capped platinum particles synthesized using a different method were unsuccessful. Aggregation of both the gold and platinum particles was observed.

Preliminary TEM data also suggested the formation of heterodimers consisting of citrate-capped gold particles and tartaric acid-capped Fe_3O_4 particles.

Approximately 30% of the gold particles were bound to at least one Fe_3O_4 particle and 18% were isolated in heterodimers, double the values observed in the absence of the bifunctional linker. While it was predicted that the selectivity between the thiol and carboxylic acid functionalities would be greater than that associated with the

thiol and isocyanide functionalities, only 30% of gold particles were bound to at least one Fe_3O_4 compared to 54% of gold particles bound to at least one mercaptobenzoic acid-capped platinum. It was speculated that this difference could be due to greater interactions between Fe_3O_4 particles, which could limit mixing and the efficiency of dimerization.

While preliminary data does suggest the formation of heterodimers, additional experiments are required to verify this behavior. The sole characterization technique used here was TEM. As shown in Table 4-1 and Table 4-2, the statistics obtained using TEM were based on a few hundred particles and do not necessarily reflect the composition of the entire solution. In addition, nanoparticle assemblies were observed even in the absence of the bifunctional linker, which created some uncertainty as to whether these structures were covalently linked. A solution-based characterization technique could provide data that was representative of the entire solution and avoid the ambiguity associated with lattice formation upon TEM sample preparation.

There are many different variables that could affect the yield of dimers in solution, including the particle sizes and concentrations, the concentration and length of the linker molecules, the nature of the particle capping ligands and the solvent composition. An efficient characterization method is also necessary in order to properly evaluate each of these variables and maximize the efficiency of

dimerization. The rest of this work is therefore focused on developing characterization methods for nanoparticle assemblies in order to both verify the presence of dimeric structures and as a means to evaluate reaction variables.

4.3.Experimental

4.3.1.Sample Preparation

Gold-citrate particles were obtained from Ted Pella, Inc. as aqueous solutions with trace amounts of citrate, tannic acid and potassium carbonate. All other nanoparticles were synthesized according to procedures reported in Chapters 2 and 3. The OPE linker molecules were synthesized by Chandra et al., and these details are published elsewhere.⁶⁶

Gold homodimer and homotrimer samples were prepared according to previously reported procedures.^{67,68} A 2 mL aliquot of gold particle solution as received from Ted Pella, Inc. was diluted with 2.5 mL 3 mM sodium citrate solution. The pH of this solution (~8) was sufficient for deprotection of the thioacetate functionality on the linker molecule. A stoichiometric amount of linker from a 1 μ M linker solution was diluted to 500 μ L with a 2:3 THF/ethanol solution and added to the gold particles in 50 μ L aliquots over a period of several minutes. The solutions were then allowed to stir overnight. Attempts at scaling up these reactions were unsuccessful. When

larger volumes were desired, several small scale reactions were performed and the resulting solutions combined.

As discussed in Section 2.2.2.1, the concentration of gold particles decreased with increasing particle diameter. The concentrations of particles as received are listed in Table 4-3 along with the concentrations of particles after the addition of sodium citrate and linker solutions.

Table 4-3. Concentrations of gold particles

Particle Size (nm)	Initial concentration (particles/mL)*	Initial concentration (nM)*	Concentration after linker addition (nM)
5	5.0×10^{13}	83.0	33.2
10	5.7×10^{12}	9.46	3.78
15	1.4×10^{12}	2.32	0.93
20	1.4×10^{12}	1.16	0.46

* as received from Ted Pella, Inc.

Heterodimers were synthesized according to a similar procedure. A 2 mL aliquot of gold particle solution as received from Ted Pella, Inc. was added to a stoichiometric amount of a second particle solution. The concentrations of particles synthesized in house were approximated based on their size (determined by TEM), their density and the amount of precursor added during the nanoparticle synthesis. The nanoparticle mixture was then diluted with 2.5 mL 3 mM sodium citrate solution. A stoichiometric amount of linker from a 1 μ M linker solution was diluted to 500 μ L with a 2:3 THF/ethanol solution and added to the gold particles in 50 μ L aliquots over a period of several minutes. The solutions were then allowed to stir overnight.

4.3.2. Particle Characterization

TEM Images were taken with a Philips CM12 TEM operated at 100 kV. Images were captured using a Gatan 780 camera and DigitalMicrograph software. A minimum of 200 particles were counted when determining yields of nanoparticle assemblies. Large assemblies of particles on the grid were not considered in these calculations. The distances between particles were measured using Image J software, a freeware program obtained from <http://rsbweb.nih.gov/ij/>.

Optical absorbance measurements were made using a Hewlett-Packard 8452A Diode Array Spectrometer and a path length of 1.0 cm.

4.4. References

- (1) Love, J. C.; Gates, B. D.; Wolfe, D. B.; Paul, K. E.; Whitesides, G. M., *Nano Lett.* **2002**, *2*, 891-894.
- (2) Andres, R. P.; Bein, T.; Dorogi, M.; Feng, S.; Henderson, J. I.; Kubiak, C. P.; Mahoney, W.; Osifchin, R. G.; Reifenger, R., *Science* **1996**, *272*, 1323-1325.
- (3) Lu, Y.; Xiong, H.; Jiang, X. C.; Xia, Y. N.; Prentiss, M.; Whitesides, G. M., *J. Am. Chem. Soc.* **2003**, *125*, 12724-12725.
- (4) Liu, H. T.; Alivisatos, A. P., *Nano Lett.* **2004**, *4*, 2397-2401.
- (5) Collier, C. P.; Vossmeier, T.; Heath, J. R., *Annu. Rev. Phys. Chem.* **1998**, *49*, 371-404.
- (6) Colvin, V. L.; Goldstein, A. N.; Alivisatos, A. P., *J. Am. Chem. Soc.* **1992**, *114*, 5221-5230.
- (7) Grabar, K. C.; Freeman, R. G.; Hommer, M. B.; Natan, M. J., *Anal. Chem.* **1995**, *67*, 735-743.

- (8) Andres, R. P.; Bielefeld, J. D.; Henderson, J. I.; Janes, D. B.; Kolagunta, V. R.; Kubiak, C. P.; Mahoney, W. J.; Osifchin, R. G., *Science* **1996**, *273*, 1690-1693.
- (9) Chumanov, G.; Sokolov, K.; Gregory, B. W.; Cotton, T. M., *J. Phys. Chem.* **1995**, *99*, 9466-9471.
- (10) Freeman, R. G.; Grabar, K. C.; Allison, K. J.; Bright, R. M.; Davis, J. A.; Guthrie, A. P.; Hommer, M. B.; Jackson, M. A.; Smith, P. C.; Walter, D. G.; Natan, M. J., *Science* **1995**, *267*, 1629-1632.
- (11) Peschel, S.; Schmid, G., *Angew. Chem.-Int. Edit. Engl.* **1995**, *34*, 1442-1443.
- (12) Novak, J., Doctoral Thesis, **2001** Chemistry, North Carolina State University
- (13) Hidber, P. C.; Helbig, W.; Kim, E.; Whitesides, G. M., *Langmuir* **1996**, *12*, 1375-1380.
- (14) Worden, J. G.; Shaffer, A. W.; Huo, Q., *Chem. Commun.* **2004**, 518-519.
- (15) Ouyang, M.; Awschalom, D. D., *Science* **2003**, *301*, 1074-1078.
- (16) Mucic, R. C.; Storhoff, J. J.; Mirkin, C. A.; Letsinger, R. L., *J. Am. Chem. Soc.* **1998**, *120*, 12674-12675.
- (17) Ying, J. W.; Sobransingh, D. R.; Xu, G. L.; Kaifer, A. E.; Ren, T., *Chem. Commun.* **2005**, 357-359.
- (18) Yu, H.; Chen, M.; Rice, P. M.; Wang, S. X.; White, R. L.; Sun, S. H., *Nano Lett.* **2005**, *5*, 379-382.
- (19) Sebba, D. S.; Mock, J. J.; Smith, D. R.; LaBean, T. H.; Lazarides, A. A., *Nano Lett.* **2008**, *8*, 1803-1808.
- (20) Noglik, H.; Pietro, W. J., *Chem. Mat.* **1995**, *7*, 1333-1336.
- (21) Srivastava, S.; Frankamp, B. L.; Rotello, V. M., *Chem. Mater.* **2005**, *17*, 487-490.

- (22) Sung, K. M.; Mosley, D. W.; Peelle, B. R.; Zhang, S. G.; Jacobson, J. M., *J. Am. Chem. Soc.* **2004**, *126*, 5064-5065.
- (23) Ibisate, M.; Zou, Z. Q.; Xia, Y. N., *Adv. Funct. Mater.* **2006**, *16*, 1627-1632.
- (24) Jensen, T.; Kelly, L.; Lazarides, A.; Schatz, G. C., *J. Clust. Sci.* **1999**, *10*, 295-317.
- (25) Park, S. J.; Lazarides, A. A.; Mirkin, C. A.; Letsinger, R. L., *Angew. Chem.-Int. Edit.* **2001**, *40*, 2909-2912.
- (26) Peng, X. G.; Wilson, T. E.; Alivisatos, A. P.; Schultz, P. G., *Angew. Chem.-Int. Edit. Engl.* **1997**, *36*, 145-147.
- (27) McConnell, W. P.; Novak, J. P.; Brousseau, L. C.; Fuierer, R. R.; Tenent, R. C.; Feldheim, D. L., *J. Phys. Chem. B* **2000**, *104*, 8925-8930.
- (28) Gu, H. W.; Yang, Z. M.; Gao, J. H.; Chang, C. K.; Xu, B., *J. Am. Chem. Soc.* **2005**, *127*, 34-35.
- (29) Loweth, C. J.; Caldwell, W. B.; Peng, X. G.; Alivisatos, A. P.; Schultz, P. G., *Angew. Chem.-Int. Edit.* **1999**, *38*, 1808-1812.
- (30) Sardar, R.; Heap, T. B.; Shumaker-Parry, J. S., *J. Am. Chem. Soc.* **2007**, *129*, 5356-5357.
- (31) Jain, P. K.; Huang, X.; El-Sayed, I. H.; El-Sayad, M. A., *Plasmonics* **2007**, *2*, 107-118.
- (32) Musick, M. D.; Keating, C. D.; Lyon, L. A.; Botsko, S. L.; Pena, D. J.; Holliday, W. D.; McEvoy, T. M.; Richardson, J. N.; Natan, M. J., *Chem. Mat.* **2000**, *12*, 2869-2881.
- (33) Chen, G.; Wang, Y.; Tan, L. H.; Yang, M.; Tan, L. S.; Chen, Y.; Chen, H., *J. Am. Chem. Soc.* **2009**, *131*, 4218-4219.
- (34) Vossmeier, T.; Delonno, E.; Heath, J. R., *Angew. Chem.-Int. Edit. Engl.* **1997**, *36*, 1080-1083.
- (35) Brust, M.; Bethell, D.; Schiffrin, D. J.; Kiely, C. J., *Adv. Mater.* **1995**, *7*, 795-797.

- (36) Elghanian, R.; Storhoff, J. J.; Mucic, R. C.; Letsinger, R. L.; Mirkin, C. A., *Science* **1997**, *277*, 1078-1081.
- (37) Mirkin, C. A.; Letsinger, R. L.; Mucic, R. C.; Storhoff, J. J., *Nature* **1996**, *382*, 607-609.
- (38) Brust, M.; Fink, J.; Bethell, D.; Schiffrin, D. J.; Kiely, C., *J. Chem. Soc.-Chem. Commun.* **1995**, 1655-1656.
- (39) McDermott, J. J.; Velegol, D., *Langmuir* **2008**, *24*, 4335-4339.
- (40) Xu, C.; Xie, J.; Ho, D.; Wang, C.; Kohler, N.; Walsh, E. G.; Morgan, J. R.; Chin, Y. E.; Sun, S., *Angew. Chem.-Int. Edit.* **2008**, *47*, 173-176.
- (41) Yin, H. F.; Wang, C.; Zhu, H. G.; Overbury, S. H.; Sun, S. H.; Dai, S., *Chem. Commun.* **2008**, 4357-4359.
- (42) Li, Y. Q.; Zhang, G.; Nurmikko, A. V.; Sun, S. H., *Nano Lett.* **2005**, *5*, 1689-1692.
- (43) Park, S. J.; Lazarides, A. A.; Mirkin, C. A.; Brazis, P. W.; Kannewurf, C. R.; Letsinger, R. L., *Angew. Chem.-Int. Edit.* **2000**, *39*, 3845-3848.
- (44) Alivisatos, A. P.; Johnsson, K. P.; Peng, X. G.; Wilson, T. E.; Loweth, C. J.; Bruchez, M. P.; Schultz, P. G., *Nature* **1996**, *382*, 609-611.
- (45) Dadosh, T.; Gordin, Y.; Krahne, R.; Khivrich, I.; Mahalu, D.; Frydman, V.; Sperling, J.; Yacoby, A.; Bar-Joseph, I., *Nature* **2005**, *436*, 677-680.
- (46) Brousseau, L. C.; Novak, J. P.; Marinakos, S. M.; Feldheim, D. L., *Adv. Mater.* **1999**, *11*, 447-449.
- (47) Novak, J. P.; Feldheim, D. L., *J. Am. Chem. Soc.* **2000**, *122*, 3979-3980.
- (48) Novak, J. P.; Brousseau, L. C.; Vance, F. W.; Johnson, R. C.; Lemon, B. I.; Hupp, J. T.; Feldheim, D. L., *J. Am. Chem. Soc.* **2000**, *122*, 12029-12030.
- (49) Novak, J. P.; Nickerson, C.; Franzen, S.; Feldheim, D. L., *Anal. Chem.* **2001**, *73*, 5758-5761.
- (50) Lawless, D.; Kapoor, S.; Meisel, D., *J. Phys. Chem.* **1995**, *99*, 10329-10335.

- (51) Turkevich, J., *Gold Bull.* **1985**, *18*, 125-131.
- (52) Su, K. H.; Wei, Q. H.; Zhang, X.; Mock, J. J.; Smith, D. R.; Schultz, S., *Nano Lett.* **2003**, *3*, 1087-1090.
- (53) Jain, P. K.; Eustis, S.; El-Sayed, M. A., *J. Phys. Chem. B* **2006**, *110*, 18243-18253.
- (54) Storhoff, J. J.; Lazarides, A. A.; Mucic, R. C.; Mirkin, C. A.; Letsinger, R. L.; Schatz, G. C., *J. Am. Chem. Soc.* **2000**, *122*, 4640-4650.
- (55) Lazarides, A. A.; Schatz, G. C., *J. Phys. Chem. B* **2000**, *104*, 460-467.
- (56) Turkevich, J.; Garton, G.; Stevenson, P. C., *J. Colloid Sci.* **1954**, *9*, S26-S35.
- (57) Sonnichsen, C.; Reinhard, B. M.; Liphardt, J.; Alivisatos, A. P., *Nat. Biotechnol.* **2005**, *23*, 741-745.
- (58) Na, J. S.; Ayres, J.; Chandra, K. L.; Chu, C.; Gorman, C. B.; Parsons, G. N., *Nanotechnology* **2007**, *18*, 035203.
- (59) Na, J. S.; Ayres, J.; Chandra, K. L.; Gorman, C. B.; Parsons, G. N., *Nanotechnology* **2007**, *18*, 424001.
- (60) Na, J. S.; Ayres, J. A.; Chandra, K. L.; Gorman, C. B.; Parsons, G. N., *J. Phys. Chem. C* **2008**, *112*, 20510-20517.
- (61) Heimenz, P. C.; Rajagopalan, R. *Principles of Colloid and Surface Chemistry*, Marcel Dekker, Inc.: New York, 1997.
- (62) Martin, J. E.; Wilcoxon, J. P.; Odinek, J.; Provencio, P., *J. Phys. Chem. B* **2002**, *106*, 971-978.
- (63) Lee, Y. G.; Morales, G. M.; Yu, L. P., *Angew. Chem.-Int. Ed.* **2005**, *44*, 4228-4231.
- (64) Seminario, J. M.; De la Cruz, C. E.; Derosa, P. A., *J. Am. Chem. Soc.* **2001**, *123*, 5616-5617.
- (65) Friend, C. M.; Muetterties, E. L.; Gland, J. L., *J. Phys. Chem.* **1981**, *85*, 3256-3262.

- (66) Chandra, K. L.; Zhang, S.; Gorman, C. B., *Tetrahedron* **2007**, *63*, 7120-7132.
- (67) Novak, J. P.; Feldheim, D. L., *J. Am. Chem. Soc.* **2000**, *122*, 3979-3980.
- (68) McConnell, W. P.; Novak, J. P.; Brousseau, L. C.; Fuierer, R. R.; Tenent, R. C.; Feldheim, D. L., *J. Phys. Chem. B* **2000**, *104*, 8925-8930.

5. Size-Exclusion Chromatography of Particles and Particle Assemblies

As discussed in Chapter 4, the main analytical tool used to characterize nanoparticles and nanoparticle assemblies is transmission electron microscopy (TEM). While TEM is a useful technique for examining small numbers of nanoparticles, it lacks the ability to provide statistical information and size distributions representative of an entire particle solution. As discussed in Section 2.1.3, particle arrays have been formed upon depositing particles onto a TEM grid and evaporating the solvent. This phenomenon makes it difficult to distinguish molecularly-linked dimers from particles that happen to lie next to one another. Moreover, there have been reports of size-separation processes which occur during this drying process.¹⁻³ Arrays form between particles of similar sizes and are often not representative of the entire sample.² Data might be biased by the arbitrary choice as to which areas on the grid to image. In addition, TEM is time-consuming and not ideal for routine analysis. There have also been reports of particles that are unstable under the high-vacuum conditions and intense electron beams required for TEM.^{2,11} The development of solution-based characterization techniques was therefore desirable. These methods could be used as routine analytical tools, and could provide more accurate statistical information. While chromatographic methods have been extensively studied for small organic molecules, similar techniques for colloids (particularly inorganic colloids) are significantly less-developed.

One technique evaluated for the characterization of nanoparticles and particle assemblies was size-exclusion chromatography (SEC). As discussed in detail below, there are several factors that affect the resolution of nanoparticles in size-exclusion experiments which must be understood in order to determine separation conditions and interpret data. In addition to size-exclusion, there are likely other mechanisms contributing to these nanoparticle separations.

5.1. Introduction and Background

5.1.1. Size-Exclusion Chromatography – General Theory

SEC is a chromatographic technique developed to separate large molecules according to size. An SEC column consists of porous micron-sized particles, typically made from a polymer or silica-based material.^{1,12,13} As solvent flows through the column at a constant rate, a sample is introduced. The smaller analytes

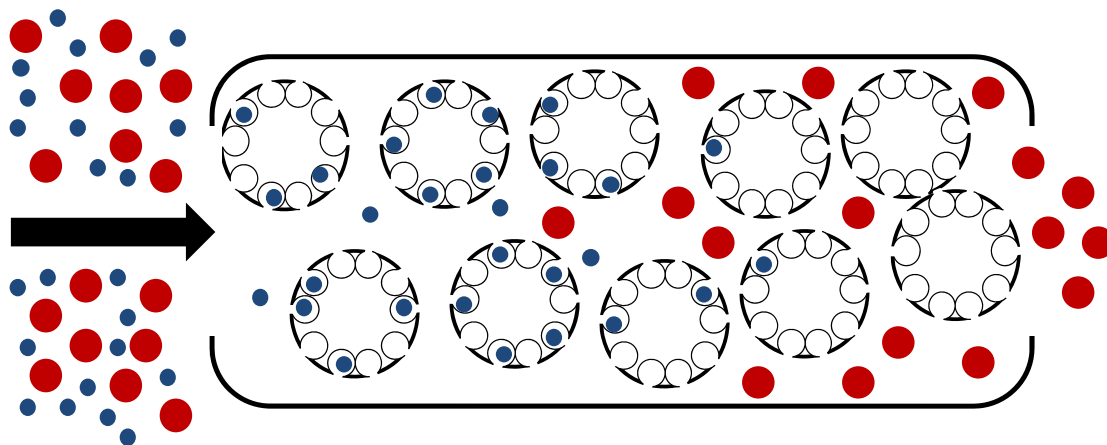


Figure 5-1. Schematic of column used for size-exclusion chromatography

readily penetrate into the pores while larger species are excluded and traverse the column at a faster rate. This general concept is represented in Figure 5-1. The time a solute spends within the SEC column is typically reported as retention volume, the volume of mobile phase required to elute the species. However, the terms retention volume and retention time are often used interchangeably. As shown in Equations 5-1 and 5-2, the retention volume is determined by a solute distribution coefficient, which reflects the concentrations of the analyte associated with both the stationary and mobile phases.

$$V_R = V_0 + K_{SEC} V_i$$

V_R = retention volume
 V_0 = free volume outside the gel particles
 V_i = volume of solvent within the pores
 K_{SEC} = solute distribution coefficient

5-1

$$K_{SEC} = \frac{(V_R - V_0)}{V_i} = \frac{c_s}{c_m}$$

5-2

c_s = concentration of analyte in stationary phase
 c_m = concentration of analyte in mobile phase

In order for the size-exclusion mechanism to be dominant in a chromatographic separation, there should ideally be no interactions between the analytes and the column material. However, in some cases, it may not be possible to eliminate specific chemical interactions. This behavior introduces elements of traditional liquid chromatography into the separation. In traditional chromatography, separation is achieved based on different chemical affinities of molecules for both the stationary and mobile phases. The retention time of a molecule is determined by a

chromatographic retention factor, which reflects the affinity of a species for the stationary phase (Equation 5-3).

$$t_R = t_M + k_A' t_M$$

t_R = retention time

t_M = time for an average molecule of the mobile phase to pass through the column

k_A' = chromatographic retention factor

5-3

While chromatographic separations are typically not reported in terms of retention volume, the expression in Equation 5-3 was multiplied by the flow rate to achieve these units as shown in 5-4.

$$V_R = u(t_M + k_A' t_M)$$

u = flow rate

5-4

A modified form of this equation was combined with Equation 5-1 in order to generate an approximate expression for the chromatographic retention volume of an analyte size-exclusion and tradition chromatographic mechanisms (Equation 5-5).

$$V_R \approx V_0 + K_{SEC} V_i + u k_A' t_M$$
5-5

Again, this equation is not directly found in the literature nor is it intended to be completely accurate; it is included here solely to indicate that an additional chromatographic term applies when interactions between an analyte and a size-exclusion column are non-negligible. In this case, the retention volume is larger than that associated with a pure size-exclusion mechanism. As retention volumes in SEC

increase with decreasing particle size, larger retention volumes due to chemical interactions can lead to an under-estimation of the analyte size.^{1,2}

In the absence of any specific chemical interactions, the retention volume for an analyte in SEC is proportional to the log of the hydrodynamic diameter.^{1-3,14-16} The size of a molecule or particle can therefore be determined from a logarithmic calibration plot. If a log relationship is not observed, there are likely other separation mechanisms occurring. Due to the high surface activity of nanoparticles, chemical interactions can often result in the irreversible adsorption of particles on the column.^{1,3,4,7,10,13,17-19} Chemical interactions and adsorption phenomenon are also indicated by asymmetrical peak shapes, which tail towards longer retention times.^{1,2} Changes in retention volumes with higher analyte concentrations are also indicative of chemical interactions.²

For nanoparticle separations, significant efforts were expended to limit chemical interactions and adsorption on the column. In addition, the column composition and the flow rate were optimized to achieve maximum resolution. For this reason, a brief discussion of factors affecting chromatographic resolution is included below.

The plate height associated with a chromatographic separation is related to the flow rate according to the van Deemter equation (Equation 5-6).¹²

$$H = A + \frac{B}{u} + Cu$$

H = plate height

A = coefficient related to multiple flow paths

B = coefficient related to longitudinal diffusion

C = coefficient related to mass transfer between phases.

5-6

The coefficient, A, is independent of the flow rate and is related to zone broadening, which occurs due to the variety of pathways by which an analyte can traverse a column. The uniformity of possible analyte paths improves with smaller particle sizes within the column. Thus, the magnitude of this term decreases with particle size, which can significantly increase the efficiency and resolution of a separation.^{10,12,16} The coefficient, B, is a longitudinal diffusion term. The longer an analyte remains in a column, the more time it has to diffuse along the length of the column, which leads to band-broadening.^{10,12} This term is therefore directly proportional to the diffusion coefficient of the analyte and inversely proportional to the flow rate. The coefficient, C, is a mass transfer coefficient which reflects how much time it takes for equilibrium to occur between the mobile and stationary phases. As the flow rate increases, there is less time for equilibrium to occur resulting in decreased resolution. The plate height as a function of flow rate is plotted in Figure 5-2 along with each term in Equation 5-5. There is an optimum flow rate for which the plate height is minimized (i.e. resolution is maximized).

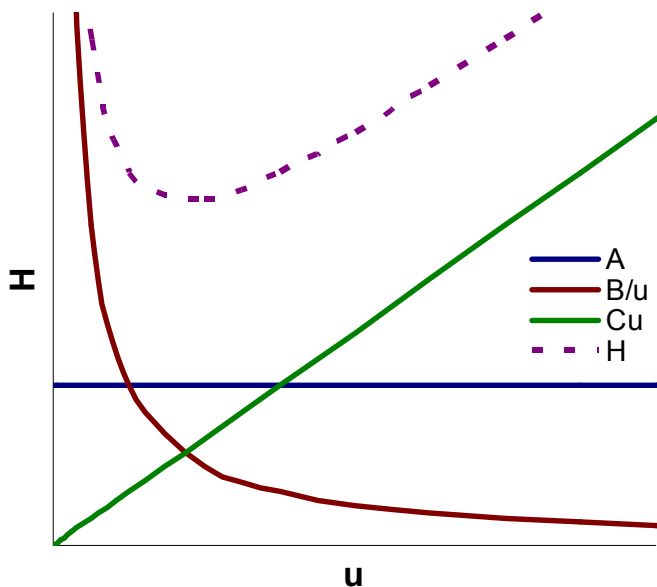


Figure 5-2. Sample van Deemter plot calculated from Equation 5-6 indicating the effects of flow rate on the plate height of a chromatographic separation

The goal of this work was to achieve efficient, high-resolution separations of nanoparticles and nanoparticle assemblies that reflect the statistical distributions present within a solution. The discussions include methods utilized to limit chemical interactions with the column and maximize resolution. The

variables considered include the column material, the composition of the mobile phase and the flow rates. As traditional chromatographic effects cannot be eliminated, these are also discussed throughout this work. Before describing the experiments performed for this project, a brief overview of literature reports describing nanoparticle chromatography is presented.

5.1.2. Liquid Chromatography of Nanoparticles in Organic Solution

While chromatographic techniques are not nearly as well-developed for nanoparticles as they are for organic molecules, there have been several reports of nanoparticle separations performed in both organic^{1,2,6,10,13,16-18,20} and

aqueous^{3,4,7,9,10,14,15,19,21} media. Separations in organic media have typically involved small clusters (1–3 nm) stabilized by organic ligands. For these cases, there was a delicate balance between size-exclusion and other chromatographic separation mechanisms.¹³ In contrast to size-exclusion, when chemical interactions dominate, smaller particles typically elute first.^{6,17,18} One report attributed this behavior to the higher solubility of smaller particles in the mobile phase.¹⁷ Another claimed that smaller alkanethiol-capped gold particles were effectively more polar than larger particles, limiting their interactions with a nonpolar stationary phase.⁶

The separation mechanism for particles varies with the nature of the particle capping ligands. For example, when hexanethiol-capped gold particles were separated in a reverse-phase column, the smallest particles were eluted first indicating a

chromatographic

separation

mechanism.¹⁷

These same

particles capped

with a mixed

monolayer of

hexanethiol and

mercapto

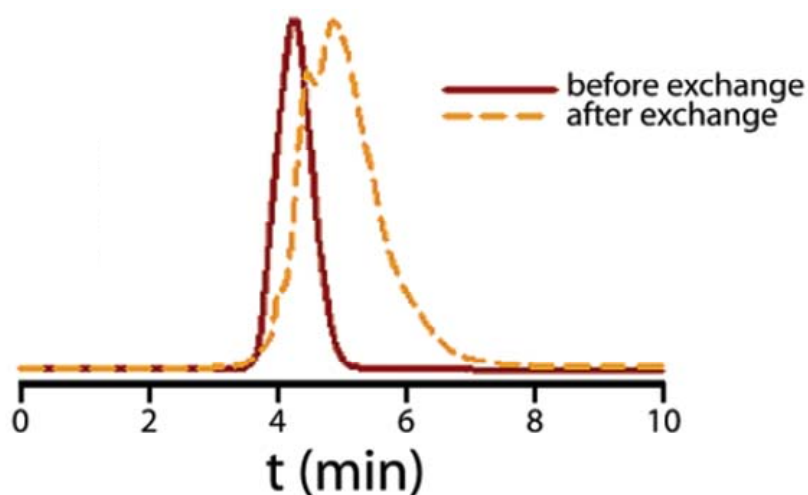


Figure 5-3. Chromatograms of monodispersed hexanethiol-capped gold nanoparticles before and after ligand-exchange with a ferrocenyl-octanethiol ligand. Figure taken from Song et al.⁶

undecanoic acid (MUA) were eluted in the reverse order indicating a size-exclusion mechanism.¹⁷ This behavior was rationalized by the increased polarity of the particles containing MUA ligands. These particles exhibited a decreased affinity towards the stationary phase, which facilitated separation by size-exclusion.¹⁷

Differences in particle capping layers can also facilitate separation. Multiple peaks have been observed for particles with uniform core sizes suggesting some polydispersity in the number of capping ligands attached to each particle.^{6,17}

Differences in capping layers have been exploited to enhance the separation of differently-sized particles. For example, one peak was observed for the separation of hexanethiol-capped gold particles.⁶ These particles were then subject to ligand-exchange with ferrocene-terminated thiols. The extent of ligand-exchange varied with particle size; more ferrocene ligands were detected on smaller particles. These differences therefore increased the resolution of the particle separation as shown in Figure 5-3.⁶

In several cases, the sizes of the nanoparticles determined by SEC were in close agreement with those determined by TEM after correcting for the thickness of the capping layer.^{10,15} In other cases, SEC provided more information about the sample than could be obtained using TEM. As mentioned previously, there have been reports of size-separation processes which occur during the preparation of samples for TEM imaging.^{1,2} The image in Figure 5-4 (A) shows an array of dodecanethiol-

capped gold particles, most of which appeared to be 3-4 nm in diameter.² Smaller, lower-contrast particles were also observed in this region, approximately 1.4-1.6 nm in diameter. However, assuming no selective particle adsorption, the SEC chromatogram in Figure 5-4 (B) indicates that the majority of particles in this sample had cores of approximately 1.6 nm. This value was calculated by subtracting the thickness of the capping ligand (2.4 nm) from the observed diameter. This example demonstrates the utility of chromatographic techniques for obtaining statistical information about a nanoparticle solution, not reflected by TEM.

As mentioned previously, one of the major difficulties associated with the chromatographic separation of nanoparticles is the aggregation and adsorption of particles. During separation, weakly bound stabilizing ligands can desorb from the

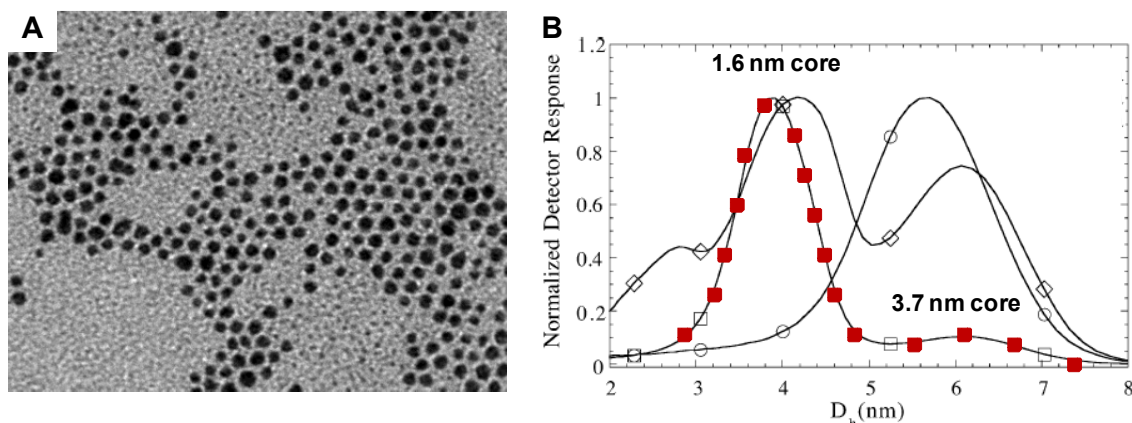


Figure 5-4. (A) TEM image of dodecanethiol-capped gold particles. The majority of particles appeared to be 3-4 nm, but lower contrast particles of approximately 1.4-1.6 nm were also observed in this region. (B) Size-exclusion chromatograms of dodecanethiol-capped gold particles. The trace corresponding to the TEM image is marked with red squares. The core sizes marked on the chromatogram were determined after subtracting the thickness of the capping layer (2.4 nm). Figure adapted from Wilcoxon et al.²

particle surfaces leading to aggregation.¹⁴ Alkanethiols have been added to the mobile phase to limit both particle aggregation and interactions with the column.^{2,10,14,16} Interactions with column were reportedly more significant when particle sizes were greater than 5nm.¹⁴ In other cases, the columns were washed with toluene following each run in attempt to remove any adsorbed particles.^{17,18}

5.1.3. Aqueous Chromatography of Nanoparticles

One of the first reports of SEC on aqueous nanoparticles involved the separation of citrate-capped gold particles using an unmodified silica column.¹⁴ Unmodified silica was chosen as it was predicted to exhibit fewer interactions with the organic citrate ions than organically-modified silica.¹⁴ The mobile phase contained additional sodium citrate in attempt to limit particle adsorption. Separation was achieved using a column consisting of 25 μm silica particles; however, irreversible adsorption occurred when 7 μm silica particles were used.¹⁴ While smaller particles yield higher resolution separations (Section 5.1.1, page 369), they also have a greater surface area which is attributed to the observed adsorption. Even with the larger particles, some gold particles were adsorbed on the column. This behavior was more prominent for larger (i.e. 20 nm) gold particles.¹⁴

In organic solution, the thickness of the capping monolayer was reflected in the effective diameter determined by SEC. Similarly, the effective diameter for electrostatically-stabilized particles was affected by the thickness of the electrical double layer.^{3,9,19,22} As the thickness of the double layer decreases with ionic strength (Section 2.1.1.1), so does the effective particle diameter. Figure 5-5 shows increases in retention times observed for cadmium sulfide particles as the ionic strength of the mobile phase was increased.⁹ It was also observed that the peak area decreased and the extent of tailing increased with increasing ionic strength, both of which indicate adsorption.⁹ The electrical double layer likely limited adsorption to the column; as its thickness decreased, adsorption became more

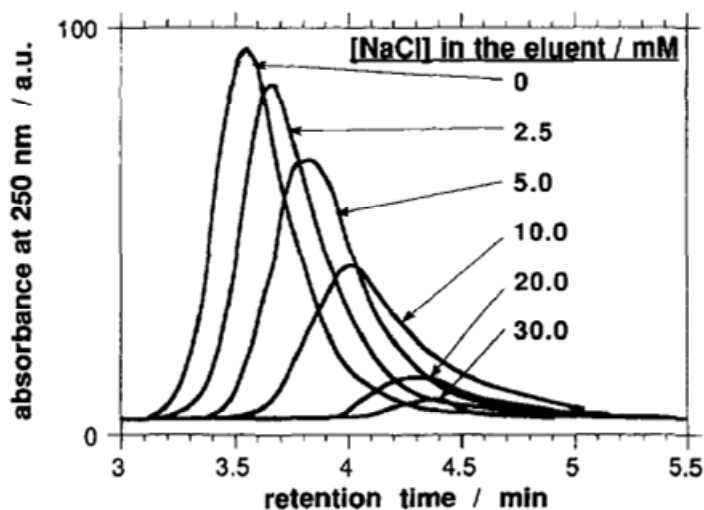


Figure 5-5. Chromatograms of CdS particles (5.7 nm) obtained using Nucleosil 500 C₄ and Nucleosil 1000 C₄ columns in series at various sodium chloride concentrations. Figure taken from Fischer et al.⁹

prevalent. The possibility that increased interactions with the column could have contributed to the increasing retention times was also explored. However, no increases in retention time were observed for similar experiments involving a column in which no size-

exclusion behavior was expected (i.e. smaller pore size so that no particles were exclude). These data supported the conclusion that the increases in retention time shown in Figure 5-5 were due to decreases in the effective particle size.⁹

In contrast to the unmodified column used for citrate-capped gold particles,¹⁴ the cadmium sulfide particles were characterized using a silica column modified with either C4⁹ or C18.³ When unmodified silica was used, particle growth occurred on the column.³ It was speculated that the silanol groups on silica surface catalyzed particle growth. This behavior was not observed when C18-modified silica was used.³

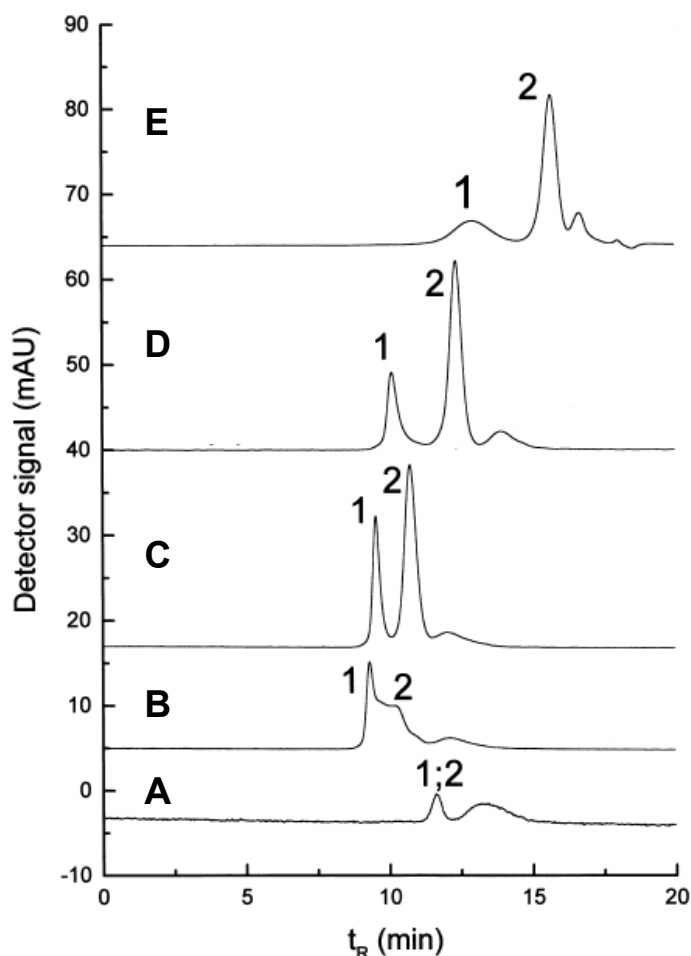


Figure 5-6. Size-exclusion chromatograms of citrate-capped gold particles (5.3 nm and 38.3 nm) with varying concentrations of sodium dodecyl sulfate in the mobile phase. (A) 0 mM (B) 0.1 mM (C) 1 mM (D) 5 mM (E) 80 mM. Figure taken from Wei et al.⁷

Particle growth was further suppressed through the addition of stabilizers to the mobile phase.³

One approach to decreasing the aggregation and adsorption of particles on an

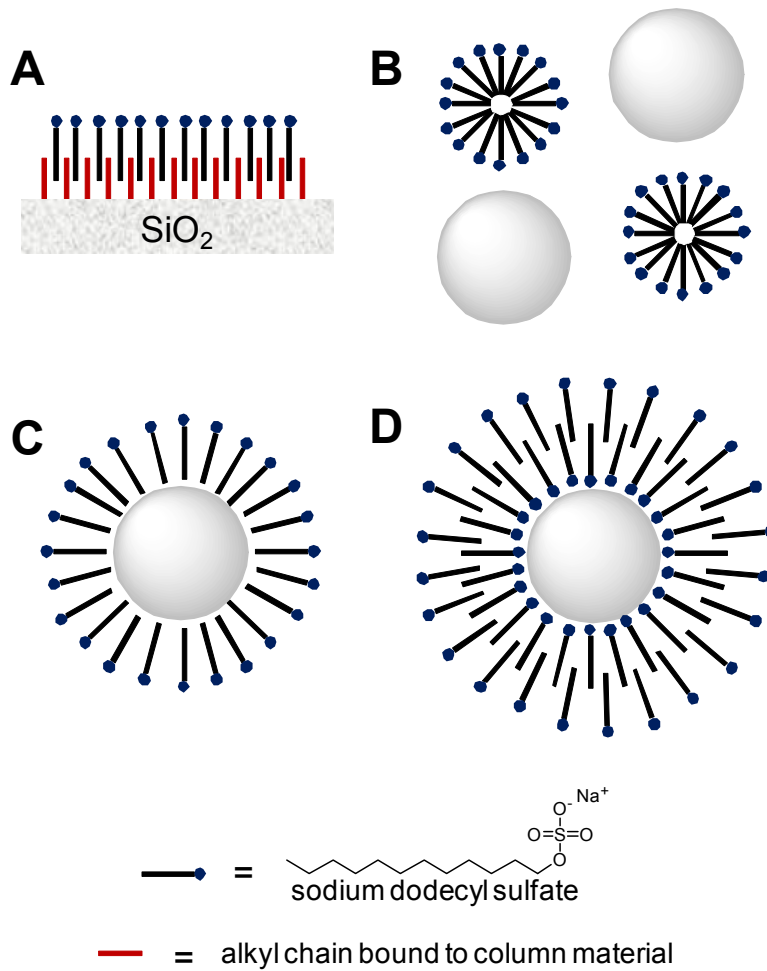


Figure 5-7. Schematics of possible interactions between sodium dodecyl sulfate (SDS) and both gold particles and size-exclusion chromatography columns (A) Interactions between SDS and silica column material coated with an alkyl chain (B) No interactions between SDS and gold particles; SDS micelles act independently of gold particles (C) Hydrophobic tails of SDS associate with gold particles (D) Inter-digitated bi-layer structure

aqueous SEC column is through the addition of a surfactant such as sodium dodecyl sulfate (SDS) to the mobile phase.^{4,7,19} Figure 5-7 shows the effects of SDS on the SEC separation of citrate-capped gold particles. Both the peak height and resolution increased in the presence of SDS.⁷

The increase in peak height was partly attributed to

interactions between the surfactant and the column packing material. Figure 5-7 (A) shows possible interactions between the hydrophobic tail of SDS and alkyl-functionalized silica. Electrostatic repulsion between this negatively-charged layer and the negatively-charged particles reduced adsorption.^{4,7}

These data also indicate a slight decrease in the retention time at low SDS concentrations followed by an increase at higher SDS concentrations. It was speculated that the initial decrease was due to interactions between the particles and SDS, which increased the apparent particle size. At higher SDS concentrations, the effects of the ionic strength of the thickness of the electrical double layer were dominant. The effective size of the particles decreased with surfactant concentration yielding longer retention times. The decrease in peak area observed at high SDS

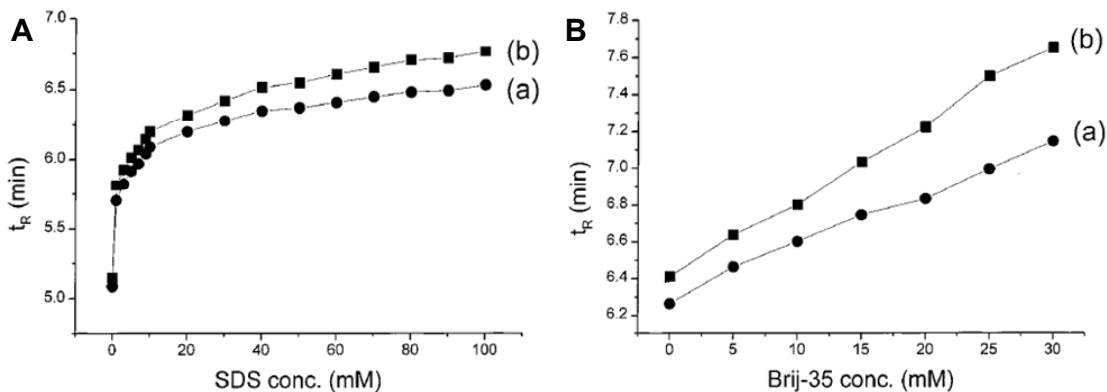


Figure 5-8. (A) Effects of the sodium dodecyl sulfate (SDS) concentration on retention times of gold nanorods (a) and gold nanoparticles (b) in size-exclusion experiments. (B) Effects of the concentration of Brij-35 added to a mobile phase consisting of 40 mM SDS. Figures taken from Wei et al.⁴

concentrations was also attributed to decreased double layer thicknesses.⁴ Another report indicates increases in retention time with SDS concentration; however, the initial decrease was not observed (Figure 5-8 (A)).⁴

Liu et al.¹⁹ presented a modified version of Equation 5-1 to account for differences in the effective diameter for particles in the presence of SDS. Equation 5-7 includes terms to account for the reduction in the effective particle diameter with increased ionic strength and the enlarged effective diameter due to interactions between the particle and SDS.

$$V_R = V_0 + K_{SEC}V_i + K_T V_i - K_P V_i \quad 5-7$$

K_T = correlation factor associated with the double-layer thickness of gold particles
 K_P = correlation factor associated with the interactions between particles and SDS

This equation indicates that there are several variables contributing to the retention time of nanoparticles within a chromatographic column, making it difficult to directly correlate retention time to core diameter. If there are other chromatographic

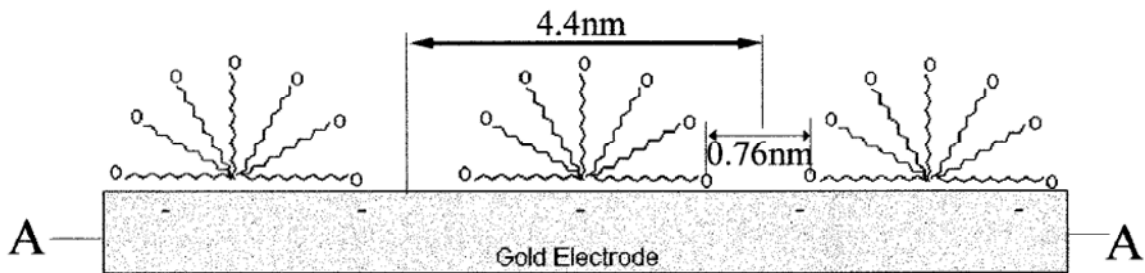


Figure 5-9. Schematic of SDS hemimicelles formed at a moderately-charged gold electrode. Image taken from Burgess et al.⁸

contributions to retention time, an additional term could add even more complexity to this relationship (Equation 5-5).

While it is speculated that SDS interacts with particles, the exact nature of this interaction remains unclear. It is possible that above the critical micellar concentration SDS micelles form, which act independently of the particles (Figure 5-7 (B)). The presence of micelles in between particles could limit aggregation. There have also been several reports claiming that the hydrophobic tail of SDS associates with gold particles as shown in (Figure 5-7 (C)).^{7,19,22} This speculation was supported by the fact that when citrate-capped gold particles were passed through C18-capped silica gel, they appeared to be largely retained on the stationary phase.^{7,19,22} While these experiments suggested that gold particles interact with alkyl chains, they do not take into account the competing presence of the sulfate ion, which may also interact with the particle surfaces. These interactions were also supported by the fact that SDS has formed hemimicelles on moderately-charged gold electrodes (Figure 5-9).⁸ In this case, both the sulfate ions and the alkyl chains interacted with the gold surface. These hemimicelles rearranged to form a monolayer at upon application of a sufficiently positive potential.⁸

Another report that supported the interaction of SDS with gold particles involved electrophoretic measurements of gold particles in the presence of SDS.⁴ In the presence of SDS, gold particles stabilized by cationic surfactants behaved as

negatively-charged species in the presence of an electric field. While an electropherogram of these gold particles in the absence of SDS was not presented for comparison, these data do suggest a strong interaction between these two species.

Wei et al.,⁷ on the other hand, presented data to suggest limited interaction between SDS and gold particles. When analytes interact with a micelle, a linear relationship is observed between $V_i/(V_R-V_0)$ and the surfactant concentration,^{7,23-25} As this relationship did not hold, it was assumed that interactions did not occur. However, as discussed in relationship to Equation 5-7, there are many variables contributing to the retention of particles under these conditions. It is therefore possible that these data do not absolutely rule out interactions between particles and SDS micelles.

While data has been presented to suggest that the hydrocarbon tail of SDS associates with gold particles as shown in Figure 5-7 (C), it is also possible that SDS forms an inter-digitated bilayer structure (Figure 5-7 (D)). In this case, the sulfate anion would likely displace the citrate anion on the gold surface. Similar structures have been observed for cationic surfactants on the surface of both gold²⁶ and nickel²⁷ particles. Spectroscopic data for tetraoctylammonium bromide and cetyltrimethylammonium bromide on gold suggested that the positively-charged bromide ions underwent hydrogen bonding with water molecules in the vicinity of the particle surfaces.²⁶ These interactions facilitated the formation of the inner-layer.

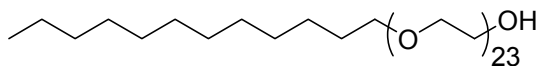


Figure 5-10. Structure of Brij-35®, polyoxyethylene (23) lauryl ether

It has been demonstrated that the presence of SDS enhances the resolution for SEC separations of gold

particles and limits particle adsorption on the column. However, the exact nature of the interactions between SDS and the particles remain unclear. Further studies are required in order to fully understand how SDS affects the apparent diameter of particles in a chromatographic separation.

While the resolution of particle separations increased in the presence of SDS, this resolution was still not sufficient to resolve different shapes of nanoparticles. Wei et al.⁴ attempted to separate gold particles from gold nanorods using SEC. The hydrodynamic diameter for a gold nanorod with a diameter of 9.7 nm and a mean aspect ratio of 4.8 was calculated to be 18.8 nm (Appendix 2). Despite the different shape, this value was similar to the diameter of the 19.3 nm spherical particles used in these experiments, making separation difficult.⁴ Separation was enhanced in the presence of a mixed-surfactant system consisting of SDS and Brij-35® (Figure 5-10).

It was speculated that the limited adsorption that occurred in the presence of SDS was due to electrostatic repulsion between the negatively charged particles and SDS adsorbed onto the column material. (Figure 5-7 (A)). The non-ionic surfactant, Brij-35®, likely interacted with the column material as well. As these molecules do not

repel the particles, some degree of adsorption likely occurred for this system. This argument was supported by the longer retention times observed in the presence of Brij-35® (Figure 5-8 (B)). Under these conditions, both size-exclusion and surface adsorption contributed to the separation mechanism. As it was believed that the adsorption behavior of gold particles is shape-dependent, the addition of Brij-35® was utilized to improve size-separation.⁴ The greatest resolution was achieved when the mobile phase consisted of 40 mM SDS and 30 mM Brij-35®.⁴ The detection of both species was enhanced by using a diode array detector. Nanorods exhibit a longitudinal plasmon resonance at significantly longer wavelengths than the transverse mode (Section 2.1.4.1.1). This absorbance can be clearly identified in

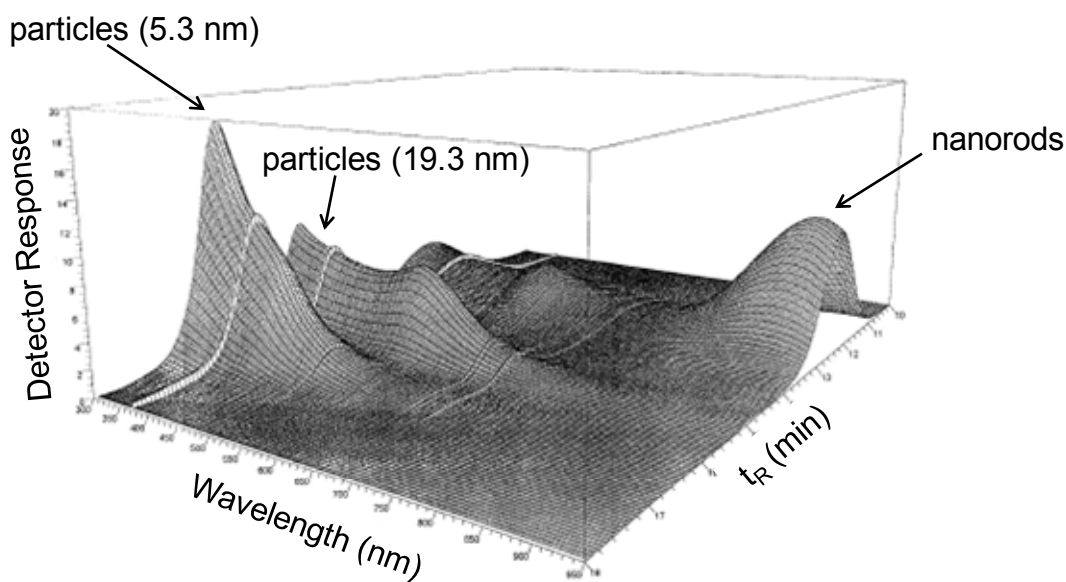


Figure 5-11. Three-dimensional size-exclusion chromatogram for a solution containing gold nanoparticles (5.3 nm and 19.3 nm) and nanorods. Mobile phase = 40 mM SDS with 10 mM Brij-35®. Figure adapted from Wei et al.⁴

the three-dimensional chromatogram shown in Figure 5-11.

5.1.4. Recycling Size-Exclusion Chromatography

Recycling size-exclusion chromatography (RSEC) is a technique that has been used to enhance the resolution in nanoparticle separations.¹⁰ These techniques effectively increase the length of the chromatographic columns without the large increases in pressure associated with long columns. Figure 5-12 (A) shows the configuration of a closed-loop RSEC system, which re-directs the solvent and the sample back through the column multiple times. The resolution increased with each pass through the column and exhibited a square root dependence on the number of cycles.¹⁰ Data obtained from the RSEC of dodecanethiol-capped gold particles are

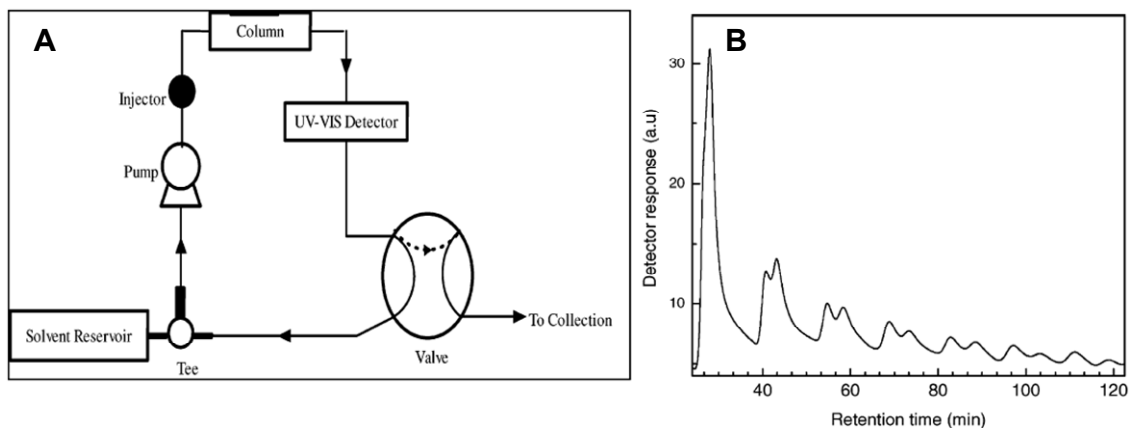


Figure 5-12. Closed-loop recycling chromatography of broadly distributed 1-decanethiol-gold nanoparticles (A) The configuration of the closed-loop recycling system. The detector, pump, and the column are all in a single closed loop. The dotted line in the valve indicates the direction of the flow when the valve is switched for collection. (B) Closed-loop recycling chromatogram of 1-decanethiol-gold nanoparticles taken on a 1000 Å column with a flow rate of 0.5 mL/min. The initially broad peak resolved into two features, which quickly dissipated due to extensive broadening introduced by recycling. Figure taken from Al-Somali et al.¹⁰

shown in Figure 5-12. While the resolution of particles increased from 0.5 to 1.2 during the cycling, significant peak broadening was also observed. This behavior was attributed to the fact that the sample repeatedly traversed the dead volume associated with both the pump and the detector.¹⁰

The alternating RSEC configuration shown in Figure 5-13 (A) proved to be more effective for improving resolution. This method involved two identical columns used

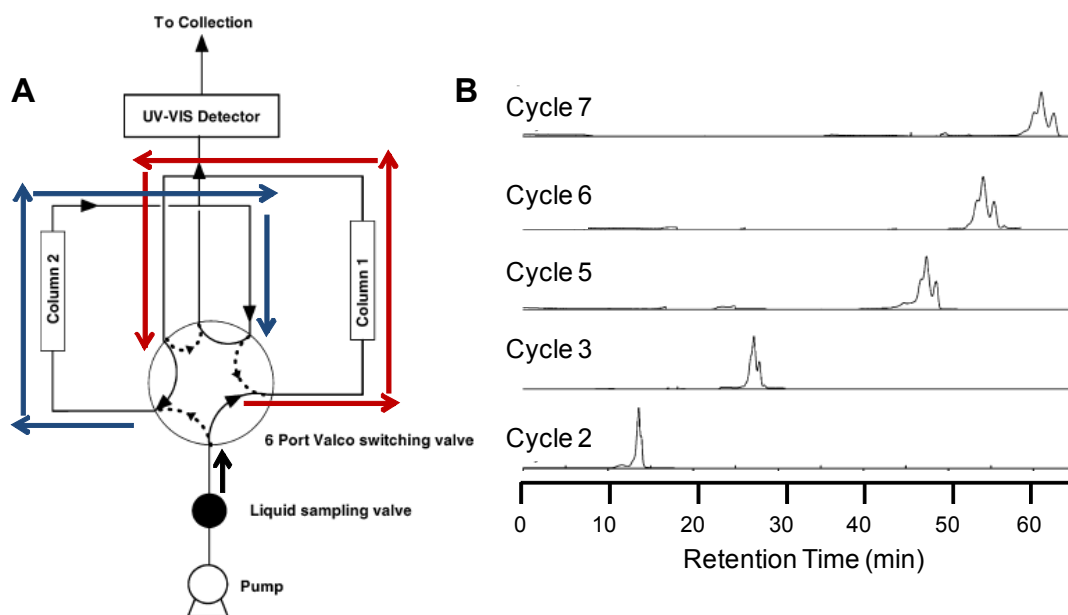


Figure 5-13. Alternate-recycling chromatography of broadly distributed 1-decanethiol-gold nanoparticles (A) configuration of the alternate-recycling system. The solvent is continually run through two columns in alternating turns. The sample first traverses the column 1 sample loop (red) followed by the column 2 sample loop (blue). At this point the sample can either go to the detector or re-enter column 1. Each column must be identical in dimensions and pore size to avoid high-pressure fluctuations. Solid arrows in the valve indicate the direction of the flow in position one. The dotted arrows indicate the direction of the flow when the valve is switched to position two. (B) Alternate-recycling chromatograms for a broadly distributed 1-decanethiol-gold nanoparticle sample at a flow rate of 1.0 mL/min. The ongoing evolution of RSEC data is shown here as a function of cycle number. Figure adapted from Al-Somali et al.¹⁰

in series. After traversing the first column, the sample entered the second column. The flow was regulated by a low-volume, high speed, six-port valve. As with the closed-loop system, the resolution increased with the square root of the cycle number.¹⁰ However, the sample did not go through the pump and the detector with each cycle so the data were not subject to the band-broadening associated with this processes. As shown in Figure 5-13 (B), the peak heights remained approximately constant through multiple cycles. This behavior also indicated minimal loss of material due to particle adsorption. The major drawback of this RSEC method is the limited peak capacity, or the number of peaks that can be resolved. There was a small peak observed at 11.6 min after cycle 2 (Figure 5-13 (B)), which was lost during the process as the other peaks were essentially magnified.¹⁰

5.1.5. SEC of Nanoparticle Assemblies

Novak et al.^{5,28} used SEC to separate assemblies of citrate-capped gold nanoparticles linked with oligomeric phenylene ethylenes (Figure 4-13). Figure 5-14 (A) shows chromatograms of 10 nm and 30 nm gold particles and a solution containing both. While these data indicated that two different particle sizes can be separated using SEC, they also showed the presence of higher-order aggregates (peak at 13.5 min). It is unclear whether these aggregates existed in solution before injection onto the column or whether they aggregated during the separation. The

mobile phase in these experiments consisted of 40 mM SDS in attempt to limit both particle aggregation and adsorption.⁵

Figure 5-14 (B) shows SEC chromatograms of solutions containing nanoparticle assemblies. In addition to peaks corresponding to individual particles, these chromatograms show peaks at shorter retention times indicative of larger structures. The retention time for the trimer was shorter than that for the dimer, which was consistent with the expected behavior.

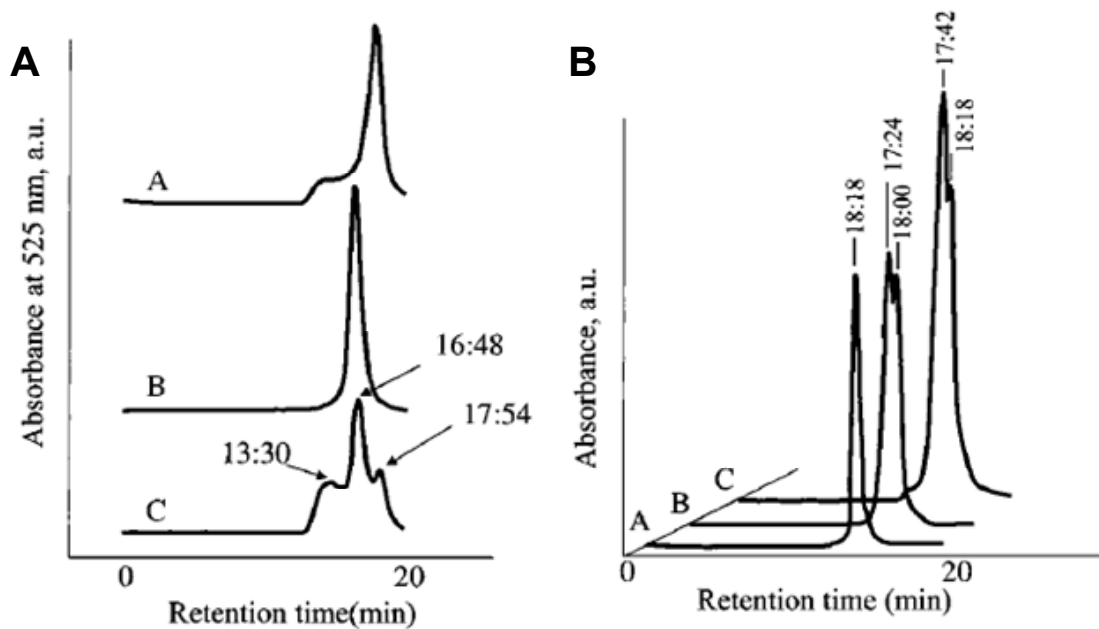


Figure 5-14. (A) Size-exclusion chromatogram showing the retention times of citrate-capped gold nanoparticles: (a) 10 nm particles (b) 30 nm particles (c) solution containing both 10 nm and 30 nm particles (B) Chromatograms for assemblies of 10 nm particles: (a) isolated particles (b) solution containing nanoparticle trimers (c) solution containing nanoparticle dimers. Figures taken from Novak et al.⁵

5.1.6. Summary

While chromatographic methods for nanoparticle separations are not nearly as well developed as comparable techniques for organic species, there have been several reports of nanoparticle separations using SEC. In some cases, specifically with organic capping ligands, specific particle/stationary phase interactions have also played a role in particle separations. The mechanism of separation has varied with the nature of the particle capping ligands, and separation has been observed for similarly-sized particles functionalized with different molecules. Due to the high surface energy associated with nanoparticles, adsorption to the column has been a significant and could make it difficult to obtain accurate statistical information.

Particles have also been separated according to size in aqueous solution. These separations have been performed using both modified and unmodified silica columns. For electrostatically-stabilized particles, the thickness of the electrical double layer contributes to the particle diameter observed using SEC. At high ionic strengths, the thicknesses of the electrical double layers decreased leading to increased adsorption on the columns.

Sodium dodecyl sulfate has been added to the mobile phase in order to limit particle adsorption and increase resolution. The effects of SDS are multi-faceted.

Interactions with between SDS and the column are believed to decrease adsorption.

It was also speculated that SDS interacts with the particles; however, the exact

nature of this interaction remains unclear. Particle interactions with SDS would increase their effective diameter while the increased ionic strength decreases the size of the electrical diameter and thus the overall diameter. The effects of ionic strength appeared to be dominant and retention times increased with SDS concentration. Beyond an optimum SDS concentration, continued increases in ionic strength led to particle adsorption.

The goal of this work was to separate nanoparticle assemblies using SEC. Data reported by Novak et al.^{5,28} suggested this was possible. Several variables were explored in order to optimize these separations. These include the column material, the composition of the mobile phase and the flow rate.

5.2. Results and Discussion

5.2.1. Organic SEC

Several attempts were made to characterize hexanethiol-capped gold²⁹ and platinum³⁰ particles using SEC. A Jordi Gel DVB (divinylbenzene) column with a 500 Å pore size was used for these experiments with little success. Significant particle adsorption was observed for both particles, even when dodecanethiol was incorporated into the mobile phase as indicated in the literature.^{2,10,14,16} In several experiments, no peaks due to eluting particles were observed. In others, very broad peaks were observed at high retention volumes and with very little consistency between runs.

As there are several literature reports of successful nanoparticle separations in organic solvent,^{1,2,6,10,13,16-18,20} it is possible these negative results were an artifact of this particular column, which had been previously been used for polymer separations. Successful separations may have been possible with a new column and further optimization of the separation parameters. However, as mentioned in previous chapters, the focus of this work was on aqueous particle assemblies. Nanoparticles which are soluble in organic solvents typically have long capping ligands, which would sterically hinder heterodimer formation. In addition, it was predicted that the success of SEC separations would be greater in aqueous media as there have been several reports of surfactants in the mobile phase which both limit adsorption and enhance resolution.

5.2.2. Aqueous SEC

5.2.2.1. Normal Phase Chromatography

Initial attempts to separate nanoparticles were based on the work of Novak et al.^{5,28} as the authors claimed to have successfully separated individual nanoparticles from dimers and trimers in solution. These separations were reportedly carried out using two silica Microsphere (Alltech, Inc) columns in series, with 500 and 350 Å pore sizes, and a mobile phase containing 40 mM SDS. A few assumptions were made in trying to replicate these conditions. The manufacturer claimed not to carry a Microsphere column, and that publication was likely referring to their Macrosphere®

product line. They had also recently discontinued columns with pore sizes greater than 300 Å. Initial separations were therefore performed using a Macrosphere® (Alltech, Inc.) column with a 300 Å pore size. It was assumed that this was the same column material used by Novak et al.,^{5,28} and that these columns were unmodified silica as initially indicated by the manufacturer and reported in the literature. After many experiments and multiple conversations with the manufacturer, it was determined that these silica columns were modified. However, the composition of the 'diol-silica' was deemed proprietary and the exact chemistry is not known.

Before injecting nanoparticle assemblies onto the column, citrate-capped gold particles of several sizes were characterized. Figure 5-15 (A) shows the SEC

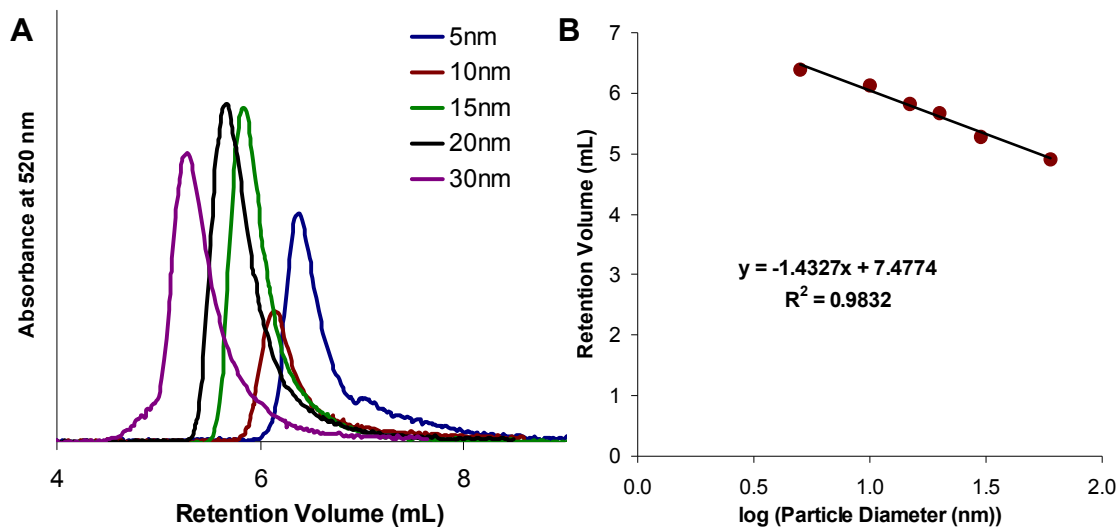


Figure 5-15. (A) SEC Chromatograms of various sizes of citrate-capped gold particles (B) Plot showing linear relationship between retention volume and log(particle diameter). Data was obtained using Alltech Macrosphere® Column (7 μm particles, 300 Å pore size), 40 mM SDS and a flow rate of 1.0 mL/min

Table 5-1. Retention Volumes Observed for Platinum Particles with Different Capping Ligands

Capping Ligand	Approximate Diameter (nm)	Retention Volume (mL)	Predicted Retention Volume for Gold Particles of this Size (mL)
Polyacrylate	3	6.9	7.0
Tiopronin	2	8.0	7.1
Mercaptobenzoic Acid	6	7.9	6.9

Retention volumes observed using a Macrosphere® Column (300 Å pore size), 40 mM SDS, and a flow rate of 0.25 mL/min

chromatograms. While separation was observed between different particle sizes, baseline resolution was not achieved. The logarithmic relationship shown in Figure 5-15 (B) indicated that the separation mechanism was primarily size-exclusion.^{1-3,14-16} However, this relationship did not hold when particles of different compositions were injected onto the column. Table 5-1 lists retention volumes for platinum particles with three different capping ligands along with the retention volumes expected for citrate-capped gold particles of the same size. These values were calculated from the linear equation shown in Figure 5-15 (B).

The retention volume observed for polyacrylate-capped platinum particles correlates with that expected for gold. However, the retention volumes for particles capped with tiopronin and mercaptobenzoic acid were larger than the expected values. This result suggests that these particles exhibit a greater affinity for this column than the citrate-capped gold particles and that chemical interactions contributed to the separation mechanism.

After characterization of individual particles, solutions containing nanoparticle dimers were injected onto the column. Figure 5-16 (A) shows SEC chromatograms of citrate-capped gold particles as a function of time after the addition of an OPE linker molecule.* In addition to the peak at 6.6 mL corresponding to isolated particles

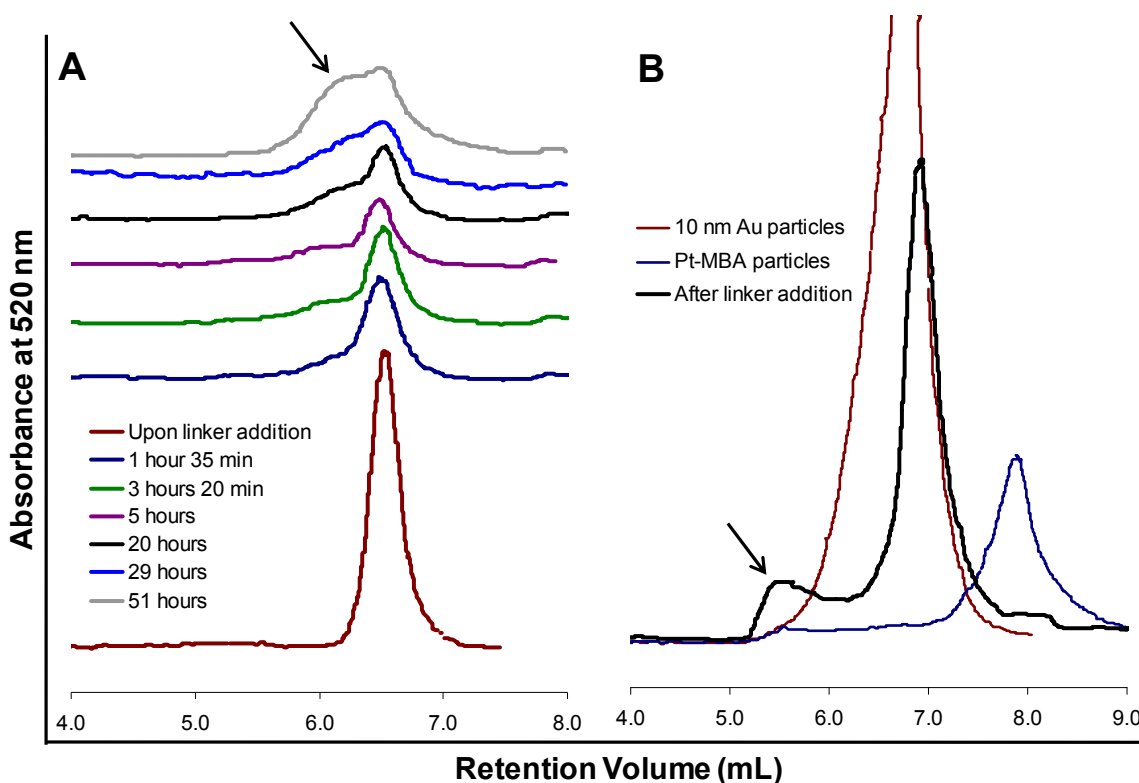


Figure 5-16. SEC Chromatograms (A) citrate-capped gold particles (5 nm) upon addition of OPE linker molecule; chromatograms were taken as a function of time after linker addition and offset along the y-axis for clarity. (B) citrate-capped gold particles (10 nm), mercaptobenzoic acid-capped platinum particles, and a solution of both particles after incubation with a bifunctional linker molecule. Chromatograms were obtained using a MacroSphere® (Alltech, Inc). column with a 300 Å pore size, a mobile phase containing 40 mM SDS and a flow rate of 0.25 mL/min

* The synthesis of nanoparticle assemblies is discussed in Chapter 4

(5 nm), a broad peak grew in at approximately 6.2 mL. Based on the calibration plot shown in Figure 5-15 (B), this value correlates to a hydrodynamic diameter of 7.8 nm. The calculated hydrodynamic diameter for two, linked 5 nm diameter particles was 8.2 nm (Table A-2-1). The similarity between these two values suggests that the peak at 6.2 mL was likely due to the presence of gold homodimers. However, there was significant overlap between the peaks associated with isolated particles and dimers; greater resolution was desired in order to accurately obtain statistical information regarding the concentration of both species in solution.

Similar conditions were used in attempt to detect heterodimers consisting of citrate-capped gold particles and mercaptobenzoic acid-capped platinum particles. Figure 5-16 (B) shows chromatograms for both the gold and platinum particles both before and after linker addition. Despite the tailing optical absorbance of platinum particles (Section 2.1.4.2), they could be detected at a wavelength of 520 nm at sufficient concentrations. At the low concentrations used for heterodimer formation, minimal absorption was observed. A detection wavelength of 520 nm was used in heterodimer experiments to detect the shift in the retention volume of the gold particles upon dimerization. Chromatograms obtained using lower detection wavelengths were often obscured by the presence of other organic species in solution.

The observed interactions between the platinum particles and the column complicated the detection of heterodimers using SEC. The hydrodynamic diameter of a gold particle was predicted to increase upon binding to a platinum particle, leading to a decrease in the retention volume. However, the platinum particle had a higher affinity for the column as indicated in Table 5-1, which could lead to increases

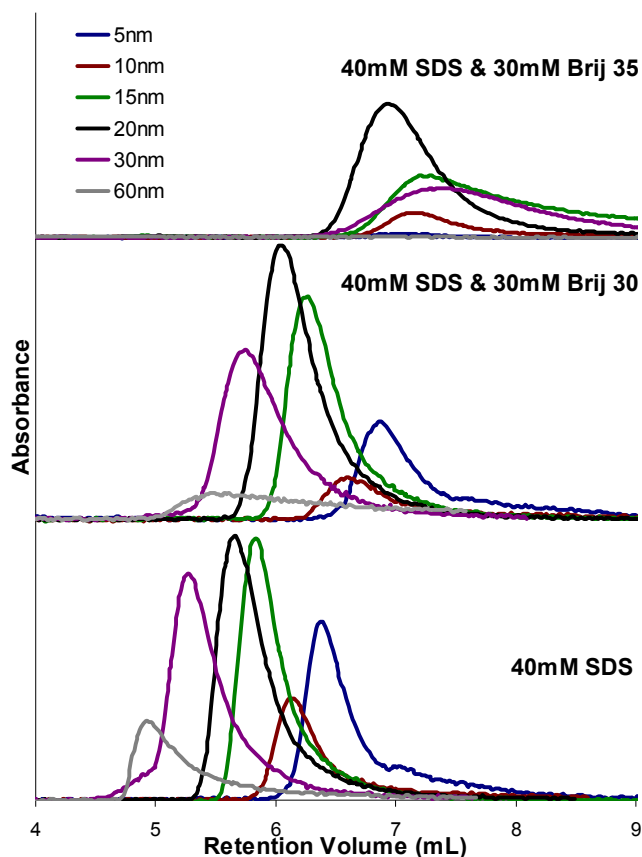


Figure 5-17. SEC chromatograms of citrate-capped gold particles with varying mobile phase compositions. Chromatograms were obtained using a MacroSphere® (Alltech, Inc). column with a 300 Å pore size.

in the particle retention times.

These competing effects were predicted to make resolution of heterodimers difficult.

Figure 5-16 (B) shows a peak at 5.6 mL, which was observed after heterodimer formation. The peak at 6.9 mL, which corresponded to isolated gold particles (10 nm) did not agree with previous measurements in which a retention time of 6.1 mL was observed. These data suggest that the

performance of the column shifted with time and made it difficult to correlate the peak at 5.6 mL with the calibration curve.

Based on the calibration curve, the hydrodynamic diameter corresponding to a 5.6 mL was approximately 20.4 nm, which is significantly greater than the predicted hydrodynamic diameter of approximately 12 nm (Table A-2-2). This observation, combined with the facts that the retention times for gold particles appeared to be increasing with the life of the column and the platinum particles exhibited a greater affinity than gold for the column, led to the conclusion that the observed peak was due to larger aggregates rather than isolated heterodimers. TEM data obtained for these structures (Section 4.2.2) indicated the presence of many different structures

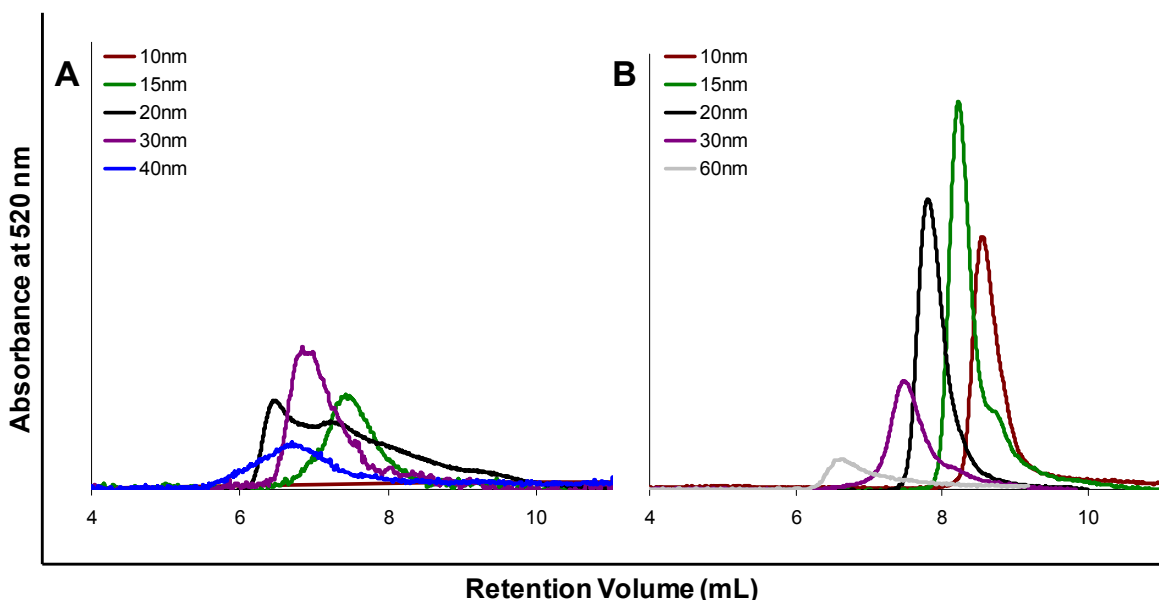


Figure 5-18. SEC Chromatograms (A) citrate-capped gold particles (B) citrate-capped gold particles after ligand-exchange with BSPP. Data obtained using two columns in series, MacroSphere® (300 Å) and Nucleosil (500 Å), 40 mM SDS and a flow rate of 0.25 mL/min

within this solution. Again, greater resolution was desired in order to effectively separate isolated particles from heterodimers, gold particle bound to more than one platinum particle and larger aggregates.

Wei et al.⁴ demonstrated improved resolution between particles of different shapes when Brij-35® (Figure 5-10) was added to the mobile phase. Figure 5-17 shows that significant particle adsorption occurred when Brij-35® was added to the mobile phase. A similar surfactant, Brij-30®, was also used with better results. This molecule contains four oxyethylene repeat units compared to Brij-35®, which contains twenty-three. It was speculated that the longer polar segments associated with the Brij-35® contributed to particle adsorption. While Brij-30® yielded better results than Brij-35®, significant peak broadening was observed, which would likely impede the resolution of nanoparticle dimers.

Another attempt to improve resolution involved adding another column in series. As mentioned previously, Macrosphere® columns with pore sizes greater than 300 Å were no longer available. Based on the assumption that these columns were composed of unmodified silica, another silica column was used for this purpose, (Nucleosil, 500 Å). The

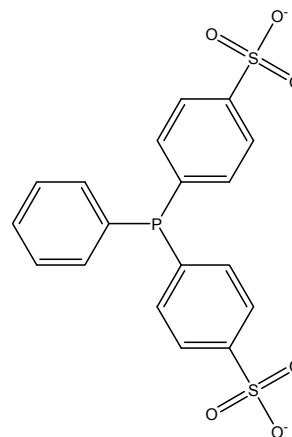


Figure 5-19. Bis(p-sulfonatophenyl)phenylphosphine (BSPP)

use of Nucleosil columns had also previously been reported for gold nanoparticle separations.^{14,19} Figure 5-18 (A) shows chromatograms of citrate-capped particles injected into this series of columns and indicates significant particle adsorption. Very broad peaks were observed with minimal peak areas. No peak was observed for 10 nm gold particles. This behavior was the first indication that the Macrosphere® column was not unmodified silica.

In attempt to stabilize the particles against adsorption on the column, the gold particles were subject to ligand-exchange with bis(p-sulfonatophenyl)phenylphosphine (BSPP, Figure 5-19), which has been shown to increase particle stability.^{5,31,32} The chromatograms shown in Figure 5-18 (B)

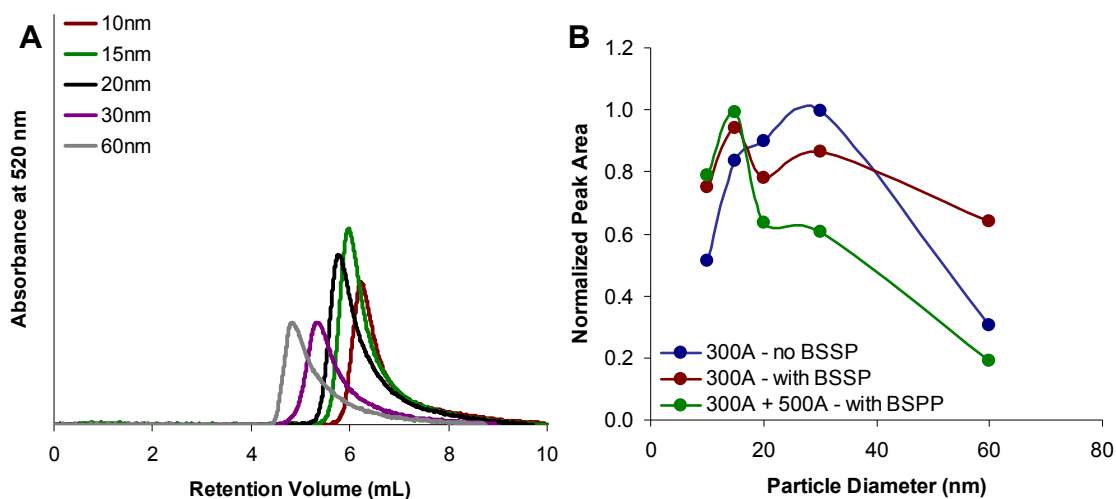


Figure 5-20. (A) SEC chromatograms of BSPP-capped gold particles. Chromatograms were obtained using a Macrosphere (Alltech, Inc). column with a 300 Å pore size. (B) Normalized peak areas as a function of particle size for different separation conditions. Normalized peak areas were calculated from the ratio of the peak areas observed for particles after passing through the column(s) to the area observed for particles which did not traverse the column(s). The lines here are not meant to indicate any type of relationship and are included only to guide the eye.

indicate that this process effectively reduced particle adsorption and improved separation. While baseline separation was still not obtained, the resolution was greater than that observed using a single column.

For comparative purposes, gold particles were then characterized using the single Macrosphere® column (300 Å). These chromatograms, shown in Figure 5-20 (A), appeared to be less-resolved than those obtained for citrate-capped gold particles under the same conditions (Figure 5-15 (A)). The normalized peak areas were calculated from the ratio of the peak areas observed for the particles after passing through the column(s) to the area observed for particles which did not traverse the column(s), and are shown in Figure 5-20 (B). While there were no apparent trends in the normalized peak areas between the citrate-capped and BSPP-capped gold particles on the Macrosphere® column, the peaks associated with BSPP-particles were significantly broader and not as tall. These data suggest that particle interactions were greater between BSPP-capped particles than citrate-capped particles on the Macrosphere® column. This behavior contradicts that observed for the Nucleosil columns, again indicating that the Macrosphere® columns were not unmodified silica. These data also indicate the sensitivity of nanoparticle separations to the nanoparticle composition and suggest that chemical interactions do contribute to the separation mechanism.

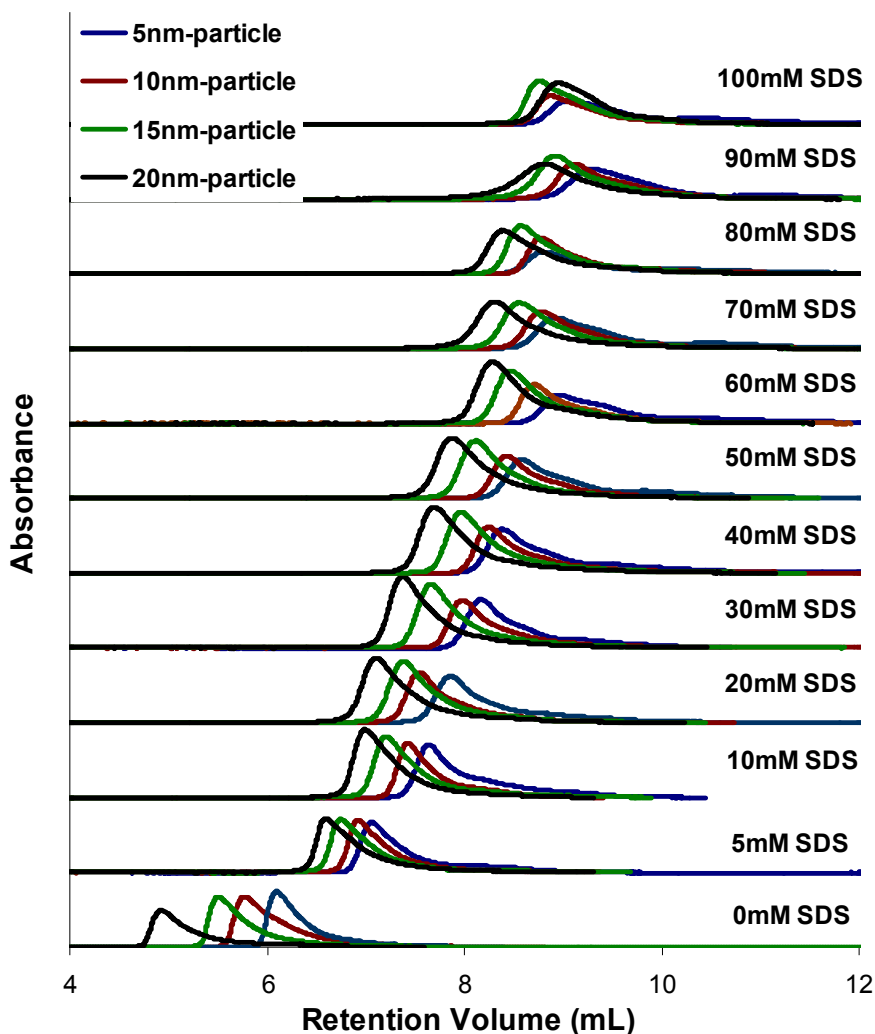


Figure 5-21. SEC chromatograms of BSPP-capped gold particles at various SDS concentrations. Data obtained using two columns in series, Macrosphere (300 Å) and Nucleosil (500 Å) and a flow rate of 0.25 mL/min

Before attempts were made to analyze nanoparticle assemblies using both column in series, additional experiments were performed to optimize resolution by varying the SDS concentration

and the flow rate. Figure 5-21 shows SEC chromatograms of gold particles after ligand-exchange with BSPP at several SDS concentrations. The retention times, which are also shown in Figure 5-22 (A) increased with SDS concentration, which is

consistent with the behavior reported by Wei et al.^{4,7} (Figure 5-6 and Figure 5-8 (A)). As discussed in Section 5.1.3 (page 378), the exact interactions between gold particles and SDS are unknown and likely complex. The increases in retention times were attributed to decreases in the thickness of the electrical double layer, which decreased the effective particle diameter and likely contributed to particle adsorption. Particle adsorption is indicated by peak tailing and broadening.

The resolution between the 5 nm and 20 nm particles was calculated for each case, and as shown in Figure 5-22 (B) exhibited a maximum between 10 and 30 mM SDS. Due to the tailing observed at the base of each peak, the peak width in these calculations was approximated as twice the width at half height.

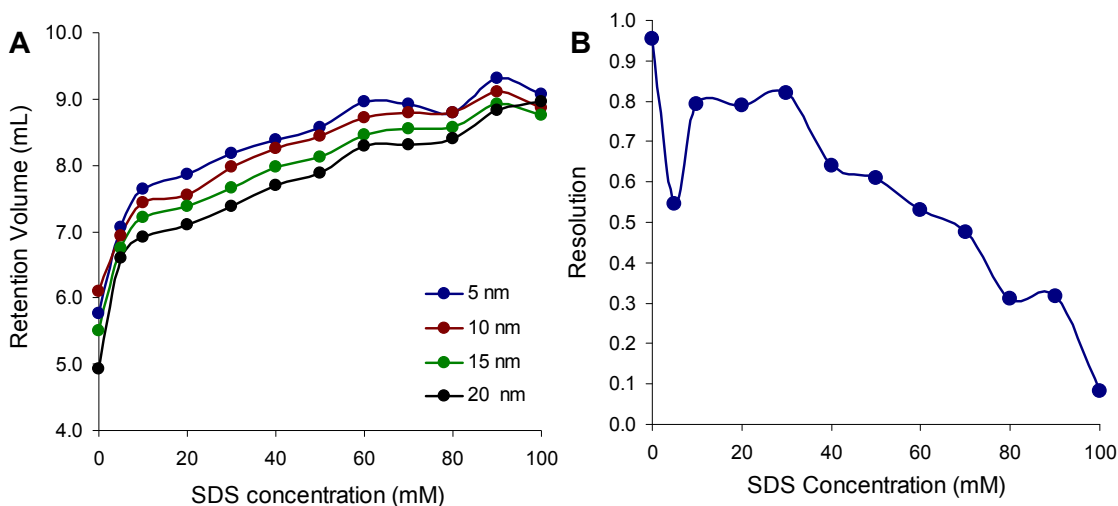


Figure 5-22. (A) Retention of BSPP-capped gold particles as a function of SDS concentration in the mobile phase (B) Resolution between 5 and 20 nm particles as a function of SDS concentration. The lines here are not meant to indicate any type of relationship and, are included only to guide the eye.

$$R_s = \frac{2\Delta Z}{W_A + W_B}$$

ΔZ = distance between peaks
 W_A, W_B = widths of two respective peaks
 Approximation: $W \sim 2W_{1/2}$; $W_{1/2}$ = width at half height

5-8

The flow rate was then varied using a mobile phase consisting of 10 mM SDS. According to the van Deemter Equation (Equation 5-6), which is plotted in Figure 5-2, there is a flow rate at which a minimum plate height (i.e. maximum resolution) is achieved. The plate height was calculated according to Equations 5-9 and 5-10, and is plotted for each particle along with the overall resolution in Figure 5-23.

$$N = 5.54 \left(\frac{V_R}{W_{1/2}} \right)^2$$

5-9

N = number of theoretical plates

$$H = \frac{L}{N}$$

5-10

L = length of column

The optimum flow rate was determined to be 0.30 mL/min. Attempts to separate nanoparticle homodimers were therefore performed using a mobile phase of 10 mM SDS and a flow rate of 0.30 mL/min. However, even under these conditions, there were difficulties with characterizing nanoparticle dimers.

As discussed in Section 4.2.1, the synthesis of nanoparticle assemblies in this work required the addition of organic solvent to solubilize the OPE linker, and sodium

citrate to deprotect the thioacetate functionalities. Both of these added reagents have consequences regarding particle stability. For these reasons, the stability of particles with these additives was also evaluated on the SEC columns. Figure 5-24 shows chromatograms of BSPP-capped particles both with and without solvent and citrate additives at several SDS concentrations. In the absence of SDS, differences in retention volumes were observed in the presence of additives; however, no clear trends were noted. In the presence of SDS, particle aggregation was observed in the presence of additives, which appeared to be dependent upon SDS concentration. Optical absorption spectra of the particle solutions in the presence of

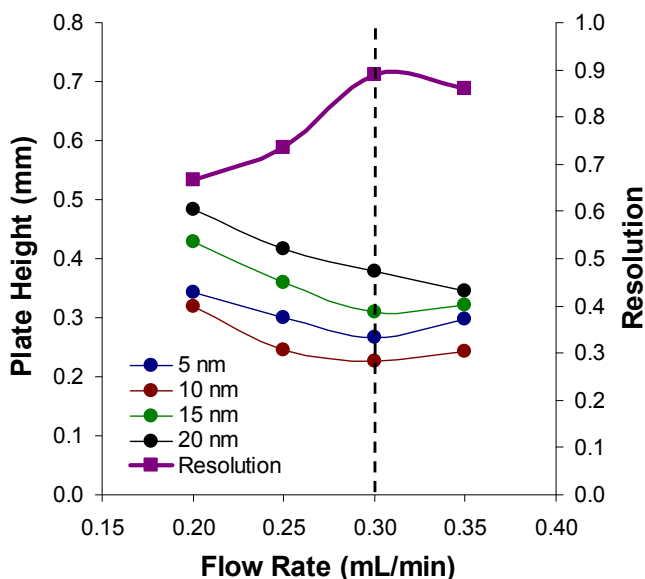
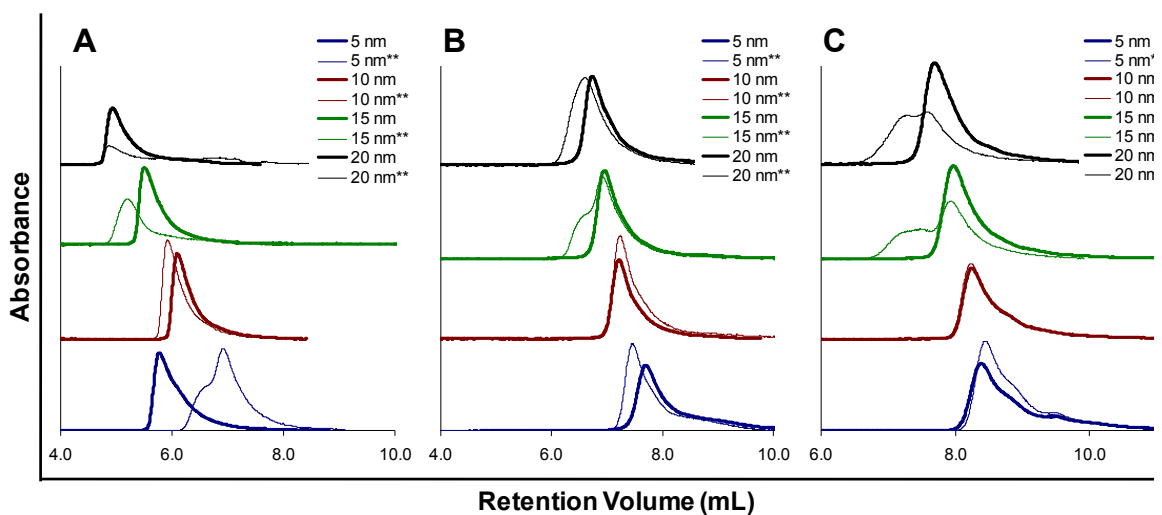


Figure 5-23. The plate height and the resolution between 5 nm and 20 nm particle as a function of flow rate. The lines here are not meant to indicate any type of relationship and, are included only to guide the eye.

SDS did not indicate aggregation (i.e. no red shift in the absorption maximum) suggesting that aggregation occurred under the higher pressure conditions of the column chromatography.

The particle aggregation observed in the presence of solvent and citrate made it difficult to detect particle dimers



**Figure 5-24. SEC chromatograms of BSPP-capped gold particles at (A) 0 mM SDS, (B) 10 mM SDS and (C) 40 mM SDS. Data was obtained using two columns in series, MacroSphere® (300 Å) and Nucleosil (500 Å) and a flow rate of 0.30 mL/min
** indicates particles with organic solvent and sodium citrate (thinner lines)**

in solution as two peaks were observed for some particles even in the absence the molecular linker. This behavior also brought into question the data obtained by Novak et al.^{5,28} (Figure 5-14 (B)) as the authors did not perform this control experiment. However, the differences in retention times observed for the dimer and trimers supports the fact that the additional peaks observed in these experiments were due to molecularly-linked species.

The aggregation behavior shown in Figure 5-24 was more prominent for larger particle sizes. A few experiments were performed in attempt to detect nanoparticle assemblies comprised of smaller gold particles. Figure 5-25 shows SEC chromatograms for dimers and trimers of 5 nm gold particles. After synthesis, some

of the assemblies were subject to ligand-exchange with BSPP. Consistent with previously reported behavior (Figure 5-18), significantly less adsorption occurred for the assemblies stabilized by BSPP. Small shoulders were observed in the SEC chromatograms for solutions containing dimers and trimers suggesting the presence of another species (Figure 5-25 (A)). However, resolution was poor and no conclusions could be drawn.

The same assemblies were characterized in the absence of BSPP. As shown in Figure 5-25 (B), the peak associated with isolated 5 nm particles was significantly smaller under these conditions (peak height comparable to the shoulder visible in (A)). However, under these conditions, small peaks were resolved which were

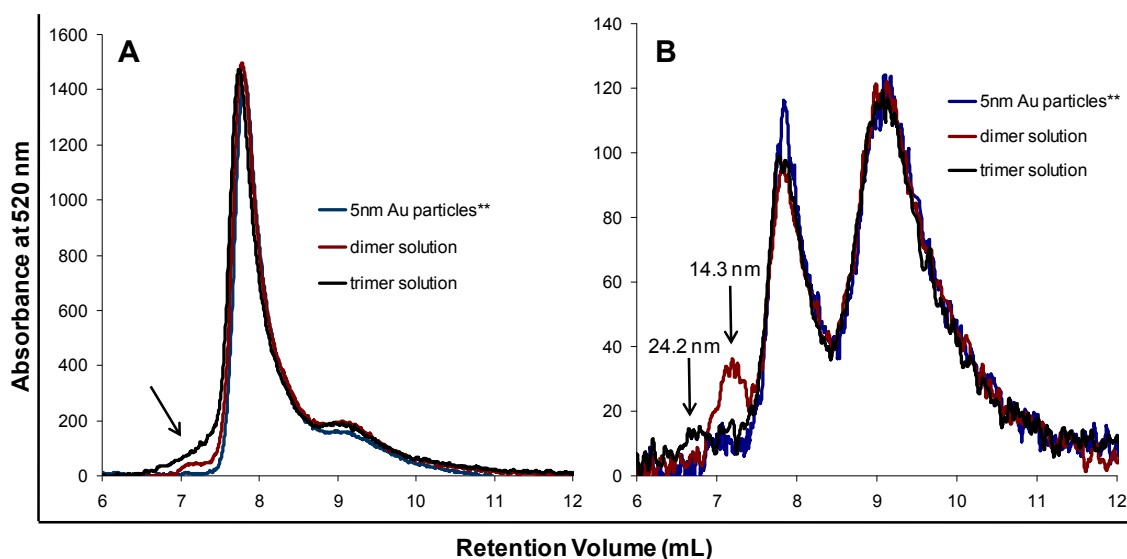


Figure 5-25. SEC chromatograms of gold nanoparticles (5 nm) and particle assemblies (A) After ligand-exchange with BSPP (B) In the absence of BSPP Data was obtained using two columns in series, Macrosphere® (300 Å) and Nucleosil (500 Å) and a flow rate of 0.30 mL/min. The absorbance units are arbitrary, but were included here for comparative purposes.

** indicates particles with organic solvent and sodium citrate

attributed to the presence of dimers and trimers in solution. Based on the logarithmic calibration plot, the dimer and trimer peaks were correlated with hydrodynamic diameters of 14.3 nm and 24.2 nm, respectively. These differ from the calculated hydrodynamic diameters for these structures, 8.2 nm and 40.9 nm (Appendix 2). However, as discussed in Appendix 2, there was a significant margin of error associated with these calculations (esp. for trimers). In addition, if the separation mechanism is not solely size-exclusion, some discrepancies would also be expected in these values. The differences in retention volumes between the two samples suggest that these peaks can be attributed to nanoparticle dimers and trimers in solution.

Despite the effort taken to optimize the separation conditions, the Macrosphere® and Nucleosil columns did not provide sufficient resolution for the separation of nanoparticle assemblies. While small peaks were observed for the assemblies in the absence of BSPP, no relevant statistical information can be obtained from these data due to obvious particle adsorption.

5.2.2.2. Reverse-Phase Chromatography

Nanoparticle separations were also attempted using non-polar stationary phases. Figure 5-26 shows chromatograms obtained using a silica column modified with an octyl capping layer (C8). The column pore size was only 80 Å; therefore, separation was not expected. This experiment was performed to evaluate the extent of particle

adsorption in a reverse-phase column. Very narrow, reproducible peaks were observed indicating minimal adsorption. The size of these peaks did not change in the presence of BSPP.

Size-exclusion experiments were then performed using a silica-C18 column with a 500 Å pore size. The C18 column was chosen for several reasons. First, the C8 material was not available at pore sizes greater than 150 Å. In addition, Fischer et al.³ reported improved separation of semiconductor particles using a silica-C18 column compared to a silica-C4 column. It was reported that the C18 capping layer was more effective at

shielding the particles from the silica cores of the particles in the stationary phase. It was also predicted that interactions between SDS and the alkyl capping layer (Figure 5-7 (A))

would be greater for the longer alkyl chain, a behavior that was also

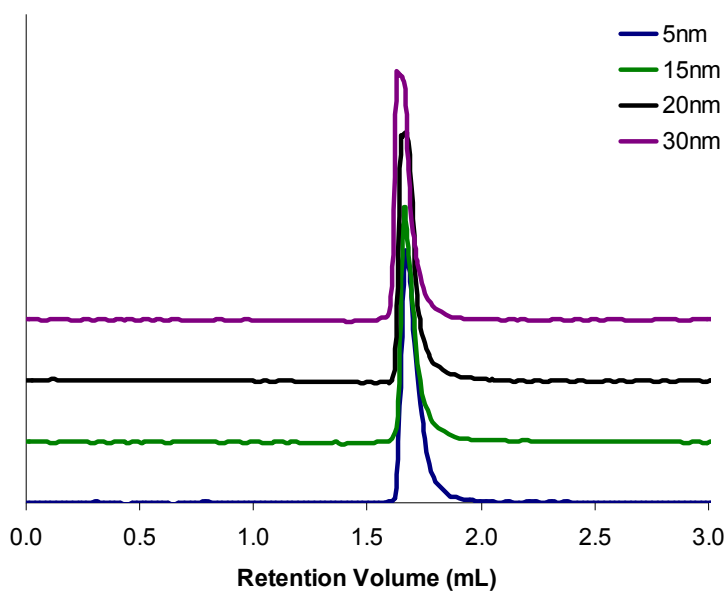


Figure 5-26. SEC Chromatograms of citrate-capped gold particles. Chromatograms were offset along the y-axis for clarity. Data were obtained using a silica-C8 column (80 Å) a mobile phase consisting of 40 mM SDS and a flow rate of 0.25 mL/min.

predicted to limit adsorption.

Contrary to predictions, the chromatograms in Figure 5-27 indicated that the extent of adsorption was greater on the C18 column compared to the C8 column. Also, the peak associated with 5 nm particles, which appeared to be just a shoulder in previous experiments using normal-phase columns (Figure 5-14 (A) and Figure 5-25 (A)) was dominant in this case, especially at high SDS concentrations. This peak was attributed to tannic acid, which is used in the synthesis of smaller gold particles (Section 2.2.2.1). Figure 5-28 shows that this peak corresponded to the retention volume of tannic acid, which, in contrast to other organics, exhibited at least some

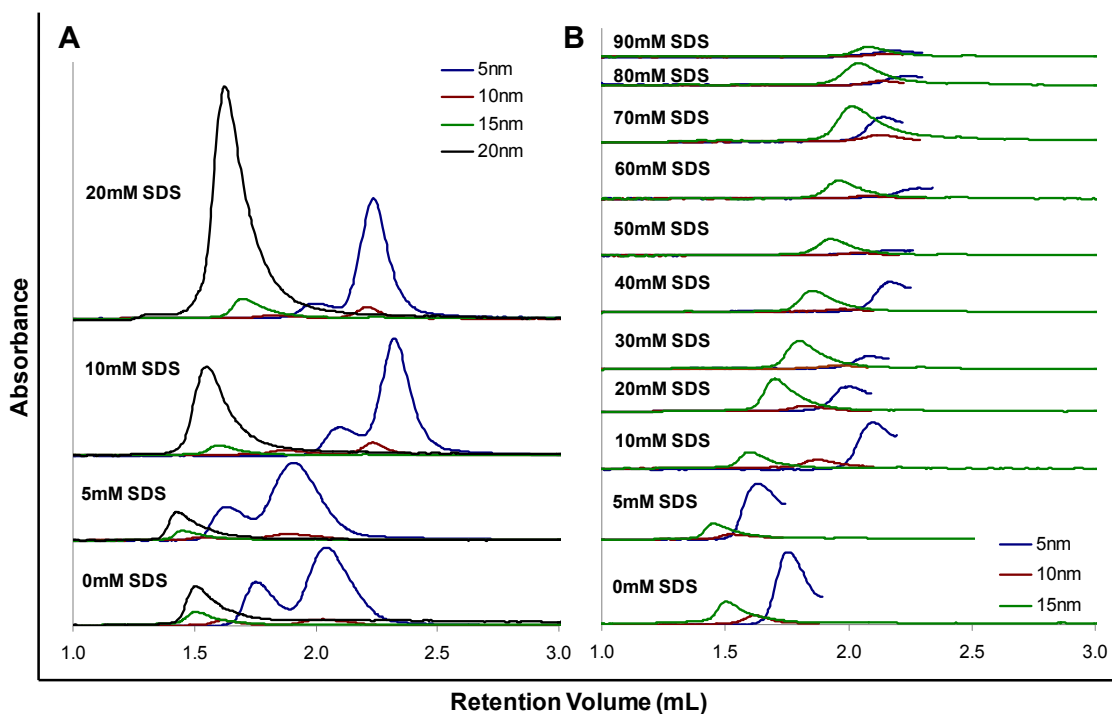


Figure 5-27. SEC Chromatograms of citrate-capped gold particles at various SDS concentrations. The chromatograms in (B) do not show the larger peaks associated with 20 nm and 5 nm particles. Data was obtained using a silica-C18 column (500 Å) and a flow rate of 0.25 mL/min

degree of absorption at 520 nm.

The adsorption behavior was dependent upon particle size as shown in both Figure 5-27 (A) and Figure 5-29. Figure 5-29 compares the normalized peak areas for citrate-capped gold particles to the data collected for the silica and C8 columns. The data collected for the C8 column is not an accurate comparison as these data were obtained using a mobile phase containing 40 mM SDS compared to the 10 mM SDS used in the other experiments. As decreases in peak area were observed with increasing SDS concentration, it is possible that these peak areas would have been greater under these conditions. Regardless, the extent of particle adsorption was

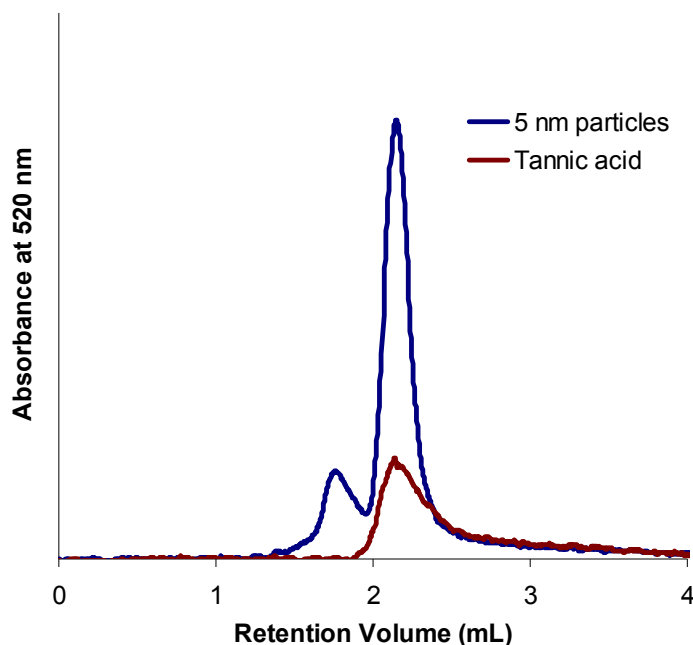


Figure 5-28. SEC chromatograms of citrate-capped gold particles and tannic acid. Data obtained using a silica-C18 column (500 Å), a mobile phase consisting of 10 mM SDS and a flow rate of 0.25 mL/min.

significantly greater for the C18 column than either the C8 column or the silica columns in the presence of BSPP.

The logarithmic relationship shown in Figure 5-30 (A) indicates that the primary separation mechanism was size-exclusion.

While the slope of this plot was less than that obtained using the silica columns in series, the peaks were significantly narrower resulting in greater overall resolution according to Equation 5-8 (Figure 5-30 (B)). The highest resolution for the C18 column was achieved using an SDS concentration of 10 mM.

As with the Macrosphere column®, chemical interactions were evident when particles of different compositions were injected onto the column. Table 5-2 lists

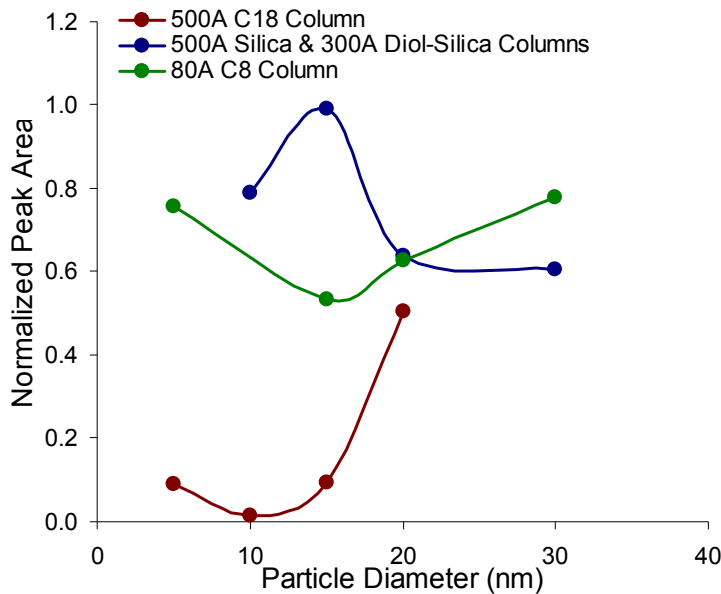


Figure 5-29. Normalized peak areas for citrate-capped gold particles characterized with several different SEC columns. The mobile phase consisted of 10 mM SDS for the silica columns and 40 mM SDS for the C8 column. Normalized peak areas were calculated from the ratio of the peak areas observed for particles after passing through the column(s) to the area observed for particles which did not traverse the column(s). The lines here are not meant to indicate any type of relationship and, are included only to guide the eye.

retention volumes for both platinum and iron oxide particles with the retention volumes expected for citrate-capped gold particles of the same size. These values were calculated from the linear equation shown in Figure 5-30 (A). The retention volume for the tartaric acid-capped particles correlates with that expected for gold. However, the retention

volumes for tiopronin-capped platinum particles were lower than the expected values. These results are consistent with those observed on the Macrosphere® column (Table 5-1). These particles exhibited a greater affinity for the polar column than the citrate-capped gold particles, and fewer interactions with the non-polar C18 column. While the size-exclusion and chromatographic processes were determined to be competitive for heterodimer separation on a polar column, these effects are likely additive for the C18 column. Higher-resolution heterodimer separations were therefore predicted for the C18 column.

The effects of the organic solvent and sodium citrate necessary for dimer formation on the SEC behavior were evaluated. The peak broadening and particle adsorption observed for the silica columns (Figure 5-24) did not occur. However, the behavior

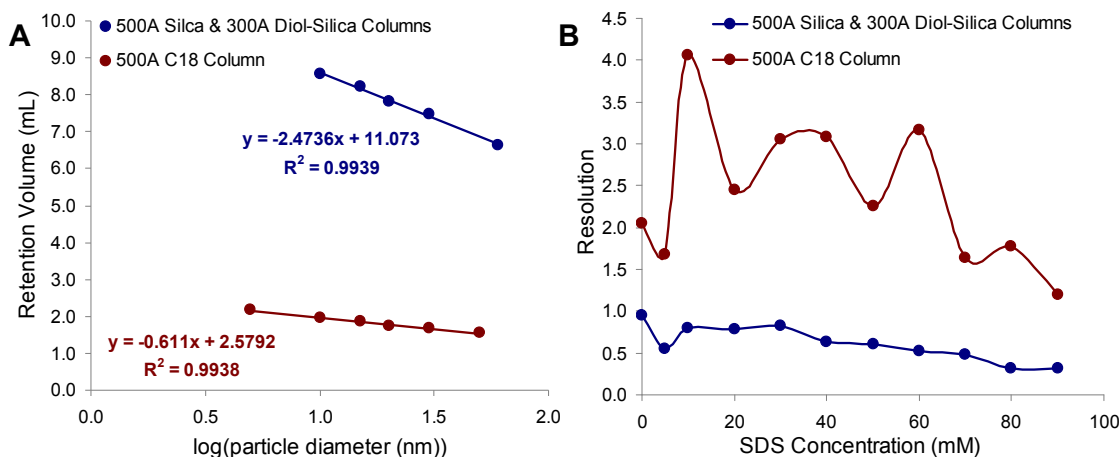


Figure 5-30. (A) Plot showing linear relationships between retention volume and log(particle diameter) for citrate-capped gold particles in both Macrosphere (300 Å) and Nucleosil (500 Å) columns in series and a silica-C18 column (500 Å) (B) Resolution between 5 and 20 nm particles as a function of SDS concentration. The lines here are not meant to indicate any type of relationship and, are included only to guide the eye.

in the presence of the molecular linker was quite unexpected. Figure 5-31 shows SEC chromatograms for gold-citrate particles (10 nm) upon the addition of a stoichiometric amount of an OPE linker molecule. Not only did a peak grow in indicating the presence of nanoparticle dimers, but both peaks grew drastically with time. The peak associated with isolated particles was barely visible on the scale of the subsequent chromatograms.

There are several factors that could have contributed to the increase in peak area. As previously described, significant particle adsorption was observed for initial particle measurements. If the extent of adsorption decreased with time, this would be indicated by an increase the peak area. The normalized peak area of the isolated 10 nm particles grew from approximately 1.5% (Figure 5-29) to 96%. This behavior was extremely reproducible and independent of any other samples were injected onto the column during the time frame of the experiment. This phenomenon

Table 5-2. Retention Volumes Observed for Platinum Particles with Different Capping Ligands

Particle	Approximate Diameter (nm)	Retention Volume (mL)	Predicted Retention Volume for Gold Particles of this Size (mL)
Tiopronin-capped platinum	2	2.0	2.4
Tartaric acid-capped Fe ₃ O ₄	8	2.1	2.0

Retention volumes observed using a silica-C18 column (500 Å pore size), 10 mM SDS, and a flow rate of 0.25 mL/min

indicates that the increases in peak size could not be attributed to changes in the stationary phase.

It is also possible that chemical changes on the particle surfaces could reduce the particles' affinity for the stationary phase, thus reducing adsorption. In order to determine whether the presence of additional sodium citrate or organic solvent could have caused these changes, chromatograms were taken of a gold nanoparticle solution containing sodium citrate and organic solvent as a function of time. Figure 5-32 shows that while the peak area did increase somewhat upon the addition of these additives (normalized peak area of about 4%), no further changes were observed in this chromatogram over a period of five days. The OPE linker was

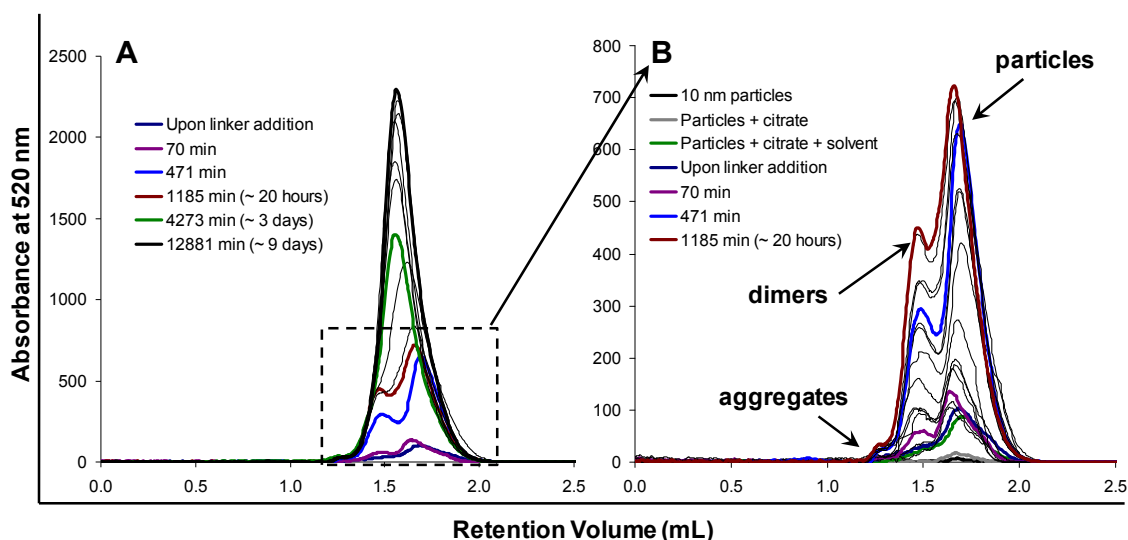


Figure 5-31. (A) SEC chromatograms of citrate-capped gold particles (10 nm) as a function of time after the addition of an OPE linker molecule. (B) Magnified view of chromatograms shown in (A). Data were obtained using a silica-C18 column, a mobile phase consisting of 10 mM SDS and a flow rate of 0.25 mL/min. The values on the y-axis are arbitrary and included only for comparative purposes

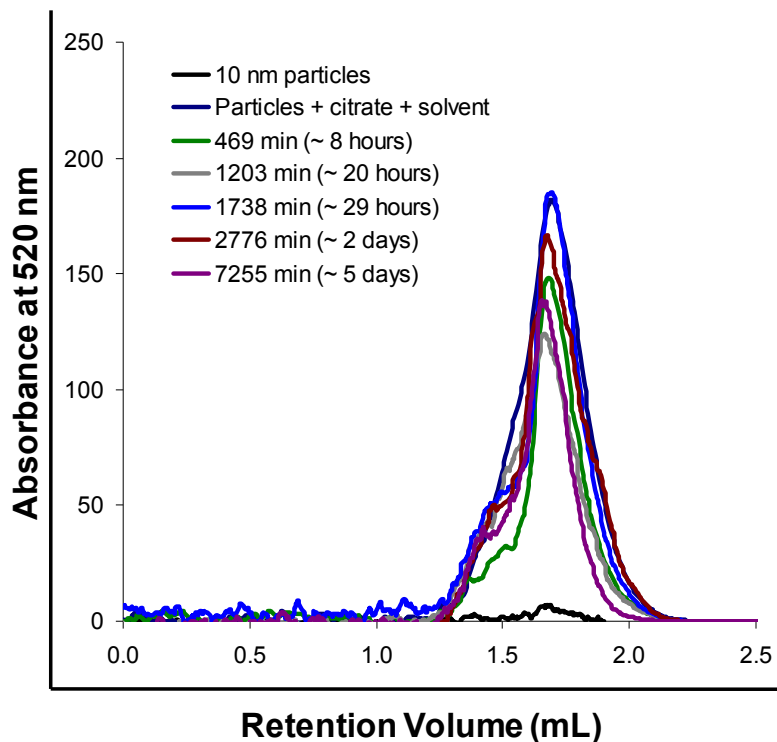


Figure 5-32. SEC Chromatograms of a solution of citrate-capped gold particles (10 nm) in a solution containing additional sodium citrate and organic solvent taken as a function of time. Data were obtained using a silica-C18 column, a mobile phase consisting of 10 mM SDS and a flow rate of 0.25 mL/min. The values on the y-axis are arbitrary and included only for comparative purposes. The peak heights are significantly lower than those observed in the presence of the molecular linker (Figure 5-31)

added in a stoichiometric amount so that there was approximately one molecule for every two particles. It was therefore doubtful that the presence of this species would have contributed greatly to the adsorption behavior of the particles in the column.

Another contributing factor to the peak area

observed in SEC chromatograms is the optical absorption behavior. The SEC chromatograms reported in this work were obtained using a UV-VIS detector at 520 nm. An increase in the absorption at this wavelength throughout the dimerization process would also cause an increase the observed peak areas.

Optical absorption spectra were also taken for the dimer solution as a function of

time. A slight increase and red-shift in the absorbance maximum was observed, which is consistent with the formation of nanoparticle dimers (Section 4.1.6). However, it is unlikely that this small increase in absorbance could account for the observed 100-fold increase in peak area.

The optical absorption spectra also show two peaks at 430 nm and 460 nm, which appear with time and then decrease in intensity as shown in the inset of Figure 5-33.

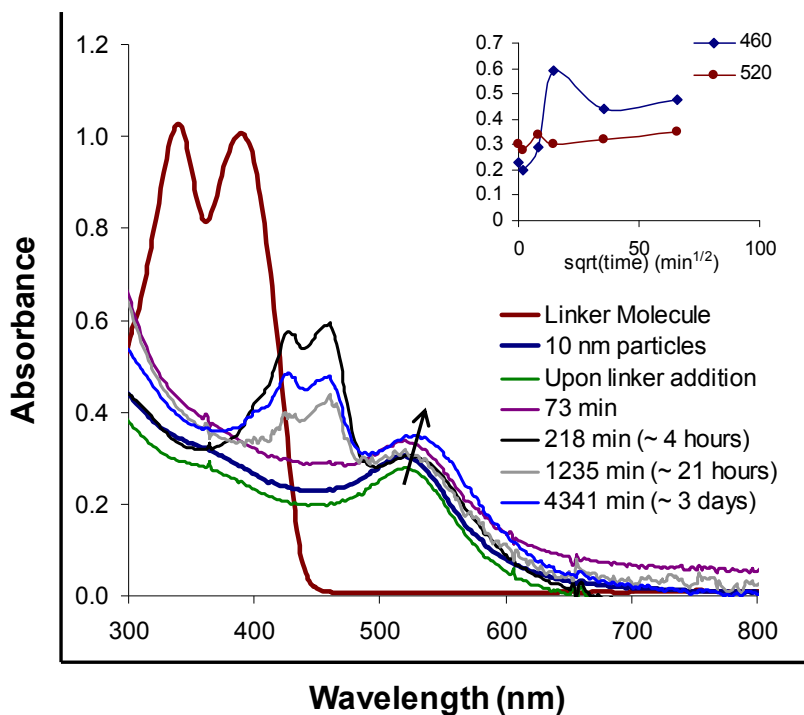


Figure 5-33. Optical absorption spectra for a solution of citrate-capped gold particles (10 nm) as a function of time after the addition of a molecular linker. The inset shows the absorption at 460 nm and 520 nm as a function of $\sqrt{\text{time}}$. The lines here are not meant to indicate any type of relationship, and are included only to guide the eye.

These two peaks do not correspond to the molecular linker. Additional experiments with several other OPE molecules indicated that these absorbances were independent of the OPE structure; similar behavior was repeatedly observed.

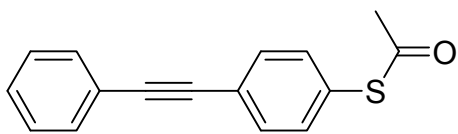


Figure 5-34. OPE molecule used in control experiment

SEC chromatograms were also taken as a function of time after the addition of a stoichiometric amount of the singly-terminated molecule shown in Figure 5-34. This

molecule was expected to bind to the nanoparticles, but not result in dimer formation. As shown in Figure 5-35 (A), an increase in peak area was observed for these experiments although no dimer peak was observed. The corresponding optical absorption spectra Figure 5-35 (B) indicated small fluctuations in the absorbance maxima without the red-shift observed in the presence of the bifunctional linker.

The increase in peak area can therefore be attributed to interactions between the

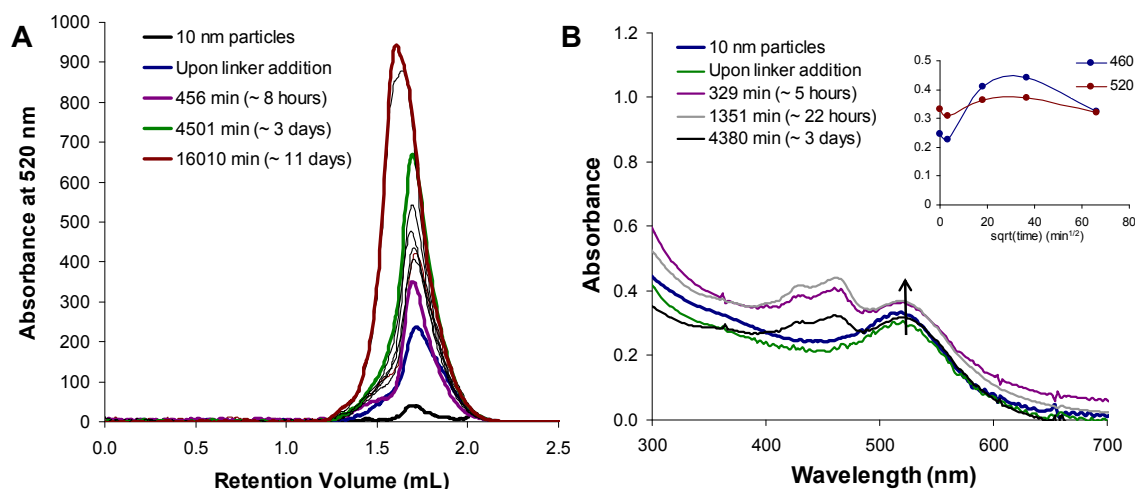


Figure 5-35. (A) SEC chromatograms of a solution of citrate-capped gold particles (10 nm) as a function of time after addition of the molecule shown in Figure 5-34 (B) Optical absorption spectra corresponding to the sample in (A). The inset shows the absorption at 460 nm and 520 nm as a function of $\sqrt{\text{time}}$. The lines here are not meant to indicate any type of relationship, and are included only to guide the eye.

particles and the molecular linkers. Again, it seems unlikely that the significant peak growth can be attributed solely to reductions in particle adsorption when only one molecule is expected to bind to each particle. However, this phenomenon was not observed when normal phase columns were used. The optical spectra shown in Figure 5-33 and Figure 5-35 indicate some changes in the optical spectra even in the absence of dimerization. A better understanding of the electronic and optical properties associated with these structures is required in order to explain these changes, which may also contribute to the observed increases in peak area.

Similar experiments were performed using particles of different sizes and different linker molecules with similar results. Figure 5-36 shows chromatograms obtained for

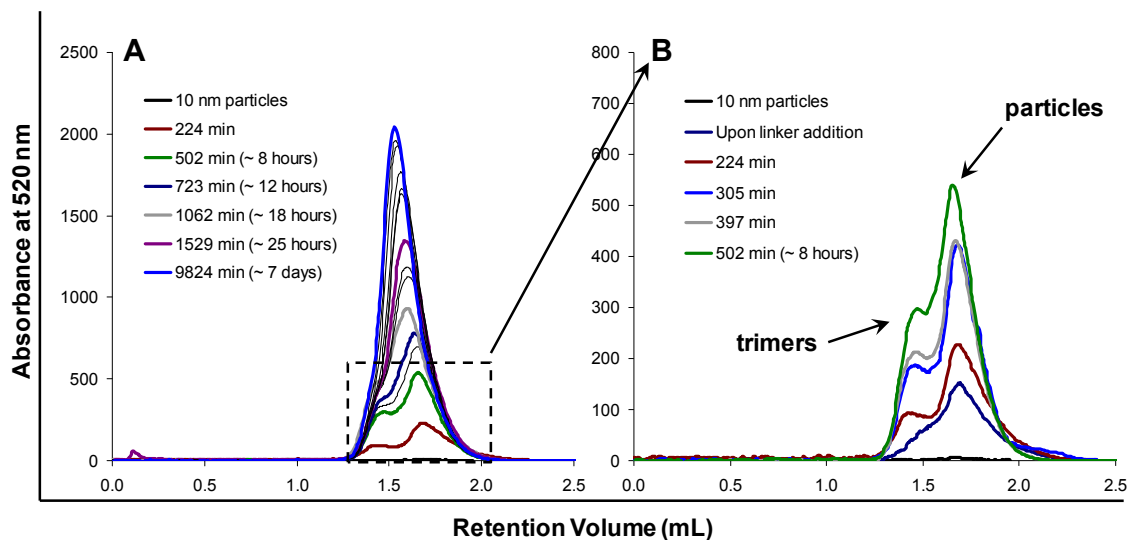


Figure 5-36. (A) SEC chromatograms of citrate-capped gold particles (10 nm) as a function of time after the addition of a three-armed OPE linker molecule. (B) Magnified view of chromatograms shown in (A). Data were obtained using a silica-C18 column, a mobile phase consisting of 10 mM SDS and a flow rate of 0.25 mL/min. The values on the y-axis are arbitrary and included only for comparative purposes

citrate-capped particles (10 nm) in the presence of a three-armed OPE, which indicated the presence of trimers. However, the retention volume of the peak associated with trimers was the same as that observed for dimers. It is possible that for this particular column the retention of particles within the column pores is similar for both dimer and trimer structures. Increases in the peak area were also observed.

The peak heights observed in the SEC chromatograms were plotted as a function of the $\sqrt{\text{time}}$ after several measurements indicated that these values grew at a rate proportional to the peak areas. If these changes were due to binding of the OPE to the gold particles, this linear relationship suggests a diffusion-limited process.^{33,34}

However, no claim was made to this effect. These plots are intended only as a

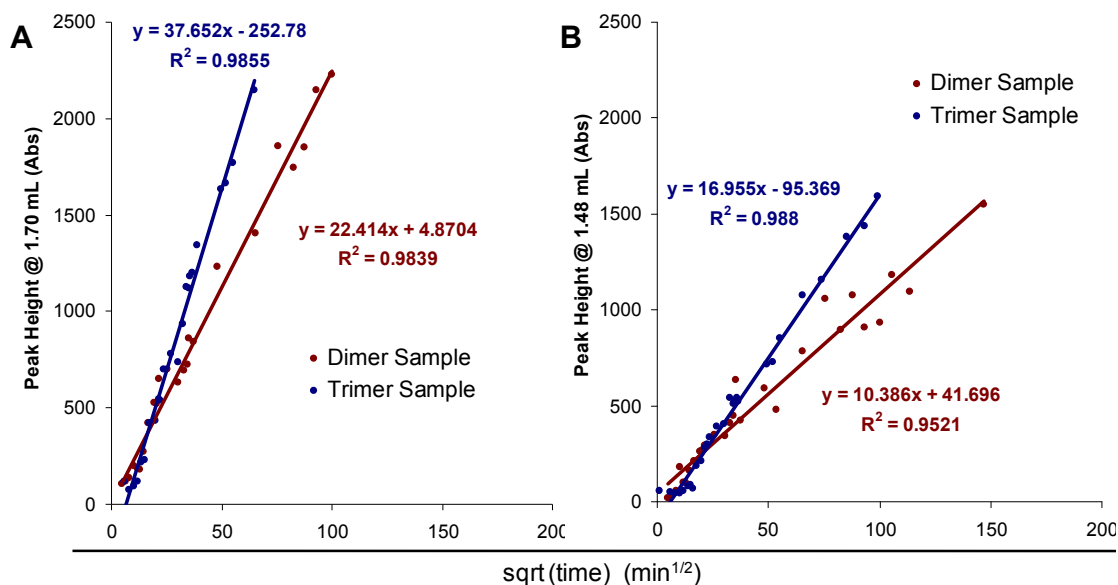


Figure 5-37. Peak heights observed in SEC chromatograms plotted as a function of $\sqrt{\text{time}}$. These data correspond to chromatograms shown in Figure 5-31 and Figure 5-36. (A) Observed heights for peaks associated with individual particles (B) Observed heights for peaks associated with dimers and trimers

means to compare data from multiple experiments.

The slopes and maximum peak heights are reported in Table 5-3 along with the retention volumes and corresponding hydrodynamic diameters for each peak. Data are not reported for 5 nm trimers as a second peak was not observed for these samples. This may be due to the fact that the trimers yields observed using TEM were typically lower for 5 nm particles (Figure 4-30A). According to the data collected, the peak growth rates and maximum peak heights increased with particle size. The maximum peak heights were similar for dimers and trimers comprised of 10 nm particles; however, the observed growth rates were greater for trimers. While

Table 5-3. Data Obtained from SEC Chromatograms of Nanoparticle Assemblies

Sample	'Particle Peak'				'Dimer/Trimer Peak'				
	V _R (mL)	D _H * (nm)	Slope**	Peak Max (Abs)	V _R (mL)	D _H * (nm)	D _H ** (nm)	Slope**	Peak Max (Abs)
5nm dimer	1.79	5.6	13.8	1000	1.51	20.2	8.2	2.9	150
10nm dimer	1.70	8.4	22.4	2200	1.48	23.2	15.8	10.4	450
10nm trimer	1.70	8.4	37.6	2200	1.48	23.2	20.2 - 42.3***	17.0	550
15nm dimer	1.56	16.0	NA****	NA****	1.29	55.8	23.3	NA****	NA****
15nm trimer	1.56	16.0	NA****	NA****	1.29	55.8	29.3 - 54.8***	NA****	NA****

* The corresponding hydrodynamic diameters based on the calibration curve in Figure 5-30 (A)

** The slopes were obtained from plots of peak height vs. sqrt(time)

*** The hydrodynamic diameters calculated in Appendix 2; a wide range was calculated for trimers

**** No kinetic data was obtained for assemblies of 15 nm particle assemblies

the phenomena contributing to peak growth are not understood, this behavior appears to be dependent upon the size and geometry of the assemblies. Preliminary data (not shown here) also suggested this behavior was dependent upon the structure of the OPE linker.

Dimers and trimers consisting of gold particles were detected using reversed-phase chromatography; however, the apparent particle adsorption observed for isolated particles and the peak growth upon linker addition suggest several other processes occurring which are not clearly understood. As a result, this technique cannot be used to obtain statistical information regarding the relative amounts of dimers and trimers in these solutions.

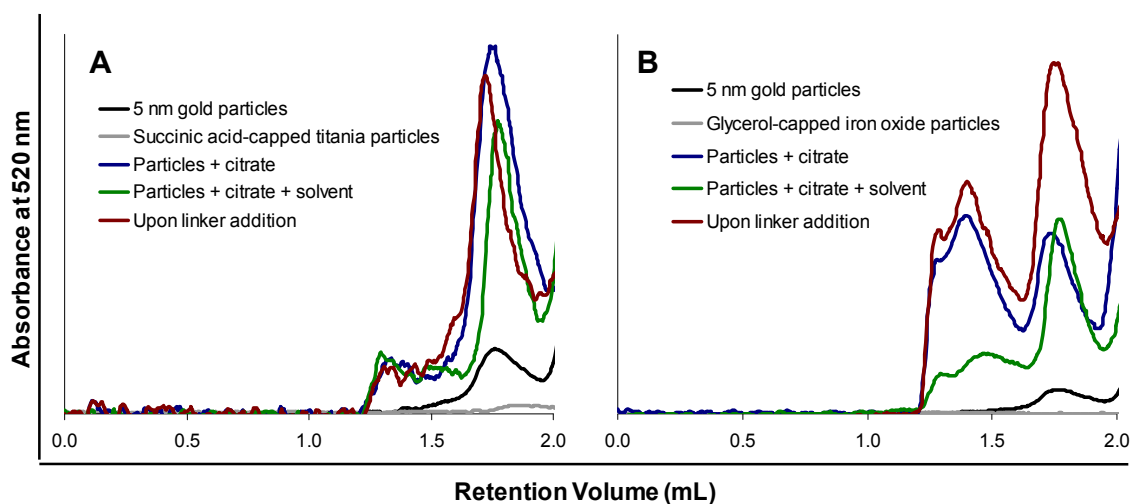


Figure 5-38. SEC chromatograms of mixed particle solutions (A) citrate-capped gold particles (5 nm) with succinic acid-capped titania particles (B) citrate-capped gold particles (5 nm) with glycerol-capped iron oxide particles. Data were obtained using a silica-C18 column, a mobile phase consisting of 10 mM SDS and a flow rate of 0.25 mL/min.

Attempts to detect nanoparticle heterodimers were unsuccessful. Figure 5-38 shows chromatograms of citrate-capped gold particles (5 nm) in the presence of both succinic-acid-capped TiO₂ and glycerol-capped Fe₃O₄

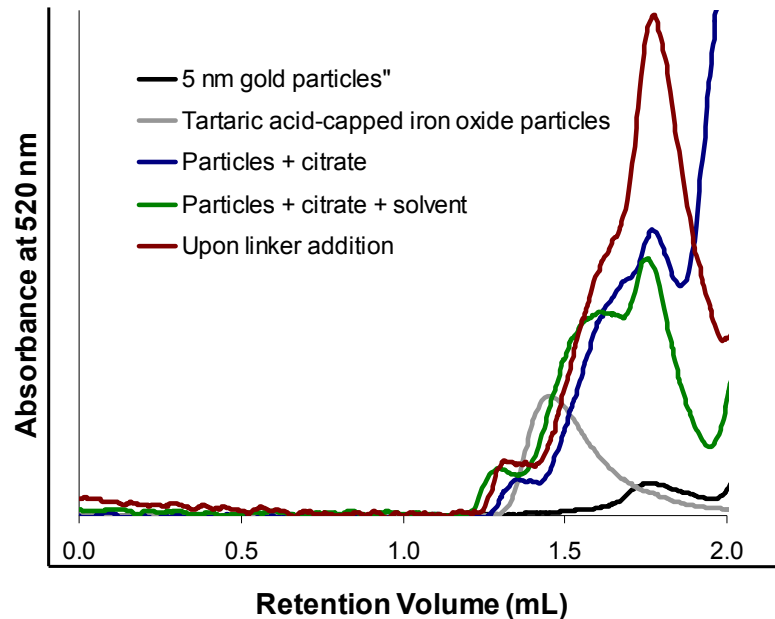


Figure 5-39. SEC chromatograms of particle solutions containing citrate-capped gold particles (5 nm) and tartaric acid-capped Fe₃O₄ particles. Data were obtained using a silica-C18 column, a mobile phase consisting of 10 mM SDS and a flow rate of 0.25 mL/min.

particles. The peak at lower retention volumes attributed to tannic acid is not shown. Neither of these metal oxide particles absorbed at 520 nm so the only peaks expected were those associated with gold. However, in both cases, additional peaks observed for particle mixtures in the absence of linker, which made it impossible to detect dimerization. Tartaric acid-capped Fe₃O₄ particles exhibited an absorbance at 520 nm, which made the SEC chromatograms even more difficult to interpret. As shown in Figure 5-39, multiple peaks were observed, which did not correlate to either of the isolated particles. Further changes in all three

chromatograms were observed as a function of time. This behavior made it even more difficult to detect dimerization.

5.2.3. Summary

The goals of this work were to separate nanoparticle assemblies from isolated particles and larger aggregates and obtain statistical information regarding the relative concentrations of these species in solution. Despite the apparent simplicity of the size-exclusion mechanism (Figure 5-1), interactions between nanoparticles and the column materials appeared to be quite complex.

Particle separations in organic solvent were unsuccessful due to irreversible adsorption on the column. While it is possible a new column and further optimization of separation parameters could have improved the results, efforts were shifted to the characterization of aqueous nanoparticles.

The separation of aqueous particles was attempted using both normal-phase and reverse-phase chromatographic columns. Particle separation was achieved using a 300 Å Macrosphere® diol-silica column; however, resolution was limited and larger pore sizes were not available for this material. The logarithmic relationship between particle size and retention volume indicated that size-exclusion was the primary separation mechanism. However, this relationship did not hold when particles of different compositions were injected onto the column. This behavior suggested chemical interactions contributed to the separation mechanism. Peaks were

observed which indicated the presence of both homo- and heterodimers; however, these peaks were not clearly resolved and statistical information could not be obtained.

Adsorption of citrate-capped gold particles was significant when an unmodified silica column was used. This adsorption was significantly reduced for particles, which underwent ligand-exchange with BSPP. This behavior contradicted that observed for the Macrosphere® column for which peaks were broadened for BSPP-capped particles compared to those stabilized by citrate. This phenomenon suggested that chemical interactions were very sensitive to the particle surface chemistry. Particle aggregation was observed on the column for particles in the presence of sodium citrate and organic solvent. This behavior was more significant for larger particle sizes, and made it difficult to detect nanoparticle assemblies. Attempts to detect nanoparticle dimers and trimers composed of smaller particles, for which aggregation was not observed, were unsuccessful despite significant efforts to optimize the separation conditions (i.e. SDS concentration and flow rate).

While limited particle adsorption was observed for citrate-capped particles on a silica-C8 column (80 Å), adsorption was significant when a silica-C18 column was used. In this case, ligand-exchange with BSPP did not affect any changes. While the differences in retention volumes for this system were not as great as those observed for the normal phase columns, the peaks were significantly narrower and

the resolution was greater. Peaks attributed to nanoparticle dimers and trimers were observed for several different particle sizes. However, the peak areas increased with time making it difficult to obtain statistical information about the particle solution. If the behavior contributing to the peak growth were understood, it is possible these experiments could provide information regarding binding kinetics. Attempts were made to detect heterodimers using this column were unsuccessful due to the presence of multiple peaks even in the absence of the molecular linker. Both particle solutions likely contained excess ligands, and mixing the two could have affected changes in the particle surface chemistry and the retention volumes. In addition, aggregation on the column could have contributed to the presence of additional peaks.

As particle separations were sensitive to the surface chemistry of the particle in addition to the nature of the mobile and stationary phases, heterodimer detection using SEC will likely be quite difficult. It is unlikely that the conditions suited for the characterization of one particle will also be ideal for another. It is possible that further experiments could prove useful in detecting homodimers and trimers. While the pore size of the silica-C8 column was too small for nanoparticle separation, the extent of particle adsorption was significantly less than that observed for the silica-C18 column. If appropriate pore sizes of this material could be located, these columns could prove useful in particle separations. However, due to the apparently

unavoidable problem of particle adsorption, a behavior which seems to be size-dependent, it is unlikely that accurate statistical information could be obtained from these data. If nanoparticle separation were to be achieved, SEC could be used to observe relative changes in a particle solution as the conditions of the dimer synthesis were changed. However, quantitative data will not likely be achievable.

5.3. Experimental

Citrate-capped gold particles were obtained from Ted Pella, Inc. as aqueous solutions with trace amounts of citrate, tannic acid and potassium carbonate. All other nanoparticles were synthesized according to procedures reported in Chapters 2 and 3. Dimers and trimers were synthesized according to methods described in Chapter 4. For SEC kinetic experiments, approximately 30-40 μL of the nanoparticle solutions were removed at several points throughout the course of the reaction. For UV-VIS kinetic experiments, the nanoparticle solutions were transferred from the reaction vials into a cuvette for analysis and then returned to the appropriate vial.

The SEC instrumentation consisted of an isocratic HPLC pump equipped with a Rheodyne 7512 Manual Injector, and a Vestec UV-VIS detector connected to a Power Mac 7200/90 through a Remove Measurements Systems ADC-1 Analog-to-Digital Converter. Unless otherwise indicated, the detection wavelength was set to 520 nm. The sample loop was 20 μL and five different columns were used as indicated in the text.

- For organic separations, a Jordi Gel DVB column (Alltech, Inc.) was used. The particle size was 5 μm , the pore size 500 Å and the column dimensions 10 mm \times 250 mm.
- Macrosphere® (Alltech, Inc.) 300 Å column with 7 μm particles and dimensions of 7.5 \times 300 mm. The column material was a 'diol-silica', the chemistry of which the manufacturer would not disclose.
- Nucleosil unmodified silica column (Macherey-Nagel) with a 500 Å pore size, 7 μm particles and dimensions of 4.6 \times 250 mm
- Econosphere® (Alltech, Inc) 500 Å column with of 7 μm silica-C8 particles and dimensions of 4.6 \times 250 mm
- Nucleosil Silica-C18 column (Macherey-Nagel) with a 500 Å pore size, 7 μm particles and dimensions of 4.6 \times 250 mm

HPLC grade THF and toluene were purchased from Fischer Scientific, and used for separations in organic solvent after filtering through a 0.20 μm nylon filter membrane (Alltech) and degassing using a vacuum aspirator.

The water for aqueous mobile phases was obtained from a Milli-Q50 Ultrapure Water System. The concentration of sodium dodecyl sulfate (MP Biomedicals, Ultra Pure) varied from 0 mM to 100 mM as indicated in the text. All solutions were

filtered through a 0.20 μm nylon filter membrane (Alltech) and degassed using a vacuum aspirator.

The columns were washed with an SDS solution in between each sample injection. Several measurements were repeated to ensure reproducibility.

Optical absorbance spectra were obtained using a Hewlett-Packard 8452A Diode Array Spectrometer and a path length of 1.0 cm.

5.4. References

- (1) Wilcoxon, J. P.; Martin, J. E.; Provencio, P., *Langmuir* **2000**, *16*, 9912-9920.
- (2) Wilcoxon, J. P.; Provencio, P., *J. Phys. Chem. B* **2003**, *107*, 12949-12957.
- (3) Fischer, C. H.; Giersig, M.; Siebrands, T., *J. Chromatogr. A* **1994**, *670*, 89-97.
- (4) Wei, G. T.; Liu, F. K.; Wang, C. R. C., *Anal. Chem.* **1999**, *71*, 2085-2091.
- (5) Novak, J. P.; Nickerson, C.; Franzen, S.; Feldheim, D. L., *Anal. Chem.* **2001**, *73*, 5758-5761.
- (6) Song, Y.; Heien, M.; Jimenez, V.; Wightman, R. M.; Murray, R. W., *Anal. Chem.* **2004**, *76*, 4911-4919.
- (7) Wei, G. T.; Liu, F. K., *J. Chromatogr. A* **1999**, *836*, 253-260.
- (8) Burgess, I.; Jeffrey, C. A.; Cai, X.; Szymanski, G.; Galus, Z.; Lipkowski, J., *Langmuir* **1999**, *15*, 2607-2616.
- (9) Fischer, C. H.; Kenndler, E., *J. Chromatogr. A* **1997**, *773*, 179-187.

- (10) Al-Somali, A. M.; Krueger, K. M.; Falkner, J. C.; Colvin, V. L., *Anal. Chem.* **2004**, *76*, 5903-5910.
- (11) Schnabel, U.; Fischer, C. H.; Kenndler, E., *J. Microcolumn Sep.* **1997**, *9*, 529-534.
- (12) Skoog, D. A.; Holler, J. F.; Nieman, T. A. *Principles of Instrumental Analysis*; 5 ed.; Hartcourt Brace College Publishers: Philadelphia, 1998.
- (13) Wilcoxon, J. P.; Craft, S. A., *Nanostruct. Mater.* **1997**, *9*, 85-88.
- (14) Siebrands, T.; Giersig, M.; Mulvaney, P.; Fischer, C. H., *Langmuir* **1993**, *9*, 2297-2300.
- (15) Fischer, C. H.; Weller, H.; Katsikas, L.; Henglein, A., *Langmuir* **1989**, *5*, 429-432.
- (16) Wilcoxon, J. P.; Martin, J. E.; Provencio, P., *J. Chem. Phys.* **2001**, *115*, 998-1008.
- (17) Jimenez, V. L.; Leopold, M. C.; Mazzitelli, C.; Jorgenson, J. W.; Murray, R. W., *Anal. Chem.* **2003**, *75*, 199-206.
- (18) Song, Y.; Jimenez, V.; McKinney, C.; Donkers, R.; Murray, R. W., *Anal. Chem.* **2003**, *75*, 5088-5096.
- (19) Liu, F. K.; Wei, G. T., *Chromatographia* **2004**, *59*, 115-119.
- (20) Wellsted, H.; Sitsen, E.; Caragheorgheopol, A.; Chechik, V., *Anal. Chem.* **2004**, *76*, 2010-2016.
- (21) Choi, M. M. F.; Douglas, A. D.; Murray, R. W., *Anal. Chem.* **2006**, *78*, 2779-2785.
- (22) Liu, F. K.; Wei, G. T., *Anal. Chim. Acta* **2004**, *510*, 77-83.
- (23) Okada, T., *Anal. Chem.* **1988**, *60*, 1511-1516.
- (24) Armstrong, D. W., *Sep. Purif. Methods* **1985**, *14*, 213-304.
- (25) Marina, M. L.; Garcia, M. A., *J. Liq. Chromatogr.* **1994**, *17*, 957-980.
- (26) Nikoobakht, B.; El-Sayed, M. A., *Langmuir* **2001**, *17*, 6368-6374.

- (27) Wu, S. H.; Chen, D. H., *Chem. Lett.* **2004**, 33, 406-407.
- (28) Novak, J., Doctoral Thesis, **2001** Chemistry, North Carolina State University
- (29) Brust, M.; Fink, J.; Bethell, D.; Schiffrin, D. J.; Kiely, C., *J. Chem. Soc. - Chem. Commun.* **1995**, 1655-1656.
- (30) Eklund, S. E.; Cliffler, D. E., *Langmuir* **2004**, 20, 6012-6018.
- (31) Parak, W. J.; Gerion, D.; Pellegrino, T.; Zanchet, D.; Micheel, C.; Williams, S. C.; Boudreau, R.; Le Gros, M. A.; Larabell, C. A.; Alivisatos, A. P., *Nanotechnology* **2003**, 14, R15-R27.
- (32) Loweth, C. J.; Caldwell, W. B.; Peng, X. G.; Alivisatos, A. P.; Schultz, P. G., *Angew. Chem. Int. Ed.* **1999**, 38, 1808-1812.
- (33) Schuck, P.; Minton, A. P., *Anal. Biochem.* **1996**, 240, 262-272.
- (34) Barrett, C. R.; Nix, W. D.; Tetelman, A. S. In *The Principles of Engineering Materials*; Prentice Hall: Englewood Cliffs, NJ, 1973, pp 159-161.

6. Electrophoresis of Particles and Particle Assemblies

Another technique explored for the separation of nanoparticles and particle assemblies was electrophoresis. Analytical and preparative-scale separations were performed using gel, capillary and continuous free-flow electrophoresis. As discussed in detail below, there are several factors that affect the mobility and resolution of nanoparticles in electrophoretic experiments which must be understood in order to determine separation conditions and interpret data. While the general theory of electrophoretic separations is the same for all three techniques discussed here, each one has its own set of variables which must be considered in order to achieve separation.

6.1. Background and Introduction

6.1.1. Electrophoresis – General Theory

Electrophoresis refers to the movement of a charged molecule or particle under the influence of an applied electric field. The velocity of a charged species is proportional to the applied field strength as shown in Equation 6-1 where v is the electrophoretic velocity, μ_{ep} is electrophoretic mobility and E is the electric field strength. The electrophoretic mobility is determined by the charge-to-size ratio as

shown in Equation 6-2 where q is the total charge on a particle, η is the solution viscosity and r is the hydrodynamic radius of the molecule or particle.

$$v = \mu_{ep} E \tag{6-1}$$

$$\mu_{ep} = \frac{q}{6\pi\eta r} \tag{6-2}$$

Separation is achieved according to differences in electrophoretic mobilities among charged species in solution as shown in Figure 6-1. Positively charged species migrate toward the anode, exhibiting positive mobilities while negatively charged species migrate towards

the cathode exhibiting negative mobilities

The first platform established for electrophoretic separations was gel electrophoresis in which the sample was dissolved in a buffer that was

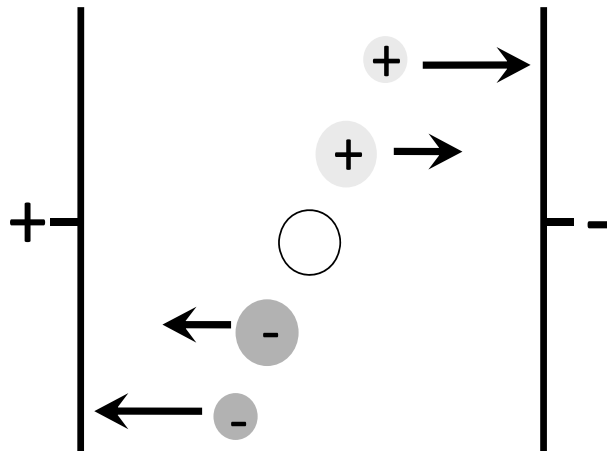


Figure 6-1. Electrophoretic velocity of charged molecules in an electric field is dependent upon charge-to-size ratio

contained the pores of a semi-solid gel. The process has been compared to thin layer chromatography in that multiple samples can be spotted on the same gel. After an electric field has been applied for a period of time, the separated bands are observed visually or through staining. This method is routinely used for the separation of biological molecules such as proteins, amino acids and DNA.⁸⁻¹²

6.1.2. Capillary Electrophoresis

Capillary electrophoresis (CE), as the name suggests, involves electrophoretic separations within a buffer-filled capillary.¹³ Charged molecules injected into the capillary exhibit an electrophoretic velocity under an applied potential. In addition, they are subject to electroosmosis, the net flow of solvent through the capillary under the influence of an electric field. Most capillaries used for CE are made of fused silica, which contains surface silanol groups. In the presence of a buffer with a pH > 3, these silanol groups ionize creating a negative charge along the capillary wall. Cations in the buffer are attracted to the negatively-charged capillary wall creating an electrical double layer as shown in Figure 6-2(A). These cations migrate toward the cathode, and as they are solvated, they create a net flow of solvent through the capillary. The rate of electroosmotic flow (EOF) is the same for all dissolved species regardless of size or charge, and the total velocity of a sample is determined by the sum of the electrophoretic and electroosmotic components (Equation 6-3). In general, EOF is towards the cathode and exhibits a velocity greater than the

electrophoretic velocity of charged solutes so that all species elute from this end of the capillary as shown in Figure 6-2 (B). This allows for the use of an on-column detector similar to those commonly used for chromatography, smaller sample volumes and higher-resolution detection. The direction of EOF can be reversed by coating the capillary wall with a cationic surfactant.

As shown in Figure 6-2(B), the order of elution is (1) cations with greatest mobility, (2) cations with lesser mobility, (3) neutral species, (4) anions with lesser mobility and (5) anions with greatest mobility. Anions with the greatest mobility migrate last.^{8,13,17}

$$v = (\mu_{eo} + \mu_{ep})E = \frac{(\mu_{eo} + \mu_{ep})V}{L} \quad 6-3$$

μ_{eo} = electroosmotic mobility
V = applied voltage
L = length of capillary

The rate of EOF can significantly affect the resolution of analytes. High rates decrease the amount of time each species spends in the capillary. While this decrease limits effects such as longitudinal dispersion and band-broadening, it also limits the selectivity of the separation and consequently the resolution. Highest resolution is achieved when the rate of EOF (towards the cathode) balances the electrophoretic velocity of anions (towards the anode); however, these conditions result in longer analysis times.¹³ The rate of EOF can be adjusted by controlling the

pH, solution viscosity, ionic strength, voltage and the dielectric constant of the buffer.¹³ Higher pH values can yield a higher degree of silanol ionization, creating

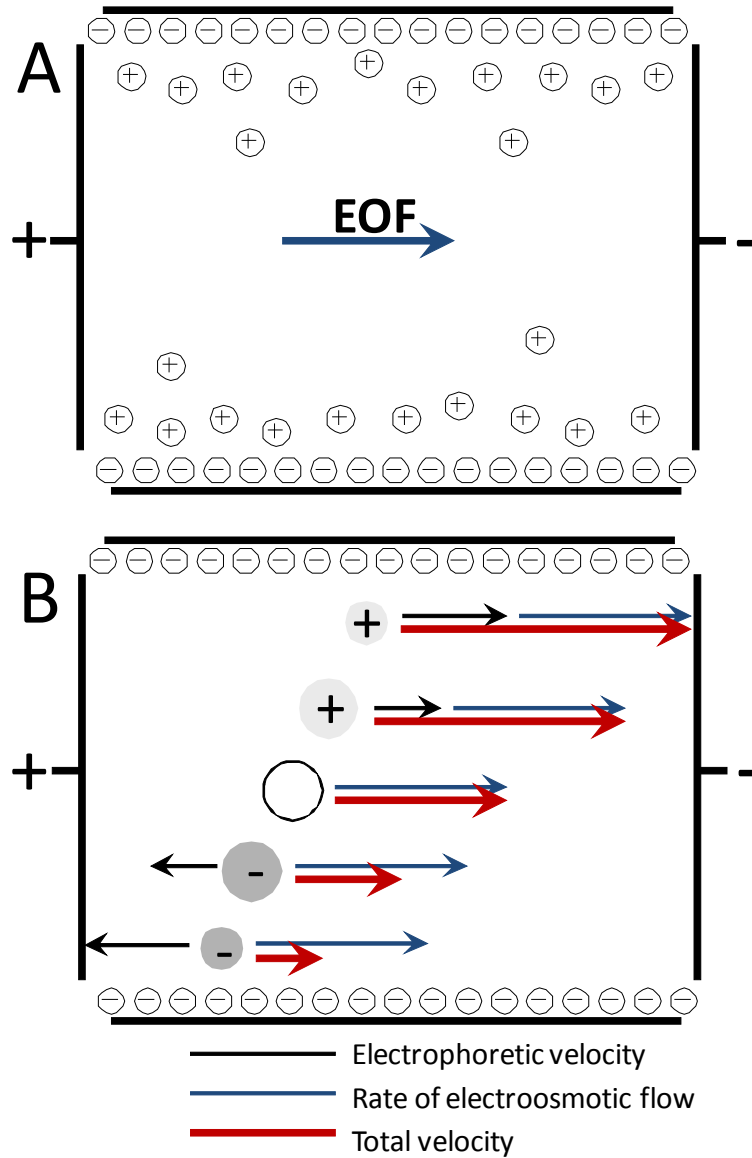


Figure 6-2. (A) Electrical double layer along capillary wall creates electroosmotic flow (B) The total velocity of ions is determined by the sum of the electrophoretic and electroosmotic components

more charge in the electrical double layer and greater EOF rates. On the other hand, an increase in the ionic strength will decrease the thickness of the double layer along the capillary wall and consequently limit the rate of EOF.^{13,17} While buffer conditions can be altered to control the relative rates of EOF, these values are often irreproducible due to different conditions of the fused silica surface, especially in cases where solutes adsorb on the capillary affecting its overall charge.

Variations in EOF can be limited by using solutions containing ionic surfactants such as sodium dodecyl sulfate (SDS) which possess relatively constant values over wide pH ranges.^{13,17} There have been also been attempts to control EOF by using polymeric coatings which exhibit more consistent charge distributions than silica over wide pH ranges and that are less prone to solute adsorption.^{13,21}

Changes in buffer composition not only affect the rate of EOF, but also have consequences on the electrophoretic velocity of analytes. While lower pH values can be desirable to limit the rate of EOF, higher pH values can increase the degree of ionization of solution anions increasing their mobility and improving resolution. In addition, adsorption of solutes onto the capillary wall can cause peak tailing and reduce separation efficiency. These effects are minimized in the pH range 8-11. In this range, many proteins are negatively charged and electrostatic repulsion between them and the negatively-charged capillary wall limit adsorption.¹³

Another consideration when performing electrophoretic separations is Joule heating. When voltage is applied across the capillary, the resulting electric current generates heat. If not properly dispersed, this heat leads to a radial temperature profile within the capillary and band broadening. Smaller capillary diameters can reduce this effect by allowing for more efficient cooling and limiting the extent of the parabolic temperature profile. The most commonly reported capillary diameter in the literature is 75 μm ; solvent boiling has been reported for larger capillaries.²² The tradeoff here is that the larger surface-to-volume ratio inside the capillary can, in principle, lead to higher degrees of wall adsorption. Joule heating increases with the ionic strength of the buffer solution and with applied voltage for non-thermostated systems. It has been shown that using a thermostated system with cooling capabilities can significantly reduce the voltage dependence on resolution.¹⁸

For general capillary electrophoretic separations, there are tradeoffs associated with the choice of both the ionic strength and the pH of the buffer. Greater ionic strengths decrease the rate of EOF, but can lead to more significant Joule heating which degrades resolution. Lower pH values decrease the rate of EOF, but also decrease the degree of ionization of both the capillary wall and solute anions. This can lead to higher degrees of adsorption along the capillary and limited electrophoretic velocities, which can impede separation. These variables have

additional consequences when looking at more complex electrophoretic systems such as those involving micelles and larger particles.

6.1.3. Micellar Electrokinetic Chromatography

As described above, electrophoretic separations require charged analytes.

However, incorporating micelles into electrophoretic experiments can facilitate the separation of both charged and neutral solutes. In this technique, commonly called micellar electrokinetic chromatography (MEKC), micelles act as a pseudo-stationary phase similar to those encountered in chromatographic separations.^{17,23-25} For neutral analytes, the separation mechanism is based on the chromatographic partitioning between the micellar phase and the aqueous mobile phase. This combines the high efficiency associated with CE with a chromatographic separation mechanism. Most often micelles are formed from an anionic surfactant such as sodium dodecyl sulfate (SDS). Anionic micelles migrate towards the anode, the opposite direction of EOF, and therefore move slowly through the capillary. Organic solutes distribute themselves between the micellar and aqueous phases according to their relative hydrophobicity. Neutral solutes that exhibit no interactions with the micelle, move through the capillary at the rate of EOF and elute at time, t_0 . Solutes that are irreversibly solubilized within the micelle migrate at the same rate as the micelle and elute at time, t_{mc} . All other neutral solutes elute in between these two values.

The efficiency and resolution of separation in MEKC can be affected by both the elution range of the micelle and the retention factor associated with each analyte. The elution range is defined by the ratio of t_0/t_{mc} , which, for neutral solutes, ranges between 0 and 1. As t_{mc} approaches infinity, the elution ranges tends to zero and the micellar phase becomes stationary. The literature reports values of approx. 0.25 for t_0/t_{mc} ; however, resolution can be improved by decreasing this ratio to as low as 0.01-0.03.²³ Decreasing this value can be achieved by reducing the rate of EOF, which is commonly done by adding organic modifiers to the mobile phase or coating the capillaries.²³ The retention factor for an analyte in an MEKC separation can be calculated according to Equation 6-4 as a function of the analyte retention time, t_R , t_0 and t_{mc} . This value can also be correlated to the concentration of surfactant according to Equation 6-4. For low micelle concentrations, the retention factor, and consequently, the retention time of each analyte increases linearly with the surfactant concentration. At higher surfactant concentrations, the micelle shape can change from spherical to rod-like or cylindrical, which can change the partitioning behavior.

The separation conditions for each analyte can be optimized in MEKC. If the analyte elutes too closely to either t_0 or t_{mc} , resolution is poor. The retention factor for optimum resolution is given by Equation 6-5. The optimum surfactant concentration can then be calculated by combining Equations 6-4 and 6-5 to get Equation 6-6.

$$k' = \frac{t_R - t_0}{t_0 \left(1 - \frac{t_R}{t_{mc}} \right)} = \frac{\mu - \mu_0}{\mu_{mc} - \mu} = PV([S] - cmc) \quad 6-4$$

t_R = retention time of analyte
 t_0 = elution time of unretained solute or EOF
 t_{mc} = elution time of micelle
 μ = mobility in the presence of micelles
 μ_0 = mobility in the absence of micelles
 P = partition coefficient – defined by concentration of solute in micellar phase/concentration in aqueous phase
 V = molar volume of surfactant
 $[S]$ = surfactant concentration
 cmc = critical micellar concentration

$$k'_{opt} = \sqrt{\frac{t_{mc}}{t_R}} \quad 6-5$$

$$[S]_{opt} = \frac{k'_{opt}}{VP_{wm}} + cmc \quad 6-6$$

The separation of charged solutes by MEKC is slightly more complicated as both chromatographic and electrophoretic effects must be taken into account.

Electrostatic interactions between charged solutes and micelles also need to be considered. Depending on the relative charges, either ion-pairing or Coulombic repulsion between solute and surfactant can occur. A charged analyte can therefore traverse the capillary either by itself in the aqueous phase, ion-paired with surfactant monomer or partitioned into the micellar phase.²⁵ In contrast to neutral solutes, a charged analyte can elute at times greater than t_{mc} . In addition to the effects of pH on the electrophoretic velocity of analytes and the rate of EOF as discussed above, pH affects the partitioning of charged solutes in MEKC. For example, the partition

coefficient of an acidic solute decreases with increasing pH as the higher charge increases its solubility in the aqueous phase as well as the electrostatic repulsion to the micelle.

The presence of micelles in the separation of charged solutes adds additional complexity to an electrophoretic separation. Buffer conditions such as pH, ionic strength and surfactant concentration affect the efficiency of separation in more ways than those discussed in reference to traditional CE. These variables have further consequences when looking at larger particles in an electrophoretic experiment.

6.1.4. Particle Electrophoresis

While the electrophoretic force experienced by an ion or small molecule in an electric field is only opposed by the viscous resistance of the medium, the electrophoretic motion of a charged particle is slightly more complicated. The following discussion of particle mobility assumes that all particles are non-conducting. However, it has been shown experimentally that mercury droplets demonstrate the behavior described below and this theory can therefore be extended to conducting particles.⁶ It also assumes significantly small concentrations of particles in solution so that particle-particle interactions can be ignored. However,

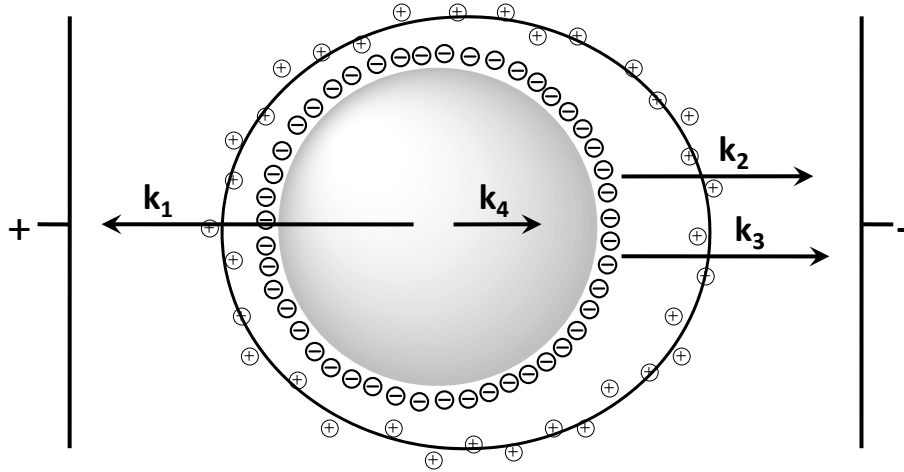


Figure 6-3. Forces acting on a charged particle in an electric field
 k_1 = electrophoretic force exerted on particle by electric field; k_2 = Stokes friction; k_3 =
 retarding force; k_4 = force due to relaxation effect
 Figure adapted from Wiersema's work, 'Calculation of the Electrophoretic Mobility of
 a Spherical Particle'⁵

there have been many works published indicating that particle-particle interactions under the influence of an electric field can be non-negligible.²⁶⁻³²

Figure 6-3 shows the four forces acting on a particle as outlined in the works of Wiersema⁵ and O'Brien¹. In addition to the force exerted by the electric field (k_1) and the frictional force (k_2), there are two additional forces associated with the electrical double layer.⁵ The electric field exerts a force on the ions in the double layer. The counterions, in turn, generate an electric field which creates a retarding force (k_3) in the opposite direction of particle motion.^{1,5,6} The relaxation effect (k_4) is attributed to the fact that, while the negatively-charged particle is attracted to the anode, the cations in the double layer are attracted to the cathode. As a result, the double layer

lags behind the particle. This deformation creates a viscous drag on the particle which is greater than the frictional force exerted on an uncharged particle. In the majority of discussions related to particle electrophoresis, the relaxation effect is the most significant opposing force, and leads to the different behavior of particles in an electric field compared to that observed for smaller ions.

Charged particles in an electric field are often characterized by the value, ka , which

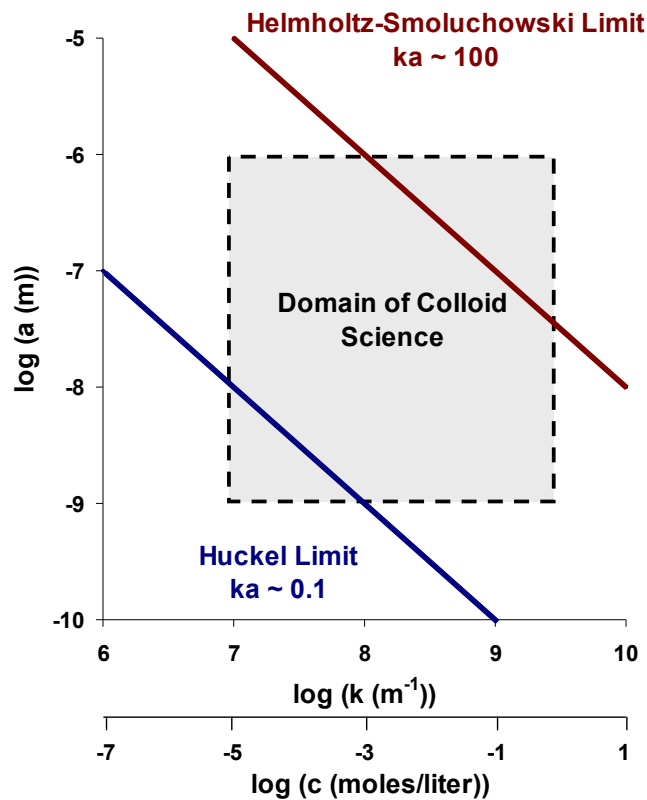


Figure 6-4. The limits of Smoluchowski and Huckel in terms of particle radius and double-layer thickness compared to the domain in which the majority of colloids exist. The second x-axis represents concentrations of a 1:1 electrolyte solution that correspond to these κ values.

Huckel's theory only applies to small particles at very low ionic strengths (large double layer) while Smoluchowski's limit applies to larger particles at high ionic strengths (thin double layer). Relaxation effects need to be considered for the area in between these limits.

Figure adapted from Heimez et al.⁶

is the ratio of the particle radius to the thickness of the double layer; a is the particle radius and κ^{-1} is the double layer thickness. Smoluchowski calculated the mobility of particles in the limit of large ka , i.e. where the double layer is small compared to the radius of the particle. For this case, the relaxation effect is not a considerable contribution and the expression he derived for mobility is a function of the particle's ζ -potential, the viscosity and dielectric constant of the solution (equation 6-8).^{3,5,14} Likewise, Huckel derived an expression for the mobility of particles in the limit of small ka , i.e. where the double layer is large compared to the radius of the particle (equation 6-8).^{3,5,14} Again, relaxation effects are negligible. Note that in both of these limits, the mobility is independent of the particle radius. Rather, it increases linearly with ζ -potential. The expressions of Huckel and Smoluchowski are proportional, differing only by a factor of 1.5.¹⁴

$$\mu_{ep} = \frac{3\zeta\epsilon_r\epsilon_0}{2\eta} \quad 6-7$$

Smoluchowski Limit (large ka)

ζ = zeta potential of particle
 ϵ_r = dielectric constant of medium
 ϵ_0 = dielectric constant of vacuum
 η = viscosity of medium

$$\mu_{ep} = \frac{\zeta\epsilon_r\epsilon_0}{\eta} \quad 6-8$$

Huckel limit (small ka)

However, as shown in Figure 6-4, most particles fall somewhere between these limits. For moderate values of ka , i.e. $0.01 < ka < 100$, the relaxation effect is more prominent and these simple analytical solutions are no longer sufficient.^{1,5} Henry took into account the effects of the double layer and determined mobility as a function of ka which varied between the Smoluchowski and Huckel limits.^{3,5,14,33} However, these calculations did not take into account the deformation of the double layer. Wiersema⁵ and O'Brien¹ both performed extensive calculations to account for these forces and their effects on particle mobility. To eliminate the effects of temperature and viscosity, Wiersema reported all values in terms of dimensionless mobilities and ζ -potentials which are defined according to Equations 6-9 and 6-10.^{5,34} He calculated dimensionless mobility (E) as a function of ka for different values of dimensionless ζ -potential (y_0) and showed that particle mobility decreases with ka , exhibits a minimum in the range $1 < ka < 10$ and then increases again. As the value of ka increases beyond the Huckel limit, the double-layer thickness becomes finite and the relaxation effect becomes more prominent reducing overall particle mobility. There is a point at which continued increases in ionic strength decrease the thickness of the double-layer so that relaxation forces are weaker and mobilities again increase. This behavior is shown later in Figure 6-6 where it is compared to experimental data.

$$E = \frac{6\pi\eta e}{\epsilon kT} \mu_{ep}$$

E = dimensionless mobility
k = Boltzmann's constant

6-9

$$y_o = \frac{e\zeta}{kT}$$

y_o = dimensionless ζ -potential

6-10

O'Brien got similar results, only he plotted E as a function of y_o for various ka values.

Figure 6-5 was taken from O'Brien's

work showing the data for $ka > 3$.^{5,34}

At low values of ζ -potential, all values approach those obtained by Huckel's equation regardless of the ka value. Above $ka \sim 4$, the mobility increases with ζ -potential, exhibiting a maximum in the range of $4 < y_o < 7$, with higher values corresponding to higher ka values. It is noted that at high ka values, E(y) curves tend to the linear Smoluchowski form ($E=1.5y_o$) although they never become totally independent of ka.

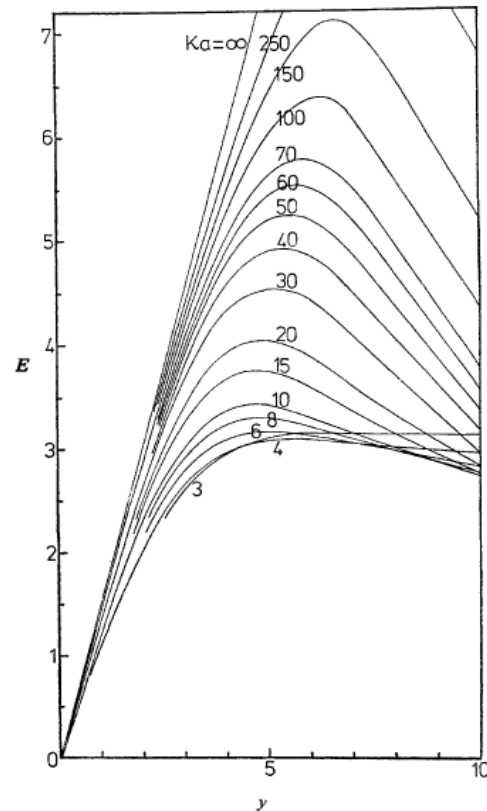


Figure 6-5. Variation of mobility with zeta potential for a spherical colloidal particle in KCl at ka values > 3

Figure taken from O'Brien and White¹

The behavior is explained by the fact that with increasing ζ - potential, the retarding force and relaxation effects increase at a faster rate than the electrophoretic driving force. For ζ -potentials less than 25mV and at low ka values (< 2.75) there is minimal distortion of the double layer and these effects are not observed.

The predictions of the theory developed by both Wiersema⁵ and O'Brien¹ have been observed experimentally. Both Figure 6-5 and Figure 6-6 show that above a threshold value, mobility increases with ka . Larger particle sizes and higher ionic strengths both contribute to larger ka values and consequently larger mobilities. Thus, for particles of equal ζ -potential and intermediate ka values, size-dependent separations can be achieved with larger particles exhibiting greater mobilities.³⁵

Electrophoretic mobilities have been shown to increase linearly with radius for polystyrene particles,^{16,35-37} gold particles,^{4,15,38} and gold/silver core/shell particles.³⁹ Larger silica particles have also exhibited greater mobilities than smaller ones.^{16,35} It has also been shown that particles exhibit greater mobility at higher ionic strengths, improving overall resolution in size-dependent separations.^{16,34} Liu et al. suggest that, as with size-exclusion chromatography (SEC), the decrease in the double layer thickness corresponding to high ionic strengths increases mobility due the decrease in the effective particle diameter.⁴ However, according to the calculations of Wiersema and O'Brien, these effects should not be as significant as those due to relaxation.

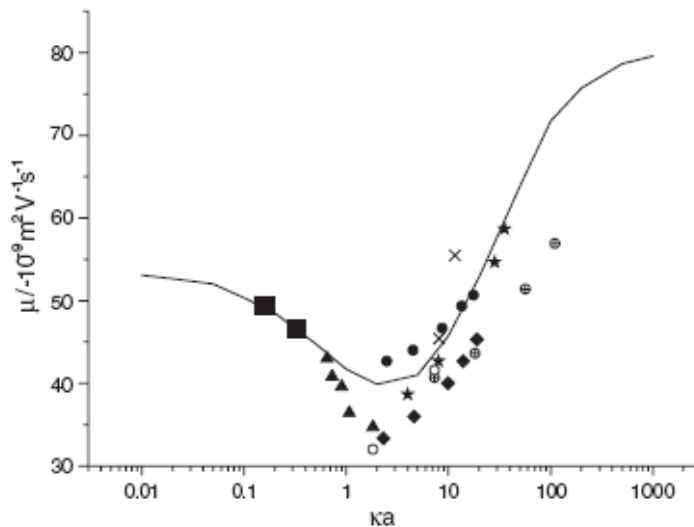


Figure 6-6. Electrophoretic mobility of nanoparticles with ζ -potential of 102.6 mV
Figure taken from Bucking et al.³

- Theoretical prediction by Wiersema et al.⁵
- Gold nanoparticles reported by Bucking et al.²
- ▲ Gold nanoparticles reported by Schnabel et al.⁵
- ◆ Gold nanoparticles reported by Liu and Wei³
- Gold nanoparticles reported by Liu et al.⁶
- * Silica particles reported by Vanifatova⁷
- × Latex nanoparticles reported by Petersen and Ballou^{4,5}
- ⊕ Polystyrene nanoparticles reported by Hwang et al.

Other studies have reported behavior which seemed to be contradictory to that predicted by Wiersema⁵ and O'Brien¹. Schnabel et al.¹⁴ observed electrophoretic mobilities of gold particles that decreased with increasing diameter.

This behavior was attributed to interactions with the capillary walls, which created more of a chromatographic type of separation mechanism.

However, Figure 6-6, taken from Bucking et al.,³ compares the results of this and several other works to the theoretical calculations performed by Wiersema, and shows that the ka values in this study are below the mobility minimum in Wiersema's calculations. In this regime, all other factors being the same, smaller particles exhibit greater mobilities. The mobility minimum reported by

Wiersema corresponds to the point at which the relationship between particle size and particle mobility is reversed.³ Bucking et al.³ and Peterson et al.² also reported separations of gold particles where smaller particles exhibited greater mobility. Thus, in order to determine particle size from electrophoretic mobility, very strict control over buffer conditions, ζ -potential and ka values is required.

Liu et al. examined the effect of sodium dodecyl sulfate (SDS) on the size-dependent separation of gold particles.⁴ The behavior shown in Figure 6-7 was attributed to the interaction of the hydrophobic tail of SDS with the gold particles, which increased the effective surface charge and consequently the particle mobility.

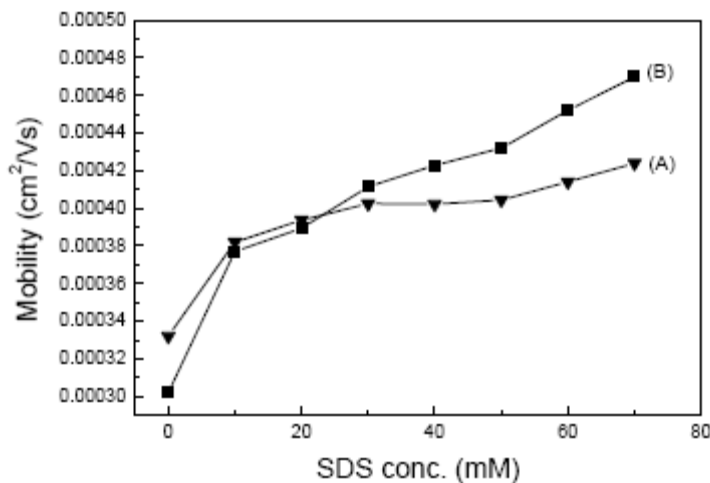


Figure 6-7. Effects of SDS concentration on the electrophoretic mobility of gold nanoparticles. CAPS, 10 mM, pH 10.0, applied voltage 20 kV (A) 5.3 nm (B) 19.0 nm Figure taken from Liu and Wei²

While this phenomenon could explain these data, there is some question about the nature of this interaction and there were several other variables that were not considered. There have been several investigations into the

interaction of SDS with gold, which are discussed in more detail in Chapter 5. They include interaction of with a charged gold electrode,⁴⁰ the adsorption of gold particles onto C18-silica,^{4,41} a shift in the plasmon resonance for gold particles in the presence of SDS,⁴² and the behavior of particles with SDS in both electrophoretic⁴³ and size-exclusion experiments.⁴² While these studies all suggest there is some type of interaction between gold particles and SDS, much of this data is inconclusive and the exact nature of this interaction is not yet known.

Relaxation effects should also be considered when interpreting Liu's data as ionic strength increases with SDS concentration. This effect of added SDS was determined to be comparable to that of NaCl in SEC experiments,^{42,44} and could therefore have similar effects in the context of CE. The magnitude of k_a increases with SDS concentration as shown in Table 6-1. These calculations are only approximate as they do not account for any NaOH that was added to modify the pH. However, if one compares these values to Wiersema's calculations in Figure 6-6, it seems reasonable to suggest the mobility minimum exists somewhere in this range of k_a values accounting for both the increase in the mobility differences and the reversal of elution order. If Liu's conclusion is correct and the overall charge of the particles increased due to their association with SDS⁴, this would also contribute to increased relaxation effects according to O'Brien's calculations shown in Figure 6-5.¹

Because of the high concentration of surfactant in solution, one cannot dismiss the possibility that there were also some elements of MEKC present in the study performed by Liu et al.⁴ Above the critical micellar concentration (cmc) of SDS, 8.1 mM,^{17,23,25} the increase in mobility appears linear, which is consistent with micellar partitioning according to Equation 6-4. A typical micelle is on the order of 3-5 nm,²³ which is of the same order magnitude as the nanoparticles used in this study. Therefore, it is questionable whether typical micellar partitioning would occur. There has been one study indicating that it does not occur in the context of an SEC experiment.⁴² However, as discussed above, there are several different factors contributing to particle mobility. If the hydrophobic tail of SDS associates with gold particles as some studies suggest,^{4,41-43} some elements of MEKC may be present in

Table 6-1. Approximate k_a values for 5.3 nm and 19 nm gold particles in 10 mM CAPS buffer with varying concentrations of SDS.*

SDS concentration (mM)	Debye Length (nm)	k_a^{**} (a = 2.65nm)	k_a^{**} (a = 9.5nm)
0	3.04	0.87	3.13
10	2.15	1.23	4.42
20	1.75	1.51	5.41
30	1.52	1.74	6.25
40	1.36	1.95	6.99
50	1.24	2.14	7.65
60	1.15	2.31	8.27
70	1.07	2.47	8.84

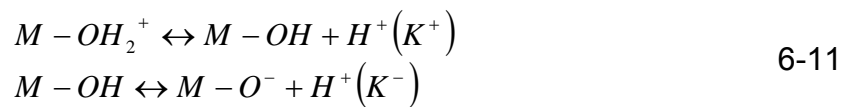
*These calculations do not account for any NaOH added to modify the pH

** a is the particle radius so these values correlate to particles with mean diameters of 5.3 and

this separation. A system involving charged particles in the presence of surfactant is complicated and many different variables need to be considered.

While the discussion thus far has focused on how the relaxation effect can facilitate size-dependent separations among particles with similar ζ -potentials, this consideration does not negate the role of surface charge in determining electrophoretic mobilities. Jones et al. separated latex particles according to both the nature and number of functional groups attached to them.⁴⁵ As with smaller anions, pH can affect the degree of ionization of surface-bound ligands and consequently their mobility. O'Brien predicted that, due to the relaxation effect, the change in the hydrogen ion concentration at the particle surface could also affect the degree of dissociation of carboxylic acid-terminal groups.¹

Quang et al.⁷ examined the effects of buffer conditions on the charge and mobility of metal oxide particles. In their analysis, metal oxide particles were treated as diprotic acid.



The pH greatly affects the surface charge of the particle and consequently the mobility. An expression was derived for the electrophoretic mobility in terms of the molar fractions of the positive and negative species.⁷

$$\mu_{ep} = \frac{\mu_+ + \mu_- K_+ K_- / [H^+]^2}{1 + K_+ / [H^+] + K_+ K_- / [H^+]^2} \quad 6-12$$

Figure 6-8 (A) and (B) shows data taken for several different metal oxide particles compared to calculations using the above equation. For all particles, mobility was positive at low pH conditions where the first reaction dominated and became negative at higher pH values where the second reaction took over.⁷ The point at which the mobility is zero is the isoelectric point or the point of zero charge. At this point the adsorption of cations was counterbalanced by the adsorption of anions and the ζ -potential was zero. In this study, the observed isoelectric points agreed with those reported in the literature. Higher pH values yielded more negative mobility values and greater resolution separations.

In addition, more negatively charged particles exhibited larger degrees of electrostatic repulsion and thus greater stability. Figure 6-8 (B) shows that the mobility leveled out for both γ -Al₂O₃ and TiO₂ particles above pH 8-9, and the electropherograms in Figure 6-8 (C) show that both individual types of particles eluted from the column to give a single peak at pH 9.0. However, Figure 6-8 (C) also shows that a mixture of these two types of particles under the same conditions exhibited a single, poorly-resolved peak with multiple spikes suggesting that the mixture of particles aggregated. The improvement in resolution with pH as shown in Figure 6-8 (D) was attributed to a greater degree of electrostatic repulsion, which

provided the particle mixture with a greater degree of kinetic stability. Quang et al.⁷ also demonstrated that at a constant pH value, resolution decreased with ionic strength due to a decrease in the electrical double layer thickness, which negatively

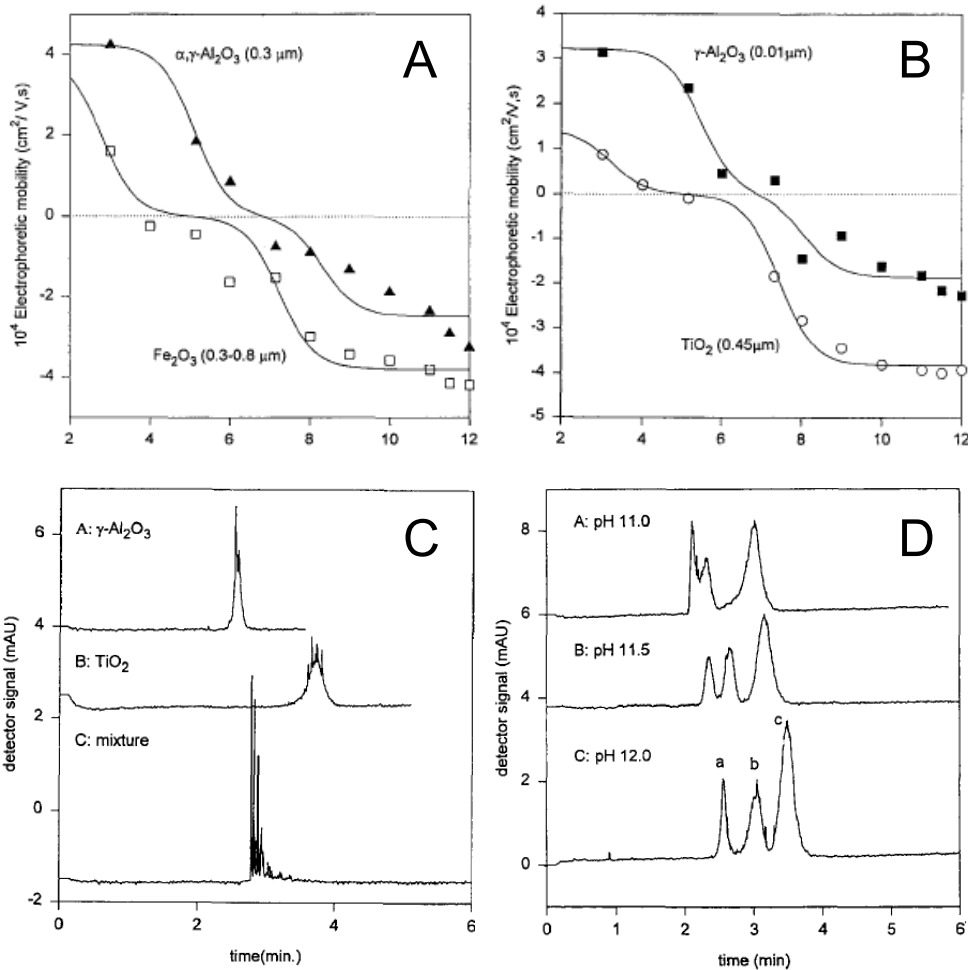


Figure 6-8. (A) Electrophoretic mobilities of $\alpha, \gamma\text{-Al}_2\text{O}_3$ and Fe_2O_3 as a function of pH. Symbols and solid lines represent the measured electrophoretic mobilities and theoretical best-fits to the two-site disassociation model (B) Electrophoretic mobilities of $\gamma\text{-Al}_2\text{O}_3$ and TiO_2 as a function of pH (C) Electropherograms of $\gamma\text{-Al}_2\text{O}_3$ and TiO_2 at pH 9.0 (D) Electropherograms of a mixture of (a) $\alpha, \gamma\text{-Al}_2\text{O}_3$, (b) $\gamma\text{-Al}_2\text{O}_3$ and (c) TiO_2 as a function of pH Figures taken from Quang et al.³

affects particle stability.

These data suggest that, when studying particle mixtures, or hetero-structures, the conditions need to be chosen not only to maximize mobility and separation but also to ensure particle stability against aggregation. In the context of Wiersema's calculations, the difference in electrophoretic mobility for particles of different sizes is greater at higher ionic strengths.^{3,5} However, under these conditions, the decrease in the electrical double layer thickness negatively affects particle stability. At the same time, higher pH values increase the charge on the particle surfaces, increasing particle mobility and maximizing electrostatic repulsion, which improves particle stability.

In contrast to most electrophoretic separations, which are performed in buffered electrolyte systems, Quang's study of metal oxide particles was done in a sodium nitrate electrolyte system in which there were no interactions between the particles and the ions in the mobile phase.⁷ However, ions in typical buffers interact with and affect the mobility of particle analytes. In general, interactions with buffer anions increase particle mobility. Ducette et al.⁴⁶ studied the effects of buffer composition on the mobility of oxide particles; phosphate, carbonate and borate anions all had significant effects on the mobility of titania, alumina and hematite. This study shows that the relative mobilities of these metal oxide particles changed according to the buffer anion, but that these interactions are complex and no general statements can

be made about the relative interactions of buffer anions with oxide particle surfaces.⁴⁶

In summary, previous studies have demonstrated that, as with the separation of smaller ions, there is a tradeoff associated with the ionic strength and pH of the buffer for particle separations. Generally, higher ionic strengths yield higher k_a values which lead to greater particle mobility and higher resolution. For capillary-based separations, high ionic strength also decreases the rate of EOF, which can improve resolution. However, as discussed above, increased ionic strength has consequences associated with particle stability and Joule heating. Increases in pH can increase the charge on particle anions, increasing their mobility and increased electrostatic repulsion has been shown to improve the stability of some metal oxides. However, there have been some studies that suggest that other particles, such as gold with carboxylate functionalities, aggregate in basic conditions.⁴⁷ For capillary-based separations, higher pH values increase the rate of EOF which degrades resolution. In addition, the buffer ions can affect particle mobility either through interactions with the particle surface or their contribution to the relaxation effect. All of these factors need to be taken into account when choosing operating conditions for electrophoretic particle separations.

6.1.5. Gel Electrophoresis of Particles

Electrophoresis of particles in a gel differs from that in solution in that an additional factor, the interaction of particles with the gel, must be considered.⁴⁸ The gel acts as a sieving network, which impedes the movement of molecules according to their size and conformation differences so that the molecular mobility is dependent on the effective molecular radius.¹⁷ This behavior is often exploited in SDS-PAGE protein separations. SDS binds to a protein giving it a net negative charge. The charge/mass ratio is the same for all proteins and these separations are based solely on size.^{6,9,10,12,17,49}

Gel electrophoresis has been used to separate nanoparticles according to the nature of the attached ligands. For instance, several groups have used this technique to determine the number and size of DNA strands attached to gold particles^{50,51} in addition to their conformation.⁵² Au particles conjugated with DNA having greater than 30-50 base pairs exhibited lower mobilities than the isolated particles or DNA.⁵⁰ This behavior was attributed to the larger size of the former particles compared to the latter ones. Similar results were achieved for the attachment of gold particles to polyethylene glycol (PEG) units with molecular weights greater than 5000 g/mol.^{53,54}

These data contradict those obtained for semiconductor particles in which complexation with a silanol shell increased the mobility of CdSe/ZnS core/shell

particles.⁵⁵ This result is explained by the fact that these particles are essentially neutral at the buffer pH, and the incorporation of a silanol shell results in a much greater charge and thus a greater mobility. The gold particles discussed previously were already sufficiently charged that the addition of DNA affected the size more than the overall charge.

Zanchet et al.⁵⁶ suggest that the separation mechanism for particles varies with agarose concentration in the gel. The particle charge is the dominant factor in determining particle mobility at low gel concentrations (e.g. < 1%) while particle size has a greater influence at higher concentrations (e.g. > 3%).⁵⁷ The effect of charge in 1% agarose gels was also documented for CdSe/ZnS particles which demonstrated distinct changes in mobility with pH.⁵⁵ Increasing the pH from 5.4 to 7.2 increased the mobilities of both siloxane and mercaptopropionic acid-coated semiconductor particles due to increases in particle charge.

Gel electrophoresis has also been used to separate gold particles according to size and shape.⁵⁸ Gold particles capped with 11-mercaptoundecanoic acid have been separated by size in Tris/borate/EDTA (TBE) with smaller particles exhibiting greater mobilities.⁵⁸ This result indicates that, under these conditions, relaxation effects are not significant. It has been suggested that the sieving effect in the gel results in the decreased mobility of larger particles.^{56,57} Likewise, Zanchet et al. attributed the lower mobilities observed for their DNA-linked, gold nanoparticle dimers to their

larger size.⁵⁷ Similar results were reported by Claridge et al. for trimer and tetramer structures.⁵⁹ In both of these studies, the linker lengths were significantly greater than the particle diameters.

6.2. Results and Discussion

6.2.1. Gel Electrophoresis of Particle and Assemblies

The goal of this work was to separate dimers and trimers of gold nanoparticles from the isolated particles in solution and any other aggregates that might be present. All examples in the literature indicate that the sieving mechanism governs separation behavior in a gel. It was, therefore, predicted that smaller particles would exhibit greater mobility than larger ones, and, likewise, isolated particles would exhibit greater mobility than larger assemblies.

One of the problems associated with using a gel is the irreversible adsorption of particles. In attempt to avoid this, all particles and particle assemblies underwent ligand-exchange with Bis(p-sulfonatophenyl)phenyl phosphine (BSPP) before separation. This ligand is bulkier than the citrate ions leading to greater stability, and, like citrate, it has a negative charge and thus contributes to the negative charge on the particle surface.^{51,52,57,59} Electrophoretic separations with citrate-particles in the absence of BSPP resulted in aggregation.⁵¹ The added stability created by the

BSPF functionality also allowed the particle solutions to be concentrated before being loaded in the gel, which increased their visibility.

Figure 6-9 (A) shows that while difficult to visualize, particles can be separated according to size using gel electrophoresis. As predicted, smaller particles exhibited greater mobilities. The mixture was compared with isolated particles to confirm band assignments. The bands were relatively wide and exhibited some tailing effects which limited resolution. In addition, bands for 30 nm and 60 nm particles were not

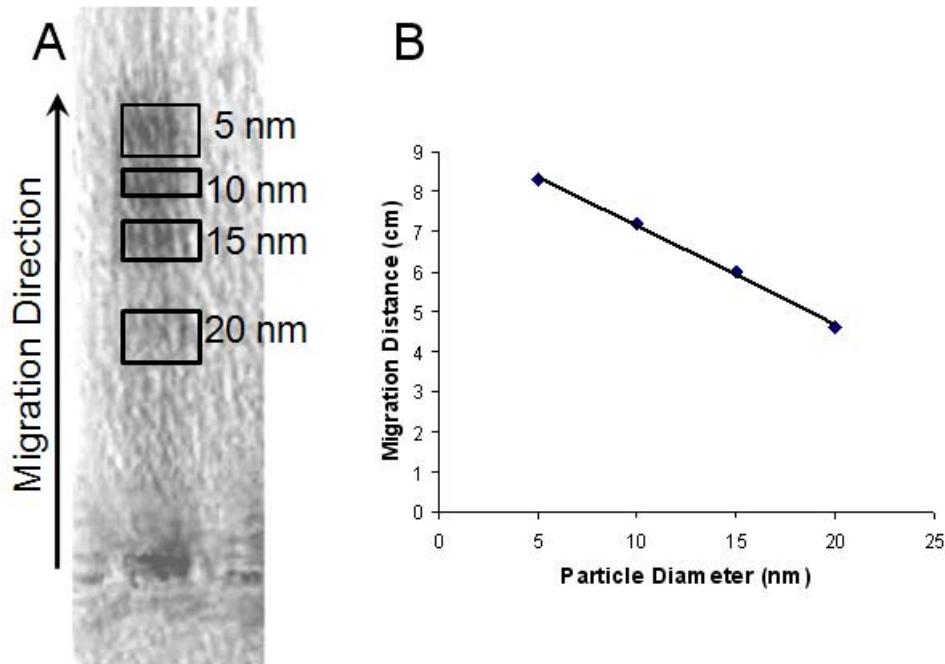


Figure 6-9. Gel electrophoresis of gold particles in 2% agarose gel (A) A mixture of 5 nm, 10 nm, 15 nm, 20 nm, 30 nm and 60 nm particles (B) A plot of migration distance vs. particle diameter showing that mobility decreases with particle size *
* Distances were measured from center of each band on the scanned image; may not reflect exact distances traveled on the gel.

observed. The absence of these particles could be due to the fact that the pore size in the gel was too small to allow them to migrate or that these particles were less stable and aggregated on the gel. It is also possible that the concentrations of these particles were too low to be observed. However, as discussed in Chapter 2, while the concentrations of larger particles in solution are significantly lower, their extinction coefficients at 520 nm are much greater and thus their absorbances are similar.

Gel electrophoresis was then applied to the separation of gold nanoparticle dimers and trimers from the isolated particles and other aggregates in solution. Figure 6-10 (A) shows the attempted separation of 5 nm dimers from the isolated particles. As the particle assemblies were synthesized in the presence of 3 mM sodium citrate and 2:3 THF/ethanol solution according to the protocol in Chapter 3, particles with these additives were run for comparison to the particle assemblies. The solution containing dimers of 5 nm particles showed a wider band than that associated with the isolated particles, but the gel did not exhibit sufficient resolution to discriminate between the dimers and individual particles. There also appears to be significant tailing. Similar results were observed for solutions containing assemblies of 10 nm particles. (Figure 6-10(B)). However, the samples containing 15 nm particles showed significant aggregation and band broadening even in the absence of the linker molecule. This behavior is most likely due to particles sticking to the gel.

Similar results were observed for dimers of 20 nm and 40 nm particles. While ligand-exchange with BSPP was sufficient to stabilize 15 and 20 nm particles sizes in the absence of additional sodium citrate and organic solvent, irreversible adsorption occurs in the presence of these additives. Similar results were shown for 15 nm and 20 nm particles analyzed with size-exclusion chromatography on a silica column in Chapter 5. For this case, the decreased stability of larger particles was attributed to both their greater Hamaker constants (Section 2.1.1.1) and the absence of tannic acid in these particle solutions.

It is possible that conditions could have been optimized to improve separations, at

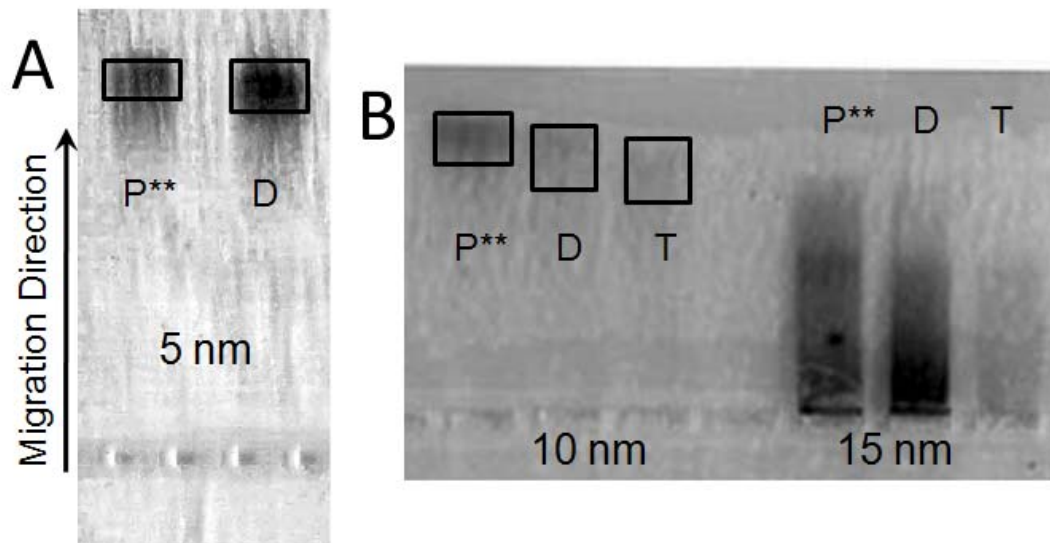


Figure 6-10. Gel electrophoresis of particle assemblies in 2% agarose gel (A) Solution containing dimers of 5 nm particles compared to solution of isolated 5 nm particles (B) Solutions containing dimers and trimers composed of 10 nm and 15 nm particles compared to solutions of isolated particles. P = particles with 3 mM sodium citrate and 2:3 THF:EtOH; D = dimers; T = trimers**

least for the smaller particles. All separations were performed in a 2% agarose gel. It has been shown that for gold-DNA conjugates, the mobility differences increase with agarose concentration.⁵⁷ However, it has also been noted that higher gel concentrations generally lead to greater degrees of band-broadening and do not improve separations.⁵⁷ It is also possible that changing the buffer composition could have improved separations. Regardless, interactions between the particles and the gel were determined to be significant and even if resolution was improved, this technique would still not provide quantitative data regarding the concentrations of dimers in solution. In addition, it was difficult to visualize small concentrations of particles in the gel.

At this point, efforts were shifted to capillary electrophoresis which has the potential for higher resolution, has less surface area to interact with the particles and is equipped with online absorbance detection so that small concentrations of particles can be detected.

6.2.2. Capillary Electrophoresis of Particles and Assemblies – General Considerations

Many different variables need to be considered when choosing conditions for the capillary electrophoretic separation of particles. As outlined in Section 6.1.4, both pH and ionic strength need to be chosen to maximize particle separation and prevent particle adsorption and aggregation. There are limited reports in the

literature on capillary electrophoresis of nanoparticles. Schnabel et al.¹⁴ used an acetic acid/acetate buffer at pH 5.0 to separate gold particles; however, higher pH values were desired for both particle stability and mobility. Hwang et al.²⁰ used trishydroxymethylaminomethane (Tris) buffer at a pH 9.2; however, Liu et al.⁴ observed greater particles mobilities in N-cyclohexyl-3-aminopropane sulfonic acid (CAPS) buffer than for Tris buffer at the same concentration. Liu et al. used CAPS in the presence of SDS for the separation of gold,^{4,15,38} silver⁶⁰ and Au/Ag core/shell particles,³⁹ and these conditions were adapted for the separation of gold particles in these experiments.

In addition to the greater mobility differences for particles in the presence of SDS (Figure 6-7), there have been reports that SDS stabilizes particles against aggregation in both electrophoretic⁶⁰ and size-exclusion^{41-43,61} separations. SDS has also been reported to yield relatively constant EOF values over wide pH ranges.^{13,17} While the exact interaction between SDS and charged particles is not known, it has proved beneficial in particle electrophoretic separations.

As discussed in Section 6.1.4, the presence of high concentrations of SDS introduces aspects of MEKC to the nanoparticle separations. For this reason, a UV-active compound that exhibits negligible interactions with micelles was added to the sample as an EOF marker. Mesityl oxide (MO) moves through the capillary at the rate of EOF and elutes at time, t_0 . Octanophenone (OP) was also added to the

sample as it is UV-active and is irreversibly solubilized within SDS micelles. OP migrates at the same rate as the micelle and elutes at time, t_{mc} . The structures of molecules involved in the CE separation of nanoparticles are shown in Figure 6-11.

In addition the particle stability provided by SDS in the mobile phase, actions were taken to stabilize the gold-citrate particle samples against aggregation. Bucking et al.³ reported that citrate-ligated particles were not suitable for capillary electrophoresis because the citrate-ligand desorbed from the particles too easily,

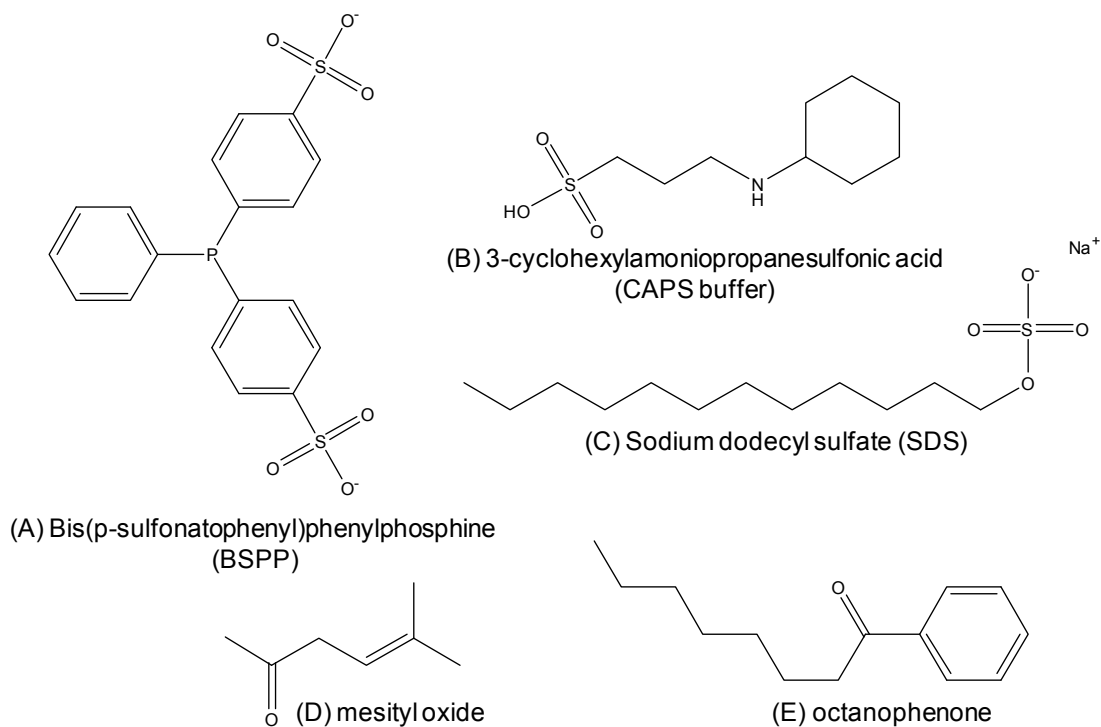


Figure 6-11. Molecules involved in CE experiments (A) Gold-citrate particles underwent ligand-exchange with BSPP for added stability (B) CAPS buffer (C) SDS was added to mobile phase (D) Mesityl oxide was added to the sample and elutes at t_0 (E) Octanophenone was added to the sample and elutes at t_{mc} .

and the nanoparticle solutions degraded. In addition, the sample volumes in CE are small ($< 1 \mu\text{L}$)⁶² making optical detection of nanomolar concentrations difficult. For these reasons, particles characterized in this study underwent ligand-exchange with BSPP in the same manner as the samples used for gel electrophoresis. BSPP has been shown to add stability to gold citrate particles,^{61,63,64} which is helpful in preventing adsorption and aggregation during electrophoresis. In addition, this added stability made it possible for particles to be concentrated before analysis for easier detection.

As with the gel electrophoresis, the goal of this work was to separate dimers and trimers of gold nanoparticles from the isolated particles in solution and any other aggregates that might be present. Unlike separations in the gel, the sieving mechanism is not present, and separations in CE were predicted to be based solely on electrophoretic phenomena and exhibit mobilities similar to those calculated by Wiersema⁵ and O'Brien.¹ The nature of these separations is expected to be size-dependent with larger particles exhibiting greater (i.e. more negative) mobilities. Whether due to interactions with SDS or simply the magnitude of relaxation effects present, Liu et al. observed linear relationship between particle size and mobility in 10mM CAPS buffer with 70mM SDS.^{4,15,38} Likewise, it was expected that particle dimers and trimers would exhibit greater mobilities than isolated particles.

6.2.3. Capillary Electrophoresis of Gold-Citrate Particles

Before particle assemblies were injected into the capillary, attempts were made to optimize conditions for the separation of gold particles by CE. Gold particles were separated in CAPS Buffer (10 mM) with 70mM SDS at pH values ranging from 9.5 to 10.7. Figure 6-12 (A) shows electropherograms of particles with mean diameters of 5, 10, 15 and 20 nm at pH 9.7, and data for all pH values are shown in Figure 6-13. Some particle separation was observed; however, it was minimal and significant overlap was observed in the overlaid data. Similar results were observed at higher pH values. It was predicted that a lower pH would decrease the rate of EOF and

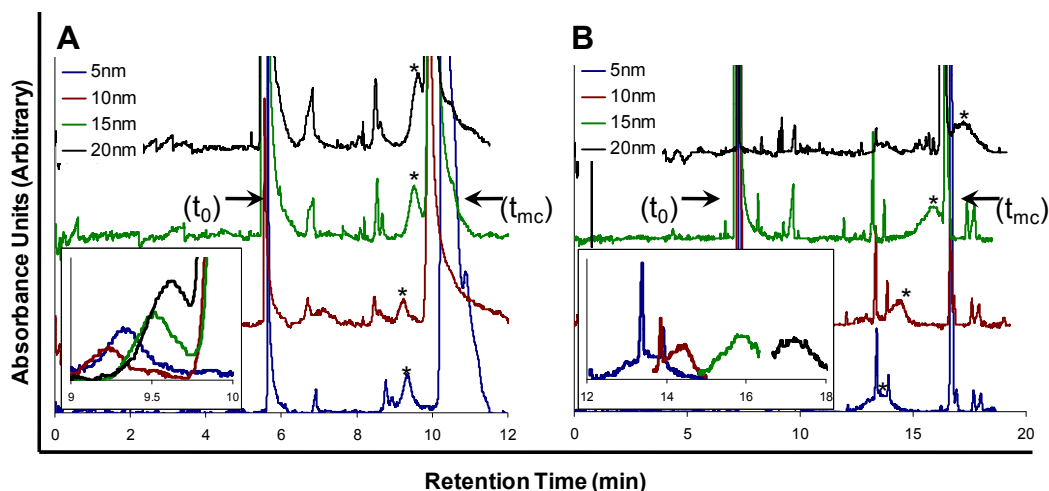


Figure 6-12. Electropherograms of 5 nm, 10 nm, 15 nm and 20 nm gold-citrate particles
(A) CAPS Buffer, pH 9.8 (B) Phosphate Buffer, pH 8.0
Applied voltage = 18 kV, $\lambda_{\text{det}} = 254 \text{ nm}$; EOF marker = mesityl oxide (t_0); Micellar marker = octanophenone (t_{mc}). The peaks associated with nanoparticles are marked with an *, and the insets show the overlaid electropherograms of the particle peaks.

possibly improve separation. However, CAPS has a pka of 10.40, and is only effective in a range, $9.7 < \text{pH} < 11.1$. Figure 6-13 (B) shows that the separation improved slightly when the pH was lowered to 9.5; however, these data varied somewhat from run to run as the pH was just outside the effective range for CAPS buffer. Phosphate buffer was chosen as it has a pka(2) of 7.20 and is effective in the range, $5.8 < \text{pH} < 8.0$. Figure 6-12 (B) shows that separation did improve with the phosphate buffer; however, peaks are also significantly broader.

There were most likely several factors contributing to both the increased separation and broader peaks observed with the phosphate buffer. Both CAPS and phosphate buffers were run at multiple pH values, and Table 6-2 lists the corresponding ionic strengths. These values were greater for the phosphate buffers, which could partially account for the increased separation as relaxation effects play a greater role

Table 6-2. Ionic strengths, Debye lengths and ka values for buffers used in CE experiments

Buffer	pH	Ionic Strength	Debye Length (nm)	κa^* (a=2.5nm)	κa^* (a=5.0nm)	κa^* (a=7.5nm)	κa^* (a=10nm)
CAPS	9.5	0.081	1.07	2.34	4.67	7.01	9.35
	9.7	0.081	1.07	2.34	4.69	7.03	9.38
	10.2	0.082	1.06	2.36	4.71	7.07	9.42
	10.7	0.085	1.04	2.40	4.80	7.19	9.59
Phosphate	7.3	0.108	0.93	2.70	5.40	8.09	10.79
	8.0	0.122	0.87	2.69	5.37	8.06	10.74

* a is the particle radius so these values correlate to particles with mean diameters of 5, 10, 15 and 20 nm

at higher k_a values.^{1,5} The decreased double-layer thicknesses associated with higher ionic strengths could also account for the peak broadening due to adsorption along the capillary wall. As predicted, the lowered pH decreased the rate of EOF

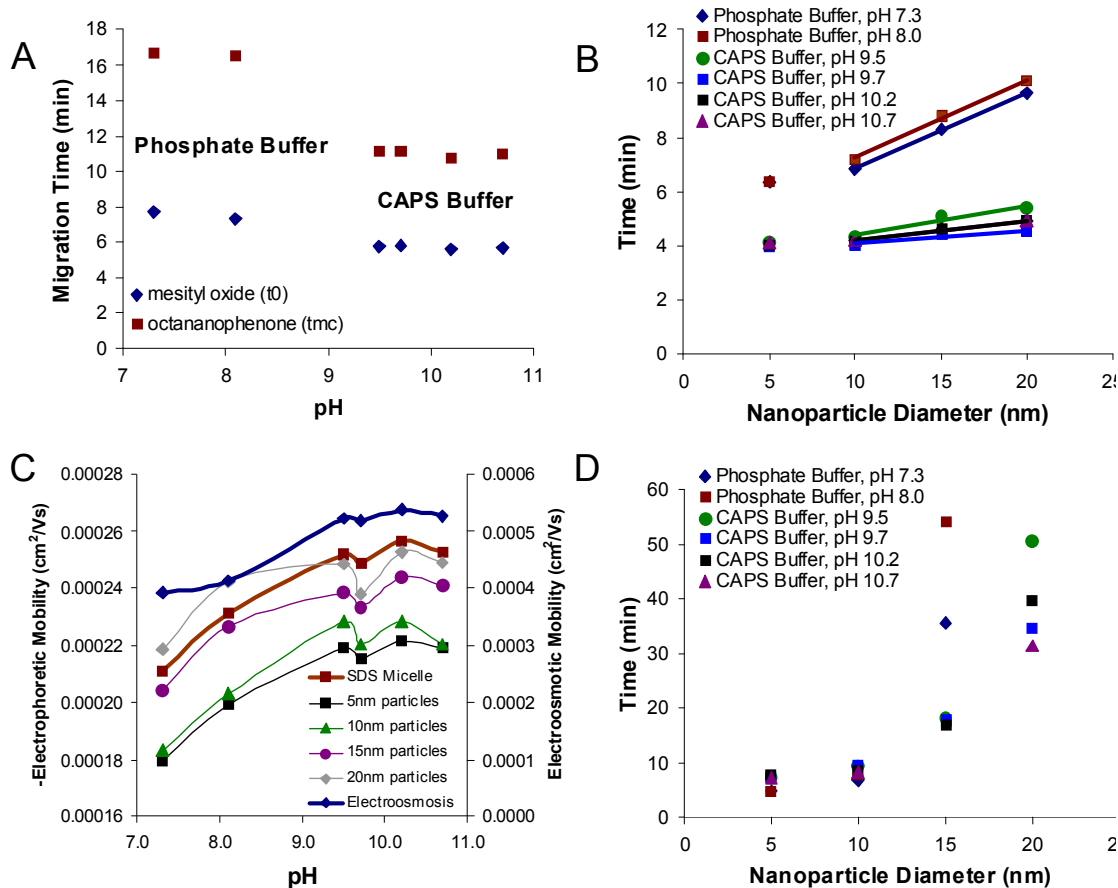


Figure 6-13 The dependence of pH on gold particle migration times, mobilities and interaction parameters (A) Migration times of mesityl oxide (t_0) and octananophenone (t_{mc}) as a function of pH (B) Migration time relative to EOF vs. nanoparticle diameter at several pH values (C) Electroosmotic and electrophoretic mobilities as a function of pH. Note that the electrophoretic mobilities are negative, and particles move in the direction opposite EOF. The lines between data points do not represent a curve fit, they are included simply to guide the eye (D) Interaction parameters of gold particles vs. nanoparticle diameter as several pH values. All experiments were performed with an applied voltage of 18 kV.

and improved separation. The lowered pH could have also decreased the effective charge on both the capillary wall and the particles contributing to the observed peak broadening.

The results for particle separations at all pH values are shown in Figure 6-13 and summarized in Table 6-3. The migration time for mesityl oxide was used to calculate electroosmotic mobility (EOM) of each buffer solution according to Equation 6-3.

There were negligible differences in EOM between solutions composed of the same buffering agent. However, phosphate buffer did exhibit less mobility than the CAPS buffer. The electrophoretic mobilities of both the SDS micelles and the gold particles were similarly calculated, and Figure 6-13 (C) shows that these values increase (i.e. become more negative) with increasing pH and then level out. This can be explained by an increase in the effective particle charge with pH.

There were negligible differences in mobility observed between 5 nm and 10 nm particles, and migration times appeared to increase linearly for sizes greater than 10 nm. This linear relationship may be less than convincing with only the three data points shown in Figure 6-13 (B); however, Figure 6-14 shows that this relationship extends for particle sizes up to at least 40 nm. These data were not included in the comparison above, because there was less control over the pH and ionic strength in this particular separation. The linear relationship above 10 nm particle size indicates that, in this regime, relaxation effects are present and separation is size-dependent

with larger particles exhibiting greater mobilities. As mentioned earlier, similar behavior has been observed for polystyrene particles,^{16,35-37} gold particles,^{4,15,38} and gold/silver core/shell particles.³⁹ The slopes of these plots are listed in Table 6-3, and the greatest separation was observed for phosphate buffer at pH 8.0.

The minimal differences in mobility between the 5 nm and 10 nm gold particles can be explained in the context of the calculations of Wiersema⁵ and O'Brien.¹ Figure 6-6 shows Wiersema's theoretical predictions, which indicate that a minimum in mobility exists in the range $1 < ka < 10$, and experimental data that suggests this

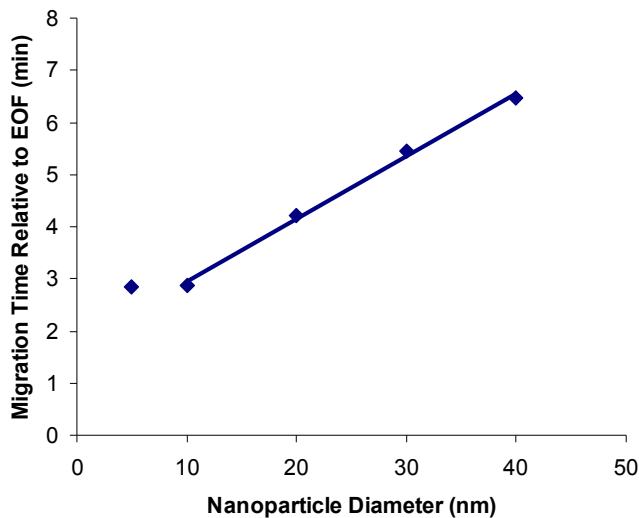


Figure 6-14. Migration time vs. nanoparticle diameter for gold particles in 10 mM CAPS Buffer, 70 mM SDS, pH ~ 8-9 (measured by pH paper)

minimum occurs at $ka \sim 2$. At the mobility minimum, the relationship between particle size and mobility is reversed, and minimal differences in mobility are observed. Table 6-2 lists the ka values for these particles, which correlate to the observed mobility minima in Figure 6-6. These values could account for the behavior shown in Figure 6-13

(B) and Figure 6-14.

As mentioned earlier, the presence of large concentrations of SDS in the buffer introduces aspects of MEKC to the separation, and octanaphenone was added to the sample to mark the micellar migration time, t_{mc} . The interaction parameters associated with MEKC were also calculated according to Equation 6-4 and plotted in Figure 6-13 (D). If the particles interact with the micelles, this parameter indicates the extent of this interaction. If, however, the particles do not interact with SDS, these values are less significant. It was predicted that the interaction parameters would be greater at lower pH values due to increased electrostatic repulsion between the particles and the micelles. This was not observed for 5 nm and 10 nm particles, which exhibit similar interaction parameters at all pH values. The 15 nm particles exhibit similar interaction parameters in CAPS buffer, but higher values in

Table 6-3. Data obtained from plots of migration time vs. particle diameter for buffers at different pH values.

Buffer	pH	Slope	Intercept	R ² value
CAPS	9.5	0.108	3.326	0.943
	9.7	0.049	3.619	0.927
	10.2	0.075	3.440	0.990
	10.7	0.071	3.515	NA*
Phosphate	7.3	0.282	4.033	0.999
	8.0	0.289	4.365	0.996

* This equation was calculated from only two points

phosphate buffer. With the exception of the data point at pH 9.7, which deviates from the trend, the interaction parameter for 20 nm particles increases with decreasing pH in CAPS buffer as expected. The

interaction parameters were not plotted for 20 nm particles in phosphate buffer as they elute after t_{mc} (Figure 6-12 (B)), which yields a negative interaction parameter according to Equation 6-4. The quantitative implication for this is not clearly understood as the total mobility is the sum of both electrophoretic and chromatographic components. These data do not shed any light on the particle-micelle interactions.

The voltage dependence on the electrophoretic separation was also investigated.

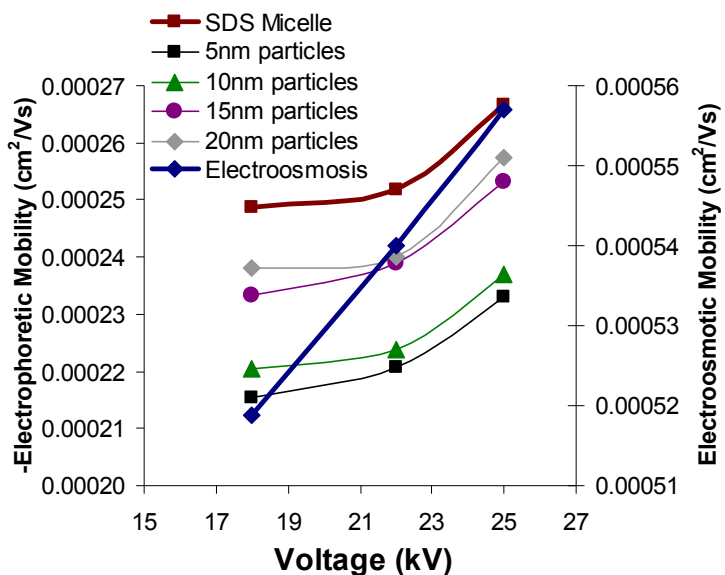


Figure 6-15. Electroosmotic and electrophoretic mobilities as a function of applied voltage
 Note that the electrophoretic mobilities are negative, and particles move in the direction opposite EOF. The lines between data points do not represent a curve fit; they are included simply to guide the eye

According to Equation 6-

2, electrophoretic

mobilities should be

independent of the

applied voltage.

However, both the rate of

EOF and the

electrophoretic velocity

increase with applied

field. The increased rate

of EOF generally reduces

the amount of time in the

capillary with negative

effects on the separation. In addition, increased temperature due to Joule heating and can decrease the viscosity, increasing mobilities. If the capillary is sufficiently thermostated, Joule heating and mobility differences should be limited.¹⁸ While the capillary in these experiments was maintained at a temperature of 25°C, there were still some increases in particle mobility as shown in Figure 6-15. The increase in electroosmotic mobility significantly reduces the migration times and reduces the separation between particles as shown in Table 6-4. For this reason, the applied voltage for subsequent dimer separations was maintained at 18 kV despite the longer analysis times. In addition, it is desirable to keep the power passing through the capillary less than 1W/m, and the current increases along with the voltage. For CAPS buffer, the current increased from 15 μA (0.41 W/m) to 22 μA (0.85 W/m) as the voltage was increased from 18 to 25 kV. However, the conductivity of the phosphate buffer was greater, and the current was 30 μA (0.83 W/m) at 18 kV and increased to 40 μA at 22 kV (1.35 W/m), which was outside the desired range. Higher currents lead to higher degrees of Joule heating. This was another reason the voltage was kept lower.

6.2.4. Capillary Electrophoresis of Nanoparticle Assemblies

Initial attempts at detecting nanoparticle assemblies were made before the optimization of experimental conditions as described above. Dimers and trimers of gold nanoparticle homodimers and trimers were injected under the conditions used by Liu et al.^{4,15} for separating gold particles. The buffer solution contained 10 mM CAPS, 70 mM SDS and was raised to a pH of approximately 11.0 using 0.1 N sodium hydroxide solution. CAPS is only an effective buffer in the range of $9.7 < \text{pH} < 11.1$, and the pH in these initial experiments was loosely monitored using pH

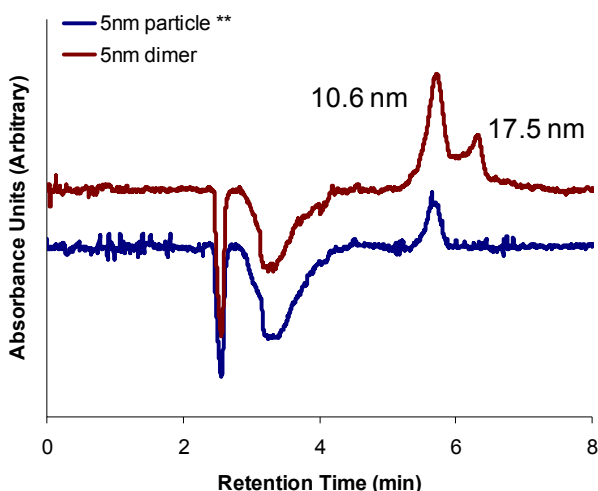


Figure 6-16. Capillary electropherogram of solution containing 5nm nanoparticles and dimers linker contained three phenyl rings 10 mM CAPS, 70 mM SDS, pH ~ 11.0, 18 kV, $\lambda_{\text{det}} = 290 \text{ nm}$ ** particle solution containing additional sodium citrate and organic solvent

paper. Assuming some margin of error, it is not unlikely that the pH could have gone outside of this range, affecting the buffering capability of the solution. In addition, the volume of the 0.1 N sodium hydroxide solution was only approximately measured (i.e. number of drops) so the ionic strength of these solutions

was not accurately known. Regardless, the data collected during these initial experiments was promising.

Figure 6-16 shows a capillary electropherogram of a solution containing dimers of 5nm gold particles. The EOF marker (toluene) did not show up in these runs, and the negative peak was attributed to air. Two peaks were observed for the solution containing dimers. Ideally, a linear calibration curve similar to the one in Figure 6-14 could have been used to correlate each peak with a hydrodynamic radius. However, this was difficult to do in this size range as the retention times for particles with diameters of 5 nm and 10 nm were approximately the same; the linear fit only applied to particles with diameters greater than 10 nm. The calculated hydrodynamic radius for a dimer containing 5nm particles is 8.2 nm (Appendix 2). If size were the only factor, one would have expected the dimer to exhibit the same retention times as both 5 nm and 10 nm particles. While not accurate, a linear calibration curve was used to correlate these peaks with hydrodynamic radii, and it was noted that the ratio between these two values ($10.6 \text{ nm}/17.5 \text{ nm} = 0.61$) was the same as that of the expected values ($5 \text{ nm}/8.2 \text{ nm} = 0.61$). While not conclusive, this supported the hypothesis that the second peak could be attributed to particle dimers.

Assemblies containing dimers and trimers of 10 nm particles were analyzed under the same conditions and the results are shown in Figure 6-17. Toluene, the EOF

marker, was visible in Figure 6-17(A); however, the retention time associated with it varied from run to run indicating the buffer solution may have been out of its effective pH range. The retention times were altered in Figure 6-17(B) so that they are displayed relative to the EOF marker. The peaks were correlated to hydrodynamic radii using a calibration curve similar to that in Figure 6-14. It is noted that there are some variations in retention times between samples, but this would be expected if the buffer was out of its effective range.

As with the samples containing 5 nm particles, the solutions containing dimers exhibited two peaks. The calculated hydrodynamic radius for a dimer consisting of

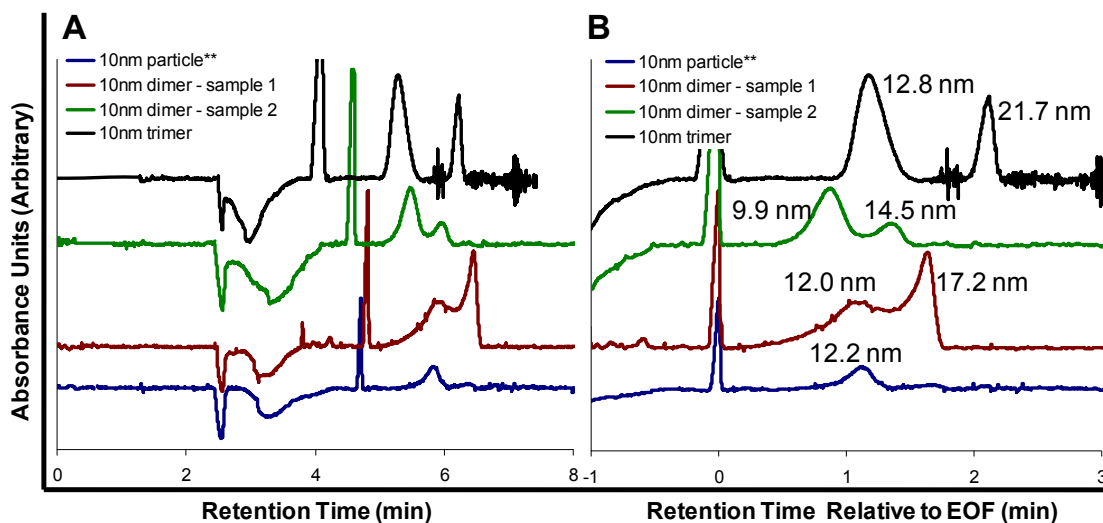


Figure 6-17 (A) Capillary electropherograms of solutions containing 10 nm particles, dimers and trimers (B) electropherograms altered to reflect time relative to EOF (toluene)

The linker for dimers contained three phenyl rings; linker for trimers contained seven phenyl rings

10 mM CAPS, 70 mM SDS, pH ~ 11.0, 18 kV, $\lambda_{det} = 290$ nm

** particle solution containing additional sodium citrate and organic solvent

10 nm particles was 15.8 nm (Appendix 2), which was in reasonably good agreement with the peaks observed in Figure 6-17. The hydrodynamic radius initially calculated for a trimer consisting of 10 nm particles was 20.2 nm, which was also in reasonably good agreement with these electropherograms.

These data were initially promising and significant efforts were expended in attempt to reproduce them. However, a closer look at the data brings up several discrepancies. Because of the polydispersity inherent in the nanoparticle solutions, they typically exhibit broad peaks. When these particles were grouped together, one would have expected the dispersity to be at least as broad. The peaks widths appeared to be similar for the two peaks observed in Figure 6-16 and for the second dimer sample in Figure 6-17. However, the second peak observed for the first dimer sample in Figure 6-17 appeared significantly narrower than the first suggesting that it may not be due to particle dimers. In addition, the peak height was significantly greater for this peak than the first peak, which contradicts TEM data indicating that 60-70% of the particles in these solutions were isolated and did not form dimeric structures (Chapter 4). Similar inconsistencies were observed in the electropherogram obtained for the solution containing trimers. The second peak was taller and narrower than was expected for nanoparticle trimers. In addition, as described in more detail in Appendix 2, the original calculation for the hydrodynamic radius of a trimer (20.2 nm) was likely inaccurate and this value could be as great as

42.3 nm. While these data were initially very promising, several inconsistencies were observed and they could not be reproduced.

These experiments were attempted again after optimizing the separation conditions as described in Section 6.2.3. While phosphate buffer yielded greater particle separation, it also produced broader peaks so CAPS buffer was again used in attempt to separate dimers from individual particles. Mesityl oxide was used as an EOF marker; however, octanophenone was not included to mark the micelle migration time to avoid any potential overlap between this peak and the dimer peak. Again, initial data were promising. Both panels of Figure 6-18 shows

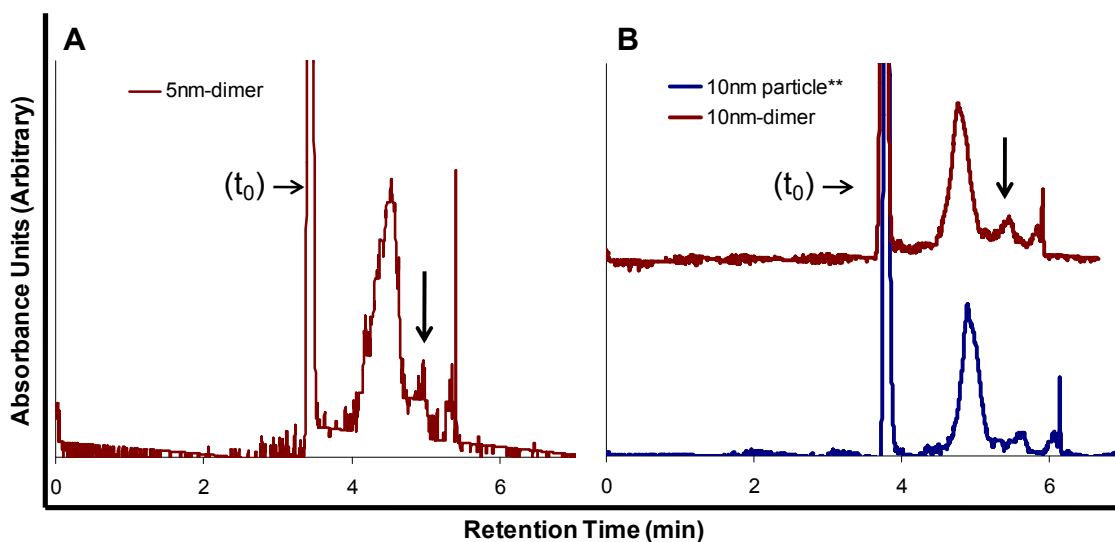


Figure 6-18 (A). Capillary electropherogram of solution containing 5nm particles and dimers
(B) electropherograms of solutions containing 10nm particles and dimers

Linker for dimers contained seven phenyl rings

10 mM CAPS, 70 mM SDS, pH =9.8, 18 kV, $\lambda_{det} = 214 \text{ nm}^{***}$

** particle solution containing additional sodium citrate and organic solvent

*** The detector was broken and would not reach a wavelength greater than 214 nm; however, particles absorb in this range and this should not have affected separation

electropherograms, which appear to have a second small peak following the particle peak (marked with arrows) which could be attributed to dimers in solution. However, this same peak was observed for the 10 nm particle solution containing no dimers.

In attempt to rule out decomposition of the sample solution, this experiment was performed again with freshly made samples and buffer. These results are shown in Figure 6-19 and again do not confirm the presence of dimers in these solutions. A second peak was observed in the electropherogram associated with the dimer solution containing 5 nm particles. However, an overlay of an electropherogram containing octanophenone to mark t_{mc} indicates that this peak overlaps that of the micelle marker. It could therefore be attributed to any organics (e.g. excess linker molecule) that traveled the capillary within the SDS micelles. It is noted that a small peak at the same retention time was observed for the sample containing only particles. There were no obvious peaks associated with dimers or trimers in Figure 6-19(B) showing electropherograms of solutions containing 10 nm particles. However, it was noted that there were small peaks in all electropherograms corresponding to t_{mc} . Despite the fact that initial data were promising, successful separations of dimers and trimers from individual particles were not achieved using capillary electrophoresis.

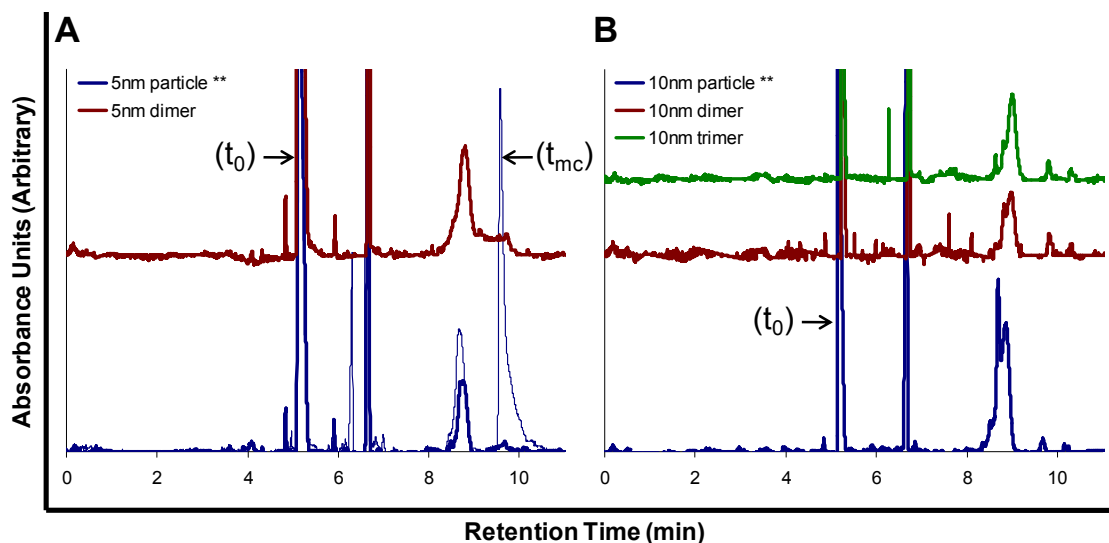


Figure 6-19 (A). Capillary electropherograms of solutions containing 5 nm particles and dimers (B) electropherograms of solution containing 10 nm particles, dimers and trimers linker for dimers contained seven phenyl rings; linker for trimers contained seven phenyl rings

10 mM CAPS, 70 mM SDS, pH =9.6, 18 kV, $\lambda_{det} = 214 \text{ nm}^{*}$**

**** particle solution containing additional sodium citrate and organic solvent**

***** The detector was broken and would not reach a wavelength greater than 214 nm; however, particles absorb in this range and this should not have affected separation**

After this chapter was written, Ivanov et al.⁶⁵ published a paper, which discussed the stability of gold nanoparticles in capillary electrophoresis. The authors claimed that stability is dependent upon surface functionalization. With an applied voltage of 20 kV, the concentration at which aggregation was observed for gold particles capped with 6-mercaptohexanoic acid in a tetraborate buffer was 1.8 nM while concentrations of 2.3 nM were required to aggregate particles coated with 6-aminohexanethiol. The authors also claimed that citrate particles are unstable inside a capillary; however, the references that they cited described the adsorption of negatively-charged particles onto a positively-charged capillary.^{66,67} Regardless,

Bucking et al.³ reported that citrate-ligated particles were not suitable for capillary electrophoresis because the citrate-ligand desorbed from the particles too easily (Section 6.2.2, page 95). In this work, both BSPP and SDS likely increased the stability of particles within the capillary. However, the sample concentrations used here ranged from 1.5 to 1320 nM (Table 6-7 and Table 6-8) and were significantly higher than the aggregation concentrations cited by Ivanov et al.⁶⁵ It is therefore likely that aggregation phenomena could have been present and contributed to the irreproducible data. However, because of the small sample volumes associated with CE (< 1 μ L),⁶² particles could not be detected at concentrations much lower than those used in these experiments. Thus, it appears that any future, successful CE experiment would have to employ a narrow range of concentration (e.g. 1-2 nM).

6.2.5. Capillary Electrophoresis of Platinum Particles

As with homodimer separation, heterodimer separation was never definitively achieved using capillary electrophoresis. However, platinum particles with two different capping ligands were injected into the capillary under the conditions listed in Figure 6-14. The retention times are listed in Table 6-8 and compared to retention the retention times observed for gold particles of similar size. Because there was negligible separation for gold particles less than 10 nm, the retention times were predicted to be the same for both particles. The retention times were not expected to be comparable to those observed for gold, because the effective charge on the

capping ligands was most likely different. The fact that the retention times for platinum were greater than those expected for gold of the same size indicated that these particles exhibited greater (negative) mobilities than those observed for gold and therefore likely exhibited greater charges.

Table 6-4. Retention times of platinum particles obtained using capillary electrophoresis

Capping Ligand	Approximate Particle Size (nm)	Retention Time (min)	Predicted Retention Time for Gold Particles of the Same Size (min)
Tiopronin	2	3.2	2.8
Mercaptobenzoic Acid	6	3.5	2.8

Based on these retention times, it was determined that heterodimer separation using capillary electrophoresis could exhibit greater resolution than homodimer separations. As described in more detail earlier in this chapter, the larger structures associated with dimers were expected to yield greater retention times. In addition, binding gold particles to platinum particles which exhibit greater mobilities and longer retention times would theoretically increase the separation between the isolated gold particles and the heterodimeric structures. As discussed in Chapter 5, these two effects were competing in size-exclusion chromatography (SEC) while in CE they are additive. Such studies of gold-platinum heterodimer structures, however, were not attempted.

6.2.6. Continuous Free-Flow Electrophoresis of Particles and Assemblies – General Considerations

Continuous free-flow electrophoresis (CFFE) is a two-dimensional technique, in which particles are separated by an electrophoretic mechanism while continuous solvent flow facilitates the collection of separated material in multiple fractions.^{2,68}

Figure 6-20 is a schematic of the instrument set-up which shows buffer being pumped in a direction perpendicular to the applied field.

McCann et al.⁶⁸

reported the separation of latex particles according to continuous electrophoresis.

Most of their separations showed increasing migration distances with particles size.

However, as the

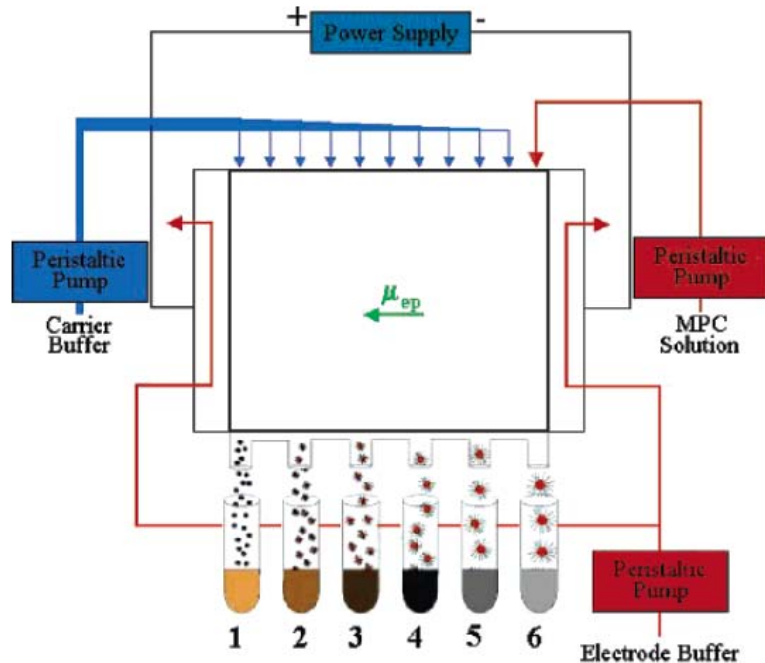


Figure 6-20. Schematic of Continuous Free-Flow Electrophoresis Apparatus
Figure taken from Peterson et al.¹

ionic strength was decreased and k_a values were reduced to the range of 2-5, the order of mobility was reversed in accordance with the relaxation effect described by Wiersema and O'Brien.^{1,5}

More recently, Peterson et al. reported the separation of tiopronin-capped gold particles in 50 mM phosphate buffer.² Under these conditions, smaller particles exhibited greater mobility indicating that the relaxation effect was not significant. Increasing the pH from 7.0 to 8.7 increased the deprotonation of the terminal carboxylic acid on the tiopronin capping ligand and thus the charge on the particles resulting in increased mobilities and better separations.

In CFFE, Joule heating can cause problems other than simple band broadening due to a radial temperature profile. Temperature gradients can create eddies and non-uniform flow throughout the chamber, which can negatively affect separations. For this reason, the ionic strength of these buffer solutions must be kept low despite the fact that capillary experiments have indicated that size-dependent resolutions are greater at higher ionic strengths. While SDS concentrations of 70 mM exhibited greater mobility differences, as shown in Figure 6-7, concentrations of less than 10 mM were required for CFFE separations to keep the current below 250 mA. At these ionic strengths, it was predicted that relaxation effects would not be significant and smaller particles would exhibit greater mobilities than larger ones. Likewise, isolated particles would exhibit greater mobilities than larger assemblies.

6.2.7. Continuous Free-Flow Electrophoresis of Particles and Assemblies – Results and Discussion

Before attempts were made to separate particle assemblies with CFFE, individual particles were injected to examine their mobility in the chamber and optimize conditions. Particles with a diameter of 5 nm were chosen as they are initially more concentrated than the larger sizes, which was desirable for collecting fractions. As with the previous electrophoretic separations, particles underwent ligand-exchange with BSPP and were concentrated using a centrifugation filter. Figure 6-21 shows a photograph of the 5 nm particles migrating through the chamber.

The fractions collected after the CFFE separation of 5nm particles were characterized by UV-VIS spectroscopy. The resulting spectra are shown in Figure 6-23. The fraction number corresponding to a particle that travels straight through the chamber with no

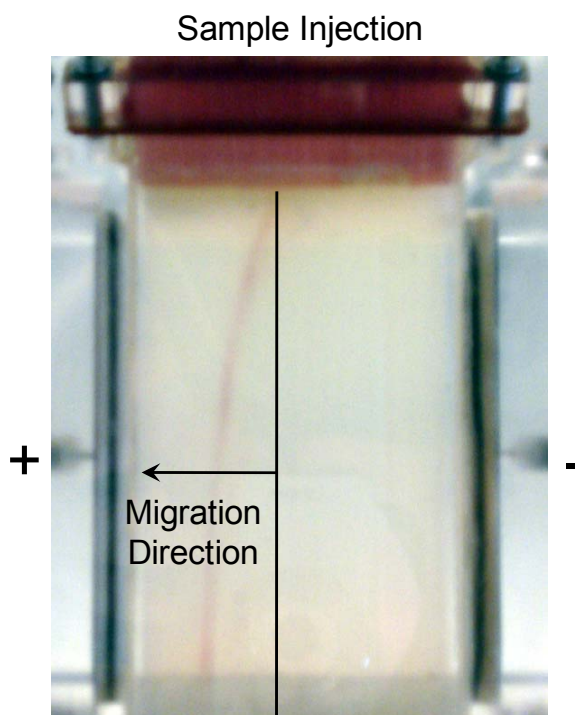


Figure 6-21. Photograph taken of 5nm particles in the CFFE chamber

migration is zero. Fraction numbers increase from there in the direction of migration. The characteristic absorbance associated with gold particles was observed in fractions 11-18 with the highest concentration of particles observed in fraction 12. The peak blue shifted with increasing fraction number, indicating that, as predicted, smaller particles exhibited greater mobilities.⁶⁹

CFFE was then applied to the separation of nanoparticle dimers from the isolated particles. As the particle assemblies were synthesized in the presence of 3 mM sodium citrate and 2:3 THF:ethanol solution according to the protocol in Chapter 4, particles with these additives were run for comparison to the particle assemblies. These particles traveled further than the previous sample, with the highest concentration of particles collected in fraction 19. It is unclear whether this difference was due to the additives in the particle solution or slight differences in the properties of the buffer solution, which are listed in Table 6-9.

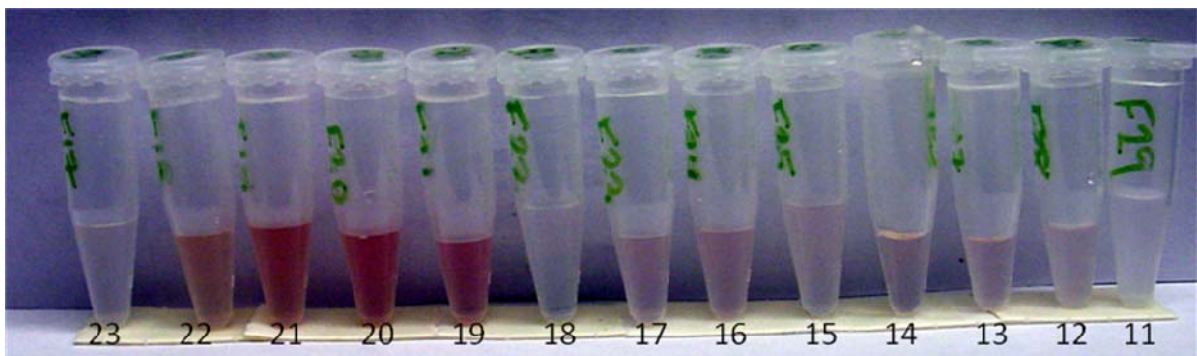


Figure 6-22. Concentrated fractions collected after the CFFE separation of particle solution containing dimers of 5 nm particles

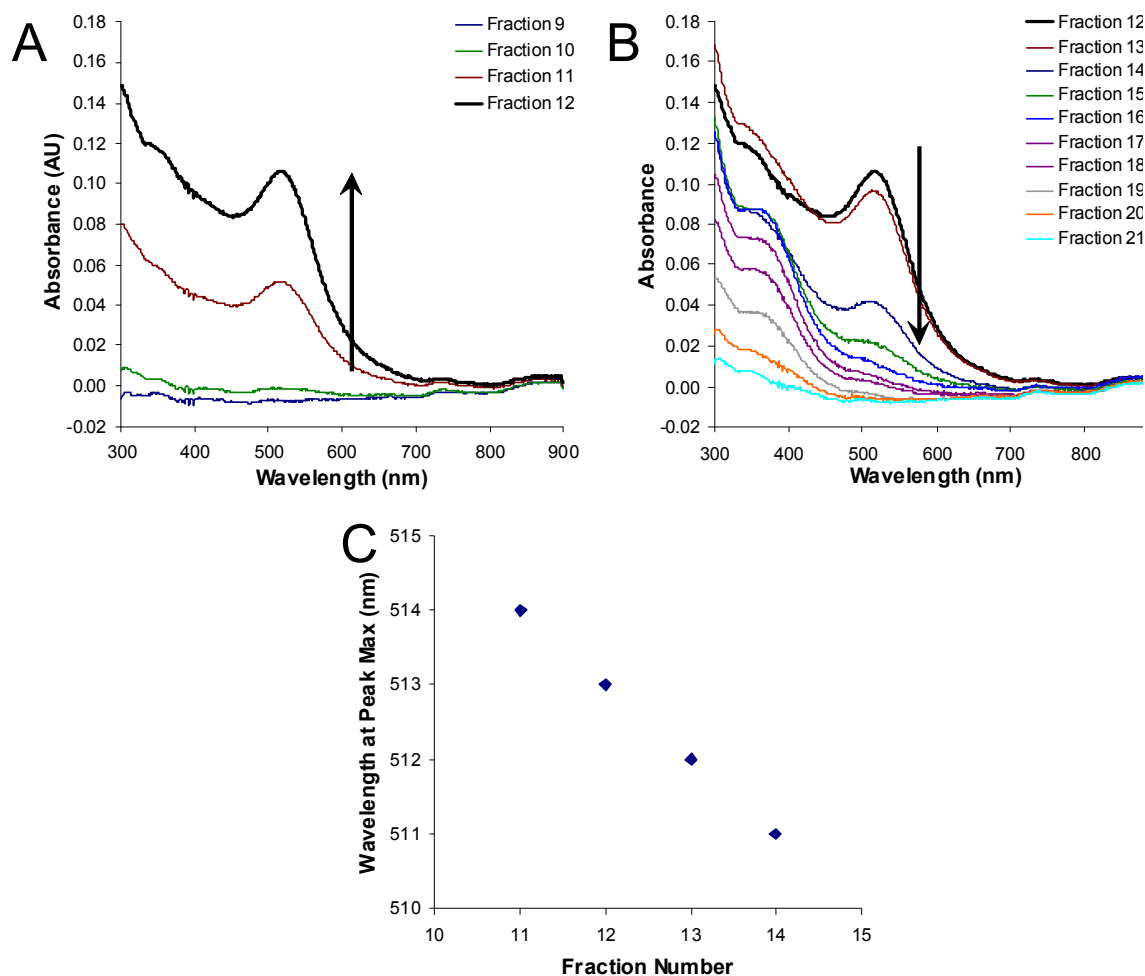


Figure 6-23. UV-VIS spectra of fraction collected after CFFE separation of 5 nm gold particles (A) Intensity increases for fractions 9-12 (B) Intensity decreases for fraction 12-21 (C) Plot of the peak maximum versus fraction number

For the separation of the solution containing dimers, the SDS concentration was reduced to the critical micellar concentration, 8.1 mM,^{17,23,25} because currents greater than 250 mA were observed. Lowering the SDS concentration reduced the current to 134 mA. In these separations, it was predicted that there would be a fork

in the particle flow profile as the sample traversed through the chamber. (Figure 6-21). This, however, was not detected. After separation, color was observed in fractions 19-22. It wasn't until samples were concentrated by centrifugation filtration that color was observed in some of the lower-numbered fractions as shown in Figure 6-22. Very faint color was observed in fractions 12-17. The UV-VIS spectra of the concentrated fractions are shown in Figure 6-24. While the absorbance was low, absorption peaks corresponding to gold particles were observed in fractions 12, 14, 16 and 17. These peaks are broad, but it appears that these peaks are slightly red-

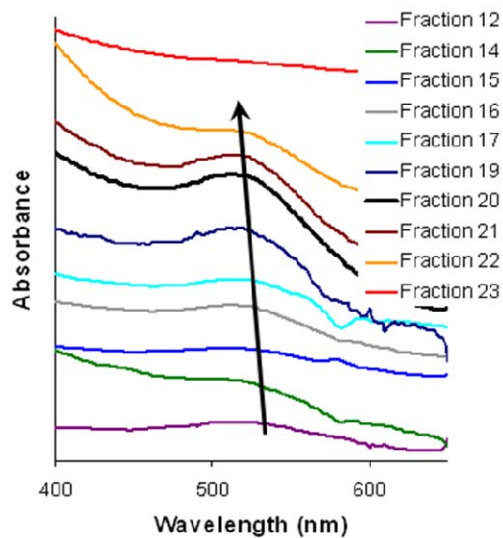


Figure 6-24. UV-VIS spectra of concentrated fractions collected after the CFFE separation of particle solution containing 5nm dimers
Spectra were offset along the y-axis for clarity.

shifted compared to fractions 19-22 associated with isolated particles. It has been documented that gold particles bound together in dimers exhibit slight red-shifts compared to isolated particles.⁷⁰

The collected fractions were then analyzed by TEM. While they did not show complete isolation of dimers from the individual particles, higher

concentrations of dimers were observed in lower-numbered fractions, which correspond to assemblies that exhibit decreased mobility. Sample images are shown in Figure 6-25 and statistics are reported in Table 6-5 and Table 6-6. Based on visual observations and UV-VIS spectra, it appeared that there were no particles present in fraction 18. It was, therefore, predicted that there would be a sharp transition between the concentration of dimers observed in fraction 17 compared to fraction 19. However, Table 6-6 shows a similar concentration was observed between fractions 16 and 20.

These data suggest that the separation of dimers from isolated particles by CFFE is possible; however, conditions need to be optimized to improve separation efficiency so that dimers are completely isolated from the individual particles. While it is not possible to increase the SDS concentration as this results in high currents and non-uniform flow through the chamber, Figure 6-7 suggests that while mobilities were lower, particle separation might be greater at lower SDS concentrations. The main reason for including SDS in the buffer for CE experiments is to prevent particle aggregation and adsorption on the capillary wall. As the particle solutions are extremely diluted in CFFE experiments and not subject to high pressures or capillary walls, separations were also attempted in the absence of SDS. In these experiments there were additional difficulties. The samples appeared extremely dilute. This was attributed to the presence of organic solvent in the particle solution,

which is less dense than water and thus has the tendency to float to the top of the

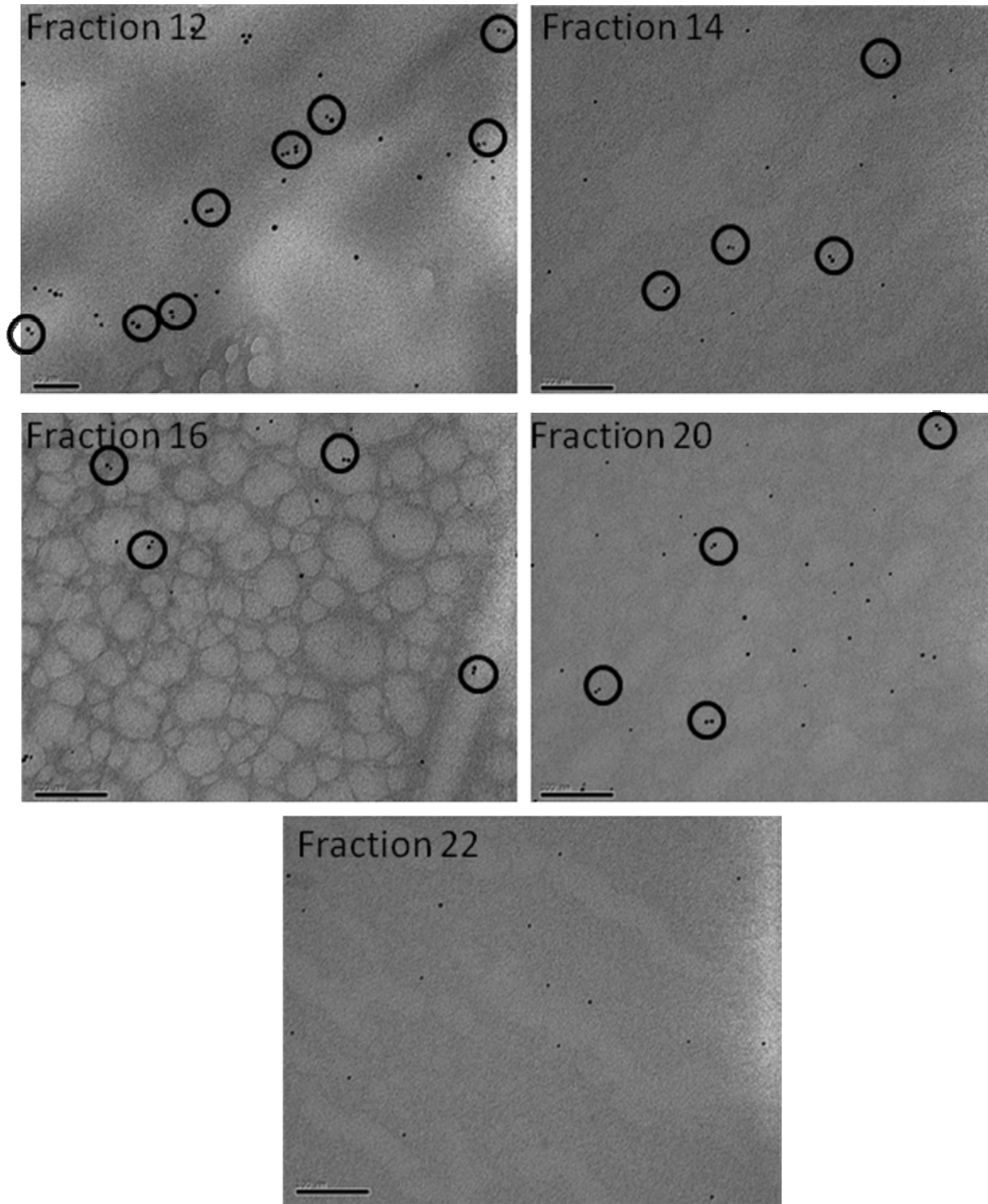


Figure 6-25. Sample TEM images of fractions collected after CFFE separation of particle solution containing dimers of 5 nm gold particles

Table 6-5. Statistics for particle solutions containing dimers determined by TEM before CFFE separation

	Total # counted	# isolated	# in dimers	# in trimers
Without Linker	467	413 (88%)	42 (9%)	12 (3%)
With Linker	446	301 (67%)	136 (30%)	9 (2%)

Table 6-6. Statistics for fractions collected after CFFE of gold dimers

Fraction #	# counted	# isolated	# in dimers	# in trimers
22	80	76 (95%)	4 (5%)	NA
21	99	77 (78%)	22 (22%)	NA
20	124	102 (82%)	22 (18%)	NA
16	68	56 (82%)	12 (18%)	NA
15	163	84 (52%)	52 (32%)	27 (16%)
14	129	81 (63%)	42 (33%)	6 (4%)
13	117	77 (66%)	34 (29%)	6 (5%)
12	157	80 (51%)	74 (47%)	3 (3%)

chamber. Samples were dialyzed in attempt to remove the organic solvent; however, this did not improve the separation.

Conclusions

Three electrophoretic techniques were evaluated for their ability to separate nanoparticle assemblies from isolated particles in solution.

Gel electrophoresis proved effective in separating gold particles of different sizes.

The separation was determined by the sieving mechanism of the gel, and smaller

particles exhibited greater mobility. The separation of nanoparticle assemblies from individual particles was unsuccessful, however. Solutions containing dimers of 5 nm and 10 nm particles exhibited wider bands than those associated with the isolated particles, but the gel did not exhibit sufficient resolution to discriminate between the different species. Larger particles exhibited irreversible adsorption to the gel even in the absence of the linker molecule. This was attributed to particle instability associated with the presence of sodium citrate and organic solvent in the sample solution.

Capillary electrophoresis also proved effective in separating gold particles of different sizes. The separation mechanism was due to differences in electrophoretic mobility with larger particles exhibiting greater mobilities due to relaxation effects. Particles exhibited greater mobilities in CAPS buffer than in phosphate buffer. This could be attributed to the higher pH, but it is also possible that particle interactions with the buffer played a role. The observed particle separation was greater in phosphate buffer. There were several factors that could have contributed to this including the lower rate of EOF at lower pH and the higher ionic strength of this buffer which increases the extent of relaxation effects. While separation was greater for particles in phosphate buffer, the peaks were also significantly broader.

While the data collected for the separation of dimers and trimers using capillary electrophoresis initially appeared promising, it was not reproducible and there were

some inconsistencies in these data. It was determined that the additional peaks observed for solutions containing dimers could not be conclusively attributed to the presence of dimers in solution. As these peaks coincide with t_{mc} , they could be due to additional organics present in solution that traversed the capillary within the micelles.

In addition the particle stability provided by SDS in the mobile phase, actions were taken to stabilize the gold-citrate particle samples against aggregation. Bucking et al.³ reported that citrate-ligated particles were not suitable for capillary electrophoresis because the citrate-ligand desorbed from the particles too easily, and the nanoparticle solutions degraded. More recently, Ivanov et al.⁶⁵ reported aggregation of gold particles at concentrations as low as 1.8 nM. While both BSPP and SDS likely increased the stability of particles within the capillary, aggregation phenomena may still have been present. However, because of the small sample volumes associated with CE (< 1 μ L),⁶² particles were not detected at concentrations much lower than those used in these experiments.

According to UV-VIS measurements, continuous free-flow electrophoresis appears to have separated a sample of 5 nm particles according to small size differences, with smaller particles exhibiting greater mobilities. Buffers with higher ionic strengths could not be used with this technique as Joule heating, which occurs at higher currents creates temperature gradients in the chamber which create eddies

and non-uniform flow. Preliminary experiments indicate that the separation of dimers from isolated particles is possible although further optimization is required.

6.3. Experimental

6.3.1. Sample Preparation.

Gold-citrate particles were obtained from Ted Pella, Inc. as aqueous solutions with trace amounts of citrate, tannic acid and potassium carbonate, and Bis(p-sulfonatophenyl)phenyl phosphine (BSPP) was obtained from Strem Chemicals, Inc.

For particle separations, six different samples were prepared from 5 nm, 10 nm, 15 nm, 20 nm, 30 nm and 60 nm particles, respectively. They were subject to ligand-exchange with BSPP according to a documented procedure.⁶¹ Approximately 1 mg BSPP was added per mL of nanoparticle solution, and then solutions were

Table 6-7. Concentrations of gold particles used in separations

Particle Size (nm)	Initial concentration (nM)*	Final concentration for gel experiments (nM)**	Final concentration for capillary experiments (nM)**	Final concentration for CFFE experiments (nM)
5	83.0	138.3	830	300
10	9.46	15.77	95	NA
15	2.32	3.87	23	NA
20	1.16	1.93	12	NA
30	0.33	0.55	3.3	NA
40	0.15	NA	1.5	NA
60	0.04	0.07	NA	NA

*as received from Ted Pella, Inc.

** approximate after concentration with centrifugation filter

stirred at room temperature for 3 hours. The solutions were then concentrated using a Millipore centrifugation filter (regenerated cellulose, MWCO 10,000). The initial and final concentrations for each particle size are listed in Table 6-7.

Gold dimer and trimer samples were prepared according to documented procedure.^{70,71} A 2 mL aliquot of gold particles solution as received from Ted Pella, Inc. was diluted with 2.5 mL 3 mM sodium citrate solution. The pH of this solution (~8) was sufficient for deprotection of the thioacetate functionality on the linker molecule. A stoichiometric amount of linker from a 1 μ M linker solution was diluted to 500 μ L with a 2:3 THF/ethanol solution and added to the gold particles in 50 μ L aliquots over a period of several minutes. The solutions were then allowed to stir overnight. Attempts at scaling up these reactions were unsuccessful. When larger volumes were desired, several small scale reactions were performed and the resulting solutions combined. After dimer/trimerization, particle solutions were subject to ligand-exchange with BSPP as described above. It has been reported

Table 6-8. Concentrations of gold particles in solutions containing dimers and trimers

Particle Size (nm)	Initial concentration (nM)*	Concentration after linker addition (nM)**	Final concentration for gel experiments (nM)**	Final concentration for capillary experiments (nM)**	Final concentration for CFFE experiments (nM)
5	83.0	33.2	1660	1320	200
10	9.46	3.8	190	150	NA
15	2.32	0.9	45	36	NA

*as received from Ted Pella, Inc.

**particles are diluted due to the addition of 3 mM sodium citrate and the linker solution

*** approximate after concentration with centrifugation filter

that BSPP displaces the citrate ion adsorbed to gold particles, but not the thiol-terminated linker molecule.⁶¹ These solutions were then concentrated using a centrifugation filter. The concentrations of particles in solution both before and after concentration are listed in Table 6-8

6.3.2. Gel Electrophoresis

10X Tris-borate-EDTA (TBE) was obtained from Sigma-Aldrich and diluted to a 1X concentration. 2% agarose gels were prepared by adding 0.8 g agarose to 40mL 1 x (TBE) buffer (89mM tris-borate, and 2mM EDTA). Most reports of gel electrophoresis involving nanoparticles utilize an agarose gel instead of the polyacrylamide gels typically used for protein-separations because of their larger pore sizes, typically > 50 nm compared to 3-5 nm.^{57,58} The solution was brought to a boil in a conventional microwave oven and then cooled to room temperature in a horizontal gel plate. The gel was then immersed in 1 x TBE buffer before samples were loaded. Samples consisted of 10 μ L concentrated particle solutions as described above and 4 μ L glycerol. A voltage of 100 Volts was applied for approximately 45-50 min at which point separations were observed visually.

6.3.3. Capillary Electrophoresis

N-cyclohexyl-3-aminopropanesulfonic acid (CAPS) buffer (99% biochemistry grade) was purchased from ACROS Organics. Monosodium and disodium phosphate were

purchased from Sigma-Aldrich (Cell Culture grade), and sodium dodecyl sulfate was purchased from MP Biomedicals (Ultra Pure). All water used for buffer solutions was obtained from a Milli-Q50 Ultrapure Water System

CE separations were performed using a homemade system consisting of a Spellman SL30 power source and a Vestec UV detector set to 254 nm. The temperature was regulated using a temperature-controlled water bath, which was set to 25 °C. A fused silica capillary with a polyimide exterior coating and a 50 µm inner diameter was obtained from Polymicro Technologies. The capillary was cut to 65 cm with a detection window 15 cm from the capillary end. The capillary was pre-treated each day experiments were done by flushing sequentially with water (10 min), methanol (10 min), water (10 min), 0.1N NaOH (20min), water (10min) and buffer (10 min). In addition, it was flushed with buffer for 5 minutes in between each run.

All buffers were filtered through at 0.2 µm filter prior to use. CAPS buffers were prepared at 10 mM, and the pH was adjusted by adding 150 µL, 250 µL, 400 µL and 1000 µL of 0.1 N NaOH solution to 20 mL buffer solution to achieve pH values of 9.5, 9.7, 10.2 and 10.7, respectively. Phosphate buffers were prepared at two pH values. A pH of 7.3 was measured for a solution containing 4.9 mM NaH₂PO₄ and 10.9 mM Na₂HPO₄, and a pH of 8.0 was measured for a solution containing 1.2 mM NaH₂PO₄ and 16.9 mM Na₂HPO₄. pH values were measured using a VWR

sympHony pH meter. SDS (70 mM) was added to buffer solutions after pH values were measured.

An applied voltage of 18 kV was use for most separations; although the voltage dependence was tested at 22 kV and 25 kV. The current was approximately and 12-15 μ A for CAPS buffers and 25-30 μ A for phosphate buffers. The times for each gravity injection varied depending on the sample concentration. Injection times for 5 nm, 10 nm, 15 nm and 20 nm particles were 15 sec, 25 sec, 40 sec and 50 sec, respectively.

6.3.4. Continuous Free-Flow Electrophoresis

These experiments were a collaborative effort with Dave Cliffl's group at Vanderbilt University. After synthesis, samples were shipped to Brian Hixon (Cliffl's grad student). Brian performed the separations and then shipped them back to NCSU for TEM analysis. The experimental set-up was similar to that reported in their previous paper.² The buffer conditions are listed in Table 6-9, the applied voltage was 200 V,

Table 6-9. Buffer conditions for CFFE separations

Sample	Buffer Composition	Buffer pH	Buffer Conductivity	Current through Chamber
5nm particles	8 mM Tris-borate 10mM SDS	8.33	745 uS/cm	136 mA
5nm particles with 3mM sodium citrate and 2:3 THF:EtOH	8 mM Tris-borate 10mM SDS	8.50	725 uS/cm	184 mA
5nm dimers	8 mM Tris-borate 8.3mM SDS	8.39	679 uS/cm	134 mA

and the buffer flow rate was ~ 8 mL/min.

The separated fractions were collected in test tubes and then shipped back to NCSU. At this point, they were concentrated using a Millipore centrifugation filter (regenerated cellulose, MWCO 10,000) to a volume of approximately 500 μ L (from approx. 5 mL) before analysis by UV-VIS and TEM.

Absorbance measurements were made using a Hewlett-Packard 8452A Diode Array Spectrometer, and a path length of 1.0 cm. TEM images were taken with a Philips CM12 TEM operated at 100 kV. Images were captured using a Gatan 780 camera and captured with Digital Micrograph software.

6.4. References

- (1) O'Brien, R. W.; White, L. R., *J. Chem. Soc.: Faraday Trans.* **1978**, *74*, 1607-1626.
- (2) Peterson, R. R.; Cliffler, D. E., *Anal. Chem.* **2005**, *77*, 4348-4353.
- (3) Bucking, W.; Nann, T., *Lee Proceedings-Nanobiotechnology* **2006**, *153*, 47-53.
- (4) Liu, F. K.; Wei, G. T., *Anal. Chim. Acta* **2004**, *510*, 77-83.
- (5) Wiersema, P. H.; Loeb, A. L.; Overbeek, J. T., *J. Colloid Interface. Sci.* **1966**, *22*, 78-&.
- (6) Heimenz, P. C.; Rajagopalan, R. In *Principles of Colloid and Surface Chemistry*; Marcel Dekker, Inc.: New York, 1997, pp 534-571.
- (7) Quang, C.; Petersen, S. L.; Ducatte, G. R.; Ballou, N. E., *J. Chromatogr. A* **1996**, *732*, 377-384.

- (8) Skoog, D. A.; Holler, J. F.; Nieman, T. A. *Principles of Instrumental Analysis*; 5 ed.; Hartcourt Brace College Publishers: Philadelphia, 1998.
- (9) Righetti, P. G., *J. Chromatogr. A* **2005**, 1079, 24-40.
- (10) Chiou, S. H.; Wu, S. H., *Anal. Chim. Acta* **1999**, 383, 47-60.
- (11) Serwer, P.; Griess, G. A., *J. Chromotogr. B* **1999**, 722, 179-190.
- (12) Barany, M.; Barany, K.; Giometti, C. S., *Anal. Chim. Acta* **1998**, 372, 33-66.
- (13) Li, S. F. Y. *Capillary Electrophoresis - Principles, Practice and Applications*; Elsevier: New York, 1992; Vol. 52.
- (14) Schnabel, U.; Fischer, C. H.; Kenndler, E., *J. Microcolumn Sep.* **1997**, 9, 529-534.
- (15) Liu, F. K.; Lin, Y. Y.; Wu, C. H., *Anal. Chim. Acta* **2005**, 528, 249-254.
- (16) Vanifatova, N. G.; Spivakov, B. Y.; Mattusch, J.; Wennrich, R., *Talanta* **2003**, 59, 345-353.
- (17) Foret, F.; Krivankova, L.; Bocek, P. *Capillary Zone Electrophoresis*; Weinham: New York, 1993.
- (18) Petersen, S. L.; Ballou, N. E., *Anal. Chem.* **1992**, 64, 1676-1681.
- (19) Jorgenson, J. W., *Anal. Chem.* **1986**, 58, A743-&.
- (20) Hwang, W. M.; Lee, C. Y.; Boo, D. W.; Choi, J. G., *Bull. Korean Chem. Soc.* **2003**, 24, 684-686.
- (21) Liu, Y.; Joseph C, F.; Bledsoe, J. M.; Henry, C. S., *Anal. Chem.* **2000**, 72, 5939-5944.
- (22) Jorgenson, J. W.; Lukacs, K. D., *Anal. Chem.* **1981**, 53, 1298-1302.
- (23) Kuhn, R.; Hoffstetter-Kuhn, S. *Capillary Electrophoresis: Principles and Practice*; Springer-Verlag: Berlin, 1993.
- (24) Watzig, H.; Degenhardt, M.; Kunkel, A., *Electrophoresis* **1998**, 19, 2695-2752.

- (25) Nielsen, K. R.; Foley, J. P. In *Capillary Electrophoresis Theory and Practice*; Camilleri, P., Ed.; CRC Press: Boca Raton, Florida, 1998, pp 135-182.
- (26) Nichols, S. C.; Loewenberg, M.; Davis, R. H., *J. Colloid Interface. Sci.* **1995**, *176*, 342-351.
- (27) Ohshima, H.; Healy, T. W.; White, L. R.; O'Brien, R. W., *J. Chem. Soc.: Faraday Trans.* **1984**, *80*, 1299-1317.
- (28) Loewenberg, M.; Davis, R. H., *J. Fluid Mech.* **1995**, *288*, 103-122.
- (29) Zeng, S. L.; Zinchenko, A. Z.; Davis, R. H., *J. Colloid Interface. Sci.* **1999**, *209*, 282-301.
- (30) Swaminathan, T. N.; Hu, H. H., *J. Colloid Interface. Sci.* **2004**, *273*, 324-330.
- (31) Tu, H. J.; Keh, H. J., *J. Colloid Interface. Sci.* **2000**, *231*, 265-282.
- (32) Wang, H.; Zeng, S. L.; Loewenberg, M.; Davis, R. H., *J. Colloid Interface. Sci.* **1997**, *187*, 213-220.
- (33) Stigter, D.; Mysels, K. J., *J. Phys. Chem.* **1955**, *59*, 45-51.
- (34) Shaw, J. N.; Ottewill, R. H., *Nature* **1965**, *208*, 681-&.
- (35) Radko, S. P.; Chrambach, A., *J. Chromatogr. B* **1999**, *722*, 1-10.
- (36) Vanifatova, N. G.; Spivakov, B. Y.; Mattusch, J.; Wennrich, R., *J. Chromatogr. A* **2000**, *898*, 257-263.
- (37) Vanorman, B. B.; McIntire, G. L., *J. Microcolumn Sep.* **1989**, *1*, 289-293.
- (38) Liu, F. K., *J. Chromatogr. A* **2007**, *1167*, 231-235.
- (39) Liu, F. K.; Tsai, M. H.; Hsu, Y. C.; Chu, T. C., *J. Chromatogr. A* **2006**, *1133*, 340-346.
- (40) Burgess, I.; Jeffrey, C. A.; Cai, X.; Szymanski, G.; Galus, Z.; Lipkowski, J., *Langmuir* **1999**, *15*, 2607-2616.
- (41) Liu, F. K.; Wei, G. T., *Chromatographia* **2004**, *59*, 115-119.

- (42) Wei, G. T.; Liu, F. K., *J. Chromatogr. A* **1999**, 836, 253-260.
- (43) Wei, G. T.; Liu, F. K.; Wang, C. R. C., *Anal. Chem.* **1999**, 71, 2085-2091.
- (44) Fischer, C. H.; Kenndler, E., *J. Chromatogr. A* **1997**, 773, 179-187.
- (45) Jones, H. K.; Ballou, N. E., *Anal. Chem.* **1990**, 62, 2484-2490.
- (46) Ducatte, G. R.; Ballou, N. E.; Quang, C. Y.; Petersen, S. L., *J. Microcolumn Sep.* **1996**, 8, 403-412.
- (47) Su, C. H.; Wu, P. L.; Yeh, C. S., *Bull. Chem. Soc. Jpn.* **2004**, 77, 189-193.
- (48) Allison, S. A.; Xin, Y.; Pei, H. X., *J. Colloid Interface Sci.* **2007**, 313, 328-337.
- (49) Stastna, M.; Radko, S. P.; Chrambach, A., *Electrophoresis* **2001**, 22, 66-70.
- (50) Qin, W. J.; Yung, L. Y. L., *Langmuir* **2005**, 21, 11330-11334.
- (51) Lou, X. H.; Wang, C. Y.; He, L., *Biomacromolecules* **2007**, 8, 1385-1390.
- (52) Parak, W. J.; Pellegrino, T.; Micheel, C. M.; Gerion, D.; Williams, S. C.; Alivisatos, A. P., *Nano Lett.* **2003**, 3, 33-36.
- (53) Sperling, R. A.; Pellegrino, T.; Li, J. K.; Chang, W. H.; Parak, W. J., *Adv. Funct. Mater.* **2006**, 16, 943-948.
- (54) Liu, Y. L.; Shipton, M. K.; Ryan, J.; Kaufman, E. D.; Franzen, S.; Feldheim, D. L., *Anal. Chem.* **2007**, 79, 2221-2229.
- (55) Gerion, D.; Pinaud, F.; Williams, S. C.; Parak, W. J.; Zanchet, D.; Weiss, S.; Alivisatos, A. P., *J. Phys. Chem. B* **2001**, 105, 8861-8871.
- (56) Zanchet, D.; Micheel, C. M.; Parak, W. J.; Gerion, D.; Alivisatos, A. P., *Nano Lett.* **2001**, 1, 32-35.
- (57) Zanchet, D.; Micheel, C. M.; Parak, W. J.; Gerion, D.; Williams, S. C.; Alivisatos, A. P., *J. Phys. Chem. B* **2002**, 106, 11758-11763.

- (58) Xu, X. Y.; Caswell, K. K.; Tucker, E.; Kabisatpathy, S.; Brodhacker, K. L.; Scrivens, W. A., *J. Chromatogr. A* **2007**, *1167*, 35-41.
- (59) Claridge, S. A.; Goh, S. L.; Frechet, J. M. J.; Williams, S. C.; Micheel, C. M.; Alivisatos, A. P., *Chem. Mater.* **2005**, *17*, 1628-1635.
- (60) Liu, F. K.; Ko, F. H.; Huang, P. W.; Wu, C. H.; Chu, T. C., *J. Chromatogr. A* **2005**, *1062*, 139-145.
- (61) Novak, J. P.; Nickerson, C.; Franzen, S.; Feldheim, D. L., *Anal. Chem.* **2001**, *73*, 5758-5761.
- (62) Rose, D. J.; Jorgenson, J. W., *Anal. Chem.* **1988**, *60*, 642-648.
- (63) Parak, W. J.; Gerion, D.; Pellegrino, T.; Zanchet, D.; Micheel, C.; Williams, S. C.; Boudreau, R.; Le Gros, M. A.; Larabell, C. A.; Alivisatos, A. P., *Nanotechnology* **2003**, *14*, R15-R27.
- (64) Loweth, C. J.; Caldwell, W. B.; Peng, X. G.; Alivisatos, A. P.; Schultz, P. G., *Angew. Chem. Int. Ed.* **1999**, *38*, 1808-1812.
- (65) Ivanov, M. R.; Bednar, H. R.; Haes, A. J., *ACS Nano* **2009**, *3*, 386-394.
- (66) Pumera, M.; Wang, J.; Grushka, E.; Polsky, R., *Analytical Chemistry* **2001**, *73*, 5625-5628.
- (67) Neiman, B.; Grushka, E.; Lev, O., *Analytical Chemistry* **2001**, *73*, 5220-5227.
- (68) McCann, G. D.; Vanderho, J. W.; Strickle, A.; Sacks, T. I., *Sep. Purif. Methods* **1973**, *2*, 153-198.
- (69) Khlebtsov, N. G.; Bogatyrev, V. A.; Dykman, L. A.; Melnikov, A. G., *J. Colloid Interface Sci.* **1996**, *180*, 436-445.
- (70) McConnell, W. P.; Novak, J. P.; Brousseau, L. C.; Fuierer, R. R.; Tenent, R. C.; Feldheim, D. L., *J. Phys. Chem. B* **2000**, *104*, 8925-8930.
- (71) Novak, J. P.; Feldheim, D. L., *J. Am. Chem. Soc.* **2000**, *122*, 3979-3980.

7. Small Angle X-Ray Scattering

Small Angle X-Ray Scattering (SAXS) was also investigated for the characterization of nanoparticle assemblies in solution. Both the chromatographic and electrophoretic techniques discussed previously suffered from adverse interactions with a stationary phase. These techniques also involved buffered mobile phases and surfactants, which affected both the nanoparticle surface chemistry and stability. The advantage of SAXS was that nanoparticle solutions could be characterized as synthesized. The incident x-rays interacted with the bulk particle solutions, without the need for additional solution additives or external forces.

7.1. Background and Introduction

As x-rays exhibit wavelengths in the range of 0.01 to 10 nm, they are extremely useful for characterizing materials on this length scale. X-ray diffraction can be used to determine crystal structure dimensions as indicated in Figure 7-1. In this

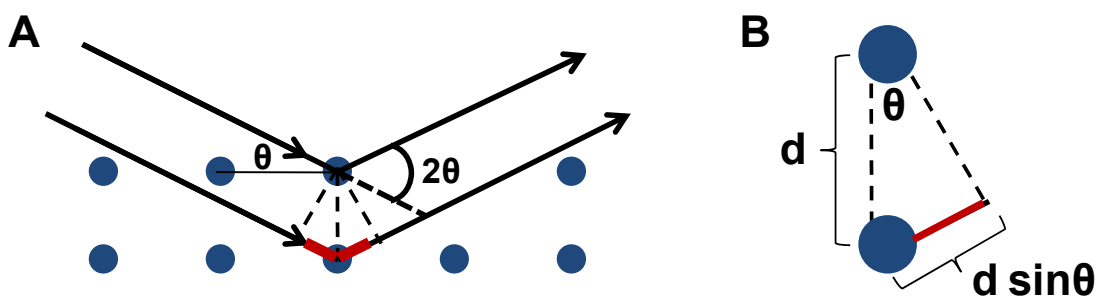


Figure 7-1. (A) Schematic of x-rays interacting with crystalline lattice (B) Higher magnification view of (A) showing the trigonometric basis for Bragg's Law

schematic, monochromatic x-rays are scattered from two atomic planes at an angle (θ) equal to the angle of incidence. Constructive interference between the two scattered rays occurs when the difference in the two path lengths is equal to an integer number of wavelengths. The trigonometric relationship in Figure 7-1(B) indicates that this path difference is also related to the lattice spacing, and is the basis for Bragg's Law (Equation 7-1).²

$$n\lambda = 2d \sin \Theta$$

n = integer
 λ = wavelength of x-rays
d = lattice spacing
 θ = scattering angle

7-1

X-ray diffraction experiments have been used to determine structural information on a sub-nanometer level. Under these conditions, the scattering angle is large enough that the detector can be placed in relatively close proximity to the sample.

As the feature sizes increase, the scattering angle becomes narrower. Small-angle x-ray scattering (SAXS) is typically used to obtain structural information for polymers, proteins and colloidal materials on length scales of approximately 5 to 25 nm.² The angular distribution of the scattered rays can provide information regarding the size, the size distributions and surface area to volume ratios of these structures. So that small scattering angles can be detected, the detectors in SAXS experiments are typically placed at larger distances from the sample as shown in Figure 7-2.

The mathematics associated with SAXS are complex and not discussed here. Experimental data is usually presented as the scattering intensity plotted as a function of the scattering vector, which is defined in Equation 7-2.

$$q = \frac{4\pi \sin \Theta}{\lambda} \quad 7-2$$

q = scattering vector

$$I(\Theta) \propto P(\Theta)S(\Theta) \quad 7-3$$

I(θ) = scattering intensity
P(θ) = shape factor or form factor
S(θ) = static structure factor

The scattering intensity is proportional to two parameters defined as the static structure factor and the shape factor (Equation 7-3).³⁻⁵ For dispersed particles, which do not interact with each other, S(θ) = 1. When particles interact with each other, the structure factor is non-unity and indicates the degree of ordering within a given solution.^{3,4} The scattering intensity can therefore indicate not only the size and shape of particles, but also the interactions between them.

There have been several reports in the literature in which interactions between nanoparticles have been observed using SAXS.³⁻⁸ For example, SAXS was used to study oligonucleotide-linked gold particles similar to those shown in Figure 4-5.⁵ These data indicated the presence of short-range order within the solution. Both small-angle and wide-angle x-ray scattering profiles have been combined to determine both the crystal structure of and interactions between cadmium selenide

nanocrystals.^{6,8} Several of these experiments required intense synchrotron x-ray sources to resolve the low scattering vectors associated with structures on the order of a few nanometers.^{5,7}

Before similar experiments were attempted to detect the presence of nanoparticle dimers and trimers in solution, Mathew A. Marcus, a collaborator at Lawrence

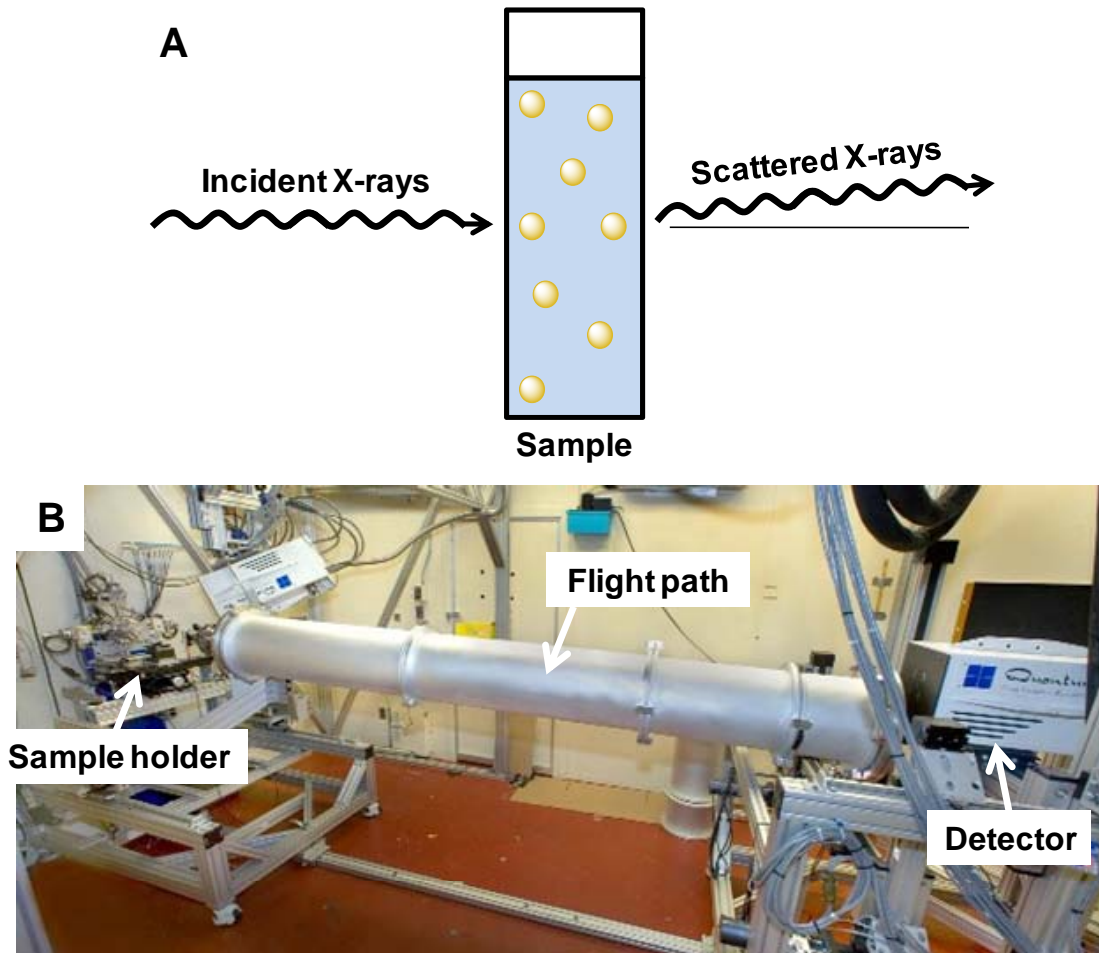


Figure 7-2. (A) Schematic of small x-ray scattering associated with a colloidal solution (B) Images of SAXS set-up at Lawrence Berkeley National Lab. The flight path was adjustable from 1.3 m to 4.3 m.

Berkeley National Lab, modeled these systems. Figure 7-3 shows calculated SAXS data for solutions containing nanoparticle dimers. These calculations indicated that nanoparticle dimers could be detected using SAXS, even at relatively low dimer concentrations.

SAXS experiments were performed in attempt to determine the relative

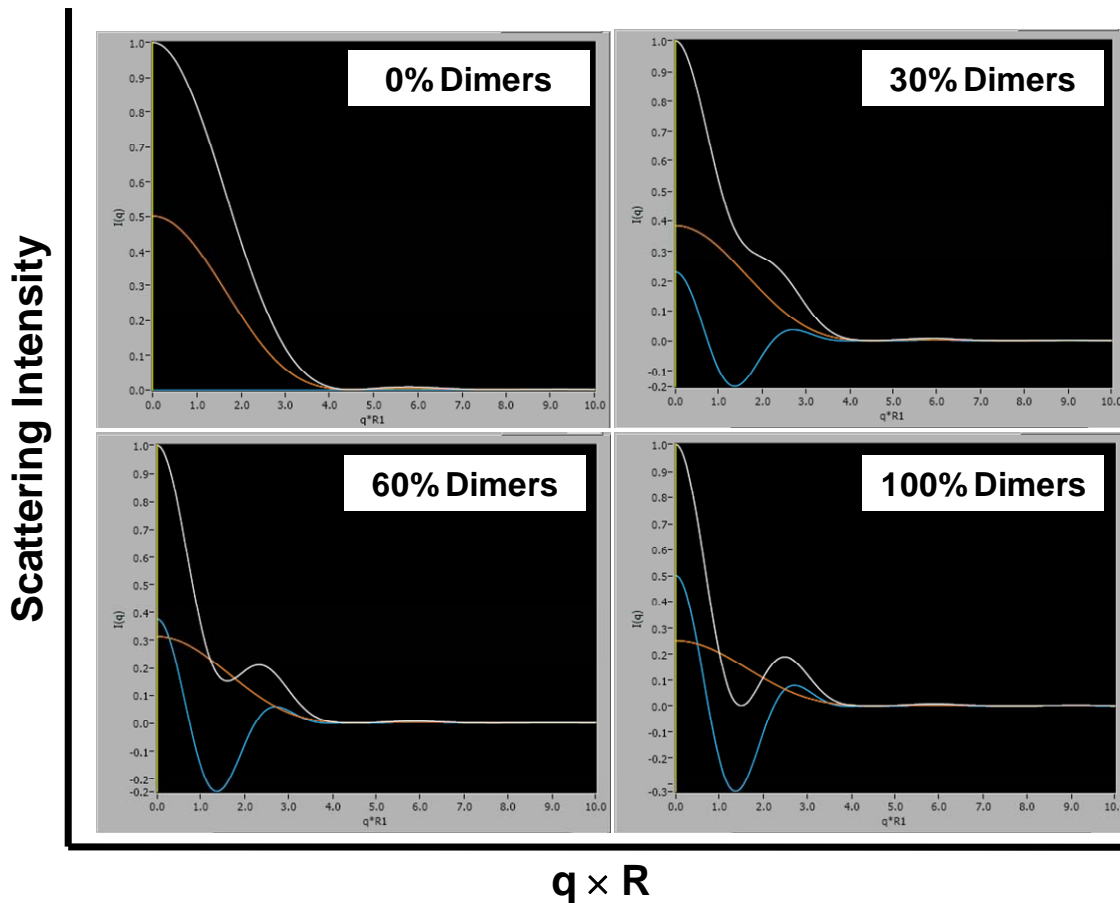


Figure 7-3. Calculated scattering intensity profiles for nanoparticle solutions containing nanoparticle homodimers (10 nm). The red line reflects the scattering intensity from half of the nanoparticles in solution, the blue line is a cross-term which reflects the structure factor and the white line is the total scattering intensity. These calculations assumed a particle polydispersity of 10% and a linker length of 0.10 nm. The LabView program which produced these data was written by Mathew A. Marcus of Lawrence Berkeley National Lab, and the details of his model are reported elsewhere.¹

concentrations of nanoparticle assemblies and isolated particles in solution.

7.2. Results and Discussion

Before nanoparticle assemblies were characterized, scattering profiles were taken for isolated particles in the presence of citrate and organic solvent as these additives have been reported to affect particle stability. Figure 7-4 shows scattering profiles obtained for citrate-capped gold particles (10 nm) in the presence of these additives. These profiles did not exhibit any changes over a period of 6 hours and a curve fit to these data yielded a particle diameter of 9.3 nm. This experiment confirmed that the additional citrate and organic solvent did not result in any significant particle aggregation, and the scattering profiles yielded size information consistent with TEM

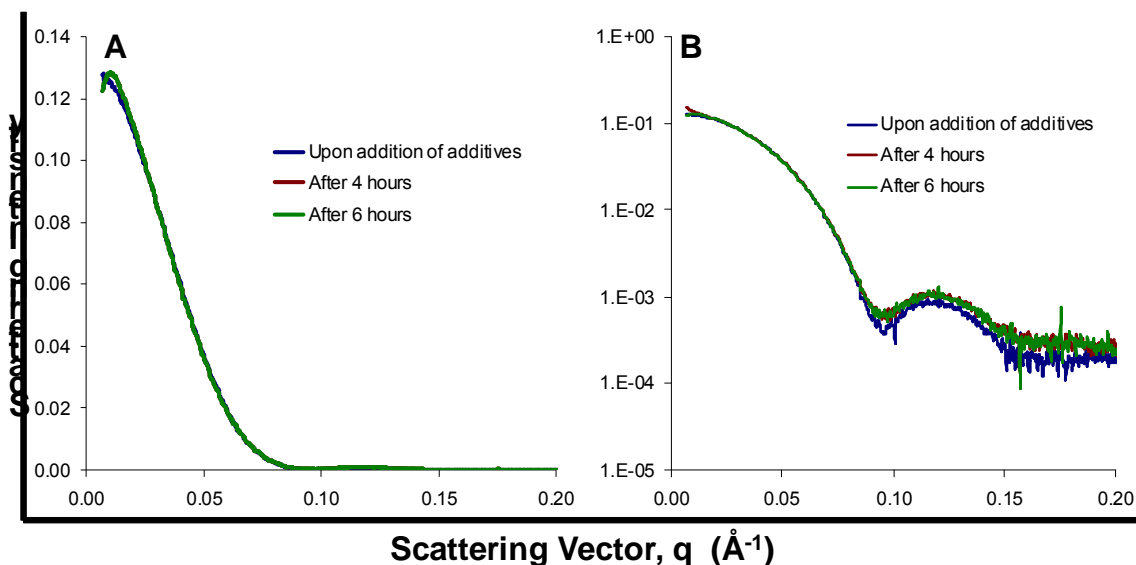


Figure 7-4. (A) Scattering profiles for citrate-capped gold particles (10 nm) in the presence of sodium citrate and organic solvent taken over a period of six hours (B) The scattering profiles in (A) plotted on a logarithmic scale.

data.

Figure 7-5 shows similar data obtained upon the addition of an OPE linker molecule. Significant changes in the scattering profile were observed with time. However, these changes occurred at a very low scattering vector and were indicative of larger-scale aggregates rather than nanoparticle dimers. The scattering intensity of larger aggregates is significantly greater than that observed for smaller structures. Therefore, this behavior does not necessarily indicate dimers were not formed in solution. The scattering of these structures was just not visible in the presence of the larger aggregates.

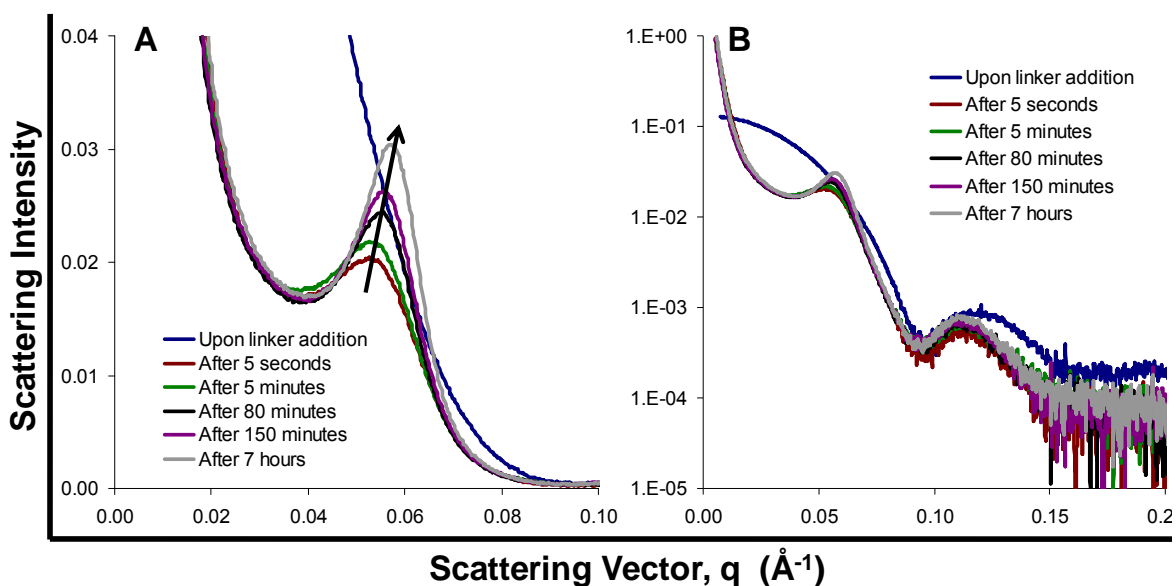


Figure 7-5. (A) Scattering profiles for citrate-capped gold particles (10 nm) as a function of time after the addition of a stoichiometric amount of an OPE linker molecule (B) The scattering profiles in (A) plotted on a logarithmic scale

One possible factor contributing to the formation of larger aggregates in these experiments was the lack of stirring of the nanoparticle solution during analysis. The nanoparticle solutions were mixed prior to being transferred to 1 mm glass capillaries and placed in a sample holder. However, samples analyzed after being stirred for several hours also indicated the presence of large aggregates. This behavior was observed for particles with 5 nm, 10 nm, 15 nm and 20 nm diameters. Due to limited time available on the beamline, experiments could not be repeated in attempt to limit aggregation behavior.

Despite the numerous advantages of the SAXS approach to characterizing nanoparticle assemblies, statistical data could not be obtained as the scattering of dimers and trimers was obscured by the presence of larger aggregates, which exhibited greater scattering intensities. It is possible that more valuable data could have been obtained if there had been sufficient time at the beamline to develop methods for preventing aggregate formation.

7.3.Experimental

Nanoparticle dimers were synthesized according to the methods described in Chapter 4. These syntheses were performed at the beamline rather than in a synthetic lab. The lack of appropriate equipment and functional magnetic stirrers could have contributed to aggregation phenomena. Kinetic experiments were

performed by mixing the nanoparticle and linker solution and then transferring small amounts to a 1 mm glass capillary which was inserted into a sample holder.

SAXS experiments were performed using a synchrotron x-ray source on Beamline 7.3.3 of the Advanced Light Source facility at Lawrence Berkeley National Lab. The x-ray wavelength used was 0.124 nm (10 keV). The flight path was adjustable from 1.3 m to 4.3 m. A 1.5 m flight path was used for 5 nm particles. a 2 m flight path was used for 10 nm and 15 nm particles, and a 4 m flight path was used for 20 nm particles.

Data work-up and curve-fitting was performed by Mathew A. Marcus of Lawrence Berkeley National Lab.

7.4. References

- (1) Marcus, M. A., *Unpublished Work* Lawrence Berkeley National Lab **2007**
- (2) Cullity, B. D.; Stock, S. R. *Elements of X-Ray Diffraction*; Prentice Hall: Upper Saddle River, NJ, 2001.
- (3) Korgel, B. A.; Fitzmaurice, D., *Physical Review B: Condensed Matter* **1999**, *59*, 14191-14201.
- (4) Connolly, S.; Fullam, S.; Korgel, B.; Fitzmaurice, D., *J. Am. Chem. Soc.* **1998**, *120*, 2969-2970.
- (5) Park, S. J.; Lazarides, A. A.; Storhoff, J. J.; Pesce, L.; Mirkin, C. A., *J. Phys. Chem. B* **2004**, *108*, 12375-12380.
- (6) Murray, C. B.; Kagan, C. R.; Bawendi, M. G., *Science* **1995**, *270*, 1335-1338.

(7) Wilcoxon, J. P.; Martin, J. E.; Provencio, P., *Langmuir* **2000**, *16*, 9912-9920.

(8) Kagan, C. R.; Murray, C. B.; Bawendi, M. G., *Phys. Rev. B* **1996**, *54*, 8633-8643.

8. Ligand-Exchange Kinetics

As discussed in Section 1.2.2, the relative binding kinetics of the two different functional groups could be significant to both understanding heterodimer formation and optimizing reaction conditions (Figure 1-18). Molecules can bind to nanoparticles through either ligand-exchange reactions or insertion into a defect site. As ligand-exchange is generally faster on edges and vertexes of particles, two regions are often observed in the kinetic profiles of such reactions as shown in Figure 8-1. In the first region, binding occurs at these defect sites and the second region exhibits slower kinetics as ligands bind to the crystalline terraces on the particles.¹⁻³ Because the percentage of defect sites is greater for small particles, the amount of exchange and the exchange kinetics are expected to vary with particle size.² Kinetics are also dependent on the nature of the capping ligand and the electronic charge on the particle.¹

The measurement of binding kinetics required analytical techniques capable of detecting binding. These

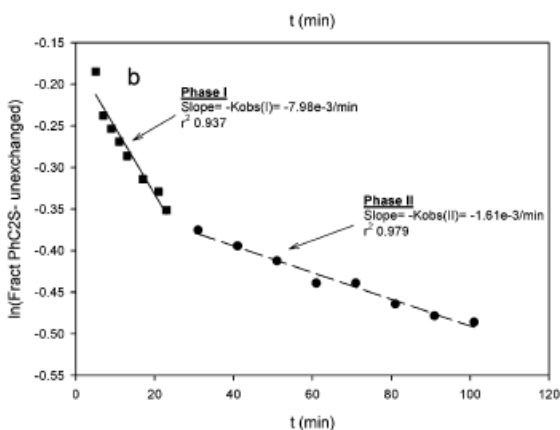


Figure 8-1. Pseudo-first-order rate plots for the exchange of phenylethanethiolate by p-nitrophenol onto Au₁₄₀(SC₂Ph)₅₃. The natural log of the free ligand concentration was plotted versus time. Figure taken from Guo et al.²

techniques are not well developed for ligands on nanoparticles. Preliminary experiments to evaluate isocyanide binding kinetics involved monitoring the shift in the isocyanide peak using infrared spectroscopy. Fluorescence quenching was also evaluated as a method to detect binding.

8.1. Infrared Spectroscopy

Initial attempts to measure isocyanide binding kinetics on platinum particles were performed using methods similar to those reported by Walker et al.⁵ Hexanethiol-capped platinum particles⁶ were incubated with the isocyanide-terminated OPE shown in Figure 8-2 in a liquid IR cell, and spectra were taken as a function of time over a period of 75 minutes. The free isocyanide peak at 2120 cm^{-1} broadened and shifted to 2158 cm^{-1} (Figure 8-3(A)) consistent with binding.⁷⁻¹² A small peak also grew in at 2261 cm^{-1} . The exact nature of this vibration is not known; however, a similar peak at 2272 cm^{-1} has been observed in the IR spectra of diisocyanides on gold and palladium substrates.⁷ It was speculated that this absorbance was due to either a different bonding arrangement on the surface or possibly the photo- or thermal oxidation of the isocyanide to an isocyanate.⁷

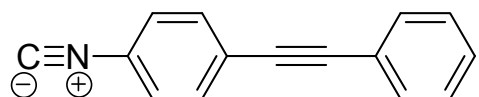


Figure 8-2. Isocyanide-functionalized OPE molecule used in IR kinetic experiments

The binding kinetics were assumed to be pseudo-first order with respect to the free ligand concentration so that a rate constant

could be determined by monitoring the disappearance of the free isocyanide. The concentration was assumed to be proportional to the area under each peak which was determined after fitting each peak to a Gaussian-Lorentzian function. The natural log of these values was plotted as a function of time as shown in Figure 8-3 (B). From the linear curve fit shown, a rate constant of $1.5 \times 10^{-3} \text{ s}^{-1}$ was obtained. However, as in previous studies, it did appear that the rate of ligand exchange was initially fast and then slowed down. Because there was significant deviation from a linear curve fit associated with these data, it was difficult to clearly establish the two different regions of ligand-exchange.

As the heterodimers in this work were synthesized in water, similar experiments were attempted in water. These were more difficult as water strongly absorbs in the

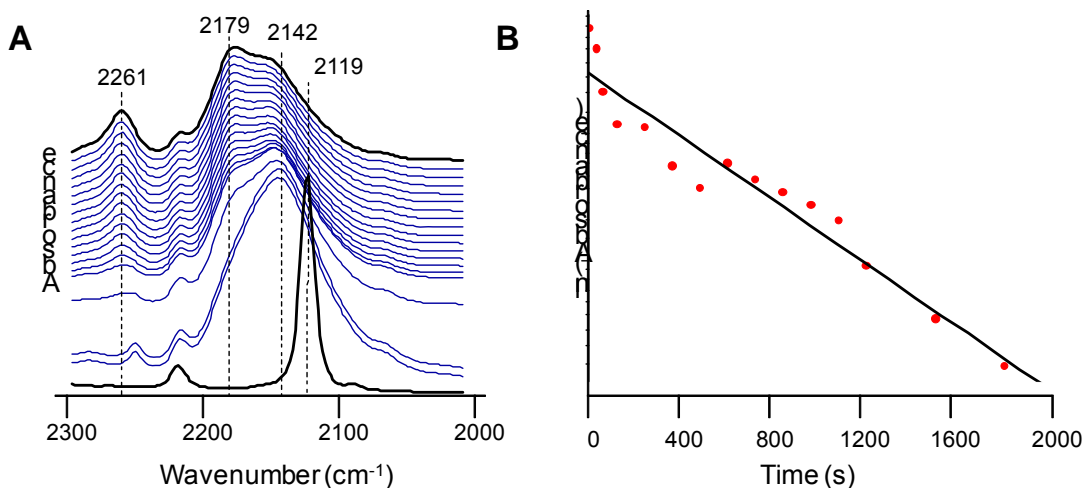


Figure 8-3. (A) IR spectra of the isocyanide-functionalized OPE shown in Figure 8-2 during incubation with hexanethiol-capped platinum particles monitored over a period of 75 minutes. The lowest spectrum was taken of the linker molecules in the absence of platinum particles. **(B)** The disappearance of the free isocyanide at 2120 cm^{-1} with time.

infrared region, but a spectrum for the isocyanide-terminated OPE was obtained using single-bounce attenuated total reflectance (ATR). However, as shown in Figure 8-4, this molecule exhibited a peak in at 2167 cm^{-1} in aqueous solution even in the absence of nanoparticles. This peak was attributed to hydrogen bonding interactions involving the polar isocyanide in aqueous solution.^{13,14} As this absorbance occurred in the region where the bound isocyanide peak was expected, it was difficult to accurately characterize binding and kinetic experiments were not attempted.

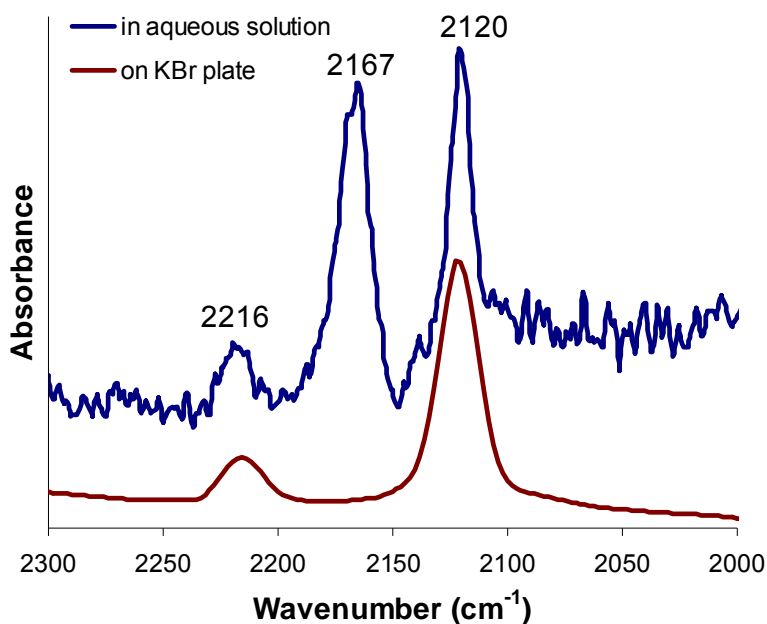


Figure 8-4. IR spectra of isocyanide-functionalized OPE obtained both after deposition onto a KBr plate and in aqueous solution

While infrared spectroscopy was a useful technique for establishing the binding kinetics of isocyanides in organic solution, it was not suitable for evaluating binding in aqueous solution, and there is no specific IR handle to detect the binding of thiols. Other

analytical techniques were therefore explored to characterize the binding of OPE molecules to metal nanoparticles.

8.2. Fluorescence Quenching

Fluorescence quenching experiments were also performed in attempt to analyze binding kinetics. Static quenching has been observed for fluorescent molecules upon binding to a nanoparticle due to electron transfer from the molecular excited state to the particle. For example, a fluorescent carboxylic acid-terminated terthiophene was quenched upon addition to TiO_2 particles (Figure 8-5).⁴ In this case, the fluorescence intensity was monitored as TiO_2 was added to the terthiophene solution. In addition to the quenching behavior, the absorption peak red-shifted slightly from 379 to 384 nm upon binding.⁴ Similar quenching behavior

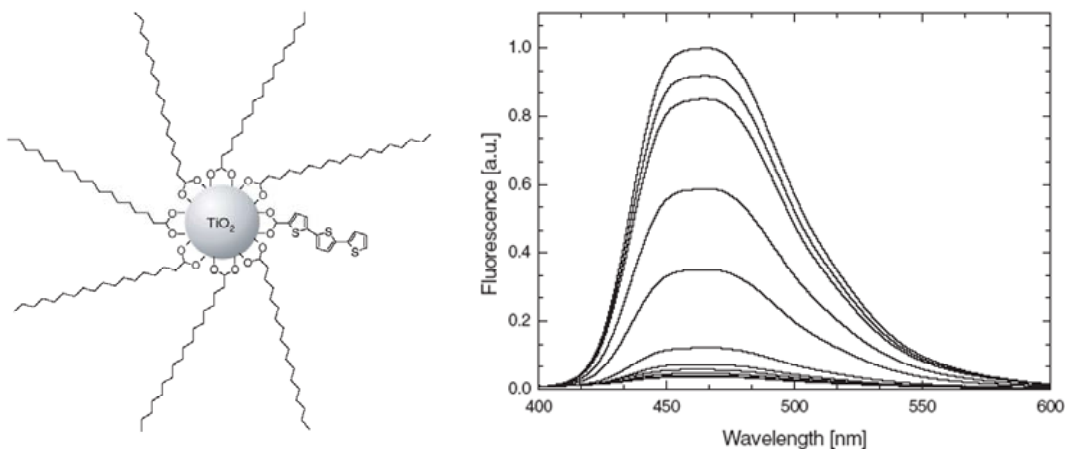


Figure 8-5. Fluorescence quenching observed upon binding of a fluorescent carboxylic acid-terminated thiophene to stearic-acid coated TiO_2 . Figure taken from Beek et al.⁴

has been

observed upon

binding fluorescent

labels to gold

particles.¹⁵⁻²⁰

Similar techniques

were explored to

demonstrate the binding of bifunctional OPEs to gold and platinum particles (Figure 8-6). These molecules exhibited fluorescent behavior similar to that observed for other OPEs in the literature (Figure 8-7).²¹⁻²⁵ These spectra exhibited the same shape when excited at each of the three absorbance wavelengths; however, as expected, the emission intensity decreased with decreasing excitation wavelength.

There are some additional complications associated with performing quenching experiments with water-soluble particles. Water²⁶ and oxygen²⁷ are also capable of quenching fluorescence, and it is difficult to exclude oxygen from aqueous systems. Preliminary experiments were designed to determine if linker quenching due to water could be separated from quenching due to nanoparticle binding. Figure 8-8 shows spectra taken over a period of 1200 minutes. No fluorescence quenching was observed.

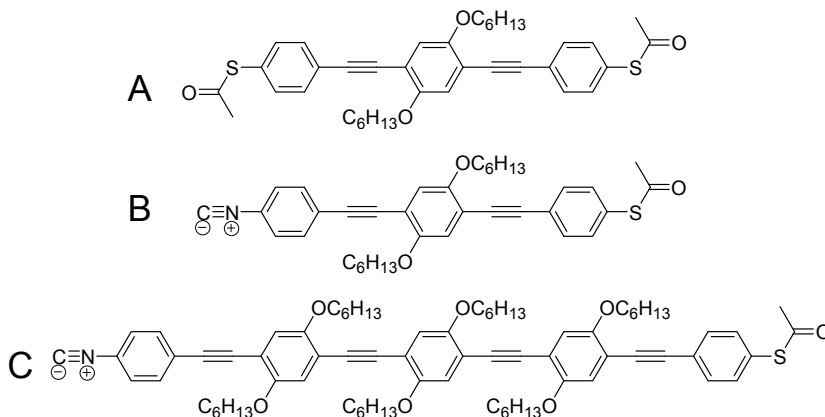


Figure 8-6. Bifunctional linker molecules used in fluorescence quenching experiments

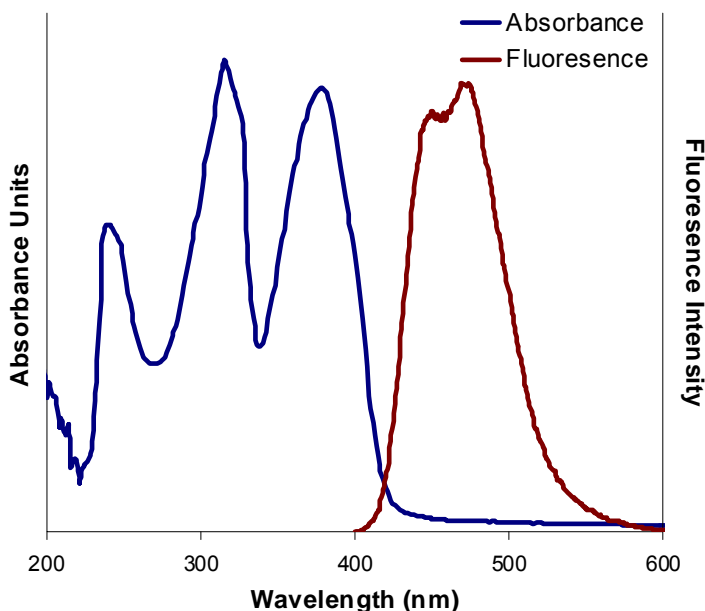


Figure 8-7. Optical absorbance and fluorescence spectra for Linker B. Fluorescence spectrum was obtained after excitation at 380 nm.

However, quenching was observed in the presence of both gold and platinum nanoparticles. Figure 8-9 (A) shows quenching observed as citrate-capped gold particles (5 nm) were added to a solution of Linker B

(Figure 8-6). The quenching efficiencies were

quantified using Stern-Volmer plots. According to Equation 8-1, a plot of the fluorescence ratio versus the particle concentration should be linear with a slope equal to the Stern-Volmer quenching constant.²⁶

$$\frac{F_0}{F} = 1 + K_{SV}[Q]$$

F_0 = fluorescence in the absence of quenching species

F = fluorescence

$[Q]$ = concentration of the quenching species

K_{SV} = Stern-Volmer quenching constant

8-1

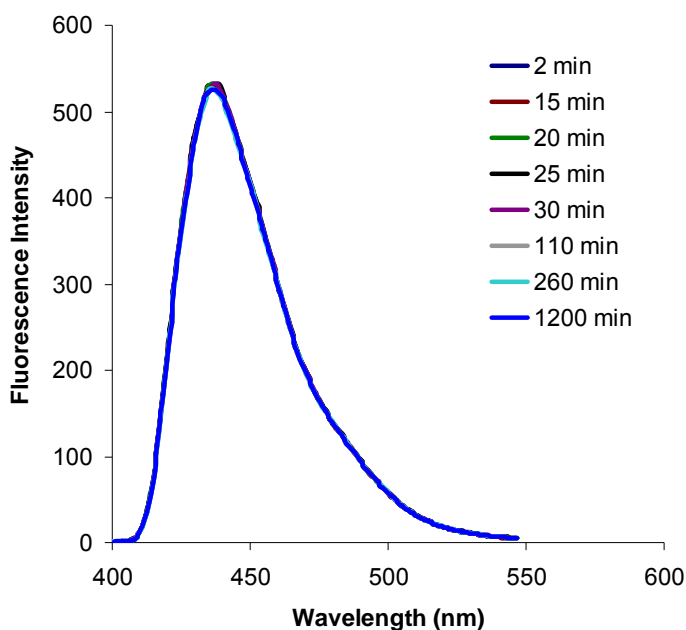


Figure 8-8. Fluorescence spectra of Linker A in aqueous solution recorded over a period of 1200 minutes.

Figure 8-9 (B) shows Stern-Volmer plots for the quenching observed as citrate-capped gold particles (5 nm) were added to solutions of Linker A and Linker B (Figure 8-6). The quenching constants for these and other experiments are reported in Table 8-1.

The high quenching constants observed indicated efficient quenching between the nanoparticles and the OPE linker molecules. The calculated values were approximately 10^7 - 10^8 M^{-1} , which are comparable to the value of 10^7 reported for the quenching of $[\text{Ru}(\text{bpy})_3]^{2+}$ by gold

Table 8-1. Stern-Volmer Quenching Constants

Linker	Particle	$K_{sv} 10^8$ (M^{-1})	Particle	$K_{sv} 10^8$ (M^{-1})	Particle	$K_{sv} 10^8$ (M^{-1})	Particle	$K_{sv} 10^8$ (M^{-1})
A	Au* (10nm)	5.8	Au* (5nm)	0.6	Pt** (8nm)	2.8	Pt** (3nm)	0.2
B	Au* (10nm)	7.2	Au* (5nm)	1.1	Pt** (8nm)	5.4	Pt** (3nm)	1.1
C	Au* (10nm)	7.7	Au* (5nm)	1.0	Pt** (8nm)	7.9	Pt** (3nm)	0.9

* gold particles were stabilized with citrate anions

** platinum particles were stabilized with polyacrylic acid

nanoparticles.²⁸ For all of the particles investigated, larger quenching constants were observed for the bifunctional linkers (Figure 8-6 (B,C)) compared to the linker molecule terminated with thioacetate functionalities on both ends (Figure 8-6 (A)). This result likely indicates a more favorable binding equilibrium for the isocyanide functional group to both gold and platinum particles; however, experiments involving molecules containing only one binding group would need to be performed to verify this trend. In the presence of bifunctional molecules, it was not possible to tell which functional group was binding. However, the fact that higher quenching constants were observed in the presence of both gold and platinum particles for the OPEs containing isocyanide functionalities does suggest that binding may have occurred

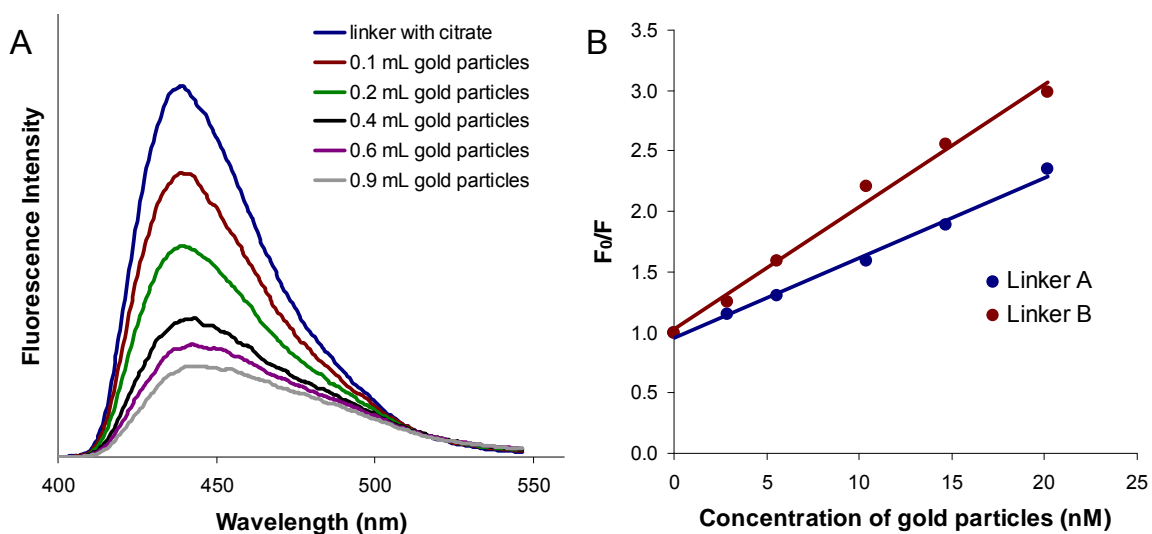


Figure 8-9. (A) Fluorescence spectra taken for Linker B as citrate-capped gold particles (5 nm) were added to the solution (B) Stern-Volmer plot of quenching observed as citrate-capped gold particles (5 nm) were added to solutions of Linker A and Linker B

through this functional group in both cases. These data are another indication that the selectivity of binding associated with orthogonal self-assembly may need to be evaluated for particles of different sizes and capping ligands.

High quenching constants were also observed for larger particle sizes. This behavior is consistent with that observed the quenching of $[\text{Ru}(\text{bpy})_3]^{2+}$ by gold nanoparticles.²⁸ The Stern-Volmer constant observed when these complexes were quenched by 2.2 nm gold particles ($1.2 \times 10^7 \text{ M}^{-1}$) was approximately two orders of magnitude greater than that observed in the presence of 1.8 nm gold particles ($5.2 \times 10^5 \text{ M}^{-1}$). This behavior can be explained by the higher surface area of the larger particles, which is available for binding. Negligible differences were observed in the quenching efficiencies for linkers of different lengths.

While the fluorescence quenching observed for the OPE molecules in the presence of both gold and platinum particles could be due to the formation of covalent bonds, dynamic quenching due to collisions within solution has also been reported.²⁸ In order to determine whether collisional quenching occurred, gold particles were added to a solution of Linker A (Figure 8-6) in the absence of sodium citrate. The pH of this solution (~ 6) was not believed to be high enough to facilitate the deprotection of the acetyl groups and thus covalent binding was not expected. However, fluorescence quenching was observed. This behavior created some uncertainty regarding the mechanisms associated with the observed quenching.

There were also some problems regarding the reproducibility of these experiments. There were likely several processes occurring in solution, and this technique could therefore not be used to accurately determine binding kinetics.

8.3. Summary and Conclusions

Both infrared spectroscopy and fluorescence quenching were explored as methods to evaluate binding kinetics. While infrared spectroscopy proved useful for establishing the binding kinetics of isocyanides in organic solution, it was not suitable for evaluating binding in aqueous solution, and there was no specific IR handle to detect the binding of thiols. The fluorescence of three OPE molecules was quenched in the presence of both gold and platinum particles. However, quenching was also observed under conditions under which no covalent binding was expected. This behavior created some uncertainty regarding the mechanisms associated with the observed quenching. There were also some problems regarding the reproducibility of these experiments. There were likely several processes occurring in solution, and this technique could therefore not be used to accurately determine binding kinetics.

8.4. Experimental

Unless otherwise mentioned, all reagents were obtained from Fisher Scientific. Gold-citrate particles were obtained from Ted Pella, Inc. as aqueous solutions with

Table 8-2. Concentrations of gold particles

Particle Size (nm)	Initial concentration (particles/mL)*	Initial concentration (nM)*
5	5.0×10^{13}	83.0
10	5.7×10^{12}	9.46

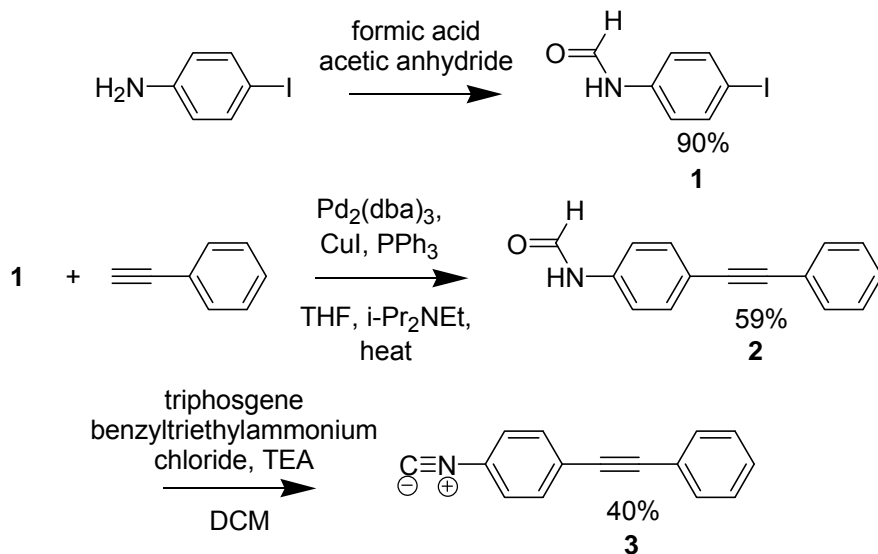
* as received from Ted Pella, Inc.

trace amounts of citrate, tannic acid and potassium carbonate. Particle concentrations are reported in Table 8-2.

The bifunctional OPE linker molecules (Figure 8-6) were synthesized by Chandra et al., and these details are published elsewhere.²⁹

8.4.1. Synthesis of 1-Isocyano-4-phenylethynyl-benzene (Figure 8-2)

This molecule was synthesized according to Scheme 8-1.



Scheme 8-1. Synthesis of 1-Isocyano-4-phenylethynyl-benzene

with a reflux condenser. Formic acid (6.8 mL, 88%, 160 mmol) was then added dropwise. The flask was heated to 60 °C and was stirred for 30 minutes before being cooled to -10 °C. A solution of 4-iodoaniline (11.0 g, 50 mmol) in THF (30 mL) was slowly added to the reaction mixture, which was then allowed to stir overnight. Solvent was removed by rotary evaporation and water was added, yielding a white precipitate which was then filtered and washed with water. The material was recrystallized from dichloromethane/hexanes to afford the desired intermediate, **1**, (11.2 g, 90%). ¹H NMR (300 MHz, CDCl₃) δ (ppm) 8.68 (d, J = 11.7 Hz, 0.36 H), 8.41 (br s, 0.68 H), 7.67 (d, J = 8.7 Hz, 2H), 6.85 (d, J = 8.7 Hz, 1H).

Inside a nitrogen-filled dry box, compound **1** (2.06 g, 9.39 mmol) was added to an oven-dried Schlenk flask along with tri(dibenzylideneacetone) bispalladium (0.21 g, 11.9 mmol), copper iodide (0.28 g, 1.45 mmol), triphenylphosphine (0.26 g, 0.99 mmol), ethyl benzene (1.3 mL, 11.9 mmol), distilled diisopropyl amine (6 mL), and anhydrous THF (15 mL). The flask was sealed, removed from the dry box, and stirred at 60 °C for 24 hours. The solution was then cooled to room temperature, the solvents were removed by rotary evaporation, and the residue was re-dissolved in methanol and filtered through a Celite plug. Purification by flash column chromatography (1:1 hexanes/ethyl acetate) yielded the desired intermediate, **2**, (1.23 g, 59%). ¹H NMR (400 MHz, d⁶-acetone) δ (ppm) 9.44 (br s, 0.5H), 8.92 (d, J

= 11.2 Hz, 0.5H), 8.40 (d, J = 1.6 Hz, 0.5H), 7.74 (m, 2H), 7.53 (m, 4H), 7.41 (m, 3H), 7.32 (d, 0.5H).

Compound **2** (0.94 g, 4.26 mmol) was added to a Schlenk flask containing triphosgene (1.64 g, 5.5 mmol). The flask was sealed, evacuated and back-filled with argon ($\times 4$) and cooled to 0 °C before the addition of distilled dichloromethane (25 mL), triethylamine (20 mL) and benzyltriethylammonium chloride (0.50 g, 2.20 mmol) in dichloromethane (15 mL) under positive argon pressure. The solution was stirred overnight as the solution slowly warmed to room temperature. The solution was then washed with water, dried with magnesium sulfate and filtered. The solvents were removed by rotary evaporation. Purification by flash column chromatography (10:1 hexanes/ethyl acetate) yielded the desired product, **3**, (0.35 g, 40%). ^1H NMR (300 MHz, CDCl_3) δ (ppm) 7.53 (m, 4H), 7.37 (m, 4H).

8.4.2. Synthesis of Hexanethiol-capped Platinum Particles

Particles were synthesized as reported in the literature.⁶ $\text{H}_2\text{PtCl}_6 \cdot 6\text{H}_2\text{O}$ (0.30 g, 0.58 mmol) and 20 mL anhydrous THF were added to a Schlenk flask inside an N_2 -filled dry box. The flask was sealed with a septum and removed from the box. While stirring under nitrogen, 83 μL hexanethiol was added and the solution stirred for 30 min. Then, 15 mL lithium triethylborohydride (LiTEBH) was added dropwise to the solution, which turned dark brown. After stirring for an additional 30 min, ethanol was added to quench the excess LiTEBH. The majority of solvent was removed via

rotary evaporation and the particles precipitated from solution with acetonitrile. The particles were filtered on a fine frit and washed with ethanol and acetonitrile. The resulting particles were approximately 2 nm as evidenced by TEM and exhibited a tailing optical absorbance.

8.4.3. Synthesis of Polyacrylate-capped Platinum Particles

Particles were synthesized according to a procedure in the literature.³⁰⁻³² A solution of K_2PtCl_4 (1.22 g, 25 mmol) and sodium polyacrylate (0.42 g, 0.2 mmol based on average MW 2100) was prepared in water (250 mL). After argon was bubbled through the solution for approximately 20 min, the solution was aged to facilitate hydrolysis of the PtCl_4^{2-} ions (i.e. $\text{Cl}^- \rightarrow \text{H}_2\text{O}$ ligand exchange).³² The particle size was increased as the aging time was varied from 1 hour to 4 days. Hydrogen was then bubbled through the solution for approximately five minutes in order to reduce the platinum ions. The reaction was allowed to progress in a sealed flask for 12 hours at room temperature. No purification was performed.

8.4.4. Analytical Techniques

8.4.4.1. Transmission Infrared Spectroscopy

Measurements were made using a Perkin-Elmer Spectrum RX1 Spectrometer under an N_2 atmosphere with a resolution of 4 cm^{-1} . Organic solutions were placed on a KBr plate and the solvent was allowed to evaporate. Kinetic measurements were

performed in a liquid IR cell composed of two KBr plates. Measurements were performed in cyclohexane as it does not absorb in the regions of interest.³³

8.4.4.2. Attenuated Total Reflectance Spectroscopy

Measurements were made using an FTS 3000 spectrometer equipped with a single reflection ATR accessory (Pike Technologies) containing a germanium crystal. A small volume (146 μL) of 1-isocyano-4-phenylethynyl-benzene solution in THF was mixed with water (1 mL). A single droplet of the resulting solution was placed on the germanium crystal.

8.4.4.3. Optical Absorbance Spectroscopy

Optical absorbance measurements were made using a Hewlett-Packard 8452A Diode Array Spectrometer and a path length of 1.0 cm.

8.4.4.4. Fluorescence Spectroscopy

Fluorescence measurements were made with a Perkin-Elmer LS50B Spectrometer. The organic linker molecules were introduced to the aqueous particle solutions in THF.

8.5. References

- (1) Song, Y.; Murray, R. W., *J. Am. Chem. Soc.* **2002**, *124*, 7096-7102.
- (2) Guo, R.; Song, Y.; Wang, G.; Murray, R. W., *J. Am. Chem. Soc.* **2005**, *127*, 2752-2757.

- (3) Hostetler, M. J.; Templeton, A. C.; Murray, R. W., *Langmuir* **1999**, *15*, 3782-3789.
- (4) Beek, W. J. E.; Janssen, R. A. J., *Adv. Funct. Mater.* **2002**, *12*, 519-525.
- (5) Walker, B. R.; Wassel, R. A.; Stefanescu, D. M.; Gorman, C. B., *J. Am. Chem. Soc.* **2004**, *126*, 16330-16331.
- (6) Eklund, S. E.; Cliffler, D. E., *Langmuir* **2004**, *20*, 6012-6018.
- (7) Swanson, S. A.; McClain, R.; Lovejoy, K. S.; Alamdari, N. B.; Hamilton, J. S.; Scott, J. C., *Langmuir* **2005**, *21*, 5034-5039.
- (8) Bong, D.; Tam, I.; Breslow, R., *J. Am. Chem. Soc.* **2004**, *126*, 11796-11797.
- (9) Horswell, S. L.; Kiely, C. J.; O'Neil, I. A.; Schiffrin, D. J., *J. Am. Chem. Soc.* **1999**, *121*, 5573-5574.
- (10) Avery, N. R.; Matheson, T. W., *Surface Science* **1984**, *143*, 110-124.
- (11) Shih, K. C.; Angelici, R. J., *Langmuir* **1995**, *11*, 2539-2546.
- (12) Murphy, K. L.; Tysoe, W. T.; Bennett, D. W., *Langmuir* **2004**, *20*, 1732-1738.
- (13) Witanowski, M.; Sicinska, W.; Webb, G. A., *Magn. Reson. Chem.* **1992**, *30*, 169-172.
- (14) Gramstad, T.; Tjessem, K., *J. Mol. Struct.* **1978**, *48*, 147-151.
- (15) Aguila, A.; Murray, R. W., *Langmuir* **2000**, *16*, 5949-5954.
- (16) Imahori, H.; Kashiwagi, Y.; Endo, Y.; Hanada, T.; Nishimura, Y.; Yamazaki, I.; Araki, Y.; Ito, O.; Fukuzumi, S., *Langmuir* **2004**, *20*, 73-81.
- (17) Sudeep, P. K.; Ipe, B. I.; Thomas, K. G.; George, M. V.; Barazzouk, S.; Hotchandani, S.; Kamat, P. V., *Nano Lett.* **2002**, *2*, 29-35.
- (18) Ghosh, S. K.; Pal, A.; Kundu, S.; Nath, S.; Pal, T., *Chem. Phys. Lett.* **2004**, *395*, 366-372.

- (19) Dubertret, B.; Calame, M.; Libchaber, A. J., *Nat. Biotechnol.* **2001**, *19*, 365-370.
- (20) Cheng, P. P. H.; Silvester, D.; Wang, G. L.; Kalyuzhny, G.; Douglas, A.; Murray, R. W., *J. Phys. Chem. B* **2006**, *110*, 4637-4644.
- (21) Schenning, A. P. H. J.; Tsipis, A. C.; Meskers, S. C. J.; Beljonne, D.; Meijer, E. W.; Bredas, J. L., *Chem. Mater.* **2002**, *14*, 1362-1368.
- (22) Khatyr, A.; Ziessel, R., *J. Org. Chem.* **2000**, *65*, 3126-3134.
- (23) Lahiri, S.; Thompson, J. L.; Moore, J. S., *J. Am. Chem. Soc.* **2000**, *122*, 11315-11319.
- (24) Prince, R. B.; Saven, J. G.; Wolynes, P. G.; Moore, J. S., *J. Am. Chem. Soc.* **1999**, *121*, 3114-3121.
- (25) Zhou, C.-Z.; Liu, T.; Xu, J.-M.; Chen, Z.-K., *Macromolecules* **2003**, *36*, 1457-1464.
- (26) Atkins, P. *Physical Chemistry*, Fifth ed.; W.H. Freeman and Company: New York, 1994.
- (27) Skoog, D. A.; Holler, F. J.; Nieman, T. A. *Principles of Instrumental Analysis*; Fifth ed.; Harcourt Brace & Company: Orlando, Florida, 1998.
- (28) Huang, T.; Murray, R. W., *Langmuir* **2002**, *18*, 7077-7081.
- (29) Chandra, K. L.; Zhang, S.; Gorman, C. B., *Tetrahedron* **2007**, *63*, 7120-7132.
- (30) Ahmadi, T. S.; Wang, Z. L.; Henglein, A.; ElSayed, M. A., *Chem. Mat.* **1996**, *8*, 1161-&.
- (31) Rampino, L. D.; Nord, F. F., *J. Am. Chem. Soc.* **1941**, *63*, 2745-2749.
- (32) Henglein, A.; Ershov, B. G.; Malow, M., *J. Phys. Chem.* **1995**, *99*, 14129-14136.
- (33) Lambert, J. B.; Shurvell, H. F.; Lightner, D. A.; Cooks, R. G. *Organic Structural Spectroscopy*, Prentice Hall, Inc.: Upper Saddle River, New Jersey, 1998.

9. Conclusions and Project Outlook

The formation of covalently-linked nanoparticle assemblies proved to be a very complex and challenging task. Despite the prevalence of nanoparticle literature, the synthesis of nanoparticles that were stable yet did not sterically hinder dimer formation was quite difficult. Not only was it necessary for particles to be stable as-synthesized, but additional complications were introduced upon the mixing of two nanoparticle solutions, and the addition of sodium citrate and organic solvent, both of which were detrimental to particle stability.

Preliminary TEM data suggested the formation of heterodimers consisting of citrate-capped gold particles and mercaptobenzoic acid-capped platinum particles.

Approximately 54% of the gold particles were bound to at least one platinum and 16% of the gold particles were isolated in heterodimers. Other structures included gold particles that were bound to more than one platinum, gold homodimers, platinum homodimers and assemblies containing both gold and platinum. Further experiments could not be performed due to the irreproducibility of the platinum particle synthesis.

Preliminary TEM data also suggested the formation of heterodimers consisting of citrate-capped gold particles and tartaric acid-capped Fe_3O_4 particles.

Approximately 30% of the gold particles were bound to at least one Fe_3O_4 particle

and 18% were isolated in heterodimers, double the values observed in the absence of the bifunctional linker. While it was predicted that the selectivity between the thiol and carboxylic acid functionalities would be greater than that associated with the thiol and isocyanide functionalities, only 30% of gold particles were bound to at least one Fe_3O_4 compared to 54% of gold particles bound to at least one mercaptobenzoic acid-capped platinum particle. It was speculated that this difference could be due to greater interactions between Fe_3O_4 particles, which could limit mixing and the efficiency of dimerization.

While preliminary TEM data did suggest the formation of heterodimers, additional experiments were required to verify this behavior. The statistics obtained using TEM were based on a few hundred particles and did not necessarily reflect the composition of the entire solution. In addition, nanoparticle assemblies were observed in the absence of the bifunctional linker, which created some uncertainty as to whether these structures were covalently linked. Solution-based characterization techniques were evaluated for their ability to provide data that was representative of an entire solution without the ambiguity associated with aggregation upon TEM sample preparation. A routine, solution-based technique is also desirable in order to evaluate how solution variables affect the efficiency of dimer formation.

Size-exclusion chromatography (SEC) was evaluated for its ability to detect nanoparticle assemblies. While size-exclusion appeared to be the primary separation mechanism for citrate-capped gold particles, chemical interactions with the column material were significant when other particles were injected onto the columns. Chromatographic separation was extremely sensitive to the nature of the particle, the column and the mobile phase. Separation conditions likely need to be optimized for each individual particle, which complicates heterodimer characterization. The optimum conditions for the separation of one particle may not be suitable for another. Particle adsorption to the column was also significant and appeared to be size-dependent. While nanoparticle assemblies were detected using SEC, these data could not be used to obtain accurate statistical information about the relative concentrations of isolated particles, assemblies and larger aggregates in solution.

Capillary electrophoresis (CE) was also evaluated for its ability to characterize nanoparticle assemblies. While CE data for the separation of dimers and trimers initially appeared promising, they were not reproducible. Data were difficult to interpret as the surface chemistry and electrophoretic behavior of particles were likely affected by the buffer composition and presence of surfactant. The low particle concentrations and solution volumes used in these experiments also made detection difficult.

Small angle x-ray scattering (SAXS) posed several advantages over chromatographic and electrophoretic techniques, which suffered from adverse interactions with a stationary phase and required buffered mobile phases and surfactants. Using SAXS, nanoparticle solutions could be characterized as-synthesized without the need for solution additives or application of external forces. While this technique proved effective for detecting nanoparticle binding, the scattering of dimers and trimers was obscured by the presence of larger aggregates, which exhibited greater scattering intensities. It is possible that more valuable data can be obtained once methods to prevent the formation of larger-scale aggregates have been developed.

It is possible that several of the challenges associated with heterodimer formation and characterization can be overcome. One of the greatest challenges was the synthesis of stable nanoparticles. The synthesis of longer OPE molecules could allow the use of more stable nanoparticles with longer capping ligands; however these syntheses were time-consuming and inefficient as each phenylethylene repeat unit required a separate reaction and work-up. In addition, solubility became more of a challenge with increasing linker lengths.

The addition of citrate and organic solvent to aqueous nanoparticle solutions also proved to be detrimental to particle stability. The synthesis of longer OPEs could facilitate heterodimer formation in organic solvent despite the sterically-bulky

capping ligands associated with most organically-soluble particles. In this case, a mixed solvent system would not be necessary. Another possibility is to synthesize OPEs with water-solubilizing side groups so that they can be introduced into aqueous nanoparticle solutions without the need for organic solvent. The synthesis of OPEs with functional groups, which do not require deprotection, could also limit the need for basic additives to nanoparticle solutions.

Despite the problems encountered with obtaining statistical information using chromatographic separation methods, these techniques could prove useful for observing relative changes in dimer yields as reaction conditions are changed. A more accurate picture of nanoparticle solutions will likely require data from multiple analytical techniques.

Appendices

Appendix 1. Collaborative Publications Involving the Integration of Nanoparticles and Nanoparticle Assemblies into Lithographic Architectures

The concepts described in this work for fabricating electronic devices are multifaceted, involving everything from the synthesis of the linker molecules to incorporating them into lithographic architectures. While the focus of this dissertation has been on the synthesis and characterization of nanoparticles and nanoparticle assemblies, significant efforts have been put forth to integrate these particles and assemblies into lithographic architectures and to evaluate the electronic behavior and the stability of these systems. The research group of Dr. Gregory Parsons in the Department of Chemical and Biomolecular Engineering at NCSU focused on this aspect of the project, which has resulted in several publications. These publications are included here to demonstrate the applicability of these types of structures to molecular electronics as well as to highlight many of the issues that still need to be overcome. The two students responsible for the majority of this work are Changwoong Chu and Jeong-Seok Na.

The first paper¹ included here is an overview of several of the issues associated with the synthesis and characterization of nanoparticle assemblies for electronic applications. The issues discussed here spanned from the synthesis of the organic linker molecules to the fabrication of the lithographic trench. The remaining papers²⁻⁵ involve primarily the study of the electronic behavior of particles and assemblies

within these lithographic features. The second paper² evaluated the effects of molecular structure on the electrical properties of nano-scale junctions involving gold contacts with the greatest conductance measured for highly delocalized structures with isocyanide terminal groups.

The next three papers³⁻⁵ reported the observed behavior of gold homodimers assembled within a lithographic trench. The first of these papers³ evaluated the most effective method for assembling dimers within the trench, with junctions created using dielectrophoretic trapping demonstrating greater overall stability than those created using the receding meniscus method. The presence of the molecular linker was confirmed by resistance measurements, which were consistent with previously reported values for similar structures, and the conduction mechanisms were evaluated. While these molecular junctions exhibited long-term stability under vacuum, current fluctuations and instability were observed under ambient conditions and attributed to water molecules adsorbed from the air into the molecular junction. The next paper⁴ reported the stability of stabilizing these molecular junctions through the atomic layer deposition (ALD) of Al_2O_3 . While the current flow through these electronic junctions varied through the ALD process, it remained relatively constant under atmospheric conditions after ALD was complete suggesting this method could be used to stabilize these types of molecular junctions. The last paper in this series⁵ looked more closely at the encapsulation of gold nanoparticle homodimers through

the ALD of Al_2O_3 , and attempted to evaluate the factors contributing to the instability of both the coated and uncoated molecular junctions.

An unpublished manuscript⁶ is also referenced here, and describes electronic measurements involving gold nanoparticle trimers assembled into a lithographic trench in a manner similar to that previously described for dimers. While it appears that trimers were successfully assembled into the trench and some current modulation was observed with gate bias, the overall success rate was low. Additional experiments need to be done to confirm the presence of the molecule in these electronic junctions, increase reproducibility and understand the gating mechanism before this work can be published.

While there are still some issues that need to be addressed, these publications demonstrate the applicability of these types of nanoparticle assemblies to electronic applications, as both molecular wires and three-terminal devices. They also provide evidence supporting the presence of the molecular linkers within the particle assemblies.

Below are the titles and authors for each of the papers and manuscript described above, each followed by a brief summary.

Paper 1: Ayres, J.; Walker, B.; Chandra, K. L.; Stefanescu, D.; Chu, C.; Parsons, G.; Gorman, C., 'Hierarchical Assembly of Interconnects for Molecular Electronics' *Proc. of SPIE* **2005**, 6003, 60030J.¹

As mentioned above, this paper gave a broad overview of several challenges associated with our approach to creating electronic junctions that bridge the molecular and the lithographic length scales. The discussion included the selectivity of binding of thiols and isocyanides on gold and platinum, respectively. Organic synthetic challenges were also addressed, specifically those involving the selective functionalization of linker molecules in ways that allow purification by common laboratory techniques and that produce high yields. Data was presented demonstrating the fabrication of sub 100nm lithographic trenches using a shadowed evaporation technique in addition to I-V measurements of both particles and molecules assembled in these trenches.

Paper 2: Chu, C.; Ayres, J. A.; Stefanescu, D. M.; Walker, B. R.; Gorman, C. B.; Parsons, G. N., 'Enhanced Conduction through Isocyanide Terminal Groups in Alkane and Biphenylene Molecules Measured in Molecule/Nanoparticle/Molecule Junctions', *J. Phys. Chem. C*, **2007**, 111, 8080-8085.²

This paper evaluated the effects of the molecular structure on the electrical properties of nano-scale junctions, and was based on single nanoparticles bridging gold contacts covered with molecular monolayers. The molecular structures evaluated included biphenyl, diphenyl acetylene and alkane molecules with both thiol and isocyanide terminal functionalities. While the synthetic procedures are not

discussed in this dissertation, I performed the synthesis of the alkyl isocyanides in addition to the biphenyl and biphenyl acetylene molecules.

As discussed in Chapter 1, it was expected that the molecular structures that exhibited the greatest electron delocalization would exhibit greater degrees of electron transport. This behavior was again demonstrated. In addition, it was observed that for all structures, those with an isocyanide functionality exhibited conductances approximately an order of magnitude greater than those observed for the same molecules terminated with thiols. The reasoning for this behavior remains unclear. However, this work highlights the importance of the metal/linker contact in determining the electrical properties of a junction. The data presented here are specific to molecular junctions with gold, and this behavior cannot be assumed for other metals (e.g. platinum).

After this paper was submitted, a similar article appeared claiming that greater conductances were observed for thiol-gold contacts compared to isocyanide-gold contacts.⁷ Based on this report, it was speculated that the contact geometry and molecular conformation play important roles in the electron transport behavior. These factors are likely affected by the methods used to create the junction, and will likely be difficult to evaluate.

Paper 3: Na, J. S.; Ayres, J.; Chandra, K. L.; Chu, C.; Gorman, C. B.; Parsons, G. N., 'Conduction Mechanim and Stability of Single Molecule Nanoparticle/Molecule/Nanoparticle Junctions', *Nanotechnology* **2007**, *18* 035203.³

The data presented in this paper involve the assembly and subsequent characterization of nanoparticle dimers in a lithographic trench. Gold-gold homodimers were synthesized using citrate-capped gold nanoparticles as described in Chapter 4. These assemblies were then inserted into lithographic architectures using both the receding meniscus method, described in the previous paper, and dielectrophoretic trapping, with junctions created using the latter method demonstrating greater overall stability. Images of the assembled dimers agreed with the predictions from simulations based on electric field gradients.

The stability of these electronic junctions was evaluated both under vacuum and ambient atmosphere. Consistent I-V data for a single sample was obtained under vacuum over a period of weeks and through 100 I-V cycles over a period of approximately 7 hours, indicating stable contacts between both within the nanoparticle dimer and between the electrode and the nanoparticles. The measured resistance was consistent with those previously observed for oligomeric phenylene ethylenes. Behavioral variations between different samples were attributed to different contact properties between the nanoparticles and the electrodes. While stable under vacuum, these junctions exhibited gradual increases in current when

exposed to ambient atmosphere. This was attributed to water molecules adsorbed from the atmosphere into the molecular junctions.

Current-voltage measurements were made at temperatures ranging from 80 K (-193 °C) to 290 K (17 °C) in order to evaluate the conduction mechanisms. A transition between direct tunneling (temperature-dependent) to Fowler-Nordheim tunneling (temperature-independent) was observed at approximately 1.5 Volts.

These data demonstrated the ability to bridge the molecular and the lithographic length scales through nanoparticle assemblies and support the data in Chapter 4 suggesting the formation of molecularly-bridged dimers. They also brought about questions regarding the long-term stability of these junctions under atmospheric conditions. These questions were addressed in subsequent publications.

Paper 4: Na, J. S.; Ayres, J.; Chandra, K. L.; Gorman, C. B.; Parsons, G. N., 'Real-time Conductivity Analysis Through Single-Molecule Electrical Junctions', *Nanotechnology* **2007**, *18* 424001.⁴

This paper again addressed the behavior of gold nanoparticle homodimers within a lithographic trench. The conductance through these junctions was measured under several conditions, both during and after dielectrophoretic assembly. As previously reported, these molecular junctions appeared to be stable under vacuum, but exhibited current fluctuations and an overall increase in electron transport when exposed to ambient conditions. It was also noted that high applied voltages (e.g. ≤ 3

Volts) resulted in the coalescence of the nanoparticles so that current measurements no longer reflected electron transport through the molecular linker.

These molecular junctions were subject to the atomic layer deposition (ALD) of Al_2O_3 in attempt to preserve their stability in ambient conditions. ALD of Al_2O_3 was chosen it required relatively low processing temperatures, and it was predicted to fully conform to the molecular junctions with precise thickness control. Before attempting ALD, the effects of temperature on the stability of the electronic junctions were evaluated. While high temperatures resulted in irreversible conductance changes, the small changes observed upon thermal treatment at $50\text{ }^\circ\text{C}$ were mostly reversible and thus this condition was chosen for the ALD process.

While the current flow through these electronic junctions varied throughout the ALD process, it remained relatively constant under atmospheric conditions after ALD was complete. These data indicate that the ALD of Al_2O_3 effectively encapsulated these junctions so that they long-term exhibited stability in ambient conditions.

Paper 5: Na, J. S.; Ayres, J. A.; Chandra, K. L.; Gorman, C. B.; Parsons, G. N., 'Nanoencapsulation and Stabilization of Single-Molecule/Particle Electronic Nanoassemblies Using Low Temperature Atomic Layer Deposition', *J. Phys. Chem. C* **2008**, *112*, 20510-20517.⁵

This paper looked more closely at the encapsulation of gold nanoparticle homodimers through the ALD of Al_2O_3 , and attempted to evaluate the factors contributing to the instability of both the coated and uncoated molecular junctions.

Instability in the uncoated molecular junctions could be attributed to changes at either the molecule/nanoparticle interface or the nanoparticle/electrode interface. A control experiment was performed in which an 80 nm citrate-capped nanoparticle was trapped in the lithographic trench. The current increase observed for this case was significantly smaller than that observed for molecularly-linked particle dimers indicating that the nanoparticle/electrode interface played a minimal role in the observed current instability. The current changes observed for the dimeric structures could be attributed to disruption of the gold-sulfur bond, desorption of contaminants (e.g. water) from the air that create additional pathways for electronic conductance or any alteration in the electronic or physical configuration of the linker molecule. While the observed initial decreases in current could be attributed to hydration of the thiolate, it was concluded that the most significant contribution to the instability of these molecular junctions was adsorption of contaminants from air. This conclusion was supported by the observations that current changes for devices exposed to air for only a few days were mostly reversible while longer-term exposure resulted in irreversible changes. Contaminant desorption has previously been reported to become progressively more difficult with extended exposures.

As reported in the previous paper, low-temperature ALD encapsulated and stabilized these molecular electronic junctions so that minimal conductance changes were observed in air for periods greater than 15 days. Several experiments were

performed to confirm the presence of these molecular junctions after ALD. The measured resistance in the coated junctions was comparable to that measured previously measured for uncoated junctions and values reported in the literature for similar molecules. In addition, the conduction mechanisms were similar to those reported for uncoated junctions with a transition to Fowler-Nordheim tunneling observed as field strength is increased followed by breakdown of the junction.

While the ALD of Al_2O_3 appeared to increase the long-term stability of these molecular junctions, samples measured immediately after the coating process showed conductivity values larger than the those observed for the uncoated samples. ALD was performed at temperatures ranging between 30 and 100 °C, and the magnitude of these conductance changes increased with the processing temperature. For dimer samples coated at 30 and 50 °C, the current slowly reverted to pre-coating values over a period of 1-2 days and then remained relatively stable for long periods (i.e. up to 19 days). For dimer samples coated at 70 and 100 C, the current increased by a factor of 10-100 and remained high. Samples coated at even higher temperatures, 200-230 °C, exhibited behavior consistent with degradation of the molecular electronic junctions. The initial increase and subsequent decrease in current observed after low-temperature ALD could be attributed to exposure to air and water during the coating process. Again, a control experiment was performed with an 80 nm gold particle and indicated improved nanoparticle/electrode contact

after ALD treatment, indicating that any inconsistencies were due to changes within the molecular junction.

Unpublished manuscript: Na, J. S.; Ayres, J.; Chandra, K. L.; Gorman, C. B.; Parsons, G. N.; 'Toward Three Terminal Molecular Devices using Nanoparticle/Y-type Molecule/Nanoparticle Trimeric Structures' North Carolina State University, 2008.⁶

In this work, nanoparticle trimers consisting of three 15 nm citrate-capped gold particles were dielectrophoretically assembled into a lithographic trench in a manner similar to that previously described for nanoparticle dimers. As discussed in Chapter 1, the third terminal was desirable in order to obtain switching behavior for the future development of a molecular-scale transistor. The SiO₂ layer coating the bottom of the trench was subject to reactive ion etching so that the one of the particles in the trimer was in close proximity to the underlying doped silicon substrate. While there was observed current modulation with gate bias in some experiments, the overall success rate was low. This was attributed to the device geometry with small variations in particle size and trimer orientation reducing electronic coupling. Additional experiments need to be done to confirm the presence of the molecule in these electronic junctions, increase reproducibility and understand the gating mechanism before this work can be published.

While there are still several aspects of this work that need to be further explored, these data demonstrate the possible applicability of these types of structures to three-terminal electronic devices, which was the overall motivation of this project.

1.1.References

- (1) Ayres, J.; Walker, B.; Chandra, K. L.; Stefanescu, D.; Chu, C.; Parsons, G.; Gorman, C., *Proc. of SPIE* **2005**, 6003, 60030J.
- (2) Chu, C.; Ayres, J. A.; Stefanescu, D. M.; Walker, B. R.; Gorman, C. B.; Parsons, G. N., *J. Phys. Chem. C* **2007**, 111, 8080-8085.
- (3) Na, J. S.; Ayres, J.; Chandra, K. L.; Chu, C.; Gorman, C. B.; Parsons, G. N., *Nanotechnology* **2007**, 18, 035203.
- (4) Na, J. S.; Ayres, J.; Chandra, K. L.; Gorman, C. B.; Parsons, G. N., *Nanotechnology* **2007**, 18, 424001.
- (5) Na, J. S.; Ayres, J. A.; Chandra, K. L.; Gorman, C. B.; Parsons, G. N., *J. Phys. Chem. C* **2008**, 112, 20510-20517.
- (6) Na, J. S.; Ayres, J.; Chandra, K. L.; Gorman, C. B.; Parsons, G. N.; North Carolina State University, 2008.
- (7) Kim, B.; Beebe, J. M.; Jun, Y.; Zhu, X. Y.; Frisbie, C. D., *J. Am. Chem. Soc.* **2006**, 128, 4970-4971.

Appendix 2. Geometric Calculations Involving Nanoparticle Dimers and Trimers

The methods used to calculate the hydrodynamic radii of nanoparticle dimers and trimers are described below in addition to the geometrical constraints associated with the formation of trimers.

A-2.1 Hydrodynamic Radii of Nanoparticle Dimers

Hydrodynamic radii for nanoparticle dimers were calculated two different ways. First, the volume of a dimer was approximated as a rod as shown in Figure A-2-1. This approximation is only valid for dimers where both particles are the same size. The hydrodynamic radius of a rod was calculated according to Equation A-2-1 where x is the length of the rod and r is the radius. These values were determined from the

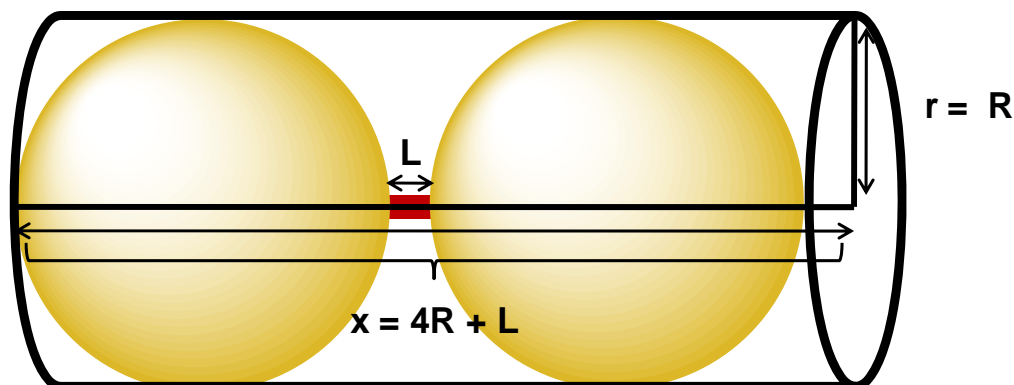


Figure A-2-1. Nanoparticle homodimer approximated as a rod. R is the nanoparticle radius and L is the linker length.

nanoparticle radius, R, and the linker length, L as shown in Figure A-2-1.

$$R_H^3 = \frac{3xr^2}{4} \quad \text{A-2-1}$$

Using linker lengths shown in Figure A-2-2, the hydrodynamic radii of homodimers were calculated for various particle sizes and are listed in Table A-2-1.

The other method used was based on the ‘dumbbell’ model developed by De La Torre et al.¹ to describe the hydrodynamic properties of macromolecules. This method involved calculating the frictional coefficients of two spheres held at a fixed distance by a frictionless spacer, as shown in Figure A-2-1, and can be used to

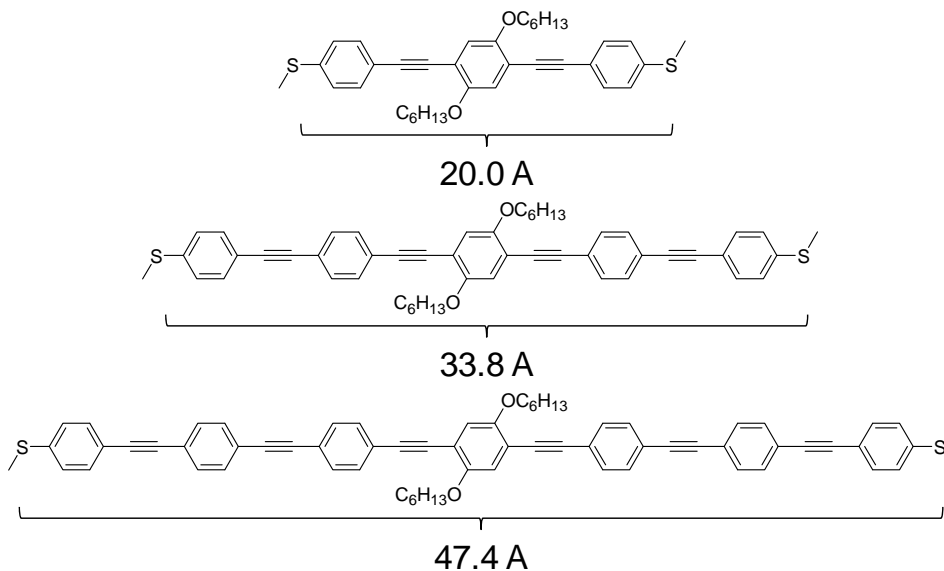


Figure A-2-2. Calculated linker lengths.

Distances were measured between the two terminal sulfur atoms after energy was minimized using the MM2 function in Chem 3D Software. These linker lengths are only approximate as they do not take into account the length of the gold-sulfur bond.

explain the properties of nucleoprotein complexes and globular proteins connected by a thin spacer.

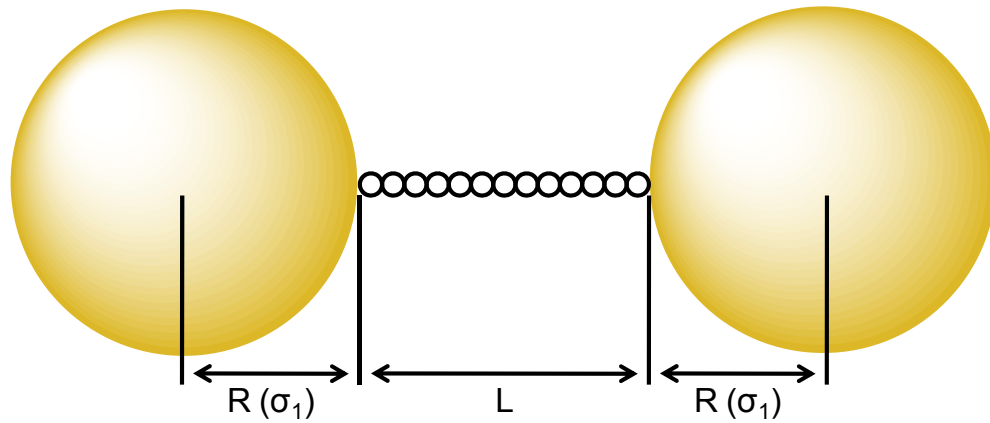


Figure A-2-3. Schematic of 'dumbbell' used to calculate hydrodynamic radii of nanoparticle dimers. Schematic adapted from De La Torre et al.¹

The frictional coefficient is related to the hydrodynamic radius of a structure according to Equation A-2-2. The majority of the calculations were therefore focused on determining the frictional coefficient using Equations A-2-3 through A-2-9. These calculations were performed using Maple software. Hydrodynamic radii were calculated for homodimers using two different linker lengths and are compared to radii calculated using the rod-approximation in Table A-2-1.

$$R_H = \frac{f}{6\pi\eta_0}$$

R_H = hydrodynamic radius
 f = frictional coefficient
 η_0 = solvent viscosity

A-2-2

$$(\Xi)_{\alpha\alpha} = \frac{[\zeta_1 + \zeta_2 - \zeta_1\zeta_2(T_{12})_{\alpha\alpha}]}{1 - \zeta_1\zeta_2(T_{12})_{\alpha\alpha}} \quad \text{A-2-4}$$

α represents one of the Cartesian coordinates, x, y, z
 ζ = translational frictional coefficient
 T = hydrodynamic interaction tensor

$$\zeta_i = 6\pi\eta_0\sigma_i \quad \text{A-2-5}$$

σ_i = radius of the i^{th} sphere

$$T_{ij}^{(d)} = \begin{bmatrix} (T_{ij})_{xx} & 0 & 0 \\ 0 & (T_{ij})_{yy} & 0 \\ 0 & 0 & (T_{ij})_{zz} \end{bmatrix} \quad \text{A-2-6}$$

$$(T_{ij})_{xx} = \frac{1}{(4\pi\eta_0 R_{ij})} \left[1 - \frac{(\sigma_i^2 + \sigma_j^2)}{3R_{ij}^2} \right] \quad \text{A-2-7}$$

$$(T_{ij})_{yy} = (T_{ij})_{zz} = \frac{1}{8\pi\eta_0 R_{ij}} \left[1 + \frac{(\sigma_i^2 + \sigma_j^2)}{3R_{ij}^2} \right] \quad \text{A-2-8}$$

$$R_{ij} = L + 2\sigma_1 \quad \text{A-2-9}$$

The data shown in Table A-2-1 indicate that the rod-approximation yields hydrodynamic radii very similar to those obtained using the more detailed dumbbell model; the values differ by approximately 4-7% for the linker lengths used here. The hydrodynamic radii obtained using the dumbbell model were slightly larger than those obtained using the rod- approximation. This was expected as the dumbbell model

takes into account the additional viscous drag forces between the particles, yielding a larger apparent size (smaller diffusion coefficient in Equation A-2-3). This also explains why the difference between the two values was slightly greater for the longer linker.

Table A-2-1. Hydrodynamic radii calculated for homodimers of various sizes using both the rod-approximation and the dumbbell model.

Particle Diameter (nm)	2.0 nm linker			4.8 nm linker		
	D _H (nm) (rod)	D _H (nm) (dumbbell)	Percent Difference (%)	D _H (nm) (rod)	D _H (nm) (dumbbell)	Percent Difference (%)
5	7.7	8.2	6.1	8.2	8.7	5.7
10	14.9	15.8	5.7	15.5	16.6	6.6
15	22.1	23.3	5.1	22.7	24.2	6.2
20	29.3	30.8	4.9	30.0	31.8	5.7
30	43.7	45.8	4.6	44.4	46.9	5.3
40	58.2	60.7	4.1	58.8	61.9	5.0
50	72.6	75.7	4.1	73.2	76.9	4.8
60	87.0	90.6	4.0	87.7	91.9	4.6

While the model demonstrated by De La Torre et al.¹ was for two equivalent spheres, these calculations were modified to incorporate two spheres of varying sizes. Values for various heterodimers are listed in Table A-2-2. It is noted that as the size difference decreased, the effect of the smaller particle diminished.

Table A-2-2. Hydrodynamic radii calculated for heterodimers of various sizes using the dumbbell model

Particle 1 Diameter (nm)	Particle 2 Diameter (nm)	D _H (nm) (dumbbell)
2	5	6.1
2	10	10.7
2	20	20.5
5	5	8.2
5	10	12.3
5	20	21.5
5	30	31.1
10	10	15.8
10	20	24.1
10	30	33.1
10	40	42.6

Calculations were performed using Maple software and a linker length of 2.0 nm

The code below shows the calculations for a heterodimer consisting of a 5 nm particle ($R = 2.5$ nm), a 10 nm particle ($R = 5$ nm) and a linker length of 2.0 nm.

Calculations were performed using Maple software.

```

- > restart;
- > with(linalg);
Warning, the protected names norm and trace have been redefined and
unprotected

[BlockDiagonal, GramSchmidt, JordanBlock, LUdecomp, QRdecomp, Wronskian, addcol,
  addrow, adj, adjoint, angle, augment, backsub, band, basis, bezout, blockmatrix, charmat,
  charpoly, cholesky, col, coldim, colspace, colspan, companion, concat, cond, copyinto, crossprod,
  curl, definite, delcols, delrows, det, diag, diverge, dotprod, eigenvals, eigenvalues, eigenvectors,
  eigenvects, entermatrix, equal, exponential, extend, ffgausselim, fibonacci, forwardsub, frobenius,
  gausselim, gaussjord, geneqns, genmatrix, grad, hadamard, hermite, hessian, hilbert, htranspose,
  ihermite, indexfunc, innerprod, intbasis, inverse, ismith, issimilar, iszero, jacobian, jordan, kernel,
  laplacian, leastsqrs, linsolve, matadd, matrix, minor, minpoly, mulcol, mulrow, multiply, norm,
  normalize, nullspace, orthog, permanent, pivot, potential, randmatrix, randvector, rank, ratform,
  row, rowdim, rowspace, rowspan, rref, scalarmul, singularvals, smith, stackmatrix, submatrix,
  subvector, sumbasis, swapcol, swaprow, sylvester, toeplitz, trace, transpose, vandermonde,
  vecpotent, vectdim, vector, wronskian]
- > with(Student[LinearAlgebra]);
Warning, the assigned name GramSchmidt now has a global binding

Warning, the protected name . has been redefined and unprotected

[&x, .., AddRow, AddRows, Adjoint, ApplyLinearTransformPlot, BackwardSubstitute, BandMatrix,
  Basis, BilinearForm, CharacteristicMatrix, CharacteristicPolynomial, ColumnDimension,
  ColumnSpace, CompanionMatrix, ConstantMatrix, ConstantVector, CrossProductPlot,
  Determinant, Diagonal, DiagonalMatrix, Dimension, Dimensions, EigenPlot, Eigenvalues,
  EigenvaluesTutor, Eigenvectors, EigenvectorsTutor, Equal, GaussJordanEliminationTutor,
  GaussianElimination, GaussianEliminationTutor, GenerateEquations, GenerateMatrix,
  GramSchmidt, HermitianTranspose, Id, IdentityMatrix, IntersectionBasis, InverseTutor,
  IsDefinite, IsOrthogonal, IsSimilar, IsUnitary, JordanBlockMatrix, JordanForm,
  LUdecomposition, LeastSquares, LeastSquaresPlot, LinearSolve, LinearSolveTutor,
  LinearSystemPlot, LinearTransformPlot, MinimalPolynomial, Minor, MultiplyRow, Norm,
  Normalize, NullSpace, Pivot, PlanePlot, ProjectionPlot, QRdecomposition, RandomMatrix,
  RandomVector, Rank, ReducedRowEchelonForm, ReflectionMatrix, RotationMatrix,
  RowDimension, RowSpace, SetDefault, SetDefaults, SumBasis, SwapRow, SwapRows, Trace,
  Transpose, UnitVector, VectorAngle, VectorSumPlot, ZeroMatrix, ZeroVector]

```

> **Txx:=(4*pi*visc*R)^(-1)*(1-(sig1^2+sig2^2)/(3*R^2));** (components of the hydrodynamic interaction tensor)

$$T_{xx} := \frac{1 - \frac{\text{sig1}^2 + \text{sig2}^2}{3 R^2}}{4 \pi \text{visc} R}$$

> **Tyy:=(8*pi*visc*R)^(-1)*(1+(sig1^2+sig2^2)/(3*R^2));**

$$T_{yy} := \frac{1 + \frac{\text{sig1}^2 + \text{sig2}^2}{3 R^2}}{8 \pi \text{visc} R}$$

> **T:=matrix([[Txx,0,0],[0,Tyy,0],[0,0,Tyy]]);** (hydrodynamic interaction tensor)

$$T := \begin{bmatrix} \frac{1 - \frac{\text{sig1}^2 + \text{sig2}^2}{3 R^2}}{4 \pi \text{visc} R} & 0 & 0 \\ 0 & \frac{1 + \frac{\text{sig1}^2 + \text{sig2}^2}{3 R^2}}{8 \pi \text{visc} R} & 0 \\ 0 & 0 & \frac{1 + \frac{\text{sig1}^2 + \text{sig2}^2}{3 R^2}}{8 \pi \text{visc} R} \end{bmatrix}$$

> **del1:=6*pi*visc*sig1;** (translational frictional coefficient associated with particle 1)

$$\text{del1} := 6 \pi \text{visc} \text{sig1}$$

> **del2:=6*pi*visc*sig2;** (translational frictional coefficient associated with particle 2)

$$\text{del2} := 6 \pi \text{visc} \text{sig2}$$

> **fx1:=(del1+del2-(del1*del2*Txx));** (numerator of friction tens

$$f_{x1} := 6 \pi \text{visc} \text{sig1} + 6 \pi \text{visc} \text{sig2} - \frac{9 \pi \text{visc} \text{sig1} \text{sig2} \left(1 - \frac{\text{sig1}^2 + \text{sig2}^2}{3 R^2} \right)}{R}$$

> **fyy1:=(del1+del2-(del1*del2*Tyy));**

$$f_{yy1} := 6 \pi \text{visc} \text{sig1} + 6 \pi \text{visc} \text{sig2} - \frac{9 \pi \text{visc} \text{sig1} \text{sig2} \left(1 + \frac{\text{sig1}^2 + \text{sig2}^2}{3 R^2} \right)}{2 R}$$

> **T1:=matrix([[fxx1,0,0],[0,fyy1,0],[0,0,fyy1]]);**

$$T1 := \begin{bmatrix} 6 \pi \text{ visc sig1} + 6 \pi \text{ visc sig2} - \frac{9 \pi \text{ visc sig1 sig2} \left(1 - \frac{\text{sig1}^2 + \text{sig2}^2}{3 R^2}\right)}{R}, 0, 0 \\ 0, 6 \pi \text{ visc sig1} + 6 \pi \text{ visc sig2} - \frac{9 \pi \text{ visc sig1 sig2} \left(1 + \frac{\text{sig1}^2 + \text{sig2}^2}{3 R^2}\right)}{2 R}, 0 \\ 0, 0, 6 \pi \text{ visc sig1} + 6 \pi \text{ visc sig2} - \frac{9 \pi \text{ visc sig1 sig2} \left(1 + \frac{\text{sig1}^2 + \text{sig2}^2}{3 R^2}\right)}{2 R} \end{bmatrix}$$

> **fxx2:=(1-(del1*del2*Txx)); (denominator of friction tensor)**

$$fxx2 := 1 - \frac{9 \pi \text{ visc sig1 sig2} \left(1 - \frac{\text{sig1}^2 + \text{sig2}^2}{3 R^2}\right)}{R}$$

> **fyy2:=(1-(del1*del2*Tyy));**

$$fyy2 := 1 - \frac{9 \pi \text{ visc sig1 sig2} \left(1 + \frac{\text{sig1}^2 + \text{sig2}^2}{3 R^2}\right)}{2 R}$$

> **T2:=matrix([[fxx2,0,0],[0,fyy2,0],[0,0,fyy2]]);**

$$T2 := \begin{bmatrix} 1 - \frac{9 \pi \text{ visc sig1 sig2} \left(1 - \frac{\text{sig1}^2 + \text{sig2}^2}{3 R^2}\right)}{R}, 0, 0 \\ 0, 1 - \frac{9 \pi \text{ visc sig1 sig2} \left(1 + \frac{\text{sig1}^2 + \text{sig2}^2}{3 R^2}\right)}{2 R}, 0 \\ 0, 0, 1 - \frac{9 \pi \text{ visc sig1 sig2} \left(1 + \frac{\text{sig1}^2 + \text{sig2}^2}{3 R^2}\right)}{2 R} \end{bmatrix}$$

> **interaction:=evalm(T1/T2);** (friction tensor is the numerator over the denominator)

interaction :=

$$\begin{bmatrix} \frac{9 \pi \text{ visc sig1 sig2} \left(1 - \frac{\text{sig1}^2 + \text{sig2}^2}{3 R^2} \right)}{6 \pi \text{ visc sig1} + 6 \pi \text{ visc sig2} - \frac{R^3 - 9 \pi \text{ visc sig1 sig2} R^2 + 3 \pi \text{ visc sig1}^3 \text{ sig2} + 3 \pi \text{ visc sig1 sig2}^3}{R}} R^3, & 0, & 0 \\ 0, & - \frac{2 \left(6 \pi \text{ visc sig1} + 6 \pi \text{ visc sig2} - \frac{9 \pi \text{ visc sig1 sig2} \left(1 + \frac{\text{sig1}^2 + \text{sig2}^2}{3 R^2} \right)}{2 R} \right) R^3}{-2 R^3 + 9 \pi \text{ visc sig1 sig2} R^2 + 3 \pi \text{ visc sig1}^3 \text{ sig2} + 3 \pi \text{ visc sig1 sig2}^3}, & 0 \\ 0, & 0, & - \frac{2 \left(6 \pi \text{ visc sig1} + 6 \pi \text{ visc sig2} - \frac{9 \pi \text{ visc sig1 sig2} \left(1 + \frac{\text{sig1}^2 + \text{sig2}^2}{3 R^2} \right)}{2 R} \right) R^3}{-2 R^3 + 9 \pi \text{ visc sig1 sig2} R^2 + 3 \pi \text{ visc sig1}^3 \text{ sig2} + 3 \pi \text{ visc sig1 sig2}^3} \end{bmatrix}$$

> **invinter:=inverse(interaction);** (friction coefficient calculated from the trace of the inverse of the hydrodynamic interaction parameter)

$$\text{invinter} := \begin{bmatrix} \frac{R^3 - 9 \pi \text{ visc sig1 sig2} R^2 + 3 \pi \text{ visc sig1}^3 \text{ sig2} + 3 \pi \text{ visc sig1 sig2}^3}{3 \text{ visc } \pi (2 \text{ sig1} R^3 + 2 \text{ sig2} R^3 - 3 \text{ sig1 sig2} R^2 + \text{sig1}^3 \text{ sig2} + \text{sig1 sig2}^3)}, & 0, & 0 \\ 0, & \frac{-2 R^3 + 9 \pi \text{ visc sig1 sig2} R^2 + 3 \pi \text{ visc sig1}^3 \text{ sig2} + 3 \pi \text{ visc sig1 sig2}^3}{3 \text{ visc } \pi (-4 \text{ sig1} R^3 - 4 \text{ sig2} R^3 + 3 \text{ sig1 sig2} R^2 + \text{sig1}^3 \text{ sig2} + \text{sig1 sig2}^3)}, & 0 \\ 0, & 0, & \frac{-2 R^3 + 9 \pi \text{ visc sig1 sig2} R^2 + 3 \pi \text{ visc sig1}^3 \text{ sig2} + 3 \pi \text{ visc sig1 sig2}^3}{3 \text{ visc } \pi (-4 \text{ sig1} R^3 - 4 \text{ sig2} R^3 + 3 \text{ sig1 sig2} R^2 + \text{sig1}^3 \text{ sig2} + \text{sig1 sig2}^3)} \end{bmatrix}$$

> **Tr:=trace(invinter);** (trace of the inverse)

$$\text{Tr} := \frac{R^3 - 9 \pi \text{ visc sig1 sig2} R^2 + 3 \pi \text{ visc sig1}^3 \text{ sig2} + 3 \pi \text{ visc sig1 sig2}^3}{3 \text{ visc } \pi (2 \text{ sig1} R^3 + 2 \text{ sig2} R^3 - 3 \text{ sig1 sig2} R^2 + \text{sig1}^3 \text{ sig2} + \text{sig1 sig2}^3)} + \frac{2 (-2 R^3 + 9 \pi \text{ visc sig1 sig2} R^2 + 3 \pi \text{ visc sig1}^3 \text{ sig2} + 3 \pi \text{ visc sig1 sig2}^3)}{3 \text{ visc } \pi (-4 \text{ sig1} R^3 - 4 \text{ sig2} R^3 + 3 \text{ sig1 sig2} R^2 + \text{sig1}^3 \text{ sig2} + \text{sig1 sig2}^3)}$$

```

> f:=(3/Tr); (frictional coefficient)
f:=3 / 
$$\left( \frac{R^3 - 9 \pi \text{ visc } \text{sig1 } \text{sig2 } R^2 + 3 \pi \text{ visc } \text{sig1}^3 \text{ sig2} + 3 \pi \text{ visc } \text{sig1 } \text{sig2}^3}{3 \text{ visc } \pi (2 \text{ sig1 } R^3 + 2 \text{ sig2 } R^3 - 3 \text{ sig1 } \text{sig2 } R^2 + \text{sig1}^3 \text{ sig2} + \text{sig1 } \text{sig2}^3)} \right. \\ \left. + \frac{2(-2 R^3 + 9 \pi \text{ visc } \text{sig1 } \text{sig2 } R^2 + 3 \pi \text{ visc } \text{sig1}^3 \text{ sig2} + 3 \pi \text{ visc } \text{sig1 } \text{sig2}^3)}{3 \text{ visc } \pi (-4 \text{ sig1 } R^3 - 4 \text{ sig2 } R^3 + 3 \text{ sig1 } \text{sig2 } R^2 + \text{sig1}^3 \text{ sig2} + \text{sig1 } \text{sig2}^3)} \right)$$

> RH:=f/(6*pi*visc); (hydrodynamic radius calculated from frictional coefficient)
RH:=1 / 
$$\left( 2 \left( \frac{R^3 - 9 \pi \text{ visc } \text{sig1 } \text{sig2 } R^2 + 3 \pi \text{ visc } \text{sig1}^3 \text{ sig2} + 3 \pi \text{ visc } \text{sig1 } \text{sig2}^3}{3 \text{ visc } \pi (2 \text{ sig1 } R^3 + 2 \text{ sig2 } R^3 - 3 \text{ sig1 } \text{sig2 } R^2 + \text{sig1}^3 \text{ sig2} + \text{sig1 } \text{sig2}^3)} \right. \right. \\ \left. \left. + \frac{2(-2 R^3 + 9 \pi \text{ visc } \text{sig1 } \text{sig2 } R^2 + 3 \pi \text{ visc } \text{sig1}^3 \text{ sig2} + 3 \pi \text{ visc } \text{sig1 } \text{sig2}^3)}{3 \text{ visc } \pi (-4 \text{ sig1 } R^3 - 4 \text{ sig2 } R^3 + 3 \text{ sig1 } \text{sig2 } R^2 + \text{sig1}^3 \text{ sig2} + \text{sig1 } \text{sig2}^3)} \right) \pi \text{ visc} \right)$$

> pi:=evalf(Pi);
pi := 3.141592654
> visc:=1.002*10^(-21); units=N*s/nm^2; (viscosity of water at room temperature)
visc := 0.1002000000 10-20
units =  $\frac{Ns}{nm^2}$ 
> L:=2.0; (linker length)
L := 2.0
> sig1:=2.5; (radius of particle 1)
sig1 := 2.5
> sig2:=5; (radius of particle 2)
sig2 := 5
> R:=sig1+sig2+L;
R := 9.5
> evalf(RH);
6.168715985
> DH:=2*RH;
DH := 12.33743197

```

A-2.2 Hydrodynamic Radii of Nanoparticle Trimers

As there was no hydrodynamic model for a trimer geometry in the literature and the rod approximation was shown to be a reasonable estimate of the hydrodynamic radius of nanoparticle dimers, this approach was extended to evaluate the hydrodynamic radii of nanoparticle trimers. However, comparing the geometry of the structure shown in Figure A-2-3 and the rod in Figure A-2-1, it can be seen that the ratio between the radius and length of each structure differ significantly. The trimer structure does not really emulate a rod, but more of a short, wide cylinder. The equation for the hydrodynamic radius of a rod (A-2-1) was derived based on the

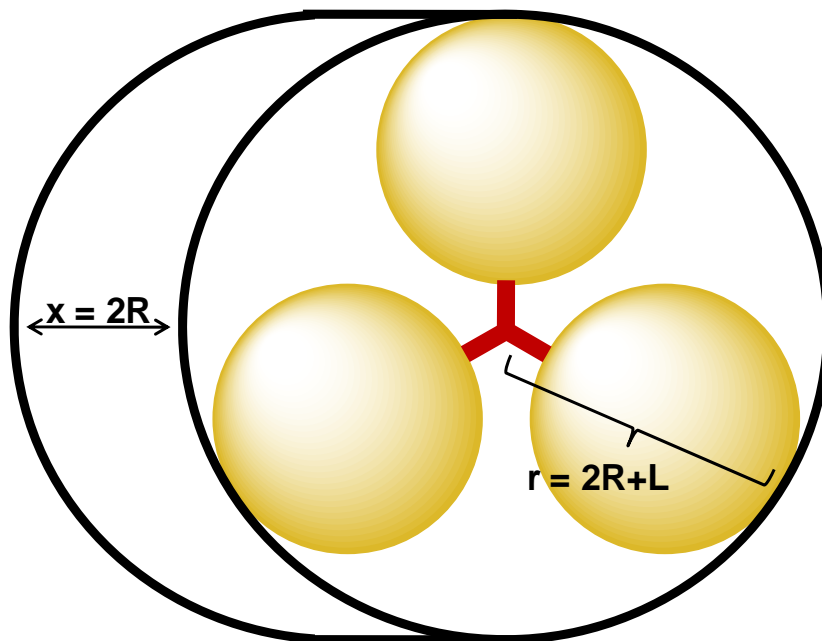


Figure A-2-3. Nanoparticle trimer approximated as a cylinder. R is the nanoparticle radius and L is the linker length

assumption that there is minimal transport in the lateral direction. The radius of the rod, r , has more of an effect on its apparent size than its length, l . This behavior is not necessarily the case for the shorter cylinder shown in Figure A-2-3. It has been documented that the axial ratio (Equation A-2-10) affects the hydrodynamic radius²⁻⁴ and lends another degree of uncertainty to the values obtained for nanoparticle trimers using the rod approximation. Previously developed models are especially inadequate when this ratio is small, which is the case for nanoparticle trimers.⁴

$$p = \frac{x}{2R}$$

p = axial ratio
 x = length of cylinder
 R = radius of cylinder

A-2-10

De La Torre et al.^{2,4} discuss a method that is valid for $2 \leq p \leq 30$. As the lengths of the cylinders used to approximate trimers are less than the corresponding radii, $p < 0.5$ for the cases described here. It is unclear to what extent the hydrodynamic behavior will differ at these smaller ratios. However, De La Torre's calculations were applied to this system.

Both the translational and rotational diffusion coefficients can be calculated based on the axial ratio according to Equations A-2-11 and A-2-12.^{2,4} The terms v and δ are referred to as end-effect corrections, are functions of p and converge to asymptotic values as $p \rightarrow \infty$.² These polynomial expressions were determined from a fit to numerical data. It was assumed that the rotational diffusion coefficient has a

negligible effect of the hydrodynamic radius, which was calculated from the translational diffusion coefficient using equations A-2-2 and A-2-3. A list of trimer hydrodynamic radii calculated using both De La Torre's method and the rod approximation (Equation A-2-1) are listed in Table A-2-3 for various particle sizes and linker lengths. The linker lengths for various trimer structures are shown in Figure A-2-5.

$$\frac{3\pi\eta_0LD_t}{kT} = \ln p + v \quad \text{A-2-11}$$

D_t = translational diffusion coefficient
 v = constant based on axial ratio

$$\frac{\pi\eta_0L^3D_r}{3kT} = \ln p + \delta \quad \text{A-2-12}$$

D_t = translational diffusion coefficient
 δ = constant based on axial ratio

$$v = 0.312 + 0.565p^{-1} - 0.100p^{-2} \quad \text{A-2-13}$$

$$\delta = -0.662 + 0.917p^{-1} - 0.050p^{-2} \quad \text{A-2-14}$$

Table A-2-3. Hydrodynamic radii calculated for homotrimers composed of nanoparticles of various sizes using both the rod-approximation and the cylindrical model based on the axial ratio.

Particle Diameter (nm)	Linker with 1.7 nm arms (7 total rings)				Linker with 2.4 nm arms (10 total rings)			
	D_H (nm) (rod)	p	D_H (nm) (cylinder)	Percent Difference (%)	D_H (nm) (rod)	p	D_H (nm) (cylinder)	Percent Difference (%)
5	11.0	0.37	40.9	73	11.8	0.38	49.0**	76
10	20.2	0.43	42.3	52	21.0	0.40	52.7	60
15	29.3	0.45	54.8	47	30.1	0.43	61.7	51
20	38.4	0.46	68.4	44	39.2	0.45	74.2	47

** This value was calculated slightly differently; see detail below

The hydrodynamic radius calculated for the 5 nm trimer with the longer linker was calculated slightly differently than the other values. Figure A-2-4 shows the calculated translational diffusion coefficient as a function of cylinder radius for a constant cylindrical length of 5 nm. The diffusion coefficient decreases with increasing radius, and as it approaches zero the calculated hydrodynamic radius approaches an asymptote at approximately $r = 7.6$ nm. The radius of a trimer

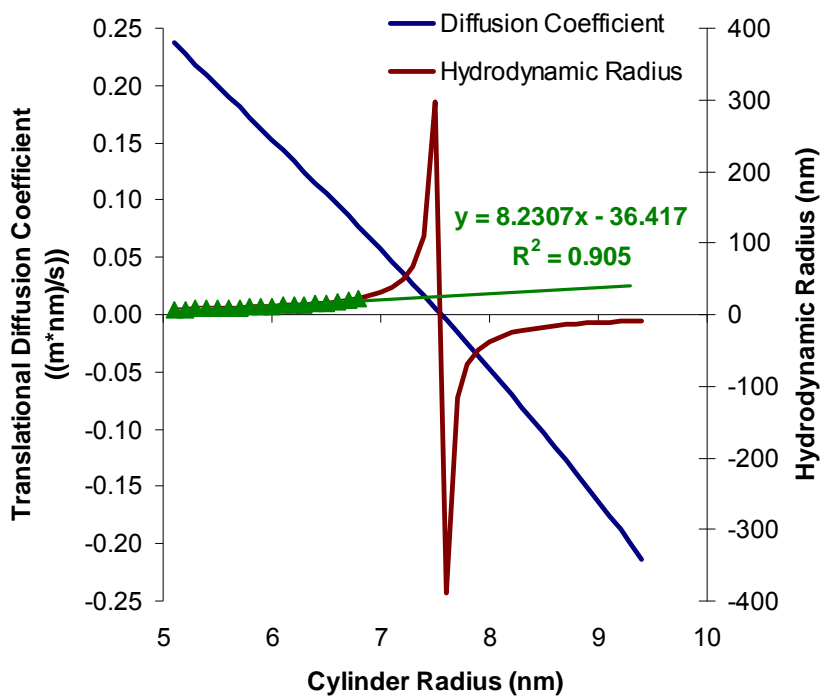


Figure A-2-4 Translational diffusion coefficient and hydrodynamic radius as a function of cylindrical radius for a cylinder with a constant length of 5nm. The green curve is a linear extrapolation used to approximate the behavior of cylinders with large radii. The diffusion coefficient is not in conventional units; however, they cancel out in the hydrodynamic radius calculation.

consisting of 5 nm particles and a 2.4 nm linker is 7.4 nm. The equations derived by De La Torre et al. therefore yielded extremely high values for the hydrodynamic radius of this structure. A linear extrapolation (green) was used

to approximate the hydrodynamic radius for the 5 nm trimer. Again, as De La Torre claimed that his method was only applicable for axial ratios in the range, $2 \leq p \leq 30$,^{2,4} the accuracy of these calculations is unknown.

Table A-2-3 shows that the values calculated using the two different methods vary significantly, especially for smaller particles (44-76%). The hydrodynamic radius of a rod assumes high aspect ratios and negligible lateral motion so is not entirely accurate in this case. While the methods proposed by De La Torre et al.^{2,4} are likely more accurate as they take into account the cylindrical axial ratio, the authors do not claim these are applicable for aspect ratios, $p < 2$.

The code below calculates the hydrodynamic radius of a nanoparticle trimer consisting of 10nm particles and a linker with an arm length of 1.7 nm. Calculations were performed using Maple software.

```

[ > restart;
[ > v:=0.312+0.565*p^(-1)-0.100*p^(-2);  function determined from
numerical results

$$v := 0.312 + \frac{0.565}{p} - \frac{0.100}{p^2}$$

[ >
[ > Dt:=(ln(p)+v)*k*T)/(3*pi*visc*x);  translational diffusion
coefficient

$$Dt := \frac{1}{3} \frac{\left( \ln(p) + 0.312 + \frac{0.565}{p} - \frac{0.100}{p^2} \right) k T}{\pi \text{ visc } x}$$

[ > pi:=evalf(Pi);

$$\pi := 3.141592654$$

[ > visc:=1.002*10^(-21);

$$\text{visc} := 0.1002000000 \cdot 10^{-20}$$

[ > k:=11.38*10^(-23);

$$k := 0.1138000000 \cdot 10^{-21}$$

[ > T:=293;

$$T := 293$$

[ > RH:=(k*T)/(6*pi*visc*Dt);  hydrodynamic radius

$$RH := \frac{0.5000000000 \cdot x}{\ln(p) + 0.312 + \frac{0.565}{p} - \frac{0.100}{p^2}}$$

[ > r:=11.7;

$$r := 11.7$$

[ > x:=10;

$$x := 10$$

[ > p:=x/(2*r);

$$p := 0.4273504274$$

[ > evalf(RH);

$$21.15157009$$


```

A-2.3 Geometry of Nanoparticle Trimers

Calculations were also performed for nanoparticle trimers. For a given linker length, there is a maximum particle size that is geometrically feasible for trimer formation. The method for calculating these values is shown in Figure A-2-5 and values for several different linker lengths are listed in Table A-2-4.

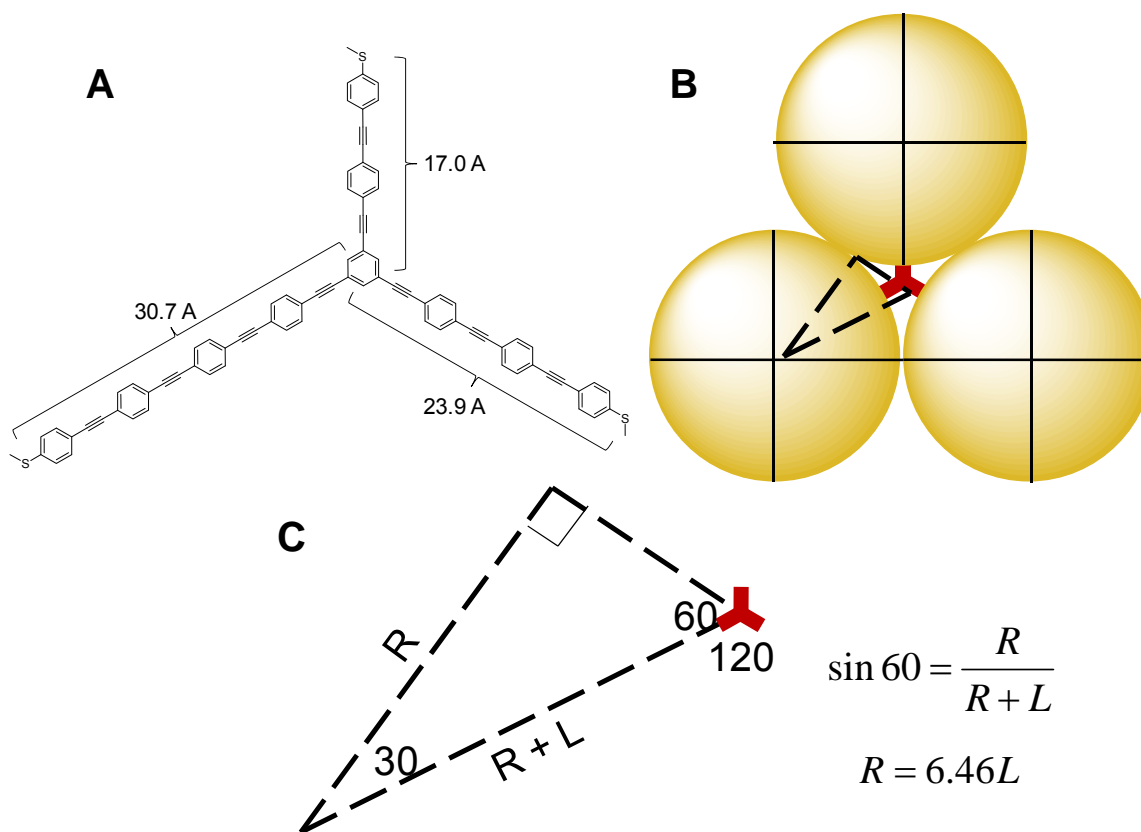


Figure A-2-5. (A) Schematic of three-armed linker molecule with different linker lengths (B) trimer geometry (C) high magnification schematic of trimer geometry showing how maximum particle size was calculated**

** Distances were measured between the two terminal sulfur atoms after energy was minimized using the MM2 function in Chem 3D Software. These linker lengths are only approximate as they do not take into account the length of the gold-sulfur bond

Table A-2-4. Maximum particle sizes feasible for nanoparticle trimers with different linker lengths

# rings in molecule	L (nm) (linker)	R (nm) (particle)	D (nm) (particle)
7	1.70	11.0	22.0
10	2.39	15.4	30.9
13	3.07	19.8	39.7

The values listed in Table A-2-4 indicate the size at which the particle cores will be touching each other in a nanoparticle trimer. However, for electronic applications, the particles should not touch. These structures were designed so that current traverses the molecular linker and does not travel between particles. These calculations also did not take the capping ligand into account. It is also undesirable for current to tunnel through the capping ligand so an accurate picture of the gap between particles in a nanoparticle trimer is required.

The gold particles used in this study were capped with citrate anions. While the nature of the gold-citrate interaction is unknown, the thickness of the citrate layer on gold was approximated as 0.4 nm using Chem Draw 3D software. However, this value could feasibly be anywhere between 0.3 and 0.6 nm depending upon the orientation of the molecule. Figure A-2-6 shows how the gap distance was calculated, and calculated values are listed in Table A-2-5. While the gap distances increases somewhat with linker length, there is really no appreciable gap for trimers comprised of particles greater than 15 nm.

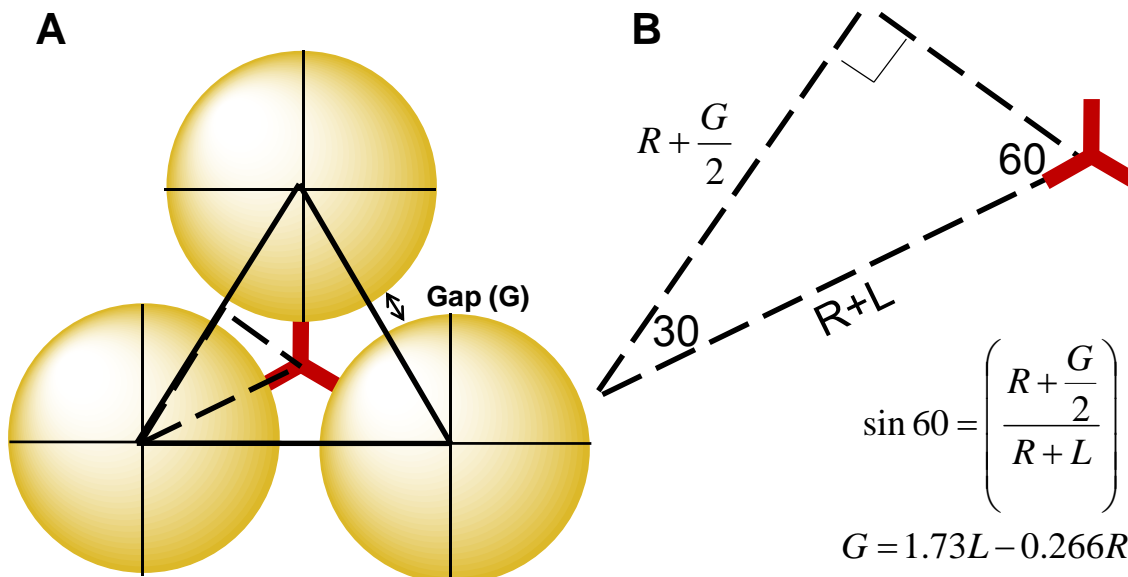


Figure A-2-6 (A) Trimer geometry showing gap between particles (B) High-magnification schematic showing how the gap between the particles was calculated

Table A-2-5. Values calculated for the gap between particles both with and without consideration for the citrate capping layer**

Diam.	Rad.	G (L=1.70)		G (L=2.39)		G (L=3.07)**	
		no cit	cit	no cit	cit	no cit	cit
5	2.5	2.3	1.5	3.5	2.7	4.6	3.8
10	5	1.6	0.8	2.8	2.0	4.0	3.2
15	7.5	0.9	0.1	2.1	1.3	3.3	2.5
20	10	0.3	NA	1.5	0.7	2.7	1.9
30	15	NA	NA	0.1	NA	1.3	0.5

** thickness of citrate capping layer approximated to be 0.4nm using Chem Draw 3D after MM2 Energy Minimization. The distance between two of the carbonyl carbons was measured. NA indicates that there was no gap (a negative value)

A-2.4 References

- (1) Garciadelatorre, J.; Bloomfield, V. A., *Biopolymers* **1977**, *16*, 1747-1763.
- (2) Tirado, M. M.; Martinez, C. L.; Delatorre, J. G., *J. Chem. Phys.* **1984**, *81*, 2047-2052.
- (3) Tirado, M. M.; Garciadelatorre, J., *J. Chem. Phys.* **1979**, *71*, 2581-2587.
- (4) Delatorre, J. G.; Martinez, M. C. L.; Tirado, M. M., *Biopolymers* **1984**, *23*, 611-615.